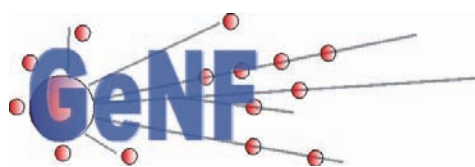


## GeNF – Experimental Report 2007



**Geesthacht Neutron Facility**



**Editors:**

*P. K. Pranzas*

*A. Schreyer*

*R. Willumeit*



**GeNF – Experimental Report 2007**

**Editors:**

***P. K. Pranzas***

***A. Schreyer***

***R. Willumeit***

**(Institute of Materials Research)**

Die Berichte der GKSS werden kostenlos abgegeben.  
The delivery of the GKSS reports is free of charge.

*Anforderungen/Requests:*

GKSS-Forschungszentrum Geesthacht GmbH  
Bibliothek/Library  
Postfach 11 60  
21494 Geesthacht  
Germany  
Fax.: +49 4152 87-17 17

Als Manuskript vervielfältigt.  
Für diesen Bericht behalten wir uns alle Rechte vor.

ISSN 0344-9629

GKSS-Forschungszentrum Geesthacht GmbH · Telefon (04152) 87-0  
Max-Planck-Straße 1 · 21502 Geesthacht / Postfach 11 60 · 21494 Geesthacht



GKSS 2008/6

## GeNF – Experimental Report 2007

Philipp Klaus Pranzas, Andreas Schreyer, Regine Willumeit (Editors)

*387 pages*

### Abstract

At the Geesthacht Neutron Facility GeNF about 203 experiments were performed in 2007 by GKSS and by or for external users, partners or contractors. In most cases the measurements were performed and analysed in cooperation by the guests and by the GKSS staff or by the permanent external user group staff. The activities, which are based on a proposal procedure and on the in house R&D program, are reported in 70 contributions in the present annual experimental report for the year 2007. The contributions may contain one or also several combined experiments.

During 2007 the GKSS research reactor FRG-1 achieved an operation time of 204 days at the full 5 MW reactor power providing a neutron flux of ca.  $1.4 \cdot 10^{14}$  thermal neutrons/cm<sup>2</sup> s. In May/June 2007 the FRG-1 was upgraded with a new cold neutron source yielding a flux increase at the five instruments using cold neutrons of up to 40 %.

The focus of the in house R&D work at GeNF instruments in 2007 was the characterisation of nano-structures in engineering materials, the analysis of stresses and textures in welds and technical structures at SANS-2, DCD, ARES-2 and TEX-2, the structural investigation of hydrogen containing substances such as polymers, colloids and biological macromolecules at SANS-1 as well as the characterisation of magnetic thin films at NeRo, PNR, POLDI and RÖDI. The modern experiment control hardware and software based on LabView was continuously improved on all instruments.

In the appendices I and II the experimental reports of the GKSS outstation at the FRM II are attached as well as of the GKSS outstation at DESY. At the neutron reflectometer REFSANS at FRM II measurements are possible using a broad range of the scattering vector with reflectivities up to  $10^{-7}$ . Three reports show the activities of GKSS in the field of texture measurement at the instrument STRESS-SPEC. The instrument HARWI II at DESY is accepted very well by the community and is overbooked in all fields (tomography, diffraction, etc.) by a factor of 3. The engagement of GKSS at the new PETRA III storage ring at DESY is demonstrated in the reports about the High Energy Materials Science (HEMS) beamline and the Imaging beamline at PETRA III.

## Jahresbericht 2007 über die Experimente an GeNF

### Zusammenfassung

An der Geesthachter Neutronenforschungseinrichtung GeNF wurden von GKSS und von oder für externe Nutzer, Partner oder Auftraggeber etwa 203 Experimente in 2007 durchgeführt. In den meisten Fällen wurden die Messungen gemeinschaftlich von den Gastwissenschaftlern

und GKSS-Personal vorgenommen und ausgewertet. Die Experimente, die in der Regel über das Antragsverfahren und über das GKSS-eigene F&E-Programm abgewickelt wurden, werden in diesem Jahresbericht in Form von 70 Experimentierberichten dargestellt. Dabei können die Berichte einzelne Experimente oder auch mehrere zusammengefasst beschreiben.

Während 2007 erreichte der Forschungsreaktor FRG-1 204 Volllasttage bei 5 MW und bei einem Fluss von  $1,4 \cdot 10^{14}$  thermischen Neutronen je  $\text{cm}^2$  und s. Um die Attraktivität der Quelle für die Restlaufzeit sicherzustellen, wurde durch eine Änderung der Form des Moderatortopfes der KNQ der kalte Neutronenfluss erhöht. Hierzu wurde ein Reserve-Moderatortopf entsprechend modifiziert und im Mai 2007 gegen den bisher benutzten Moderatortopf ausgetauscht. Im Juni 2007 konnte das Wiederanfahrprogramm des Reaktors mit dem Erreichen der vollen Reaktorleistung abgeschlossen werden. An den Instrumenten konnte eine Erhöhung des kalten Neutronenflusses von bis zu 40 % nachgewiesen werden.

Der Schwerpunkt der GKSS-eigenen Forschungsarbeiten lag in 2007 im Bereich der Charakterisierung von Nanostrukturen in Werkstoffen, der Analyse von Eigenspannungen und Texturen in Schweißverbindungen und technischen Strukturen an SANS-2, DCD, ARES-2 und TEX-2, im Bereich der Strukturanalyse von wasserstoffhaltigen Substanzen wie Polymere, Kolloide und Biomolekülen an SANS-1 sowie im Bereich der Charakterisierung magnetischer Schichtstrukturen an NeRo, PNR, POLDI und RÖDI. An den Instrumenten werden ständig neue Probenumgebungen (Magnete, Kryostate, Öfen, usw.) entwickelt und eingesetzt sowie die auf Labview basierende moderne und nutzerfreundliche Steuersoftware angepasst und verbessert.

In Anhängen werden die Experimentberichte des Neutronenreflektometers REFSANS an der GKSS- Außenstelle am FRM II sowie der Beamline HARWI II am Synchrotronring DORIS III an der GKSS-Außenstelle bei DESY aufgelistet. Am Instrument REFSANS wurde gezeigt, dass hochaufgelöste Messungen über einen weiten Bereich des Streuvektors mit Reflektivitäten von bis zu  $10^{-7}$  möglich sind mit einem großen Potential für weitere Verbesserungen. Drei Berichte zeigen die Aktivitäten von GKSS im Bereich der Texturmessung am Instrument STRESS-SPEC. HARWI II ist bei der Nutzergemeinde sehr begehrt und ist inzwischen in allen Bereichen (Tomographie, Diffraktion, etc.) dreifach überbucht. Das Engagement von GKSS am neuen PETRA III Speicherring am DESY ist in den Berichten über die High Energy Materials Science (HEMS) Beamline und die Imaging beamline an PETRA III dargestellt.

## CONTENTS

### Preface

- GeNF Operation
- Operation of FRG-1
- GeNF Instruments (overview)

<b>SANS-1</b>	<b>19</b>
<i>M. Almgren, M.-J. Stébé</i> Contrast variation SANS studies of micelles in mixed perfluorinated and normal non-ionic surfactants	21
<i>M. Almgren</i> Contrast variation SANS studies of micelles in mixed perfluorinated and hydrogenated surfactants	25
<i>M. V. Avdeev, A. V. Feoktystov</i> SANS contrast variation in ferrofluids as polydisperse multicomponent superparamagnetic systems	27
<i>L. Vekas, D. Bica, M. V. Avdeev</i> SANS analysis of ferrofluids produced by laser pyrolysis	29
<i>M. Balasoiu, M. L. Craus, A. M. Moisin, V. Tripadus</i> Effect of Ce and Gd doping on the microstructure properties of PT ceramics investigated by SANS	31
<i>S. Filippov, P. Štěpánek</i> Conformation of hydrophilic polymers hydrophobically modified by sterically-hindered Phenols	35
<i>S. V. Grigoriev, V. K. Ivanov, G. P. Kopitsa</i> The study of evolution of fractal properties of amorphous Zr, Zn, Ti and Ce-based xerogels by SANS	39
<i>J. Preu, T. Gutberlet, T. Heimburg</i> Interaction of Angiotension II with lipid membranes	43
<i>L. He, A. Middelberg, H. Wang</i> Small angle neutron scattering study of galectin-PEG conjugates	45
<i>G. Bryant, C. Garvey, B. Kent</i> Determination of microphase sugar concentrations in model biological membrane systems by SANS	47
<i>M. Knaapila, A. Monkman</i> A SANS study of polyfluorene phase behaviour in solution	51
<i>C. Meesters, A. Brack, H. Hartmann, H. Decker</i> SANS on the pre-pore state of the $\alpha$ -Toxin <i>Staphylococcus aureus</i>	53
<i>K. Oehlke, K. Schwarz</i> Determination of the partitioning of emulsifiers in emulsion in dependence of their concentrations	55

<i>J. Preu, T. Gutberlet, T. Heimbürg</i> Network formation in lipid membranes	57
<i>S. Rangelov, S. Halacheva</i> The Effect of PPO Block Size on the Self-Assembly of Polyglycidol-Based Analogues to Pluronics	59
<i>M. Tokita, H. Miki, S. Mukai</i> Structure of Opaque Poly(acrylamide) Gels Revealed by SANS and CLSM	61
<b>SANS-2</b>	<b>65</b>
<i>L. Dahbi, W. Pyckhout-Hintzen</i> Hierarchy of hyperbranched polymer by SANS	67
<i>G. Cheng, Y. Melnichenko, K. Hong, H. Fengjun</i> Conformation of comb-like thermosensitive polymers	71
<i>A. Michels, R. Birringer, P. K. Pranzas</i> Magnetic microstructure of nanocrystalline gadolinium	73
<i>A. Ulbricht, F. Bergner</i> Nature of defects formed in neutron-irradiated Fe-Cr model alloys	77
<i>E. Eidenberger, P. Staron</i> SANS experiments with unpolarized neutrons to study precipitation of intermetallic phase in a Fe-Co-Mo alloy	79
<i>E. Eidenberger, S. Mayer, P. Staron</i> SANS experiments with unpolarized neutrons to study precipitations in hot-work tool steels	81
<i>P. Staron, W. V. Vaidya</i> Precipitates in a laser beam welded butt-joint of aluminium sheets	85
<i>D. Schwahn, V. Pipich</i> Formation of large scale structures in a binary polymer blend with components of asymmetric mobility	87
<i>A. Michels, M. Elmas, F. Döbrich, J. Kohlbrecher, R. Birringer</i> Dipole-Field-Induced Spin Disorder In Nanoporous Inert-Gas Condensed Materials	93
<i>H. Eckerlebe</i> Characterisation of Hydrogen Distribution in Roller Steel With the Help of Small-Angle Neutron Scattering	95
<i>A. Kulkarni, A. M. Bivigou Koumba, A. Laschewsky, M. Sharp, C. M. Papadakis</i> Small angle neutron scattering analysis of amphiphilic triblock copolymer gels	97
<i>G. P. Kopitsa, D. N. Lazukov, N. N. Tiden</i> The study of the nature of the low-temperature inter-ion correlations in CeAl <sub>3</sub> by means of SANS	99

<i>S. V. Grigoriev, N. A. Grigoryeva, A. S. Sinitskiy</i> Polarized SANS study of geometrically frustrated 3-dimensional nanoscale ferromagnetic structures	103
<i>K. Napolskii, N. Sapoletova, N. Grigoryeva</i> Polarized SANS study of the magnetic inverse photonic crystals	107
<i>K. Napolskii, N. Grigoryeva, S. V. Grigoriev</i> Polarized SANS study of the Co nanowires in anodic aluminum oxide films	113
<i>S. V. Grigoriev, N. Grigoryeva, K. Napolskii, A. V. Syromyatnikov</i> SANS study of highly-ordered Al <sub>2</sub> O <sub>3</sub> matrix: test of the theory	117
<i>S. V. Grigoriev, N. Grigoryeva, K. Napolskii, A. V. Syromyatnikov</i> Polarized SANS study of highly-ordered massives of the magnetic Ni nanowires embedded into Al <sub>2</sub> O <sub>3</sub> matrix	121
<i>K. Napolskii, A. Vyacheslavov</i> SANS study of the magnetic nanocomposites based on mesoporous aluminosilicates	125
<i>V. Dyadkin, D. Lamago, S. V. Grigoriev</i> Principal interactions in helical system Mn <sub>1-y</sub> Fe <sub>y</sub> Si	129
<i>S. V. Grigoriev, E. Moskvina, V. Dyadkin, D. Menzel</i> Spin chirality of the helix in Fe <sub>1-x</sub> Co <sub>x</sub> Si	133
<i>S. V. Grigoriev, N. Grigoryeva, K. Napolskii</i> Polarized SANS study of the magnetic Ni inversed photonic crystal in the magnetic field applied along different principal direction of its FCC structure	137
<i>S. V. Grigoriev, V. Dyadkin, D. Lamago</i> Critical scattering in helical system Mn <sub>1-y</sub> Fe <sub>y</sub> Si	143
<i>S. V. Grigoriev, V. Dyadkin, D. Menzel</i> Critical scattering in helical system Fe <sub>1-x</sub> Co <sub>x</sub> Si	145
<i>S. V. Grigoriev, V. V. Piyadov, T. Taniguchi</i> The study of the static and dynamic spin chirality in the spin-glass system Au <sub>1-x</sub> Mn <sub>x</sub> by small angle scattering of polarized neutrons	149
<b>DCD</b>	<b>151</b>
<i>S. King, H. Jarvie</i> Fractal Structure of Natural Aquatic Nanocolloids	153
<b>PNR</b>	<b>155</b>
<i>D. M. Solina, R. Kaltofen, U. Tietze</i> Dipole-Field-Induced Spin Disorder in Nanoporous Inert-Gas Condensed Materials	157
<i>D. M. Solina, C.-H. Lai</i> Investigation of exchange bias between MnPt and CoFe layers	159

<b>NeRo</b>	<b>161</b>
<i>A. B. Rodríguez-Rodríguez, M. Geoghegan, A. M. Higgins</i> Morphology of Organic Thin Film Transistors with Polymer Brush Gate Dielectrics Synthesized by Atom Transfer Radical Polymerization	163
<i>Y. Chetverikov, S.V. Grigoriev</i> Magnetic field effect on the spin structure of Dy/Y multilayer system	167
<i>S. V. Grigoriev, N. A. Grigoryeva, A. A. Vorobiev</i> Neutron reflectometry from the layer of Co/SiO <sub>2</sub> nanocomposites on the GaAs substrate	171
<i>F. Feyerabend, M. Störmer</i> Neutron reflectivity studies of phospholipid layers on a thin titanium-alloy film on Si(100) Substrate	175
<i>W. Kreuzpaintner, D. Lott</i> Diffuse neutron scattering analysis on a laterally nanostructured	177
<b>ARES-2</b>	<b>181</b>
<i>M. Piza, P. Staron</i> Residual stresses in steel plates with a friction weld	183
<i>J. Dos Santos, P. Staron</i> Residual stresses in a friction stir welded butt-joint of Al and steel	185
<i>C. Redl, P. Staron</i> Residual stress in tool steel rods	187
<i>W. V. Vaidya, M. Koçak, P. Staron</i> Residual stresses in a laser beam welded butt-joint of aluminium sheets	189
<i>W. Machold, F. Bayraktar, P. Staron</i> Influence of the welding sequence on residual stresses in laser welded T-joints of an airframe aluminium alloy	191
<b>TEX-2</b>	
<i>S. Yi, H.-G. Brokmeier</i> Texture variation during heat treatment of extruded AZ31	195
<i>W. Skrotzki, J. Hüttenrauch</i> Texture measurements on ultrafine-grained aluminium produced by accumulative roll bonding	199
<i>T. Lychagina, D. Nikolayev</i> Texture investigation of magnesium alloys	203
<i>M.Y. Zheng, K. Xiao, K. Wu, W. M. Gan, H.-G. Brokmeier</i> Effect of texture on the damping behavior of the ECAPed AZ31 Mg alloy	205

<i>W. Skrotzki</i>	
Texture measurements on ECAP deformed Al-Mg alloys	209
<i>W. M. Gan, M.Y. Zheng, X. J. Wang, H. Chang, K. Wu, H.-G. Brokmeier</i>	
Investigation on the texture gradient in the equal channel angular pressed (ECAP) pure Mg	211
<i>X. J. Wang, W.M. Gan, M.Y. Zheng, K. Wu, H. Chang, H.-G. Brokmeier</i>	
Texture Development in AZ91 alloy and SiCp/AZ91 composites under extrusion processing	213
<i>M. Shahzad, L. Wagner, H.-G. Brokmeier</i>	
Texture development of Mg AZ-80 and Mg-ZK60 extruded at different temperatures	219
<i>W. Skrotzki, R. Chulist</i>	
Cast and rolling textures of NiMnGa alloys	221
<i>R. E. Bolmaro, V. L. Sordi, M. Ferrante</i>	
Texture Characterization of Pb and Pb-62%Sn alloys deformed by ECAE	225
<i>W. W. Schmahl, C. Merkel, A. Götz</i>	
NiTi – Shape Memory Alloy Texture	227
<i>H. Siemes</i>	
Texture of hematite ore deformed to high strains in torsion	229
<i>R. E. Bolmaro, R. D. Martino</i>	
Texture Characterization of a poly-structured rock from Sierras de Córdoba (Argentina)	233
<i>R. E. Bolmaro, A. V Druker</i>	
Texture Characterization of FeMn Shape Memory Alloys	235
<i>Z. Zuberova, H.-G. Brokmeier</i>	
Texture of Mg-AZ31 after squeeze casting (SC), hot rolling (HR) and equal channel angular pressing (ECAP)	237
<b>POLDI</b>	<b>239</b>
<i>P. Mani, D. Lott, J.Fenske</i>	
Investigation of temperature behaviour of the magnetic phase transition in Fe <sub>50</sub> Pt <sub>50-x</sub> Rh <sub>x</sub> thin films	241
<b>GENRA-3</b>	<b>245</b>
<i>P. K. Pranzas, O. Metz, M. Dornheim</i>	
Neutron Radiography Characterization of the Hydrogen Distribution in RT Hydride Tanks	247
<b>Note: EU Support</b>	<b>249</b>

<b>APPENDIX I</b>	<b>251</b>
<b>Reports of experiments carried out at the instruments REFSANS and SRESS-SPEC at the GKSS outstation at the Forschungsneutronenquelle Heinz Maier-Leibnitz (FRM II) in Garching in support of internal and external users.</b>	

<b>APPENDIX II</b>	<b>277</b>
<b>Reports of experiments carried out at the GKSS outstation at DESY in Hamburg in support of internal and external users.</b>	



## **PREFACE**

### **GeNF Operation**

The Geesthacht Neutron Facility (GeNF) is operated as an open facility for external users for about 2/3 of the available beam time and it is used for GKSS in house research within its materials science programme for the remaining 1/3. The external users come either from national and international scientific research institutions, universities and industry, or they own and operate experiments at GeNF as permanent external partners.

The beam time allocations for GeNF instruments are established on the base of a continuous proposal procedure which can react in a flexible and fast way on new proposals. Proposals can be submitted at any time. In 2007 about 203 experiments were performed at GeNF by or for external users, partners or contractors as well as for the in house research programmes. A part of these activities – mainly the part of external use based on proposals – is reported in the present annual experimental report for the year 2007. In many cases several experiments are concentrated in one experimental report.

### **Operation of FRG-1**

In 2007 the total FRG operation time was 211 days providing neutrons, of these it ran for 204 days at its full power of 5 MW providing a neutron flux of ca.  $1.4 \cdot 10^{14}$  thermal neutrons/cm<sup>2</sup> s. In May/June 2007 the FRG-1 was upgraded with a new cold neutron source yielding a flux increase at the instruments using cold neutrons of up to 40 %.

### **GeNF Instruments**

The current set of instruments at GeNF is shown in figure A and listed in table A. The available sample environment equipment is listed in table B.

In 2007 the modern experiment control hardware and software based on LabView was continuously improved on all instruments. The focus of the GKSS in-house research at GeNF is the characterisation of nanostructures, textures and residual stresses in materials at the instruments SANS-2, DCD, ARES-2 and TEX-2, the structural investigation of hydrogen containing substances such as polymers, colloids and biological macromolecules at SANS-1 as well as the characterisation of magnetic and polymer thin films at PNR, NeRo, POLDI and RÖDI.

At the small-angle scattering and reflectometry instrument REFSANS of GKSS at the Heinz Maier-Leibnitz (FRM II) reactor measurements are possible using a broad range of the scattering vector with reflectivities up to  $10^{-7}$ . More details can be found in the reports in appendix I. GKSS also contributes to the construction of the new SANS-1 instrument at FRM II together with the Technical University of Munich (TUM). Furthermore, GKSS, HMI and TUM operate the residual stress and texture instrument STRESS-SPEC together at the FRM II.

At the HARWI II beamline at the synchrotron storage ring DORIS at DESY in Hamburg 49 experiments in the fields tomography, residual stress and texture research were performed. HARWI II is accepted very well by the community and is overbooked in all fields (tomography, diffraction, etc.) by a factor of 3. The two new beamlines at the new third generation synchrotron source PETRA III at DESY, the High Energy Materials Science (HEMS) beamline and the Imaging beamline, are currently under construction. For details see the report in appendix II.



# Geesthacht Neutron Facility (GeNF)

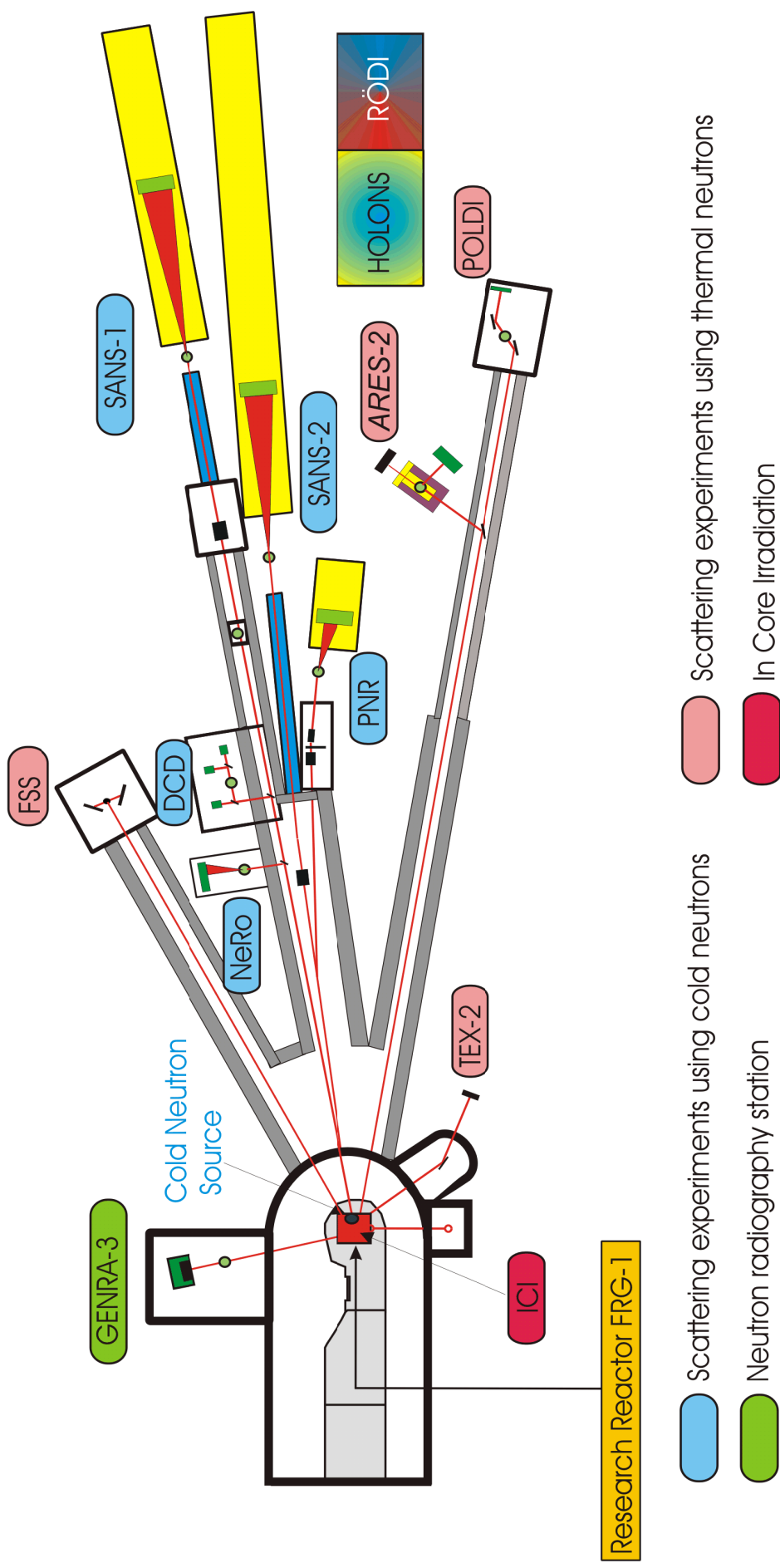


**Figure A:** Arrangement of the Instruments at GeNF.

**Table A:** List of GeNF Instruments.

<b>Instrument</b>	<b>Short Instrument Description /Main Tasks</b>	<b>Characteristic Data</b>	<b>Operator / Local Contact</b>
<b>SANS-1</b>	<u>S</u> mall <u>A</u> nge <u>N</u> eutron <u>S</u> cattering using cold non-polarised/polarised neutrons primarily to investigate molecular biology, colloids and polymers	$\Phi_{\max} = 1 \cdot 10^6 \text{ cm}^{-2} \text{ s}^{-1}$ (coll. 2 m, $\lambda = 0.82 \text{ nm}$ ) $\Delta\lambda/\lambda = 0.1$ ( $\lambda = 0.82 \text{ nm}$ ) Particle sizes: 2–80 nm 2-D position-sens. $^3\text{He}$ -detector	GKSS/ Regine Willumeit Vasy Haramus
<b>SANS-2</b>	<u>S</u> mall <u>A</u> nge <u>N</u> eutron <u>S</u> cattering using cold non-polarised/polarised neutrons to characterise precipitates, clusters, interfaces, grain sizes, magnetic structures etc. in materials (metals, polymers, colloids a.o.)	$\Phi_{\max} = 2 \cdot 10^7 \text{ cm}^{-2} \text{ s}^{-1}$ (coll. 1 m, $\lambda = 0.5 \text{ nm}$ ) $\Delta\lambda/\lambda = 0.1$ Particle sizes: 1–100 nm 2-D position-sens. $^3\text{He}$ -detector	GKSS/ Melissa Sharp Helmut Eckerlebe
<b>DCD</b>	<u>D</u> ouble <u>C</u> ystal <u>D</u> iffractometer for ultra small angle neutron scattering (USANS) using non-polarised cold neutrons to characterise large creep pores, fatigue and sintering cavities, precipitates, voids, bubbles, etc. in materials	$\Phi \approx 550 \text{ cm}^{-2} \text{ s}^{-1}$ $\Delta\lambda/\lambda = 1 \cdot 10^{-5}$ ( $\lambda = 0.443 \text{ nm}$ ) Particle sizes: 30 nm–24 $\mu\text{m}$ $3 \times ^3\text{He}$ - detectors	GKSS/ Melissa Sharp
<b>ARES-2</b>	Diffractometer for the <u>A</u> nalysis of <u>R</u> esidual <u>S</u> tresses in specimens with technical sizes (up to 200 kg) using thermal non-polarised neutrons	$\Phi \approx 3 \cdot 10^5 \text{ cm}^{-2} \text{ s}^{-1}$ (perfect Si-monochr.) $\Delta d/d \approx 4 \cdot 10^{-3}$ take-off angle: $57^\circ - 120^\circ$ 2-D position-sens. $^3\text{He}$ -detector	GKSS/ Peter Staron
<b>NeRo</b>	<u>N</u> eutron <u>R</u> eflectometer to study magnetic and other surfaces, layers, thin films and membranes using cold non-polarised/polarised neutrons with high resolution	$\Phi = 5 \cdot 10^4 \text{ cm}^{-2} \text{ s}^{-1}$ (standard collimation) $\Delta\lambda/\lambda = 0.02$ ( $\lambda = 0.433 \text{ nm}$ ) 2-D position-sens. $^3\text{He}$ -detector, $^3\text{He}$ - pencil counter	GKSS/ Dieter Lott
<b>PNR</b>	<u>P</u> olarised <u>N</u> eutron <u>R</u> eflectometer for the study of magnetic and non-magnetic surfaces, layers, thin films and membranes using cold non-polarised or polarised neutrons with high flux	$\Phi_{\text{nonpol}} = 1 \cdot 10^5 \text{ cm}^{-2} \text{ s}^{-1}$ $\Phi_{\text{nonpol}} / \Phi_{\text{pol}} = 3 / 1$ $\Delta\lambda/\lambda = 0.05$ ( $\lambda \geq 0.635 \text{ nm}$ ) 2-D position-sens. $^3\text{He}$ -detector	GKSS/ Danica Solina

**Table A:** List of GeNF Instruments (continued).

<b>Instrument</b>	<b>Short Instrument Description /Main Tasks</b>	<b>Characteristic Data</b>	<b>Operator / Local Contact</b>
<b>RÖDI</b>	X-ray ( <u>R</u> öntgen) <u>D</u> iffractometer to investigate residual stresses, textures and thin films	Seifert XRD 3003 PTS Heavy load goniometer	GKSS/ Peter Staron
<b>TEX-2</b>	Four circle neutron <u>I</u> EXture diffractometer to characterise textures in metallic, ceramic and geologic materials using thermal non-polarised neutrons	$\Phi = 0.3\text{--}2\cdot 10^6 \text{ cm}^{-2} \text{ s}^{-1}$ take-off angle: $17\text{--}57^\circ$ (in $10^\circ$ -steps) $\lambda$ -range: 0.08–0.27 nm $^3\text{He}$ -single detector, 2-D position-sens. $^3\text{He}$ -detector 300 x 300 mm	TEXMAT – Technische Universität Clausthal/ Heinz-Günter Brokmeier
<b>POLDI</b>	<u>P</u> OLarised <u>D</u> iffractometer; 3-D depolarisation analysis is used to investigate magnetic properties and correlations in magnetic materials; additional time of flight option in non-polarised mode	$\Phi_{\text{max}} = 0.8\cdot 10^5 \text{ cm}^{-2} \text{ s}^{-1}$ (polarized) take-off angle: $10^\circ < 2 \Theta_M < 65^\circ$ $\lambda$ -range: 0.1 nm - 0.36 nm $^3\text{He}$ -single detector	GKSS/ Jochen Fenske Dieter Lott
<b>HOLONS</b>	<u>H</u> OLOgraphy and <u>N</u> eutron <u>S</u> cattering to investigate the properties in functional materials of photonics (e.g. photopolymers and photorefractive crystals) and to study light-induced changes simultaneously by light and neutron diffraction	holographic setup in SANS-2: angular resol. $\leq 0.01^\circ$ ; anglul.setting acc = 0.001° lasers (excitation & diffract.): Ar <sup>+</sup> -laser (single&multi line mode: 25 W /visible, 5.5 W / UV), HeNe-lasers (green, red)	Universities of Vienna and Osnabrück/ Romano Rupp
<b>GENRA-3</b>	<u>G</u> Eesthacht <u>N</u> eutron <u>R</u> Adiography facility for non-destructive analysis of materials by static and dynamic imaging	$\Phi_{\text{therm}} / \Phi_{\text{epi}} = 1.4\cdot 10^6 / 8\cdot 10^3 [\text{cm}^{-2} \text{ s}^{-1}]$ image: 15 x 15 to 45 x 45 $\text{cm}^2$ max. size of specimen: 100 x 200 $\text{cm}^2$	GKSS/ P. Klaus Pranzas
<b>GBET</b>	<u>G</u> eesthachter <u>B</u> oron- capture ( <u>E</u> infang) <u>I</u> therapy originally designed to study cell cultures in tumours with enriched boron; now available as a cold neutron irradiation facility	$\Phi = 1.6\cdot 10^8 \text{ cm}^{-2} \text{ s}^{-1}$ ( $\lambda_{\text{m}} = 0.6 \text{ nm}$ ) irrad. area : 30 x 40 $\text{mm}^2$ $E_{\text{m}} = 2.3 \text{ meV}$	GKSS/ Hans-Ulrich Ruhnau
<b>ICI</b>	<u>I</u> n <u>C</u> ore <u>I</u> rradiation – service for industry and others, different core positions, pneumatic dispatch system available	$\Phi_{\text{therm}} = 2 \text{ to } 8\cdot 10^{13} \text{ cm}^{-2} \text{ s}^{-1}$ $\Phi_{\text{fast}} = 0.02 \text{ to } 0.06 \Phi_{\text{therm}}$ max. sample size: 40 mm $\varnothing$ x 100 mm	GKSS/ Wolfgang Knop

**Table B:** GeNF Sample Environment.

Instrument	Cryostat	Magnets	Temp. Conditioning	Other Devices
<b>SANS-1</b>	<sup>3</sup> He / <sup>4</sup> He – Cryostat: horizontal dilution-refrigerator with NMR sample coil and microwave source: T-range: 120 mK - RT; NMR: 106 and 16 MHz; Microwave: tunable: 68 to 74 GHz sample dimension: 2.8 x 17 x 19 mm <sup>3</sup> (optimum design for NMR coil), NMR is made for <sup>1</sup> H and <sup>2</sup> H resonance in 2.5 Tesla continuous wave mode;	<ul style="list-style-type: none"> <li>• electro magnet: 2.5 T</li> </ul>	heater from 5 to 80 °C heater from 80 to 200 °C	
<b>SANS-2</b>	<ul style="list-style-type: none"> <li>• several refrigerator cryostats, temp. -range: 4–475 K flexible operation in various instruments</li> </ul>	<ul style="list-style-type: none"> <li>• <b>B-E 25:</b> up to 2 Tesla with closed cycle refrigerator (T: 8–300 K)</li> <li>• <b>B-E 15:</b> up to 1.5 Tesla with closed cycle refrigerator (T: 4–475 K)</li> <li>• <b>B-E 10:</b> up to 1 Tesla with closed cycle refrigerator (T: 4–475 K), alternative furnace (T: 300–900 K)</li> <li>• <b>superconducting magnets:</b> up to 5 Tesla with longitudinal (T: 8–300 K) or vertical field (T: 4–280 K)</li> </ul>	heater (electric) / cooler (thermostat liquid circuit): T-range: -30–400 °C vacuum or inert gas atmosphere furnaces (temperatures up to 1000 °C)	<ul style="list-style-type: none"> <li>– side detector for measurements at large angles</li> <li>– sample container for big samples</li> <li>– lasers</li> </ul>
<b>DCD</b>		<ul style="list-style-type: none"> <li>• <b>electro magnet:</b> &gt; 0.9 Tesla</li> </ul>	heater up to 80 °C	Sample changer with up to 6 positions
<b>ARES-2</b>			furnace (up to 700 °C)	Eulerian cradle (with x, y, z tables), load frame

**Table B:** GeNF Sample Environment (continued).

<b>Instrument</b>	<b>Cryostat</b>	<b>Magnets</b>	<b>Temp. Conditioning</b>	<b>Other Devices</b>
<b>PNR</b>	<ul style="list-style-type: none"> <li>refrigerator cryostat Model Leybold RGD 210, temp.-range: 12–475 K</li> <li>refrigerator cryostat Model ARS DE 210 SE, temp.-range: 4–300 K flexible operation in various instruments</li> </ul>	<ul style="list-style-type: none"> <li>electro magnet: up to 0.9 Tesla</li> </ul>	<ul style="list-style-type: none"> <li>heater / cooler (thermostat liquid circuit): T-range: -30–250 °C</li> </ul>	
<b>NeRo</b>	<ul style="list-style-type: none"> <li>refrigerator cryostat Model Leybold RGD 210, temp.-range: 12–475 K</li> <li>refrigerator cryostat Model ARS DE 210 SE, temp.-range: 4–300 K flexible operation in various instruments</li> </ul>	<ul style="list-style-type: none"> <li>electro magnet: up to 0.9 Tesla</li> <li>superconducting magnet: up to 5 Tesla with closed cycle refrigerator (T: 8–300 K) suitable for polarised neutrons</li> </ul>	<ul style="list-style-type: none"> <li>2 x vacuum furnaces: T-range: RT – 200 °C <ul style="list-style-type: none"> <li>one especially. for annealing purposes under PC control</li> </ul> </li> <li>heater/cooler (thermostat liquid circuit): T-range: -30–250 °C</li> </ul>	<ul style="list-style-type: none"> <li>2D-analyser for measurements of magnetic diffuse reflectivity</li> </ul>
<b>TEX-2</b>				<ul style="list-style-type: none"> <li>loading device: range of cycling load: tension up to 1.5 t, compression up to 2.0 t,</li> <li>sophisticated set of sample holders</li> </ul>
<b>POLDI</b>	<ul style="list-style-type: none"> <li>refrigerator cryostat T &gt; 10 K</li> <li>refrigerator cryostat Model Leybold RGD 210, temp.-range: 12–475 K</li> </ul>	<ul style="list-style-type: none"> <li>DC magnetic field &lt; 160 A/cm</li> <li>pulsed field &lt; 6.5 kA/cm</li> <li>superconducting magnet: up to 5 Tesla (T: 8–300 K)</li> </ul>		





**Small-angle scattering instrument SANS-1**

**Short Instrument Description:**

The small angle neutron scattering instrument SANS-1 using cold non-polarised/polarised neutrons serves primarily to investigate molecular biology, colloids and polymers.

**Local Contact:**

**Dr. Regine Willumeit**

Phone/Fax : +49 4152 87-1291 / +49 4152 87-1356

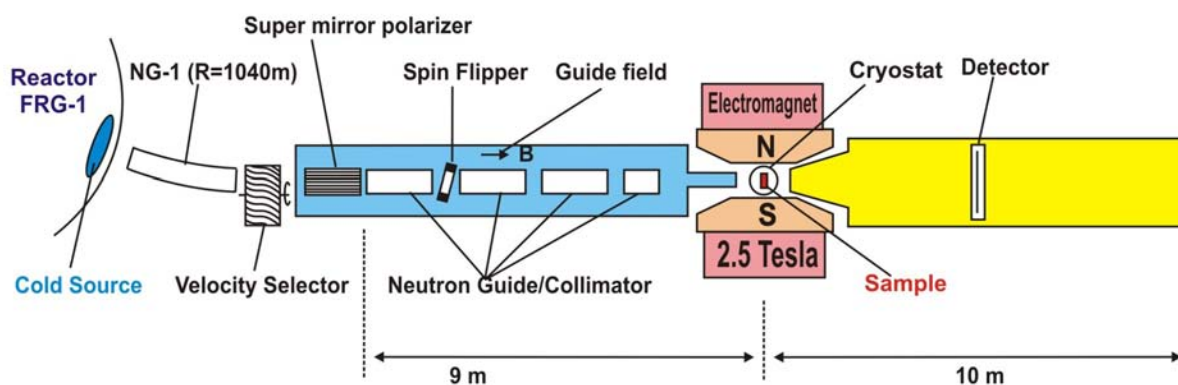
e-mail: [regine.willumeit@gkss.de](mailto:regine.willumeit@gkss.de)

**Dr. Vasyil Haramus**

Phone/Fax : +49 4152 87-1290 / +49 4152 87-1356

e-mail: [vasyl.haramus@gkss.de](mailto:vasyl.haramus@gkss.de)

**Schematic view of SANS-1:**



**Instrument Details:**


Beamline:	Beamline 8 – NG-1, radius of curvature R = 1040 m, cross section 3 x 4 cm <sup>2</sup> , cold neutrons
Monochromator	helical slot selector
Wavelength range behind polariser and selector:	≥ 0.45 nm;
Wavelength resolution	$\Delta\lambda / \lambda = 0.1$ ( $\lambda = 0.82$ nm)
Length L of collimation:	2 m, 4 m, 6 m, 8 m, 10 m
Flux at specimen:	$\Phi = 0.05\text{--}1 \cdot 10^6$ cm <sup>-2</sup> s <sup>-1</sup> see table

**Instrument Details** (continued):

Range of momentum transfer:	$0.05 \leq Q \leq 3 \text{ nm}^{-1}$
Distance sample to detector:	$0.7 \text{ m} \leq d \leq 9.7 \text{ m}$
Detector: active area: effective pixel size: background:	2-dim position-sensitive $^3\text{He}$ -counter 50 x 50 cm <sup>2</sup> 0.2 x 0.3 cm <sup>2</sup> 1 cps
Polarized target station:	dilution refrigerator (120 mK) 2.5 T C-shaped electro-magnet microwave emitter (68–74 GHz) NMR circuit for protons and deuterons selective nuclear spin depolarisation
Other sample environment	thermostat (5 °C to +80 °C and 80 °C to 200 °C) automatic sample change 10 positions

**Flux of non-polarized cold neutrons at the sample position:**

length of collimator [m]	2	4	6	8	10
$\Phi [10^3 \text{ n cm}^{-2} \text{ s}^{-1}]$ ( $\lambda = 0.82 \text{ nm}$ )	1000	600	200	120	65

	<b>EXPERIMENTAL REPORT</b>	<b>GeNF SANS-1</b>
<b>Contrast variation SANS studies of micelles in mixed perfluorinated and normal non-ionic surfactants</b>		
<b>Proposer:</b>	<b>Mats Almgren<sup>1</sup></b> , <sup>1</sup> Uppsala University, Uppsala, Sweden	
<b>Co-Proposer(s):</b>	<b>Marie-José Stébé<sup>2</sup></b> , <sup>2</sup> University of Nancy, Nancy, France	
<b>Experimental Team:</b>		
<b>User Group Leader:</b>	<b>Mats Almgren<sup>1</sup></b>	
<b>Instrument Responsible:</b>	<b>Vasyl Haramus<sup>3</sup></b> , <sup>3</sup> GKSS Research Centre Geesthacht, Germany	
<b>Date(s) of Experiment:</b>	17 <sup>th</sup> – 20 <sup>th</sup> April 2007	

## Objectives

Mixtures of fluorocarbon and hydrocarbon surfactants in aqueous solution either assemble to form mixed micelles, or to form coexisting populations of hydrocarbon-rich and fluorocarbon-rich micelles. In earlier experiments (2004–2006) it was shown that contrast variation SANS results give strong support for the demixing of micelles into hydrocarbon-rich and fluorocarbon-rich populations in solutions containing a fluorinated and a normal ionic surfactant.<sup>1–3</sup> These were the first times such a demixing was verified by SANS studies. We have now extended the measurements to a non-ionic system mixtures of C<sub>8</sub>F<sub>17</sub>C<sub>2</sub>H<sub>4</sub>(OC<sub>2</sub>H<sub>4</sub>)<sub>9</sub> and C<sub>12</sub>H<sub>25</sub>(OC<sub>2</sub>H<sub>4</sub>)<sub>8</sub> that according to other reports makes non-ideally mixed micelles.<sup>4</sup> The problems caused by micellar interactions should be minimized in this system.

## Experiment

SANS with contrast variation by using D<sub>2</sub>O/H<sub>2</sub>O mixtures for solvent would, at a first glance, appear as ideally suited for such studies: one solvent mixture would make one type of micelles invisible, another the other type of micelles, and a scattered intensity would remain for the demixed system at the nominal match point for the mixed surfactants, where the scattering would all but disappear for an ideally mixed system. Only few studies of this kind have been made prior to our series of measurements.<sup>1–3</sup> The early studies seemed to suggest that the systems selected all contained mixed micelles. On a closer inspection of the results, however, in the light of our later findings, it appears that this conclusion is maybe not inescapable.

In ref.2 a simplified theory for the intensity as a function of the contrast is presented:

$$\frac{d\Sigma}{d\Omega}(0) = n_m V_m^2 \left[ \sigma^2 (\rho_{FS} - \rho_{HS})^2 + (\bar{\rho} - \rho_S)^2 \right] \quad (1)$$

It is assumed a distribution of composition over globular, non-interacting micelles of equal size (or a size polydispersity not coupled to the composition variation). The half-width of the composition distribution is given by  $\sigma$ ,  $\rho$  stands for the scattering length density, subscript HS for hydrogeneous surfactant, FS fluorinated surfactant, S for solvent, and the bar designates the nominal matchpoint for the surfactant mixture,  $n_m$  is the number density of micelles, and  $V_m$  the dry volume of a micelle. Besides the width of the composition distribution – which is the only information about the distribution that can be obtained from the scattered intensity at zero angle – the micelle aggregation number and the scattering length density at the minimum are determined.  $\frac{d\Sigma}{d\Omega}(0)$  was obtained from an IFT analysis of scattering results for  $q \geq 0.02 \text{ \AA}^{-1}$ ,

obtained using low concentrations of surfactants (to reduce excluded volume interactions) and a substantial salt concentration to minimize electrostatic interactions. It was obvious from the results that intermicellar interactions were still somewhat important. In the most recent contribution,<sup>1</sup> direct modelling was made in addition to the IFT calculations, using models with globular micelles having either a Gaussian or a prescribed composition distribution and an effective hard sphere interaction. The results from the direct modelling and the IFT calculations were similar with respect to the width of the composition distribution.

We have now used the technique on a non-ionic system without electrostatic interactions between the micelles. A suitable system, of great interest on its own rights, was recently studied in detail by Stébé and coworkers.<sup>4</sup> Mixtures of  $C_8F_{17}C_2H_4(OC_2H_4)_9$  and  $C_{12}H_{25}(OC_2H_4)_8$  in dilute water solution form micelles that are globular and of similar size in the mixture as in the pure components (according to dynamic light scattering results). The ternary phase diagram of the system was determined at two temperatures, and showed that at high surfactant concentrations the micellar solution separated into two liquid phases, one with fluorosurfactant rich micelles, the other with mainly normal surfactants. At still higher concentrations both pure surfactants form hexagonal phases that were only slightly miscible. It seemed probable that two types of micelles would coexist in the solution at low surfactant concentrations.

### Achievements and Main Results

Figure 1 presents the variation of zero  $q$  intensity with the scattering length density of the solvent, and the fit of these values to eqn. (1).

In Table 1 we have collected all results for all systems studied in this way. The results for the present system, shown as the last row in the table, can be compared with those for  $C_{12}PC + HFDePC$ , with the same length and composition of the hydrophobic tails of the surfactants. The non-ionic surfactant mixture form larger micelles, with a less broad composition distribution, than the cationic pair.

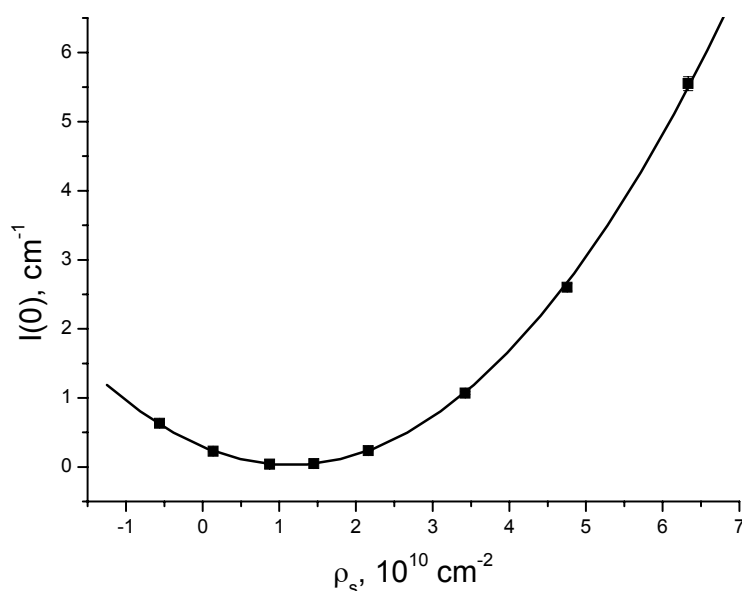


**Figure 1:**  $I(0) = \frac{d\Sigma}{d\Omega}(0)$ , obtained from an IFT analysis, for mixtures of 22 mM  $C_8F_{17}C_2H_4(OC_2H_4)_9$  (= HFDeEO<sub>9</sub>) and 22mM  $C_{12}H_{25}(OC_2H_4)_8$  (=  $C_{12}EO_8$ ), fitted to eqn. 1.

**Table 1:** Aggregation number, half-width of micelle composition distribution and match point (given as  $x_{D2O}$  of the corresponding solvent mixture) for all systems studied. The results from the present study are given in the last row.


System	$N_{agg}$	$\sigma$	$\bar{\rho}$	$\bar{\rho}_{calc}$
C <sub>16</sub> TAC + HFDePC 25°C	76	0.33	0.35	0.35
C <sub>16</sub> TAC + HFDePC 60°C	54	0.20	-	0.35
C <sub>16</sub> PC + HFDePC 25°C	71	0.39	0.38	0.375
C <sub>16</sub> PC + HFDePC 60°C	54	0.22	0.37	0.375
C <sub>12</sub> PC + HFDePC 25°C	47	0.22	0.46	0.42
SDS + SDS-d25 25°C	78	0.005	0.57	0.59
SDeS + SPFO 25°C	56	0.07	0.41	0.42
<b>C<sub>12</sub>EO<sub>8</sub> + HFDeEO<sub>9</sub> 25 °C</b>	<b>85</b>	<b>0.15</b>	<b>0.247</b>	<b>0.238</b>

The results thus indicate that the measured width of the composition distribution in all the mixed systems of hydrogenated and fluorinated surfactants is larger than in the ideal system, composed of SDS and its deuterated analog. While being broader than this measured value, the width is small for SDeS and SPFO, the system with shortest tails of the surfactants. The half-width value corresponds to the theoretically expected value of a randomly mixed system. The non-ionic system show a substantial broadening of the composition distribution, but probably not so much that a bimodal distribution has evolved.

## References

- [1] Almgren, M.; Garamus, V., Asakawa, T., Jiang, N. *J Phys. Chem. B* 2007, *111*, 7133
- [2] Almgren, M.; Garamus, V., *J. Phys. Chem. B* 2005, *109*, 11348–11353
- [3] Kadi, M.; Hansson, P.; Almgren, M.; Bergström, M.; Garamus, V. *Langmuir* 2004, *20*, 3933
- [4] Blin, J. L.; Henzel, N.; Stébé, M. J., *J. Colloid Interface Sci.* 2006, *302*, 643



	<b>EXPERIMENTAL REPORT</b>	<b>GeNF SANS-1</b>
<b>Contrast variation SANS studies of micelles in mixed perfluorinated and hydrogenated surfactants</b>		
<b>Proposer:</b> Mats Almgren, Uppsala University, Uppsala, Sweden <b>Co-Proposer(s):</b>		
<b>Experimental Team:</b> <b>User Group Leader:</b> Mats Almgren <b>Instrument Responsible:</b> Vasyl Haramus, GKSS Research Centre Geesthacht, Germany		
<b>Date(s) of Experiment:</b> 20 <sup>th</sup> – 27 <sup>th</sup> November 2007		

## Objectives

Mixtures of fluorocarbon and hydrocarbon surfactants in aqueous solution either assemble to form mixed micelles, or to form coexisting populations of hydrocarbon-rich and fluorocarbon-rich micelles. We have used this procedure for studies of a number of mixed systems, both ionic and non-ionic, from an ideally mixed system, represented by SDS and its perdeuterated analogue, to strongly non-ideal fluorocarbon-hydrocarbon surfactant mixtures, some of which gave so broad composition distributions that they must be bimodal. The broadening of the composition distribution, eventually leading to demixing, increases with the size of the hydrophobic part of the surfactants, but appears mainly independent of the headgroups. In order to test this dependence in more detail we now complement the earlier measurements with an anionic surfactant system, having the same hydrophobic parts as previously measured cationic and non-ionic surfactants.

## Experiment

SANS with contrast variation by using D<sub>2</sub>O/H<sub>2</sub>O mixtures for solvent as well suited for such systems: one mixture would make one type of micelles invisible, another the other type of micelles, and a scattered intensity would remain for the demixed system at the nominal match point for the mixed surfactants, where the scattering would all but disappear for an ideally mixed system.

For non-interacting particles of equal size and shape with a composition polydispersity the scattered intensity at zero angle is given by<sup>1</sup>,

$$\frac{d\Sigma}{d\Omega}(0) = n_m V_m^2 \left[ \sigma^2 (\rho_{FS} - \rho_{HS})^2 + (\bar{\rho} - \rho_S)^2 \right] \quad (1)$$

The width of the composition distribution is given by  $\sigma$ ,  $\rho$  stands for the scattering length density, subscripts HS for hydrogenous surfactant, FS fluorinated surfactant, S for solvent, and the bar designates the nominal matchpoint for the surfactant mixture,  $n_m$  is the number density of micelles, and  $V_m$  the dry volume of a micelle. Besides the width of the composition distribution – which is the only information about this distribution that can be obtained from the scattered intensity at zero angle – the micelle aggregation number and the scattering length density at the minimum are determined.

In the present study we measured mixtures of sodium dodecylsulfate (SDS) and sodium perfluorononanoate (SPFN), using 40mM of each surfactant, aqueous 0.200 M LiCl, at seven contrasts obtained by varying the D<sub>2</sub>O mole fraction from 0.1 to 1.0. Due to the high Krafft point of this surfactant mixture, the temperature was chosen as 30 °C.

Preliminary evaluation of the results using eq. (1) as described earlier gave  $N_{agg} = 58$  and  $\sigma = 0.16$ . The minimum scattered intensity was found close to the calculated matchpoint.

## Achievements and Main Results

Results from the previous experiments are summarized in the following table.

System	$N_{agg}$	$\sigma$	$\bar{\rho}$	$\bar{\rho}_{calc}$
C <sub>16</sub> TAC + HFDePC 25°C	91	0.33	0.35	0.35
C <sub>16</sub> TAC + HFDePC 60°C	65	0.20	-	0.35
C <sub>16</sub> PC + HFDePC 25°C	89	0.39	0.38	0.375
C <sub>16</sub> PC + HFDePC 60°C	68	0.22	0.37	0.375
C <sub>12</sub> PC + HFDePC 25°C	62	0.22	0.46	0.42
SDS + SDS-d25 25°C	78.5	0.005±0.030	0.57	0.59
SDeS + SPFO 25°C	56	0.07±0.024	0.41	0.42
C <sub>8</sub> F <sub>17</sub> C <sub>2</sub> H <sub>4</sub> (OC <sub>2</sub> H <sub>4</sub> ) <sub>9</sub> + C <sub>12</sub> H <sub>25</sub> (OC <sub>2</sub> H <sub>4</sub> ) <sub>8</sub> 25°C	85	0.15±0.006	0.25	0.24
<b>SDS + SPFN 30°C</b>	<b>58</b>	<b>0.16±0.01</b>	<b>0.40</b>	<b>0.41</b>


The results from the study of the first four systems have been published.<sup>1,2,3</sup> The width of the composition distribution decreases with increasing temperature, as expected, but it is still much larger than the value for ideal mixing,  $\sigma = 0.1$  for  $N_{agg} = 50$ , as could be expected for a non-ideally mixed system, even if there is no clear demixing into two micelles populations. Note that  $\sigma$  is always smaller than  $\sigma = 0.5$ , the value for complete demixing into pure micelles of the two components. A square distribution of compositions from 0 to 1 – which is the broadest unimodal distribution – would have  $\sigma = 0.289$ .

The results from the present study of SPFN and SDS in 200mM LiCl are given in bold face as the last entry in the table. The results, still tentative, indicate that the system is clearly non-ideal, with  $\sigma = 0.16$ . This result should be compared to those of C<sub>12</sub>PC + HFDePC and C<sub>8</sub>F<sub>17</sub>C<sub>2</sub>H<sub>4</sub>(OC<sub>2</sub>H<sub>4</sub>)<sub>9</sub> + C<sub>12</sub>H<sub>25</sub>(OC<sub>2</sub>H<sub>4</sub>)<sub>8</sub>, in which the fluorocarbon chains and the hydrocarbon chains have the same length. The width of the composition distributions are comparable: 0.22 and 0.15, respectively.

## References

- [1] Almgren, M.; Garamus, V., J Phys. Chem. B 2005, 109, 11348–11353
- [2] Kadi, M.; Hansson, P.; Almgren, M.; Bergström, M.; Garamus, V., Langmuir 2004, 20, 3933.
- [3] Almgren, M.; Garamus, V. M., Asakawa, T., Jiang, N., J Phys. Chem. B 2007, 111, 7133–7141.



	<b>EXPERIMENTAL REPORT</b>	<b>GeNF SANS-1</b>
<b>SANS contrast variation in ferrofluids as polydisperse multicomponent superparamagnetic systems</b>		
<b>Proposer:</b>	<b>M. V. Avdeev<sup>1</sup></b> , <sup>1</sup> FLNP, JINR, Dubna, Russia	
<b>Co-Proposer(s):</b>	<b>A. V. Feoktystov<sup>1</sup></b>	
<b>Experimental Team:</b>		
<b>User Group Leader:</b>	<b>M. V. Avdeev<sup>1</sup></b>	
<b>Instrument Responsible:</b>	<b>Vasyl Haramus<sup>2</sup></b> , <sup>2</sup> GKSS Research Centre Geesthacht, Germany	
<b>Date(s) of Experiment:</b>	18 <sup>th</sup> June – 1 <sup>st</sup> July, 2 <sup>nd</sup> – 9 <sup>th</sup> December 2007	

## Objectives

The aim of the performed experiment was the study of a classical organic ferrofluid (nanomagnetite dispersed into benzene and coated with single layer of oleic acid for stabilization) by a new method developed in [1]. The data of the SANS contrast variation (non-polarized mode) were treated in terms of the basic functions approach [2] for the case of polydisperse and multicomponent magnetic particles. The current work was the continuation of the previous experiments with the similar magnetic fluid where myristic acid was used instead of oleic acid [3]. As it has been shown recently [4], in organic media shorter saturated monocarboxylic acids (myristic and lauric acids, 14 and 12 C-groups in linear tails, respectively) stabilize magnetite particles of smaller size and reduced polydispersity in comparison with unsaturated oleic acid (18 C-groups in bent tail).

## Experiment

The initial magnetic fluid on D-benzene (CFATR, Romania) with the magnetite volume fraction of 10 % was diluted down to 0.7 % with different mixtures of D- and H-benzene with variation of the D-benzene relative content in the final solution from 0.1 to 1. Measurements were made at ten points over this interval. The special attention was given to the vicinity of the match point estimated as ~0.6 of the D-benzene relative content.

## Achievements and Main Results

The obtained scattering curves for different contrasts are presented in Fig.1. Some aggregation in the fluids was detected, which we connect with the age effect (about one year after preparation). The intensity at zero angle and visible squared radius of gyration were obtained by the Guinier approximation to these curves over  $q$ -interval 0.1-0.25 nm<sup>-1</sup>, where the effect of aggregates was small. According to [1] dependences of these parameters on the modified contrast,  $\Delta\rho$ , have the form:

$$I(0) = n(\Delta\rho)^2 \langle V_c^2 \rangle + n \langle (\bar{\rho} - \bar{\rho}_e)^2 V_c^2 \rangle, \quad (1a)$$

$$\tilde{R}_g^2 = \left( \frac{\langle V_c^2 R_c^2 \rangle}{\langle V_c^2 \rangle} + \frac{A}{\Delta\rho} - \frac{B}{(\Delta\rho)^2} \right) / \left( 1 + \frac{D}{(\Delta\rho)^2} \right), \quad (1b)$$

where  $n$  is the particle number density;  $R_c$ ,  $V_c$  are the radius of gyration and volume related to the whole particle shape; and  $A$ ,  $B$ ,  $D$  are parameters comprising different averages over the polydispersity function. Brackets  $\langle \dots \rangle$  in (1) denote the averaging over the polydispersity function. Here, this function concerns the magnetite core in the particle. The corresponding treatment of the experimental integral parameters are shown in Fig. 2.

The effective match point is determined as  $0.63 \pm 0.03$  of the D-benzene relative content in the solvent, which corresponds to the scattering length density of  $(3.86 \pm 0.15) \times 10^{10} \text{ cm}^{-2}$ . The fit of Eq. (1b) to the experimental data results in the squared radius of gyration  $R_c^2 = 6450 \pm 65 \text{ \AA}^2$ , or  $R_c = 80.3 \pm 0.4 \text{ \AA}$ . Taking into account the quasi-spherical shape of particles one obtains for the characteristic radius of the whole particle the value of  $103.3 \pm 0.5 \text{ \AA}$ . It is twice larger compared to  $52 \text{ \AA}$  in the previous experiment with the samples stabilized by myristic acid [3], which is in agreement with the results on the scattering of polarized neutrons [4]. Obtained parameters of (1) are to be compared with the values calculated by the polydispersity function from direct modelling of the curves.

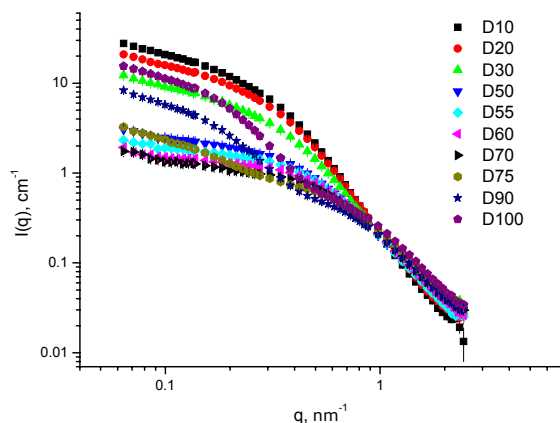


**Figure 1:**


Scattering curves obtained during the SANS contrast variation for 0.7 % ferrofluid magnetite/oleic acid/benzene. In the sample names the content of deuterated benzene (per cent) is indicated.

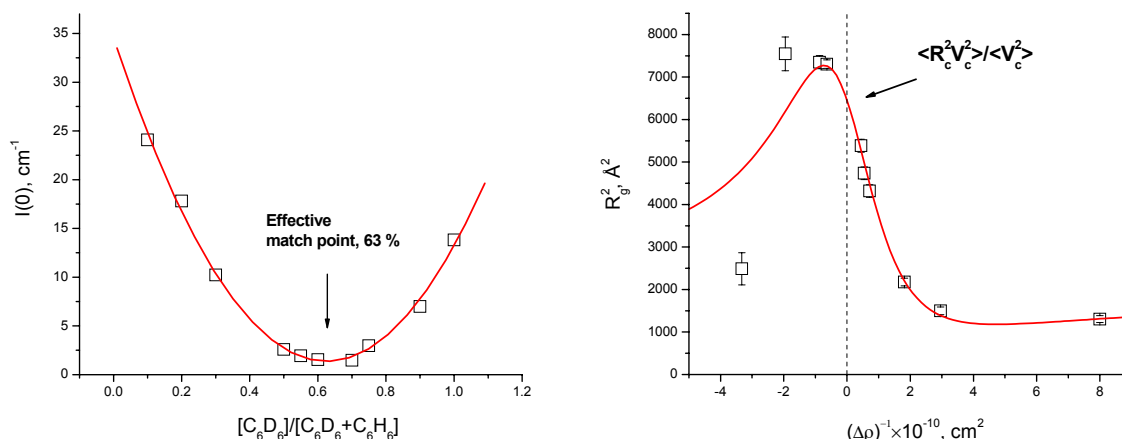


**Figure 2:** Integral parameters of the SANS curves as a result of the contrast variation. (Left) Intensity at zero angle as a function of the content of deuterated benzene in the carrier. Line shows the fit to the parabolic dependence in accordance with (1a). (Right) Squared visible radius of gyration as a function of the inversed modified contrast. Line is a result of fitting by (1b).

## References

- [1] M. V. Avdeev, J. Appl. Cryst., 40 (2007) 56–70.
- [2] H. B. Stuhmann, In Modern aspects of small-angle scattering. Ed. Brumberger, H., Kluwer Acad. Publishers, Dordrecht (1995) 221–254
- [3] M. V. Avdeev, A. V. Feoktystov, V. M. Garamus, In GeNF Annual Report 2006, GKSS 2007/6 (2007).
- [4] M. V. Avdeev, D. Bica, L. Vékás, O. Marinica, M. Balasoia, V. L. Aksenov, L. Rosta, V. M. Garamus, A. Schreyer, J. Mag. Mater. 311 (2007) 6–9.

	<b>EXPERIMENTAL REPORT</b>	<b>GeNF SANS-1</b>
<b>SANS analysis of ferrofluids produced by laser pyrolysis</b>		
<b>Proposer:</b> <b>Co-Proposer(s):</b>	<b>L. Vekas<sup>1</sup></b> , <sup>1</sup> CFATR, Timisoara, Romania <b>D. Bica<sup>1</sup></b>	
<b>Experimental Team:</b> <b>User Group Leader:</b> <b>Instrument Responsible:</b>	<b>M. V. Avdeev<sup>2</sup></b> , <sup>2</sup> FLNP, JINR, Dubna, Russia <b>L. Vekas<sup>1</sup></b> <b>Vasyl Haramus<sup>3</sup></b> , <sup>3</sup> GKSS Research Centre Geesthacht, Germany	
<b>Date(s) of Experiment:</b>	9 <sup>th</sup> – 18 <sup>th</sup> December 2007	

## Objectives

Ferrofluids are colloidal systems composed of isolated particles with nanometre-sized dimensions that are stabilized by surfactant molecules and dispersed in solvent media. In the ideal case, these non-interacting systems derive their unique magnetic properties mostly from the reduced size of the isolated nanoparticles, and contributions from interparticle interactions are negligible. In the case of ferrite nanoparticles, such as magnetite, maghemite or cobalt ferrite, the most efficient route is the chemical co-precipitation process. Thus, for ferrofluids with magnetite there are several examples where the isolated particles are confirmed by structural methods as small-angle neutron scattering (SANS) [1, 2].

In the current experiments a new class of ferrofluids with iron oxide particles produced by laser pyrolysis [3, 4] was studied by SANS. This work was done complementary to other methods including TEM, HRTEM, X-ray diffraction, magnetization analysis. Despite indications of aggregates the newly synthesized ferrofluids show high stability. The aim of the SANS experiments was to clarify the structure of these aggregates and compare their organization with that in the initial iron oxide powder, dispersed then in various solvents.

## Experiment

Experiments with initial iron-oxide powder (sample name SF) were made after the powder was put into the quartz cell (1.5 mm thick). Further experiments were performed with liquid samples, ferrofluids based on H-carriers (transformer oil, water). In this case the used surfactant is almost matched, so SANS comes mainly from magnetic material dispersed in the liquid.

## Achievements and Main Results

As one can see from the SANS curve (Fig.1), the SF powder represent a system of clusters composed of particles with characteristic size of about 7 nm. The last value was estimated from the the point where the scattering starts to deviate from the power-law type when decreasing  $q$ . It was made in accordance with the relation  $q \sim 2\pi/D$ . The corresponding mean value of size is denoted as  $\langle D \rangle_v$ , which means “visible”. It covers both the real mean size and polydispersity index in a way  $\langle D \rangle_v = (\langle D^2 V^2 \rangle / \langle V^2 \rangle)^{1/2}$ , where  $V$  is the particle volume. If one takes into account that particles are polydisperse, the obtained value is quite small. For the log-normal type of the particle size distribution the estimates give  $D_0 \sim 5$  nm,  $S \sim 0.25$ . For comparison, the particle size distribution of nanomagnetite obtained in the course of the

reaction of co-precipitation and dispersed into transformer oil ( $\langle D^2 V^2 \rangle / \langle V^2 \rangle^{1/2} = 15$  nm, which corresponds to significantly larger parameters  $D_0 \sim 7$  nm,  $S \sim 0.38$ ).

After dispersing the powder in various solvents, SANS curves show approximately the same behaviour (Fig.1). This means that large aggregates of magnetic particles (size more than 120 nm) are stabilized in the fluids. The structure of the aggregates repeats that in the initial powder. In this connection, two interesting features for the studied systems should be pointed out. First, despite the large aggregates the fluids are well stable. Second, the complementary analysis of the magnetization for the fluids gives a characteristic magnetic size close to that of magnetic particles composing aggregates. The last fact indicates that effectively there are no strong correlations between magnetic moments of the particles in the aggregates. Based on the strong evidence of the presence of fractal aggregate in the fluids by SANS, this gives rise to an interesting problem on correlation between magnetic moments of particles in a fractal cluster.

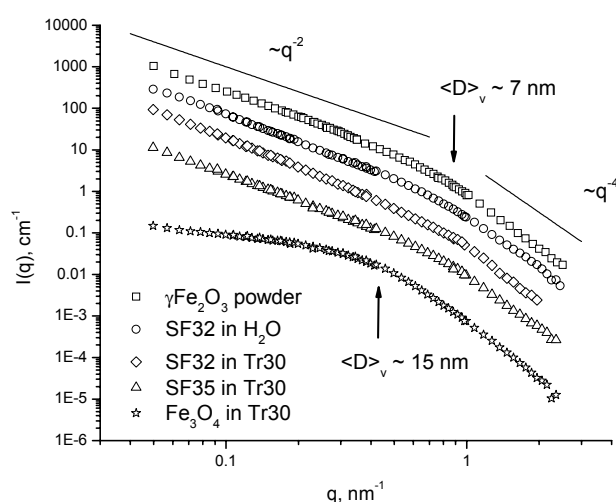


**Figure 1:**


SANS data for the studied systems. For convenient view data of SF32 in Tr30 is divided by coefficient 5, data of SF35 in Tr30 is divided by coefficient 20. For comparison the SANS curve for magnetite particles ( $\text{Fe}_3\text{O}_4$ ) dispersed in Tr30 is shown (divided by coefficient 100). Line of the power-law type on the top shows the scattering from fractal clusters with the fractal dimension 2. Arrows indicate points used for estimating the characteristic size of basic particles.

## Acknowledgement

The SF powder and MF sample were obtained in the framework of the CEEEX project FeMANANOF supported by the Romanian Ministry of Education and Research.

## References

- [1] M. V. Avdeev, V. L. Aksenov, M. Balasoïu, V. M. Garamus, A. Schreyer, Gy. Török, L. Rosta, D. Bica, L. Vékás, *J. Coll. Interface Sci.* 295 (2006) 100–107
- [2] M. V. Avdeev, D. Bica, L. Vékás, O. Marinica, M. Balasoïu, V. L. Aksenov, L. Rosta, V. M. Garamus, A. Schreyer, *J. Mag. Mag. Mater.* 311 (2007) 6–9
- [3] Dumitrache, F., I. Morjan, R. Alexandrescu, V. Ciupina, G. Prodan, I. Voicu, C. Fleaca, I. Albu, M. Savoïu, I. Sandu, E. Popovici, I. Soare, *Appl. Surf. Sci.* 247 (2005) 25–28
- [4] Popovici, E., F. Dumitrache, I. Morjan, R. Alexandrescu, V. Ciupina, G. Prodan, L. Vékás, D. Bica, O. Marinica, E. Vasile, *Appl. Surf. Sci.* (2007), doi:10.1016/j.apsusc.2007.09.022

	<b>EXPERIMENTAL REPORT</b>	<b>GeNF SANS-1</b>
<b>Effect of Ce and Gd doping on the microstructure properties of PT ceramics investigated by SANS</b>		
<b>Proposer:</b>  <b>Co-Proposer(s):</b>	<b>Maria Balasoiu<sup>1</sup></b> , <sup>1</sup> National Institute of Physics and Nuclear Engineering, Bucharest <b>M. L. Craus<sup>2</sup></b> , <sup>2</sup> National Institute of Research and Development for Technical Physics, Iasi, Romania <b>A. M. Moisin<sup>3</sup></b> , <sup>3</sup> INCDIE ICPE-CA, Bucharest, Romania	
<b>Experimental Team:</b> <b>User Group Leader:</b> <b>Instrument Responsible:</b>	<b>V. Tripadus<sup>1</sup></b> <b>Maria Balasoiu<sup>1</sup></b> <b>Vasyl Haramus<sup>4</sup></b> , <sup>4</sup> GKSS Research Centre Geesthacht, Germany	
<b>Date(s) of Experiment:</b>	1 <sup>st</sup> – 7 <sup>th</sup> November 2007	

## Objective

Ferroelectric materials such as  $\text{PbTiO}_3$  (PT) or  $\text{PbZr}_x\text{Ti}_{1-x}\text{O}_3$  (PZT) ceramics are ferroelectric oxides characterized by a nonvolatile, reversible polarization field that has been successfully used in radiation hard memories, high density storage media and integrated components for applications in dynamic and nonvolatile random access memories, as well as in surface acoustic wave devices, micromechanical devices and ferroelectric field effect devices [1–4]. The importance of PT and PZT ceramics results also from the large number of additives that have been successfully used to tailor the desired end use. It has been reported in the literature that the composition of PZT at the morphotropic phase boundary (MPB) of the  $\text{PbTiO}_3$ – $\text{PbZrO}_3$  phase diagram modified with rare-earth additives has maximum piezoelectric and electromechanical coupling coefficients [5–8].

The present study has been performed with the aim of investigating the microstructure of Ce doped PT ceramics.

## Experiment

$\text{Pb}_{0.84}\text{Ce}_{0.08}(\text{Ti}_{0.98}\text{Mn}_{0.02})\text{O}_3$  samples were synthesized by standard ceramic technology at 1180 °C, 1230 °C, 1280 °C temperatures.

## Achievements and Main Results

Before SANS, conventional  $\theta$ – $2\theta$  X-ray diffraction scans using  $\text{CoK}\alpha$  radiation were recorded in order to identify the crystallographic phases and to determine the average coherent sizes and the microstrains of the samples (Fig. 1a).

From XRD data we can conclude that all three  $\text{Pb}_{0.84}\text{Ce}_{0.08}(\text{Ti}_{0.98}\text{Mn}_{0.02})\text{O}_3$  perovskites samples sintered at 1180 °C, 1230 °C, 1280 °C temperatures contain a single phase similar to makedonite (Fig. 1a and 1b). The variation of the lattice constants with temperature has been obtained (Table 1).

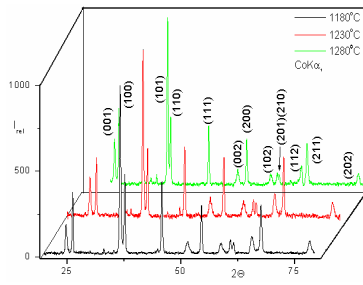


**Figure 1a:** Diffractograms of  $\text{Pb}_{0.84}\text{Ce}_{0.08}(\text{Ti}_{0.98}\text{Mn}_{0.02})\text{O}_3$  perovskites samples sintered at various temperatures.

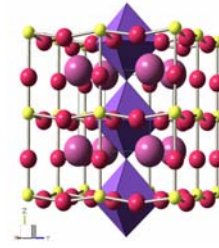


**Figure 1b:** Unit cell of  $\text{Pb}_{0.88}\text{Ce}_{0.08}\text{Ti}_{0.98}\text{Mn}_{0.02}\text{O}_3$  (yellow sphere – Ti/Mn cations; purple sphere – Pb/Ce cations; red sphere – oxygen anions; violet polyhedra –  $(\text{Ti}, \text{Mn})\text{O}_6$ ).

SANS experimental curves presents Porod region (Fig. 2). Porod analysis is a common technique used in the characterization of two-phase systems. For a sample that contains sharp interfaces between two regions with different scattering length densities  $\Delta\rho$ , the scattering intensity has the asymptotic form (Porod's law):

$$(d\Sigma/d\Omega)(Q) = K_p Q^{-4} + B,$$

where B is a (small) residual background term,  $K_p$  is the Porod constant.

$K_p [= 2\pi(S/V)(\Delta\rho)^2]$  and  $S/V$  is the specific surface.  $K_p$  is usually found experimentally by making a Porod plot of  $I(Q)Q^4$  versus  $Q^2$  after subtraction of B. The Porod constant will permit the characterization of the pores in each sample (Table1).

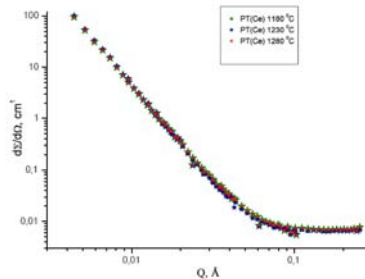


**Figure 2:** Experimental SANS curves of  $\text{Pb}_{0.84}\text{Ce}_{0.08}(\text{Ti}_{0.98}\text{Mn}_{0.02})\text{O}_3$  perovskites samples sintered at various temperatures.

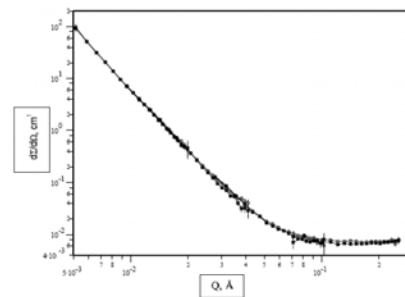


**Figure 3:** Experimental SANS curves of  $\text{Pb}_{0.84}\text{Ce}_{0.08}(\text{Ti}_{0.98}\text{Mn}_{0.02})\text{O}_3$  sample prepared at  $1180^\circ\text{C}$  and of the same sample kept in  $\text{D}_2\text{O}$  water for 48 hours.

**Table 1:** Porod constant and unit cell parameters variation with temperature for the  $\text{Pb}_{0.84}\text{Ce}_{0.08}(\text{Ti}_{0.98}\text{Mn}_{0.02})\text{O}_3$  sample.

Sintering temperature, $^\circ\text{C}$	$K_p, 10^7 \text{ cm}^{-1} \text{ \AA}^{-1}$	a=b ( $\text{\AA}$ )	c( $\text{\AA}$ )
1180	0.58	3.957(1)	4.181(6)
1230	0.41	3.925(8)	4.140(7)
1280	0.43	3.938(3)	4.080(0)

$\text{Pb}_{0.84}\text{Ce}_{0.08}(\text{Ti}_{0.98}\text{Mn}_{0.02})\text{O}_3$  sample prepared at 1180 °C was kept in  $\text{D}_2\text{O}$  water for 48 hours. SANS curves of  $\text{Pb}_{0.84}\text{Ce}_{0.08}(\text{Ti}_{0.98}\text{Mn}_{0.02})\text{O}_3$  dry sample and those kept in  $\text{D}_2\text{O}$  water for 48 hours are presented in Fig. 3.


Detailed results analysis is in progress.

## References

- [1] J. F. Scott and C. A. Paz de Araujo, *Science* 246, (1989) 1400
- [2] S. L. Swartz and V. E. Woods, *Condens. Matter News* 1, (1992) 4
- [3] G. H. Haertling, *J. Vac. Sci. Technol. A* 9, (1991) 414
- [4] C. H. Ahm, R. H. Hammond, T. H. Geballe, M. R. Beasley, J.-M. Triscone, M. Decroux, O. Fischer, L. Antognazza, and K. Char, *Appl. Phys. Lett.* 70, (1997) 206
- [5] J. Pinteá, A-M. Moisin, A. Dumitru, *Rom. Rep. in Physics*, Vol. 56, N0.3 (2004) 441–444
- [6] A. Garg, D.C. Agrawal, *J. Mat. Sci: Mat in Electronics* 10 (1999) 649–652
- [7] A-M. Moisin, A. Dumitru, E. Andronescu, G. Ghitulica, *JOAM*, Vol. 8, No. 2 (2006) 553–554
- [8] E. Dimitriu, R. Ramer, F. Craciun, G. Prodan, V. Ciupina, *JOAM* , Vol. 8, No.1 (2006) 55–59





	<b>EXPERIMENTAL REPORT</b>	<b>GeNF SANS-1</b>
<b>Conformation of hydrophilic polymers hydrophobically modified by sterically-hindered phenols</b>		
<b>Proposer:</b>  <b>Co-Proposer(s):</b>	<b>Sergey Filippov<sup>1</sup>,</b> <sup>1</sup> Ústav makromolekulární chemie AV ČR, Prague, Czech Republic <b>Petr Štěpánek<sup>1</sup></b>	
<b>Experimental Team:</b> <b>User Group Leader:</b> <b>Instrument Responsible:</b>	<b>Petr Štěpánek<sup>1</sup></b> <b>Vasyl Haramus<sup>2</sup>,</b> <sup>2</sup> GKSS Research Centre Geesthacht, Germany	
<b>Date(s) of Experiment:</b>	1 <sup>st</sup> – 7 <sup>th</sup> May 2007	

## Objectives

Aim of this project was the investigation of polysaccharides (dextran and starch) hydrophobically modified by sterically-hindered phenols (SHP)<sup>1-2</sup>. They represent a novel class of amphiphilic molecules possessing an enhanced biological activity<sup>3</sup>. The solubility of such polymers may be controlled by varying the nature of the hydrophilic polymer and the degree of modification with biologically active units, which usually are hydrophobic substances. It is highly probable that a hydrophobic modification affects also a polymer's conformation including a persistence length and radius of gyration that also might affect the biological functionality of these perspective biomedical substances. Therefore the knowledge of a persistence length ( $l_p$ ) of the conjugate was of great importance.

We believe that for the first time a comparative systematic investigation of a conjugates' persistence length and  $R_g$  have been conducted so as to shuffle all possible reasons, which might influence a polymers' conformation in aqueous solution.

## Experiment

To assess a polymers molecular conformation a variety of parameters were varied:

*Degree of substitution (DS):* to estimate importance of a substitution degree, the conjugates were synthesized with different numbers of a modifier attached to a polymer chain. It was varying from 0.2 up to 10 mol.%.

*Hydrophobicity of substituent:* some of polymers possessed a modifier benzaldehyde (BA) which was twice less hydrophobic then sterically hindered phenols (SHP).

*Polymer's molecular weight:* All other things being equal, some of the polymers were synthesized with different molecular weights: 18.000, 37.000, 69.000 and 430.000 g/mole.

*Nature of polymer backbone:* a variety of polymers have been modified with sterically hindered phenols to validate biological functionality of conjugates. Among them dextrans and hydroxyethyl starch have been tested.

To evaluate  $R_g$  and  $l_p$  values two approaches were applied – a graphical analysis and fitting procedure.

The values of  $R_g$  were obtained using the Guinier approximation  $I(q) = I(0)\exp(-q^2 R_g^2/3)$  by plotting  $\ln I(q)$  of  $q^2$ . Another graphical approach was a plotting of  $I \times q$  values as a function of  $q$ . That allowed us to get information about a persistence length of the polymers. Fitting routines incorporate an extraction of  $R_g$  and persistence length values by fitting a scattering curve by Debye<sup>4</sup> and Sharp-Bloomfield<sup>5</sup> models.

## Achievements and Main Results

Figures 1a,b present the typical scattering curves of a dextran modified by a substituent with different hydrophobicity (SHP and BA), and the fit to Debye and Sharp-Bloomfield models.

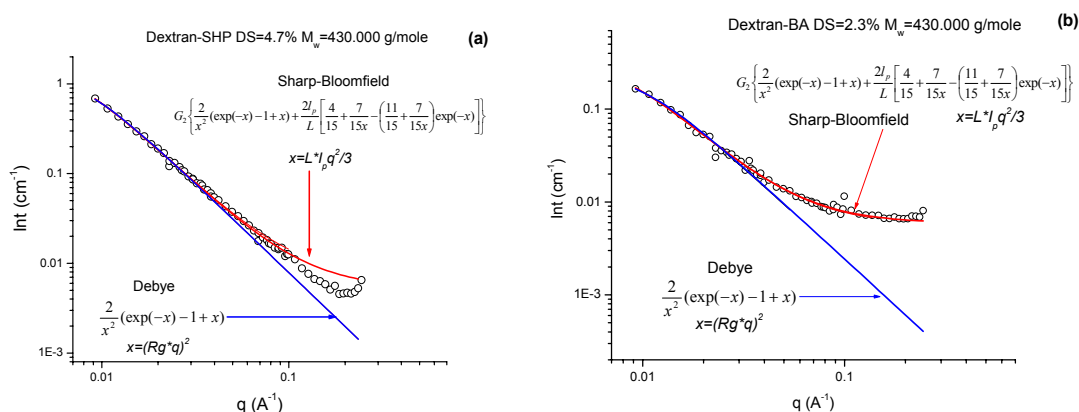


**Figure 1:** SANS data and best fits using Debye and Sharp-Bloomfield models for dextran samples modified by sterically hindered phenols **(a)** and benzaldehyde **(b)** substituent.

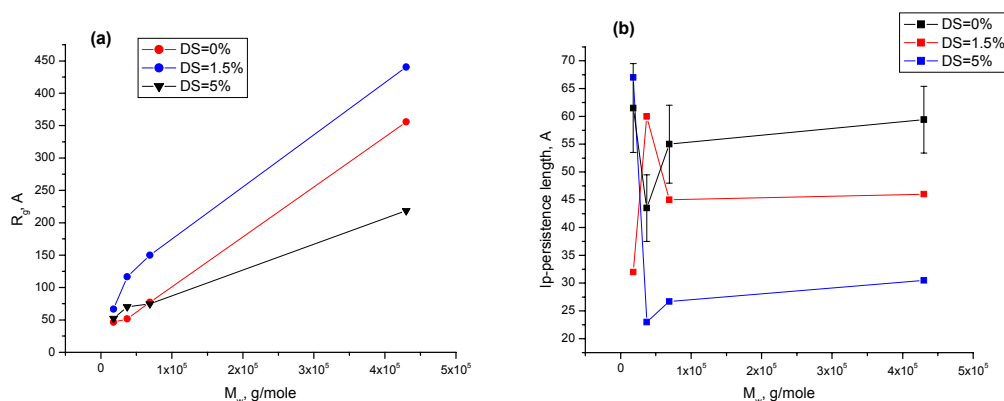


**Figure 2:** **(a)** Dependence of  $R_g$  as a function of a molecular weight for the dextran-SHP samples for different substitution degrees; **(b)** Dependence of  $l_p$  as a function of a molecular weight for the dextran-SHP samples for different substitution degrees.

One can see that Sharp-Bloomfield model much better describes a scattering profile than a Debye model. Apparently, it is because S-B model includes into consideration not only a coil regime but also a rodlike behavior. We found that for a vast majority of polymers it is possible to fit a whole scattering data range by S-B equation (Figure 1b). The results of the fitting together with the values obtained from a graphical analysis are presented in Table 1. It appears that there is a correlation between the data obtained from fitting and graphical approaches. There is a significant discrepancy between the data (marked red) only for the polymers with a highest molecular mass. Obviously, values of  $R_g$  for that polymers is too big for a fulfillment of a  $qR_g < 1$  condition which is mandatory for a correct Guinier analysis.

The dependence of  $R_g$  as a function of molecular mass for dextran-SHP samples are presented in Figure 2a. One can see that decreasing of a substitution degree makes this dependence steeper. It indicates that a conformation of polymers is changing with a modification. Dextran molecules possessing highest substitution degree have more compact conformation in contrast with non-modified or low-modified polymers. This fact is in accordance with the values of a persistence length obtained from S-B model (Figure 2b). That means

that a hydrophobic modification results in the decreasing of a persistence length making such polymers more compact comparing with non-modified polymers. The similar situation is observed for a substituent with lower hydrophobicity. That proves that a driving force of such changes is the hydrophobicity of the pendant. For samples with a starch as a backbone the situation is quite similar.

In other words, we observed that an insertion of hydrophobic groups into a hydrophilic chain results to a worsening of a thermodynamic quality of a solvent which leads to a shrinking of single molecules.


**Table 1:**

Substituent	M <sub>w</sub> , g/mole	DS	R <sub>g</sub> , nm Guinier	R <sub>g</sub> , nm Sh+BI	I <sub>p</sub> , Å Sh+BI	I <sub>p</sub> , Å Guinier
	18.000	0	3.3	4.6	61.5	-
SHP	18.000	1.6	13	6.6	32	51
SHP	18.000	4.7	6.0	5.1	67	-
	37.000	0	4.6	5.1	43.5	-
SHP	37.000	1.7	9.2	11.6	60	61.4
SHP	37.000	5.7	7	7	23	22.4
	69.000	0	8	7.7	55	61
SHP	69.000	1.6	10.9	15	45.3	46
SHP	69.000	5.2	12.5	7.4	26.7	27
	430.000	0	13.3	35.5	59.4	61
SHP	430.000	0.8	11.6	49	72.5	76
SHP	430.000	1.3	12.5	44	40(46)	57
SHP	430.000	4.7	11.9	21.8	30.5	25.5
SHP	430.000	5.2	10.4	7	15.8	21.8
	430.000	0	13.3	35.5	59.4	61
BA	430.000	2.3	11.7	18.8	56	76
BA	430.000	6.8	12.1	23.7	89	102
BA	430.000	10.3	11.5	19.7	35	41.6
	37.000	0	4.6	5.1	43.5	-
BA	37.000	0.9	5.1	6.5	49	57
BA	37.000	2.5	7.4	8.9	73	83
BA	37.000	9.7	7.8	6.2	27	27

## References

- [1] D. Aref'ev, N. Domnina, E. Komarova, A. Bilibin, Eur. Polym. J. 36 (2000) 857
- [2] O.Yu. Sergeeva, D. V. Aref'ev, N.S. Domnina, E.A. Komarova, Russian Journal of Applied Chemistry 78 (2005) 940
- [3] N. S. Domnina, O.Yu. Sergeeva, N. K. Merkulova, M. G. Pliss, R. S. Khrustaleva, Psychopharmacology and Biological Narcology (in Russian) 2 (2002) 391
- [4] Debye, P. J. Phys. Colloid Chem. (1947), 51, 18
- [5] Sharp, P.; Bloomfield, V. A. Biopolymers (1968), 6, 1201



	<b>EXPERIMENTAL REPORT</b>	<b>GeNF SANS-1</b>
<b>The study of evolution of fractal properties of amorphous Zr, Zn, Ti and Ce-based xerogels by SANS</b>		
<b>Proposer:</b>	<b>S. V. Grigoriev<sup>1</sup></b> , <sup>1</sup> Petersburg Nuclear Physics Institute, Gatchina, Russia	
<b>Co-Proposer(s):</b>	<b>V. K. Ivanov<sup>2</sup></b> , <sup>2</sup> Institute of General and Inorganic Chemistry, Moscow, Russia	
<b>Experimental Team:</b>	<b>G. P. Kopitsa<sup>1</sup></b>	
<b>User Group Leader:</b>	<b>S. V. Grigoriev<sup>1</sup></b>	
<b>Instrument Responsible:</b>	<b>Vasyl Haramus<sup>3</sup></b> , <sup>3</sup> GKSS Research Centre Geesthacht, Germany	
<b>Date(s) of Experiment:</b>	11 <sup>th</sup> – 16 <sup>th</sup> April 2007	

### Objective

The **goal** of this proposal is to study evolution of fractal properties of amorphous and semi-amorphous xerogels (including Zn-, Ti-, Zr- and Ce-based xerogels) during both thermal decomposition and hydrothermal treatment resulting in formation of nanocrystalline oxide materials by means of small-angle neutron scattering (SANS).

Recently it was established that xerogels of several metal hydroxides may possess surface or volume fractal properties [1–3]. It should be noted that methods of xerogels synthesis are well established and reproducible, while variation of synthetic conditions allows to change composition and structure of xerogels, so these materials can be judged to be promising model objects which can be used in study of peculiarities of fractal properties evolution during various physico-chemical processes.

According to several general principles [3–6], any solid-state (for instance topochemical) transformation should obviously result in change of fractal dimension of reactant or disappearance of its fractal structure, but the corresponding data is nearly absent. Our previous results indicate that thermal decomposition of salts of 3d metals can result in formation of oxide materials with surface fractal properties [7,8]. It was found that formation of fractals during topochemical reactions is probably a fundamental law, and such a supposition was confirmed by analysis of surface of various individual oxides including zirconia, ceria, iron(III) oxide, tungsten oxide etc. Thus we can also suppose that decomposition of xerogels under mild conditions can preserve their fractal structure so that resulting oxide nanopowders will be also mass or surface fractals. In turn, fractal dimension of the powders will depend on conditions of thermal treatment and nature of precursor.

In this project evolution of fractal properties will be examined by analysis of structure of nanocrystalline samples obtained by thermal decomposition and hydrothermal treatment of xerogels. It is planned to combine investigation of fractal properties of the samples by means of SANS with examination of mechanism of high temperature processes and properties of resulting nanopowders by other methods including *in situ* Calvet calorimetry, electron microscopy, TGA, IR, XRD, BET and several other techniques already used by the authors during study of both solid state and hydrothermal processes at elevated temperatures [9–11].

### Experiment

Five series of the samples of Zr, Zn, Ce and Ti-based xerogels, prepared by sol-gel method, and its evolution at different stages of the thermal decomposition and hydrothermal treatment were studied. The samples were kept in quartz cells with a path length of 1 mm.

## Achievements and Main Results

### 1. The amorphous xerogels ZrO<sub>2</sub>

Figure 1 shows the scattering curves  $d\Sigma(q)/d\Omega$  of the check sample of the amorphous xerogel ZrO<sub>2</sub> and samples obtained at different stages of the hydrothermal treatment ( $T_h$ ). According to this figure, the increase of  $d\Sigma(q)/d\Omega$  occurs with the increasing of the temperature  $T_h$ . It indicates that the fluctuations of the nuclear density in the amorphous xerogel ZrO<sub>2</sub> increase with the increasing of  $T_h$ . At once this increase is visibly uneven and depend on the treatment temperature  $T_h$ .

The analysis of the experimental data shown that, firstly, the check sample of the amorphous xerogel ZrO<sub>2</sub> consists of aggregates with fractal surface ( $D_s = 6 - n = 2.49 \pm 0.14$ ) that are formed from the initial small monodisperse monomer particles. It verify results obtained in our early work [12], where the fractal properties of the amorphous xerogels ZrO<sub>2</sub> with different acidity  $pH$  of medium were studied. Secondly, it was found that the hydrothermal treatment results in the sharp grown of the size of the initial monomer particles from  $R_C \approx 2$  nm (check sample) to 20 nm (at  $T_h = 240^\circ\text{C}$ ). At once, as is seen from figure 1, these particles have the strongly developed surface with the fractal dimension  $D_s = 2.44 \pm 0.06$  which is practically equal to  $D_s$  of aggregates in the check sample.

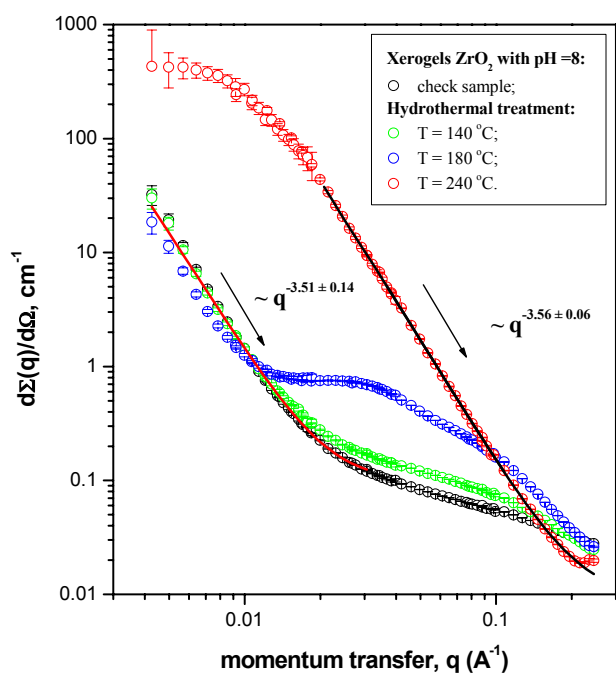


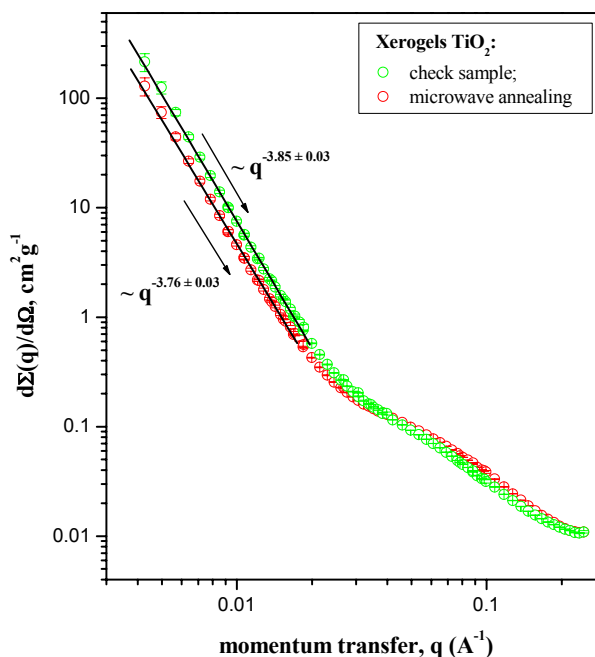
**Figure 1:**

Momentum-transfer dependences of the SANS cross section  $d\Sigma(q)/d\Omega$  from the samples of ZrO<sub>2</sub> obtained at different stages of the hydrothermal treatment.

The momentum dependences of the SANS cross section  $d\Sigma(q)/d\Omega$  measured for the check sample of the amorphous xerogel TiO<sub>2</sub> and one obtained after the microwave annealing are shown in Fig. 2 on the log-log scale. As is seen in this figure, for both samples the  $d\Sigma(q)/d\Omega$  behaves as  $q^{-n}$  at  $q < q \approx 0.025 \text{ \AA}^{-1}$ . It was found that the exponent  $n$  is equal to  $3.85 \pm 0.03$  and  $3.76 \pm 0.03$  for the samples before and after microwave annealing, respectively. It correspond to the scattering on the surface fractal with the dimension  $D_s = 2.15$  and  $2.24$ , respectively. The obtained results clearly shown that the effect of the microwave treatment on the structure of the amorphous xerogel TiO<sub>2</sub> occurs at  $q < 0.025 \text{ \AA}^{-1}$  and consists in the increasing of the fractal dimension  $D_s$ . At high- $q$  region, as is seen from figure 2, this effect is insignificant.

**Figure 2:**

Momentum-transfer dependences of the SANS cross section  $d\Sigma(q)/d\Omega$  from the check and microwave annealing samples of  $\text{TiO}_2$ .




The treatment of the data for samples of Zn and Fe-based xerogels and interpretation of all obtained data are in progress.

## References

- [1] W. L. Huang, S. H. Cui, K. M. Liang et al.; J. Phys. Chem. Solids. 2002. V. 63. P.645–650
- [2] T. López, F. Rojas, R. Alexander-Katz et al.; J. Solid State Chem. 2004. V. 177. pp. 1873–1885
- [3] A. C. Geiculescu, H. J. Rack. J. Non-Cryst. Solids. 2002. V. 306. P. 30–41
- [4] H. Schmalzried. Chemical kinetics of solids. Weinheim: VCH, 1995. 433 p
- [5] A. Galwey, Thermochim. Acta. 2000. V. 355. pp. 181–238
- [6] W. G. Rothschild. Fractals in Chemistry. Wiley-Interscience, 1998, 231 p
- [7] V. K. Ivanov, A.N. Baranov, N. N. Oleinikov, Yu. D. Tret'yakov. Russ. J. Inorg. Chem. 2002. V. 47. pp. 1769–1772
- [8] V. K. Ivanov, A. N. Baranov, N. N. Oleinikov, Yu. D. Tret'yakov. Inorganic Materials. 2002. V. 38. pp. 1224–1227
- [9] A. E. Baranchikov, V. K. Ivanov, N. N. Oleynikov et al.; Mendeleev Commun. 2004. pp.143–144
- [10] P. E. Meskin, V. K. Ivanov, A. E. Baranchikov et al.; Ultrasonics Sonochemistry. 2006. V. 13. pp. 47–53
- [11] A. S. Vanetsev, V. K. Ivanov, N. N. Oleynikov et al.; Mendeleev Commun. 2004. pp.145–146
- [12] G. P. Kopitsa, V. K. Ivanov, S. V. Grigoriev, P. E. Meskin, O. S. Polezhaeva and V. M. Garamus. JETP Letters. 2007. V. 85(2), p.132





	<b>EXPERIMENTAL REPORT</b>	<b>GeNF SANS-1</b>
<b>Interaction of Angiotension II with lipid membranes</b>		
<b>Proposer:</b>	<b>J. Preu<sup>1</sup></b> , <sup>1</sup> PSI, Villigen, Switzerland	
<b>Co-Proposer(s):</b>	<b>T. Gutberlet<sup>1</sup>, T. Heimborg<sup>2</sup></b> , <sup>2</sup> NBI, Copenhagen, Denmark	
<b>Experimental Team:</b>		
<b>User Group Leader:</b>	<b>T. Gutberlet<sup>1</sup></b>	
<b>Instrument Responsible:</b>	<b>Vasyl Haramus<sup>3</sup></b> , <sup>3</sup> GKSS Research Centre Geesthacht, Germany	
<b>Date(s) of Experiment:</b>	<b>3<sup>rd</sup> – 8<sup>th</sup> October 2007</b>	

## Objectives

The renin-angiotensin system plays a critical role in circulatory homeostasis. Part of this system is the peptide hormone Angiotensin II (Ang II), a potent vasoconstrictor that aids the in blood pressure regulation, as well as in body fluid balance maintenance. Ang II derives from the precursor angiotensinogen, through enzymatic reaction catalyzed by renin and the angiotensin converting enzyme (ACE). On the heart, acting in both endocrine and paracrine fashions Ang II regulates contractility, remodelling, growth, apoptosis, and reduces cell coupling and conduction velocity in cardiac muscles. Ang II has two major receptor subtypes, the Ang II type 1 receptor (AT<sub>1</sub>-receptor) and the Ang II type 2 receptor (AT<sub>2</sub>-receptor). Although both types of receptors were found in cardiac muscle cells, only AT<sub>1</sub>-receptor was found to mediate classical cardiovascular functions like blood pressure elevation, vasoconstriction, aldosterone release and renal absorption of water and sodium.

In renal diseases or hypertension, changes in the renin-angiotensin system occur. Therefore hypertension can be treated by  $\beta$ -blockers, inhibiting the conversion of angiotensinogen to Angiotension I, or by specific inhibition of the AT<sub>1</sub>-receptor by Ang II antagonists like losartan and its active derivate E-3174. Using differential scanning calorimetry (DSC) and electron spin resonance spectroscopy (ESR) Theodoropoulou *et al.* studied the molecular basis of the interaction of losartan with membranes [1]. Mimicking the cell membrane by using dimyristoyl phosphatidylcholin (DMPC) dispersions, they observed with increased concentration of losartan a thermodynamic behavior similar as found in dispersions of the charged lipid dimyristoyl phosphatidylglycerol (DMPG).

In the present study we try to elucidate the structural changes induced by Ang. II on different lipid dispersions dependent on temperature and Ang II concentration.

## Experiment

An aqueous buffer solution containing concentrations of 0.2 mM, 0.5 mM and 1 mM of the peptide hormone was prepared. The same amount of chain-deuterated DMPC was added to the Ang II-containing buffer. For all preparations a lipid concentration of 10 mM DMPG was used and unilamellar vesicles were produced by extrusion at a temperature above the main phase transition of the lipid. Pure D<sub>2</sub>O was used as solvent for all sample preparations. Measurements were done for three different temperatures, 15 °C, 22 °C and 35 °C.

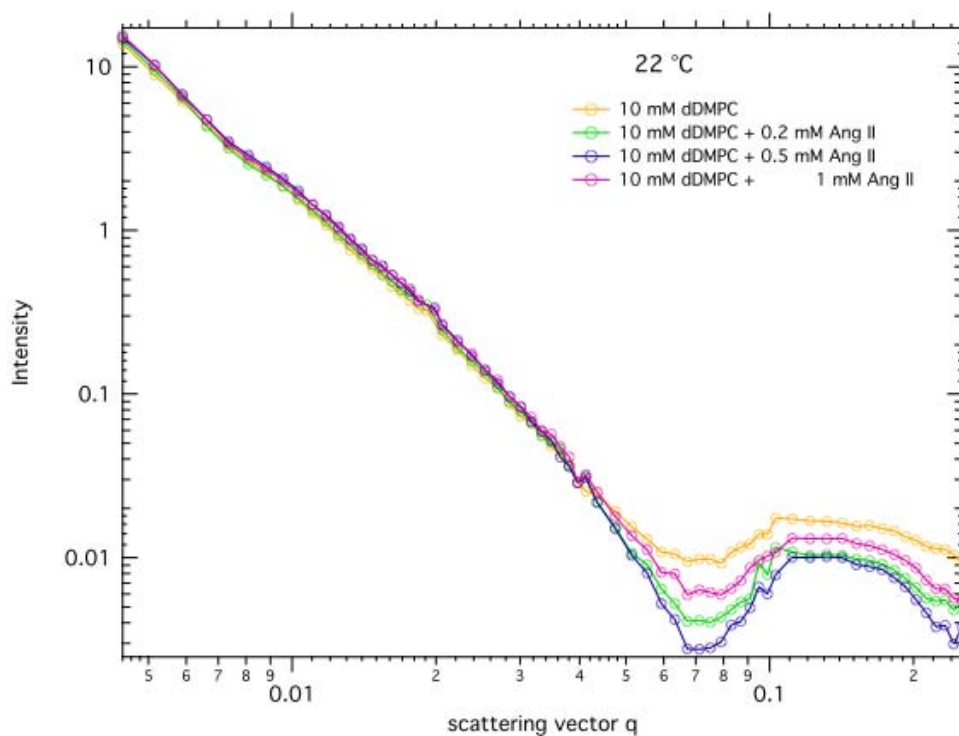



**Figure 1:** Scattering intensity ( $\text{cm}^{-1}$ ) as a function of the scattering vector  $q$  ( $\text{\AA}^{-1}$ ) for samples measured at  $22\text{ }^{\circ}\text{C}$  with Ang II concentrations of 0.2 mM, 0.5 mM and 1 mM.

### Achievements and Main Results

The SANS measurements provide evidence that there is only a weak interaction regarding structural changes between DMPC and Ang II at all measured temperatures. DSC studies of Losartan and DMPC showed a melting behaviour of the lipid system similar as found in pure DMPG. Similar DSC experiments of Ang II and DMPC showed only weak changes in the heat capacity profiles. These results would be consistent with the neutron scattering experiments. They present evidence that Ang II does not intercalate in the bilayer introducing charges into the membrane system. The size of the vesicles and the thickness of the bilayer remain unchanged, suggesting a different type of interaction e.g. adsorption by electrostatic interaction between Ang II and the lipid headgroup, which is subject of further investigations.

### Reference

- [1] Teodoropoulou et al., *Biochimica et Biophysica Acta* 1461 (1999), 135–146

	<b>EXPERIMENTAL REPORT</b>	<b>GeNF SANS-1</b>
<b>Small angle neutron scattering study of galectin-PEG conjugates</b>		
<b>Proposer:</b>	<b>L. He<sup>1,1</sup></b> , <sup>1</sup> Centre for Biomolecular Engineering, University of Queensland, St. Lucia, Australia	
<b>Co-Proposer(s):</b>	<b>A. Middelberg<sup>1</sup></b>	
<b>Experimental Team:</b>	<b>H. Wang<sup>1</sup></b>	
<b>User Group Leader:</b>	<b>A. Middelberg<sup>1</sup></b>	
<b>Instrument Responsible:</b>	<b>Vasyl Haramus<sup>2</sup></b> , <sup>2</sup> GKSS Research Centre Geesthacht, Germany	
<b>Date(s) of Experiment:</b>	10 <sup>th</sup> – 20 <sup>th</sup> September 2007	

## Objectives

The proposed project aims to study the structure of PEG-galectin conjugates. Poly(ethylene glycol)-conjugated proteins (i.e. PEGylated proteins) have attracted increasing attentions because PEGylation can significantly increase in vivo circulation half lives of therapeutic proteins while reducing immunogenicity [1]. The structure properties of PEG-protein conjugates however, have not been well understood. The SANS study of PEG-protein conjugates in this project will be focused on human Galectin-2 (hGal-2), a carbohydrate binding protein showing great potential for medical application. This study will potentially elucidate how PEG interacts with a protein, and subsequently reveal the functional roles of PEG in changing protein biological and physical properties.

## Experiment

s20 mM phosphate buffer containing 0.1 M NaCl and 0.1 M lactose was used to prepare amples of PEG, galectin-2 and PEG-galectin-2, and the ratio of D<sub>2</sub>O/H<sub>2</sub>O in the buffer was varied to give contrast variation. The quartz cuvettes (1 mm path length) containing the sample solutions were placed in a thermostatted sample holder to maintain a temperature of 20 °C.

## Achievements and Main Results

Our SANS experiments were started with free PEG-5000 in D<sub>2</sub>O. The results show that the free PEG molecules are highly hydrated in solution and it has typical feature of polymers in a good solvent, similar to those reported on PEG-3400 in literature [2]. PEG-galectin-2 conjugates were measured in 100 %, 42 % (matching point of protein) and 17.9 % (matching point of PEG) D<sub>2</sub>O. Due to poor contrast, scattering intensity in 42 % and 17.9 % D<sub>2</sub>O was very low, and direct determination of individual structure of PEG and galectin-2 from those contrast measurement was impossible. The data measured in 100 % D<sub>2</sub>O have a strong signal and are discussed in detail here. The spectra at different concentrations were normalized by dividing the scattering intensities through the concentration and were compared in Figure 1. At low scattering angle, the normalized scattering intensities at protein concentration of 1.97 mg/mL and 3.93 mg/mL are in good agreement with each other. However, the normalized intensity decrease when the concentration are increased to 8.23 mg/mL and 13.7 mg/mL, indicating that there are inter-particle interaction at high protein concentration. Guinier plot analysis shows that there is a concentration dependence of apparent radii of gyration of PEG-gal2, with the value decreasing from 32 Å at a concentration of 1.97 mg/mL to 26 Å at a concentration of 13.7 mg/mL. The results suggest that excluded volume effects, arising from steric clashes between PEG molecules at high concentration, constrain the


number of possible conformation of PEG and thus decrease the effective size of PEG-conjugates. Details analysis is currently being carried out to understand how PEG conformation of the conjugate is changed with concentration. This will potentially reveal structure-stability correlation of PEG-protein conjugates in solution.

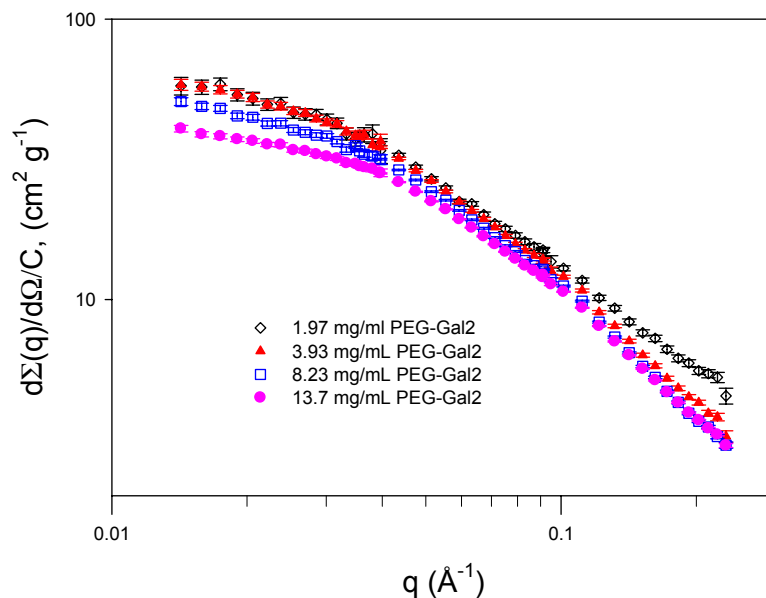


**Figure 1:** Normalized SANS spectra of PEG-galectin-2 conjugate in 20 mM phosphate buffer (0.1 M NaCl, 100 mM lactose, pH 7.2, D<sub>2</sub>O) at different protein concentrations. The spectra were normalized by dividing scattering intensity  $I$  with the conjugate concentration (based on the mass of protein only).

## References

- [1] Veronese, F. M.; Harris, J. M.; Preface – Introduction and overview of peptide and protein pegylation. *Advanced Drug Delivery Reviews* 54 (2002), 453–456.
- [2] Thiyagarajan, P.; Chaiko, D. J.; Hjelm, R. P.; A Neutron-Scattering Study of Poly(Ethylene Glycol) in Electrolyte-Solutions. *Macromolecules* 28 (1995), 7730–7736.

	<b>EXPERIMENTAL REPORT</b>	<b>GeNF SANS-1</b>
<b>Determination of microphase sugar concentrations in model biological membrane systems by SANS</b>		
<b>Proposer:</b> <b>Co-Proposer(s):</b>	<b>Gary Bryant</b> <sup>1</sup> , <sup>1</sup> RMIT University, Melbourne, Australia <b>Chris Garvey</b> <sup>2</sup> , <sup>2</sup> Institute for Environmental Research, ANSTO, Sydney, Australia	
<b>Experimental Team:</b> <b>User Group Leader:</b> <b>Instrument Responsible:</b>	<b>Ben Kent</b> <sup>1</sup> <b>Gary Bryant</b> <sup>1</sup> <b>Vasyl Haramus</b> <sup>3</sup> , <sup>3</sup> GKSS Research Centre Geesthacht, Germany	
<b>Date(s) of Experiment:</b>	2 <sup>nd</sup> –13 <sup>th</sup> July 2007	

## Objective

The presence of solutes such as sugars is known to inhibit deleterious phase changes in biological membranes at low hydration (eg [1–3]), such as the bilayer fluid lamellar  $L_{\alpha}$  to non-bilayer inverse hexagonal ( $H_{II}$ ) phase transition. While the effects of solutes on lipid phase behaviour are now well known, there is disagreement in the literature about the mechanism by which the solutes affect the lipid phase behaviour. Specifically, there is debate about whether the effects are caused by direct interactions between the solutes and the lipids ([4–6]), or by non-specific effects related to the volumetric, osmotic and solution properties of the solutes (eg [7–10]). Central to the resolution of this question is the location of the sugars within the lipid/water/sugar system.

Previously, Deme and Zemb [11] demonstrated using contrast variation SANS that an excess water/solute microphase exists in equilibrium with a lamellar lipid/water/solute microphase in fully hydrated bilayer lipid samples. Furthermore, the solute is preferentially excluded from the interlamellar region. Expanding on this work, the RMIT soft condensed matter physics group established the presence of a water/solute microphase in partially hydrated bilayer samples and the preferential exclusion of the sugar from the interlamellar region in these samples [12].

These experiments extend the RMIT group's previous work on bilayer samples to determine the existence of a separate water/solute microphase in  $H_{II}$  systems and to quantify the degree to which sugar is excluded from the water core surrounded by the lipid columns. The results from these experiments will be used to elucidate the mechanisms by which solutes inhibit deleterious phase changes in biological membranes, and to improve theoretical models which currently fit the data only semi-quantitatively [13], probably because they assume that all of the sugars reside between the membranes.

## Experiment

The synthetic phospholipid 1,2-Dioleoyl-*sn*-Glycero-3-Phosphoethanolamine (DOPE) 50 % hydration by weight was used as a model system. Samples were prepared with pure DOPE and Glucose- $d_7$ :DOPE: 0.5:1 at four  $D_2O/H_2O$  ratios: 0 %, 40 %, 70 % and 100 %  $D_2O$ . Previous small angle x-ray scattering (SAXS) experiments established these samples are in the  $H_{II}$  phase at 25 °C. Background samples equal to the equivalent  $D_2O$  content (0 %, 23.5 %, 38.5 % and 53.5 %  $D_2O$ ) of each sample were measured and subtracted from the scattering data. All measurements were performed at 25 °C.

The distribution of sugar throughout the system was determined by applying analysis similar to that of Deme and Zemb [11]. We obtained SANS measurements of each samples for each  $D_2O / H_2O$  contrast values above in the  $Q$  range  $4.98 \times 10^{-3}$  to  $2.44 \times 10^{-1} \text{ \AA}^{-1}$ . Contrast match points were then extrapolated from graphs of square root of intensity vs contrast for various values of  $q$  in the low  $Q$  decay region, and used in analysis as described in [12].

### Achievements and Main Results

Figures 1(a) and 2(a) show on an absolute scale the SANS scattering curves for the pure lipid and lipid + glucose samples respectively. The square root of intensity vs. %  $D_2O$  plots for several values of  $Q$  are shown to the right – Figures 1(b) and 2(b).

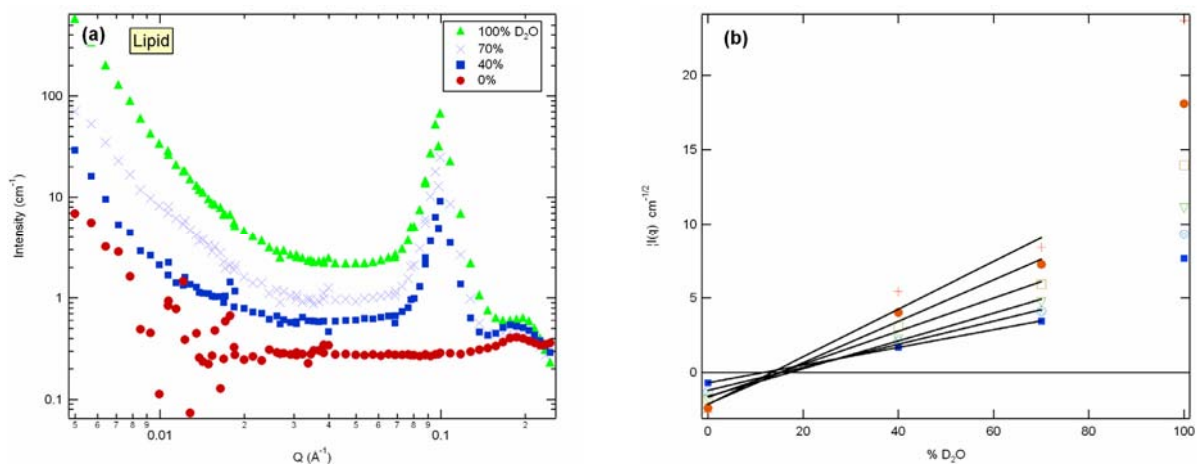
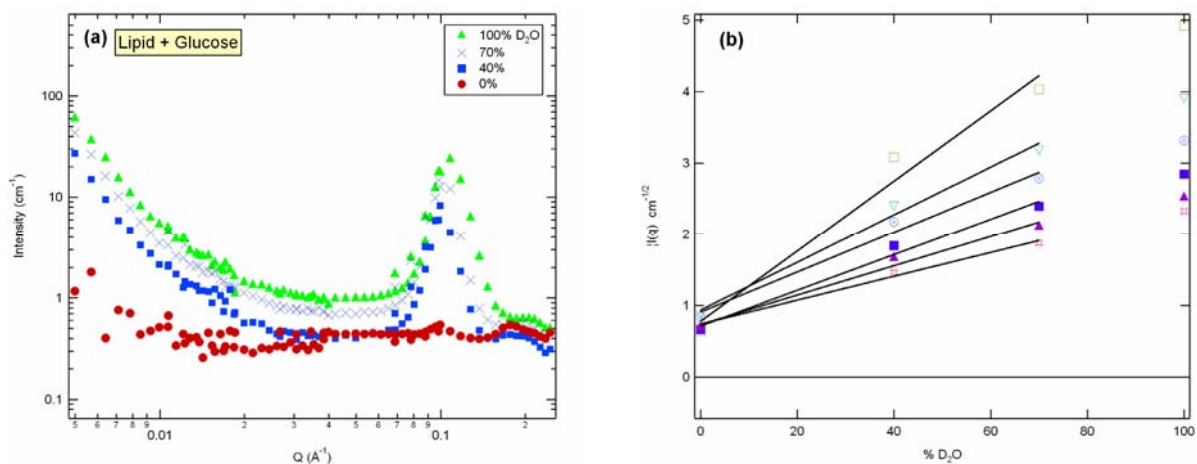


**Figure 1a, 1b:** Pure lipid samples – SANS scattering curves for each water contrast (left), the corresponding square root of Intensity vs. % $D_2O$  plots (right) for various values of  $Q$ .



**Figures 2a, 2b:** Lipid + Glucose samples – SANS scattering curves for each water contrast (left), the corresponding square root of Intensity vs. % $D_2O$  plots (right) for various values of  $Q$ .

Lines of best fit – shown in black – have been fitted to the three lower  $D_2O$  contrasts. The 100 %  $D_2O$  contrast samples were found to have inconsistent results with the trend of the other contrasts and were disregarded in the determination of contrast match points. The contrast match points were calculated to correspond to  $(15.3 \pm 1.44)\%$   $D_2O$  for the pure lipid samples and  $(-30.1 \pm 9.5)\%$   $D_2O$  for the lipid + glucose samples. This corresponds to scattering length densities of the solvent matching the membrane phase of  $5.03 \times 10^{-7} \text{ \AA}^{-2}$  and  $1.53 \times 10^{-6} \text{ \AA}^{-2}$  for the lipid and lipid + glucose systems respectively.


Following the analysis described by Deme and Zemb [12] the glucose volume fraction of the membrane phase is calculated to be  $-0.060 \pm 0.016$ . Clearly this is unphysical. Assuming the contrast match point for the lipid samples is correct, total exclusion of glucose from the membrane phase would result in a lipid + glucose contrast match point of 3.5% D<sub>2</sub>O, while total exclusion of glucose from the excess phase would yield a contrast match point of 19 % D<sub>2</sub>O. It is as yet unclear why the lipid + glucose samples have contrast match point outside this range. It is possible that measurements taken near the contrast match point are disproportionately affected by incoherent background intensity. Other sources of error are also being investigated. Analysis is continuing. Results have been presented at the 6th AINSE/ANBUG Neutron Scattering Symposium, Sydney, Australia, 2007.

## References

- [1] Crowe, J.H., L.M. Crowe, and D. Chapman, *Preservation of Membranes in Anhydrobiotic Organisms: The Role of Trehalose*. *Science* (Washington, D. C., 1883-), 1984. 223: p. 701–703
- [2] Crowe, J.H. and L.M. Crowe, *Effects of Dehydration on Membranes and Membrane Stabilization at Low Water Activities*. Academic Press, in *Biological Membranes*, D. Chapman, Editor. 1984: London
- [3] Crowe, J.H. and L.M. Crowe, *Stabilization of Membranes in Anhydrobiotic Organisms.*, in *Membranes, Metabolism and Dry Organisms.*, A.C. Leopold, Editor. 1986, Cornell University Press: New York
- [4] Crowe, L.M., D.S. Reid, and J.H. Crowe, *Is Trehalose Special for preserving Dry Biomaterials?* *Biophysical Journal*, 1996. 71: p. 2087–2093
- [5] Crowe, J.H. and L.M. Crowe, *Evidence for Direct Interaction between Disaccharides and Dry Phospholipids*. *Cryobiology*, 1993. 30: p. 226–227
- [6] Oliver, A.E., L.M. Crowe, and J.H. Crowe, *Methods for dehydration-tolerance: Depression of the phase transition temperature in dry membranes and carbohydrate vitrification*. *Seed Science Research*, 1998. 8: p. 211–221
- [7] Koster, K.L., K.J. Maddocks, and G. Bryant, *Exclusion of maltodextrins from phosphatidylcholine multilayers during dehydration: effects on membrane phase behaviour*. *European Biophysics Journal*, 2003. 32: p. 96–105
- [8] Bryant, G., K.L. Koster, and J. Wolfe, *Membrane behaviour in seeds and other systems at low water content: the various effects of solutes*. *Seed Science Research*, 2001. 11: p. 17–25
- [9] Koster, K.L., Y. Ping Lei, M. Anderson, S. Martin, and G. Bryant, *Effects of vitrified and nonvitrified sugars on phosphatidylcholine fluid-to-gel phase transitions*. *Biophysical Journal*, 2000. 78(4): p. 1932
- [10] Wolfe, J. and G. Bryant, *Cellular cryobiology: thermodynamic and mechanical effects*. *International Journal of Refrigeration*, 2001. 24: p. 438–450
- [11] Demé, B. and T. Zemb, *Measurement of sugar depletion from uncharged lamellar phases by SANS contrast variation*. *Journal of Applied Crystallography*, 2000. 33: p. 569–573
- [12] Lenne, T., G. Bryant, C.J. Garvey, U. Keiderling, and K.L. Koster, *Location of sugars in multilamellar membranes at low hydration*. *Physica B: Condensed Matter*, 2006. 385-386(Part 2): p. 862–864
- [13] Lenné, T., G. Bryant, R. Holcomb and K. L. Koster, *How much solute is needed to inhibit the gel to fluid membrane phase transition at low hydration?*, *Biochim. Biophys. Acta*, 2007, doi:10.1016/j.bbamem.2007.01.008





	<b>EXPERIMENTAL REPORT</b>	<b>GeNF SANS-1</b>
<b>A SANS study of polyfluorene phase behaviour in solution</b>		
<b>Proposer:</b>	<b>Matti Knaapila<sup>1</sup></b> , <sup>1</sup> MAX-lab, Lund University, Sweden	
<b>Co-Proposer(s):</b>	<b>Andy Monkman<sup>2</sup></b> , <sup>2</sup> University of Durham, UK	
<b>Experimental Team:</b>		
<b>User Group Leader:</b>	<b>Andy Monkman<sup>2</sup></b>	
<b>Instrument Responsible:</b>	<b>Vasyl Haramus<sup>3</sup></b> , <sup>3</sup> GKSS Research Centre Geesthacht, Germany	
<b>Date(s) of Experiment:</b>	28 <sup>th</sup> September – 3 <sup>rd</sup> October 2007	

## Objective

Polyfluorenes are a specific class of electroluminescent polymers. Structurally, they are so called hairy rods consisting of a rodlike backbone with flexible side chains. We have recently clarified how the phase behaviour of linear and branched side chain polyfluorene solutions depends on the solvent quality[1–2]. Next we have detailed how the phase behaviour depends on the side chain quality[3]. For instance, we have found that the shorter side chain polyfluorenes form large (10–100 nm) sheet-like assemblies (thickness of 2–3 nm). The larger length scale structures of these sheets show an odd-even dependence on the side chain (spacer) length – the sheets of poly(9,9-hexylfluorene) and poly(9,9-octylfluorene) are broader and thinner, whereas poly(9,9-heptylfluorene) and poly(9,9-nonylfluorene) sheets are thicker with a putative double layer structure. Poly(9,9-dodecylfluorene) does not follow this sequence and only part of the polymer is assembled into a sheet-like structure, the rest remaining dissolved at the molecular level. As a natural continuation, the idea of present work was to clarify how this picture changes when the degree of side chain branching is varied. To study this, a selection of block copolymers was synthesized so that the degree of branching varied while the number of side chain beds remained constant.

## Experiment

The phase behavior of poly(9,9-dioctylfluorene)/(9,9-bis-(2-ethylhexyl)-fluorene) random copolymer, where the ratio of octyl chains over ethylhexyl chains varied from one extreme to the another, was studied in methylcyclohexane. A poly[9,9-bis(2-ethylhexyl)-fluorene-2,7-diyl] with fluorenone units was used for comparison.

## Achievements and Main Results


The experiment was very successful and the beamline performance was excellent (see examples of the data in Fig. 1). The sheets and isotropic rodlike polymer phases were found and the phase transition determined as a function of temperature and the degree of branching. The side chain branching was found to decrease the sheet-rod transition temperature and the sheets were found when the fraction of octyl side chains is at least 90 %. The SANS data are being combined with SAXS, WAXS, and photoabsorption spectroscopy data plus the prediction of the mean field theory but it is yet too early to make final conclusions [4].

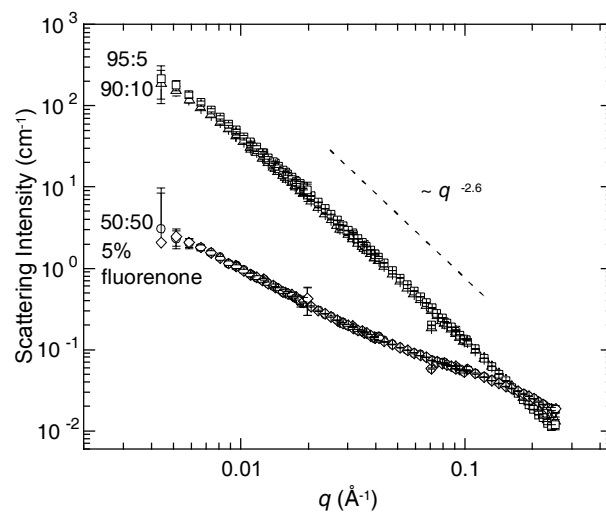


**Figure 1:** Typical SANS curves obtained during the last GKSS measurement. The given ratios refer to the copolymer composition.

## References

- [1] M. Knaapila, V. M. Garamus et al. *Macromolecules*, 2006, Vol. 39, pp. 6505–6512
- [2] M. Knaapila, L. Almásy, V. M. Garamus et al. submitted to *Polymer*
- [3] M. Knaapila, F. B. Dias, V. M. Garamus et al. *Macromolecules*, 2007, Vol. 40, pp. 9398–9405
- [4] M. Knaapila, R. Stepanyan, M. Torkkeli, V. M. Garamus et al. manuscript in preparation

	<b>EXPERIMENTAL REPORT</b>	<b>GeNF SANS-1</b>
<b>SANS on the pre-pore state of the <math>\alpha</math>-Toxin <i>Staphylococcus aureus</i></b>		
<b>Proposer:</b> <b>Co-Proposer(s):</b>	<b>Christian Meesters<sup>1</sup></b> , <sup>1</sup> University of Mainz, Inst. of Mol. Biophysics	
<b>Experimental Team:</b> <b>User Group Leader:</b> <b>Instrument Responsible:</b>	<b>Antje Brack<sup>1</sup>, Hermann Hartmann<sup>1</sup></b> <b>Heinz Decker<sup>1</sup></b> <b>Vasyl Haramus<sup>2</sup></b> , <sup>2</sup> GKSS Research Centre Geesthacht, Germany	
<b>Date(s) of Experiment:</b>	28 <sup>th</sup> – 30 <sup>th</sup> March, 8 <sup>th</sup> – 14 <sup>th</sup> November 2007	

## Objectives

$\alpha$ -toxin (or  $\alpha$ -hemolysin) from the gram-positive pathogenic bacterium *S. aureus* is a well-studied model to elucidate membrane-insertion mechanisms of soluble proteins. The protein is toxic for a wide range of mammalian cells, particularly erythrocytes, hence the name  $\alpha$ -hemolysin. It serves primarily as a tool to convert host tissue into nutrient ground for the bacteria [1]. The protein is secreted as a water-soluble, 34-kDa monomer that binds to target membranes and then oligomerizes to form membrane-inserted heptameric channels [2, 3]. While the crystal structure of the final pore was solved [4], intermediate structures are yet to be elucidated.

We possess a mutant (H35R) which assembles onto the membrane, but is unable to form a channel [5]. This state can be considered a pre-pore state and elucidating its structure could give the long wanted structure of an intermediate conformation of the pore forming process.

SANS is the method of choice as assembly of the pre-pore requires a membrane and SANS allows distinguishing between lipid and protein. Taken the C7-symmetry of the pore, respectively pre-pore, into account SANS data can allow rigid body modelling based on the structure of the pre-pore.

## Experiment

We aimed to match the lipids as the demand for preparing various solutions containing protein would exceed the amount of protein available. Similar approaches are followed in biochemistry occasionally [6]. Since different relative deuterium concentrations are required for matching different, yet similar, lipid compositions [6, 7], as a first step vesicle emulsions with different D<sub>2</sub>O/H<sub>2</sub>O mixtures were prepared to find the right deuterium content for our lipid composition. All vesicles used were composed of 30 % cholesterol (Sigma, C8667), 15 % L- $\alpha$ -Phosphatidyl-ethanolamine (Sigma, P6386), 15 % 1,2-Diacyl-sn-glycero-3-phospho-L-serine (Sigma, P6641), and 40 % N-acyl-4-sphingeny-1-O-phosphorylcholine (mainly 16:0; Sigma, S0756); all molar ratios. Lipids were dried under a stream of dry nitrogen and sequentially subjected to vacuum (< 1 mbar). As vesicles of the required diameter of not more than 50 nm cannot be considered as stable, the dried lipids were dissolved in buffer (70 mM Na-Phosphatebuffer, pH 7.2) at GKSS and subsequently extruded. After subtracting the buffer intensity at zero scattering angle was estimated using the Guinier approximation.

For the actual measurement protein (the pre-pore forming mutant and the wild type protein as reference) was prepared as outlined [8] and incubated with vesicles of 140 nm diameter with log-norm distribution (as controlled by dynamical light scattering) under matching conditions (see below) for several hours to achieve a maximum yield of membrane-bound protein. The samples subsequently got concentrated using membrane filters.

## Achievements and Main Results

The match point for our lipid composition could be determined as  $14.3 \pm 2.6$  % D (see figure 1, left part), which is in good agreement with results reported earlier [6]. There are only four experimental points as two samples were partly lost during the extruding process and could not be analysed.

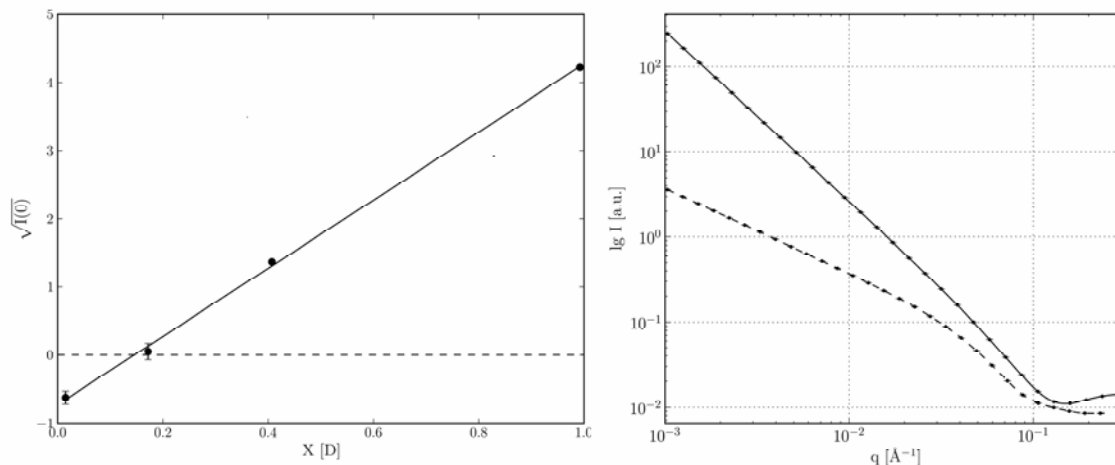



**Figure 1:** Left: Forward scattering of the lipid mixture with different amount of deuterium. Plotted is the root of  $I(q)$  vs. the fraction of deuterium. Right: Scattering curves of wild type protein (continuous line) and pre-pore protein (dashed line) with sample error bars. (see text)

The actual scattering experiment turned out to be less successful: While matching of the lipids was achieved and scattering intensity was sufficiently high to yield interpretable curves, the protein apparently was aggregated. To which degree cannot be answered now. We intend to examine the sample by electron microscopy, as preliminary data treatment indicated the presence of disk-like structures. This points to a more specific aggregation in terms of (para-)crystalline arrays on the membranes, due to too dense protein.

## References

- [1] Dinges, M. M., Orwin, P. M. and Schlievert, P. M.; Clin Microbiol Rev 13 (2000), 16–34.
- [2] Gouaux, J. E.; Braha, O.; Hobaugh, M. R.; Song, L.; Cheley, S.; Shustak, C. and Bayley, H.; Proc Natl Acad Sci U S A 91 (1994), 12828–12831.
- [3] Valeva, A.; Palmer, M. and Bhakdi, S.; Biochemistry 36 (1997), 13298–304.
- [4] Song, L.; Hobaugh, M. R.; Shustak, C.; Cheley, S.; Bayley, H. and Gouaux, J. E.; Science 274 (1996), 1859–66.
- [5] Valeva, A.; Weisser, A.; Walker, B.; Kehoe, M.; Bayley, H.; Bhakdi, S. and Palmer, M.; Embo J 15 (1996), 1857–64.
- [6] Bu, Z.; Wang, L. and Kendall, D. A.; J Mol Biol 332 (2003), 23–30.
- [7] Gilbert, R.J. et al.; J Mol Biol 293 (1999), 1145–1160.
- [8] Palmer, M.; Jursch, R.; Weller, U.; Valeva, A.; Hilgert, K.; Kehoe, M. and Bhakdi, S.; J Biol Chem 268 (1993), 11959–11962.

	<b>EXPERIMENTAL REPORT</b>	<b>GeNF SANS-1</b>
<b>Determination of the partitioning of emulsifiers in emulsion in dependence of their concentrations</b>		
<b>Proposer:</b> Kathleen Oehlke <sup>1</sup> , <sup>1</sup> Food Technology Division, CAU Kiel <b>Co-Proposer(s):</b>		
<b>Experimental Team:</b> <b>User Group Leader:</b> Karin Schwarz <sup>1</sup> <b>Instrument Responsible:</b> Vasyi Haramus <sup>2</sup> , <sup>2</sup> GKSS Research Centre Geesthacht, Germany		
<b>Date(s) of Experiment:</b> 6 <sup>th</sup> –10 <sup>th</sup> , 17 <sup>th</sup> –18 <sup>th</sup> November 2006		

## Objectives

In emulsions the interface and the micelles can solubilise different amounts of small molecules like antioxidants, depending on solubilisation properties of the solutes and the respective solubilisation capacities of the phases. The activity of such compounds can greatly be influenced by their partitioning behaviour<sup>[1]</sup>. For investigations concerning the partitioning of solutes, the amount of emulsifier present in the individual pseudophases is of particular interest. SANS is a powerful tool to characterize multiphase systems and has already been used to investigate the effect of additional emulsifier on the structure of emulsions<sup>[2]</sup>. In particular effects on the shape and size of Brij, SDS and CTAB micelles in the presence of antioxidants were successfully analysed by SANS<sup>[3]</sup>.

This experiment was carried out to verify the hypothesis, that the excess emulsifier is present in the form of micelles<sup>[2]</sup>. In addition, for nonionic emulsifiers it is assumed, that the excess emulsifier may also aggregate at the interface leading to an increase of the thickness and / or packing density of the interfacial layer<sup>[4]</sup>.

## Experiments

The experiments included a) the quantification of the emulsifier at the interface and b) to investigate whether the interfacial concentration will remain constant when the total emulsifier concentration is increased. Thereby the hypothesis should be verified, that the excess emulsifier is present in the form of micelles<sup>[2]</sup>. In addition, for nonionic emulsifiers it is assumed, that the excess emulsifier may also aggregate at the interface leading to an increase of the thickness and / or packing density of the interfacial layer<sup>[4]</sup>.

The emulsifiers SDS, CTAB and Brij 58 were used different concentrations (10, 20, 30 mM), which made it possible to determine the effect of the excess emulsifier on the micelle concentration and / or on the structure of the interfacial layer. Contrast variation was achieved by the measurements of emulsions with D<sub>2</sub>O, emulsifier and Oil and emulsions with D<sub>2</sub>O, d-emulsifier and Oil, respectively. Micellar solutions were used as control samples.

In former studies with emulsions, deuterated alkanes were used as oil phase<sup>[2]</sup>. As the use of alkanes yields very small droplet sizes and incorporation of alkanes into micelles partitioning results may be misinterpreted. Therefore, the oil phase consisted of corn oil in this study. The systems contained 0.2 M acetic buffer solution (pH 5.00), 10, 20 and 30 mM emulsifier and 10 % corn oil.

## Achievements and Main Results

In emulsions with Brij 58 the presence evidence for the presence of micelles could not be provided. This coincides with an increased density of the interfacial layer. However, the thickness of the interface was not affected by an increased emulsifier concentration. The interface between emulsifier and water phase can be described as increasingly smooth, whereas the oil-emulsifier interface is more diffusive.

The increase of SDS (Fig. 1) and CTAB concentrations resulted in the presence of different amounts of micelles. Still, the micellar size in emulsions was found to be larger than in micellar solutions under the same conditions. This is discussed to be due to the incorporation of oil into the micellar core. From calculations the incorporation of 2–3 triglyceride molecules is supposed.

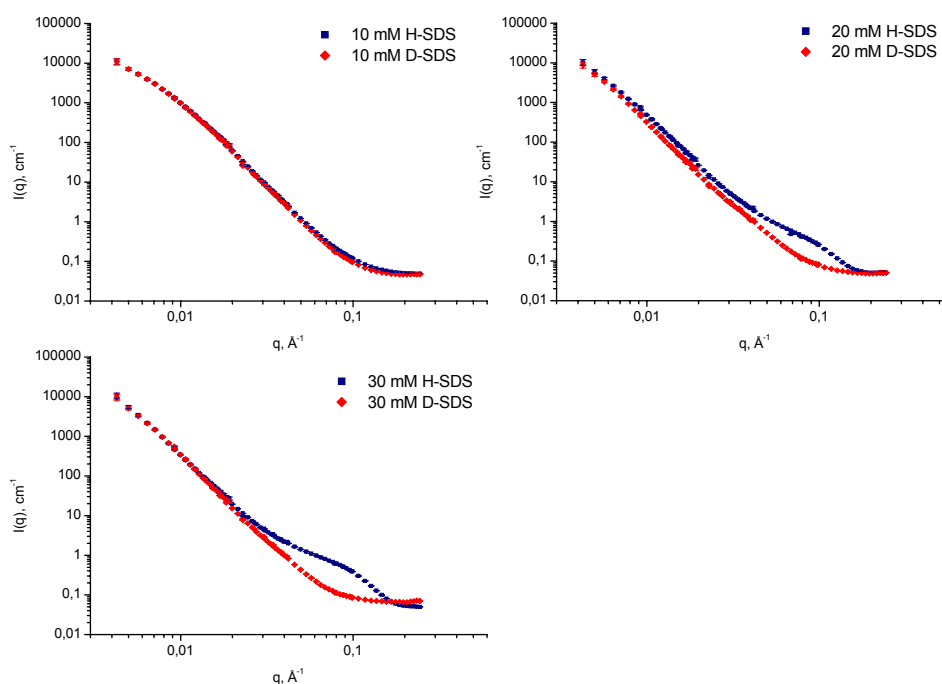



**Figure 1:** Scattering curves of emulsions with 10, 20 and 30 mM SDS with different contrasts (h-SDS and d-SDS). The differences in the shape of the scattering curves at large  $q$  are attributable to the presence of SDS micelles which are matched in the case of d-SDS.

The headgroup area of SDS and CTAB molecules was determined. For emulsions with SDS it was found to be  $62.5 \text{ \AA}^2$  for all samples. Conversely, for CTAB the results indicate a change of the packing density when the CTAB concentration is increased.

## References

- [1] Stöckmann, H.; Schwarz, K. & Huynh-Ba, T.; JAOCS 77 (2000), 535–542
- [2] Staples, E.; Penfold, J. & Tucker, I.; J. Phys. Chem. B 104 (2000), 606–614
- [3] Heins, A.; Garamus, V.; Steffen, B.; Stöckmann, H.; Schwarz, K.; Food Biophysics 1 (2006), 189–201
- [4] Coupland, J. N. & McClements, D. J.; Trends in Food Science & Technology 7(1996), 83–91

	<b>EXPERIMENTAL REPORT</b>	<b>GeNF SANS-1</b>
<b>Network formation in lipid membranes</b>		
<b>Proposer:</b>	<b>J. Preu<sup>1</sup></b> , <sup>1</sup> PSI, Villigen, Switzerland	
<b>Co-Proposer(s):</b>	<b>T. Gutberlet<sup>1</sup>, T. Heimborg<sup>2</sup></b> , <sup>2</sup> NBI, Copenhagen, Denmark	
<b>Experimental Team:</b>		
<b>User Group Leader:</b>	<b>T. Gutberlet<sup>1</sup></b>	
<b>Instrument Responsible:</b>	<b>Vasyl Haramus<sup>3</sup></b> , <sup>3</sup> GKSS Research Centre Geesthacht, Germany	
<b>Date(s) of Experiment:</b>	15 <sup>th</sup> – 19 <sup>th</sup> July 2007	

## Objectives

Pure lipid membranes are used as models for more complex biological membranes with potential use in pharmacology. Some phospholipids exhibit a number of different lamellar and nonlamellar phases undergoing a cooperative melting reaction. This is linked to the loss in conformational order of the lipid chains and can result in extended networks (see Schneider et al.), bearing a morphological resemblance to lattice networks of tubular myelin as found by long surfactant in the alveolar fluid. The associated transitions are depending on temperature, pressure, lipid concentration and sample environment, such as ionic strength.

For DMPG dispersions these transitions have been studied, using calorimetry, electron microscopy, viscosity measurements, fluorescence spectroscopy and light scattering. It was demonstrated by Schneider et al. that aqueous dispersions of DMPG at low ionic strength display an extended and complex melting regime, having influence on the viscosity and the structure. This striking change in material properties of the lipid suspension has been related to a structural transition from a vesicular state below the transition to a long-range bilayer network in the transition region. Above the range of calorimetric events, vesicles, but of different morphology, again prevail. Throughout the transition region, the lipid membranes assume an entirely different mean curvature. The structural changes seem evident in electron microscopy (Schneider et al.). Heimborg & Biltonen have described the structure of irregular connected bilayers as a so-called sponge phase. Riske et al. assumed vesicle disaggregation in the intermediate phase. As recently published by Alakoskela & Kinnunen both theories can be excluded. Applying fluorescence spectroscopy and dynamic light scattering, they assume that neither vesicle disaggregation nor bilayer connectivity can be used as an explanation for the shape transition.

## Experiment

To provide a more detailed insight into the structural changes found close to the chain-melting transition in aqueous dispersions of DMPG SANS measurements of DMPG at different ionic strength and temperatures, in particular at 0, 50, 150 and 500 mM NaCl and at temperatures of 15, 22 and 35 °C were conducted. For all preparations a lipid concentration of 10 mM DMPG was used and unilamellar vesicles were produced by extrusion at a temperature above the main phase transition. The contrast of solvent towards the lipid mixture was varied using pure D<sub>2</sub>O as a solvent for the sample preparation. Additionally a sample with a lipid concentration of 1 mM DMPG was measured to look at concentration dependent effects.

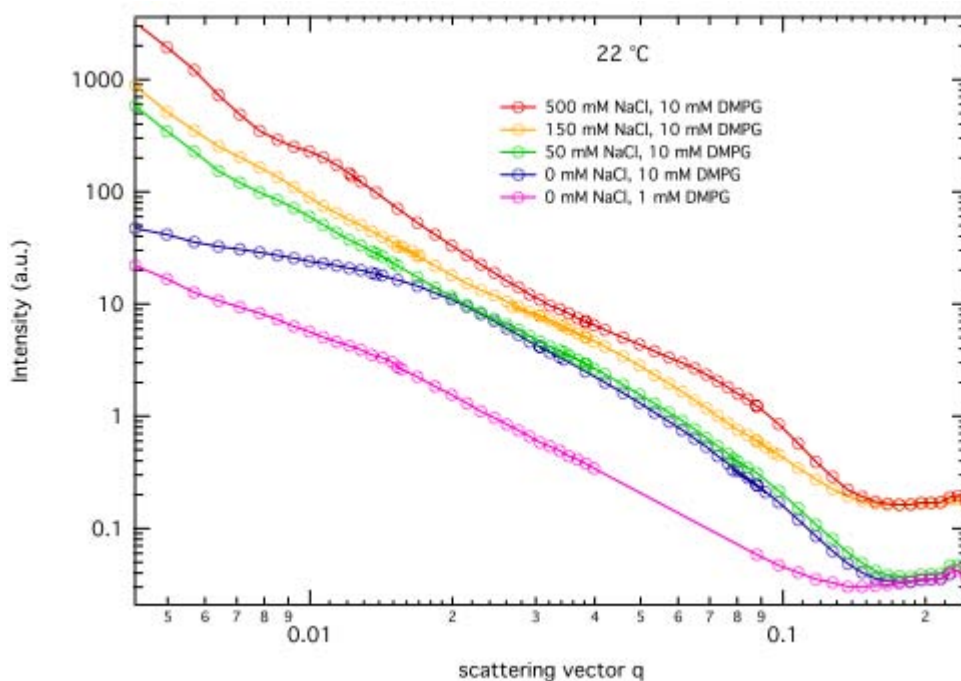


**Figure 1:** Scattering intensity as a function of the scattering vector for the samples of 10 mM DMPG measured at 22 °C with NaCl concentrations of 0, 50, 150 and 500 mM, and an additional sample containing 1 mM DMPG in pure D<sub>2</sub>O.

### Achievements and Main Results

Below the temperature of the main phase transition unilamellar vesicles were observed. Above the main phase transition the vesicles are multilamellar, with the number of lamellas increasing with the ionic strength. The measurements provided evidence that the sample tends to aggregate, resulting in a drastic reduction of the data quality. The main aim of the measurements was to study the presumably non-vesicular structure that occurs during the main phase transition between 20 and 28 °C. With the ongoing aggregation and sedimentation of the DMPG vesicles a reliable interpretation of the measurement is not possible. Experiments with a better time resolution or with a rotating sample holder should give required better data to prove the structure in this system.

### References

- [1] Schneider, M. F. et al., PNAS, 96 (1999), 14312
- [2] Heimburg, T.; Biltonen, R. L., Biochemistry, 33 (1994), 9477–9488
- [3] Riske, K. A. et al., CPL, 89 (1997), 31–4
- [4] Alakoskela, J.-M.; Kinnunen, P. K. J., Langmuir 23 (2007), 4203–4213



**The Effect of PPO Block Size on the Self-Assembly  
of Polyglycidol-Based Analogues to Pluronic**

<b>Proposer:</b>	<b>Stanislav Rangelov</b> <sup>1</sup> , <sup>1</sup> Institute of Polymers, Bulgarian Academy of Sciences, Sofia, Bulgaria
<b>Co-Proposer(s):</b>	<b>Silvia Halacheva</b> <sup>1,2</sup> , <sup>2</sup> Department of Chemistry, University of Bath, Bath, UK
<b>Experimental Team:</b>	
<b>User Group Leader:</b>	<b>Stanislav Rangelov</b> <sup>1</sup>
<b>Instrument Responsible:</b>	<b>Vasyl Haramus</b> <sup>3</sup> , <sup>3</sup> GKSS Research Centre Geesthacht, Germany
<b>Date(s) of Experiment:</b>	14 <sup>th</sup> – 26 <sup>th</sup> October 2007

### Objectives

The main objectives of this work are to complement earlier studies [1–3] on the self-assembly in aqueous solution of amphiphilic copolymers based on polyglycidol (PG). The copolymers are considered as analogues to the commercially available and extensively investigated *Pluronic*, poly(ethylene oxide)-poly(propylene oxide)-poly(ethylene oxide), PEO-PPO-PEO, block copolymers in which the flanking PEO blocks are substituted by blocks of structurally similar PG blocks. The structural formulae of the monomer units of PEO, PPO, and PG are presented in Figure 1.

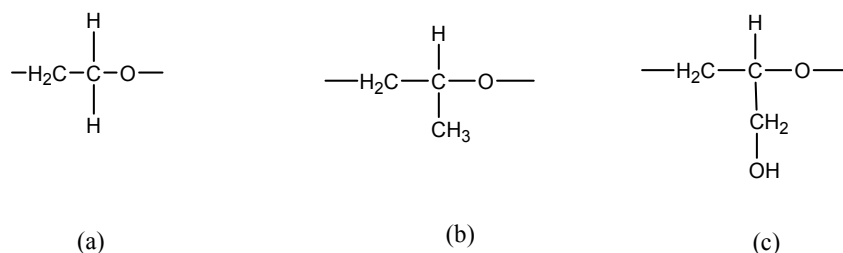


**Figure 1:** Monomer units of **(a)** poly(ethylene oxide), **(b)** poly(propylene oxide), and **(c)** linear polyglycidol.

The current experiments add to data that have been collected on similar copolymers having a twice-shorter middle block of PPO. In particular we aimed at (i) determining the size of the PPO cores at different temperatures, (ii) investigating the internal structure of the large particles formed by some of the copolymers, and (iii) determining how the aggregates or PPO domains are arranged at elevated concentrations and temperatures. Combining the results from the present study and earlier ones allows following the effect of the PPO block size on the self-assembly in aqueous solution of the polyglycidol-based copolymers.

### Experiment

Five copolymers were selected for the study. Their composition, PG contents, and total molecular weights are summarized in Table 1. The samples run were in the 2–33 wt.% concentration range at temperatures 25, 40, 50, and 60 °C. Four sample-to-detector distances (0.7, 1.8, 4.5, and 9.7 m) were used, which, with a neutron wavelength of 8.1 Å gives a q-range of approximately 0.005–0.25 Å<sup>-1</sup>.

**Table 1:** Abbreviations, composition, polyglycidol content, and total molecular weight of the copolymers studied. G and PO denote PG and PPO monomer units, respectively.

Abbreviation	Composition	PG content (wt.%)	Molecular weight
LGP134	(G) <sub>18</sub> (PO) <sub>68</sub> (G) <sub>18</sub>	40	6700
LGP135	(G) <sub>27</sub> (PO) <sub>68</sub> (G) <sub>27</sub>	50	8000
LGP136	(G) <sub>40</sub> (PO) <sub>68</sub> (G) <sub>40</sub>	60	9900
LGP137	(G) <sub>63</sub> (PO) <sub>68</sub> (G) <sub>63</sub>	70	13300
LGP138	(G) <sub>135</sub> (PO) <sub>68</sub> (G) <sub>135</sub>	80	24000

## Achievements and Main Results

Figures 2 and 3 present the evolutions of the scattering curves with (i) copolymer composition at constant temperature and concentration and (ii) temperature for LGP135 at fixed concentration, respectively. The scattering patterns are characterized by peaks attributed to inter-correlation between the PPO domains. At lower concentrations broad maxima or shoulders, rather than peaks, were observed.

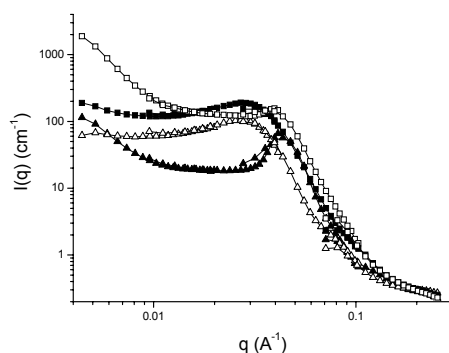


**Figure 2:** SANS profiles obtained from 33 wt.% aqueous solutions of LGP134 (open squares), LGP135 (closed squares), LGP136 (open triangles), LGP137 (closed triangles) at 40 °C.

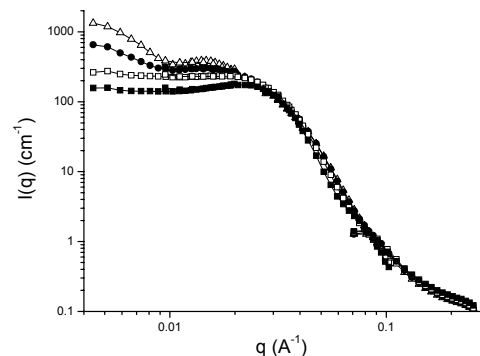


**Figure 3:** SANS profiles obtained from 20 wt.% aqueous solutions of LGP135 at 25 °C (closed squares), 40 °C (open squares), 50 °C (closed circles), and 60 °C (open triangles).

The complete analysis and interpretation of the data are still underway. The data are analyzed on an absolute scale and fitted by means of a least-squares method using recently developed models for *Brij* and *Pluronic* micelles [4, 5]. These are advanced models based on Monte Carlo simulations, where the scattering from both the core and corona is taken into account [6, 7]. Preliminary results from the fitting procedures gave aggregation numbers from 40 to 90 depending on the copolymer composition and temperature, which corresponds to core radii in the 45–70 Å range.

## References

- [1] Halacheva, S.; Rangelov, S.; Tsvetanov, Ch. *Macromolecules* 39 (2006), 6845-52
- [2] Rangelov, S.; Almgren, M.; Halacheva, S.; Tsvetanov, Ch. *J. Phys. Chem. C* 111 (2007), 13185-91
- [3] Halacheva, S.; Rangelov, S.; Garamus, V. *Macromolecules* 40 (2007), 8015-21
- [4] Sommer, C.; Pedersen, J. S.; Garamus, V. M. *Langmuir* 21 (2005), 2137
- [5] Liu, Y. C.; Chen, S. H.; Huang, J. S. *Macromolecules* 31 (1998), 2236
- [6] Svaneborg, C.; Pedersen, J. S. *Macromolecules* 35 (2002), 1028
- [7] Svaneborg, C.; Pedersen, J. S. *J. Chem. Phys.* 112 (2000), 9661

	<b>EXPERIMENTAL REPORT</b>	<b>GeNF SANS-1</b>
<b>Structure of Opaque Poly(acrylamide) Gels Revealed by SANS and CLSM</b>		
<b>Proposer:</b> <b>Co-Proposer(s):</b>	<b>Masayuki Tokita<sup>1</sup></b> , <sup>1</sup> Kyushu University, Fukuoka 810-8560, Japan	
<b>Experimental Team:</b> <b>User Group Leader:</b> <b>Instrument Responsible:</b>	<b>Hirohisa Miki<sup>1</sup>, Sada-atsu Mukai<sup>1</sup></b> <b>Masayuki Tokita<sup>1</sup></b> <b>Vasyl Haramus<sup>2</sup></b> , <sup>2</sup> GKSS Research Centre Geesthacht, Germany	
<b>Date(s) of Experiment:</b>	21 <sup>st</sup> – 27 <sup>th</sup> September 2007	

## Objectives

Poly(acrylamide) gels are known to be opaque when the concentration of the cross-linker is increased<sup>1,2</sup>. In Figure 1, we show the photograph of the gels. The total concentration of the gel is fixed at 700 mM, while the mole fraction of the cross-linker is changed from 0.01, 0.03, 0.05, and 0.1 from left to right. It is clear that the opaqueness of the gel increases with the concentration of the cross-linker

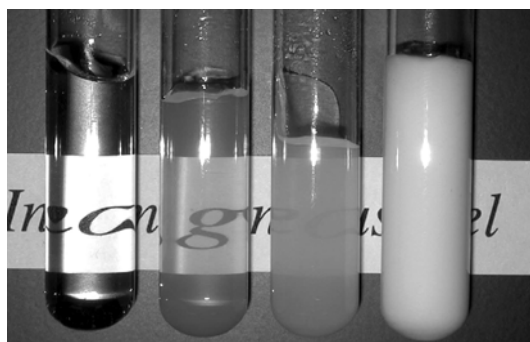


**Figure 1:** The appearance of the opaque poly(acrylamide) gels.

Usually, the mole fraction of the cross-linker is fixed at about 0.01 when the gel is used as a medium for the electrophoresis. Since the opaqueness of the gel is of importance in the practical use of the gel, the structure and the properties of the opaque gel has been studied<sup>3,4</sup>. Recently, the structure of the opaque poly(acrylamide) gels has been studied by using the confocal laser scanning microscope (CLSM)<sup>5</sup>. The real space structure of the gel that is observed by CLSM indicate that the opaque poly(acrylamide) gel consists of the fractal aggregate of the colloidal particles of about few hundred nanometres in diameter. The hydrodynamic friction between the polymer network and the gel fluid has been also studied<sup>6</sup>. The friction of the gel thus determined has been discussed in terms of the structure of the polymer network that is revealed by the CLSM. The results indicate that the frictional property of the gel is well described by the structural parameters of the colloid gel of poly(acrylamide). Although the structure of the gel is studied by the CLSM, the information on the fine structure of the opaque poly(acrylamide) gel has yet to be obtained because the spatial resolution of the CLSM is limited to about few hundred nanometres.

## Experiment

The opaque poly(acrylamide) gels are obtained by a photo-polymerization method. The details of the synthesise of the gel is described in previous reports<sup>5,6</sup>. The total amount of the polymer network is fixed at 700 mM while the mole fraction of the cross-linker is changed

from 0.2 to 0.5. Hereafter, samples are abbreviated as 0.2-Bis, 0.3-Bis, 0.4-Bis, and 0.5-Bis for the mole fraction of the cross-linker at 0.2, 0.3, 0.4, and 0.5. The sample gels are prepared in D<sub>2</sub>O as a solvent. The sheet shaped gels thus prepared are soaked in D<sub>2</sub>O to remove the unreacted substances. The sample gel is transferred into a quartz cell of 1.5 mm in thickness and then the SANS measurements are carried out.

### Achievements and Main Results

The angular dependence of the scattering intensity from the opaque gels is shown in Fig. 2 in a double logarithmic manner. The absolute values of the scattering function,  $S(q)$ , of the higher cross-linker concentrations are multiplied by a numerical factors to avoid the overlap of the results.

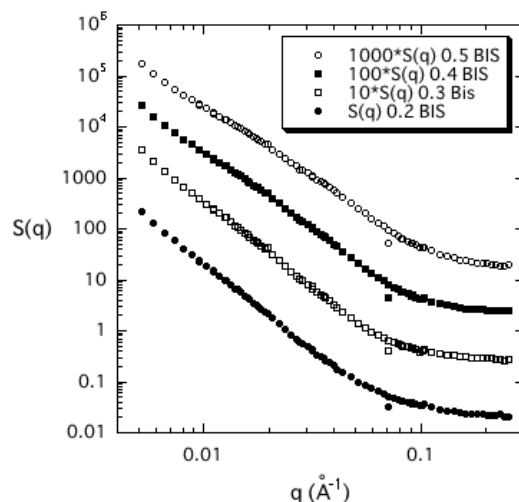


**Figure 2:** The double logarithmic plot of the scattering function.

The results of  $S(q)$  for the 0.5-Bis, 0.4-Bis, and 0.3-Bis are multiplied by a factor of 1000, 100, and 10, respectively. It is clear from this figure that the scattering function of the gel,  $S(q)$ , is well described by the straight lines at small scattering vectors. The power law behaviours of the scattering intensity is analysed by the least square fitting to the following function.

$$S(q) = A q^{-b} + C \quad (1)$$

Best fitting values of  $A$  and  $b$  are listed in the following Table. It is find that the  $S(q)$ 's of 0.2-Bis and 0.3-Bis gels are well explained by the equation 1). On the other hand, we find that the scattering functions of 0.4-Bis and 0.5-Bis gels are the overlap of two limiting functions. The scattering function is explained by a simple power law function with  $C = 0$  and  $b \sim 2.7$  in the region of  $q < 0.02$  ( $\text{\AA}^{-1}$ ) while the scattering function is well explained by the equation 1) where  $q > 0.02$  ( $\text{\AA}^{-1}$ ). These results suggest that the structures of the 0.4-Bis and 0.5-Bis are the mass fractals with the fractal dimension of  $D_m \sim 2.7$  in the length scale larger than 5 nm.

In Figure 3, we show the CLSM images of the 0.5-Bis gel gained at three magnifications. The brighter regions of the images correspond to the region where the density of the FITC is higher. Since the polymer network of the gel is labelled by FITC in our case, the brighter region is the region where the density of the polymer network is higher. It is clearly shown in these images that the polymer network of the opaque poly(acrylamide) gel consists of the fractal aggregate of the colloidal particles of a diameter of about few hundred nanometres. The previous results, in which the diameter of the colloidal particles are measured, indicate that the average diameter of the particle is found to be 420, 300, and 180 nm in the case of 0.5-Bis, 0.4-Bis, and 0.3-Bis gels<sup>5</sup>.

**Table 1:** Fitting results.

Sample	0.2-Bis	0.3-Bis	0.4-Bis		0.5-Bis	
			q < 0.02	q > 0.02	q < 0.02	q > 0.02
A	$3.0 \times 10^{-6}$	$3.0 \times 10^{-6}$	$6.0 \times 10^{-5}$	$6.0 \times 10^{-6}$	$1.3 \times 10^{-4}$	$1.7 \times 10^{-5}$
B	3.39	3.51	2.83	3.42	2.64	3.16

The two dimensional distribution of the particles (brighter region) in the CLSM images is analyzed by the box counting method. The results yields that the distribution of the particles in the images is well described by the fractal dimension of  $D_m \sim 1.7$ . The fractal dimension thus determined by the CLSM images is less than the one determined by the SANS measurements. The results suggest that  $D_{m \text{ SANS}} = D_{m \text{ CLSM}} + 1$ . It may be, however, reasonably understood that the CLSM images are the two-dimensional slice of the three-dimensional aggregate of the colloidal particles while the SANS measurements represent the structures of the opaque gels as it is. It is further suggested from the SANS measurements that the colloidal particles, which are observed in the CLSM images, consist of the aggregates of further smaller particles of the diameter of about 5 nm. It may be of importance to discuss the origin and the mechanism of the formation of such smaller particles in the reaction systems. We show in this study that the combined use of the SANS and the CLSM will promote the better understanding of the structure of the colloid gel.

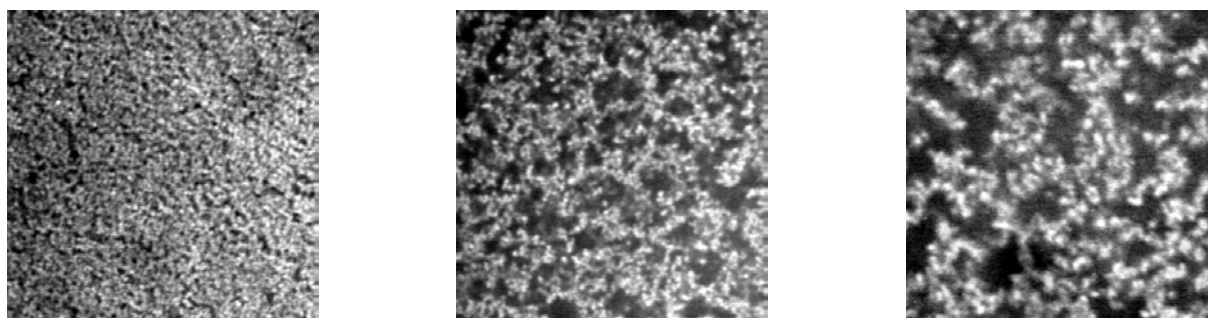


**Figure 3:** The CLSM images of the 0.5-Bis gel. The magnifications of the images are 10 $\times$ , 40 $\times$ , and 100 $\times$  from left to right. The one side of the images is 200 pixels which correspond to 192, 48.8, and 18.9  $\mu\text{m}$  for 10 $\times$ , 40 $\times$ , and 100 $\times$ , respectively.

## References

- [1] Richards, E. G.; Temple, C. J., *Nature* 220 (1971), 92
- [2] Bansil, R.; Gupta, M. K., *Ferroelectrics* 30 (1980), 63
- [3] Asnaghi, D.; Giglio, M.; Bossi, A.; Righetti, P. G., *Macromolecules* 30 (1997), 6194
- [4] Benguigui, L.; Boue, F., *Eur. Phys. J. B11* (1999), 439
- [5] Doi, Y.; Tokita, M., *Langmuir* 21 (2005), 5285
- [6] Doi, Y.; Tokita, M., *Langmuir* 21 (2005), 9420



**Small-angle scattering instrument SANS-2**

**Short Instrument Description:**

Small angle neutron scattering using cold non-polarised/polarised neutrons is a powerful tool for investigating the structure of matter in the range between 1 and 100 nm. It is a non destructive method with a wide range of applications in:

- Metal physics (precipitates, clusters, interfaces, grain boundaries,...)
- Materials science (defects, porosity,...)
- Nanocrystalline materials (grain size, magnetic structures,...)
- Polymers and polymer systems (blends, mixtures, structure and morphology,...)
- Biology (viruses, proteins,...)
- Complex liquids (microemulsions, colloids, liquid crystals,...)

**Local Contact:**

Dr. Melissa Sharp

Phone/Fax : +49 (0)4152 87 – 1209 / +49 (0)4152 87 – 1338

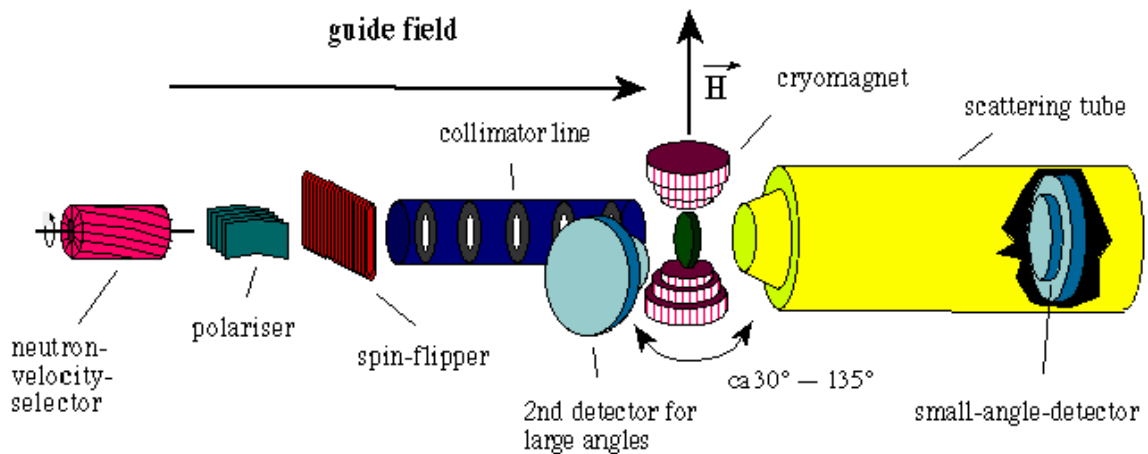
e-mail: [melissa.sharp@gkss.de](mailto:melissa.sharp@gkss.de)

Helmut Eckerlebe

Phone/Fax : +49 (0)4152 87 – 1202 / +49 (0)4152 87 – 1338

e-mail: [helmut.eckerlebe@gkss.de](mailto:helmut.eckerlebe@gkss.de)


**Schematic View of SANS-2:**



**Instrument Details:**

Beamline:	beamline 8 – cold neutron guide NG-2, radius of curvature $R = 900$ m, cross section $3 \times 4$ cm <sup>2</sup>
Monochromator:	helical slot velocity selectors (Dornier)
Wavelength range at sample position:	0.3 to 2.0 nm
Wavelength resolution:	$\Delta\lambda/\lambda = 0.1$ (2 additional velocity selectors with $\Delta\lambda/\lambda = 0.05$ and $0.2$ available)
Length of collimation:	max. 16 m (2 m elements)
Flux at sample position:	$\Phi_{\max} = 2 \cdot 10^7$ cm <sup>-2</sup> s <sup>-1</sup> (1 m collimation, $\lambda = 0.5$ nm)
Range of momentum transfer:	$0.01 \leq q \leq 3$ nm <sup>-1</sup> (small-angle scattering) $q \leq 25$ nm <sup>-1</sup> (wide-angle scattering with 2. detector)
Distance sample to detector:	$1.0 \text{ m} \leq d \leq 22 \text{ m}$ optional 2. detector for wide angles: $d = 1$ m
Detector: active area: resolution: background:	2-dim position-sensitive <sup>3</sup> He-counter 50 x 50 cm <sup>2</sup> 0.25 x 0.25 cm <sup>2</sup> < 0.5 cps
Supplementary equipment:	<ul style="list-style-type: none"> <li>– several electro-magnets up to 2.0 T (horizontal and vertical fields)</li> <li>– superconducting magnets up to 5.0 T</li> <li>– several cryostats (4– 400 K)</li> <li>– furnace (-30 °C to +900 °C, atmospheric condition, inert gas and vacuum)</li> <li>– linear translation, rotary, tilting and lift tables (freely programmable sample position)</li> <li>– “HOLONS”: holographic combined with SANS setup (see table A)</li> </ul>
Special features:	<ul style="list-style-type: none"> <li>– Sample environment space is variable from a few mm up to 2500 mm</li> <li>– User-friendly software for data reduction and evaluation running on PC (SANDRA a. o.)</li> </ul>



	<b>EXPERIMENTAL REPORT</b>	<b>GeNF SANS-2</b>
<b>Hierarchy of hyperbranched polymer by SANS</b>		
<b>Proposer:</b>	<b>L. Dahbi<sup>1</sup></b> , <sup>1</sup> Forschungszentrum Juelich, Germany	
<b>Co-Proposer(s):</b>	<b>W. Pyckhout-Hintzen<sup>1</sup></b>	
<b>Experimental Team:</b>	<b>L. Dahbi<sup>1</sup>, W. Pyckhout-Hintzen<sup>1</sup>, M. Sharp<sup>2</sup>, H. Eckerlebe<sup>2</sup></b>	
<b>User Group Leader:</b>	<b>W. Pyckhout-Hintzen<sup>1</sup></b>	
<b>Instrument Responsible:</b>	<b>M. Sharp<sup>2</sup></b> , <sup>2</sup> GKSS Research Centre Geesthacht, Germany	
<b>Date(s) of Experiment:</b>	16 <sup>th</sup> – 22 <sup>nd</sup> April 2007	

## Objective

We study the hierarchical relaxation of a non linearly stretched model polymer among linear chains of different lengths. This study aims at the understanding of the relaxation of a hyperbranched architecture while entangled to certain degrees with the linear matrix via quenched SANS experiments using our elongational stretching rheometer. Quenching decouples the characteristic microscopic polymeric relaxation times from the laboratory time frame.

The originality of this system lies in the fact that the relaxation time scales of both constituents can be controlled from fully separated (3 orders of magnitude, long linear matrix) to intimately mixed and concurrent (linear chain comparably sized). This experiment will therefore shed light on the relaxations of the fast arms via arm breathing modes and/or constraint-release events from the linear chain.

## Experiment

As the reference state the sample is measured in the isotropic state after which a relatively fast stretch on the timescale of the arm segments is applied. The elongation  $\lambda = 2$  achieved within 2 seconds at  $T = -25^\circ\text{C}$  was chosen. This assures non-linear dynamics of the arms to be observed. The immediately quenched state after the stretch is expected to be nearly affine. Several further states of the sample relaxation time axis were investigated by proceeding through a sequence of annealing of the sample, each annealing being followed by an immediate quench of the sample below its  $T_g$ .

Both investigated blend systems were studied at comparable states of strain and relaxation time in order to clarify the effect of the matrix length on the time dependence of the relaxation of the arms and its impact on the processability of polymers in general.

## Achievements and Main Results

As necessary primary measurement, the sample in its isotropic state must be characterized to define the reference values. This involves  $R_g$ ,  $q$ -dependence, absolute molecular weight...

To allow the sample to relax, it was brought above  $T_g$  over a time-temperature ramp and converted to the equivalent time at room temperature to be located in the hump of  $G''(\omega)$  (fig1b). This method, due to its capacity to fully decouple the measuring time from the microscopic time, makes it an excellent candidate for studying long-time relaxations of the sample which cannot be accessed via typical inelastic studies. All SANS measurement were realized at  $-90^\circ\text{C}$ .

The results plotted here (fig 1a) represent the scattering function of the hyperbranched polyisoprene polymer in a fully deuterated matrix of linear polyisoprene ( $M_w=200k$ ) along the principal axes as a function of  $q$  for different relaxation time after subtraction of an incoherent background to yield the  $q^{-2}$  behaviour at high  $q$ . The central curve (black dots) is the isotropic state for comparison.

The curves above the isotropic curve are the measurement in the direction perpendicular to the stretch whereas the one below the isotropic curve represent the measurement in the direction parallel to the deformation. The upturn at low  $q$  is due to a non-zero isotope interaction parameter between both types of monomers whereas another contribution due to the different topologies cannot be excluded.

The insert correspond to the 2D graph measured at an intermediate sample-detector distance of 4 meters, which  $q$ -range represents parts of the relaxing arms as well as the tube of fluctuation.

In the direction parallel to the stretch, the molecules have the highest radius of gyration ( $\lambda R_g$  just after the elongation in the case of an affine deformation) and conversely the smallest radius gyration in the direction perpendicular to the stretch, which explain the shift and the decrease of intensity in the direction parallel to the stretch and the reverse shift and increase in the other direction. The intensities at high  $q$  after a slight annealing (10% of the total relaxation time of the arms) do not evolve much in time from comparison to the anisotropy observed immediately after the stretch. A minor loss of anisotropy is observed, as well as a slight decrease of  $R_g$  in the direction parallel to the elongation and a slight increase of  $R_g$  can be suspected.

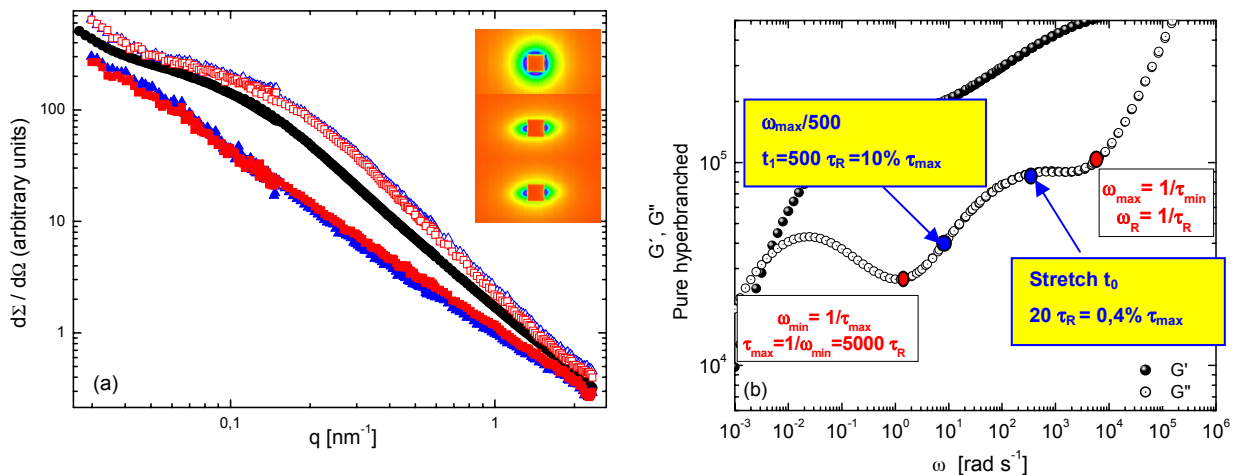


**Figure 1:** **a)** Intensity measured in the isotropic state (central curve), in the direction perpendicular to the stretch (above the isotropic curve, open symbols) and in the direction parallel to the stretch (below the central curve, closed symbol). The intensity recorded immediately after the stretch is represented by blue triangles and the one after a relaxation of 10 % of total relaxation time of the arms by red squares.

**Insert:** 2D patterns recorded at a sample-detector distance of 4 meters. From top to bottom: isotropic state, immediately after elongation, after a relaxation of 10 % of  $\tau_{max}$  ( $500 \tau_R$ ),  $\tau_{max}$  being the total relaxation time of the arms.

**b)** Storage (solid symbols) and Loss modulus (open symbols) versus frequency.

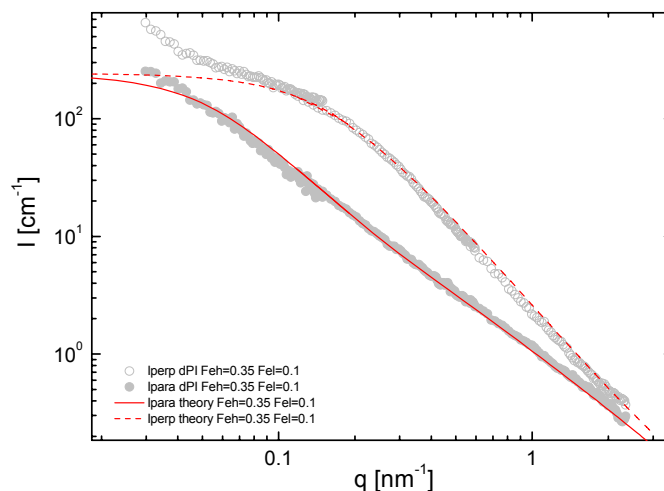


**Figure 2:** Comparison Experience-Theory (fully deuterated PI matrix (dPI)). Intensity measured after a relaxation time of 10 % of  $\tau_{\max}$  (gray dots) corresponding to a fraction of relaxed arms of  $F_{eh}=0,35$  and of relaxed linear chain of  $F_{el}=0,1$  and calculated theoretical scattering function (red lines). The calculated scattering function is in excellent agreement with the experimental data for scattering vector  $q > 0.08 \text{ nm}^{-1}$ .

The results obtained with the second system displayed similar features for the relaxed and elongated state but further measurement with same relaxation time for both systems are necessary to compare the influence of the matrix length on the dynamics of the relaxation of the arms of the hyperbranched polymer (To save place, the data are not presented here but are attached to this report).

The intensity scattered by the second system (only partially deuterated matrix) was much lower than the first one (factor of 10). Some experimental problems related to the setup came across with the temperature control and are being solved in our workshop.


However, this first allocated beamtime allowed us to show the feasibility of this study. We do observe changes in the relaxation of the arms and both system are excellent candidates for modelling industrial procedures in detail. The obtained details will enter rheological modelling of flow and lead to optimal blending recipes after generality has been proven.

Further experiments must therefore be carried out to extend the study to longer relaxation time as well as other elongation time and elongation factors to fully understand the dynamics of the relaxation process of the arms. The description of the scattering function is being improved to take into account the upturn at very low  $q$  that is due to different contributions.

## References

- [1] M. Heinrich et al., *Macromolecules*, 37 (2004), 5055
- [2] A. Blanchard et al, *Physical Review Letters*, 95 (2005), 166001



	<b>EXPERIMENTAL REPORT</b>	<b>GeNF SANS-2</b>
<b>Conformation of comb-like thermosensitive polymers</b>		
<b>Proposer:</b>	<b>Gang Cheng<sup>1</sup></b> , <sup>1</sup> NSSD, Oak Ridge National Laboratory, Oak Ridge, TN 37830	
<b>Co-Proposer(s):</b>	<b>Yuri Melnichenko<sup>1</sup></b> , <b>Kunlun Hong<sup>1</sup></b> , <b>Hua Fengjun<sup>1</sup></b>	
<b>Experimental Team:</b>	<b>Gang Cheng<sup>1</sup></b> , <b>Melissa Sharp<sup>2</sup></b>	
<b>User Group Leader:</b>	<b>Tom Mason<sup>1</sup></b>	
<b>Instrument Responsible:</b>	<b>Melissa Sharp<sup>2</sup></b> , <sup>2</sup> GKSS Research Centre Geesthacht, Germany	
<b>Date(s) of Experiment:</b>	16 <sup>th</sup> – 20 <sup>th</sup> April 2007	

## Objective

Comb like polymers consist of a backbone chain with multiple trifunctional branch points from each of which a linear side chain emanates. These polymers have received a great deal of attention due to their unique architecture and sensitivity to the molecular parameters (e.g. DP of the backbone and side chains), chemical composition as well as external perturbations [1–2]. Theoretical and computer simulation studies have focused on the local and global conformation of the polymers as well as on scaling relations between the sizes, persistence length and the molecular weight; however, many of theoretical predictions can not be verified due to a limited number of experimental investigations [1–2].

Amphiphilic polymers constitute a special class of comb-like polymers where the backbone and side chains have different hydrophobicity [3–4]. PEG-grafted comb like polymers with hydrophobic backbones have been proposed as an alternative to

poly(Nisopropylacrylamide) (PNIPAM) for many applications such as drug delivery [5]. In addition to temperature, the polymer conformation can be controlled by choosing different solvents [18]. For comb-like polymers with a hydrophobic backbone and hydrophilic side chains, the solvent quality is expected to affect the conformation much more than that for other comb like polymers.

In this work, we report our preliminary results of SANS investigations of the conformation of Oligo(Ethylene Glycol) grafted Poly(styrene) (OEG-PS) in toluene. The conformation of OEG-PS in other solvents is being studied.

## Experiment

Data were taken at SDD=15 m, 3 m, and 0 meters.

## Achievements and Main Results


As shown in Figure 1, the SANS data were taken for 1.0 wt.% OEG-PS in toluene-d<sub>8</sub>. The polymers have a fixed length of the side chains and the backbone length varies. The polymers assume the shape of a rigid cylinder when the degree of polymerization (DP) of the backbone is low. With increase of the DP of the backbone, the polymers start to exhibit flexibility. The OEG-PS homopolymer behave as a flexible cylinder when the DP is high enough, as shown in Figure 1. The uppermost curve corresponds to a flexible cylinder where the contour length is 232 Å, Kuhn length is 73 Å and the cross section radius is 13 Å.

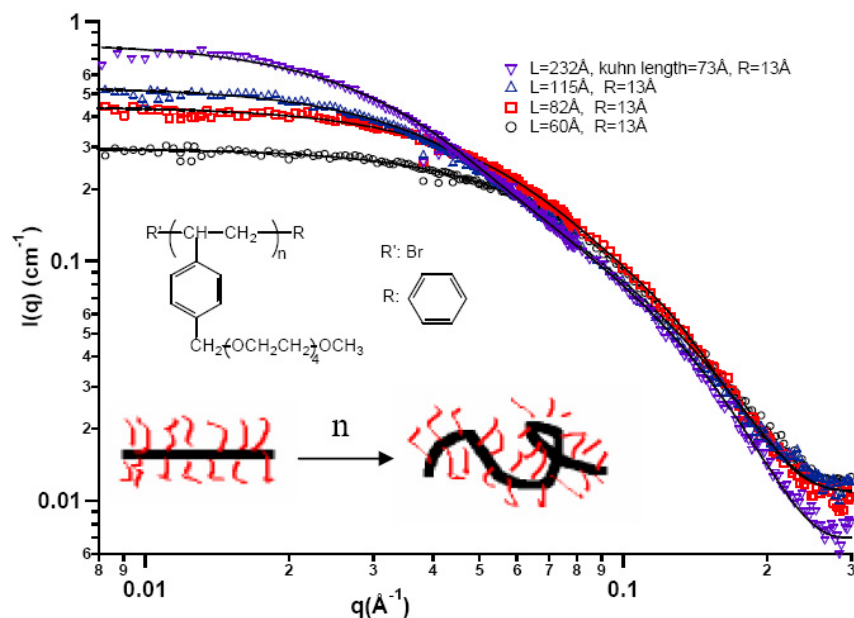


**Figure 1:** SANS data of OEG-grafted PS in 1.0 wt.% toluene-d8 solutions. The difference between different curves is the degree of polymerization of the backbone,  $n$ . The solid lines are fits to a rigid cylinder model or to a flexible cylinder model.

## References

- [1] Zhang B, Gröhn F., Pedersen JS, Fisher K, Schmidt M. *Macromolecules* 39 (2006), 8440
- [2] Rathgeber S, Pakula T, Wilk A, Matyjaszewski K, Lee H-I, Beers KL. *Polymer* 47 (2007), 7318
- [3] Kuhlman WA, Olivetti EA, Griffith LG, Mays AM. *Macromolecules* 39 (2006), 5122
- [4] Ito K, Kawaguchi S. *Colloids and Surfaces A: Physicochemical and Engineering Aspects* 153 (1999), 173
- [5] Lutz J-F, Weichenhan K, Akdemir Ö, Hoth A. *Macromolecules* 40 (2007), 2503

	<b>EXPERIMENTAL REPORT</b>	<b>GeNF SANS-2</b>
<b>Magnetic microstructure of nanocrystalline gadolinium</b>		
<b>Proposer:</b>	<b>A. Michels<sup>1</sup>,</b> <sup>1</sup> Technische Physik, Universität Saarbrücken, Saarbrücken, Germany	
<b>Co-Proposers:</b>	<b>R. Birringer<sup>1</sup>, P. K. Pranzas<sup>2</sup>,</b> <sup>2</sup> GKSS Research Centre Geesthacht, Germany	
<b>Experimental Team:</b>	<b>A. Michels<sup>1</sup>, F. Döbrich<sup>1</sup>, M. Elmas<sup>1</sup>, M. Sharp<sup>2</sup></b>	
<b>User Group Leader:</b>	<b>R. Birringer<sup>1</sup></b>	
<b>Instrument Responsible:</b>	<b>M. Sharp<sup>2</sup></b>	
<b>Date(s) of Experiment:</b>	September 2007	

## Objective

In nanocrystalline bulk ferromagnets the magnetic microstructure, i.e., the variation of the direction of the magnetization vector, is (compared to coarser-grained microstructures) highly nonuniform on a scale of a few nanometres. The origin of this nonuniformity is mainly related to the fact that at each grain boundary the set of crystallographic easy axes for the magnetization changes its orientation randomly. As is well known, the downscaling of the average particle size and the associated spin disorder at the nanoscale do influence the macroscopic magnetic properties of a magnetic material: famous examples include the observation of remanence enhancement in nanocrystalline hard magnets [1,2] or the tremendous decrease in coercivity [3], observed in nanocrystalline Fe-based soft magnets. Therefore, studying the detailed nature of this nonuniformity is of importance for understanding the macroscopic magnetic properties of nanocrystalline materials.

Polycrystalline rare-earth metals with average grain sizes in the nanometre range can be considered as a “simple” model system in order to scrutinize the influence of disorder (internal interfaces) and the consequences of crossing length scales (grain size  $\leftrightarrow$  exchange length) on the magnetic properties. The relatively small magnetic anisotropy ( $L = 0$ ) and high Curie temperature ( $T_C = 293$  K) renders Gd unique among the rare-earth magnets. Furthermore, in the localized  $4f$  systems the position-dependent RKKY interaction should make magnetism particularly sensitive to structural disorder and imperfections (grain boundaries) present in nanocrystalline bulk material, whereas the signature of defects in  $3d$  band magnets is expected to be less pronounced due to screening and delocalization. As a consequence of its extraordinary large absorption cross section for thermal and cold neutrons, conventional Gd can generally not be investigated by means of neutron methods. Therefore, only very few neutron studies on bulk Gd, mostly on single crystals consisting of the low-capturing isotope  $^{160}\text{Gd}$ , exist [4–8]. Here, we report the first experimental investigation of *polycrystalline bulk* Gd with a *nanometre crystallite size* by means of magnetic small-angle neutron scattering (SANS).

## Experiment

Nanocrystalline bulk Gd was synthesized by means of the inert-gas condensation technique [9] using the isotope  $^{160}\text{Gd}$  as starting material (enrichment: 98.6 %), yielding a volume-weighted average crystallite size  $D = 21$  nm of the as-prepared nc  $^{160}\text{Gd}$  sample and a mass density of about 99 % of the coarse-grained material value. An incident neutron wavelength  $\lambda = 5.8$  Å was used in SANS. The external magnetic field ( $0\text{T} \leq \mu_0 H \leq 5\text{T}$ ) was applied perpen-

dicular to the wave vector of the primary beam. Sample temperatures were 78 K and 5 K with a temperature stability of about  $\pm 1$  K. The nc  $^{160}\text{Gd}$  specimen had the shape of a circular disc with a diameter of 8 mm and a thickness of 275  $\mu\text{m}$ . At 78 K, sample transmission increased from 15.2 % at zero field to 18.5 % at 5 T.

## Achievements and Main Results

A general expression for the spin-dependent magnetic SANS cross section allowing for multiphase composition has been given in [10], which reduces for the case of an unpolarized incident neutron beam to  $d\Sigma/d\Omega(\vec{q}) = d\Sigma_R/d\Omega + d\Sigma_M/d\Omega$  with

$$\frac{d\Sigma_R}{d\Omega}(\vec{q}) = \frac{8\pi}{V} \left[ |\tilde{N}|^2 + b_H^2 |\tilde{M}_z|^2 \sin^2 \theta \right] \quad (1)$$

$$\text{and } \frac{d\Sigma_M}{d\Omega}(\vec{q}) = \frac{8\pi}{V} \left[ b_H^2 |\tilde{M}_x|^2 + b_H^2 |\tilde{M}_y|^2 \cos^2 \theta - b_H^2 (\tilde{M}_y \tilde{M}_z^* + \tilde{M}_y^* \tilde{M}_z) \sin \theta \cos \theta \right]. \quad (2)$$

$d\Sigma_M/d\Omega$  denotes the spin-misalignment scattering cross section and  $d\Sigma_R/d\Omega$  is the so-called residual nuclear and magnetic scattering cross section, which is measured at complete saturation.  $d\Sigma_R/d\Omega$  contains the nuclear SANS and the part of the magnetic SANS which is related to *longitudinal* magnetization fluctuations, whereas  $d\Sigma_M/d\Omega$  depends on the *transverse* spin components. The quantities  $V$ ,  $\tilde{N}$ ,  $\tilde{M}_i$  and  $\theta$  refer to, respectively, the scattering volume, the Fourier transform of the nuclear scattering length density  $N(\vec{x})$ , the Fourier transform of the Cartesian components of the magnetic scattering length density  $\vec{M}(\vec{x})$  and the angle between the scattering vector  $\vec{q}$  and the direction  $\vec{e}_z = (0,0,1)$  of the externally applied magnetic field. In this geometry,  $\vec{e}_x = (1,0,0)$  is the direction of the incident beam, and  $b_H = 2.7 \times 10^{-15} \text{ m}/\mu_B$ . For a magnetically saturated microstructure,  $d\Sigma_M/d\Omega = 0$ , and the scattering pattern on the area detector exhibits the well-known  $\sin^2 \theta$  anisotropy; it can be clearly seen in fig. 1a, where we display  $d\Sigma/d\Omega$  of nc  $^{160}\text{Gd}$  at an external field of 5 T. When the field is switched off,  $d\Sigma/d\Omega$  is essentially isotropic (fig. 1b), consistent with an expected random orientation of domains. Departure from these well-known angular variations of  $d\Sigma/d\Omega$  becomes visible at intermediate applied fields: the SANS signal at 30 mT (fig. 1c) is enhanced along H, in accordance with the  $\cos^2 \theta$  term in the expression for  $d\Sigma_M/d\Omega$ . Such a behaviour is expected for single-phase materials near saturation whenever the magnitude of the longitudinal magnetization component  $M_z$  is nearly uniform, *i.e.*,  $M_z \approx M_S$ . Although being a single-phase material, nc Gd unexpectedly exhibits the clover-leaf anisotropy, *i.e.* strong contributions to  $d\Sigma_M/d\Omega$  proportional to  $\sin \theta \cos \theta$  (figs. 1d and 1e), which is known to be particularly relevant in multiphase magnetic nanocomposites [10]. As a likely explanation for the origin of the clover-leaf anisotropy in nc Gd, we suggest the presence of a perturbed magnetization distribution  $\mathbf{M}(\mathbf{x})$  originating from the core regions of grain boundaries [11]. In particular, we are led to assume that the defect character of grain boundaries results in a jump of  $\mathbf{M}(\mathbf{x})$ , and, herewith, in *nano-scale* transverse,  $M_y(\mathbf{x})$ , and longitudinal,  $M_z(\mathbf{x})$ , magnetization fluctuations on a characteristic length scale of the order of the average crystallite size. Such a defect structure would presumably yield a contribution  $d\Sigma_M/d\Omega \sim \tilde{M}_y \tilde{M}_z \sin \theta \cos \theta$  to the spin-misalignment scattering. What is more, the atomic site disorder in the boundary core region may lead to interfacial anisotropy and by virtue of the oscillatory RKKY interaction even to antiferromagnetic coupling. This view is supported by grain-size dependent magnetization data (not displayed). At all applied fields, the magnetization of the nc Gd samples is strongly reduced as compared to coarse-grained Gd; for instance, even at  $\mu_0 H = 1 \text{ T}$  and for  $D = 33 \text{ nm}$ , the magnetization is reduced by about 25 %. By stepwise annealing of the nc sample, resulting in concomitant grain growth, we find from a  $M(H)$  loop at 5 K the zero-temperature single-crystal value for the saturation magnetization of Gd,  $\mu_0 M_S = 2.69 \text{ T}$  [12].



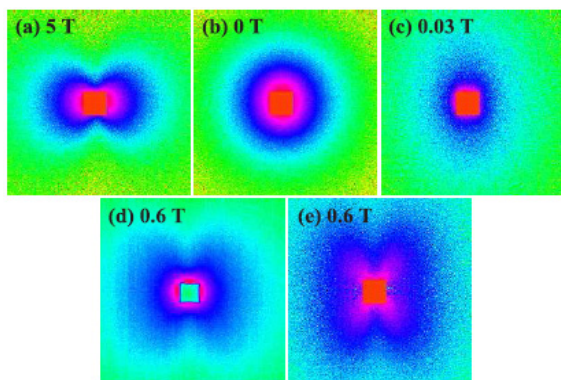


**Figure 1:**

(a)–(c) Total experimental SANS cross section  $d\Sigma/d\Omega$  of nanocrystalline  $^{160}\text{Gd}$  at  $T=78\text{ K}$  and at different applied magnetic fields  $H$  as indicated (logarithmic scale). Pixels in the corners of the detector correspond to  $q = 1.0\text{ nm}^{-1}$  [in (a) and (b)] and to  $q = 0.2\text{ nm}^{-1}$  [in (c)].

(d) Total SANS intensity at  $\mu_0 H = 0.6\text{ T}$  and at  $T = 78\text{ K}$  (raw data).

(e) Difference-intensity data at  $0.6\text{ T}$ , *i.e.*, the total intensity at  $5\text{ T}$  has been subtracted from the total intensity at  $0.6\text{ T}$ .

In (d) and (e), pixels in the corners correspond to  $q = 0.45\text{ nm}^{-1}$ .  $H$  is vertically oriented.

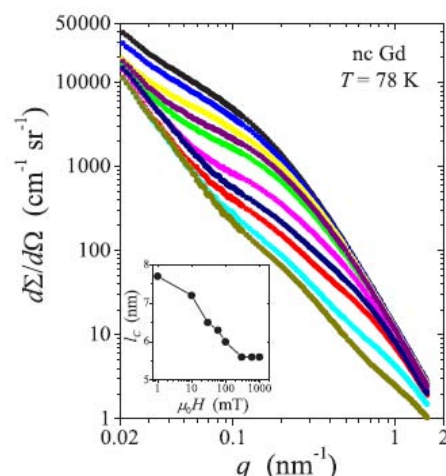



**Figure 2:**

Radially-averaged total scattering cross section  $d\Sigma/d\Omega$  of nanocrystalline  $^{160}\text{Gd}$  as a function of momentum transfer  $q$  and at several applied magnetic fields ( $T = 78\text{ K}$ ) (log-log scale). Field values (in mT) from top to bottom: 0, 10, 30, 60, 100, 300, 600, 1000, 2500, 5000. The inset depicts the field dependence of the spin-misalignment length  $l_c$  (semi-log scale). Line is guide to the eye.

Figure 2 depicts the field-dependent radially-averaged SANS cross section  $d\Sigma/d\Omega$  of nc Gd at  $T = 78\text{ K}$ . Between nominally  $0\text{ T}$  and  $5\text{ T}$ ,  $d\Sigma/d\Omega$  exhibits at all momentum transfers  $q$  a strong dependence on the applied field  $H$ , an observation which demonstrates the dominating spin-misalignment scattering contribution to  $d\Sigma/d\Omega$ . However, in contrast to nc Ni and Co [13], where the strongest  $H$ -dependence of  $d\Sigma/d\Omega$  was observed at the smallest  $q$ ,  $d\Sigma/d\Omega$  of nc Gd reveals the most pronounced change at intermediate  $q$ , *e.g.*,  $d\Sigma/d\Omega$  between  $0\text{ T}$  and  $5\text{ T}$  decreases by a factor of about 23 at  $q = 0.1\text{ nm}^{-1}$ . The existence of a relatively strong field dependence of  $d\Sigma/d\Omega$  at the largest  $q$  (factor 2.6) suggests that significant spin disorder is present on a real-space length scale which extends from the average grain size,  $q > 2\pi/D = 0.3\text{ nm}^{-1}$ , down to only a few nanometers, at  $q \approx 2\text{ nm}^{-1}$ . Intraparticle spin misalignment has also been found in a SANS study on the related rare-earth metal Tb [14], where it has been attributed to inhomogeneous microstrain. Calculation of the autocorrelation function of spin-misalignment allows one to determine a characteristic length scale  $l_c$  of spin misalignment [14, 15], which can be taken as a measure for the average distance over which perturbations in the spin structure decay. The inset in fig. 2 shows the field dependence of  $l_c$  in nc Gd. As was concluded from the radially-averaged  $d\Sigma/d\Omega$ ,  $l_c$  varies exclusively on a length scale smaller than  $D$ , with values between about 5–10 nm. This observation further sustains our view that the dominating source of spin disorder in nc Gd presumably originates from the defect cores of grain boundaries.

## References

- [1] Koon N. C., Das B. N., Appl. Phys. Lett. 39 (1981), 840
- [2] Croat J. J., IEEE Trans. Magn. 18 (1982), 1442
- [3] Herzer G., IEEE Trans. Magn. 26 (1990), 1397
- [4] Cable J. W., Wollan E. O., Phys. Rev. 165 (1968), 733
- [5] Koehler W. C., Child H. R., Nicklow R. M., Smith H. G., Moon R. M., Cable J. W., Phys. Rev. Lett. 24 (1970), 16
- [6] Child H. R., Phys. Rev. B 18 (1978), 1247
- [7] Will G., Nathans R. and Alperin H. A., J. Appl. Phys. 35 (1964), 1045
- [8] Moon R. M., Koehler W. C., Cable J. W. and Child H. R., Phys. Rev. B 5 (1972), 997
- [9] Michels D., Krill III C. E. and Birringer R., J. Magn. Mater. 250 (2002), 2003
- [10] Michels A., Vecchini C., Moze O., Suzuki K., Pranzas P. K., Kohlbrecher J., Weissmüller J., Phys. Rev. B 74 (2006), 134407
- [11] Skomski R., J. Phys.: Condens. Matter 15 (2003), R841
- [12] Legvold S., in Ferromagnetic Materials, edited by Wohlfarth E. P., Vol. 1 (North-Holland Publishing Company, Amsterdam), 1980 pp. 183–295
- [13] Weissmüller J., Michels A., Barker J. G., Wiedenmann A., Erb U. and Shull R. D., Phys. Rev. B 63 (2001), 214414
- [14] Weissmüller J., Michels A., Michels D., Wiedenmann A., Krill III C. E., Sauer H. M. and Birringer R., Phys. Rev. B 69 (2004), 054402
- [15] Michels A., Viswanath R. N., Barker J. G., Birringer R. and Weissmüller J., Phys. Rev. Lett. 91 (2003), 267204

	<b>EXPERIMENTAL REPORT</b>	<b>GeNF SANS-2</b>
<b>Nature of defects formed in neutron-irradiated Fe-Cr model alloys</b>		
<b>Proposer:</b>	<b>Andreas Ulbricht<sup>1</sup></b> , <sup>1</sup> Forschungszentrum Dresden-Rossendorf (FZD), Germany	
<b>Co-Proposer(s):</b>	<b>Frank Bergner<sup>1</sup></b>	
<b>Experimental Team:</b>	<b>Andreas Ulbricht<sup>1</sup>, Cornelia Heintze<sup>1</sup></b>	
<b>User Group Leader:</b>	<b>Frank Bergner<sup>1</sup></b>	
<b>Instrument Responsible:</b>	<b>Helmut Eckerlebe<sup>2</sup></b> , <sup>2</sup> GKSS Research Centre Geesthacht, Germany	
<b>Date(s) of Experiment:</b>	13 <sup>th</sup> – 18 <sup>th</sup> July 2007	

## Objective

Reduced activation ferritic-martensitic (RAFM) Cr-steels are candidate materials for future applications in fusion and generation IV fission research and technology. Previous SANS experiments for this class of materials indicated defects on the nanometer size scale to be formed as a result of neutron irradiation [1–5].

The experiment was devoted to the investigation of Eurofer97, which is in the focus of current coordinated European research activities [6], and related Fe-Cr model alloys. The investigation of binary Fe-Cr alloys will significantly contribute to the understanding of the behaviour of more complex alloys.

## Experiment

Samples of Fe-Cr alloys with 2.5, 4.7, 9 and 12.5 at.% Cr, respectively, and Eurofer97 were investigated in the unirradiated condition and the model alloy Fe-9at.%Cr in the neutron-irradiation condition of 0.6 dpa (displacements per atom). Slices of 7 mm x 7 mm, thickness 1 mm, were used. The SANS measurements were carried out at a wavelength of 0.53 nm with three sample – detector distances of 1, 4 and 16 m and corresponding collimation length. The samples were placed in a saturation magnetic field (about 1.7 T). Scattering data were corrected for sample transmission, detector response and background. Absolute calibration was done by means of a vanadium measurement. Raw data analysis was performed using software routines provided by GKSS.

## Achievements and Main Results

Fig. 1 shows the coherent nuclear scattering of the Fe-9Cr model alloy in different conditions obtained after subtraction of the incoherent term of  $0.00755 \text{ cm}^{-1} \text{ sr}^{-1}$  (see corresponding value in fig. 4). Fig. 2 shows the coherent magnetic scattering (separated from the total and nuclear scattering) of the same conditions. We observed a pronounced increase of scattering intensity for the irradiated condition at scattering vectors  $Q > 0.2 \text{ nm}^{-1}$  for both, nuclear and magnetic scattering. The reason of the increase of intensity are irradiation-induced clusters with a size distribution presented in Fig. 3. The A-ratio is about 2.8. This value is far from a value of 1.4 corresponding to nano-voids as scattering objects. This indicates that the irradiation-induced clusters are a Cr-rich  $\alpha'$ -phase. A total of 0.27 vol.-% of irradiation-induced clusters was estimated.

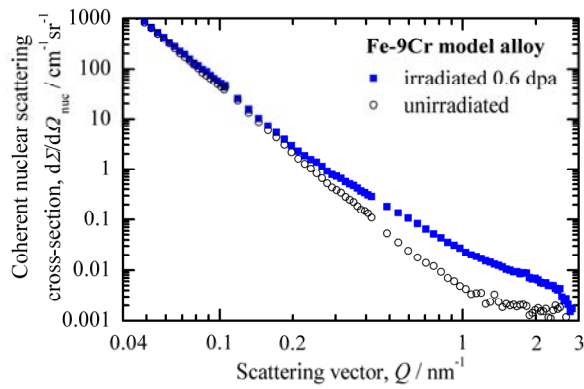


**Figure 1:** Coherent nuclear scattering cross-sections of Fe-9Cr model alloy.

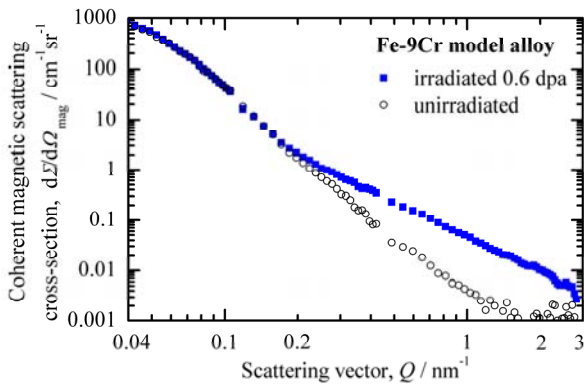


**Figure 2:** Coherent magnetic scattering cross-sections of Fe-9Cr model alloy.

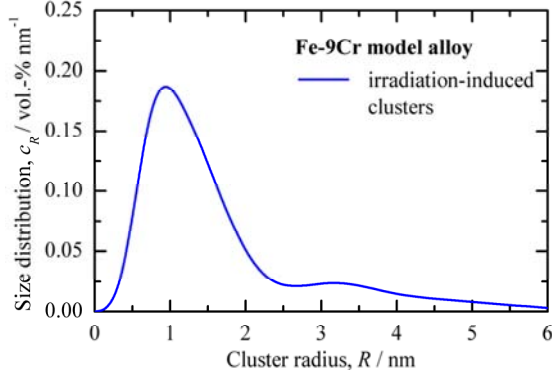


**Figure 3:** Size distribution of irradiation-induced clusters calculated from figure 2.

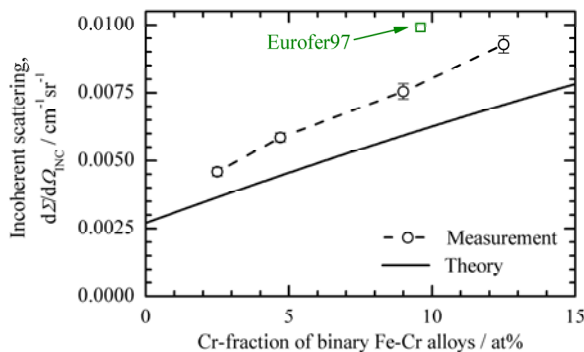



**Figure 4:** Measured incoherent scattering and comparison with theory.

The measured incoherent contributions of the different materials in the unirradiated condition are summarized in Fig. 4. A theoretical curve representing the dependence of the incoherent scattering for binary Fe-Cr on the Cr content is also shown. We find agreement between theory and experiment with respect to the order of magnitude and the tendency with increasing Cr content. The deviation of the measured incoherent scattering intensity from the theoretical curve may be due to point defects, impurities and grain boundaries. In Eurofer97 additional contributions to the incoherent scattering are caused by the alloying elements, in particular those responsible for solution hardening (e. g. Mn).

## References

- [1] Jia, X.; Dai, Y.; Victoria, M.; The impact of irradiation temperature on the microstructure of F82H martensitic/ferritic steel irradiated in a proton and neutron mixed spectrum, *Journal of Nuclear Materials* 305 (2002), 1–7
- [2] Mathon, M.-H.; de Carlan, Y.; Geoffroy, G.; Averty, X.; Alamo, A.; de Novion, C.-H.; A SANS investigation of the irradiation-enhanced  $\alpha$ - $\alpha'$  phases separation in 7-12Cr martensitic steels, *Journal of Nuclear Materials* 312 (2003) 236–248
- [3] Copolla, R.; Dewhurst, C.; Lindau, R.; May, R. P.; Möslang, A.; Valli, M.; Polarized SANS study of microstructural evolution under neutron irradiation in a martensitic steel for fusion reactors, *Physica B* 345 (2004) 225–230
- [4] Copolla, R.; Lindau R.; Magnani, M.; May, R. P.; Möslang, A.; Rensman, J. W.; van der Schaaf, B.; Valli M.; Microstructural investigation, using small-angle neutron scattering, of neutron irradiated Eurofer97 steel, *Fusion Engineering Design* 75-79 (2005) 985–988
- [5] Große, M.; Dai, Y.; Van Petegem, S.; Irradiation-induced structural changes in martensitic steel T91, *Journal of Nuclear Materials* 356 (2006) 112–117
- [6] Lucon, E. et al.; The European effort towards the development of a demo structural material: Irradiation behaviour of the European reference RAFM steel EUROFER, *Fusion Engineering Design* 81 (2006) 917–923

	<b>EXPERIMENTAL REPORT</b>	<b>GeNF SANS-2</b>
<b>SANS experiments with unpolarized neutrons to study precipitation of intermetallic phase in a Fe-Co-Mo alloy</b>		
<b>Proposer:</b>	<b>E. Eidenberger<sup>1</sup></b> , <sup>1</sup> University of Leoben, Department of Physical Metallurgy and Materials Testing, Leoben, Austria	
<b>Co-Proposer(s):</b>	<b>P. Staron<sup>2</sup></b> , <sup>2</sup> GKSS Research Centre Geesthacht, Germany	
<b>Experimental Team:</b>	<b>E. Eidenberger<sup>1</sup>, P. Staron<sup>2</sup></b>	
<b>User Group Leader:</b>	<b>H. Clemens<sup>1</sup></b>	
<b>Instrument Responsible:</b>	<b>M. Sharp<sup>2</sup></b>	
<b>Date(s) of Experiment:</b>	22 <sup>nd</sup> – 27 <sup>th</sup> August.2007	

## Objectives

The Model alloy Fe-25Co-15Mo (wt.%) has been studied since the 1930s because of its very promising hardening potential [1]. However, only today it has become possible to produce such alloys in industrial processes. In the investigated alloy, hardening takes place via the precipitation of a single intermetallic phase, the so-called  $\mu$ -phase. These precipitates lead to hardness values up to 65 HRC and to high thermal stability. Aim of this study is to gather knowledge of the precipitate formation and the kinetics of the precipitation reaction in order to be able to optimize the material properties.

## Experiment

Two detector distances (1 m and 3 m) were used with appropriate collimations to cover scattering vectors  $q$  from  $0.1 \text{ nm}^{-1}$  to  $2 \text{ nm}^{-1}$ . The measurements were performed using unpolarized neutrons at a wavelength of  $\lambda=0.58 \text{ nm}$  and a wavelength spread of  $\Delta\lambda/\lambda=10\%$ . The neutron beam impinging on the samples had a diameter of 3 mm. The samples were magnetized to saturation in a field of 2 T. Measured intensities were corrected for sample transmission, background and detector efficiency. The nuclear cross sections were measured at azimuthal detector angles of  $\alpha=0^\circ$  and  $180^\circ$ , while the sum of nuclear and magnetic cross section was measured at angles of  $\alpha=90^\circ$  and  $270^\circ$ , where  $\alpha$  is the angle between the scattering vector and the magnetization. The scattered intensity was averaged over sectors of  $20^\circ$  around the given mean angles. Absolute cross sections were calculated by comparison with the incoherent scattering of vanadium. A detector resolution of  $128 \times 128$  pixels was used for the analysis.

The investigated samples were heat treated prior to the SANS measurements. Solution annealing at  $1180 \text{ }^\circ\text{C}$  for 5 min and quenching with  $\lambda=0.3$  was conducted for all samples.  $\lambda$  stands for the quenching parameter and is the time (in seconds) the sample needs to cool down from  $800 \text{ }^\circ\text{C}$  to  $500 \text{ }^\circ\text{C}$ , divided by a factor of 100. After that, the samples were annealed at  $500 \text{ }^\circ\text{C}$  for different times (3, 10, 100, 300, 1000 min).

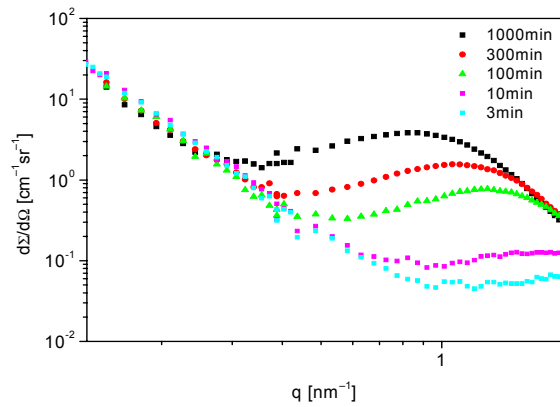


**Figure 1:** Magnetic scattering curves of steel samples aged for 3, 10, 100, 300, and 1000 min.

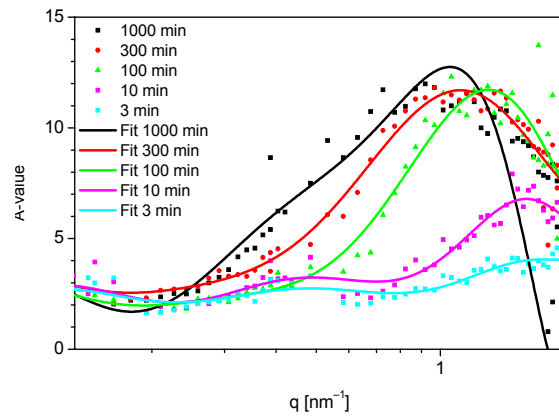


**Figure 2:** Ratio A of nuclear and magnetic scattering intensity.

### Achievements and Main Results

The measured curves exhibit a pronounced maximum due to interparticle interference (Fig. 1). Larger structures are also present in the samples, but they do not change during the heat treatments. The shift of the maximum to lower  $q$  values indicates growth and coarsening of the precipitates.


The ratio  $A$  of nuclear to magnetic scattering gives information about the chemical composition of precipitates. The  $A$ -values derived from the measured scattering curves are shown in Fig. 2. The maximum  $A$ -Value of the samples annealed for 3 and 10 min is 5 and 8, respectively, whereas the value for the samples annealed for longer time is about 12. This indicates that the chemical composition of the particles changes in the early stages of precipitation, but reaches equilibrium composition after 100 min. The scattering curves will be further analyzed in terms of sizes and volume fractions of precipitates for comparison with theoretical models.

Further investigations with SANS are going to be performed on additional samples in the time frame of 10–100 min of annealing time to gather more information about the change in chemical composition of precipitates in the early decomposition stages. For this, in-situ SANS experiments using a special furnace are planned because in this way the decomposition can be studied at different temperatures very effectively. Additional in-situ SAXS measurements have already been carried out recently at the GKSS beamline HARWI II at HASYLAB. Later, the results of both scattering experiments will be combined and compared with model predictions.

### Reference

- [1] Köster W., Tonn W.: Das System Eisen-Kobalt-Molybdän, Archiv für das Eisenhüttenwesen 12, pp. 627–630, (1932)



	<b>EXPERIMENTAL REPORT</b>	<b>GeNF SANS-2</b>
<b>SANS experiments with unpolarized neutrons to study precipitations in hot-work tool steels</b>		
<b>Proposer:</b>	<b>E. Eidenberger<sup>1</sup>, S. Mayer<sup>1</sup></b> <sup>1</sup> University of Leoben, Department of Physical Metallurgy and Materials Testing, Leoben, Austria	
<b>Co-Proposer:</b>	<b>P. Staron<sup>2</sup>,</b> <sup>2</sup> GKSS Research Centre Geesthacht, Germany	
<b>Experimental Team:</b>	<b>E. Eidenberger<sup>1</sup>, P. Staron<sup>2</sup></b>	
<b>User Group Leader:</b>	<b>H. Clemens<sup>1</sup></b>	
<b>Instrument Responsible:</b>	<b>M. Sharp<sup>2</sup></b>	
<b>Date(s) of Experiment:</b>	<b>22<sup>nd</sup> – 27<sup>th</sup> August 2007</b>	

## Objectives

Hot-work tool steels have to possess excellent mechanical and thermo-physical properties in order to fulfil the requirements for their application fields which are mainly light-alloy processing and die-casting. Nowadays the dimensions of hot-work tools in industry are constantly increasing causing the problem that the cooling rate decreases when reaching the core of the tool. This leads to a bainitic transformation and the occurrence of precipitates, which have a strong influence on the mechanical properties of tool steels [1, 2]. The previous characterization of the microstructural constituents was carried out by means of scanning electron microscopy (SEM) and transmission electron microscopy (TEM) (Fig. 1) in order to find the reason for the unfavourable characteristics. As shown in Fig. 1, with decreasing cooling rates the specimens exhibit an increasing amount of globular precipitates along prior austenite grain boundaries, which were identified by EDS analyses to be Cr-Mo- and V-Mo- rich carbides, and also a large number of precipitates within the grains, which could not be resolved by means of conventional TEM. High-resolution (HR-) TEM would provide a direct imaging of those nm-sized particles, but the analyzed volume is very small. On this account, SANS was selected since it provides a direct measuring of the particle size distribution down to the nanometre scale by probing a relatively large sample volume.

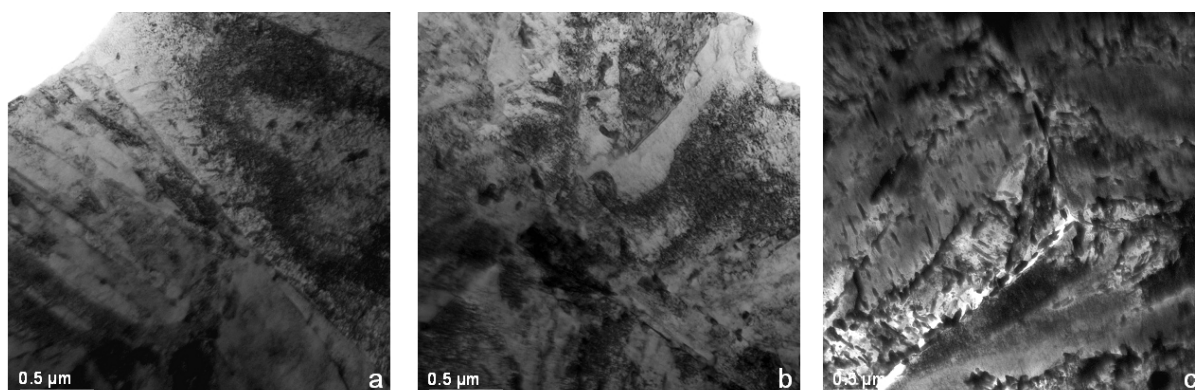


**Figure 1:** Bright-field TEM micrographs of the hardened and heat treated (HT) condition as a function of the  $\lambda$ -value: **a)** 0.6, **b)** 12 and **c)** 28 using the example of W400.

## Experiment

The precipitation behaviour of hot-work tool steel grades W300 (X37CrMoV5-1) and W400 (X38CrMoV5-1) is investigated. The nominal compositions of the materials are given in Table 1. All specimens were heat-treated prior to testing using the following parameters: austenitizing at 990 °C (W400) or 1020 °C (W300) for 30 min, quenching with  $\lambda$ -values of 0.6, 12 and 28 and double tempering for 2 hrs at 610 °C to achieve a working hardness of 44-46 HRC.  $\lambda$  stands for the quenching parameter and is the time (in seconds) the sample needs to cool down from 800 °C to 500 °C, divided by a factor of 100.

**Table 1:** Nominal compositions of W300 and W400 (wt.-%).

	<b>C</b>	<b>Si</b>	<b>Mn</b>	<b>Cr</b>	<b>Mo</b>	<b>V</b>
W300	0.38	1.10	0.40	5.00	1.30	0.40
W400	0.36	0.20	0.25	5.00	1.30	0.45

Four detector distances (1 m, 3 m, 9 m and 21 m) were used with appropriate apertures and collimators to cover scattering vectors  $q$  from 0.02 nm<sup>-1</sup> to 2 nm<sup>-1</sup>. The measurements were performed using unpolarized neutrons at a wavelength of  $\lambda = 0.58$  nm and a wavelength spread of  $\Delta\lambda/\lambda = 10\%$ . The neutron beam impinging on the samples had a diameter of 4 mm. The samples were magnetized to saturation in a field of 2 T. Measured intensities were corrected for sample transmission, background and detector efficiency. The nuclear cross sections were measured at azimuthal detector angles of  $\alpha = 0^\circ$  and  $180^\circ$ , while the sum of nuclear and magnetic cross section was measured at angles of  $\alpha = 90^\circ$  and  $270^\circ$ , where  $\alpha$  is the angle between the scattering vector and the magnetization. The scattered intensity was averaged over sectors of  $25^\circ$  around the given mean angles. Absolute cross sections were calculated by comparison with the incoherent scattering of vanadium. The detector resolution was reduced to 128 x 128 pixels prior to analysis.

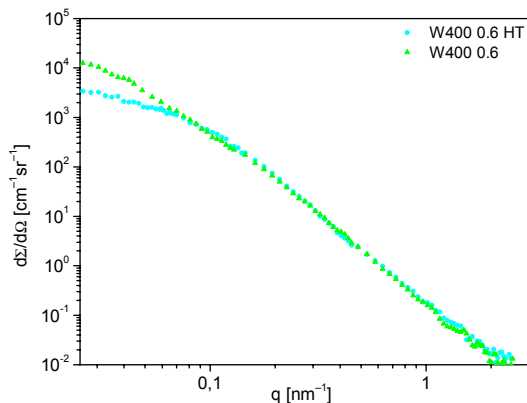


**Figure 2:** Magnetic scattering curves of the W400 alloy, hardened vs. hardened and heat treated (HT) both cooling rate of  $\lambda = 0.6$ .

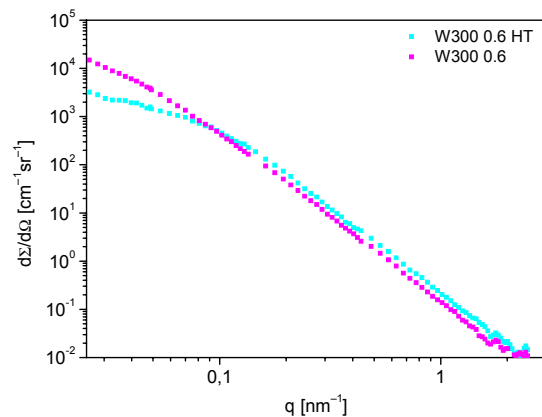


**Figure 3:** Magnetic scattering curves of the W300 alloy, hardened vs. hardened and heat treated (HT) both cooling rate of  $\lambda = 0.6$ .



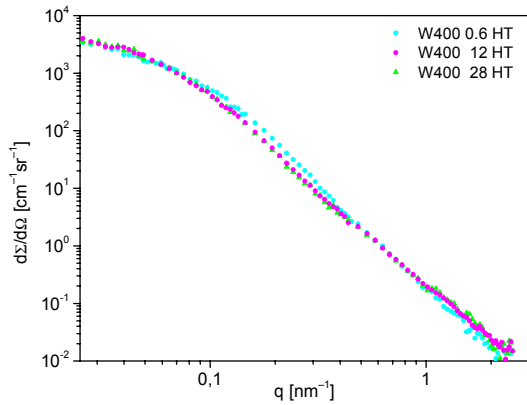


**Figure 4:** Comparison of magnetic scattering curves for different cooling rates of W400 HT.

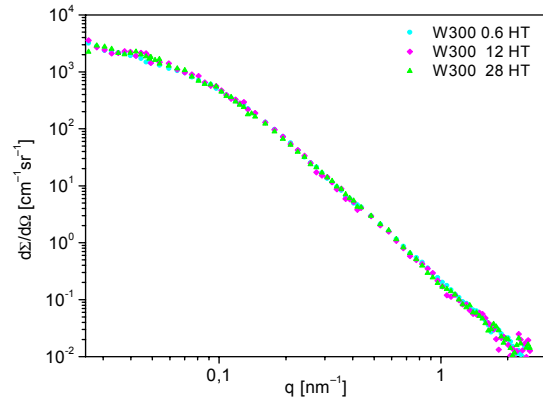


**Figure 5:** Comparison of magnetic scattering curves for different cooling rates of W300 HT.

### Achievements and Main Results


All samples contain large primary carbides and depending on heat treatment secondary hardening carbides. In comparison to the quenched sample the tempered sample shows additional scattering due to the formation of this small secondary hardening carbides (Figs. 2 and 3). The influence of the cooling rate during quenching on the secondary hardening carbides for the W400 and W300 is illustrated in Figs. 4 and 5, respectively. It can be seen that in case of W400 additional scattering is observed in the  $q$ -range of 0.1 to 0.4  $\text{nm}^{-1}$ . This indicates a slight change of size and volume fraction with decreasing cooling rate. In contrast to that the W300 does not show any changes.

The analysis of the SANS data is not yet completed. For a detailed quantitative analysis of the composition of occurring precipitates, further investigations with HR-TEM and atom probe field ion microscopy (APFIM) are going to be performed on these samples. The obtained data shall be used as input parameters for fitting the scattering curves.

### References

- [1] S. Mayer, S. Pölzl, G. Hawranek, C. Scheu, H. Leitner, H. Clemens, I. Siller: Microstructural Characterization of a Hot-Work Tool Steel with a Martensitic- Bainitic Microstructure, *Prakt. Metallogr.* 44 (2007) 4, 182–192
- [2] S. Mayer, C. Scheu, H. Leitner, H. Clemens, I. Siller: Influence of the Cooling Rate on the Mechanical Properties of a Hot-work Tool Steel, *Berg- und Hüttenmännische Monatshefte*, 152 (5) (2007) 132–136



	<b>EXPERIMENTAL REPORT</b>	<b>GeNF SANS-2</b>
<b>Precipitates in a laser beam welded butt-joint of aluminium sheets</b>		
<b>Proposer:</b> <b>Co-Proposer(s):</b>	<b>P. Staron<sup>1</sup>, <sup>1</sup>GKSS Research Centre Geesthacht, Germany</b> <b>W. V. Vaidya<sup>1</sup></b>	
<b>Experimental Team:</b> <b>User Group Leader:</b> <b>Instrument Responsible:</b>	<b>P. Staron<sup>1</sup></b> <b>N. Huber<sup>1</sup></b> <b>M. Sharp<sup>1</sup></b>	
<b>Date(s) of Experiment:</b>	21 <sup>st</sup> November 2007	

## Objective

Aluminium alloys are potential materials for lightweight structures in transportation industry [1]. Laser beam welding (LBW) is, compared to the conventional fusion welding techniques, well suited for Al alloys because of the low localised heat input leading to low distortion [2]. In addition, high strength joints can be produced with high processing speeds. In an earlier SANS investigation, the influence of different heat treatments on the precipitates within and around the weld had been studied [3]. In this investigation, the influence of a post-weld heat treatment on the precipitates that had been missing in the first investigation was determined. The purpose was to find out if the solute is lost in the welding by evaporation or is present but taken into the solution. Re-precipitation is possible only in the latter case.

## Experiment

The investigated specimen was an aluminium sheet (AA6056) with a size of 500 mm × 500 mm and a thickness of 3.2 mm that has been joined using LBW. The sheet was in the T6 temper before welding. After welding, the sheet was given an additional T6 post-weld heat treatment. The fusion zone was approximately 2 mm wide; therefore, a slit of size 2 mm × 10 mm was used with the long edge parallel to the weld. Measurements were done within the fusion zone and in the base material. The neutron wavelength was 5.7 Å. Four detector distances and corresponding collimations were used to cover a  $q$ -range from 0.03 to 2.5 nm<sup>-1</sup>. Detector images were azimuthally averaged.

## Achievements and Main Results


The previous measurements had shown that after welding the initial precipitates are dissolved within the weld and no precipitates with sizes in the nanometre range are present in the weld [3]. The current result shows that by the T6 post-weld heat treatment precipitates with sizes in the nanometre-range are created in the weld (Fig. 1). In other words, not all the solute is lost by evaporation but at least a part of it is taken into solution through welding, and re-precipitates due to the T6 temper. Interestingly, the volume fraction of the (large) precipitates is higher within the weld than that in the base metal. The question about the type of such precipitates (which can be studied only by TEM) remains open in the present investigation but there is a clear indication of precipitation, which in turn should contribute to a recovery of strength of the weld material. In a parallel study, also the influence of the T6 post-weld heat treatment on the residual stresses in the weld region is investigated [4].

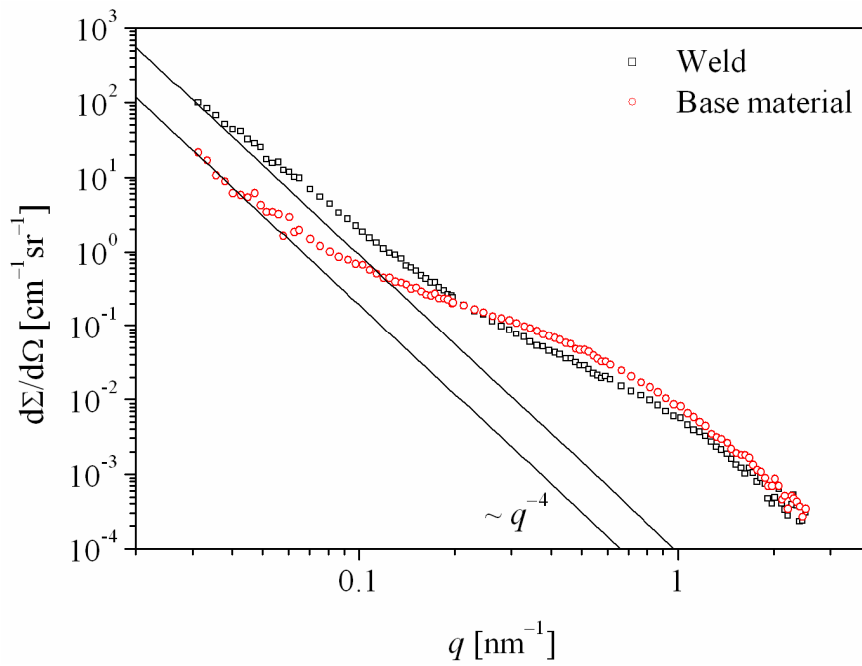


**Figure 1:** Scattering curves of weld and base material of sample laser beam welded initially in the T6 temper and post weld heat treated to T6 again.

## References

- [1] K.-H. Rendigs, Mater. Sci. Forum 242 (1997) 11–24
- [2] E. Schubert, M. Klassen, I. Zerner, C. Walz, G. Sepold, J. Mater. Processing Technol. 115 (2001) 2–8
- [3] P. Staron, W. V. Vaidya, GeNF Experimental Report 2006, p. 91
- [4] W. V. Vaidya, M. Koçak, P. Staron, GeNF Experimental Report 2007 (ARES-2 section of this document)

	<b>EXPERIMENTAL REPORT</b>	<b>GeNF SANS-2</b>
<b>Formation of large scale structures in a binary polymer blend with components of asymmetric mobility</b>		
<b>Proposer:</b> <b>Co-Proposer(s):</b>	<b>Dietmar Schwahn<sup>1</sup></b> , <sup>1</sup> Forschungszentrum Juelich, Germany <b>Vitaliy Pipich<sup>1</sup></b>	
<b>Experimental Team:</b> <b>User Group Leader:</b> <b>Instrument Responsible:</b>	<b>Vitaliy Pipich<sup>1</sup></b> , <b>Dietmar Schwahn<sup>1</sup></b> , <b>Melissa Sharp<sup>2</sup></b> <b>Dietmar Schwahn<sup>1</sup></b> <b>Melissa Sharp<sup>2</sup></b> , <sup>2</sup> GKSS Research Centre Geesthacht, Germany	
<b>Date(s) of Experiment:</b>	23 <sup>rd</sup> – 26 <sup>th</sup> April 2007	

## Objective

The glass transition temperatures of the homopolymers poly(ethylene oxide) (PEO) and poly(methyl methacrylate) (PMMA) are at, respectively, minus 57 °C and plus 120 °C and thereby the two polymers show a distinctive asymmetry with respect to their molecular mobility. Both polymers are miscible; SANS experiments propose a LCST (lower critical solution temperature) phase diagram, which is miscible at low temperature and decomposes in two macroscopic phases at extreme high temperature.

In figure 1 the temperature composition plane of the phase diagram is shown. The boarder lines of glass and crystallization transitions are depicted. The blue points represent a line which we call gelation line. In a former SANS experiment we observed a distinct suppression of thermal composition fluctuations and the formation of large scale structures below this line. There are reasons to assume that the asymmetry in chain mobility of PEO and PMMA is the reason for these large structures. A detailed exploration of these structures, e.g. their size and time evolution as well as the chain conformation is the topic of this proposal.

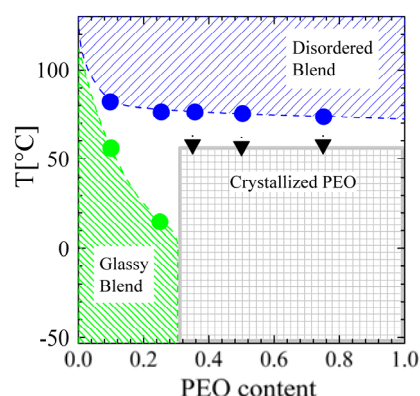


**Figure 1:** Phase diagram.

## Experiment

**Table 1:** Explore samples: Volume fraction of the polymer components.

Sample	h-PEO	d-PEO	h-PMMA	d-PMMA	PEO	PMMA	Matrix
1	0.03	-	-	0.97	0.03	0.97	d
2	0.10	-	-	0.90	0.10	0.90	d
3	0.25	-	-	0.75	0.25	0.75	d
4	0.07	0.03	0.9	-	0.10	0.90	h
5	0.22	0.03	0.75	-	0.25	0.75	h
6	0.10	-	0.87	0.03	0.10	0.90	h
7	0.25	-	0.72	0.03	0.25	0.75	h

Small angle neutron scattering (SANS) experiments were performed above and below the glass transition in the amorphous part of the PEO/PMMA phase diagram which is located below 30 % of PEO content. The composition of the explored samples is summarized in Table I. The molar weight of the components was between 20 and 28 kDa.

## Achievements and Main Results

### Scattering in Polymer Blend

In this section we present scattering from the PEO/PMMA blend with one component deuterated and the other one protonated in order to achieve a large scattering contrast. First, the measurements were performed in the “pure” glassy state at room temperature, then at 200°C after heating up the samples and waiting for about two hours for equilibration.

#### 3 % *h*-PEO in 97 % deuterated *d*-PMMA

PMMA is a “good solvent” for PEO as the Flory-Huggins (FH) interaction parameter is negative. In figure 2 scattering profiles from this sample are plotted for temperatures at 20 and 200 °C. The scattering cross section shows scattering from two scattering centers which are very different in size. At low  $Q$  below  $0.007 \text{ \AA}^{-1}$  the scattering for the two temperatures is the same with a  $Q^{-4}$  behavior which indicates a 3D compact structure with sharp interface. Figure 2(b) shows the large  $Q$  scattering patterns. In this  $Q$  range the scattering came from polymer scattering. The scattering at 200 and 250°C is largest because of enhanced thermal fluctuations characteristic for LCST systems in consistence with the larger correlation length  $\xi$  (see Table 2).

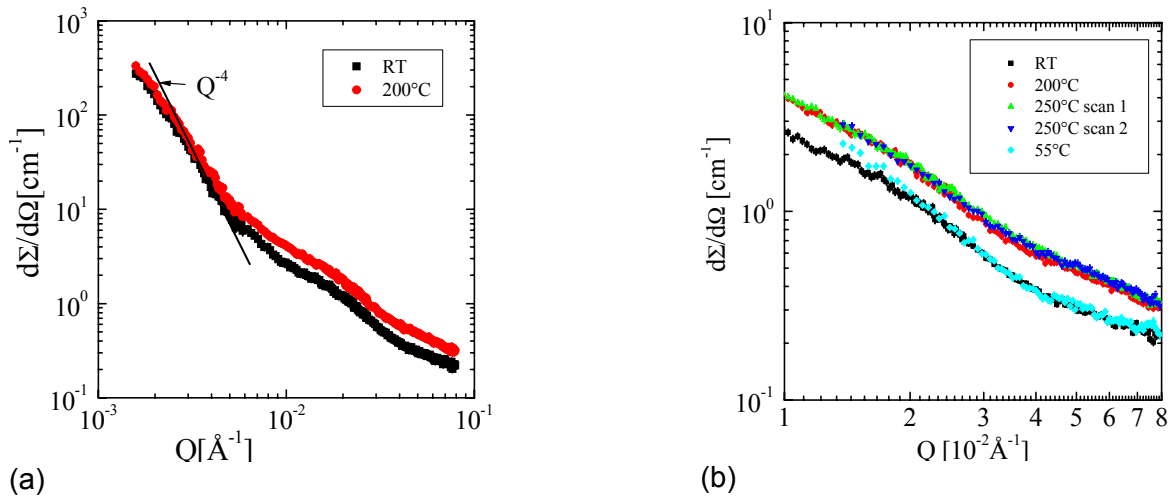


**Figure 2:** (a) Scattering profile of sample 5 at 20 and 200 °C, (b) scattering curve at large  $Q$ .

**Table 2:** Fit parameters of sample 1.

$T[^\circ\text{C}]$	$\xi[\text{\AA}]$	$I(0)[\text{cm}^{-1}]$
20	$54.9 \pm 0.02$	$2.975 \pm 0.002$
200	$59.8 \pm 0.04$	$4.923 \pm 0.007$
250	$58.8 \pm 0.04$	$4.885 \pm 0.006$

### 10 and 25 % h-PEO in deuterated PMMA matrix

In figure 3 scattering from two blends with larger PEO content are depicted for RT and 200 °C. Qualitatively, the same results were obtained as for the 3 % PEO sample in figure 2. Scattering from large heterogeneities at small Q and scattering from thermal composition fluctuations of the polymers. Again thermal fluctuations increase with temperature confirming the LCST type of the PEO/PMMA blend.

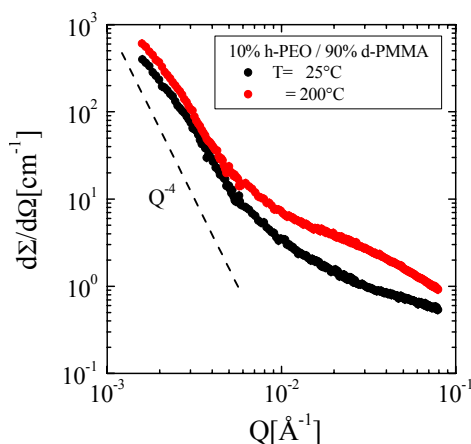


**Figure 3 (a):**  
10 % h-PEO / 90 % d-PMMA,

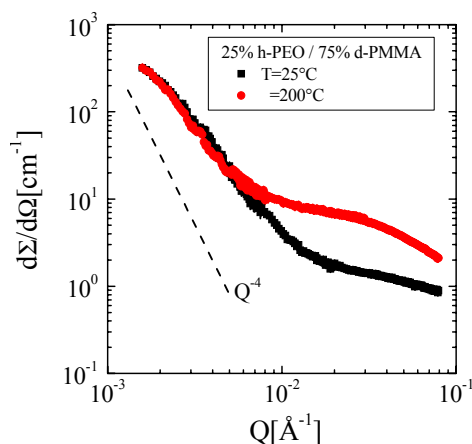


**Figure 3 (b):**  
25 % h-PEO / 75 % d-PMMA.

On the other hand the low-Q scattering part is almost not affected by annealing at 200 °C. The aim of this experiment was to find out the origin of this upturn of scattering. Theory predicts large scale composition fluctuations below the “gelation” temperature in blends with polymers of strong asymmetry in mobility. But because this scattering does not disappear at high temperature most likely mass density fluctuations, e.g. cavities are the main reason of scattering. This assumption is supported by the large scattering contrast of cavities in a deuterated matrix. Therefore, we repeated the measurements with samples of much smaller scattering contrast, e.g. with a protonated matrix.

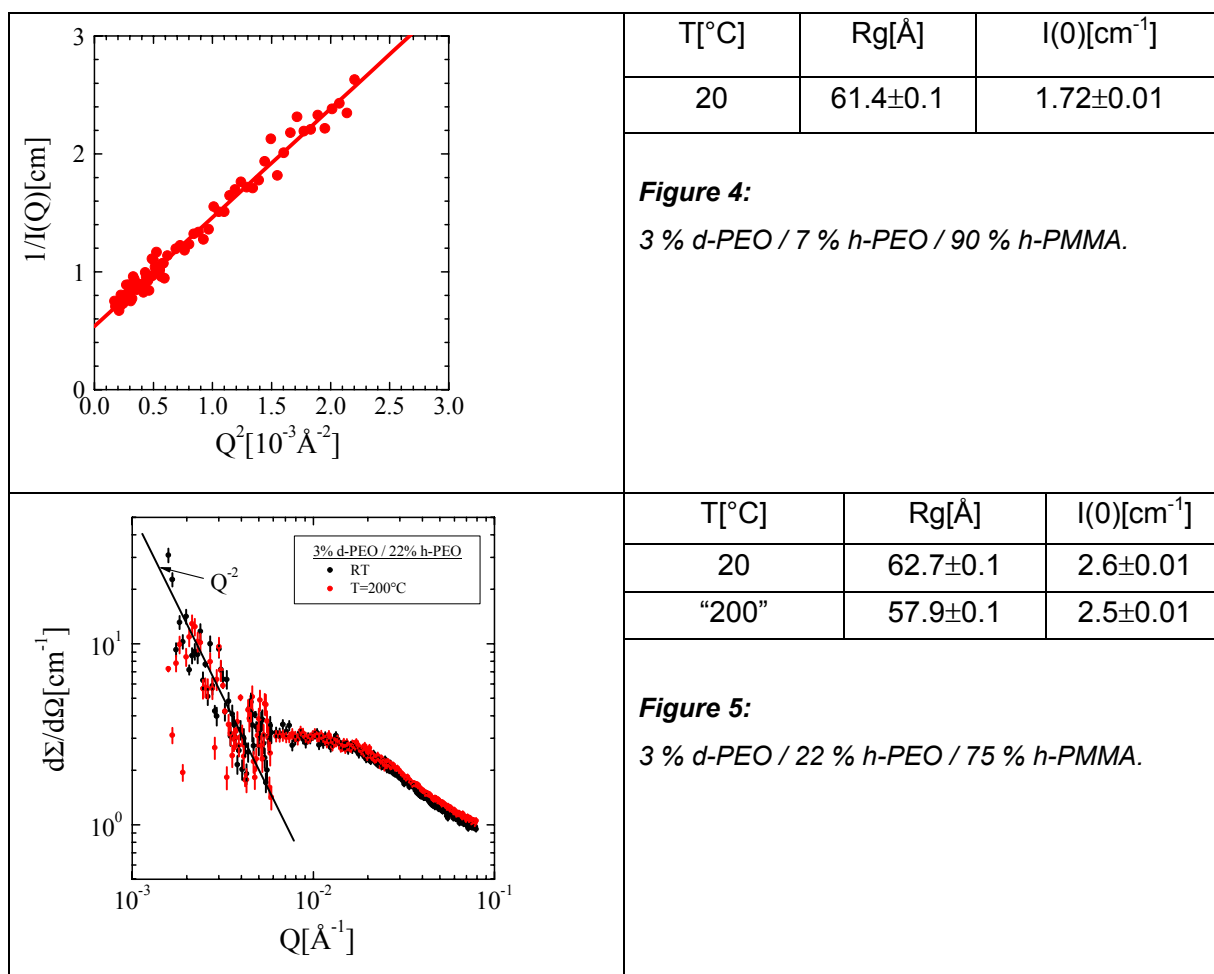
### Single Coil Scattering and Low Scattering Contrast of Cavities

In a next series of experiments we measured samples with a protonated matrix of about 30 times smaller scattering contrast for cavities. In order to visualize a possible large scale phase separation one component was always prepared as deuterated/protonated mixture which also allowed the determination of the chain conformation of PEO and PMMA in the blend.

### Deuterated PEO in protonated matrix

In sample 4 one has a 10/90 ratio of PEO/PMMA with 3 % of deuterated PEO. Figure 4 shows the data in Zimm representation delivering  $R_g$  and the scattering at  $Q=0$  of the PEO chain from fitting a straight line (table with figure 4). A small upturn (not shown in this example) at low- $Q$  range still exists but it is of approximately two orders of amplitude lower intensity in comparison with the deuterated matrix.

In sample 5, 3 % of total 25 % PEO concentration was deuterated. This sample was measured above and below glass transition temperature at 20 and 200 °C as depicted in figure 7. As for the previous sample a small upturn still exists. The radius of gyration of the d-PEO chain at room temperature is close to that of sample 4 of smaller total PEO concentration. After annealing at 200 °C we got a 10 % smaller  $R_g$  which is qualitatively consistent with observations from literature.



### Deuterated PMMA in protonated matrix

In sample 6 one has a 10/90 ratio of PEO/PMMA with 3 % of deuterated PMMA. Figure 6 shows the data in double logarithmic representation delivering  $R_g$  and the scattering at  $Q=0$  of the PMMA from the large  $Q$  data (see table). Again a small upturn at low- $Q$  range still exists. Similar results are obtained for sample 7, with less total PMMA concentration of 75 % but again with 3 % concentration deuterated PMMA. The corresponding results are depicted in figure 8. In contrast to PEO the radius of gyration of the PMMA chain slightly increases after heating up to higher temperature. The small upturn observed for all samples and temperatures in the protonated matrix tentatively follows a  $Q^{-2}$  power law. But the statistical accuracy is too bad to give a conclusive answer about the origin of this scattering.



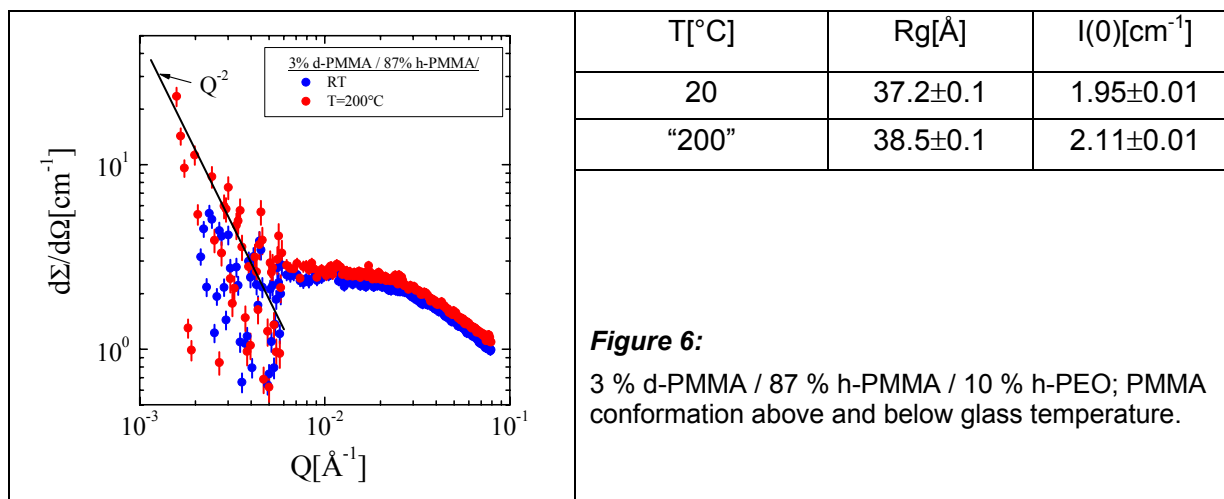


**Figure 6:**  
3 % d-PMMA / 87 % h-PMMA / 10 % h-PEO; PMMA conformation above and below glass temperature.

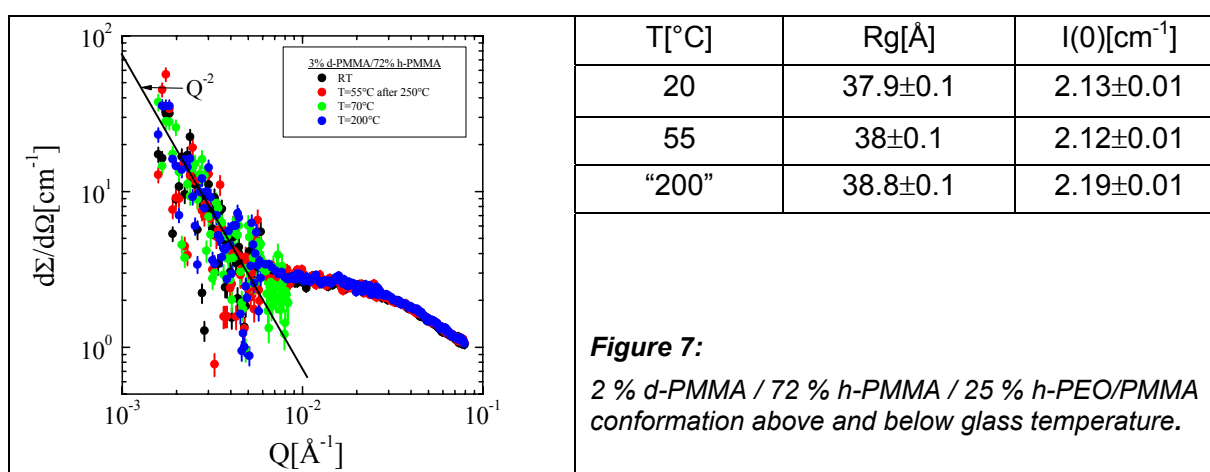



**Figure 7:**  
2 % d-PMMA / 72 % h-PMMA / 25 % h-PEO/PMMA conformation above and below glass temperature.

## Summary

In this study we determined scattering above and below the glass transition in the amorphous part of the PEO/PMMA phase diagram which is located below 30 % of PEO content. The scattering patterns always consisted of scattering from large objects (>1000 Å) at low Q and of Debye-like scattering from thermal composition fluctuations and single coils in consistency with earlier SANS experiments. The main objective of the present experiment was the characterization of large scale structures. Variation of scattering contrast from deuterated to protonated matrix, e.g. from large to about 5 to 6 times smaller mean coherent scattering length density, consistently suppressed the scattering from the "large" objects by nearly two orders of magnitude. The annealing of the samples at temperatures far above the glass transition shows only minor changes of the scattering profile. The conclusion was that the upturn at small Q is dominated from scattering of cavities. In a next experiment we have to prepare the samples more carefully in order to get more "clean" samples and also to determine the upturn from the protonated samples with much better statistical accuracy. In this way we hope get some definite information about large scale phase decomposition due to asymmetric mobility of the two polymer components.



 <p><b>GKSS</b> FORSCHUNGSZENTRUM in der HELMHOLTZ-GEMEINSCHAFT</p>	<p><b>EXPERIMENTAL REPORT</b></p>	<p><b>GeNF SANS-2</b></p>
<p><b>Dipole-Field-Induced Spin Disorder In Nanoporous Inert-Gas Condensed Materials</b></p>		
<p><b>Proposer:</b></p>	<p><b>A. Michels<sup>1</sup></b>, <sup>1</sup>Technische Physik, Universität des Saarlandes, Saarbrücken</p>	
<p><b>Co-Proposer(s):</b></p>	<p><b>M. Elmas<sup>1</sup></b>, <b>F. Döbrich<sup>1</sup></b>, <b>J. Kohlbrecher<sup>1</sup></b>, <b>R. Birringer<sup>1</sup></b></p>	
<p><b>Experimental Team:</b></p>	<p><b>M. Elmas<sup>1</sup></b>, <b>F. Döbrich<sup>1</sup></b>, <b>A. Michels<sup>1</sup></b></p>	
<p><b>User Group Leader:</b></p>	<p><b>A. Michels<sup>1</sup></b></p>	
<p><b>Instrument Responsible:</b></p>	<p><b>M. Sharp<sup>2</sup></b>, <b>H. Eckerlebe<sup>2</sup></b>, <sup>2</sup>GKSS Research Centre Geesthacht, Germany</p>	
<p><b>Date(s) of Experiment:</b></p>	<p>22<sup>nd</sup> – 27<sup>th</sup> March and 26<sup>th</sup> – 28<sup>th</sup> November 2007</p>	

## Objective

The purpose of the present research was to investigate the existence of the recently discovered clover-leaf anisotropy (see below) in the magnetic SANS cross section of nanocrystalline (nc) inert-gas condensed (igc) ferromagnets, in particular, in nc Fe. Related to the synthesis procedure, igc materials typically contain a certain volume fraction of pores: in the igc process, the starting material is evaporated into an inert-gas atmosphere, resulting in the formation of nanoscale particles which are collected and mechanically compacted under high pressure. The resulting porosity can be controlled within certain limits via the applied pressure during compaction (typically between 0.5 GPa – 2 GPa). In fact, igc samples constitute two-phase systems of non-magnetic “particles” (pores) in a magnetic matrix, which are most likely to account for dipolar stray fields in the approach-to-saturation regime, similar to nanocomposites [1]. The jump of the magnetization at the interface between a pore and the ferromagnetic matrix is maximum in such samples, and we therefore expect to observe strong dipole-field-induced spin disorder in the magnetic SANS cross section of these materials. It may therefore be expected to detect the related spin disorder in igc nanoporous magnetic materials as a clover-leaf shaped anisotropy.

## Experiment, Achievements and Main Results

The nuclear and magnetic SANS cross section  $d\Sigma/d\Omega$  of a nc ferromagnet can be expressed as the sum of two contributions [1],

$$\frac{d\Sigma}{d\Omega}(\mathbf{q}) = \frac{d\Sigma_R}{d\Omega}(\mathbf{q}) + \frac{d\Sigma_M}{d\Omega}(\mathbf{q})$$

$$\frac{d\Sigma_R}{d\Omega}(\mathbf{q}) = \frac{8\pi^3}{V} \left[ |\tilde{N}|^2 + b_H^2 |\tilde{M}_z|^2 \sin^2\theta \right] \quad (1)$$

$$\frac{d\Sigma_M}{d\Omega}(\mathbf{q}) = \frac{8\pi^3}{V} \left[ b_H^2 |\tilde{M}_x|^2 + b_H^2 |\tilde{M}_y|^2 \cos^2\theta - b_H^2 (\tilde{M}_y \tilde{M}_z^* + \tilde{M}_y^* \tilde{M}_z) \sin\theta \cos\theta \right] ,$$

where  $V$  denotes the scattering volume,  $c^*$  denotes a quantity complex-conjugated to  $c$ ,  $b_H$  is a constant,  $\theta$  is the angle between the scattering vector  $\mathbf{q}$  and the external magnetic field  $\mathbf{H}$ , and  $\tilde{N}(\mathbf{q})$  and  $\tilde{\mathbf{M}}(\mathbf{q}) = (\tilde{M}_x, \tilde{M}_y, \tilde{M}_z)$  denote, respectively, the Fourier coefficients of the nuclear and of magnetic scattering-length densities. The residual scattering cross section  $d\Sigma_R/d\Omega$  contains the *nuclear* SANS and the part of the magnetic SANS which originates from

the *longitudinal* magnetization component  $M_z$ , whereas the spin-misalignment scattering cross section  $d\Sigma_M/d\Omega$  depends on the *transversal* spin components  $M_x$  and  $M_y$ .  $d\Sigma_M/d\Omega$  vanishes at complete saturation. Important to note in the present context is the fact that Eq. (1) contains a recently discovered term [1] which varies as  $\sin\theta \cos\theta$ , the so-called clover-leaf anisotropy, resulting in maxima roughly along the detector diagonals ( $\theta = \pm 45^\circ$ ).

Note that Eq. (1) is valid for both single-phase as well as multi-phase materials. However, contributions proportional to  $\sin\theta \cos\theta$  are expected to be particularly relevant in multi-phase magnetic nanocomposites (as opposed to *homogeneous* single-phase materials), where in addition to nonuniformities in the spin orientation, variations in the magnitude of the magnetization have to be taken into account [1]. The terms  $d\Sigma_M/d\Omega \propto \sin\theta \cos\theta$  are a direct manifestation of the dipolar character of magnetic neutron scattering, and, as such, they are *a priori* unrelated to the details of the magnetic microstructure. These details affect the scattering through the Fourier coefficients  $\tilde{M}_y(\mathbf{q})$  and  $\tilde{M}_z(\mathbf{q})$  of the magnetization [compare Eq. (1)]. The clover-leaf-shaped anisotropy is by no means a subtle feature that is peculiar only to a small class of magnetic materials, rather, such an angular anisotropy is expected to be relevant in almost all nanomagnets, whenever correlations between  $\tilde{M}_y(\mathbf{q})$  and  $\tilde{M}_z(\mathbf{q})$  exist. In this context we would also like to note that we have recently observed the dipole-field effect in steel samples containing nanometer-sized NiAl precipitates [2].

We have measured the magnetic-field-dependent SANS cross section of several nc igc Fe samples with different volume fractions of porosity. As can be seen in the figure below, the clover-leaf anisotropy is indeed present in  $d\Sigma_M/d\Omega$  of nc igc Fe. This observation is particularly relevant for the interpretation of SANS data and thus for the understanding of the materials' magnetic microstructure; it is in contrast to the recent SANS results obtained by Löffler *et al.* [3] on igc nc Fe and Co, where this type of angular anisotropy has not been detected.

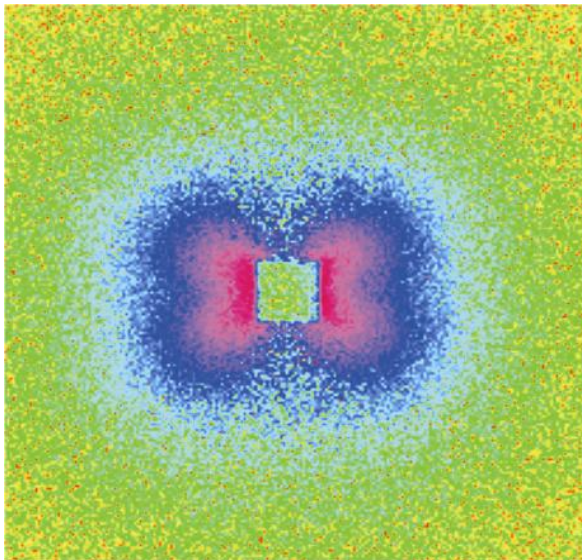



**Figure 1:**

Magnetic (difference) SANS cross section of nanocrystalline inert-gas condensed Fe at 600 mT. The scattering at 1.73 T has been subtracted. The average crystallite size is 44 nm and the volume fraction of pores is about 12 %.

## References

- [1] A. Michels, C. Vecchini, O. Moze, K. Suzuki, P. K. Pranzas, J. Kohlbrecher, J. Weissmüller, Phys. Rev. B 74 (2006), 134407
- [2] M. Bischof, P. Staron, A. Michels, P. Granitzer, K. Rumpf, H. Leitner, C. Scheu, H. Clemens, Acta Mater. 55 (2007), 2637
- [3] J. F. Löffler, H. B. Braun, W. Wagner, G. Kostorz and A. Wiedenmann, Phys. Rev. B 71 (2005), 134410

	<b>EXPERIMENTAL REPORT</b>	<b>GeNF SANS-2</b>
<b>Characterisation of Hydrogen Distribution in Roller Steel With the Help of Small-Angle Neutron Scattering</b>		
<b>Proposer:</b>	<b>Helmut Eckerlebe<sup>1</sup></b> , <sup>1</sup> GKSS Research Centre Geesthacht, Germany	
<b>Co-Proposer(s):</b>		
<b>Experimental Team:</b>	<b>Helmut Eckerlebe</b>	
<b>User Group Leader:</b>	<b>Andreas Schreyer<sup>1</sup></b>	
<b>Instrument Responsible:</b>	<b>Helmut Eckerlebe</b>	
<b>Date(s) of Experiment:</b>	April, May 2007	

## Objectives

The main task was to perform test measurements to evaluate the probability of SANS to characterize the hydrogen distribution in roller bearing steels.

Roller bearing steel samples containing up to 4 ppm hydrogen were investigated with small-angle neutron scattering (SANS). After several test measurements scanning with the neutron beam from the center to the edge of the samples it became obvious that SANS is not sensitive enough to measure the hydrogen distribution in this steel samples

## Experiment

SANS measurements were performed at the instrument SANS-2 at the Geesthacht Neutron Facility (GeNF) using the shortest possible distance between sample and detector of 1 m (neutron wavelength  $\lambda = 0.58$  nm,  $\Delta\lambda/\lambda = 0.1$ ) to cover the range of scattering vector  $q$  between  $10^{-2}$  nm<sup>-1</sup> and 3 nm<sup>-1</sup>. The samples were placed in a vacuum chamber to avoid background scattering from the humidity in the air. A magnetic field of 2 Tesla was applied to the sample perpendicular to neutron beam in order to align the magnetic structures in the steel samples and to avoid the strong scattering of large not-ordered magnetic domains. Measured intensities were corrected for sample transmissions and detector efficiency. An aperture of diameter 3 mm was used in front of the sample. The samples were scanned from the center to the edges to find differences in the hydrogen contents. Absolute cross sections were calculated by comparison with the incoherent scattering of vanadium.

## Achievement and Main Results

As an example the scattering curves of sample new roller and roller R8 is presented in Fig 1. The isotropic incoherent scattering of the steel and the hydrogen is accessible at large scattering angles only. In order to obtain better statistics, the intensity was averaged over  $2\pi$  at constant  $|q|$ . Assuming, that the microstructure of the rollers is homogeneous and has not changed during the treatment with hydrogen, the scattering of roller R8 and NR at small angles ( $|q| < 1.25$  nm<sup>-1</sup>) is identical within the margin of error. In this sample the concentration of hydrogen is below the detection limit.

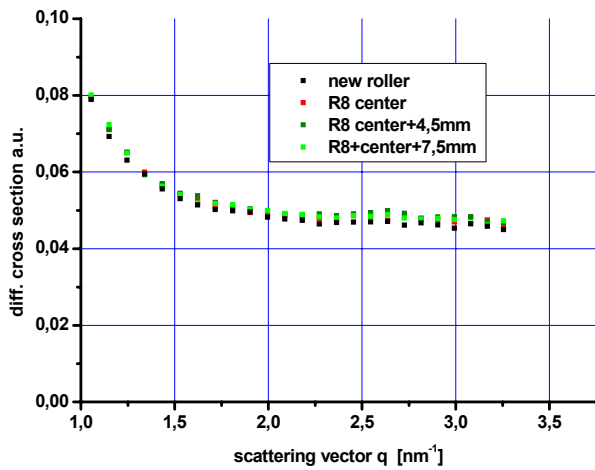


**Figure 1:**

Scattering intensity of new roller and roller R8. The intensity is radially averaged to increase the statistics

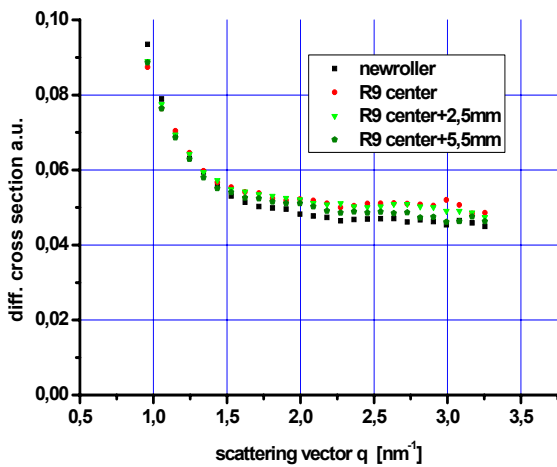



**Figure 2:**

Scattering intensity of sample roller 9. A small difference of the scattering of new roller and roller 9 is visible.

A small difference between the scattering curves of sample roller 9 and the new roller at  $|q| > 2 \text{ nm}^{-1}$  is visible in Fig. 2. The intensity scan of R9\_center and R9\_center+2.5mm is about 10 % higher than the background contribution of the ground material NR. In addition, one can clearly see that the scattering curves of r9\_center+5.5mm decreases; it is 3 % higher than the background contribution of NR only. Provided that sample R9 has no gradient in composition and microstructure, the concentration of H is equal inside of the material app.125 ppm; it decreases towards the surface of the roller. The amount of H close to the surface of is app. 45 ppm.

Several attempts can be done, to decrease the unwanted background: e.g. inelastic scattering can be lowered by cooling the specimen and multiple scattering can be avoided by thinning the sample, but at the expense of scattered intensity. If all conditions are fulfilled, the limit of detection of bound hydrogen can be less than 50 ppm.

	<b>EXPERIMENTAL REPORT</b>	<b>GeNF SANS-2</b>
<b>Small angle neutron scattering analysis of amphiphilic triblock copolymer gels</b>		
<b>Proposer:</b> <b>Co-Proposer(s):</b>	<b>C. M. Papadakis<sup>1</sup>, A. Kulkarni<sup>1</sup>,</b> <b>A. M. Bivigou Koumba<sup>2</sup>, A. Laschewsky<sup>2</sup>, M. Sharp<sup>3</sup></b> <sup>1</sup> Physikdepartment E13, TU München, Garching, Germany <sup>2</sup> Institut für Chemie, Universität Potsdam, 14476 Golm, Germany <sup>3</sup> GKSS Research Centre Geesthacht, Germany	
<b>Experimental Team:</b> <b>User Group Leader:</b> <b>Instrument Responsible:</b>	<b>A. Kulkarni<sup>1</sup>, Melissa Sharp<sup>3</sup>, C. M. Papadakis<sup>1</sup></b> <b>C. M. Papadakis<sup>1</sup></b> <b>Melissa Sharp<sup>3</sup></b>	
<b>Date(s) of Experiment:</b>	23 <sup>rd</sup> – 25 <sup>th</sup> November 2007	

## Objectives

Stimuli-responsive polymers react strongly to even weak changes of their environment and are therefore of interest for a number of applications, such as drug delivery systems, sensors and micromechanics [1–3]. In many applications, chemically connected polymer networks have been used [4], which, however, have the disadvantage that the response times depend on the network size and may be too long. An alternative approach is based on physically connected (micellar) gels from amphiphilic block copolymers with a responsive hydrophilic block and a hydrophobic block [5]. They have the advantage that the micelles are much smaller than usual, chemically connected microgels and that the gels can easily be reshaped.

## Experiment

A triblock copolymer with deuterated polystyrene (dPS) end blocks of molar mass 1150 g/mol and a poly(N-isopropylacrylamide) (PNIPAM) middle block having molar mass 23 000 g/mol was studied by small angle neutron scattering (SANS) at the SANS-2 instrument at GKSS, Geesthacht. The wavelength was 0.58 nm, and the sample-to-detector distance was varied between 1 and 9 m. The sample temperature was varied between 26 and 36 °C. The isotropic scattering was azimuthally averaged, the transmission-corrected background was subtracted and the intensities were brought to absolute scale using a vanadium single crystal. All these operations were carried out using the software SANDRA [6]. The polymer is water soluble; hence micellar solutions and gels could be prepared by dissolving the polymer in water. D<sub>2</sub>O/H<sub>2</sub>O mixtures were used to contrast-match the dPS core or the PNIPAM shell. In this way, a micellar solution at a concentration of 5 wt.-% was studied in D<sub>2</sub>O (PNIPAM shell observable) and a micellar gel at 20 wt.-% both in D<sub>2</sub>O (PNIPAM matrix observable) and in a D<sub>2</sub>O/H<sub>2</sub>O mixture of ratio 17/83 (dPS cores observable).

## Achievement and Main Results

Figure 1(a) shows SANS curves of the micellar solution in D<sub>2</sub>O at various temperatures. Below the LCST (32 °C), the curves resemble the form factor of spheres, i.e. spherical micelles. In contrast, above the LCST, a correlation peak appears which is due to the aggregation of collapsed and thus water-insoluble micelles. Similarly but more pronounced results obtained for micellar gel in D<sub>2</sub>O (Figure 1(b)). The gel curves in D<sub>2</sub>O also show the LCST at 32 °C.



Above the LCST the curves show a correlation peak and pronounced forward scattering due to the clusters formed by the aggregated micelles. Cooling back the solution to 26 °C shows that the switching behavior is reversible. The scattering of the dPS cores in the micellar gel (Figure 1(c)) does not show any change in form factor above LCST, as expected, but a correlation peak appears due to the aggregation of the micelles, i.e. a decrease of the inter micellar distance.

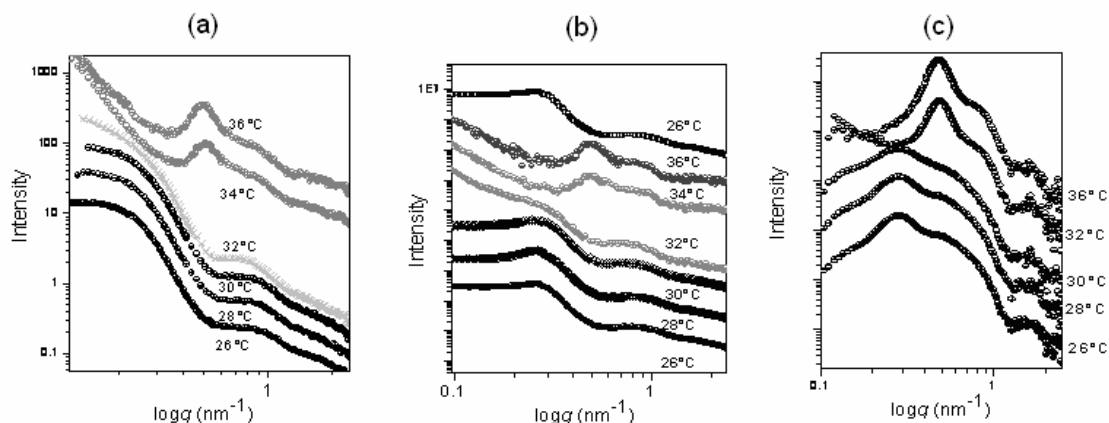


**Figure 1:** SANS curves of the deuterated triblock copolymer **(a)** solution in D<sub>2</sub>O (5 wt.-%), **(b)** gel in D<sub>2</sub>O (20 wt.-%) and **(c)** gel in D<sub>2</sub>O / H<sub>2</sub>O (20wt.-%) at various temperatures. The curves were shifted vertically.


In summary, the micelles formed by the partially deuterated triblock copolymers show a collapse due to the NIPAM shell at 32 °C. Above the LCST at 32 °C, the micelles form clusters.

This work was financially supported by DFG in the priority program SPP1259 (PA771/4).

## References

- [1] M. Shibayama et al., J. Chem. Phys. (2002) 97, 6829
- [2] D. Kuckling et al., Macromol. Mater. Eng. (2003) 288, 144
- [3] J. E. Chung, J. Controlled Release (1999) 62, 115
- [4] T. Tanaka et al., Phys. Rev. Lett. (1985) 55, 2455
- [5] F. M. Winnik et al., Macromolecules (1992) 25, 1876
- [6] P. Biemann, M. Haese-Seiller, P. Staron, Physica B (2000) 276-278, 156



	<b>EXPERIMENTAL REPORT</b>	<b>GeNF SANS-2</b>
<b>The study of the nature of the low-temperature inter-ion correlations in CeAl<sub>3</sub> by means of SANS</b>		
<b>Proposer:</b>	<b>G. P. Kopitsa<sup>1</sup></b> , <sup>1</sup> Petersburg Nuclear Physics Institute, Gatchina, 188300 Russia	
<b>Co-Proposer(s):</b>	<b>D. N. Lazukov<sup>2</sup></b> , <sup>2</sup> Russian Research Centre "Kurchatov Institute", Kurchatov sq. 1, Moscow, 123182 Russia <b>N. N. Tiden<sup>2</sup></b>	
<b>Experimental Team:</b>	<b>G. P. Kopitsa<sup>1</sup>, N. N. Tiden<sup>2</sup>, H. Eckerlebe<sup>3</sup></b>	
<b>User Group Leader:</b>	<b>S. V. Grigoriev<sup>1</sup></b>	
<b>Instrument Responsible:</b>	<b>H. Eckerlebe<sup>3</sup></b> , <sup>3</sup> GKSS Research Centre Geesthacht, Germany	
<b>Date(s) of Experiment:</b>	24 <sup>th</sup> – 29 <sup>th</sup> June 2007	

## Objectives

The goal of this proposal is to investigate the magnetic scattering from the inter-ion correlations in heavy-fermion substance CeAl<sub>3</sub> at low temperatures by means of small angle neutron scattering (SANS).

CeAl<sub>3</sub> was one of the first materials established to be a heavy-fermion compound. Nevertheless the origin of the low temperature ground state is still a subject of discussions. A wide variety of ground states and models have been proposed for CeAl<sub>3</sub> – frustrated short range order [1], antiferromagnetic order [2], anisotropic Kondo effect [3] or exciton-polaron model [4]. The recent measurements performed at time-of-flight (TOF) spectrometer have shown oscillation momentum transfer ( $Q$ ) dependence of quasi-elastic magnetic scattering intensity at  $T \sim T_K$ . These results have been treated as a presence of dynamical magnetic inter-ion correlations of the ferromagnetic type [5]. In spite of the fact that this type of correlation has been proposed in [5], the momentum transfer range has been insufficient (the smallest  $Q \sim 0.4 \text{ \AA}^{-1}$ ) to obtain the incontrovertible evidence of the type of correlations and characteristic information about inter-ion correlation – correlation length. So, to obtain such kind of information about the correlations it was necessary to perform measurements at  $Q < 0.4 \text{ \AA}^{-1}$ .

## Experiment

### 1. Sample

The polycrystalline samples of CeAl<sub>3</sub> and LaAl<sub>3</sub> (non-magnetic structural analog CeAl<sub>3</sub>) were studied. The samples are the same as used for investigations in [5,6].

### 2. Small-angle neutron scattering

The small angle neutron scattering (SANS) experiment was performed at the SANS-2 scattering facility of FRG-1 research reactor in Geesthacht (Germany), which operates in near point geometry using neutrons with the wavelength  $\lambda = 5.8 \text{ \AA}$  ( $\Delta\lambda/\lambda=0.1$ ). The range of momentum transfer  $1 \cdot 10^{-2} < q < 2.4 \cdot 10^{-1} \text{ \AA}^{-1}$  was obtained using two sample-to-detector distances (1 and 3 m). The scattered neutrons were detected by a position sensitive detector with 256x256 pixels.

The samples were mounted in the closed cycle refrigerator and the measurements were carried out at the temperatures  $T = 8, 10, 15$  and  $60 \text{ K}$ . The magnetic field  $H = 0$  and  $213 \text{ mT}$  was set perpendicular to the incident neutron beam. The measured data were calibrated by the

incoherent scattering of vanadium and corrected for the sample transmission, background scattering (from the sample holder) and detector response.

The magnetic contribution to the scattering was determined as an excess over the nuclear scattering by the sample at the temperature  $T = 60$  K:

$$I_m(q) = I(T, q) - I(T=60 \text{ K}, q) \cdot R \quad (1)$$

where:  $R = I(T, q=0) / I(T=60 \text{ K}, q=0)$  is the transmission coefficient.

Notice that the SANS measurements in all investigated  $q$ -range for both samples were carried out at the temperatures  $T = 10$  and  $60$  K only. At  $T = 8$  and  $15$  K the range of momentum transfer was  $4.5 \cdot 10^{-2} < q < 2.4 \cdot 10^{-1} \text{ \AA}^{-1}$ .

## Achievements and Main Results

The momentum dependencies of the magnetic contribution  $d\Sigma_m(q)/d\Omega$  to the small-angle neutron scattering measured in the range  $4.5 \cdot 10^{-2} < q < 2.4 \cdot 10^{-1} \text{ \AA}^{-1}$  for  $\text{CeAl}_3$  at  $T = 8, 10$  and  $15$  K (open blue circle, green diamond and red square, respectively) and for  $\text{LaAl}_3$  at  $T = 10$  K (solid circle) are shown in fig. 1. As one would expect, this contribution is practically equal to zero for non-magnetic compound  $\text{LaAl}_3$ . Figure observed for the system  $\text{CeAl}_3$  is quite another.

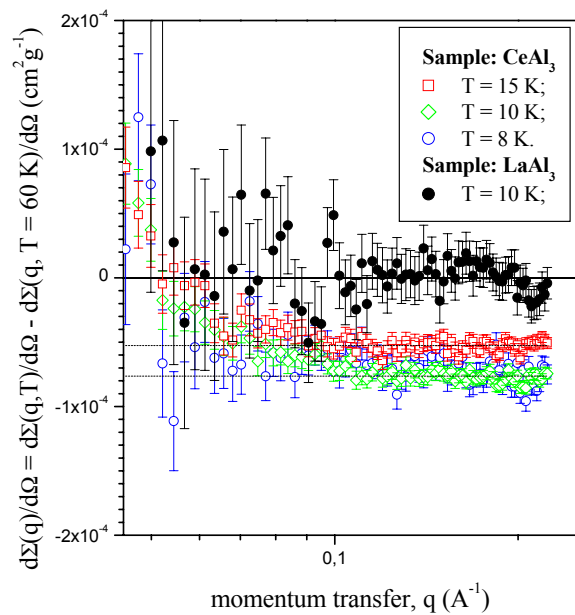


**Figure 1.**

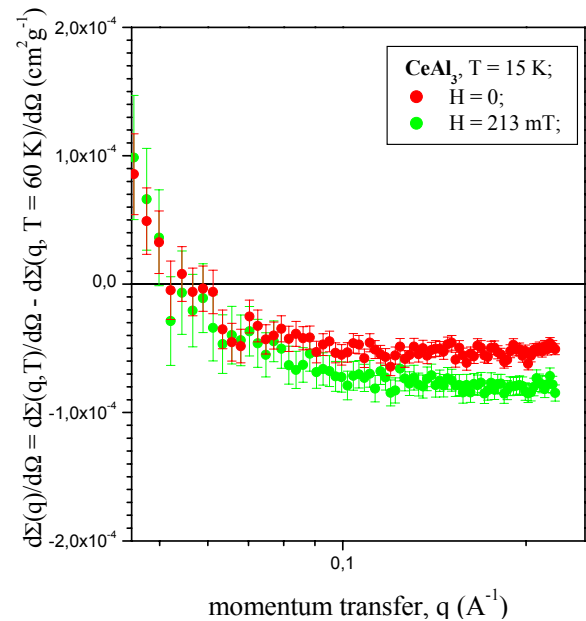


**Figure 2.**

It is clear seen that in this case the difference between the low temperature scattering and scattering at  $T = 60$  K has constant negative value at  $q > 7.5 \cdot 10^{-2} \text{ \AA}^{-1}$  which increases with the decreasing of the temperature from  $T = 15$  to  $10$  K. Further decrease of the temperature to  $T = 8$  K does not change the value of  $d\Sigma_m(q)/d\Omega$ . At  $q$  smaller than  $7.5 \cdot 10^{-2} \text{ \AA}^{-1}$  this difference tends to zero and becomes positive at  $q \approx 5.5 \cdot 10^{-2} \text{ \AA}^{-1}$ . Moreover, as it is seen from fig.2, the momentum dependence of  $d\Sigma_m(q)/d\Omega$  measured for  $\text{CeAl}_3$  at  $T = 15$  K and in the magnetic field  $H = 0$  and  $213$  mT is presented, the turn-on of the magnetic field results in a change of the value of  $d\Sigma_m(q)/d\Omega$ , which becomes equal one at  $T = 10$  K. At last the influence of the magnetic field on  $d\Sigma_m(q)/d\Omega$  at  $T = 8$  and  $10$  K was not found.

From the above, we assume that all observables, which change in spectral response of  $\text{CeAl}_3$ , connected to the transformation of magnetic component. At  $T = 60$  K we observe the scattering from the non-correlated system of Ce-spins (the incoherent paramagnetic scattering) which becomes the correlative one at low temperatures. The noticeable reduction of the

paramagnetic response with decreasing temperature is in agreement with previous data of the temperature dependence of quasi-elastic scattering [6]. The level of the paramagnetic scattering may be estimated from  $d\Sigma_m(q)/d\Omega$  at  $T = 10$  K since it does not depend on neither change of the temperature nor on the turn-on of the magnetic field.

Thus, for the correct analysis of the magnetic scattering, which was observed at low temperatures, it is necessary to make the allowance for the paramagnetic background at  $T = 60$  K. In fig. 3 the momentum dependence of the cross section  $d\Sigma_m(q)/d\Omega$  obtained for the sample  $\text{CeAl}_3$  with allowance for the paramagnetic background at  $T = 60$  K (fig. 2.) is shown on the log-log scale in all investigated range  $q$ . This scattering is weak but it is statistically permitted and increases with the decreasing of  $q$  (the slope angle is negative). Such a behavior of the cross section  $d\Sigma_m(q)/d\Omega$  corresponds to the scattering on the ferromagnetic correlations. It was found that the behavior of the  $d\Sigma_m(q)/d\Omega$  is satisfactory described by the expression:

$$d\Sigma_m(q)/d\Omega \approx A/(q^2 + \kappa^2)^{n/2} + I_{\text{inc}}, \quad (2)$$

where  $A$  is the parameter of the scattering amplitude,  $\kappa = 1/R$  is the inverse length of the scattering correlations and  $I_{\text{inc}}$  is a constant, which does not depend on  $q$  and is caused by scattering on objects with a size of order of the neutron wavelength. To obtain the final results, the expressions (2) was convolved with the resolution function of the facility, which was approximated by a Gauss function. The experimental data of  $d\Sigma_m(q)/d\Omega$  were analyzed in the range of  $q \in [0.1, 0.24] \text{ \AA}^{-1}$  by the least-squares method. The results of fitting are shown as solid lines in figure 3. It is interestingly that the lineshape in  $q$  of the magnetic contribution in the cross section  $d\Sigma_m(q)/d\Omega$  is not a Lorentzian, but can be described by the Lorentzian raised to the power of  $\sim 1.5$ . The analogous situation was observed in work [7], where the short-range correlations in  $\text{PbMg}_{1/3}\text{Nb}_{2/3}\text{O}_3$  relaxor ferroelectric were studied. This shows that the magnetic ordering in  $\text{CeAl}_3$  appears to be complex.

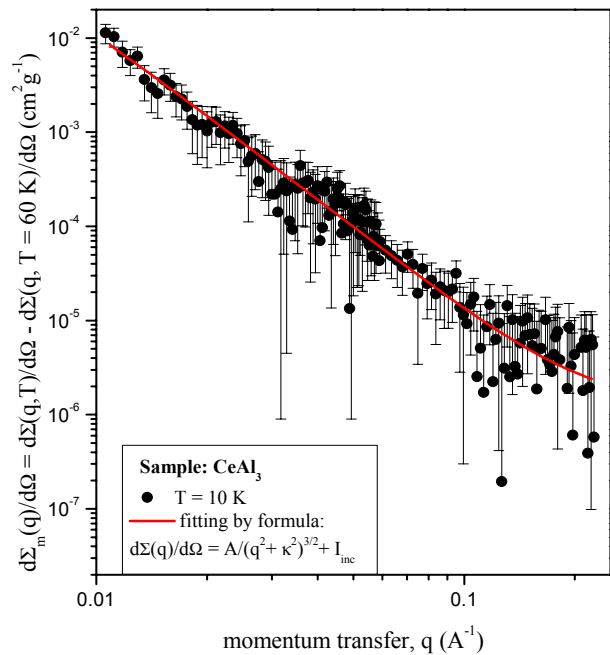



**Figure 3.**

## References

- [1] S. Barth, H. R. Ott, F. N. Gygax et al. Phys. Rev. B 39(1989), 11695
- [2] W. H. Wong and W. G. Clark, JMMM. 108 (1992) 175
- [3] E. A. Goremychkin, R. Osborn, B. D. Rainford et al., Phys. Rev. Lett. 89 (2002) 147201
- [4] N. E. Sluchanko, V.V. Glushkov, S.V. Demishev et al., Physica B: Condensed Matter, 378-380 (2006), 773–774
- [5] N. N. Tiden, P. A. Alekseev, V. N. Lazukov, A. Podlesnyak, E. S. Clementyev and A. Furrer, Solid State Communications 141 (2007), 474
- [6] V. N. Lazukov, P.A. Alekseev, N.N. Tiden, et al., JETP Lett., 2002
- [7] S. N. Gvasaliya, B. Roessli, R. A. Cowley, P. Huber and S. G. Lushnikov, J. Phys.: Condens. Matter 17 (2005) 4343



	<b>EXPERIMENTAL REPORT</b>	<b>GeNF SANS-2</b>
<b>Polarized SANS study of geometrically frustrated 3-dimensional nanoscale ferromagnetic structures</b>		
<b>Proposer:</b> <b>Co-Proposer(s):</b>	<b>S. V. Grigoriev</b> <sup>1</sup> , <sup>1</sup> PNPI, Gatchina, St-Petersburg, Russia <b>N. A. Grigoryeva</b> <sup>2</sup> , <sup>2</sup> St-Petersburg State University, St-Petersburg, Russia <b>A. S. Sinitskiy</b> <sup>3</sup> , <sup>3</sup> Moscow State University, Moscow, Russia	
<b>Experimental Team:</b> <b>User Group Leader:</b> <b>Instrument Responsible:</b>	<b>A. S. Sinitskiy</b> <sup>3</sup> , <b>N. A. Grigoryeva</b> <sup>2</sup> , <b>A. S. Mistonov</b> <sup>1</sup> , <b>H. Eckerlebe</b> <sup>2</sup> , <b>M. Sharp</b> <sup>2</sup> , <sup>2</sup> GKSS Research Centre Geesthacht <b>S. V. Grigoriev</b> <sup>1</sup> <b>Helmut Eckerlebe</b> <sup>2</sup> , <b>Melissa Sharp</b> <sup>2</sup>	
<b>Date(s) of Experiment:</b>	1 <sup>st</sup> – 5 <sup>th</sup> December 2007	

## Objective

Photonic crystals, the materials with a periodic modulation of dielectric constant, have recently received much attention from researchers [2,3]. Ones of the most intensively studied photonic crystals are artificial opals consisting of submicron monodisperse microspheres packed in a face-centered cubic cell [4–6]. Another important class of photonic crystals is inverse opals, which can be synthesized by filling the voids of opal templates with suitable structure-forming precursors and subsequent removing the initial microspheres to leave three-dimensionally ordered porous materials. This templating technique is very flexible and can be applied to the preparation of inverse photonic crystals based on metals, non-metals, oxides, semiconductors and polymers [2,3].

Recently, we were the first to report polarized SANS study of magnetic photonic crystals [1]. In our previous experiments at SANS-2 (GeNF, Geesthacht) we investigated inverse opals based on metallic Ni. We have shown that diffraction patterns typically consist of several clearly resolved sets of hexagonally arranged reflections. Particularly, we used polarized SANS to detect the transformation of the magnetic structure under applied field. Different contributions to the neutron scattering, that have been analyzed, are the nonmagnetic (nuclear) contribution, the magnetic contribution depending on the magnetic field, and the nuclear-magnetic interference indicating the correlation between the magnetic and nuclear structures.

The main goal of our present experiments was to investigate the structural and magnetic properties of various inverse opal photonic crystals by means of small angle polarized neutron scattering (SAPNS). In the present study we significantly expanded the range of photonic crystals studied by polarized SANS. We studied inverse opals based on magnetic iron oxides maghemite ( $\gamma$ -Fe<sub>2</sub>O<sub>3</sub>) and magnetite (Fe<sub>3</sub>O<sub>4</sub>) as well as several high-quality non-magnetic photonic crystals, including artificial opals made of silica and latex microspheres, and inverse opals made of SiO<sub>2</sub> and MgAl<sub>2</sub>O<sub>4</sub>. For characterization of our samples we have obtained momentum transfer dependence of SANS intensity in the wide range of  $q$ . We expected to observe the spot-like Bragg peaks from regular structure.

## Experiment

SANS measurements were carried out with the instrument SANS-2 at the Geesthacht Neutron Facility (GeNF). Polarized neutron beam with the polarization  $P_0 = 0.95$ , with a mean wavelength of  $\lambda = 0.9$  nm and a wavelength spread of  $\Delta\lambda/\lambda = 10\%$  was used. The Sample – Detector distance of 21.5 m was used with appropriate collimations to cover scattering vectors  $q$  from 0.005 to 0.06 nm<sup>-1</sup>.

## Achievements and Main Results

For most of our samples we recorded well-resolved neutron diffraction patterns consisted of several clearly resolved sets of hexagonally arranged reflexes as shown, for example, in Fig. 1 for the inverse opal based on  $\gamma\text{-Fe}_2\text{O}_3$ .

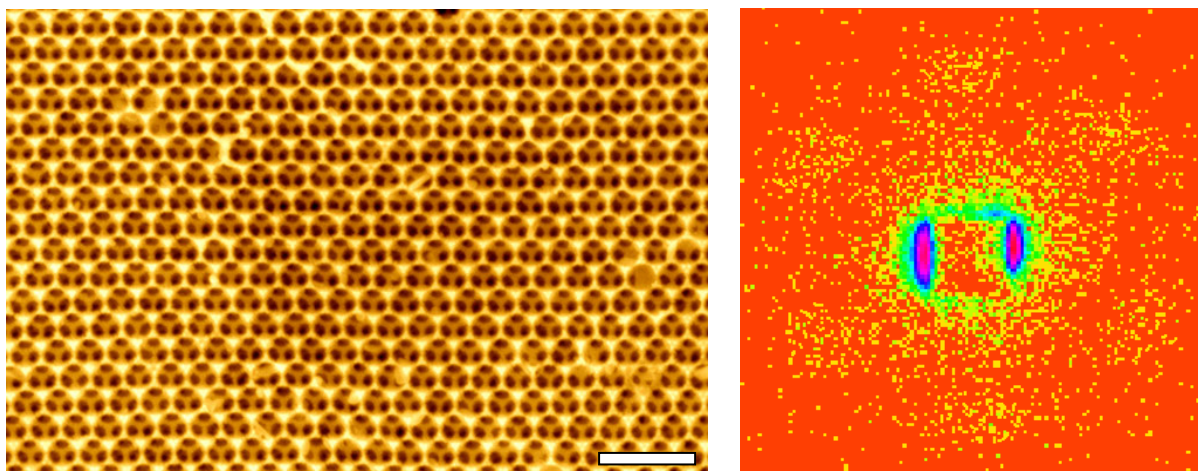


**Figure 1:** SEM image of inverse opal based on  $\gamma\text{-Fe}_2\text{O}_3$  (left) and a corresponding SANS pattern (right). Scale bar is 1  $\mu\text{m}$ .

By now, the most interesting data was obtained for an opal film made of 250 nm silica microspheres (Fig. 2), for which we ran angle-dependent measurements, i.e. recorded diffraction patterns as a function of a neutron beam incident angle.

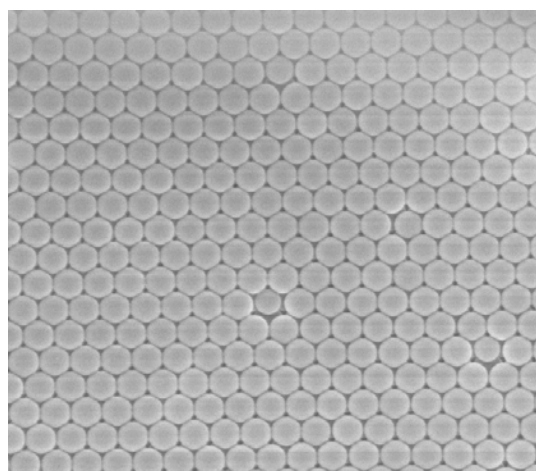


**Figure 2:** SEM image of silica opal studied in angle-dependent SANS experiments.

We recorded several specific diffraction patterns at various angles of incidence: 0, 19, 35, 55 degrees (Fig. 3). The first picture taken at 0 degrees of the incident beam, i.e. the neutron beam is perpendicular to the sample plane, shows a typical hexagonal pattern. It is interesting to note that the first order peaks close to the center are weaker than the second order reflexes. The second panel of Fig. 3, taken at 19 degrees of the incident beam, shows a rhomb-like pattern. The two reflexes of the first order on the left and right sides become very intensive but the second order reflexes on the left and right sides disappear. The third panel of Fig.3, taken at 35 degrees of the incident beam, shows the same rhomb-like pattern but those two intensive reflexes on the left and right sides become weak while the other four of the first order become stronger. The fourth panel of Fig.3, taken at 55 degrees of the incident



beam, shows the quadratic pattern of the second order reflexes with the corners on the up-down and left-right of the picture. Although such pictures have been taken for the first time using the SANS method, we believe they are very typical for the photonic crystals and can be interpreted taking into account a face-centered cubic (fcc) structure of the opal. Obviously, for a photonic crystal with fcc symmetry  $\{111\}$ ,  $\{200\}$  and  $\{220\}$  plane families are the most important for consideration. First, we assume  $(111)$  planes to be parallel to the PC film surface, and  $\langle 111 \rangle$  direction to be normal to the surface. The first panel is attributed to the case when the neutron beam is parallel to the  $\langle 111 \rangle$  direction. Furthermore, the angle between  $(111)$  plane and any of  $(-111)$ ,  $(1-11)$  or  $(11-1)$  planes is  $\Theta = 70.53^\circ$ , correlating with the first specific angle  $19.47^\circ$  ( $\sim 19^\circ$ ). Therefore, the second panel corresponds to the case when one of the  $\langle 111 \rangle$  axes is perpendicular to the neutron beam and lies horizontally. In order to have one of the  $[220]$ ,  $[202]$  and  $[022]$  axes parallel to the beam (we do not consider  $[-220]$ ,  $[-202]$  and  $[0-22]$ , since they are perpendicular to  $\langle 111 \rangle$  directions) we set the incident beam angle  $\Theta = 35.26^\circ$ , which apparently is the third specific angle on the third panel. Finally, the angle between  $(111)$  plane and any of  $\{200\}$  planes is  $\Theta_{\{200\}} = 54.74^\circ$ , which apparently is the last specific angle. Remarkably,  $\{200\}$  planes are cubic, which explains a cubic symmetry of reflexes at the last diffraction pattern.

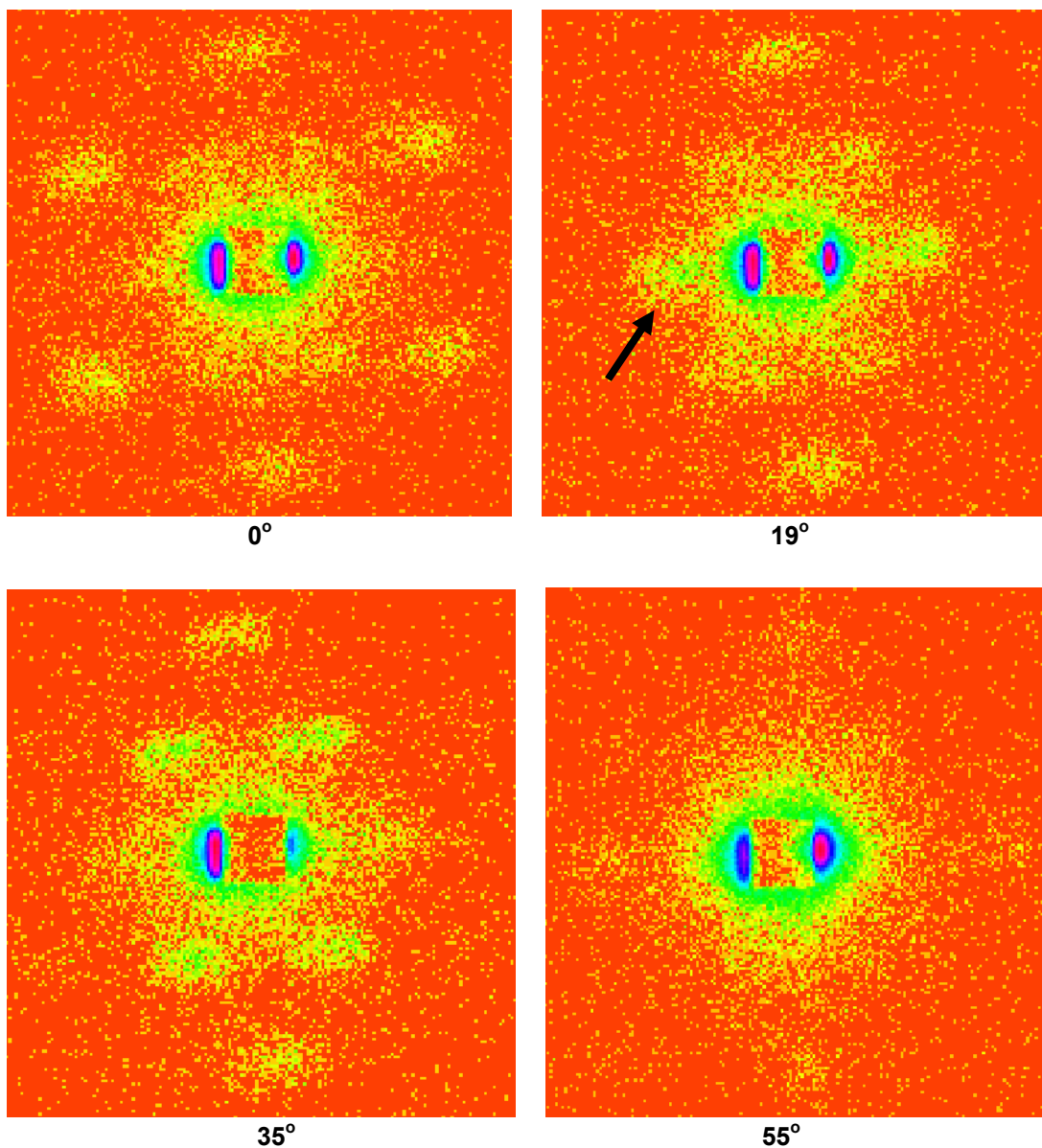


**Figure 3:** Neutron diffraction patterns recorded at some specific angles of incidence of neutron beam.

For the reflex marked by the arrow we plotted a dependence of its intensity as a function of incidence angle (Fig. 4). Four maximums corresponding to specific crystallographic directions in fcc photonic crystal are clearly seen.

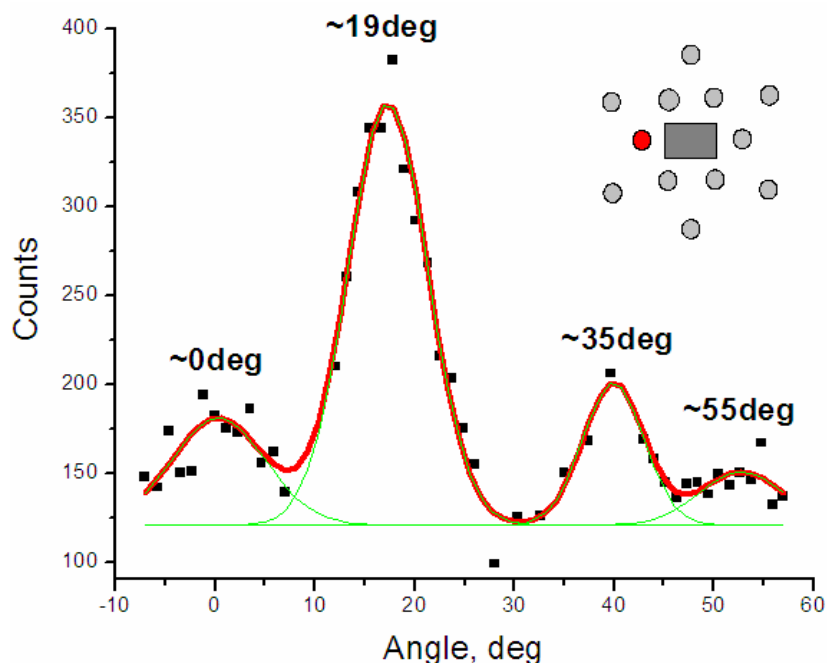



**Figure 4:** Intensity of one of diffraction reflexes as a function of a neutron beam incident angle. Black squares are experimental data, whereas red line is a fitting curve constructed as a sum of four Gaussian functions.

Thus, our preliminary results suggest that the small angle neutron diffraction can be a very powerful tool for the structural study of submicron periodic structures such as photonic crystals. The results presented above illustrate the high potential of the setup SANS-2. The work could not be done without excellent support provided by our local contact Helmut Eckerlebe and Melissa Sharp.

## References

- [1] Napolskii, K.; Sinitskii, A.; Grigoriev, S.; Grigorieva, N.; Eckerlebe, H.; Eliseev, A.; Lukashin, A.; Tretyakov, Y.; Topology constrained magnetic structure of Ni photonic crystals, *Physica B* 397 (2007), 23–26
- [2] Krauss, T.F.; De La Rue, R.M.; T Photonic crystals in the optical regime – past, present and future, *Progress in Quantum Electronics* 23 (1999), 51–96
- [3] López, C.; Materials aspects of photonic crystals, *Advanced Materials* 15 (2003), 1679–1704
- [4] Astratov, V.; Vlasov, Y.; Karimov, O.; Kaplyanskii, A.; Musikhin, Y.; Bert, N.; Bogomolov, V.; Prokofiev, A.; Photonic band gaps in 3D ordered fcc silica matrices, *Physics Letters* 222 (1996), 349–353
- [5] McComb, D.; Treble, B.; Smith, C.; De La Rue, R.; Johnson, N.; Synthesis and characterisation of photonic crystals, *Journal of Materials Chemistry* 11 (2001), 142–148
- [6] Sinitskii, A.; Khokhlov, P.; Abramova, V.; Laptinskaya, T.; Tretyakov, Y.; Optical study of photonic crystal films made of polystyrene microspheres, *Mendeleev Communications* 17 (2007), 4–6



	<b>EXPERIMENTAL REPORT</b>	<b>GeNF SANS-2</b>
<b>Polarized SANS study of the magnetic inverse photonic crystals</b>		
<b>Proposer:</b>	<b>Kirill Napolskii<sup>1</sup>, Nina Sapoletova<sup>1</sup>, <sup>1</sup>MSU, Moscow, Russia</b>	
<b>Co-Proposer(s):</b>	<b>Natalia Grigoryeva<sup>2</sup>, <sup>2</sup>SPSU, St-Petersburg, Russia</b>	
<b>Experimental Team:</b>	<b>Kirill Napolskii<sup>1</sup>, Nina Sapoletova<sup>1</sup>, Natalia Grigoryeva<sup>2</sup>, Melissa Sharp<sup>3</sup>, Helmut Eckerlebe<sup>3</sup>, <sup>3</sup>GKSS Research Centre Geesthacht, Germany</b>	
<b>User Group Leader:</b>	<b>Sergey V. Grigoriev<sup>4</sup>, <sup>4</sup>PNPI, Gatchina, Russia</b>	
<b>Instrument Responsible:</b>	<b>Melissa Sharp<sup>3</sup>, Helmut Eckerlebe<sup>3</sup></b>	
<b>Date(s) of Experiment:</b>	<b>July 2007</b>	

## Objectives

The experiments were aimed to investigate the structural and magnetic features of inverse photonic crystals using polarized small angle neutron scattering (SANS). There has been a considerable interest in the investigation of photonic crystals (PCs) due to unique possibilities that they offer in having control over photons [1–4]. PCs are predicted to exhibit a photonic band gap (PBG), for which light within a certain frequency range can not propagate in any or some directions inside the crystals, causing the unique properties of PCs, such as localization of light and control of spontaneous emission. Many applications of PCs have been proposed, ranging from low-threshold lasers and high-efficient light emitting diodes to perfect dielectric mirrors and planar waveguides.

From the point of view of materials science, PCs are the materials with a periodic modulation of dielectric constant, in which the refractive index varies on the scale of visible light wavelength. One of the main tools to affect functional properties of such materials is structure quality. Several works report on investigations of the organization of the PC's periodic structure formed during self-organization of monodispers microspheres, however most of them involve only electron microscopy studies, which are known for their locality. The diffraction methods, especially small angle scattering of synchrotron [5] and neutron radiation [6], were demonstrated to be very efficient to determine the orientation and to characterize the ordering of photonic crystal films. Here we present preliminary results on structural and magnetic properties as well as their correlations in metal (Ni, Co) inverse PCs.

## Experiment

### 1. Samples preparation

The magnetic (Ni, Co) PC films with an inverse opal structure were prepared using a templating technique [6,7]. For template preparation, monodisperse polystyrene microspheres with relative standard deviation less than 5 % were synthesized by emulsifier-free emulsion polymerization of styrene using potassium persulfate as initiator. Colloidal crystal films made of 450 nm polystyrene microspheres were grown onto conductive substrates (ITO or Au sputtered on glass slides) by the vertical deposition method. Electrochemical crystallization of metal in the voids between the spheres was carried out in three-electrode cell at room temperature. In order to obtain free-standing metal structure onto substrate the polystyrene microspheres were completely dissolved in toluene.

### 2. Small-angle neutron scattering

Polarized SANS measurements were carried out with the instrument SANS-2 at the Geesthacht Neutron Facility (GeNF). Polarized neutron beam with the polarization  $P_0 = 0.95$ ,

with a mean wavelength of  $\lambda = 1.274$  nm and a wavelength spread of  $\Delta\lambda/\lambda = 10\%$  was used. The Sample – Detector distance of 21.5 m was set with an appropriate collimation to cover scattering vectors  $q$  from 0.005 to 0.06 nm<sup>-1</sup>. An external magnetic field (up to 200 mT) was applied in the horizontal plane and perpendicular to the incident beam. We determine the total (nuclear and magnetic) scattering ( $I(q) = I^+(q) + I^-(q)$ ) and the polarization dependent part of the scattering ( $\Delta I(q) = I^+(q) - I^-(q)$ ) where  $I^+(q)$  and  $I^-(q)$  are the intensities for neutrons polarized parallel (+) and anti-parallel (-) to the magnetic field. The field-dependent scattering intensity is extracted as  $I_H(q) = I(q, H) - I(q, 0)$ .

### Achievements and Main Results

According to the SEM observations all synthesized samples possess an ordered porous structure with uniform spherical pores (Fig. 1A). The average center-to-center distance between close-packed voids is 450 nm, suggesting no structure shrinkage during the fabrication process. Due to well ordered structure with periodicity in optical wavelength region, the samples possess strong iridescence and demonstrate all rainbow colours, when varying the observation angle (Fig. 1B). It is well documented that vertical deposition method of colloidal particles on substrate mainly leads to formation of the fcc structure with  $\langle 111 \rangle$  crystallographic direction perpendicular to the film surface [8,9].

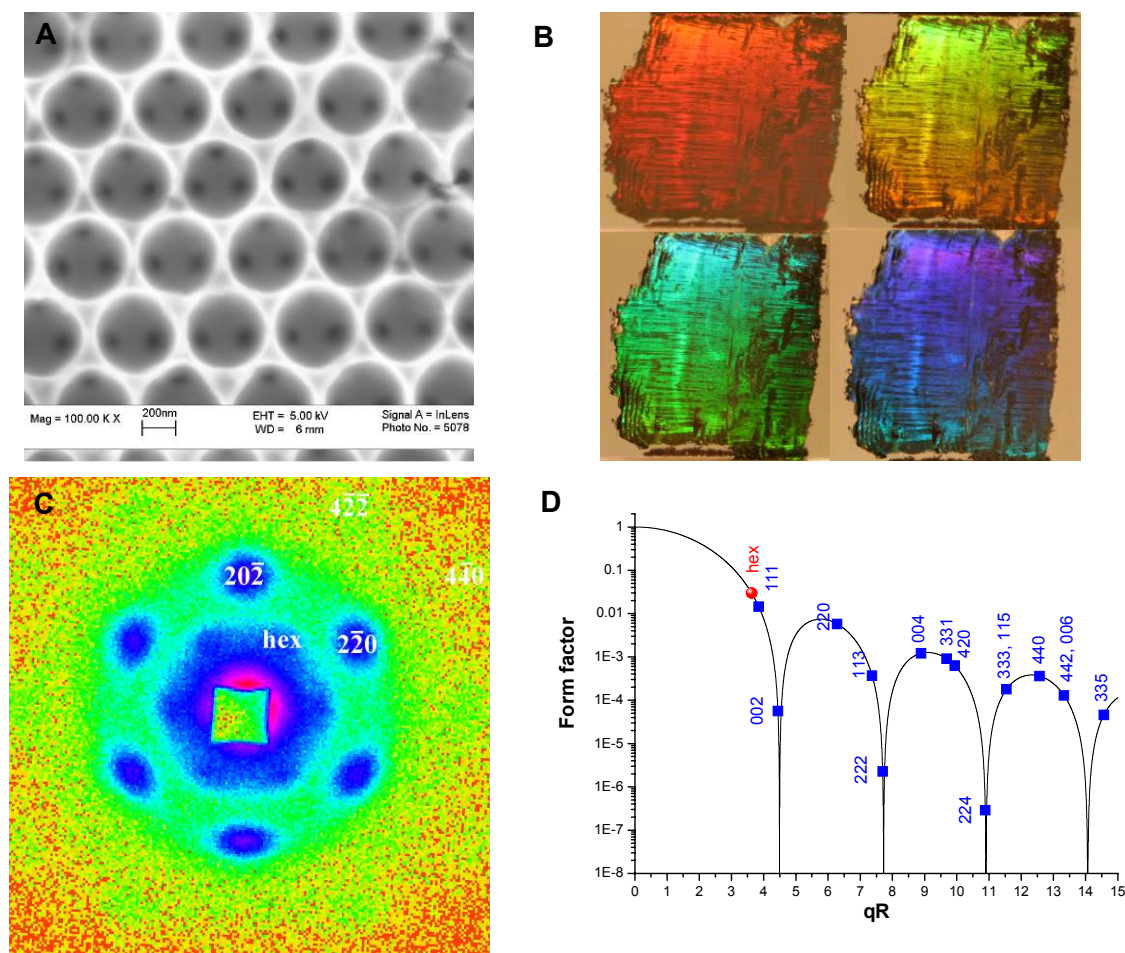


**Figure 1:** Panel A shows typical SEM images of metal (Co) inverse opals. Optical photographs of a Ni PC film demonstrate the change in the iridescent colour, when tilting the angle of observation from glancing to normal (panel B). Small angle diffraction pattern from an inverse Ni PC measured with the beam normal to the substrate (111 crystallographic direction, panel C). Panel D shows the form factor of uniform spheres (lines) and its value at the position of several Bragg peaks (points). The horizontal axis presents the values of  $qR$  ( $R$  is the sphere radius) and the vertical axis shows scattering intensity  $I(q)$  for a single particle normalized by  $I(q \rightarrow 0)$ .

Figure 1C presents typical diffraction pattern measured from metal (Ni) inverse PC. Up to fourth-order reflections have been clearly detected, suggesting the presence of strong correlations in the voids positions over significant distances. The hexagonally arranged set of reflections reflects the 3-fold symmetry along the 111 direction normal to the substrate surface. In addition to the well-pronounced fcc reflections indicated on Fig. 1C, one can also see additional reflections close to the beam-stop, which are forbidden for a perfect fcc crystal. They originate from intersections of the Ewald sphere by so-called Bragg rods, which are induced by stacking disorder in the direction normal to the substrate [10]. The intersections of the lowest-order Bragg rods (denoted by ‘hex’) have the highest form factor (Fig. 1D) and are clearly visible.

It is worth noting, that the patterns, typical of single crystal, were recorded using a large beam spot area (the aperture with 5 mm diameter is used), suggesting the well-ordering of both Ni and Co PCs on a macroscale. The positions of the diffraction maxima ( $q_{\text{hex}} = 0.016 \text{ nm}^{-1}$ ,  $q_{220} = 0.027 \text{ nm}^{-1}$  and  $q_{422} = 0.047 \text{ nm}^{-1}$ ) correspond very well to the hexagonal order of pores in plane parallel to the substrate with  $a = 460 \pm 10 \text{ nm}$  (see Fig. 3A). Thus calculated pore (sphere) diameter is  $460 \pm 10 \text{ nm}$  that in good agreement with the SEM data.

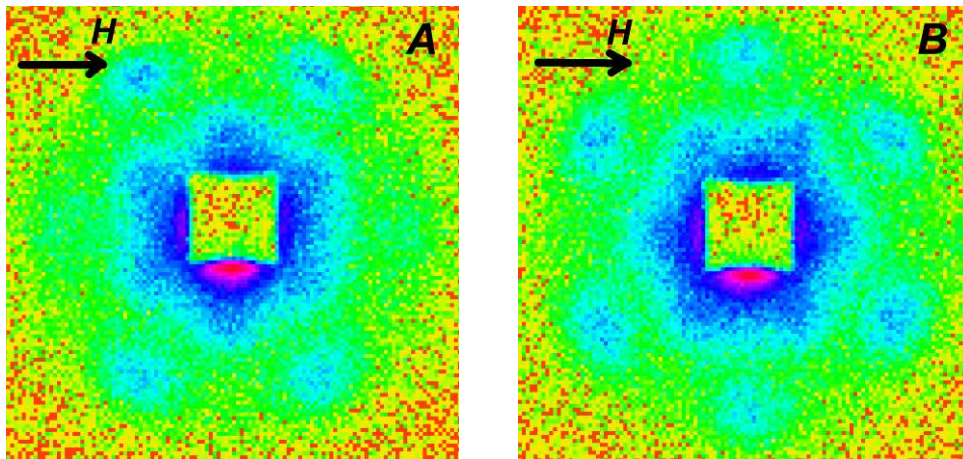


**Figure 2:** Small angle diffraction patterns from an inverse Co PC measured with different direction of magnetic field.

For investigation of unusual magnetic structure of inverse PCs the cobalt samples were selected. It is connected with higher magnetic contribution into scattering intensity for Co in comparison with Ni. An external magnetic field is applied along two different directions in crystal in order to reveal the anisotropic properties of the magnetic system (Fig. 2 A,B). It is clearly seen that even at low magnetic field ( $H < 100 \text{ mT}$ ) intensity of (2-20) and (-220) reflections which lie in horizontal plane (Fig. 2A) are nearly zero. Generally speaking, it is not surprising because magnetic contribution in the total intensity

$$\sum_m = |A_m m_{\perp q} S(q) F(q)|^2,$$

is zero at these points due to  $\overline{m_{\perp q}} = 0$ . On contrary, the intensity of peaks denoted as “hex” (Fig 2B), which lies in horizontal plane too, have much higher intensity. This fact can be explained by higher contribution of isotropic diffuse scattering at lower  $q$  as well as presence structural elements with  $\overline{m_{\perp q}} \neq 0$  in the crystallographic planes, which give “hex” reflections. Thus, at low magnetic fields the direction of magnetization of each element (tetrahedral or octahedral structural unit) is determined by the geometrical anisotropy (axis of easy magnetization).

According to the polarization dependent part of scattering ( $I(q) = I((q) + I+(q))$ ) nuclear and magnetic structures are well-correlated (Fig. 3B). The two types of contributions to the interference scattering, the diffuse small angle scattering and Bragg reflection, with domination of the second one are clearly seen.

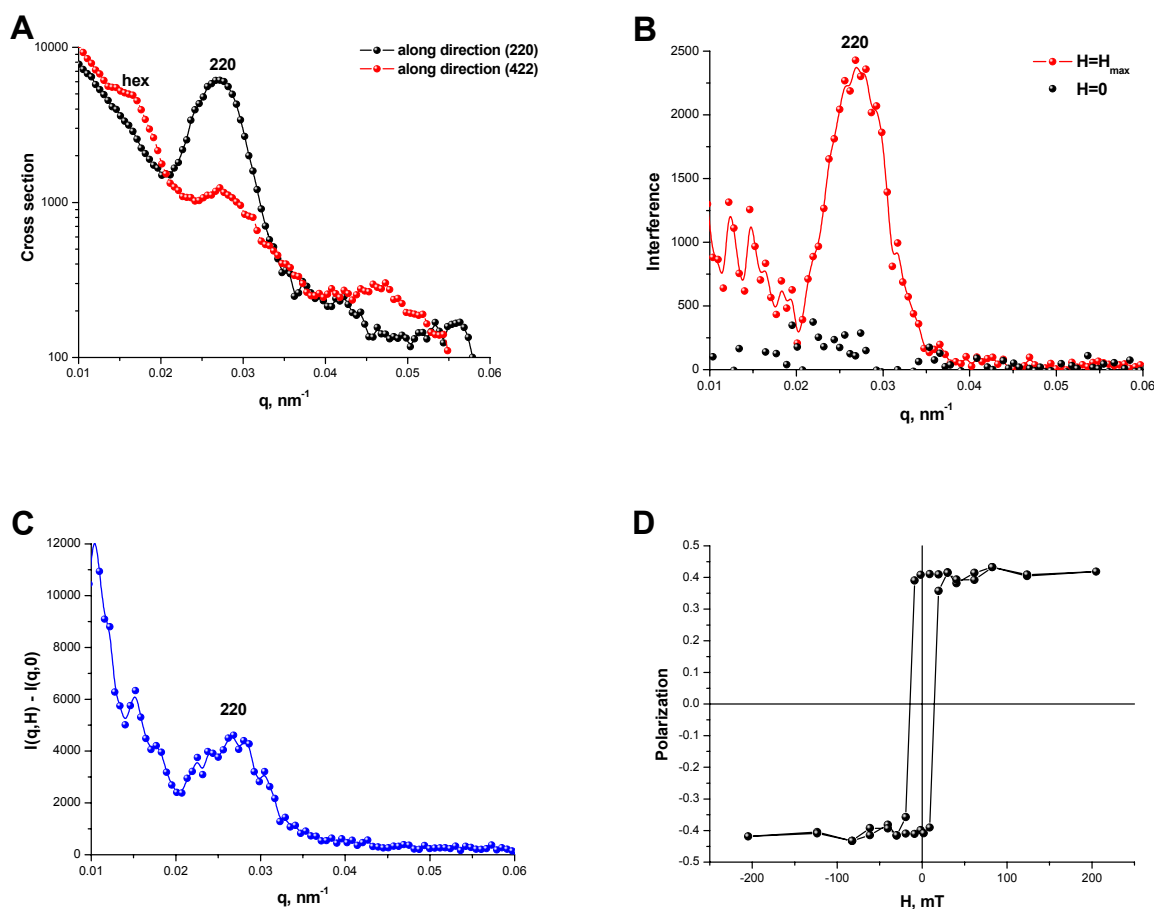


**Figure 3:** Q-dependence of total intensity for Co inverse PC (panel A). Panels B and C show interference and magnetic cross section terms versus momentum-transfer vector  $q$  for Co inverse PC. Polarization dependence on external magnetic field demonstrates remagnetisation process of Co inverse PC (panel D).

The pure magnetic contribution to the scattering, also referred to as field induced scattering, was extracted as  $I_H(q) = I(q,H) - I(q,0)$  (Fig. 3C). Increasing the strength of the magnetic field leads to decreasing the small-angle diffuse scattering and increasing the magnetic coherent reflection at  $q=0.027 \text{ nm}^{-1}$ . It is prescribed to the transition from multi- to single domain magnetic structure.

The magnetization curve is plotted using polarization values in (220) reflections (Fig. 3D). The reflections (220) are chosen due to their high intensities and low contribution of diffuse scattering in comparison with “hex” maxima. Magnetization loop have rather small coercive force ( $\sim 25 \text{ mT}$ ) and a square shape. It is connected with the structure of inverse PC (Fig. 1A). The network of tetrahedral and octahedral “islands” allows easy rotation of magnetic moment during remagnetization process.


Results presented above illustrate the high potential of the small angle neutron scattering setup at SANS-2 for the characterization of both structural and magnetic (dis)order in photonic crystals and other materials with spatially-ordered structure. We are also grateful to our local contacts, to Helmut Eckerlebe and to Melissa Sharp for their excellent support.

## References

- [1] Yablonovitch E.; Phys. Rev. Lett. 58 (1987), 2059
- [2] John S.; Phys. Rev. Lett. 58 (1987), 2486
- [3] Joannopoulos J. D., Mead R. D., Winn J. D.; Photonic crystals, Princeton Univ. Press (1995).
- [4] Busch K., John S.; Phys. Rev. E 58 (1998), 3896
- [5] Petukhov A. V., Aarts D.G.A.L., Dolbnya I.P., E.H. A. de Hoog, Kassapidou K., Vroege G. J., Bras W., Lekkerkerker H.N.W.; Phys. Rev. Lett. 88 (2002), 20830
- [6] Grigoriev S. V., Napolskii K. S., Grigoryeva N. A., Eliseev A. A., Lukashin A. V., Tretyakov Yu. D., Eckerlebe H.; JETF Letters 87, (2008), 15–21
- [7] Napolskii K. S., Sinitskii A., Grigoriev S. V., Grigorieva N. A., Eckerlebe H., Eliseev A. A., Lukashin A. V., Tretyakov Yu. D.; Physica B 397 (2007), 23
- [8] Li H.-L., Marlow F.; Chem. Mater. 18 (2006), 1803
- [9] Kuai S.-L., Hu X.-F., Hache A., Truong V.-V.; J. Cryst. Growth 267 (2004), 317
- [10] Thijssen J. H. J., Petukhov A. V., Hart D. C., Imhof A., C.H.M. van der Werf, Schropp R.E.I., A. van Blaaderen; Adv. Mater. 18 (2006), 1662





	<b>EXPERIMENTAL REPORT</b>	<b>GeNF SANS-2</b>
<b>Polarized SANS study of the Co nanowires in anodic aluminum oxide films</b>		
<b>Proposer:</b> <b>Co-Proposers:</b>	<b>Kirill Napolskii<sup>1</sup></b> , <sup>1</sup> MSU, Moscow, Russia <b>Natalia Grigoryeva<sup>2</sup></b> , <sup>2</sup> SPSU, St-Petersburg, Russia <b>Sergey V. Grigoriev<sup>3</sup></b> , <sup>3</sup> PNPI, Gatchina, , Russia	
<b>Experimental Team:</b>  <b>User Group Leader:</b> <b>Instrument Responsible:</b>	<b>Sergey V. Grigoriev<sup>3</sup></b> , <b>Kirill Napolskii<sup>1</sup></b> , <b>Alexander Vyacheslavov<sup>1</sup></b> , <b>Natalia Grigoryeva<sup>2</sup></b> , <b>Melissa Sharp<sup>4</sup></b> , <b>Helmut Eckerlebe<sup>4</sup></b> , <sup>4</sup> GKSS Research Centre Geesthacht <b>Sergey V. Grigoriev<sup>3</sup></b> <b>Melissa Sharp<sup>4</sup></b> , <b>Helmut Eckerlebe<sup>4</sup></b>	
<b>Date(s) of Experiment:</b>	27 <sup>th</sup> September – 1 <sup>st</sup> October 2007	

## Objectives

The present study is focused on the SANS investigation of the spatially ordered array of magnetic Co nanowires based on porous anodic alumina membranes. Anodic aluminum oxide (AAO) films formed by two-step anodization technique or nanoimprint technology are well-known to possess uniform pore structure with hexagonal arrangement of cylindrical channels. AAO is extremely attractive as a matrix or reactor for synthesis of nanocomposites owing to the possibility of formation of membranes with ultra high length of mesopores at very low diameters (which could be considered as one-dimensional).

One of the most important challenges in physics and materials science today is the preparation of ordered nanostructure arrays with the controlled properties and dimensions. Thus porous alumina films and nanocomposites based on AAO membranes could be used as a perfect model objects for deeper understanding of processes and unusual effects on nanolevel in spatially-ordered systems.

Many works report on the investigations of organization of the mesopore channels formed during an anodization process, however most of them involve only electron microscopy or scanning probe microscopy studies, which are known for their locality and only few rely upon small-angle scattering techniques for quantitative characterization.

It should be noted that in case of intercalation of magnetic materials inside the pores, neutron scattering enables us to investigate magnetic field dependent contribution to the Bragg reflection from superstructure of the magnetic nanowires of the spatially-ordered arrays. Therefore for deeper investigation of structural and magnetic features of nanowires array inside AAO membranes we propose to use polarized SANS technique, which allows us to determine both nuclear and magnetic scattering contribution.

## Experiment

### 1. Samples preparation

In order to obtain the highly ordered porous structure, the anodic aluminum oxide membranes were prepared by the two-step anodization technique. Subsequently, porous films were used as a matrix for the formation of Co nanowires with help of the electrocrystallization technique. These electrochemical experiments were carried out in the three-electrode cell at room temperature. The counter electrode was a Pt wire and the reference one was a saturated Ag/AgCl electrode connected to the cell via a Luggin capillary. 0.3M CoSO<sub>4</sub>, 0.05M CoCl<sub>2</sub>, 0.3M H<sub>3</sub>BO<sub>3</sub> solution was used for potentiostatic Co deposition at E<sub>d</sub> = - 0.9 V.

## 2. Small-angle neutron scattering

Polarized SANS measurements were carried out with the instrument SANS-2 at the Geesthacht Neutron Facility (GeNF). Polarized neutron beam with the polarization  $P_0 = 0.95$ , with a mean wavelength of  $\lambda = 0.7$  nm and a wavelength spread of  $\Delta\lambda/\lambda = 10\%$  was used. A film with an area of  $\sim 0.5$  cm<sup>2</sup> was oriented perpendicularly to the neutron beam and was uniformly irradiated over the entire area. Such an orientation of the sample corresponds to the pore arrangement, as well as the long axis of the magnetic nanowires, in parallel to the incident neutron beam. The chosen geometry of the experiment allows the observation of the diffraction reflection system from the ordered structure of the porous matrix, as well as from the superstructure of magnetic nanowires, in a small-angle scattering range. The Sample - Detector distance of 14 m was used with appropriate collimations to cover scattering vectors  $q$  from 0.025 to 0.2 nm<sup>-1</sup>. An external magnetic field (up to 800 mT) was applied in the horizontal plane and perpendicular to the incident beam (perpendicular to the long axis of the nanowires). We determine the total (nuclear and magnetic) scattering ( $I(q) = I^+(q) + I^-(q)$ ) and the polarization dependent part of the scattering ( $\Delta I(q) = I^+(q) - I^-(q)$ ) where  $I^+(q)$  and  $I^-(q)$  are the intensities for neutrons polarized parallel (+) and anti-parallel (-) to the magnetic field. The field-dependent scattering intensity is extracted as  $I_H(q) = I(q, H) - I(q, 0)$ .

### Achievements and Main Results

A typical diffraction pattern measured from Co nanowires arrays inside AAO membrane is shown in Fig. 1A. Up to three-order reflections have been clearly detected, suggesting the presence of strong correlations in the pores (or nanowires) positions over significant distances. The hexagonally arranged set of reflections demonstrates the 6-fold symmetry along the direction normal to the film surface. For the considered geometry the interplanar spacing  $d_{hk}$  can be calculated as  $d_{hk} = \sqrt{3}a / (2\sqrt{h^2 + hk + k^2})$ .

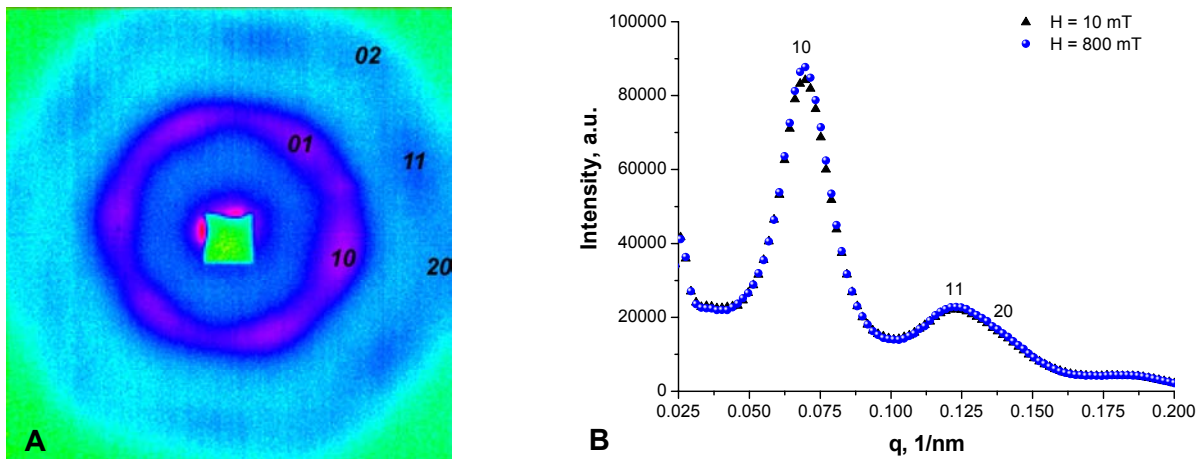


**Figure 1:** Typical 2D diffraction pattern from Co/Al<sub>2</sub>O<sub>3</sub> nanocomposite with spatially ordered structure **A**. Panel **B** shows momentum-transfer dependence of the total (nuclear and magnetic) neutron scattering intensity at  $H = 10$  and 800 mT.

The widening of reflections to 10–20 degrees in a radial direction indicates that samples have a block structure, in which different domains are disoriented a little bit in plane of the film surface. Nevertheless, the diffraction patterns, typical for a single crystal, were recorded using a large-spot-area beam (the aperture with 5 mm diameter is used), suggesting the well-ordering structure of Co/Al<sub>2</sub>O<sub>3</sub> nanocomposite on a macroscale.



Figure 1B shows the momentum-transfer dependence of the total (nuclear and magnetic) neutron scattering  $I(q)$  for the nonmagnetized ( $H = 10$  mT) and magnetized ( $H = 800$  mT) sample. Several diffraction maxima are clearly observed, indicating the highly ordered structure of the Co/Al<sub>2</sub>O<sub>3</sub> nanocomposite. The dependence  $I(q)$  is satisfactorily reproduced by the sum of the Gaussians with the centers at  $q_{10} = 0.069 \pm 0.004$  nm<sup>-1</sup>,  $q_{11} = 0.119 \pm 0.004$  nm<sup>-1</sup>,  $q_{20} = 0.138 \pm 0.004$  nm<sup>-1</sup>, and fixed half-width  $w = 0.0090 \pm 0.0005$  nm<sup>-1</sup>; and the diffuse small-angle scattering, which is represented by an exponential decay. The observed diffraction maxima are classified in the hexagonal lattice with the parameter  $a = 106 \pm 2$  nm. It should be noted that applying the external magnetic field induces noticeable increase of the diffraction peak intensity of order of 5 %.

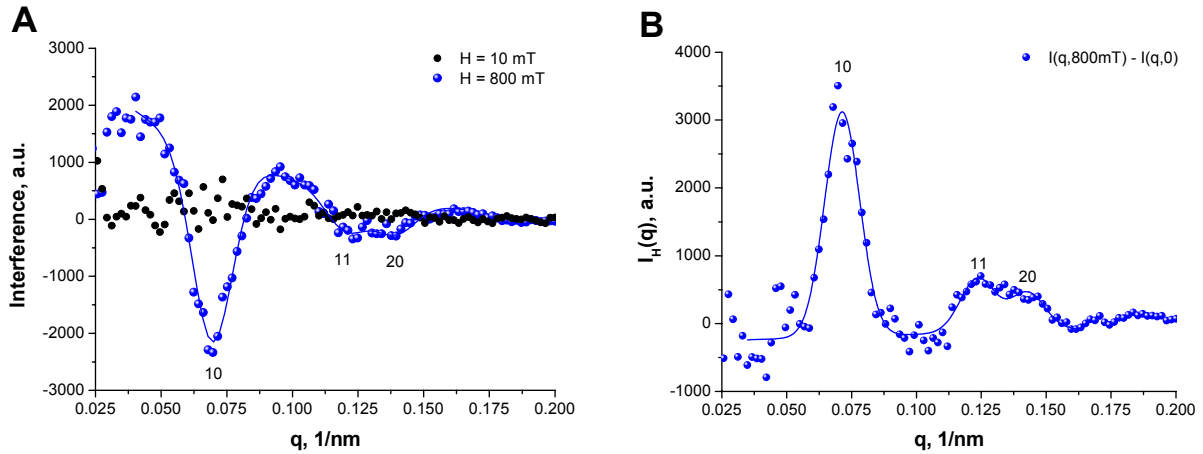


**Figure 2:** Q-dependence of the nuclear–magnetic interference  $\Delta I(q)$  at  $H = 1$  and 800 mT (A) and magnetic contribution to the scattering  $I_H(q)$  (B).

The figures 2 A,B show the nuclear-magnetic interference  $\Delta I(q)$  and the field-dependent part of neutron scattering  $I_H(q)$  as a function of  $q$ . The coincidence of the Bragg's peak position at  $q \sim 0.069$  nm<sup>-1</sup> for nuclear scattering (at zero magnetic field, fig. 1B) with the maxima in Fig. 2A, B confirms the formation of the spatially-ordered magnetic structure, e.g. the massive of 1D nanowires arrays with periodicity of 106 nm.

Both the interference  $\Delta I(q)$  and the field-induced term  $I_H(q)$  are fitted by the sum of the Gaussians with the centers at  $q = q_{ht}$  (coherent scattering) and the diffuse small-angle scattering, which is represented by the exponential decay. The amplitudes of the interference contributions in the positions of the (10) diffraction reflection are shown in Fig. 3A as functions of the external magnetic field. Note that the interference contribution is proportional to the magnetization, which exhibits the absence of any hysteresis during remagnetization of the system of magnetic nanowires in the field perpendicular to the long axis of a wire. Scattering tends to saturation in fields  $H > 500$  mT.

The measurements reveal the presence of large hysteresis of the magnetic scattering in field dependence, connected to several processes appearing with magnetization of nanowire arrays in the perpendicular external field (fig. 3B). In the ground state (at no field applied) the moments of nanowires are aligned parallel to the long axes, but are randomly distributed between +1 and -1 states. Applying the perpendicular magnetic field results in a deviation of the average wire magnetic moment from its long axes starting from  $H \approx 350$  mT. Further increase of the field aligns moments in perpendicular direction with rapid increase of scattering intensity at the Bragg position. Thus the inflection of experimental curve (Fig. 3B) at the  $H \approx 350$  mT should be attributed to the change of the magnetization mechanism in the Co nanowires array from incoherent to coherent rotation. And finally the decrease of the magnetic ordering in low fields is attributed to the demagnetization effect playing a role of

disorienting force, which also forces the formation of domain structure in the array. Further treatment of the experimental data are in progress. The data will be treated in accord with the model proposed in our recent work [1].

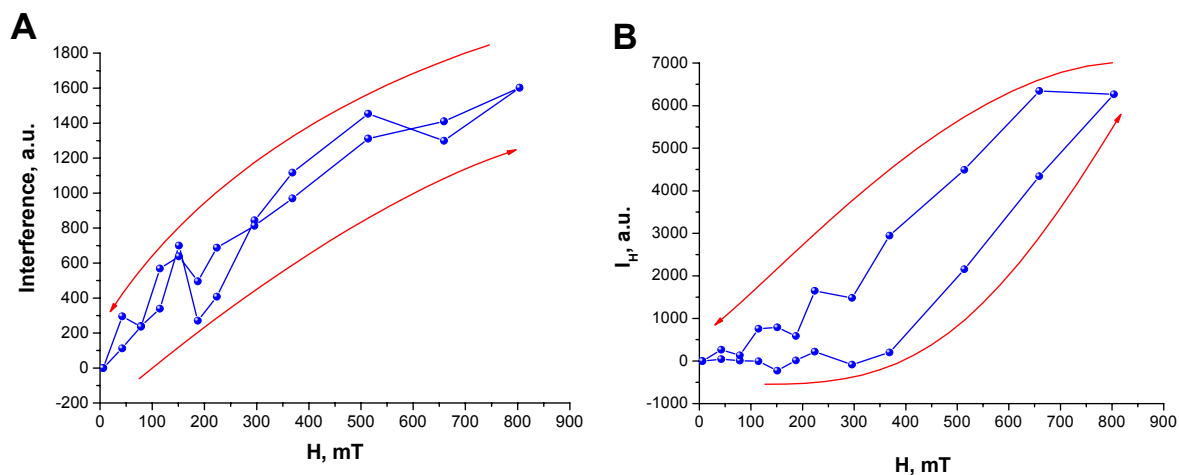



**Figure 3:** Field dependence of the amplitudes of (A) the interference contribution and (B) the magnetic coherent contribution obtained from the approximation of the experimental data.

Results presented above illustrate the high potential of the SANS-2 setup for the characterization of structural and magnetic features in spatially-ordered nanosystems. Finally, we would like to thank our local contact Dr Melissa Sharp and Helmut Eckerlebe for their excellent support.

## Reference

- [1] S. V. Grigoriev, N. A. Grigorieva, A. V. Syromyatnikov, K. S. Napolskii, A. A. Eliseev, A. V. Lukashin, Yu. D. Tretyakov, H. Eckerlebe, *JETP Letters*, Vol. 85 (2007) pp. 605–610. (Translated from *Pis'ma v Zhurnal Éksperimental'noi i Teoreticheskoi Fiziki*, Vol. 85, 2007, pp. 738–743 – Spatially ordered arrays of magnetic nanowires: polarized neutron scattering investigation.)

	<b>EXPERIMENTAL REPORT</b>	<b>GeNF SANS-2</b>
<b>SANS study of highly-ordered Al<sub>2</sub>O<sub>3</sub> matrix: test of the theory</b>		
<b>Proposer:</b> <b>Co-Proposers:</b>	<b>Sergey V. Grigoriev<sup>1</sup></b> , <sup>1</sup> PNPI, Gatchina, Russia <b>Natalia Grigoryeva<sup>2</sup></b> , <sup>2</sup> SPSU, St-Petersburg, Russia <b>Kirill Napolskii<sup>3</sup></b> , <sup>3</sup> MSU, Moscow, Russia <b>Arseny V. Syromyatnikov<sup>1</sup></b>	
<b>Experimental Team:</b> <b>User Group Leader:</b> <b>Instrument Responsible:</b>	<b>Sergey V. Grigoriev<sup>1</sup></b> , <b>Natalia Grigoryeva<sup>2</sup></b> , <b>Kirill Napolskii<sup>3</sup></b> , <b>Andrey Chumakov<sup>1</sup></b> , <b>Melissa Sharp<sup>4</sup></b> , <b>Helmut Eckerlebe<sup>4</sup></b> , <sup>4</sup> GKSS Research Centre Geesthacht <b>Sergey V. Grigoriev<sup>1</sup></b> <b>Melissa Sharp<sup>4</sup></b> , <b>Helmut Eckerlebe<sup>4</sup></b>	
<b>Date(s) of Experiment:</b>	27 <sup>th</sup> April – 30 <sup>st</sup> April 2007	

## Objectives

The anodic oxidation method is known more than 100 years and is widely used in technology for formation of protective oxide coatings on metal surfaces. The interest of scientific community was attracted again to the process of anodic oxidation of metals about 15 years ago, when spatially ordered porous alumina films were first formed by two-stage anodization process [1]. The structure of Anodic Alumina Oxide (AAO) films differs slightly depending on chemical nature of metal substrate: porous alumina, for example, reveals a hexagonal ordered system of cylindrical channels aligned perpendicular to the film surface. Our previous measurements had shown a high efficiency of the small angle neutron scattering method in investigations of these AAO membranes. In attempt to describe the result of our previous experiments we have developed a new theory of the neutron scattering on such objects [2]. If one assumes the AAO membrane with the perfect ordering of the pore structure, the intensity of the neutron scattering is proportional to the scattering length  $f_q$ :

$$I(\vec{q}) \sim f_q^2 = 4k^2 R^4 \sin^2(kL(1-n)/2) \cdot F^2(q) \cdot S^2(\vec{q}), \quad (1)$$

where  $L$  is the pore's length,  $R$  is the pore radius,  $k$  is the neutron wave number in vacuum, and  $n$  is the refraction coefficient for neutrons. For most of the materials the value of  $(1-n)$  is of order of  $10^{-5} \div 10^{-6}$ .  $F^2(q)$  is the form factor, that characterizes the scattering of the neutron wave on the cylindrical pores. It is proportional to the first order Bessel function. The last term in the product  $S^2(q)$  is the structure factor. The positions of the reflections are determined by the structure factor. They are independent on the pore radius  $R$  or the sample thickness  $L$ . The ratio of the intensities between different reflections is determined by the pore radius  $R$ . The intensity of the whole pattern strongly depends on the pore radius  $R$  and membrane thickness  $L$  and the wave number  $k$ . The present experiment was aimed to test the new theory, i.e. to compare the result of the experiment with the prediction of the theory on the quantitative level.

## Experiment

### 1. Samples preparation

Anodic Aluminum Oxide (AAO) membrane was prepared by the two-step anodization technique [1]. This method allows producing porous films with well ordered hexagonal arrays of

cylindrical channels. High purity aluminum foil was annealed at 550 °C in air in order to remove the mechanical stress and enhance the grain size in the metal. The anodization was carried out in the two-electrode cell. After the first anodization for 24 h the film of AAO was selectively etched away. After the second anodization with the oxidation time of 52 h the oxide layers have been obtained with thicknesses  $L$  of 60  $\mu\text{m}$  and the pore radius of 24 nm.

## 2. Small-angle neutron scattering

SANS measurements were carried out with the instrument SANS-2 at the Geesthacht Neutron Facility (GeNF). A neutron beam with a wavelength ranging from  $\lambda = 0.5$  nm to  $\lambda = 1.2$  nm and a wavelength spread of  $\Delta\lambda/\lambda = 10\%$  was used. A film with an area of  $\sim 0.5$  cm<sup>2</sup> was oriented perpendicularly to the neutron beam and was uniformly irradiated over the entire area. Such an orientation of the sample corresponds to the pore arrangement, as well as the long axis of the magnetic nanowires, in parallel to the incident neutron beam (Fig.1). The chosen geometry of the experiment allows the observation of the diffraction reflection system from the ordered structure of the porous matrix in the small-angle scattering range. The Sample – Detector distances of 15 and 11 m for the neutron wavelength of 0.5, 0.6, 0.7, 0.8 nm and of 0.8, 0.9, 1.0, 1.1, 1.2 nm, respectively, were used with appropriate collimations to cover scattering vectors  $q$  from 0.025 to 0.2 nm<sup>-1</sup>.

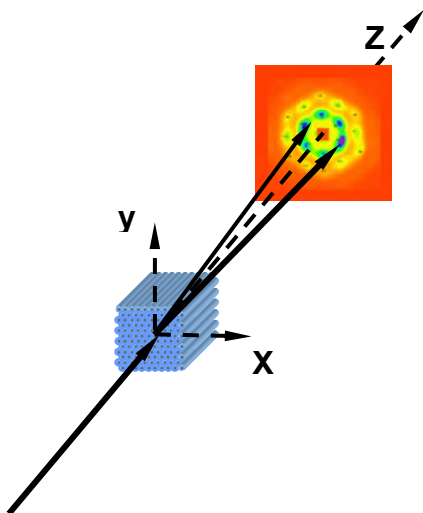


**Figure 1:**  
The schematic drawing of the experiment.  
A typical diffraction pattern obtained from AAO membrane.

## Achievements and Main Results

A typical diffraction pattern measured from AAO membrane is shown in Figure 2a. Up to three-order reflections have been clearly detected, suggesting the presence of strong correlations in the pores positions over significant distances. The hexagonally arranged set of reflections demonstrates the 6-fold symmetry along the direction normal to the film surface.

Figure 2b shows the momentum-transfer dependence of the radially-averaged neutron scattering intensity  $I(q)$  for different wavelengths normalized by the incident beam  $I_0$ . The diffraction pattern for the wavelength of 0.8 nm had been taken at two different S-D distances of 11 and 15 m. These two curves, shown in Fig. 3, coincide practically. This demonstrates the correctness of the data treatment. The dependence  $I(q)$  is satisfactorily reproduced by the sum of the Gaussians with the centers at  $q_{10} = 0.069 \pm 0.004$  nm<sup>-1</sup>,  $q_{11} = 0.119 \pm 0.004$  nm<sup>-1</sup>,  $q_{20} = 0.138 \pm 0.004$  nm<sup>-1</sup>, and a half-width  $w = 0.0100 \pm 0.0005$  nm<sup>-1</sup>; and the diffuse small-angle scattering, which is represented by the Gaussian centred at  $q = 0$ . The observed diffraction maxima are classified in the hexagonal lattice with the parameter  $a = 105 \pm 2$  nm.

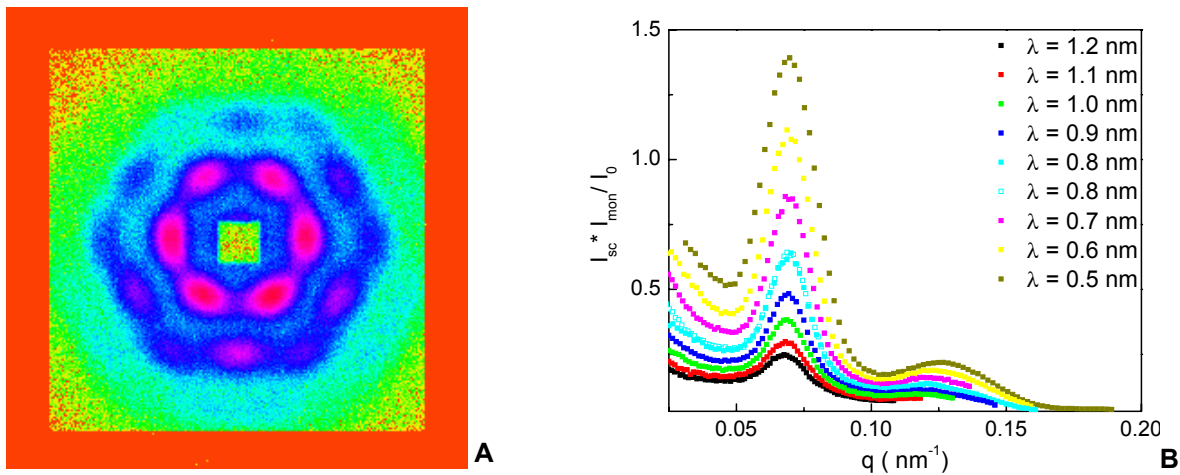
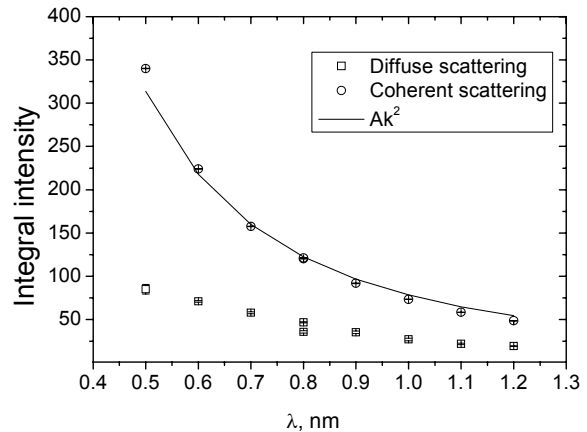


**Figure 2:** Typical 2D diffraction pattern from  $\text{Al}_2\text{O}_3$  membrane with a spatially ordered structure (A). Panel B shows momentum-transfer dependence of the neutron scattering intensity at different neutron wavelengths normalized by the incident beam  $I_0$ .

**Figure 3:**

Wavelength dependence of the integral scattering intensity for coherent scattering at  $q_{10}$  and for diffuse scattering.




The wavelength dependence of the integral scattering intensity for coherent scattering at  $q_{10}$  and for diffuse scattering at  $q = 0$  is shown in Fig. 3. As is well seen the integral intensity decreases with increase of the wavelength. This contradicts to naive expectations that the neutron cross-section in a small angle range should increase with increase of the wavelength as  $\lambda^2$ . The experiment shows the opposite: the line gives the  $k^2$ -dependence, which is proportional to  $\lambda^{-2}$ . The diffuse scattering decreases with increase of the wavelength as well but its decrease is proportional to  $\lambda^{-1}$ . Thus our preliminary treatment demonstrate the validity of the new theory and expression Eq.(1). Further treatment of the experimental data in accord with the model proposed in our recent work [2] is in progress.

Finally, we would like to thank our local contacts (Helmut Eckerlebe and Melissa Sharp) for their excellent support.

## References

- [1] H. Masuda, K. Fukuda, Science, 268, 1466 (1995)
- [2] S. V. Grigoriev, N. A. Grigorieva, A. V. Syromyatnikov, K. S. Napol'skii, A. A. Eliseev, A. V. Lukashin, Yu. D. Tretyakov, H. Eckerlebe, JETP Letters, Vol. 85 (2007) pp. 449–453. (Translated from Pis'ma v Zhurnal Éksperimental'noi i Teoreticheskoi Fiziki, Vol. 85, 2007, pp. 549–554 – Two-dimensional spatially ordered  $\text{Al}_2\text{O}_3$  systems: small angle neutron scattering investigation.)



	<b>EXPERIMENTAL REPORT</b>	<b>GeNF SANS-2</b>
<b>Polarized SANS study of highly-ordered massives of the magnetic Ni nanowires embedded into Al<sub>2</sub>O<sub>3</sub> matrix</b>		
<b>Proposer:</b> <b>Co-Proposers:</b>	<b>Sergey V. Grigoriev<sup>1</sup></b> , <sup>1</sup> PNPI, Gatchina, Russia <b>Natalia Grigoryeva<sup>2</sup></b> , <sup>2</sup> SPSU, St-Petersburg, Russia <b>Kirill Napolskii<sup>3</sup></b> , <sup>3</sup> MSU, Moscow, Russia <b>Arseny V. Syromyatnikov<sup>1</sup></b>	
<b>Experimental Team:</b> <b>User Group Leader:</b> <b>Instrument Responsible:</b>	<b>Sergey V. Grigoriev<sup>1</sup></b> , <b>Natalia Grigoryeva<sup>2</sup></b> , <b>Kirill Napolskii<sup>3</sup></b> , <b>Andrey Chumakov<sup>1</sup></b> , <b>Melissa Sharp<sup>4</sup></b> , <b>Helmut Eckerlebe<sup>4</sup></b> , <sup>4</sup> GKSS Research Centre Geesthacht <b>Sergey V. Grigoriev<sup>1</sup></b> <b>Melissa Sharp<sup>4</sup></b> , <b>Helmut Eckerlebe<sup>4</sup></b>	
<b>Date(s) of Experiment:</b>	27 <sup>th</sup> April – 30 <sup>st</sup> April 2007	

## Objectives

In recent years we have started investigations of the structural and magnetic properties of two-dimensional spatially ordered system of ferromagnetic nickel nanowires embedded into Al<sub>2</sub>O<sub>3</sub> matrix with use of Polarized Small-Angle Neutron Scattering [1]. It appears that the small-angle scattering pattern exhibits many diffraction peaks (up to the third-fourth reflection orders), which corresponds to the scattering from highly correlated hexagonal structure of pores and magnetic nanowires. Different contributions to the scattering, that have been analyzed, are the nonmagnetic (nuclear) contribution, the magnetic contribution depending on the magnetic field, and the nuclear-magnetic interference indicating the correlation between the magnetic and nuclear structures. All these contributions to the scattering appeared to be very unusual and could not be described using an ordinary theory of neutron scattering in its Born approximation. An exact theoretical solution has been obtained for describing the neutron diffraction on these objects [1]. The present experiment was aimed to test the new theory of the magnetic scattering, i.e. to compare the result of the experiment with the prediction of the theory on the quantitative level.

## Experiment

### 1. Samples preparation

Anodic Aluminum Oxide (AAO) membrane was prepared by the two-step anodization technique [1]. The resulting films with a thickness of 60 μm and the pore radius of 20 nm are used as templates to synthesize wire nanoparticles. For the controlled growth of Ni nanoparticles in the porous Al<sub>2</sub>O<sub>3</sub> matrix, electrostatic precipitation is performed in a three-electrode cell in a controlled potential regime. The duration of the Ni electrostatic precipitation is equal to 48 h, which corresponds, according to scanning electron microscopy, to the formation of wire nanoparticles with a length of 60 μm and a diameter of 40 nm.

### 2. Small-angle neutron scattering

SANS measurements were carried out with the instrument SANS-2 at the Geesthacht Neutron Facility (GeNF). Polarized neutron beam with the polarization  $P_0 = 0.95$ , with a wavelength ranging from  $\lambda = 0.5$  nm to  $\lambda = 1.2$  nm and a wavelength spread of  $\Delta\lambda/\lambda = 10\%$  was used. A film with an area of  $\sim 0.5$  cm<sup>2</sup> was oriented perpendicularly to the neutron beam and was uni-



formly irradiated over the entire area. Such an orientation of the sample corresponds to the pore arrangement, as well as the long axis of the magnetic nanowires, in parallel to the incident neutron beam. The chosen geometry of the experiment allows the observation of the diffraction reflection system from the ordered structure of the porous matrix in the small-angle scattering range. The Sample - Detector distances of 15 and 11 m for the neutron wavelength of 0.5, 0.6, 0.7, 0.8 nm and of 0.8, 0.9, 1.0, 1.1, 1.2 nm, respectively, were used with appropriate collimations to cover scattering vectors  $q$  from 0.025 to 0.2  $\text{nm}^{-1}$ . An external magnetic field (up to 800 mT) was applied in the horizontal plane and perpendicular to the incident beam (perpendicular to the long axis of the nanowires). We determine the total (nuclear and magnetic) scattering ( $I(q) = I^+(q) + I^-(q)$ ) and the polarization dependent part of the scattering ( $\Delta I(q) = I^+(q) - I^-(q)$ ) where  $I^+(q)$  and  $I^-(q)$  are the intensities for neutrons polarized parallel (+) and anti-parallel (-) to the magnetic field. The field-dependent scattering intensity is extracted as  $I_H(q) = I(q, H) - I(q, 0)$ .

### Achievements and Main Results

A diffraction pattern measured from AAO membrane with Ni nanowires embedded in it is shown in Fig.1 a. The hexagonally arranged set of reflections demonstrates the 6-fold symmetry along the direction normal to the film surface.

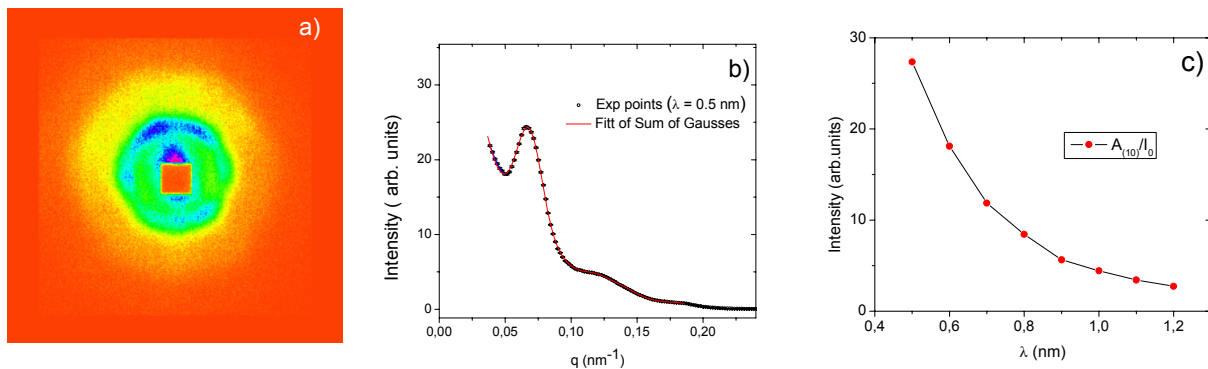


**Figure 1:** The 2D diffraction pattern from  $\text{Al}_2\text{O}_3$  membrane with Ni nanowires (a). Momentum-transfer dependence of the neutron scattering intensity at the wavelengths  $\lambda = 0.5$  nm (b). Wavelength dependence of the integral scattering intensity for coherent scattering at  $q_{10}$  (c).

The momentum-transfer dependence of the radially-averaged neutron scattering intensity  $I(q)$  is shown in Fig. 1b. The dependence  $I(q)$  is satisfactorily reproduced by the sum of the Gaussians with the centres at  $q_{10} = 0.068 \pm 0.004 \text{ nm}^{-1}$ ,  $q_{11} = 0.119 \pm 0.004 \text{ nm}^{-1}$ ,  $q_{20} = 0.138 \pm 0.004 \text{ nm}^{-1}$ , and a half-width  $w = 0.0100 \pm 0.0005 \text{ nm}^{-1}$ ; and the diffuse small-angle scattering, which is represented by the Gaussian centred at  $q = 0$ . The observed diffraction maxima are classified in the hexagonal lattice with the parameter  $a = 106 \pm 2$  nm. The wavelength dependence of the integral scattering intensity for coherent scattering at  $q_{10}$  is shown in Fig.1c. The intensity decreases with increase of the wavelength proportional to  $\lambda^{-2}$  in accord to the predictions of the theory [1].

The magnetic field dependent component the radially-averaged neutron scattering intensity  $I_H(q)$  is shown in Fig. 2a. This component is the difference between the magnetic cross sections of the sample in two significantly different states: a state close to the saturation magnetization (in the field  $H = 800$  mT) and a completely demagnetized state, i.e. without magnetic prehistory at  $H = 0$ . The main component of the magnetic cross-section at  $H = 800$  mT is the ensemble of the magnetic reflections described by the sum of the Gaussians, whose positions correspond to maxima of the nuclear scattering cross sections. On contrary, the main component of the cross section in zero magnetic field is scattering on domains; i.e.



diffuse scattering which is described by the Gaussian at  $q = 0$ , in a complete absence of any contributions to the diffraction peaks. The approximation of the experimental data in the framework of this model is shown in Fig. 2a. The dependence  $I_H(q)$  is satisfactorily reproduced by the same sum of the Gaussians as in case of the total intensity. The wavelength dependence of the integral scattering intensity for coherent scattering at  $q_{10}$  is shown in Fig. 2 b. The intensity decreases with increase of the wavelength proportional to  $\lambda^{-2}$  in accord to the predictions of the theory [1] and similar to the total intensity shown in Fig.1.

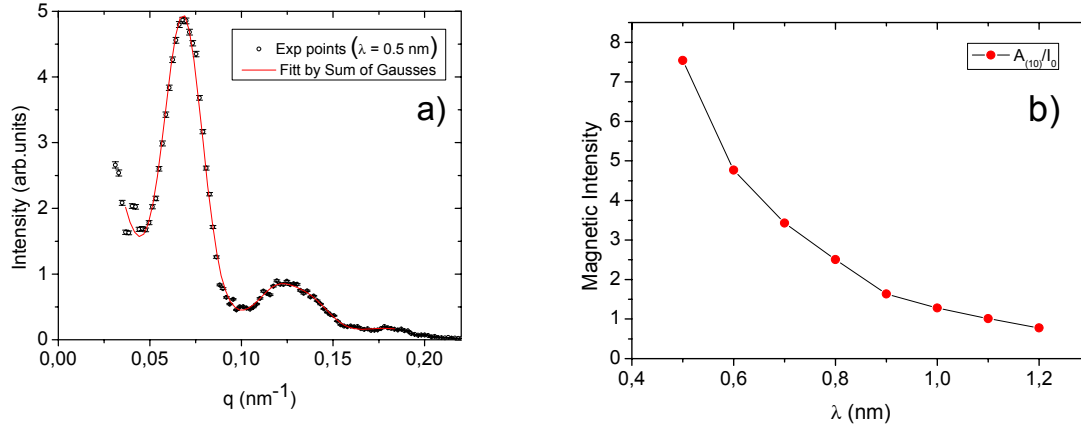


**Figure 2:** Momentum-transfer dependence of the magnetic neutron scattering intensity  $I_H(q)$  at the wavelengths  $\lambda = 0.5$  nm (a). Wavelength dependence of the integral scattering intensity for coherent scattering at  $q_{10}$  (b).

However, the azimuthal dependence of the magnetic scattering intensity is not trivial and even changes with the neutron wavelength. Figure 3 shows the intensity of the magnetic scattering normalized by the total scattering intensity denoted as  $R(\alpha) = I_H(\alpha)/\Sigma I(\alpha)$  at  $|q| = q_{(10)}$ , where  $\alpha$  is the azimuthal angle between the field direction  $\mathbf{H}$  and the scattering vector  $\mathbf{q}$ . As is well seen from Fig.3 a, the magnetic scattering  $I_H$  is maximal for  $\alpha = 0$  and 180 degrees and it is minimal at  $\alpha = 90$  and 270 degrees for short wavelengths. Thus, the magnetic scattering is preferable at  $\mathbf{q} \parallel \mathbf{H}$  and is suppressed at  $\mathbf{q} \perp \mathbf{H}$ . With increase of the wavelength the  $\alpha$ -dependence of the magnetic intensity shows a well-resolved 6-fold structure with the an equal intensity of the peaks although scattering perpendicular to  $\mathbf{H}$  remains forbidden.

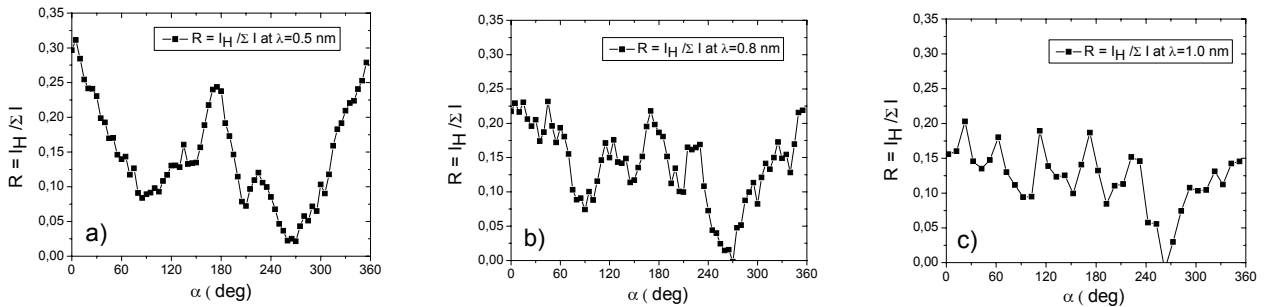


**Figure 3:** Azimuthal dependence of the normalized magnetic scattering intensity  $R(\alpha) = I_H(\alpha)/\Sigma I(\alpha)$  at  $|q| = q_{(10)}$  and neutron wavelength  $\lambda = 0.5$  nm (a), 0.8 nm (b), and 1.0 nm (c).

The  $q$ -dependence of the interference scattering contribution  $\Delta I(q)$  is shown in Fig. 4 for different directions of the scattering vector  $\alpha = 0, 30, 60, 90$  degrees at  $H = 800$  mT. As is well seen the interference scattering at  $q = q_{(10)}$  is maximal at  $\mathbf{q} \parallel \mathbf{H}$  i.e. at  $\alpha = 0$  degrees. With increase of  $\alpha$  it decreases and changes its sign at  $\alpha \sim 60$  degrees while it is negative at  $\mathbf{q} \perp \mathbf{H}$ , i.e. at  $\alpha = 90$  degrees. The situation is different at  $q \sim q_{(11)}$ . No second order reflections are

observed in the interference at  $\alpha = 0$  and 30 degrees, i.e. for  $\mathbf{q} \parallel \mathbf{H}$ . They become significant for  $\alpha = 60$  (reflection (20)) and for 90 degrees (reflection (11)). The wavelength dependence of the integral interference scattering intensity for coherent scattering at  $q_{10}$  for  $\alpha = 0$  and 90 degrees is shown in Fig. 4b. The intensity decreases with increase of the wavelength as it can be expected and similar to the total and magnetic intensity shown in Fig. 1 and Fig. 2.

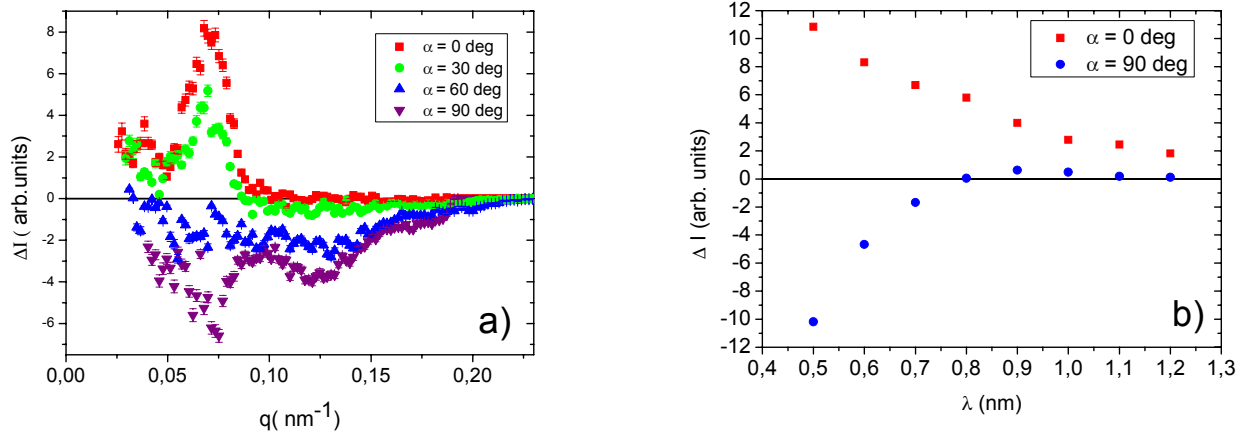


**Figure 4:** Momentum-transfer dependence of the interference neutron scattering intensity  $\Delta I(q)$  at the wavelengths  $\lambda = 0.5$  nm and for  $\alpha = 0, 30, 60, 90$  degrees (a). Wavelength dependence of the integral interference scattering intensity at  $q_{10}$  for  $\alpha = 0$  and 90 deg. (b).

To illustrate a complex behavior of the interference patterns at different wavelengths  $\lambda$  and different momentum transfer  $q$ , we plot the azimuthal dependence of the interference scattering intensity normalized by the total scattering intensity denoted as  $P(\alpha) = \Delta I(\alpha)/\Sigma I(\alpha)$  at  $|q| = q_{(10)}$  (Fig. 5). As is well seen from Fig. 5a, the interference scattering  $\Delta I$  is maximal for  $\alpha = 0$  and 180 degrees and it is minimal and negative at  $\alpha = 90$  and 270 degrees for short wavelengths.

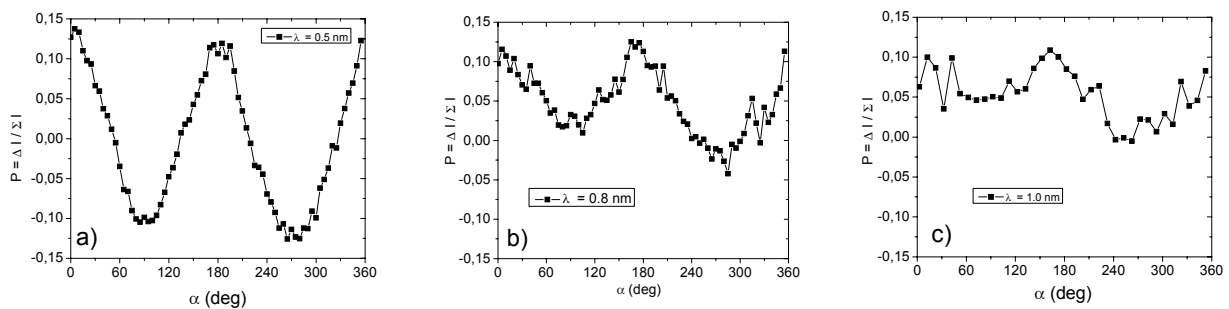



**Figure 5:** Azimuthal dependence of the normalized interference scattering intensity  $P(\alpha) = \Delta I(\alpha)/\Sigma I(\alpha)$  at  $|q| = q_{(10)}$  and neutron wavelength  $\lambda = 0.5$  nm (a), 0.8 nm (b), and 1.0 nm (c).

Further treatment of the experimental data in accord with the model proposed in our recent work [2] are in progress. Finally, we would like to thank our local contacts (Helmut Eckerlebe and Melissa Sharp) for their excellent support.

## Reference

- [1] S. V. Grigoriev, N. A. Grigorieva, A. V. Syromyatnikov, K. S. Napolskii, A. A. Eliseev, A. V. Lukashin, Yu. D. Tretyakov, H. Eckerlebe, JETP Letters, Vol. 85 (2007) pp. 605–610. (Translated from Pis'ma v Zhurnal Éksperimental'noi i Teoreticheskoi Fiziki, Vol. 85, 2007, pp. 738–743 – Spatially ordered arrays of magnetic nanowires: polarized neutron scattering investigation.)

	<b>EXPERIMENTAL REPORT</b>	<b>GeNF SANS-2</b>
<b>SANS study of the magnetic nanocomposites based on mesoporous aluminosilicates</b>		
<b>Proposer:</b>	<b>Kirill Napolskii<sup>1</sup>, <sup>1</sup>MSU, Moscow, Russia</b>	
<b>Co-Proposers:</b>	<b>Alexander Vyacheslavov<sup>1</sup></b>	
<b>Experimental Team:</b>	<b>Kirill Napolskii<sup>1</sup>, Alexander Vyacheslavov<sup>1</sup>, Andrey Eliseev<sup>1</sup>, Natalia Grigoryeva<sup>2</sup>, Helmut Eckerlebe<sup>3</sup>, Melissa Sharp<sup>3</sup></b> <sup>2</sup> SPSU, St-Petersburg, Russia, <sup>3</sup> GKSS Research Centre Geesthacht	
<b>User Group Leader:</b>	<b>Sergey V. Grigoriev<sup>4</sup>, <sup>4</sup>PNPI, Gatchina, Russia</b>	
<b>Instrument Responsible:</b>	<b>Helmut Eckerlebe<sup>3</sup>, Melissa Sharp<sup>3</sup></b>	
<b>Date(s) of Experiment:</b>	<b>1<sup>st</sup> – 15<sup>th</sup> May 2007</b>	

## Objectives

An exceptional growth of information technologies and the progress in data recording schemes resulted in downscaling magnetic bit size to several nanometers. As is known, the reduction in size of a magnetic particle leads to significant decrease of its magnetic susceptibility and the coercive force. Superparamagnetic nanoparticles are characterized by zero  $H_c$  and inability of fastening of the magnetic moment in a certain direction, which makes impossible the use of nanomagnets with a size smaller than 5–10 nm in magnetic applications. From the theoretical point of view, the most common solution of the problem is the use of strongly anisotropic nanoparticles, which could certainly increase functional properties of nanomaterials (e.g. blocking temperatures and coercive force at room temperature).

In the present work we performed synthesis and detailed characterization of cobalt nanowire arrays in mesoporous aluminosilicate (MAS) with hexagonal arrangement of 1D channels (pore diameter 2 nm). The strategy of synthesis was based on the intercalation of the hydrophobic cobalt complex  $(Co_2(CO)_8)$  to the hydrophobic part of MAS/CTAB composite with the subsequent reduction of metal. Ordering parameters and magnetic structure of nanocomposites were investigated by polarized small-angle neutron scattering (SANS) measurements.

## Experiment

### 1. Samples preparation

Mesoporous aluminosilicate was prepared by the two-step hydrothermal treatment procedure [1]. The precursor with the molar ratio of reactants:

$(16-n)SiO_2:nNaAlO_2:NaOH:564H_2O:10.5(CH_3)_4NOH$  was transferred to a stainless steel autoclave and annealed at 150 °C for 3 hours. To form mesoporous phase 9.8 g of dried seeding gel and 1.5 g of cetyltrimethylammonium bromide  $(C_{16}H_{33}(CH_3)_3NBr)$  were dissolved in 25 ml of distilled water, the mixture was transferred in autoclave and annealed at 150 °C for 48 hours. The crystalline precipitate was filtered out, washed and dried at 80 °C for 12 hours. Intercalation of cobalt precursor into the channels of mesoporous aluminosilicate was performed by soaking it in the mesitylenic solution of  $Co_2(CO)_8$  in argon atmosphere for 24 hours. After the impregnation stage the sample was washed by mesitylene to get rid of cobalt complex adsorbed on external surface and dried in an argon flow. The samples were thermally decomposed in hydrogen flow at different temperatures to formation of metal particles inside the channels.

## 2. Small-angle neutron scattering

Polarized SANS measurements were carried out with the instrument SANS-2 at the Geesthacht Neutron Facility (GeNF). Polarized neutron beam with the polarization  $P_0 = 0.95$ , with a mean wavelength of  $\lambda = 0.5$  nm and a wavelength spread of  $\Delta\lambda/\lambda = 10\%$  was used. The Sample - Detector distance of 1 m was used with appropriate collimations to cover scattering vectors  $q$  from 0.5 to 4 nm<sup>-1</sup>. An external magnetic field (0 and 800 mT) was applied in the horizontal plane perpendicular to the incident beam. In SANS experiments we determine the total (nuclear and magnetic) scattering  $I(q)$ . The field-dependent scattering intensity is extracted as  $I_H(q) = I(q, H) - I(q, 0)$ .

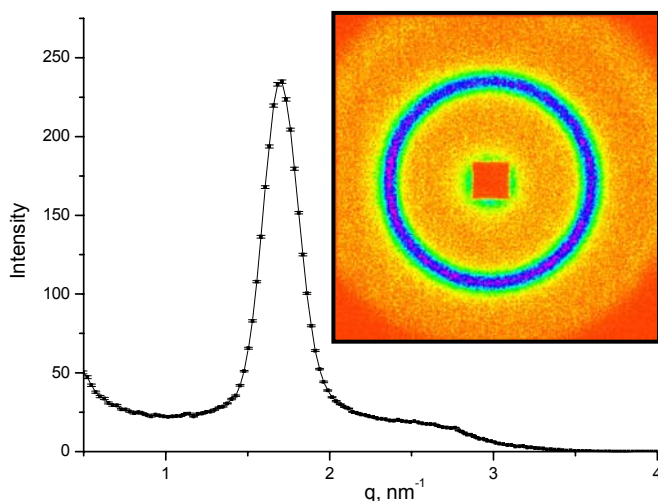


**Figure 1:**  
The  $q$ -dependence of the SANS intensity and 2D diffraction pattern from CoMAS(1:15) nanocomposite.

### Achievements and Main Results

According to XRD analysis and adsorption measurements synthesized MAS matrices possess a porous structure with an uniform pore diameter. It is well documented that a growth of Al:Si ratio in the initial aluminosilicates results in a partial disordering of pores and decreasing of a pores volume. The thermal decomposition of Co<sub>2</sub>(CO)<sub>8</sub>/MAS composites leads to a formation of the wire-like cobalt-containing anisotropic particles inside 1D pores of aluminosilicate matrix.

The ordering of magnetic structure and re-magnetization process were investigated by means of polarized SANS technique. A typical diffraction pattern from Co/MAS nanocomposite is shown in Fig. 1. The two rings with an isotropic distribution of intensity are clearly seen that corresponds to the ordered porous structure with a random orientation of aluminosilicate particles in the powder. The period of the structure  $d$  calculated using the Bragg law ( $n\lambda\theta = 2d\sin(\theta/2)$ ) is equal to 4.3 nm. An increase of Al:Si ratio leads to a decrease of the peak intensity and its widening, which correspond to disordering of the porous structure.

As powder samples consist of many randomly oriented particles, the contribution to the scattering is strongly dependent on their orientation. Obviously the particles with pores oriented parallel to the neutron beam, make the major contribution to the diffraction ring with six reflexes for each mesoporous crystallite, the particles oriented perpendicularly to the beam give two low-intensity reflexes, while nearly no contribution should be observed for other crystallites due to mismatch of the Bragg conditions for these orientations. The magnetic part of the neutron cross-section is determined by the magnetization  $m$  and corresponds to the certain length scale defined by  $q_c$ . The nuclear contribution does not depend on the external field, while magnetic cross-section is field-dependent, allowing to extract the magnetic part of scattering as  $I_H(q) = I(q, H) - I(q, 0)$ . The increase of the magnetic scattering illustrates, therefore, the correlation (collinearity) of the magnetic moments of the adjacent particles.

The sample CoMAS(1:15) have shown the highest field-dependent contribution in the series of CoMAS(n:m) nanocomposites. The magnetic scattering was extrapolated by sum of the diffuse scattering and Gauss function describing the intensity of the Bragg peak. The intensity of magnetic scattering is plotted as a function of the external field (Fig. 2). The measurements reveal the presence of large hysteresis of the  $I_H(q)$ , which is connected to several processes taking place during magnetization of nanowire arrays in the perpendicular external field. In the ground state (when no external field is applied) the moments of nanowires are aligned parallel to the long axes, but are randomly distributed between +1 and -1 states. The perpendicular magnetic field applied results in a deviation of the total wire momentum from the long axes and to decrease of the magnetization via an incoherent mechanism: disordering of the magnetic moments at the first stage. Further increase of the field aligns moments in perpendicular direction with a gradual increase of scattering intensity at the Bragg peak position. Thus, the local minima at the magnetic reversal curve ( $H \approx 300$  mT) should be attributed to the change of the magnetization mechanism from the incoherent model to the coherent rotation. Thus, the obtained data is in a good agreement with the curling magnetic reversal predicted by theoretical model for anisotropic magnetic particles [2]. An additional scattering appearing with reduce of the field from maximum (800 mT) appears due to the coherent rotation of wire magnetic moments towards easy axis, which decreases thermal fluctuations of the magnetic moments. Finally, the decrease of the magnetic ordering in low fields is attributed to the demagnetization effect playing a role of disorienting force, which also forces the formation of pseudodomain structure in the array.

We would like to thank our local contact Dr Melissa Sharp and Helmut Eckerlebe for their excellent support.

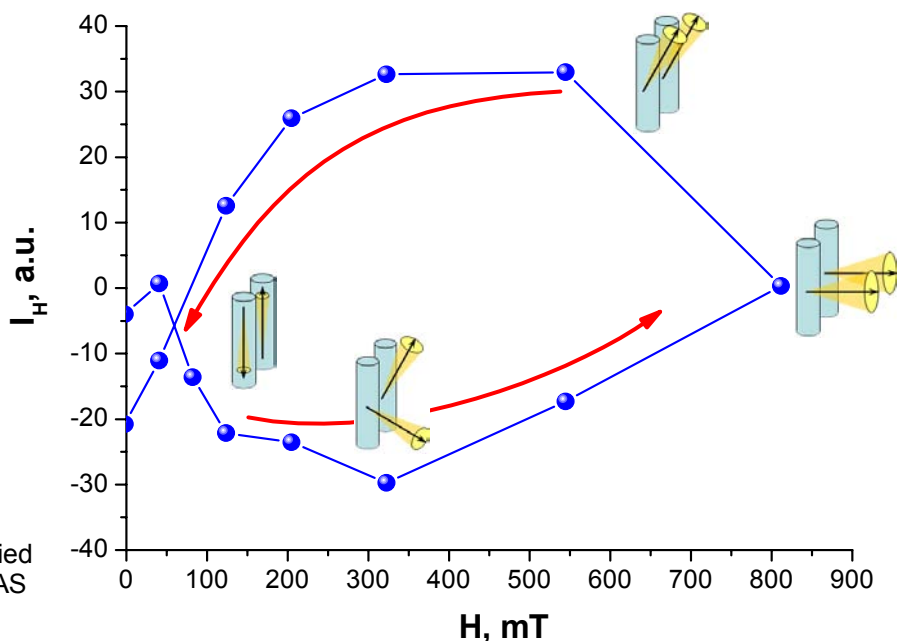



**Figure 2:** Dependence of magnetic cross section on the applied field for the sample CoMAS (1:15).

## References

- [1] A. S. Vyacheslavov, A. A. Eliseev, A. V. Lukashin, Yu. D. Tretyakov, N. A. Grigorieva, S. V. Grigoriev, H. Eckerlebe, Ordered cobalt nanowires in mesoporous aluminosilicate, *Mat. Sci. Eng. C* 27 (2007), 1411–1414
- [2] L. Sun, Y. Hao, C.-L. Chien, P.C. Searson, Tuning the properties of magnetic nanowires. *IBM J. Res. & Dev.* 49 (2005), 79–102



	<b>EXPERIMENTAL REPORT</b>	<b>GeNF SANS-2</b>
<b>Principal interactions in helical system Mn<sub>1-y</sub>Fe<sub>y</sub>Si</b>		
<b>Proposer:</b> <b>Co-Proposers:</b>	<b>Vadim Dyadkin<sup>2</sup></b> <b>Daniel Lamago<sup>1</sup>, Sergey V. Grigoriev<sup>2</sup></b> <sup>1</sup> LLB, Saclay, France <sup>2</sup> PNPI, Gatchina, St-Petersburg, RUSSIA	
<b>Experimental Team:</b> <b>User Group Leader:</b> <b>Instrument Responsible:</b>	<b>Vadim Dyadkin, Eugeny Moskvina, Daniel Lamago</b> <b>Helmut Eckerlebe<sup>3</sup>, <sup>3</sup>GKSS Research Centre Geesthacht, Germany</b> <b>Sergey V. Grigoriev<sup>2</sup></b> <b>Helmut Eckerlebe<sup>3</sup></b>	
<b>Date(s) of Experiment:</b>	July 2007	

## Objectives

The weak itinerant ferromagnet MnSi with the space group  $P2_13$  and the lattice constant  $a = 0.4558$  nm has ordered below  $T_C = 29$  K in a left-handed ferromagnetic spiral along the  $\langle 1\ 1\ 1 \rangle$  directions with a propagation vector  $\mathbf{k} = (2\pi/a) (\xi, \xi, \xi)$  where  $\xi = 0.017$  [1,2]. The helicity is realized by an antisymmetric Dzyaloshinski-Moriya (DM) exchange interaction caused by the lack of a center of symmetry in Mn atomic arrangement [3,4]. This DM interaction is isotropic itself but another weak anisotropic exchange (AE) interaction fixes a direction of the magnetic spiral along one of the cube diagonals. It is well known that the doping MnSi by Fe leads to the decrease of the average magnetic moment in these compounds [3] and  $T_C$  decreases as well. The general aim of the carried experiments was to determine general parameters of these systems (such as the spiral wave vector  $\mathbf{k}$ , the critical magnetic fields  $H_{C1}$ ,  $H_{C2}$ ,  $H_{gap}$ ) and using newly developed theory [5] to calculate principal interactions (such as the Dzyaloshinskii constant  $D$ , the spin wave stiffness  $A$ , and the spin wave gap  $\Delta$ ).

## Experiment

### 1. Sample

The single crystals Mn<sub>0.94</sub>Fe<sub>0.06</sub>Si, Mn<sub>0.92</sub>Fe<sub>0.08</sub>Si, and Mn<sub>0.9</sub>Fe<sub>0.1</sub>Si were chosen for the study. The samples were discs with a thickness of 3 mm and a diameter of 15 mm.

### 2. Small-angle neutron scattering

Small-angle neutron scattering (SANS) measurements are carried out with the instrument SANS-2 at the Geesthacht Neutron Facility (GeNF). Neutrons with a mean wavelength of  $\lambda = 0.58$  nm and a wavelength spread of  $\Delta\lambda/\lambda = 10\%$  were used. Detector distance of 4.5 m was used with appropriate collimations. The scattering intensity is measured in the following way: (i) zero field cooling from the paramagnetic state to the temperature of interest; (ii) up-rising field from  $H = 0$  to the field value of interest; (iii) descending field from  $H_{max}$  to  $H = 0$ . Using these principles the Bragg peak intensity was studied at different values of the x concentration of Fe, different values of magnetic field and different temperatures.



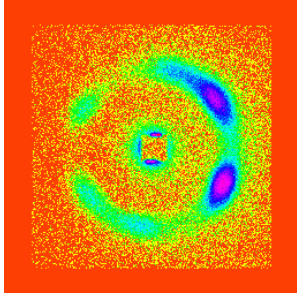


**Figure 1:** SANS map of intensity for  $\text{Mn}_{0.92}\text{Fe}_{0.08}\text{Si}$  at  $T = 8$  K.

### Achievements and Main Results

Figure 1 shows a map of the SANS intensity for the sample  $\text{Mn}_{1-y}\text{Fe}_y\text{Si}$  with  $y = 0.08$  at  $T = 8$  K. The Bragg reflections from the other samples look very similar. The scattering disappears at the critical temperature, which is determined to be equal to 16.5 K for the sample with  $y = 0.06$ ,  $T_C = 11$  K for  $y = 0.08$  and  $T_C = 7$  K for  $y = 0.1$ , respectively. Figure 2 shows the dependence of the critical temperature on the Fe concentration  $y$ . As well seen,  $T_C$  tends to 0 K with increasing the Fe concentration and, consequently, the system approaches the quantum phase transition. It is also interesting to note that the spiral wave vector  $\mathbf{k}$  of the doped samples have an ill-defined direction since the Bragg peaks are smeared and oriented along both  $\langle 111 \rangle$  and  $\langle 110 \rangle$  axes. This misorientation of the wave vector  $\mathbf{k}$  is caused by a disorder introduced by Fe doping of the MnSi compound.

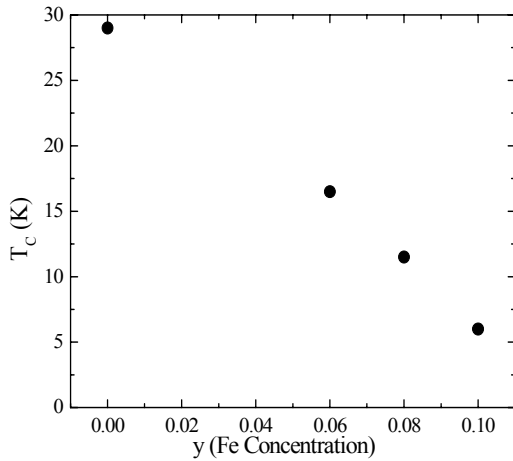


**Figure 2:** Concentration dependence of critical temperature  $T_C$ .

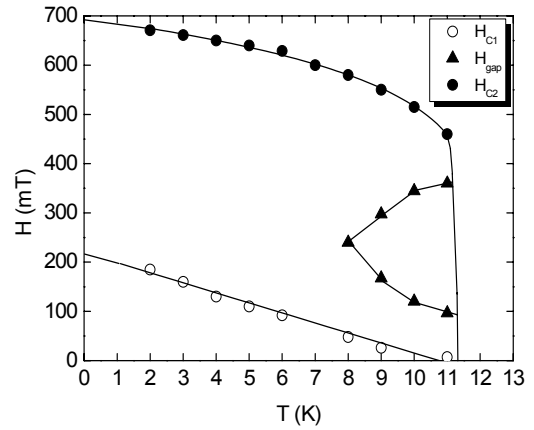


**Figure 3:** Phase diagram for the sample  $\text{Mn}_{0.92}\text{Fe}_{0.08}\text{Si}$ .

We have measured the magnetic-field dependence of the Bragg intensity at different temperatures. From these measurements one is able to determine

- (i) the value of the helical wave vector  $\mathbf{k}$ , which is inversely related to the spiral period;
- (ii) the first critical magnetic field  $H_{C1}$  where the spiral domains orient along the applied magnetic field, i.e. the anisotropy becomes smaller than the interaction of the spiral with the field;
- (iii) the second critical magnetic field  $H_{C2}$  where samples become ferromagnetic and therefore the reflections disappear;
- (iv) k-flop field  $H_{gap}$  where the wave vector revolves from  $\mathbf{k} \parallel \mathbf{H}$  to  $\mathbf{k} \perp \mathbf{H}$  in the temperature region near  $T_C$ . [4].

Using the data obtained, we plotted the H-T (magnetic field - temperature) phase diagrams for all samples under study. Figure 3 shows the phase diagram for the sample with  $y = 0.08$ . Extrapolating values of  $H_{C2}$  to  $T = 0$  and taking the middle field value for the k-flop phase near  $T_C$ , one is able to find the characteristic parameters of these compounds. We plotted them as a



function of Fe concentration  $y$  in Fig. 4. Using these parameters and newly developed theory [5] we calculated principal interactions of these systems such as

- (i) the spin wave stiffness  $A/a^2$ , where  $A = g\mu_B H_{C2}/k^2$ ,  $a$  is parameter of unit cell,  $g$  is Landè factor,  $\mu_B$  is Bohr magneton;
- (ii) the Dzyaloshinsky constant  $SD/a$ , where  $SD = Ak$ ,  $S$  is average unit cell spin;
- (iii) the spin wave gap  $\Delta = g\mu_B H_{gap}/\sqrt{2}$ .

As well seen from Fig. 5, the spin wave stiffness  $A$  decreases with the concentration  $y$  in a way very similar to the decrease of  $T_C$  with concentration (Fig. 2). The Dzyaloshinsky constant  $SD/a$  decreases as well but slower than the stiffness  $A$ . Therefore, one can conclude that the critical temperature  $T_C$  is related and probably determined by the exchange interaction, i.e. by the spin wave stiffness. These principal interactions appeared to be different from the similar system  $Fe_{1-x}Co_xSi$  [6]. This circumstance concludes that the quantum phase transitions in these two systems are governed in a completely different way, however, both these systems can be described by the same set of parameters and the same theory. We believe the comparison of these two different systems could shed a new light on the quantum phase transition problem.

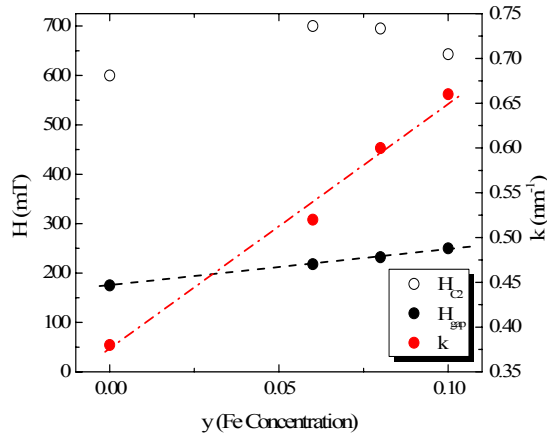


**Figure 4:** Parameters of  $Mn_{1-y}Fe_ySi$  system.

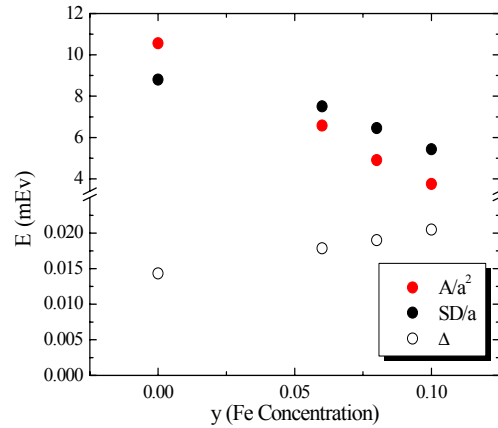



**Figure 5:** Principal interactions of  $Mn_{1-y}Fe_ySi$  system

## References

- [1] Y. Ishikawa, K Tajima, D. Bloch and M. Roth, Solid State Commun. 19 (1976), 525
- [2] Y. Ishikawa, G. Shirane, J. A. Tarvin, M. Kohgi, Phys. Rev. B 16 (1977), 4956
- [3] N. Manyala, Y. Sidis, J.F. DiTusa, G. Aeppli, D.P. Young, Z. Fisk, Nature London 404 (2000), 581–584
- [4] S. V. Grigoriev, S. V. Maleyev, A. I. Okorokov, Yu. O. Chetverikov, P. Böni, R. Georgii, D. Lamago, H. Eckerlebe, and K. Pranzas, Phys. Rev. B 74 (2006), 214414
- [5] S. V. Maleyev, Phys. Rev. B 73 (2006), 174402
- [6] S. V. Grigoriev, S. V. Maleyev, V. A. Dyadkin, D. Menzel, J. Schoenes, and H. Eckerlebe, Phys. Rev. B 76 (2007), 092407



	<b>EXPERIMENTAL REPORT</b>	<b>GeNF SANS-2</b>
<b>Spin chirality of the helix in Fe<sub>1-x</sub>Co<sub>x</sub>Si</b>		
<b>Proposer:</b>	<b>Sergey V. Grigoriev<sup>1</sup></b> , <sup>1</sup> PNPI, Gatchina, Russia	
<b>Co-Proposers:</b>	<b>Evgeny Moskvina<sup>1</sup>, Vadim Dyadkin<sup>1</sup>, Dirk Menzel<sup>2</sup></b> <sup>2</sup> Technische Universität Braunschweig, Germany	
<b>Experimental Team:</b>	<b>Sergey Grigoriev, Vadim Dyadkin, Evgeny Moskvina</b> <b>Helmut Eckerlebe<sup>3</sup></b> , <sup>3</sup> GKSS Research Centre Geesthacht, Germany	
<b>User Group Leader:</b>	<b>Sergey Grigoriev<sup>1</sup></b>	
<b>Instrument Responsible:</b>	<b>Helmut Eckerlebe<sup>3</sup></b>	
<b>Date(s) of Experiment:</b>	November 2007	

## Objectives

The cubic B20-type of mixed crystal Fe<sub>1-x</sub>Co<sub>x</sub>Si orders below T<sub>C</sub> in the one-handed helical spin structure with a small propagation vector  $k < 0.025 \text{ \AA}^{-1}$  [1,2,3,4]. At present it is widely recognized that in analogy to the magnetic structure of MnSi [5,6] and FeGe [7], the helicity is induced by the antisymmetric Dzyaloshinskii-Moriya (DM) exchange interaction caused by the lack of a symmetry centre in the arrangement of magnetic atoms Fe and Co [8,9,10]. In contrary to the case of MnSi and FeGe, the anisotropic exchange (AE) interaction and the cubic anisotropy are extremely weak in these compounds Fe<sub>1-x</sub>Co<sub>x</sub>Si. The spiral wavevector  $\mathbf{k}$  is oriented along  $\langle 100 \rangle$  axes for  $x < 0.2$  and it is almost randomly oriented for  $x > 0.2$ . The value of the wavevector  $k$  for a certain  $x$  hardly changes with temperature but  $|k|$  changes strongly with the concentration  $x$  for  $T = 0$ . It increases with increase of  $x$  for  $x < 0.2$  and decreases smoothly for  $x > 0.2$ . Thus, the concentration  $x = 0.2$  is considered as a very special point for the helix wavevector, which according to the theory [9] is determined as  $\mathbf{k} = \mathbf{SD}/A$ . Here  $\mathbf{D}$  is the Dzyaloshinskii vector and  $A$  is the spin-wave stiffness. As one can see, the sign of the Dzyaloshinskii vector is directly connected to the sign of the wavevector  $\mathbf{k}$ , which, in turn, determines the handedness (chirality) of the helical structure. The aim of the present experiment was to measure not only the length of  $\mathbf{k}$  but its sign, or chirality of the magnetic system, for different concentration  $x$  of the Fe<sub>1-x</sub>Co<sub>x</sub>Si compound using small-angle polarized neutron diffraction.

## Experiment

### 1. Sample

The single crystals Fe<sub>1-x</sub>Co<sub>x</sub>Si with  $x = 0.1, 0.15, 0.2, 0.25, 0.5$  (at.%) were chosen for the study. The samples grown by the Chokhralski method were discs with a thickness of 1 mm and a diameter of 6 mm.

### 2. Small-angle neutron scattering

Small-angle neutron scattering (SANS) measurements are carried out with the instrument SANS-2 at the Geesthacht Neutron Facility (GeNF). Polarized neutron beam with the polarization  $P_0 = 0.95$ , with a mean wavelength of  $\lambda = 0.58 \text{ nm}$  and a wavelength spread of  $\Delta\lambda/\lambda = 10 \%$  were used. Sample – Detector distance of 11 m (for  $x = 0.1, 0.15$ ), 9 m (for  $x = 0.2, 0.25$ ), 17 m (for  $x = 0.5$ ) were used with appropriate collimations to cover scattering vectors  $q$  from  $0.015 \text{ nm}^{-1}$  to  $0.2 \text{ nm}^{-1}$  ( $q = 4\pi/\lambda \cdot \sin(\theta/2)$  where  $2\theta$  is the scattering angle). A weak magnetic field (1 mT) guiding the polarization was applied horizontally and perpendicularly to the neutron beam.

## Achievements and Main Results

The polarized neutron diffraction is known as an ideal tool for measuring the spin chirality [11]. As it is known the pure magnetic elastic cross-section of the polarized neutrons consists of polarization-independent and polarization-dependent parts. The latter part is also asymmetric with respect to the momentum transfer  $\mathbf{Q}$  and associated to the average chirality of the magnetic system. It can be determined by one of the following methods: by measuring the difference between the scattering intensities taken from the incident neutron beam with the polarization along (up) and opposite (down) to the guiding magnetic field at the fixed position in the momentum space  $\mathbf{Q}$ , or, by measuring the difference between the scattering intensities at two distinct Bragg points  $\mathbf{Q}$  and  $-\mathbf{Q}$  with a fixed incident polarization. The difference between two intensities normalized to their sum is considered as a measure of the chirality of the system.

Using the position sensitive detector we measured a map of the scattering intensity at different  $\mathbf{Q}$  with a fixed incident polarization  $\mathbf{P}_0$  (Fig. 1) but particularly at two distinct Bragg points  $\mathbf{Q} = \mathbf{k}$  and  $\mathbf{Q} = -\mathbf{k}$ , providing that  $\mathbf{k} \parallel \mathbf{P}_0$ . It is well known that MnSi shows always the left-handed helix [5,6] what is well illustrated by Fig.1 a, where the scattering from MnSi sample is shown as concentrated on the left side of the detector. This sample and the corresponding scattering map is considered as an etalon for other measurements.

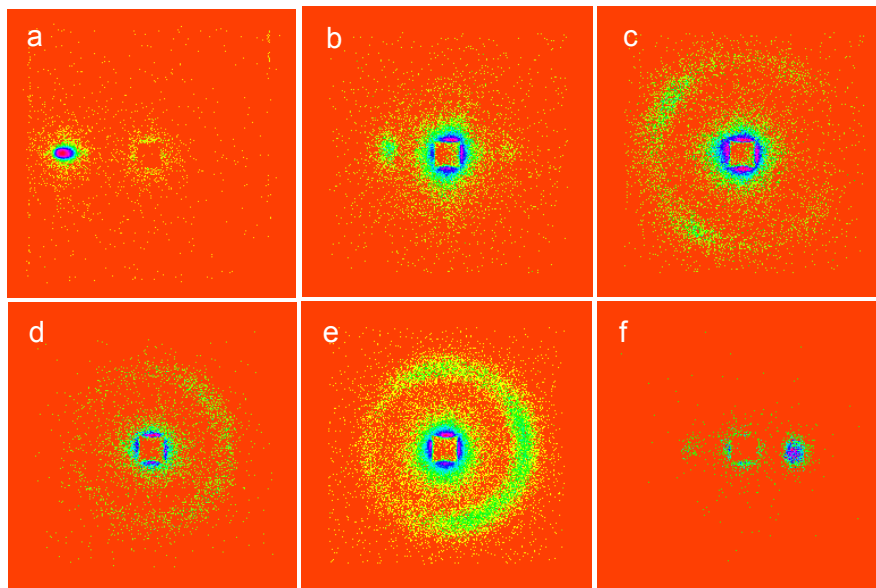


**Figure 1:** SANS maps of intensity for (a) MnSi and  $\text{Fe}_{1-x}\text{Co}_x\text{Si}$  with (b)  $x = 0.1$ ; (c)  $x = 0.15$ ; (d)  $x = 0.2$ ; (e)  $x = 0.25$ ; (f)  $x = 0.5$ .

Figure 1 shows maps of the polarized SANS intensities for five different samples  $\text{Fe}_{1-x}\text{Co}_x\text{Si}$  with  $x = 0.10$  (b),  $x = 0.15$  (b),  $x = 0.20$  (d),  $x = 0.25$  (e) and  $x = 0.50$  (f) at  $T \approx 9$  K. Comparing the maps of MnSi and  $\text{Fe}_{1-x}\text{Co}_x\text{Si}$  one can see that the samples with  $x = 0.1, 0.15$  (fig. 1 b, c) show maximum of scattering intensity at the left side of the detector similar to MnSi. It means that all three compounds (a, b, c) have the same chirality, i.e. left-handed helices. On contrary, the other three compounds with  $x = 0.2, 0.25$ , and  $0.5$  show scattering at the right side of the detector (Fig.1 d, e, f) that means: these compounds have the opposite to MnSi chirality, i.e. right-handed helices. This observation shows that there is a flop of chirality near the concentration  $x = 0.20$ . The sign of the Dzyaloshinski constant  $\mathbf{D}$  must change along with the chirality [8,9].

It is interesting to note that the handedness of the crystallographic structure of FeSi, CoSi, MnSi and  $\text{Fe}_{0.5}\text{Co}_{0.5}\text{Si}$  had been examined long ago in [12]. All of them had been revealed to belong to the left handed crystallographic system. The change of the magnetic spin chirality in the family of  $\text{Fe}_{1-x}\text{Co}_x\text{Si}$  compounds emphasize the importance of the chirality as a parameter whose change leads to the variation of the macroscopic properties such as  $T_C$  and the helix wavevector.

## References

- [1] J. Beille, J. Voiron, M. Roth, Solid State Commun. 47 (1983) 399
- [2] J. Beille, J. Voiron, F. Towfiq, M. Roth, Z.Y. Zhang, J.Phys.F: Met.Phys. 11 (1981) 2153
- [3] K. Ishimoto, H. Yamaguchi, Y. Yamaguchi, J. Suzuki, M. Arai, M. Furusaka, Y. Endoh, J.Magn.Magn.Mat. 90&91 (1990) 163
- [4] K. Ishimoto, Y. Yamaguchi, J. Suzuki, M. Arai, M. Furusaka, Y. Endoh, Physica B 213&214 (1995) 381
- [5] Y. Ishikawa, K. Tajima, D. Bloch and M. Roth, Solid State Commun. 19 (1976) 525
- [6] Y. Ishikawa, G. Shirane, J.A. Tarvin, M. Kohgi, Phys. Rev. B 16 (1977) 4956
- [7] B. Lebech, J. Bernhard, T. Freltoft, J. Phys. Condens. Matter 1, 6105 (1989)
- [8] I.E. Dzyaloshinskii, Zh. Eksp. Teor. Fiz. 46 (1964) 1420
- [9] P.Bak, M.H.Jensen, J.Phys. C13, L881 (1980)
- [10] D. Nakamishi, A. Janase, A. Hasejawa, M. Kitaoka, Solid State Commun. 35 (1980) 995
- [11] S.V. Maleyev, Phys. Rev. Lett. 75 (1995) 4682
- [12] M. Tanaka, H. Takayoshi, M. Ishida, Y. Endoh, Jour.Phys.Soc.Jap. 54 (1985) 2970

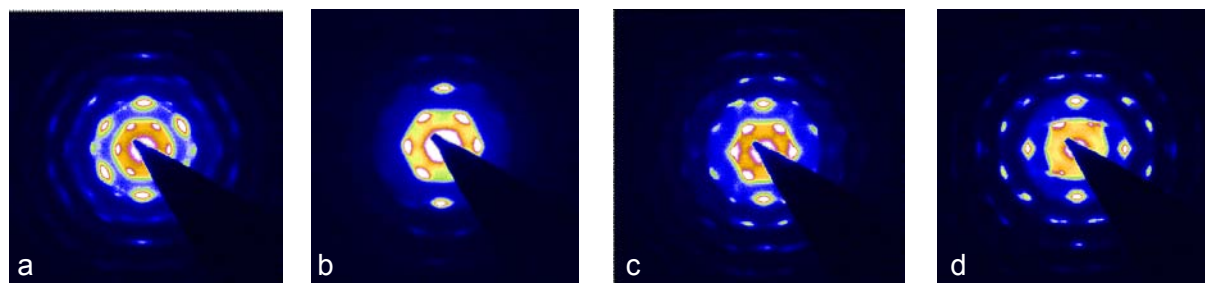


**Polarized SANS study of the magnetic Ni inversed photonic crystal in the magnetic field applied along different principal direction of its FCC structure**

<b>Proposer:</b>	<b>S. V. Grigoriev<sup>1</sup></b> , <sup>1</sup> PNPI, Gatchina, Russia
<b>Co-Proposer(s):</b>	<b>N. Grigoryeva<sup>2</sup></b> , <sup>2</sup> St-Petersburg State University, St-Petersburg, Russia <b>K. Napolskii<sup>3</sup></b> , <sup>3</sup> Moscow State University, Moscow, Russia
<b>Experimental Team:</b>	<b>N. A. Grigoryeva<sup>2</sup></b> , <b>A. A. Mistonov<sup>1</sup></b> , <b>A. V. Vasilieva<sup>1</sup></b> <b>Helmut Eckerlebe<sup>4</sup></b> , <b>Melissa Sharp<sup>4</sup></b> , <sup>4</sup> GKSS Research Centre
<b>User Group Leader:</b>	<b>Sergey V. Grigoriev<sup>1</sup></b>
<b>Instrument Responsible:</b>	<b>Helmut Eckerlebe<sup>4</sup></b> , <b>Melissa Sharp<sup>4</sup></b>
<b>Date(s) of Experiment:</b>	1 <sup>st</sup> – 9 <sup>th</sup> October 2007

**Objective**

Recently, we were the first to report polarized SANS study of magnetic photonic crystals (PC) [1]. In our previous experiments at SANS2 (GeNF, Geesthacht) we investigated inverse opals based on metallic Ni. We have shown that diffraction patterns typically consist of several clearly resolved sets of hexagonally arranged reflections. We used polarized SANS to detect the transformation of the magnetic structure under applied field. Different contributions to the neutron scattering, that have been analyzed, are the nonmagnetic (nuclear) contribution, the magnetic contribution depending on the magnetic field, and the nuclear-magnetic interference indicating the correlation between the magnetic and nuclear structures.



Angle = 0 deg

Angle = 19 deg

Angle = 35 deg

Angle = 55 deg

**Figure 1:** Small angle synchrotron diffraction patterns measured at normal incidence (a) and after sample rotation by 19 degrees (b), and by 35 degrees (c) and by 55 degrees (d).

The small angle diffraction of synchrotron radiation was demonstrated to be very efficient to determine the orientation and to characterize the ordering of photonic crystal films [2]. Our experiments with microradian synchrotron diffraction were performed on Ni inversed PCs with 450 nm periodicity of the structure. The results of the experiments are shown Fig. 1, which presents examples of the diffraction patterns measured at normal incidence (a), after sample rotation by 19 degrees (b), by 35 degrees (c) and by 55 degrees (d). The four images can be interpreted such that the crystal possesses face-centred cubic (fcc) structure. For example, the hexagonally arranged set of reflections demonstrates the 3-fold symmetry along the 111 direction normal to the substrate surface (a). The rhomb-like pattern is formed by the set of reflections when the [111] planes are oriented parallel to the beam. In this case the normal to the substrate surface is 19° turned with respect to the beam (b). The similar but somewhat richer pattern is formed when the (110) direction is oriented parallel to the

beam. In this case the normal to the substrate surface is  $35^\circ$  turned with respect to the beam (c). While the quadratic arrangements of reflections on panel (d) demonstrates the 4-fold symmetry when the beam is parallel to the (200) direction,  $55^\circ$ -inclined to the normal of the substrate surface (d).

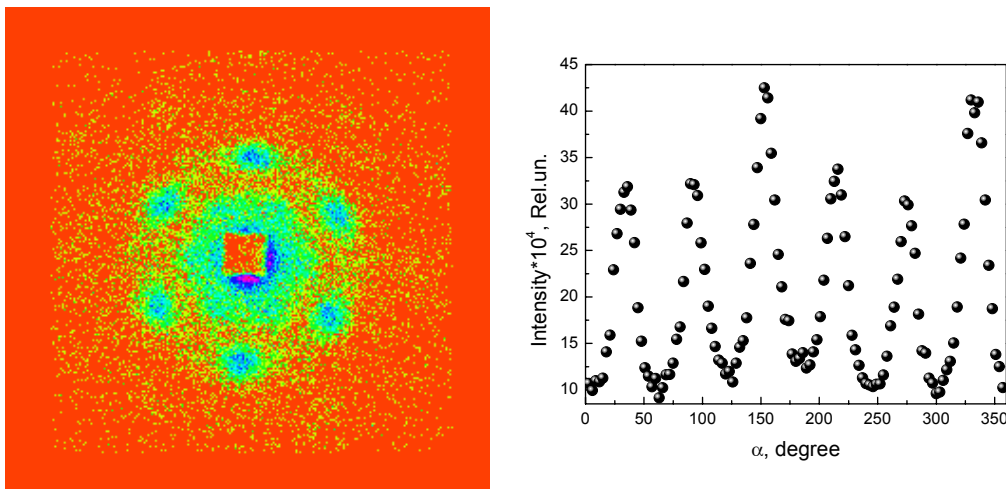
In addition to the well-pronounced fcc reflection, one can also see additional reflections, which are forbidden for a perfect fcc crystal. They originate from intersections of the Ewald's sphere by so-called Bragg rods, which are induced by stacking disorder in the direction normal to the substrate. Thus, one can conclude that the crystal is ordered to fcc structure with a weak disorder tending to the hexagonal packing. The main goal of our present experiments was to investigate magnetic properties of this Ni inverse photonic crystal using of polarized SANS in the magnetic field applied along different principal direction of its FCC structure.

## Experiment

SANS measurements were carried out with the instrument SANS-2 at the Geesthacht Neutron Facility (GeNF). Polarized neutron beam with the polarization  $P_0 = 0.95$ , with a mean wavelength of  $\lambda = 0.9$  nm and a wavelength spread of  $\Delta\lambda/\lambda = 10\%$  was used. The Sample – Detector distance of 21.5 m was used with appropriate collimations to cover scattering vectors  $q$  from 0.005 to 0.06  $\text{nm}^{-1}$ . An external magnetic field up to 160 mT was applied perpendicular to the incident beam in the (2-42) – position 1 and (111) – position 2 directions of the fcc structure and 19 degrees inclined to the incident beam along the (1-10) direction – position 3. We determine the total (nuclear and magnetic) scattering ( $I(q) = I^+(q) + I^-(q)$ ) and the polarization dependent part of the scattering ( $\Delta I(q) = I^+(q) - I^-(q)$ ) where  $I^+(q)$  and  $I^-(q)$  are the intensities for neutrons polarized parallel (+) and anti-parallel (-) to the magnetic field. The field-dependent scattering intensity is extracted as  $I_H(q) = I(q, H) - I(q, 0)$ .

## Achievements and Main Results

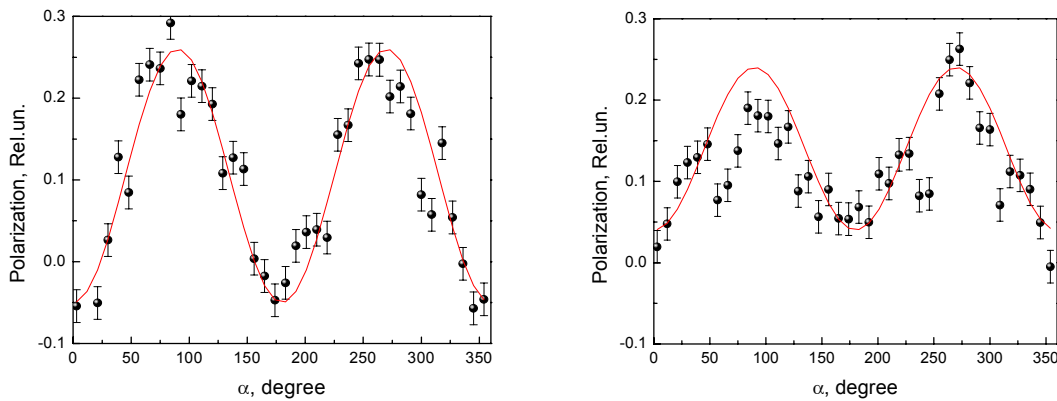
In all these measurements we recorded well-resolved neutron diffraction patterns consisted of several clearly resolved sets of hexagonally arranged reflexes as shown in Fig. 2. In order to adequately estimate the magnetic and interference scattering, an analysis of intensities as functions of  $\alpha$  has been performed, where  $\alpha$  is the angle between the direction of the scattering vector  $\mathbf{q}$  and the horizontal axis of the detector plane. Figure 2 b shows the variations of the intensity  $I(q_{20-2}, \alpha)$  on the angle  $\alpha$  at for a magnetized sample ( $H = 160$  mT). Six clearly pronounced maxima at  $60^\circ$  intervals can be well seen; they correspond to six reflections of  $\langle 20-2 \rangle$  type. The interference scattering was analyzed using the convenient definition  $P_S = \Delta I(q) / I(q)$ .



**Figure 2:** The scattering map for Ni inverse photonic crystal with peaks running from the top one clock-wise (20-2), (2-20), (0-22), etc. and  $\alpha$ -dependence of the intensity at  $|q| = q_{20-2}$ .

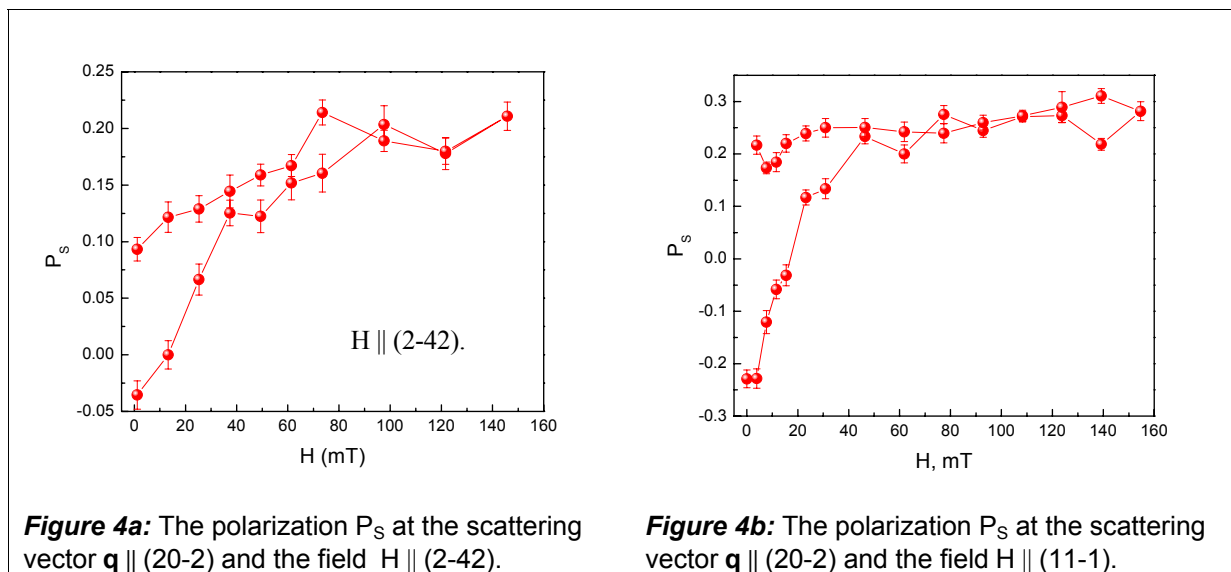


Figure 3 shows the  $\alpha$  dependence of the polarization  $P_S$  for two orientations of the magnetic field. It can be seen that  $P_S$  is adequately described by a function of the form  $\sin^2\alpha$ . The function of this form suggests that the family of the planes (20-2) was equally magnetized along the external field direction at this value of the field  $H = 160$  mT. In case the field is directed in the plane of the sample ( $H \parallel (2-42)$ ) the polarization is zero at  $\mathbf{q} \parallel (2-42)$ . In case the field is directed along the (11-1) axis, the polarization is positive at  $\mathbf{q} \parallel (2-42)$ . The variations of the polarization with the azimuth angle  $\alpha$  for the two different orientations of the magnetic field can be well interpreted taking into account the geometry of the experiment, i.e. mutual orientation of three vectors: the field and polarization axis  $\mathbf{H} \parallel \mathbf{P}$ , the average magnetization vector  $\mathbf{m}$  and scattering vector  $\mathbf{q}$ . The occurrence of the polarization (interference scattering) at the same values of  $q$  as for nuclear scattering suggests that the magnetic and nuclear structure coincide.



**Figure 3:** The  $\alpha$ -dependence of the polarization at  $|q| = q_{20-2}$  for orientations of the magnetic field along (2-42) and (11-1) axes at  $H = 160$  mT.

The magnetic field dependence of the polarization  $P_S$  for  $\mathbf{q} \parallel (20-2)$  is shown in Fig. 4a and Fig. 4b for the field directed along (2-42) and (11-1) axes, respectively. It is important to note that the observed polarization  $P_S$  is proportional to the average magnetization  $\langle \mathbf{m} \rangle$  projected onto the magnetic field direction.

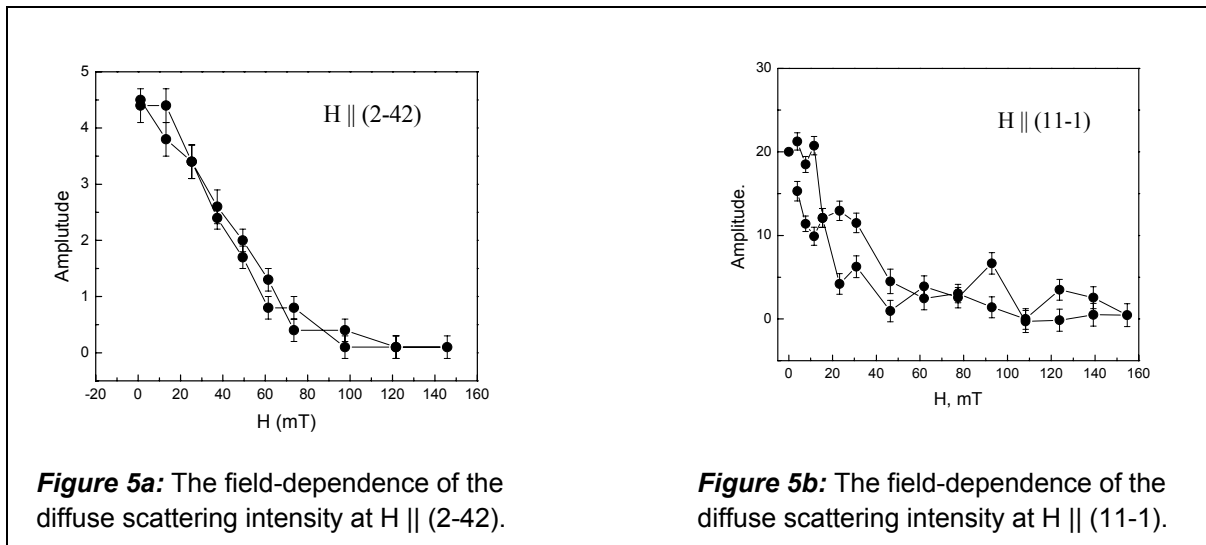


**Figure 4a:** The polarization  $P_S$  at the scattering vector  $\mathbf{q} \parallel (20-2)$  and the field  $H \parallel (2-42)$ .

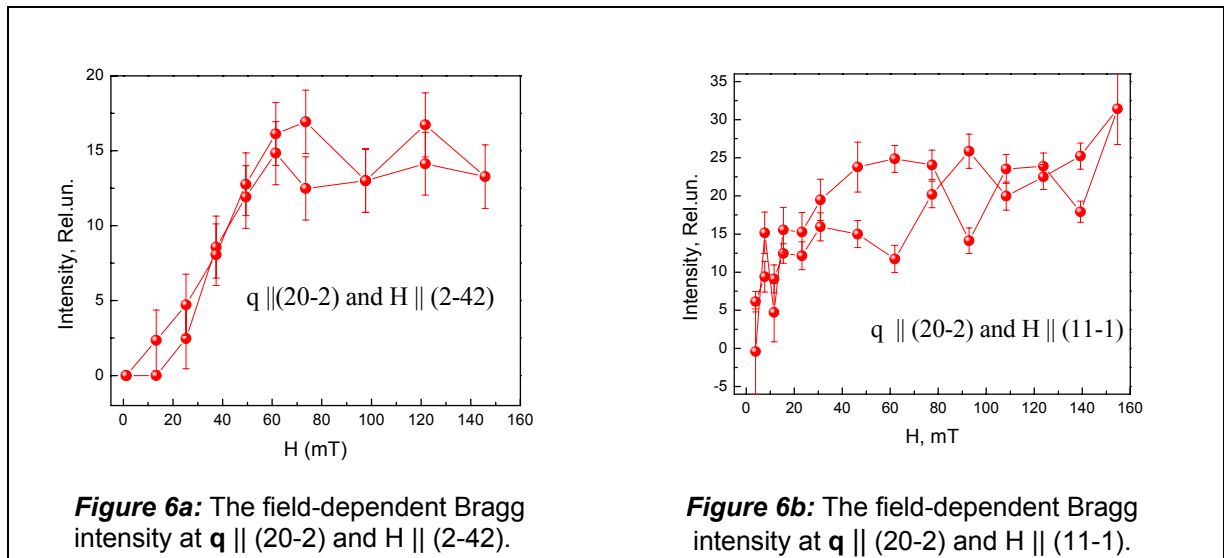
**Figure 4b:** The polarization  $P_S$  at the scattering vector  $\mathbf{q} \parallel (20-2)$  and the field  $H \parallel (11-1)$ .

As can be seen from Fig. 4 the saturation of the magnetization  $P_S$  ( $\sim \langle m \rangle$ ) takes place at 60 mT for  $H \parallel (2-42)$  and at 40 mT for  $H \parallel (11-1)$ . The magnetization curve shows also the hysteretic behaviour with the coercive force of order of 20 mT in both cases. Nevertheless, for  $H \parallel (11-1)$  the hysteresis is much more rectangular than for  $H \parallel (2-42)$ . This observation implies that the axis (11-1) is the easy axis for magnetization as compare with the (2-42) axis. This can be related to the geometrical shape of the inversed photonic crystal under study. The field dependence of the polarization  $P_S$  for other reflections  $\langle 20-2 \rangle$  shows the similar behaviour as described above.

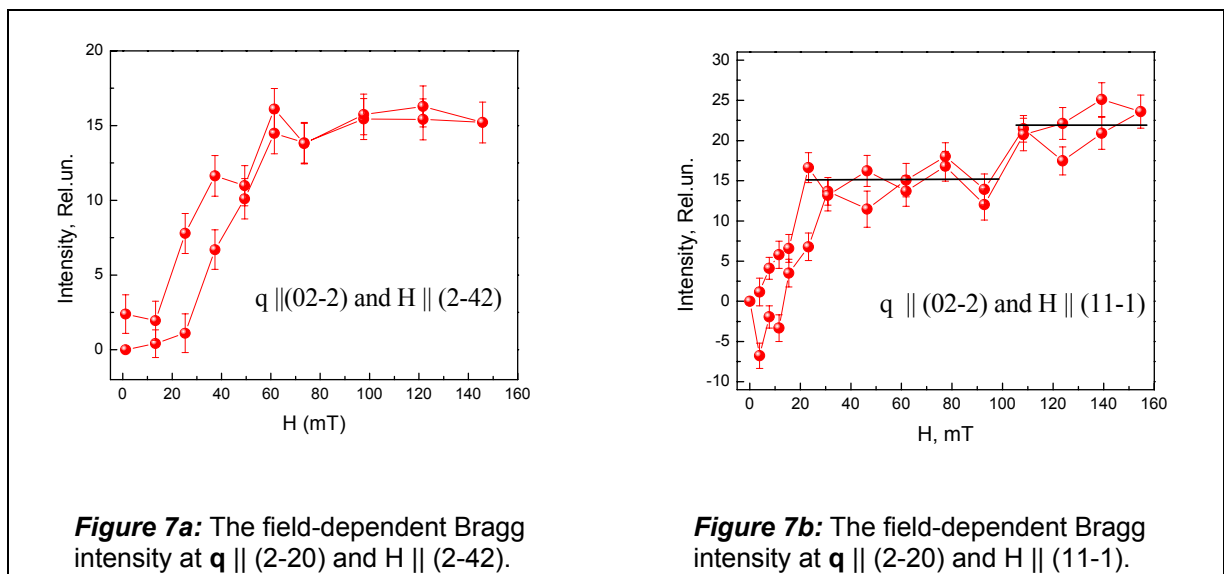
The momentum transfer dependence of the magnetic neutron scattering intensity  $I_H(q)$  has been analyzed at different scattering vectors  $\mathbf{q} \parallel (20-2)$  and  $\mathbf{q} \parallel (2-20)$ . We suppose that the magnetic scattering  $I_H(q)$  is a difference between the magnetic cross-sections of the sample in two principally different states: partially magnetized in the finite field  $H$  and fully demagnetized at  $H = 0$ . The main component of the magnetic cross-section at large field is a system of the magnetic reflections described as the sum of Gaussians with positions corresponding to the nuclear maxima. On contrary, the major component of the cross-section at  $H = 0$  is the diffuse scattering from the domains, which can be described by the squared Lorentzian in absence of any contribution the reflections. The experimental data were treated in accord to this model. The amplitude of the diffuse scattering, describing the scattering from magnetic domains, is shown in Fig. 5. It is maximal at  $H = 0$  and decreases with the field while does not vanish at  $H = 70$  mT for  $H \parallel (2-42)$  and at  $H = 40$  mT for  $H \parallel (11-1)$ . Thus domains disappear at smaller values of  $H$  for  $H \parallel (11-1)$  and than for  $H \parallel (2-42)$ . This proves also that (111) is easier for magnetization than (2-42).



All reflections of  $\langle 20-2 \rangle$  type can be divided into two subgroups: reflections (20-2) and (-202) with the angle of 90 degrees between  $\mathbf{q}$  and  $\mathbf{H}$ ; and reflections (02-2), (0-22), (2-20) and (-220) with the angle of 30-40 degrees between  $\mathbf{q}$  and  $\mathbf{H}$ . The intensities of these magnetic reflections were averaged over inside the subgroup. Fig. 6 shows the intensity of the (20-2) reflection as a function of the field for  $H \parallel (2-42)$  (a) and for  $H \parallel (11-1)$  (b), respectively. The intensity of the reflection is zero at  $H = 0$ , then it increases and reaches the saturation values at  $H = 60$  mT for  $H \parallel (2-42)$  and at  $H = 40$  mT for  $H \parallel (11-1)$ . These dependences show no hysteretic behaviour within the error bars. An interesting behaviour of the scattering intensities is observed at the reflection (02-2). They are shown in Fig. 7 as a function of the field for  $H \parallel (2-42)$  (a) and for  $H \parallel (11-1)$  (b), respectively. As for the previous case they are zero at  $H = 0$  and saturates at large  $H > 100$  mT.



On the other hand, they show several features. For  $H \parallel (2-42)$  (i) there are two critical fields. The first one at  $H_{C1} = 20$  mT, below this value the intensity is zero. It means the corresponding planes (02-2) are not magnetized. Above  $H_{C2} = 60$  mT the intensity is saturated showing full magnetization alignment along the field inside these planes. (ii) There is a small hysteresis loop inside the field range between two critical fields  $H_{C1} < H < H_{C2}$ . For  $H \parallel (11-1)$  there are two critical fields as well. The magnetic field dependence at looks the step-like function with  $H_{C1} = 20$  mT and  $H_{C2} = 100$  mT. The intensity increases in the range  $H < H_{C1}$ . A small hysteresis loop is seen at  $H < H_{C1}$ .




In conclusion, the change of the scattering intensities of the corresponding Bragg peaks can be interpreted in terms of the probability of the magnetization distribution in the octahedral and tetrahedral particles, a certain set of which is the base of the structure element of the inverted photonic crystal. In this sense, the above technique for studying PC is a direct method for measuring these probabilities.

## References

- [1] Napolskii, K.; Sinitzkii, A.; Grigoriev, S.; Grigorieva, N.; Eckerlebe, H.; Eliseev, A.; Lukashin, A.; Tretyakov, Y.; *Topology constrained magnetic structure of Ni photonic crystals*, Physica B 397 (2007), 23–26
- [2] A. V. Petukhov et al., *ESRF Highlights 2005*, 59 (2005)



	<b>EXPERIMENTAL REPORT</b>	<b>GeNF SANS-2</b>
<b>Critical scattering in helical system Mn<sub>1-y</sub>Fe<sub>y</sub>Si</b>		
<b>Proposer:</b>	<b>Sergey V. Grigoriev<sup>1</sup></b> , <sup>1</sup> PNPI, Gatchina, Russia	
<b>Co-Proposers:</b>	<b>Vadim Dyadkin<sup>1</sup>, Daniel Lamago<sup>2</sup></b> , <sup>2</sup> LLB, Saclay, France	
<b>Experimental Team:</b>	<b>Sergey Grigoriev, Vadim Dyadkin, Evgeny Moskvina<sup>1</sup></b> <b>Helmut Eckerlebe<sup>3</sup></b> , <sup>3</sup> GKSS Research Centre Geesthacht, Germany	
<b>User Group Leader:</b>	<b>Sergey Grigoriev<sup>1</sup></b>	
<b>Instrument Responsible:</b>	<b>Helmut Eckerlebe<sup>3</sup></b>	
<b>Date(s) of Experiment:</b>	November 2007	

## Objectives

The weak itinerant ferromagnet MnSi with the space group  $P2_13$  and the lattice constant  $a = 0.4558$  nm has ordered below  $T_C = 29$  K in a left-handed ferromagnetic spiral along the  $\langle 1\ 1\ 1 \rangle$  directions with a propagation vector  $\mathbf{k} = (2\pi/a)(\xi, \xi, \xi)$  where  $\xi = 0.017$ . The helicity is realized by an antisymmetric Dzyaloshinski-Moriya (DM) exchange interaction caused by the lack of a center of symmetry in Mn atomic arrangement [1]. This DM interaction is isotropic itself but another weak anisotropic exchange (AE) interaction fixes a direction of the magnetic spiral along one of the cube diagonals. It is well known that the doping MnSi by Fe leads to the decrease of the average magnetic moment in these compounds [2] and  $T_C$  decreases as well. The critical behaviour of MnSi was studied earlier [3]. Results of polarized neutron small angle scattering in the single crystal MnSi near  $T_C$  can be formulated as follows. (i) The diffuse scattering intensity above  $T_C$  looks like half-moons oriented along the incident neutron polarization. (ii) The sum of the intensities for two opposite polarizations form an anisotropic ring with weak spots. (iii) Below  $T_C$  these spots transform into the Bragg peaks originating from the helical structure. The general aim of the present experiment is to study the influence of the Fe doping on the critical behavior of the Mn<sub>1-y</sub>Fe<sub>y</sub>Si compounds.

## Experiment

### 1. Sample

The single crystal Mn<sub>0.92</sub>Fe<sub>0.08</sub>Si was chosen for the study. The sample was a disc with a thickness of 2.5 mm and a diameter of 30 mm.

### 2. Small-angle neutron scattering

Small-angle neutron scattering (SANS) measurements are carried out with the instrument SANS-2 at the Geesthacht Neutron Facility (GeNF). Polarized neutron beam with the polarization  $P_0 = 0.95$ , with a mean wavelength of  $\lambda = 0.58$  nm and a wavelength spread of  $\Delta\lambda/\lambda = 10\%$  were used. The scattered neutrons were registered by the position sensitive detector. Detector distance of 2.5 meters was used with an appropriate collimation. The incident beam was directed along the [11-2] axis, so that vectors parallel to [111] and [1-10] were in the scattering plane and perpendicular to the beam. The temperature was measured with accuracy better than 0.05 K. The magnetic field of 1 mT guiding the neutron polarization was applied in the sample's area horizontally.

## Achievements and Main Results

Maps of the polarized SANS intensities below and above  $T_c=10.4$  for two opposite neutron polarizations up and down are shown in Fig.1. Below  $T_c$  four Bragg peaks with  $k=0.61$  nm and different intensities are visible. This is possible due to the large magnetic mosaic, as in ideal case the Bragg condition would be only fulfilled for one reflection. In our geometry it is the  $[1\ 1\ 1]$  peaks, which are almost polarization-independent, as  $\mathbf{k}$  is almost perpendicular to  $\mathbf{P}$ . Reflections with  $\mathbf{k} \parallel [1\ -1\ 0]$  depend on  $\mathbf{P}$  as expected for helices with the Dzyaloshinskii vector along  $\mathbf{q}$ . Above  $T_c$ , there are half-moons only. In sum they compose a ring with the maximal intensity at  $q \sim k$ . These half-moons are induced by the critical fluctuations.

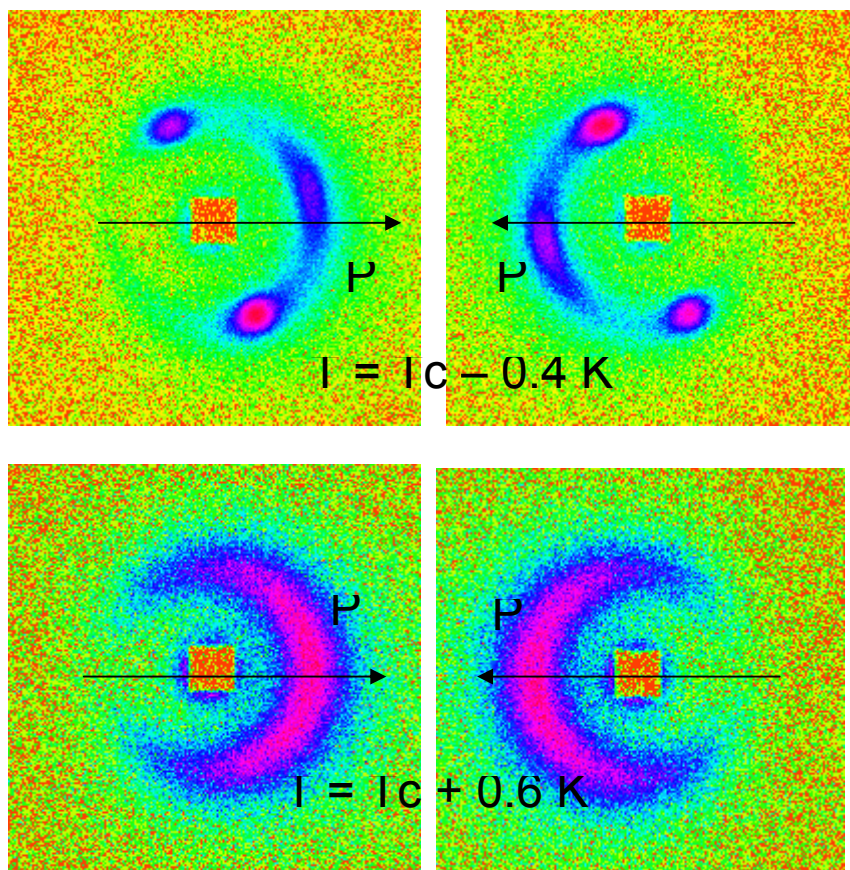



**Figure 1.**

These results are in semi-quantitative agreement with the mean-field calculations based on the Bak-Jensen model that takes into account the hierarchy of the interactions: the exchange interaction  $B$ , the isotropic Dzyaloshinskii-Moriya (DM) interaction  $D = kB$  and the weak anisotropic exchange (AE) interaction  $F \sim k^2B$ , where  $k$  is the helix wavevector and  $|k| \ll 1$ . The DM interaction is responsible for the scattering intensity concentrated in the half-moons. It is important to note that the temperature range where these half-moons exist is almost twice wider for this compound than that of the pure MnSi. We relate the temperature range, where the ring is visible  $\Delta T_{DM} = T_{DM} - T_c$ , with the value of the helix wavevector  $k^2$ . The ratio  $(k_{MnFeSi}/k_{MnSi})^2 = 2$ , which fits to the observed phenomena.

## References

- [1] P. Bak, M. H. Jensen, J.Phys.C13 (1980), L881
- [2] N. Manyala, Y. Sidis, J. F. DiTusa, G. Aeppli, D. P. Young, Z. Fisk, Nature London 404 (2000), 581–584
- [3] S. V. Grigoriev, S. V. Maleyev, A. I. Okorokov, Yu. O. Chetverikov, R. Georgii, P. Boni, D. Lamago, H. Eckerlebe, K. Pranzas, Phys.Rev.B 72 (2005), 134420



	<b>EXPERIMENTAL REPORT</b>	<b>GeNF SANS-2</b>
<b>Critical scattering in helical system Fe<sub>1-x</sub>Co<sub>x</sub>Si</b>		
<b>Proposer:</b> <b>Co-Proposers:</b>	<b>Sergey Grigoriev</b> <sup>1</sup> , <sup>1</sup> PNPI, Gatchina, Russia <b>Vadim Dyadkin</b> <sup>1</sup> , <b>Dirk Menzel</b> <sup>2</sup> , <sup>2</sup> Technische Universitat Braunschweig, Germany	
<b>Experimental Team:</b> <b>User Group Leader:</b> <b>Instrument Responsible:</b>	<b>Sergey Grigoriev</b> <sup>1</sup> , <b>Vadim Dyadkin</b> <sup>1</sup> , <b>Evgeny Moskvina</b> <sup>1</sup> <b>Helmut Eckerlebe</b> <sup>3</sup> , <sup>3</sup> GKSS Research Centre Geesthacht, Germany <b>Sergey Grigoriev</b> <sup>1</sup> <b>Helmut Eckerlebe</b> <sup>3</sup>	
<b>Date(s) of Experiment:</b>	November 2007	

## Objectives

The cubic B20-type of mixed crystal Fe<sub>1-x</sub>Co<sub>x</sub>Si orders below T<sub>C</sub> in a one-handed spin helical structure with a small propagation vector  $k < 0.25 \text{ nm}^{-1}$ . At present it is widely recognized that in analogy to the magnetic structure of MnSi and FeGe, the helicity is induced by an antisymmetric Dzyaloshinskii-Moriya (DM) exchange interaction caused by the lack of a center of symmetry in the arrangement of magnetic atoms Fe and Co [1]. This DM interaction is isotropic in cubic crystals and a weak anisotropic exchange (AE) interaction along with cubic anisotropy should fix the direction of the magnetic spiral below T<sub>C</sub>. The critical behaviour in Fe<sub>1-x</sub>Co<sub>x</sub>Si is believed to be similar to MnSi, which was studied earlier [2]. Results of polarized neutron small angle scattering in the single crystal MnSi near T<sub>C</sub> can be formulated as follows. (i) The diffuse scattering intensity above T<sub>C</sub> looks like half-moons oriented along the incident neutron polarization. (ii) The sum of the intensities for two opposite polarizations form an anisotropic ring with weak spots. (iii) Below T<sub>C</sub> these spots transform into the Bragg peaks originating from the helical structure.

The general aim of the present experiment is to study the influence of the anisotropy on the critical behavior of the Fe<sub>1-x</sub>Co<sub>x</sub>Si compounds. As was shown in [1,2] for  $x < 0.2$  the helix wavevector is clearly oriented along the  $\langle 100 \rangle$  axes, while for  $x > 0.2$  it is almost randomly oriented and the neutron scattering looks like a ring of the intensity. Thus one concludes that the anisotropy is suppressed with the increase of Co concentration [3,4].

## Experiment

### 1. Sample

The single crystal Fe<sub>0.85</sub>Co<sub>0.15</sub>Si, in which the anisotropy is significant, was chosen for the study. The sample was a disc with a thickness of 1 mm and a diameter of 10 mm.

### 2. Small-angle neutron scattering

Small-angle neutron scattering (SANS) measurements are carried out with the instrument SANS-2 at the Geesthacht Neutron Facility (GeNF). Polarized neutron beam with the polarization  $P_0 = 0.95$ , with a mean wavelength of  $\lambda = 0.58 \text{ nm}$  and a wavelength spread of  $\Delta\lambda/\lambda = 10\%$  were used. The scattered neutrons were registered by the position sensitive detector. Detector distance of 7.5 meters was used with an appropriate collimation. The incident beam was directed along the [001] axis, so that vectors parallel to [100] and [010] were in the scattering plane and perpendicular to the beam. The temperature was measured with accuracy better than 0.05 K. The magnetic field of 1 mT guiding the neutron polarization was applied in the sample's area along the [100] axis.

## Achievements and Main Results

The map of the SANS intensities below  $T_C = 18.67$  K is shown in Fig. 1a. Four Bragg peaks with  $k = 0.172 \text{ nm}^{-1}$  and different intensities are visible. This is possible due to the large magnetic mosaic, as in ideal case the Bragg condition would be only fulfilled for one reflection. In our geometry it is the [100] peak. The peaks at  $\mathbf{k} \parallel [0, 1, 0]$  are polarization-independent, as  $\mathbf{k}$  is perpendicular to  $\mathbf{P}_0 \parallel [100]$ . Reflections with  $\mathbf{k} \parallel [1 0 0]$  depend on  $\mathbf{P}_0$  as expected for helices with the Dzyaloshinskii vector along  $\mathbf{q}$ . The intensity of the [100] peak is shown in Fig. 1 b as a function of temperature. Its variation obeys the scaling law  $I = I_0 \tau^{2\beta}$ , where  $2\beta = 0.44 \pm 0.01$ . The value of the critical index  $\beta$  for this compound is close to that of MnSi [2]. Above  $T_C$  the intensity of the peak is low but still detectable within 0.3 K. Further increase of temperature leads to appearance of the ring caused by the scattering on the critical fluctuations, which disappears above 20 K, i.e. at  $\tau = 0.1$ .

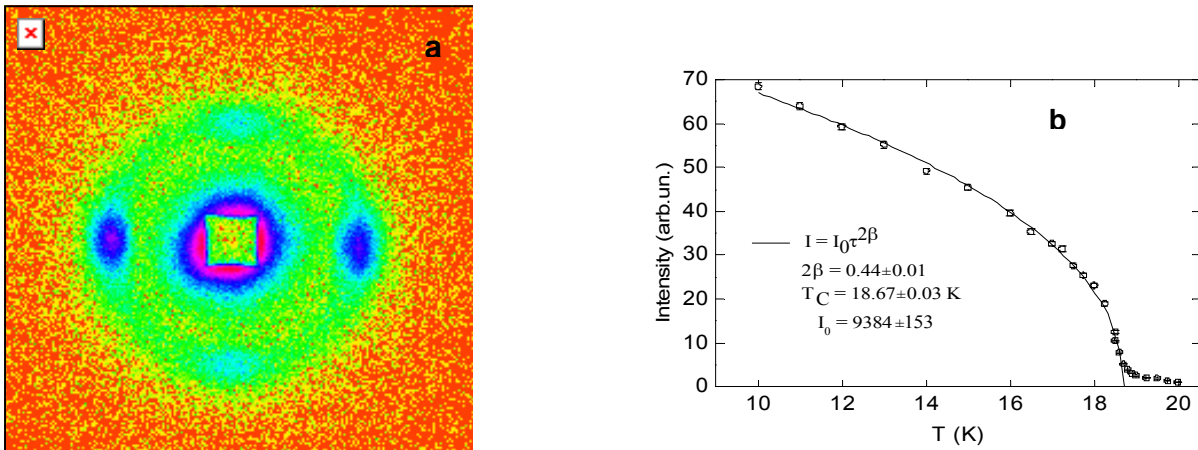


**Figure 1:** (a) The map SANS intensity at  $T = 10$  K, (b) Temperature dependence of intensity of the [100] peak.

The momentum transfer dependence of the scattering intensity at  $T = 19.0$  K (i.e. above  $T_C$ ) is presented in fig.2 a. It is well fitted by the Lorentzian with the center  $q_C = 0.172 \text{ nm}^{-1}$  and its width, or the inverse correlation length of the fluctuation  $\kappa = 0.072 \text{ nm}^{-1}$ . The temperature dependence of  $\kappa$  is presented in Fig. 2b. It is well described by the scaling law  $\kappa = \kappa_0 \tau^\nu$ , where  $\nu = 0.48 \pm 0.05$ . The resolution function with the width of  $0.03 \text{ nm}^{-1}$  has been taken into account for the latter approximation.

These results are in semi-quantitative agreement with the mean-field calculations based on the Bak-Jensen model that takes into account the hierarchy of the interactions: the exchange interaction  $B$ , the isotropic Dzyaloshinskii-Moriya (DM) interaction  $D = kB$  and the weak anisotropic exchange (AE) interaction  $F \sim k^2 B$ , where  $k$  is the helix wavevector and  $|k| \ll 1$ . The DM interaction is responsible for the scattering intensity concentrated in the ring. The AE interaction provides the anisotropy so that the correlation length diverges along  $\langle 100 \rangle$  only.



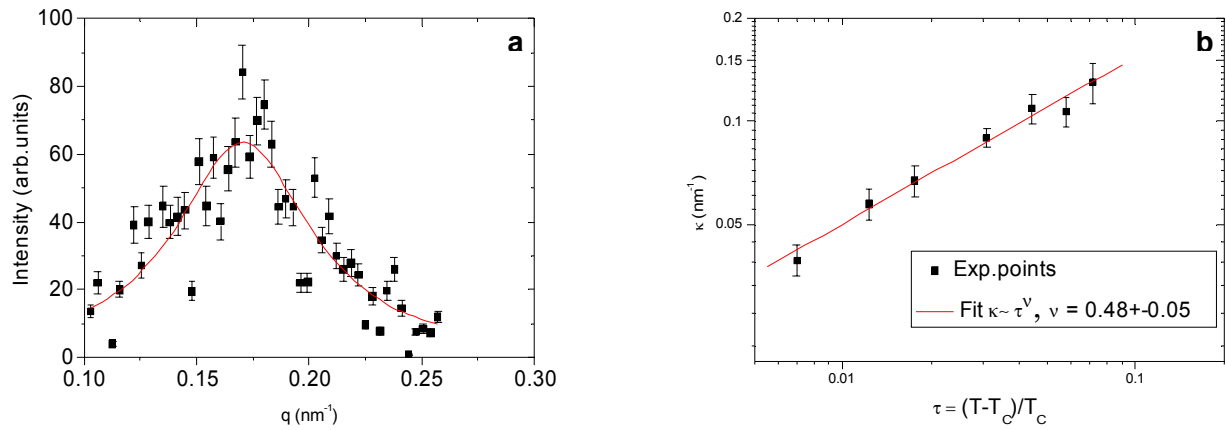



**Figure 2:** (a) The momentum transfer dependence of the scattering intensity at  $T = 19$  K. (b) The inversed correlation length as a function of the reduced temperature.

## References

- [1] P. Bak, M. H.Jensen, J.Phys.C13, L881 (1980)
- [2] S. V. Grigoriev, S. V. Maleyev, A. I. Okorokov, Yu. O. Chetverikov, R. Georgii, P. Boni, D. Lamago, H. Eckerlebe, K. Pranzas, Phys.Rev.B 72, 134420 (2005)
- [3] S. V. Grigoriev, S. V. Maleyev, V. A. Dyadkin, D. Menzel, J. Schoenes, H. Eckerlebe, Phys.Rev. B, Vol. 76, (2007) 092407
- [4] S. V. Grigoriev, V. A. Dyadkin, D.Menzel, J. Schoenes, Yu .O. Chetverikov, A. I. Okorokov, H. Eckerlebe, S.V. Maleyev, Phys.Rev. B, Vol.76, (2007) 224424



	<b>EXPERIMENTAL REPORT</b>	<b>GeNF SANS-2</b>
<b>The study of the static and dynamic spin chirality in the spin-glass system <math>Au_{1-x}Mn_x</math> by small angle scattering of polarized neutrons</b>		
<b>Proposer:</b> <b>Co-Proposers:</b>	<b>S. V. Grigoriev<sup>1</sup></b> , <sup>1</sup> PNPI, Gatchina, Russia <b>Vasily V. Piyadov<sup>1</sup>, Prof. T. Taniguchi<sup>2</sup></b> , <sup>2</sup> Osaka University, Japan	
<b>Experimental Team:</b> <b>User Group Leader:</b> <b>Instrument Responsible:</b>	<b>Sergey V. Grigoriev<sup>1</sup>, Vasily V. Piyadov<sup>1</sup>, Vadim A. Dyadkin<sup>1</sup>, Helmut Eckerlebe<sup>3</sup></b> , <sup>3</sup> GKSS Research Centre Geesthacht, Germany <b>Sergey V. Grigoriev<sup>1</sup></b> <b>Helmut Eckerlebe<sup>3</sup></b>	
<b>Date(s) of Experiment:</b>	December 2007	

### Objectives

Recently, Kawamura proposed the chiral mechanism for explanation of the spin-glass phase transition [1]. He suggested that it is not pair correlation of the Ising's spins that is the key object of such a transition, but the chiral three-spin fluctuation. Kawamura suggested that experimentally observed effects at such transitions in Heisenberg magnetics should be referred to a chiral rather than an ordinary spin glass. This approach requires reconsideration of the spin glass transition both from theoretical and experimental point of view.

It is also well known that the presence of the high-order correlations is generally strongly enhanced in the paramagnetic state close to the critical temperature. The even order correlations, involving four spins etc., change the critical exponent of the pair correlation function from the mean-field approximation 1/2 to that of the critical scaling 2/3. The odd-order correlation functions do not contribute to the static part of the magnetic susceptibility because this would contradict to the energy conservation law with respect to the time inversion. Nevertheless, the odd correlation functions may contribute to the dynamic part of the susceptibility. The lowest of them, triple vertex and the triple spin fluctuation associated with it, was introduced by Maleev [2]. As was shown later [3,4,5], the triple vertex ( $[\mathbf{S}_x \mathbf{S}_y] \mathbf{S}_z$ ) is a new entity, which is lacking in the static theory of the phase transitions. The triple dynamic spin fluctuations were detected for the first time by Okorokov [4] in the scattering of the polarized neutrons in iron. Recently it was realized that this triple vertex and its three-spin correlation function is a chiral object and is easily described in terms of chirality [5,6]. As was also shown in [5,6], both static and dynamic chirality may be detected using the Polarized Neutron Scattering with the help of the special inclined geometry of the applied magnetic field (H is inclined to the neutron wavevector k). In paramagnetic state (in the inclined geometry) neutron scattering associated with the three-spin fluctuations leads to the appearance of an asymmetric contribution to the polarization-dependent cross-section. The symmetric part of the magnetic scattering is connected to the pair correlation function. Thus, both correlation functions can be measured in the same experiment. Thus, the aim of the present experiment was to study spin excitations in the temperature range covering both Spin Glass state and paramagnetic states in one of the spin-glass systems.

### Experiment

The object for the study is the sample of  $Au_{1-x}Mn_x$  with  $x = 0.076$ , which is an example of the diluted spin glass system. The polarized SANS experiments were carried out at the SANS-2

setup at the Geesthacht Neutron Facility (GeNF). A polarized beam of neutrons with an initial polarization of  $P_0=0.95$ , the neutron wavelength  $\lambda=5.8$  Å ( $\Delta\lambda/\lambda=0.1$ ) and a divergence of 4 mrad was used. The scattered neutrons were detected by a 256x256 position sensitive detector. The detector-to-sample distance of 3045 mm was used with an appropriate collimation to cover an angular range up to 100 mrad. The sample under study has the spin-glass transition temperature  $T_{SG} = 22$  K. The scattering intensity was measured in the temperature range of 8 K – 40 K with accuracy better than 0.1 K. Following the standard procedure we determine the pure magnetic scattering by subtracting from the measured intensity the nonmagnetic background at  $T=100$  K:  $S_m(q) = S(q, T) - S(q, 100 \text{ K})$ .

## Achievements and Main Results

The temperature dependence of the integral scattering cross-section is given in Fig. 1. The cross-section increases with decreasing temperature and gets its saturation below the spin glass transition  $T_{SG}$ . The increase of the magnetic scattering shows appearance of the spin correlations in the corresponding temperature range. We evaluated the shape of these fluctuations at three different temperature regions: in the glassy state  $8 < T < 16$  K, in the transition state at  $20 < T < 26$  K, and in the paramagnetic state at  $30 < T < 40$  K. Figure 2 shows the dependences of the cross-section on the scattering vector  $q$ . It is seen that the correlations change their shapes with lowering temperature as it is expected. Further investigations of the behaviour of these fluctuations with polarized neutron technique are necessary in order to establish their chirality.

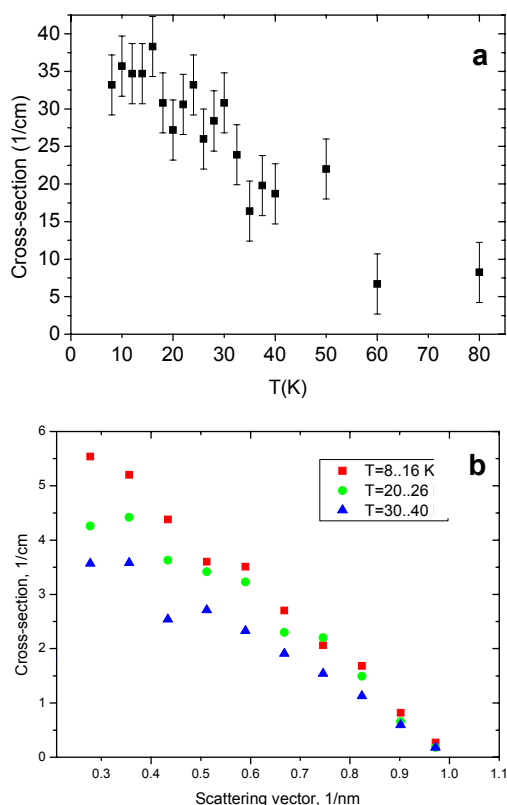


**Figure 1:**

**a:** The integral neutron cross-section as a function of temperature.

**b:** Momentum transfer dependence of the neutron cross-section in the three temperature ranges (below, within, and above TSG).

## References

- [1] H. Kawamura, M. Suan Li, Phys. Rev. Lett. 87 (2001), 187204 (1–4)
- [2] S. V. Maleyev, Sov. Phys. JETP 42 (1976), 713
- [3] A. V. Lazuta, S. V. Maleyev, B.P. Toperverg, Sov. Phys. JETP 48 (1978), 386
- [4] A. I. Okorokov, A. G. Gukasov, Ya. M. Otchik, V. V. Runov, Phys. Lett. A 65 (1978), 60
- [5] S. V. Maleyev, Phys. Rev. Lett. 75 (1995), 4682
- [6] S. V. Maleyev, Usp. Fiz. Nauk, 172 (2002), 617

Double crystal diffractometer DCD

**Short Instrument Description:**

The double crystal diffractometer for ultra small angle neutron scattering (USANS) uses non-polarised cold neutrons to characterise in materials large creep pores, fatigue and sintering cavities, precipitates, voids, bubbles, etc. with particle sizes in the range between 100 nm and 24  $\mu\text{m}$  in diameter.

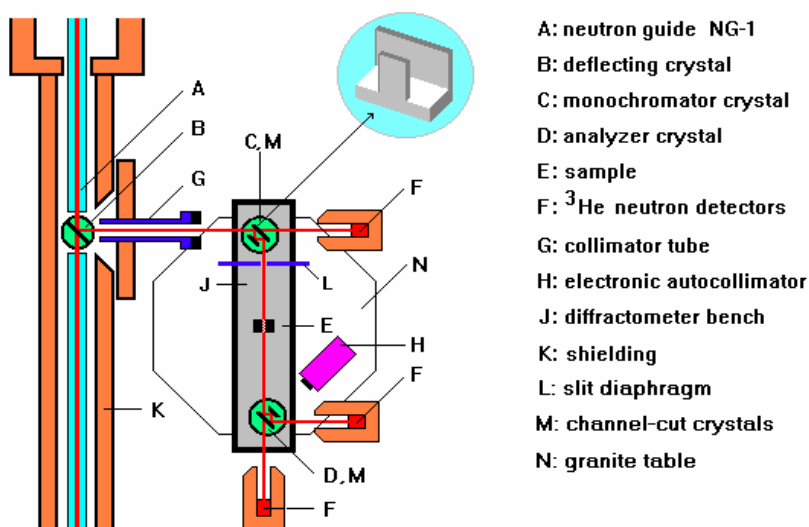
**Local Contact:**

**Dr. Melissa Sharp**

Phone/Fax : +49 (0)4152 87-1209 / +49 (0)4152 87-1338

e-mail: [melissa.sharp@gkss.de](mailto:melissa.sharp@gkss.de)


**Schematic View of DCD:**



**Instrument Details:**

Beamline:	beamline 8 – cold neutron guide NG-1, max. beam cross section 30 x 40 mm <sup>2</sup>
Deflecting crystal:	Si(111), mosaic spread 0.1 mrad
Monochromator / analyser:	channel-cut perfect Si crystals
Wavelength resolution	$\Delta\lambda/\lambda = 1 \cdot 10^{-5}$ ( $\lambda = 0.443$ nm)
Max. flux at deflecting crystal	$\Phi = 2.5 \times 10^8$ cm <sup>-2</sup> s <sup>-1</sup>
Flux at sample position:	$\Phi \approx 550$ cm <sup>-2</sup> s <sup>-1</sup> (Si(111), $\lambda = 0.443$ nm)
Range of momentum transfer:	$1 \cdot 10^{-4}$ nm <sup>-1</sup> $\leq Q \leq 5 \cdot 10^{-2}$ nm <sup>-1</sup>
Detectors:	three $^3\text{He}$ -detectors
Control of crystal alignment:	electronic autocollimator, angular resolution < 0.05 $\mu\text{rad}$
Sample environment:	thermostat (5 °C to +80 °C) electro magnet with field up to > 0.9 T automatic sample change



	<b>EXPERIMENTAL REPORT</b>	<b>GeNF DCD</b>
<b>Fractal Structure of Natural Aquatic Nanocolloids</b>		
<b>Proposer:</b>	<b>Stephen King<sup>1</sup></b> , <sup>1</sup> STFC, ISIS Facility, Rutherford Appleton Laboratory, Didcot OX11 0QX, United Kingdom	
<b>Co-Proposer(s):</b>	<b>Helen Jarvie<sup>2</sup></b> , <sup>2</sup> NERC, Centre for Ecology & Hydrology, Mclean Building, Wallingford OX10 8BB, United Kingdom	
<b>Experimental Team:</b>	<b>Stephen King<sup>1</sup>, Helen Jarvie<sup>2</sup>, Melissa Sharp<sup>3</sup></b>	
<b>Head of Institute:</b>	<b>Andrew Taylor<sup>1</sup></b> (STFC, ISIS), <b>Patricia Nuttall<sup>2</sup></b> (NERC, CEH)	
<b>Instrument Responsible:</b>	<b>Melissa Sharp<sup>3</sup></b> , <sup>3</sup> GKSS Research Centre Geesthacht, Germany	
<b>Date(s) of Experiment:</b>	11 <sup>th</sup> November – 4 <sup>th</sup> December 2007	

## Objective

Natural aquatic colloids (typically a complex mixture of inorganic and organic components, including oxides of aluminium, iron, manganese and silicon, carbonates, clays, organic humic substances, polysaccharides, bacteria and viruses) are of major environmental importance because they act as vectors for pollutant transport in rivers and through soils and groundwater, and play an important role in the biogeochemical ‘cycling’ of nutrients, trace metals and organic micro-pollutants. Indeed, pollutant association with colloids can significantly alter bioavailability, with important implications for aquatic ecology.

The proposers recently undertook a SANS study on a range of natural aquatic colloidal systems; indeed, the first-ever SANS study of its type. The results<sup>1</sup> showed that natural aquatic colloids are *mass fractal* systems with what appear to be three characteristic ranges of length scale: one ca. 3–10 nm which was attributed to ‘primary particle’ sizes, another ca. 20–50 nm suggestive of small aggregates, and the last ca. 50–200+ nm postulated to arise from transient networks of the aggregates.

One problem with those results was that the ‘cut-off lengths’ (typically >100 nm) obtained from the fractal models coincided with the limit of the Q-range accessible on conventional (pinhole) SANS instruments, but the power law behaviour of the scattering appeared to continue to much smaller Q values. It was this aspect of the scattering that the present DCD experiment sought to investigate with USANS.

## Experiment

DCD configuration:  $\lambda = 0.443$  nm, triple-bounce Si(111) @ 45°.

Samples were run at ambient temperature (20°C) and contained in 2 mm path length circular quartz cuvettes (Hellma™ type 120-QS/QX) mounted on a rotating multi-position sample changer (to offset the effects of sedimentation) supplied by the experimental team. Sample concentrations were approximately 9 wt.-% solids (equivalent volume fraction of about 3.2 %). The measurement time was approximately 48 hours per sample or background.

## Achievements and Main Results

Three different natural aquatic colloid samples, one dilution sample (Sample 4), two background samples, and a SANS intensity calibration sample were measured. The natural aquatic colloid samples included one treated with hydrogen peroxide to remove organic matter (Sample 2), and one at contrast match for the mineral component (Sample 3). Sample 1 was ‘as

collected' from the bed of a lowland UK river. The scattering measured is shown in Figure 1. Except for Sample 3, the samples were dispersed in river water.

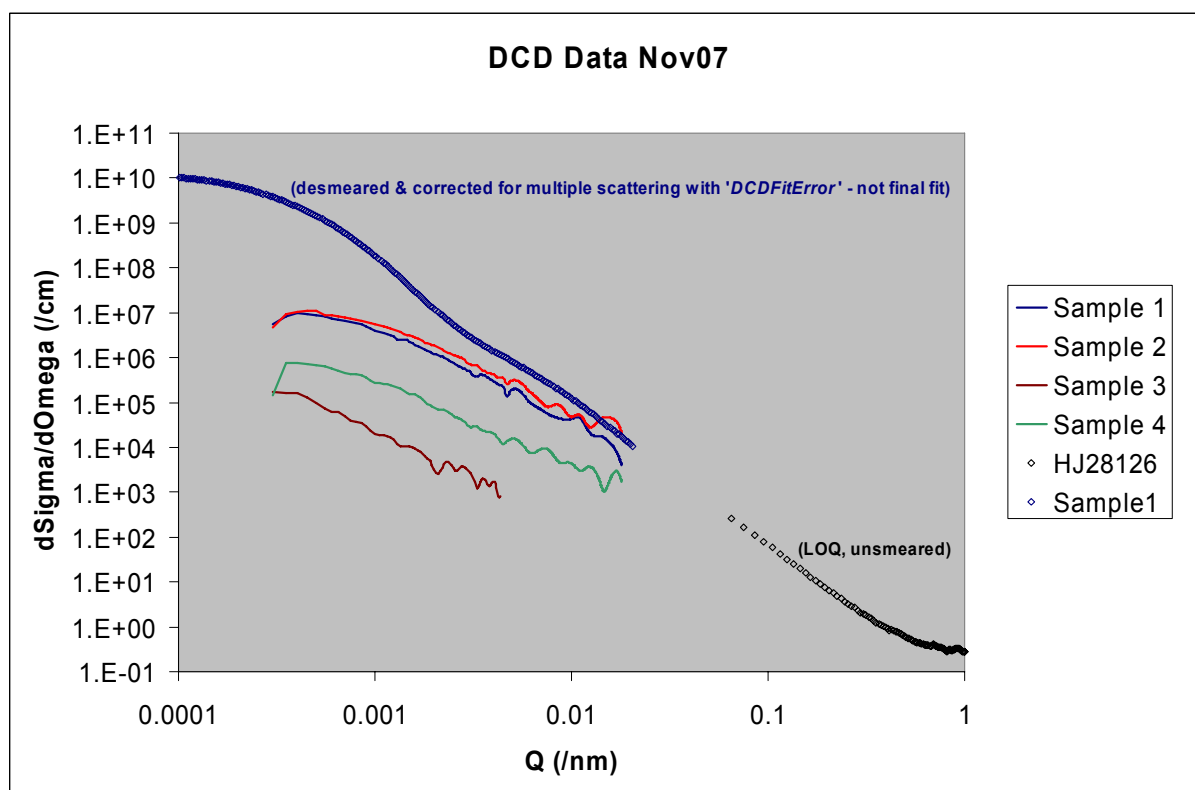


**Figure 1:** The reduced *but slit-smeared and multiply-scattered* USANS data (continuous lines) calculated from the raw detector counts with knowledge of the DCD instrument geometry and flight paths. The oscillations at intermediate  $Q$  values are artefacts of the data treatment. Also shown is an example of a desmeared, deconvoluted, data set made using the GeNF program 'DCDFitError', and representative SANS data from a similar sample measured on the LOQ instrument at ISIS. The USANS data shown are not yet on an absolute scale.

Data processing is still in progress at the time of writing. It is complicated by the degree of multiple scattering in some samples and also by their fractal nature (the GeNF analysis programs assume a particle size distribution). For this reason a dual approach is being adopted whereby the scattering is also being *calculated* from the raw detector data. When these data are desmeared they will provide a test of the output from the GeNF programs. The USANS data will then be combined with the existing SANS data for further analysis.

### Acknowledgements

Access to DCD for this work has been supported by the European Commission under the 6th Framework Programme through the Key Action: Strengthening the European Research Area, Research Infrastructures. Contract n°: RII3-CT-2003-505925. The experimental team would also like to thank Dr Sharp for her assistance with the experiment, and Drs Pranzas and Staron for helpful discussions during the course of the measurements.

### Reference

- [1] Jarvie HP, King SM, 2007 *Env. Sci. Tech.*, 41, 2868–2873  
<http://pubs.acs.org/cgi-bin/abstract.cgi/esthag/2007/41/i08/abs/es061912p.html>



**Reflectometer for polarised neutrons PNR**

**Short Instrument Description:**

The polarised neutron reflectometer is used to study magnetic and non-magnetic surfaces, layers, thin films and membranes using cold non-polarised or polarised neutrons with high flux.

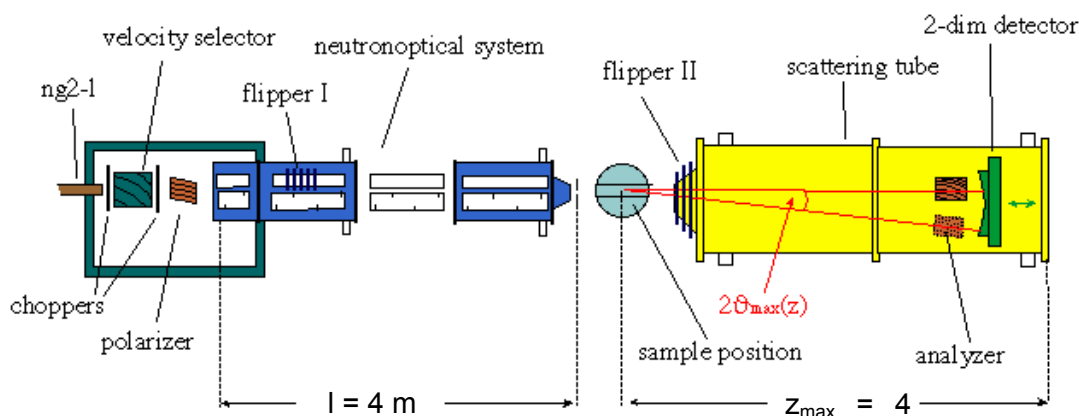
**Local Contact:**

**Dr. Danica Solina**

Phone/Fax : +49 (0)4152 87-1373 / +49 (0)4152 87-1338

e-mail: [danica.solina@gkss.de](mailto:danica.solina@gkss.de)

**Schematic View of PNR:**



**Instrument Details:**

Beamline:	beamline 8 (NG-2I), cross section 30 x 40 mm <sup>2</sup>
Monochromator:	helical slot selector
Wavelength:	$\lambda \geq 0.635$ nm
Wavelength resolution:	$\Delta\lambda/\lambda = 0.05$
TOF equipment:	2 choppers, to be used if a resolution better than 0.05 is required
Polariser:	transmission polariser
Analyser	set of bent supermirrors
Spin flipper:	hf-flipper
Collimation lengths:	4 m
Flux at sample position: (beamsize: 0.5 x 40 mm <sup>2</sup> )	$\Phi_{\text{nonpol}} = 1 \cdot 10^5 \text{ cm}^{-2} \text{ s}^{-1}$ (unpolarised) $\Phi_{\text{pol}} = 3 \cdot 10^4 \text{ cm}^{-2} \text{ s}^{-1}$ (polarised neutrons)
distance sample-detector:	3 m to 4 m
angular range:	$0^\circ \leq 2\theta \leq 8^\circ$
Detector:	2-dim position-sensitive <sup>3</sup> He-counter
Ancillary equipment:	– refrigerator cryostats – temp.-range: 4 – 475 K – electro magnet up to 0.9 T with closed cycle refrigerator (8–300 K) suitable for polarised neutrons



**Dipole-Field-Induced Spin Disorder  
In Nanoporous Inert-Gas Condensed Materials**

<b>Proposer:</b>	<b>D. M. Solina<sup>1</sup></b> ; <sup>1</sup> GKSS Research Centre Geesthacht, Germany
<b>Co-Proposer(s):</b>	<b>R. Kaltofen<sup>2</sup>, U. Tietze<sup>1</sup></b> , <sup>2</sup> IFW, Technical University, Dresden
<b>Experimental Team:</b>	<b>U. Tietze<sup>1</sup>, D. M. Solina<sup>1</sup></b>
<b>User Group Leader:</b>	<b>A. Schreyer<sup>1</sup></b>
<b>Instrument Responsible:</b>	<b>D. M. Solina<sup>1</sup></b>
<b>Date(s) of Experiment:</b>	17 <sup>th</sup> –19 <sup>th</sup> December 2007

### Objective

The phenomena of exchange bias (EB), observed as a shift in the ferromagnetic hysteresis loop owing to pinning of the ferromagnetic layer at a ferromagnetic/ anti-ferromagnetic (FM/AFM) interface is used extensively in the fabrication of magnetic recording media devices. Although EB is used, the exact nature of the coupling is poorly understood, in particular the role of the AFM layer, thus hindering the optimisation of the performance of these devices.

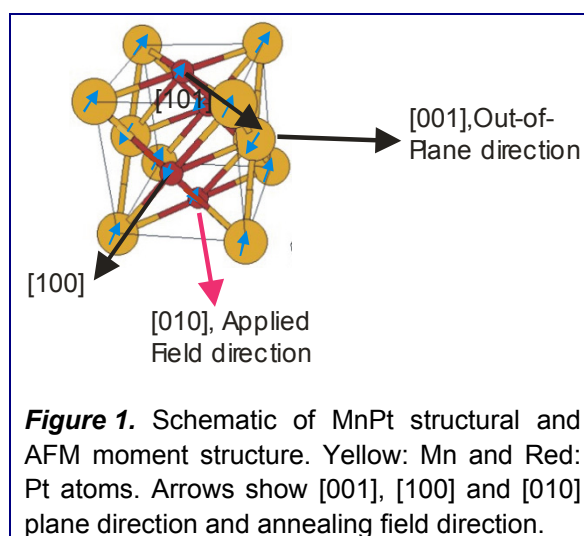
Neutron diffraction has been used to investigate the antiferromagnetic layer of a CoFe/PtMn exchange biased system and has shown that a domain wall forms in the antiferromagnetic PtMn. In addition to knowledge of the magnetic structure of the antiferromagnet it is necessary to couple this behaviour to that of the ferromagnet. Previous PNR experiments (June 2007) on a sample showed that the exchange bias had degraded with time. In this work, preliminary Polarized Neutron Reflection (PNR) measurements have been carried out on new samples (see Figure 2 for Magneto-Optical Kerr Effect) in order to study the ferromagnetic structure with applied field. This is an extension of work began in 2006.

### Sample

The layer system:

CoFe(10 nm)/MnPt(100 nm)/MgO(100) was fabricated using sputter deposition and annealed in field. MnPt is an ordered AFM that requires annealing to transform from the non-magnetic face-centred-cubic phase to the AFM face-centred tetragonal phase shown in figure 1.

Hysteresis loops show EB occurs in the annealed direction only (figure 2).



### Experiment, Achievements and Main Results

Polarized Neutron Reflectivity (PNR) measurements were carried out at remnant fields to determine whether a clear distinction is observable between Non-Spin-Flip and Spin-Flip intensities in preparation for measurements to be carried out in the new year. The Non-Spin-Flip

(++, --) and the Spin-Flip (+,-,-) intensities are due to scattering on collinear and perpendicular orientated magnetic moments in respect to the applied magnetic field, respectively. If the reversal of the magnetization in the FM occurs due to coherent rotation a significant contribution appears in the Spin Flip channel due to the presence of magnetic moments perpendicular to the applied magnetic field. In the case of domain formation the orientation of the moment remains collinear to the magnetic field and no Spin Flip intensity is observed.

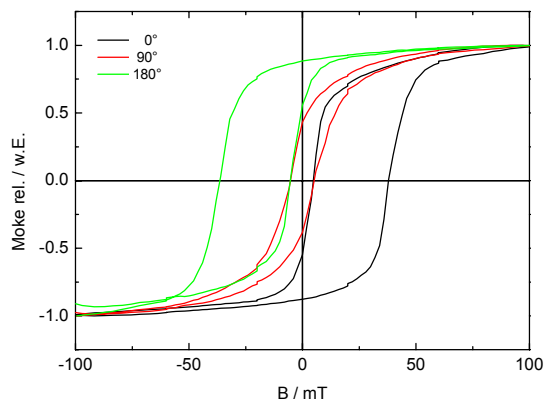


**Figure 2:**

MOKE scans for sample annealed at 375 °C for 1 h along 0°, clearly showing exchange bias at 0° and 180° and no bias 90° to the annealing direction.

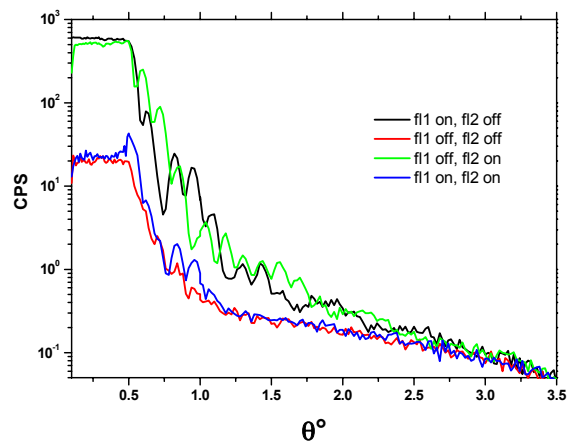


**Figure 3:**

PNR reflectivity at remanant field and saturation.

The PNR spectra illustrated in figure 3 show a clear distinction between spin flip and non spin flip components for the magnetic reflection.

**Investigation of exchange bias between MnPt and CoFe layers**

<b>Proposer:</b>	<b>D. M. Solina<sup>1</sup></b> , <sup>1</sup> GKSS Research Centre Geesthacht, Germany
<b>Co-Proposer(s):</b>	<b>C.-H. Lai<sup>2</sup></b> , <sup>2</sup> Dept. Phys., Univ. Tsing-Hua, Taiwan
<b>Experimental Team:</b>	<b>D. Lott<sup>1</sup>, D. M. Solina<sup>1</sup></b>
<b>User Group Leader:</b>	<b>A. Schreyer<sup>1</sup></b>
<b>Instrument Responsible:</b>	<b>D. M. Solina<sup>1</sup>, D. Lott<sup>1</sup></b>
<b>Date(s) of Experiment:</b>	21 <sup>st</sup> June – 2 <sup>nd</sup> .July, 2007

**Objectives**

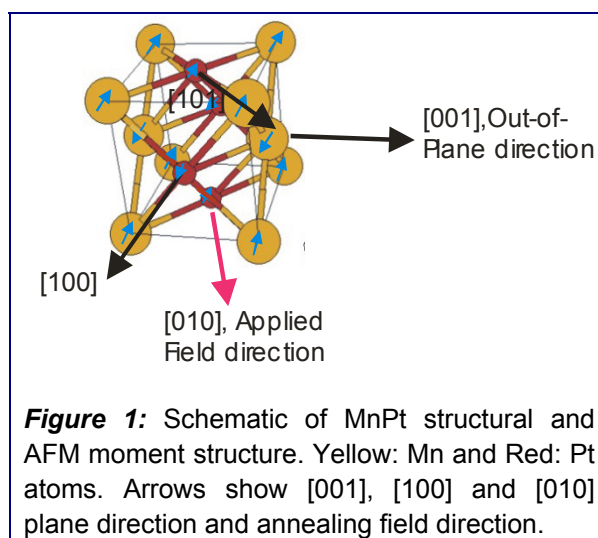
The phenomena of exchange bias (EB), observed as a shift in the ferromagnetic hysteresis loop owing to pinning of the ferromagnetic layer at a ferromagnetic/ anti-ferromagnetic (FM/AFM) interface is used extensively in the fabrication of magnetic recording media devices. Although EB is used, the exact nature of the coupling is poorly understood, in particular the role of the AFM layer, thus hindering the optimisation of the performance of these devices.

Neutron diffraction has been used to investigate the antiferromagnetic layer of a CoFe/PtMn exchange biased system and has shown that a domain wall forms in the antiferromagnetic PtMn. In addition to knowledge of the magnetic structure of the antiferromagnet it is necessary to couple this behaviour to that of the ferromagnet. In this work, Polarized Neutron Reflection (PNR) measurements have been carried out on NeRo in order to study the ferromagnetic structure with applied field. This is an extension of work begun in 2006.

**Experiment**

The layer system :

CoFe(10 nm)/MnPt(100 nm)/MgO(100) was fabricated using sputter deposition and annealed in field. MnPt is an ordered AFM that requires annealing to transform from the non-magnetic face-centred-cubic phase to the AFM face-centred tetragonal phase shown in figure 1.



**Achievements and Main Results**

Polarized Neutron Reflectivity (PNR) measurements were carried out at remnant fields and at saturation at both sides of the hystereses loop. The Non-Spin-Flip (++, --) and the Spin-Flip (+,-,+ ) intensities are due to scattering on collinear and perpendicular orientated magnetic moments in respect to the applied magnetic field, respectively. If the reversal of the magnetization in the FM occurs due to coherent rotation a significant contribution appears in

the Spin Flip channel due to the presence of magnetic moments perpendicular to the applied magnetic field. In the case of domain formation the orientation of the moment remains collinear to the magnetic field and no Spin Flip intensity is observed.

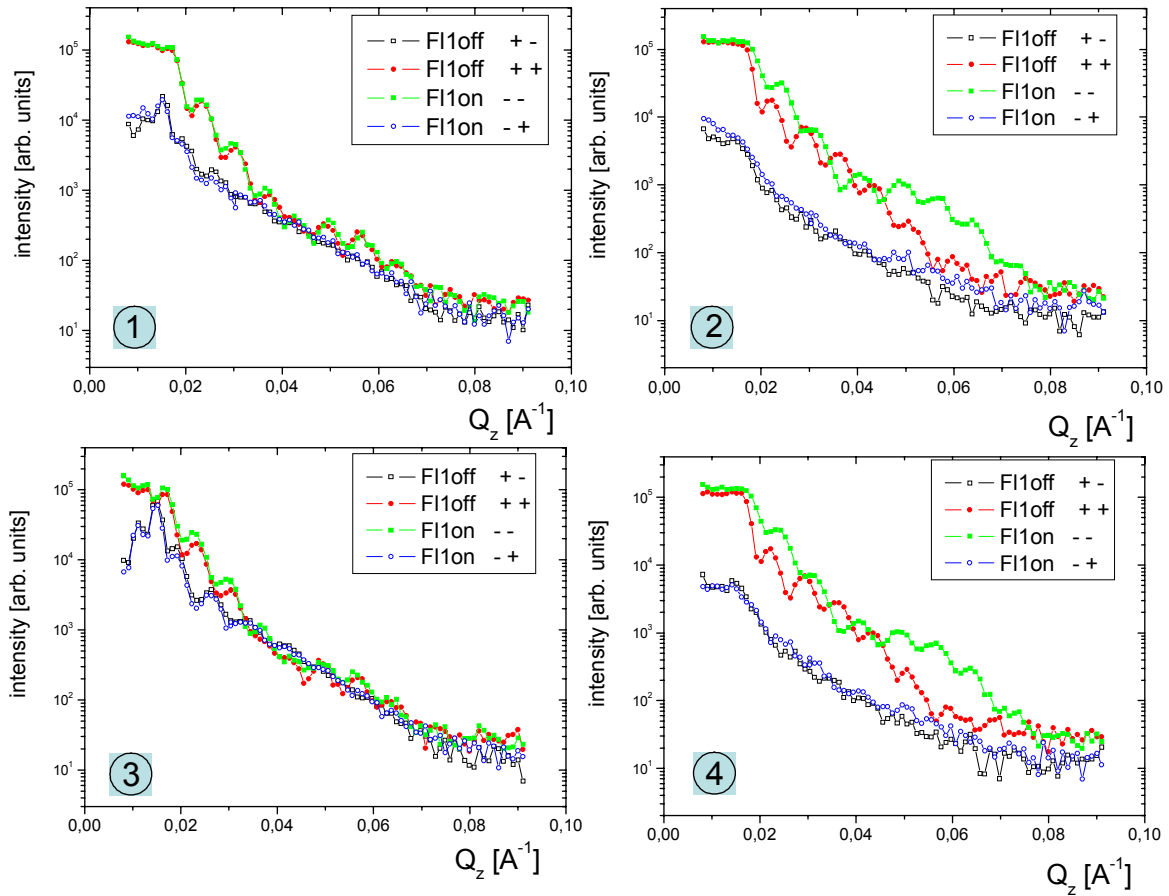


**Figure 2:** PNR reflectivity at remanent field and saturation. Scan No.1 and 2/3 and 4 are taken at negative/positive magnetic field directions at remanence and saturation, respectively.

The results in figure 2 show that the spin flip component is much stronger in one branch (3, 4) indicating coherent rotation. In the other branch (1, 2) non-spin flip is dominant suggesting switching is predominantly by domain formation. In order to obtain quantitative information, curves need to be simulated.

These results, combined with polarized neutron diffraction data obtained in Grenoble on the film will give a more complete picture of the mechanics of the ferromagnetic and antiferromagnetic layers in the process of exchange bias.

### Short Instrument Description

The Neutron Reflectometer NeRo is designed for measurements of thin film systems including polymer and magnetic systems using cold non-polarised / polarised neutrons with high resolution.

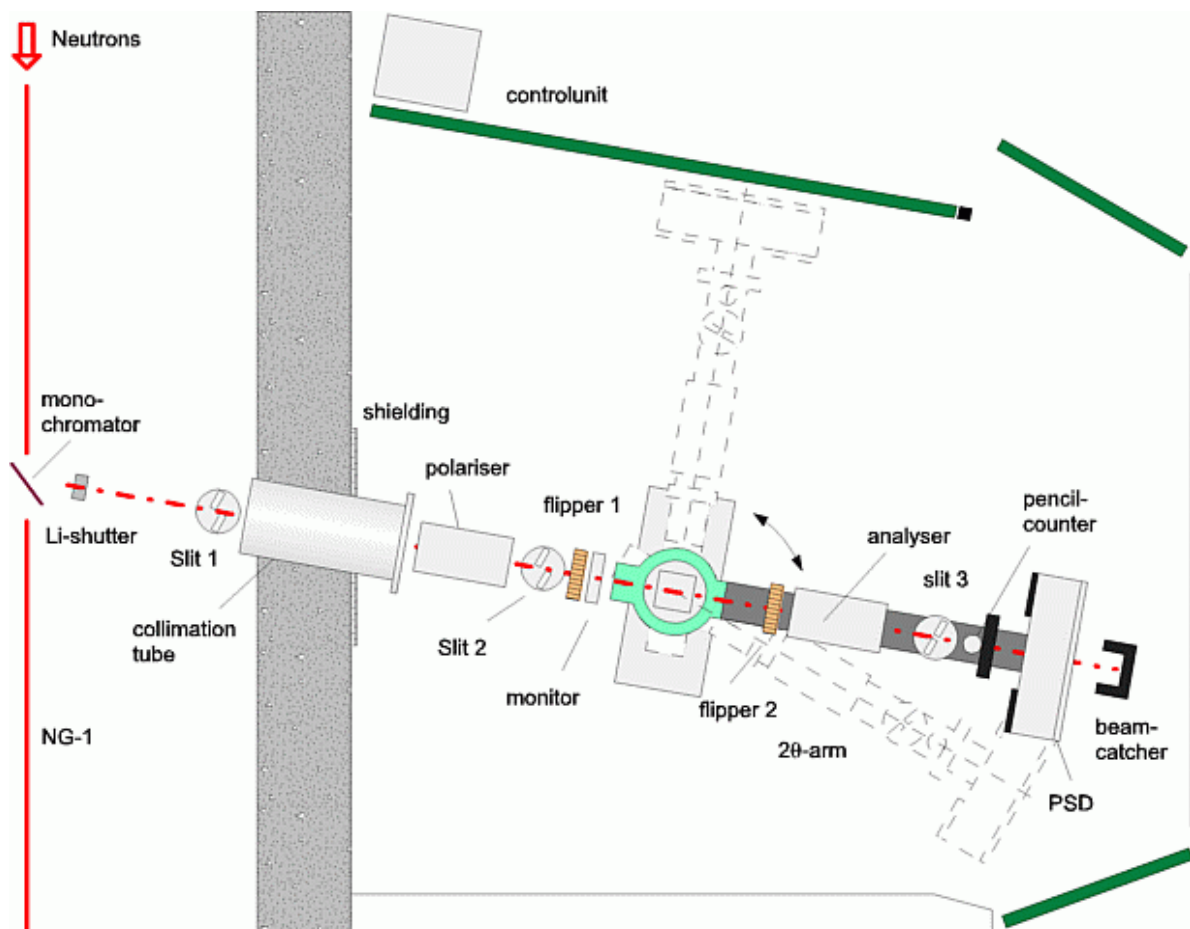
### Local Contact:

**Dr. Dieter Lott**

Phone/Fax : +49 (0)4152 87-1372 / +49 (0)4152 87-1338

e-mail: [dieter.lott@gkss.de](mailto:dieter.lott@gkss.de)


### Schematic View of NERO:



**Instrument Details:**

Beamline:	beamline 8 (NG-1)
Wavelength:	$\lambda = 0.433 \text{ nm}$ ;
Wavelength resolution	$\Delta\lambda/\lambda = 0.02$
Angular range	$-20^\circ \leq \theta \leq 100^\circ$
Flux at sample position:	$\Phi = 7 \cdot 10^4 \text{ cm}^{-2} \text{ s}^{-1}$ (unpolarised, standard collimation)
Detectors:	2-dim position-sensitive $^3\text{He}$ -counter $^3\text{He}$ pencil counter
Polarisation equipment:	Transmission polariser/analyser 2D-analyser: super-mirror stack for measurements of magnetic diffuse reflectivity 2 Mezei-flippers
Ancillary equipment:	Several refrigerator cryostats – temp.-range: 4 – 475 K electro magnet with field up to 0.9 T cryo-magnet with field up to 5 T



	<b>EXPERIMENTAL REPORT</b>	<b>GeNF NeRo</b>
<b>Morphology of Organic Thin Film Transistors with Polymer Brush Gate Dielectrics Synthesized by Atom Transfer Radical Polymerization</b>		
<b>Proposer:</b>  <b>Co-Proposer(s):</b>	<b>Ana Belén Rodríguez-Rodríguez<sup>1</sup>, Mark Geoghegan<sup>1</sup>, Anthony M. Higgins<sup>2</sup></b> <sup>1</sup> Department of Physics and Astronomy. University of Sheffield (UK) <sup>2</sup> School of Engineering. University of Swansea (UK)	
<b>Experimental Team:</b> <b>User Group Leader:</b> <b>Instrument Responsible:</b>	<b>Mark Geoghegan<sup>1</sup>, Ana Belén Rodríguez-Rodríguez<sup>1</sup></b> <b>Mark Geoghegan<sup>1</sup></b> <b>Dieter Lott<sup>3</sup>, <sup>3</sup>GKSS Research Centre Geesthacht, Germany</b>	
<b>Date(s) of Experiment:</b>	10 <sup>th</sup> – 17 <sup>th</sup> July 2007	

## Objective

Our objective was to use neutron reflectometry to study the interface between poly(methyl methacrylate) (PMMA) end-grafted to silicon substrates (brush layers) and the semiconducting polymer poly(3-hexylthiophene) (P3HT). In particular, we are interested in how heat treatment affects these interfaces as well as the performance of the corresponding field effect transistors (FETs). These two polymers form the gate dielectric and active layer respectively of the FET. The PMMA layer is a thick polymer brush, although it is a relatively thin polymer layer in terms of the most used organic dielectrics, and it is known that in its cross-linked form, the gate dielectric shows better device characteristics than the uncrosslinked polymer. These experiments are aimed at understanding the role of the interface on device performance. OFETs were fabricated at the Cavendish Laboratory (Cambridge) in collaboration with the group of Professor Henning Sirringhaus [1].

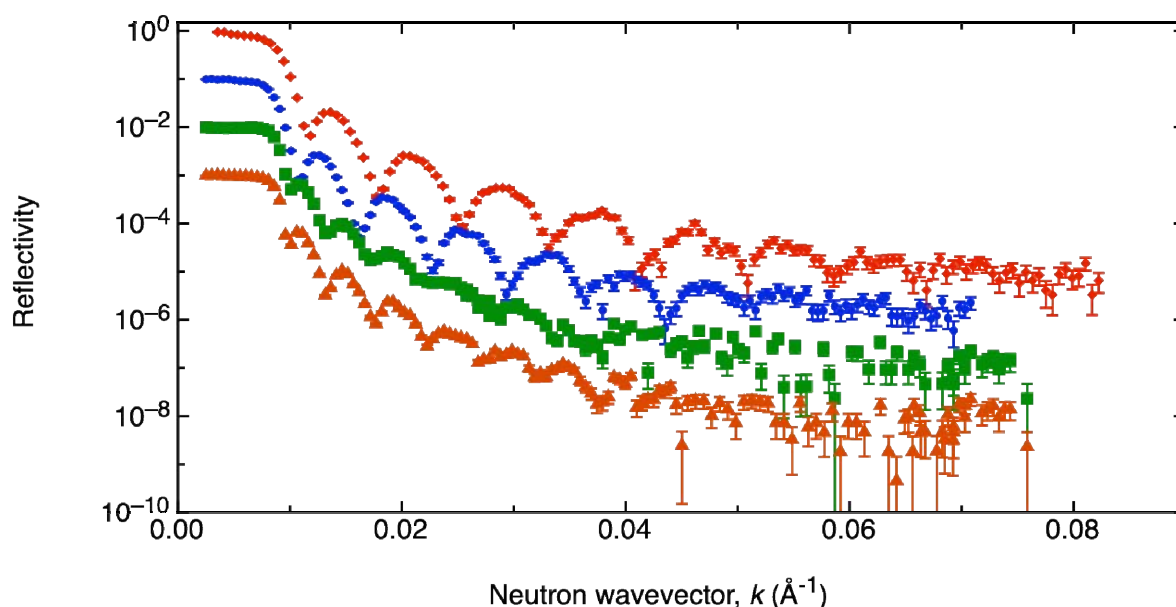
## Experiment

Together with the right choice of gate dielectric (GD) [2], the characteristics of a device greatly depend upon the properties of the interface between the electrodes and the organic semiconductor (surface roughness) and between the gate dielectric and the organic semiconductor itself (interfacial roughness) [3], [4]. Hence morphology is as important a parameter for optimum device performance as the choice of materials. In order to carry out this investigation we produced a series of bilayers consisting of a brush layer of partially deuterated PMMA (grown using atom transfer radical polymerization) grown PMMA brushes (partially deuterated), with a P3HT film on top (two different weights of P3HT were used for this experiment). P3HT was spin-casted from chloroform.

To investigate the effect of annealing procedures on the morphology of the samples, the samples underwent heat treatment for short and long periods at 78 °C and 100 °C respectively; only for short periods at 150 °C (well above the glass transition temperature ( $T_g$ ) of PMMA) and only for long periods at 40 °C. Another variable in our study is the interface roughness between the gate dielectric and the gate electrode, hence a series of samples in which brushes were grown from gold prior to their heat treatment was also produced.

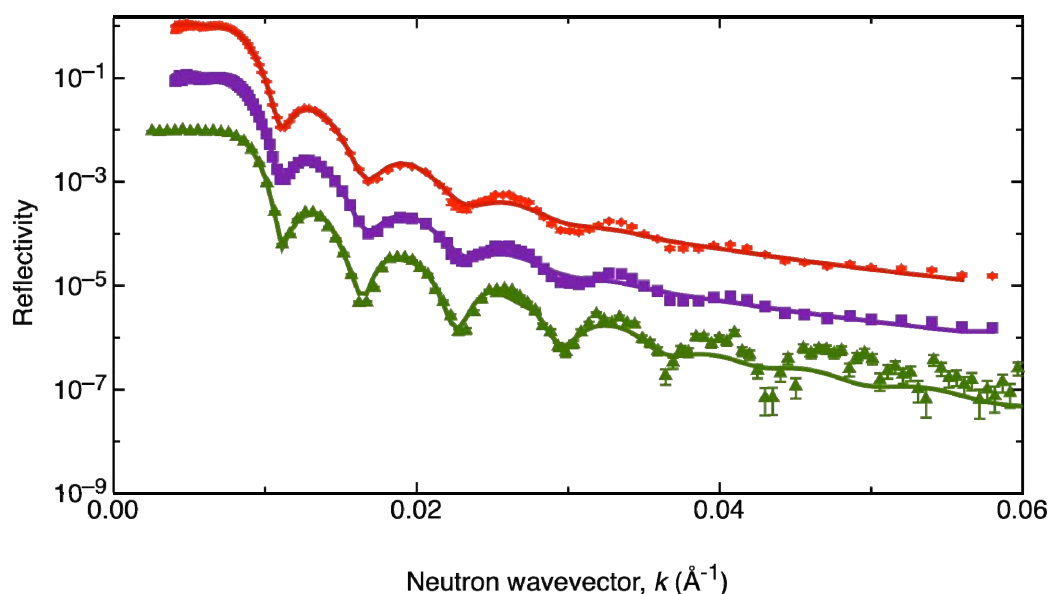
## Achievements and Main Results

Figure 1 shows some of the reflectivity data obtained at the NeRo reflectometer. The first set of curves (red and blue) prove the stability of the gate dielectric. P3HT films are known to crystallize at a very different range of temperatures, depending on factors such as molecular weight and annealing conditions. In many of those examples reported by the literature, the conductivity of the OFETs was improved by this crystallization. Annealing a sample at 100 °C (close to the  $T_g$  for PMMA) will indeed change the morphology of the bilayer without destroying it. This bilayer is stable during annealing for both the short and long periods. On the second set of curves (green and orange) the comparison between the reflectivity profiles of a sample before and after annealing are shown.



**Figure 1:** Neutron reflectivity data for silicon/partially deuterated PMMA brush/P3HT film bilayers. (red symbol=sample A after short time annealing at 100 °C; blue symbol= sample A after long time annealing at 100 °C; green symbol= sample B not annealed; orange symbol= sample B after short time annealing at 100 °C). All brushes were grown to show a similar thickness and all P3HT films were spin coated from chloroform. The curves have been offset from one another for clarity.

In figure 2 three reflectivity profiles and fits are shown. These fits were obtained using a downhill simplex fitting routine (*Mascara*, written by M Geoghegan) routine. The red curve corresponds to a sample before being annealed while the blue one is the reflectivity profile of the same sample after undergoing long time annealing. A small increase in both surface and interfacial roughness of the deuterated layer is observed after annealing. The third curve shown on figure 2 refers to a sample annealed at 40 °C for a long period. In this case, after annealing, the morphology can no longer be fitted using a bilayer morphology. (These latter data have been fitted using a trilayer model {with a surface roughness of 1 nm and interfacial roughness of 3.5 nm for the first interfacial roughness [between the top layer and the second layer] and 1.5 nm [between the second layer and the bottom layer]}, but a definitive morphology for this sample will require further fitting.)



**Figure 2:** Neutron reflectivity data and fits for silicon/partially deuterated PMMA brush/P3HT film bilayers. (red symbol= sample A not annealed<sup>1</sup>  $\sigma_{\text{surface}} = 2$  nm,  $\sigma_{\text{interface}} = 1.5$  nm, blue symbol= sample A after long time annealing at 100 °C  $\sigma_{\text{surface}} = 9$  nm,  $\sigma_{\text{interface}} = 5$  nm; green symbol= sample C after long time annealing at 40 °C). All brushes were grown to show a similar thickness and all P3HT films were spin coated from chloroform. The curves have been offset from one another for clarity.


The devices fabricated parallel to this experiment showed good electric characteristics on the process to be related to the morphology models extracted from the ongoing neutron reflectivity analysis done on these data. Although the fitting presented above is largely preliminary, the data that we obtained do seem to be of a good quality and will aid us in our investigation of FETs.

## References

- [1] J. C. Pinto et al., Organic Thin Film Transistors with Polymer Brush Gate Dielectrics Synthesized by Atom Transfer Radical Polymerization. *Advanced Functional Materials*, 2008 (doi 10.1002/adfm.200700540)
- [2] J. Veres, S. Ogier, and G. Lloyd, Gate insulators in Organic Field-Effect Transistors. *Chem. Mater.* 16 (2004), 4543–4555
- [3] L.-L. Chua, P. K.-H. Ho, H. Sirringhaus and R. H. Friend, Observation of Field-Effect Transistor Behaviour at Self-Organized Interfaces. *Adv. Mater.* 16 (2004), 1609–1615
- [4] A. M. Higgins, P. C. Jukes, S. J. Martin, M. Geoghegan, and R. A. L. Jones, A neutron reflectometry study of the interface between poly(9,9-dioctylfluorene) and poly(methyl methacrylate). *Appl. Phys. Lett.* 81 (2002), 4949–4951

<sup>1</sup> Sample measured at the Eros reflectometer (LLB (Saclay, France))



	<b>EXPERIMENTAL REPORT</b>	<b>GeNF NeRo</b>
<b>Magnetic field effect on the spin structure of Dy/Y multilayer system</b>		
<b>Proposer:</b> <b>Co-Proposer(s):</b>	<b>Yury Chetverikov<sup>1</sup></b> , <sup>1</sup> PNPI, Gatchina, St-Petersburg, Russia <b>Sergey Grigoriev<sup>1</sup></b>	
<b>Experimental Team:</b> <b>User Group Leader:</b> <b>Instrument Responsible:</b>	<b>Yury Chetverikov<sup>1</sup></b> <b>Dieter Lott<sup>2</sup></b> , <sup>2</sup> GKSS Research Centre Geesthacht, Germany <b>Sergey Grigoriev<sup>1</sup></b> <b>Dieter Lott<sup>2</sup></b>	
<b>Date(s) of Experiment:</b>	2 <sup>nd</sup> – 9 <sup>th</sup> July 2007	

## Objective

Our previous measurements with polarized neutrons on  $[\text{Dy}_{4.2 \text{ nm}}/\text{Y}_{2.8 \text{ nm}}]_{350}$  (denoted as Dy42) demonstrated that Dy/Y multilayer structures possess a coherent spin helix with a preferable chirality induced by the magnetic field. The average chirality, being proportional to the difference in the left- and right-handed helix population numbers, was measured as a polarization-dependent asymmetric part of the magnetic neutron scattering  $\gamma$ . It is introduced as a measure of the chirality  $\gamma = (I(+P) - I(-P)) / (I(+P) + I(-P))$ , where  $I(+P)$  and  $I(-P)$  are the scattering intensities with the polarization along  $I(+P)$  and opposite  $I(-P)$  the magnetic field. The magnetic field applied in the plane of the sample upon cooling below  $T_N$  is able to repopulate the otherwise equal population numbers for the left- and right-handed helices. The experimental results indicate strongly that the chirality is caused by Dzyaloshinskii-Moriya interaction due to the lack of the symmetry inversion on the interfaces.

## Experiment

At present the magnetic-field effect on the helix spin structure of another multilayer system  $\text{Y}_{50 \text{ nm}}[\text{Dy}_{3.0 \text{ nm}}/\text{Y}_{3.0 \text{ nm}}]_{150}/\text{Y}_{234 \text{ nm}}/\text{Nb}_{200 \text{ nm}}$  on a Sapphire substrate (denoted as Dy30) was investigated by means of small angle diffraction in a wide temperature range. The sample was grown along the  $c$ -axis of the hcp-structure of Dy and Y, in the same manner as in [1]. The anisotropy of the crystal fixes the direction of the magnetic spirals  $k$  along the  $c$  axis. The magnetic field  $H$  from 10 to 900 mT was applied, when necessary, perpendicularly to the incident beam and parallel to multilayer surface. The use of polarized neutrons allows one to compare magnetic and superstructure nuclear contributions to the scattering; to obtain information about spin orientation in the system, and to extract polarization-dependent chiral contribution to the scattering cross section.

## Achievements and Main Results

There are common features observed for both samples:

- I. The value and sign of the chirality depend on the strength the magnetic field which was applied in the sample's plane upon cooling and does not depend on the field direction i.e. the chirality is the same for both  $\pm H$ .
- II. The chirality, induced by the field of 0.9 T upon cooling to  $T \ll T_N$ , increases in the critical range upon warming up as shown in Fig.1. The temperature range, in which the chirality changes, is larger for the sample Dy30 (130–163 K) than for Dy42 (160–168 K).
- III. The sample, being cooled to a certain  $T$  in the field 0.9 T, gives value of the chirality different from that of the zero field cooled (ZFC) experiment ( see Fig. 1 open symbols).

On the other hand, there is a difference in the temperature-field behavior of these samples: sample Dy30 shows no chirality when it is cooled in zero field. Thus we conclude that these experiments revealed qualitatively the same effect of the magnetic field on the chirality implying that this phenomenon of the field-induced chirality is genetic for the multilayer structures of Dy and Y. The new experiments aim to study the H-T phase diagram of the sample Dy30, which is able to shed a new light to the origin of the chirality induced by the magnetic field. For this purpose the momentum transfer dependence of the scattering intensity was measured at  $T=130$  K and  $155$  K for different values of the magnetic field. The evolution of the neutron cross-section with the magnetic field is shown in Fig. 2. The peak SL (superlattice) is associated to the nuclear periodic superstructure, the peak M is the incommensurate magnetic reflex originating from the spin helix, and the other peaks (M125, M15, M2) are commensurate magnetic reflexes. The positions of peaks in dependence on the magnetic field strength are plotted in Fig. 3. The peaks evolve smoothly upon increasing of the magnetic field.

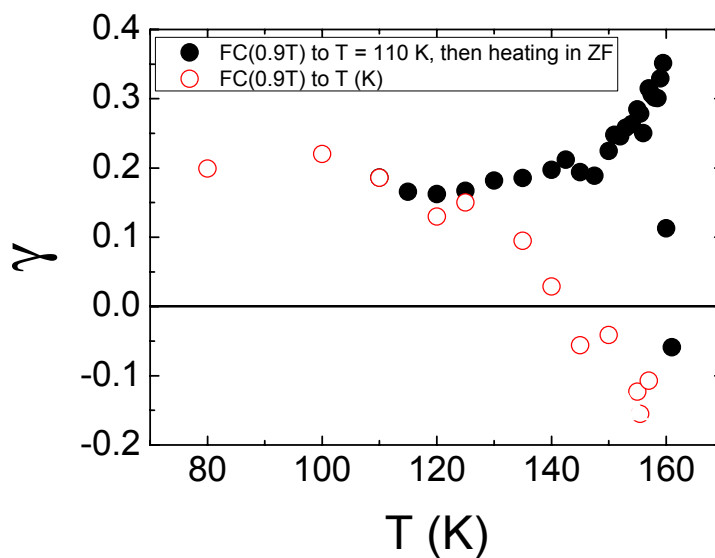


**Figure 1:** Temperature dependence of the chiral parameter  $\gamma$  for different temperature/magnetic-field prehistory of the sample (closed circles – ZF warming after FC at  $H = 0.9$  T to  $T = 110$  K; open circles – FC in  $H = 0.9$  T to the temperature of interest  $T$ ).

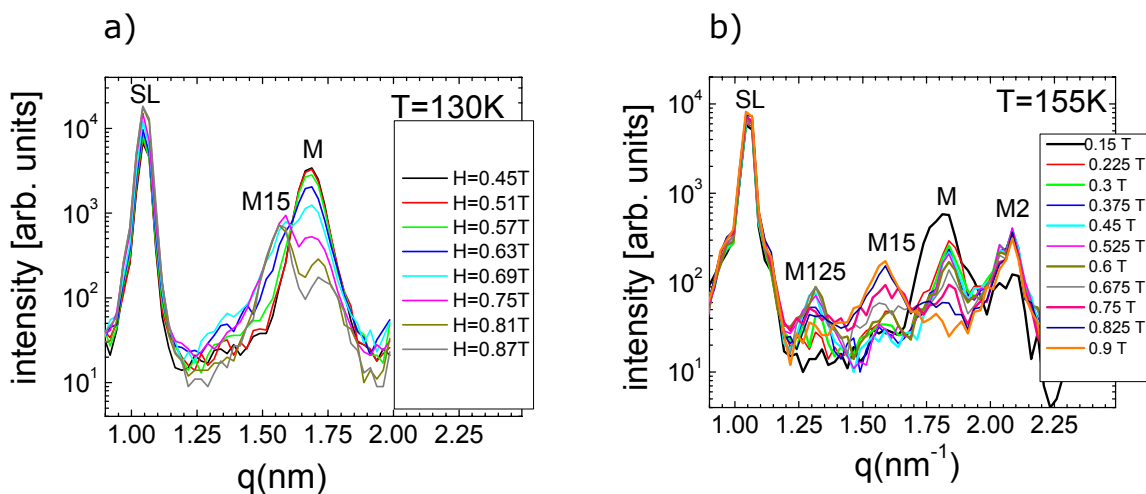


**Figure 2:** The  $q$ -dependences of the neutron scattering intensity at  $T = 130$  K (a) and  $T = 155$  K (b) measured under applied magnetic field.

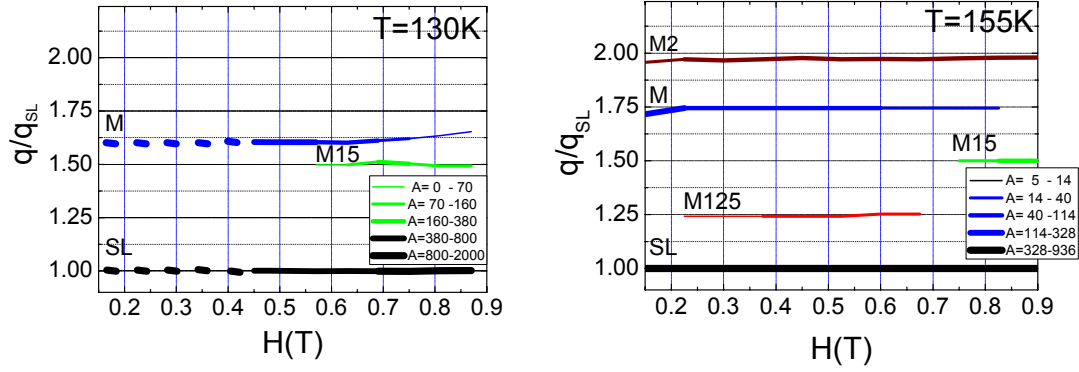


**Figure 3:** The magnetic field dependences of the Bragg peaks positions for temperatures  $T = 130$  K and  $T = 155$  K. The widths of lines are proportional to the logarithm of the peak intensity.

At  $T = 130$  K the intensity of the superstructure peak (SL) with  $q_{SL} = 1.05 \text{ nm}^{-1}$  arises while the intensity of magnetic spiral peak (M) with  $q_M = 1.611 \cdot q_{SL}$  decreases. It was interpreted as an increase of the ferromagnetic component in the layer and decrease of the spin of the helix. At the same time the M15 peak with  $q_{M15} = 1.5 \cdot q_{SL}$  appears at  $H = 0.57$  T close to peak M and it has a maximum around  $H = 0.8 - 0.9$  T. The position of peak M15 does not change while the position of the peak M changes from  $q_M(H = 0.45 \text{ T}) = 1.6 \cdot q_{SL}$  to  $q_M(H = 0.9 \text{ T}) = 1.65 \cdot q_{SL}$ . In our view it is related to the appearance of additional peaks at  $q_{M125}$  and  $q_{M175}$ , which are best visible at  $H \sim 0.6$  T and disappear at larger fields.

Close to  $T_N$ , at  $T = 155$  K, the evolution of the peaks upon increase of the field is more pronounced. Three peaks exist up to a field of 0.15 T: SL, M with  $q_M = 1.72 \cdot q_{SL}$  and M2 with  $q_{M2} = 1.95 \cdot q_{SL}$ . The intensity of the peaks SL and M2 increases with the increase of the magnetic field demonstrating the appearance of the ferromagnetic component of the spin structure inside the Dy layer. At a field of 0.23 T the intensity of the peak M decreases rapidly and two additional peaks arise at  $q_{M125} = 1.25 \cdot q_{SL}$  and  $q_{M175} = 1.75 \cdot q_{SL}$ . The intensities of these two peaks become maximal at  $H = 0.6$  T. Then they vanish again at  $H = 0.75$  T while the M15 peak with  $q_{M15} = 1.5 \cdot q_{SL}$  appears and approaches its maximum at the upper limit of the measured field at  $H = 0.9$  T.

It is obvious that the magnetic field implies a transition from the incommensurate to the commensurate spin structure for both  $T = 130$  K and 150 K. Close to  $T_N$  (155 K) these field-induced transitions are more pronounced as compared to  $T$  far away from  $T_N$  (130 K). This is correlated with the changes of the chirality close to  $T_N$  (Fig.1). Thus we observe in the Dy/Y multilayer structure two additional commensurate phases which appear with increasing magnetic field applied in the layer plane. First, the  $1/4$ -structure with the period of four Dy/Y bilayers arises in the intermediate field range and close to  $T_N$ . Second, the  $1/2$ -structure with the period of two Dy/Y bilayers appears at larger fields independent on the temperature range. The  $1/2$  structure is commonly observed in the multilayer systems under an applied magnetic field and is a result of the antiferromagnetic interlayer coupling. The  $1/4$  structure is clearly correlated with the field induced chirality shown in Fig.1 and in [2] since the appearance of this phase and the remarkable changes of the chirality occur within the same temperature and magnetic-field ranges. It should be also noticed that the interface affects strongly the spin structure of Dy layer since the effects are better pronounced for sample Dy30 than for sample Dy42. Furthermore, we speculate that the spin chirality is caused by Dzyaloshinskii-Moriya (DM) interaction which originates from the non inverse exchange coupling closed to the magnetic-nonmagnetic interfaces [3,4]. We suggest that the commensurate  $1/4$  structure, which arises under magnetic field, is chiral itself and induces chirality into the incommensurate structure when the field is switched off. Although the exact mechanism leading to these

phenomena is not clarified yet, we suggest that the field induced chirality of the Dy/Y multilayers can be interpreted as an effect of the DM interaction arising from the interfaces of the multilayer structure.

## References

- [1] Ross W. Erwin, J. J. Rhyne, M. B. Salamon, J. Borchers, S. Sinha, R. Du, J. E. Cunningham, C. P. Flynn, Phys.Rev.B 35 (1987), 6808
- [2] GeNF – Experimental Report 2006, GKSS Research Centre (2007), GKSS 2007/6, 151–153
- [3] M. Bode, M. Heide, K. von Bergmann, P. Ferriani, S. Heinze, G. Bihlmayer, A. Kubetzka, O. Pietzsch, S. Blugel, R. Wiesendanger, Nature 447 (2007) 05802
- [4] E. Y. Vedmedenko, L. Udvardi, P. Weinberger, and R. Wiesendanger; Phys. Rev 75 (2007) 104431



**Neutron reflectometry from the layer of  
Co/SiO<sub>2</sub> nanocomposites on the GaAs substrate**

<b>Proposer:</b>	<b>S. V. Grigoriev<sup>1</sup></b> , <sup>1</sup> PNPI, Gatchina, St-Petersburg, Russia
<b>Co-Proposer(s):</b>	<b>N. A. Grigoryeva<sup>2</sup></b> , <sup>2</sup> St-Petersburg State University, St-Petersburg, Russia <b>A. A. Vorobiev<sup>3</sup></b> , <sup>3</sup> ESRF, Grenoble, France
<b>Experimental Team:</b>	<b>A. A. Vorobiev<sup>3</sup></b> , <b>N. A. Grigoryeva<sup>2</sup></b> , <b>D. S. Lazarenko<sup>4</sup></b> , <b>Dieter Lott<sup>4</sup></b> , <sup>4</sup> GKSS Research Centre, Geesthacht, Germany
<b>User Group Leader:</b>	<b>Sergey V. Grigoriev<sup>1</sup></b>
<b>Instrument Responsible:</b>	<b>Dieter Lott<sup>4</sup></b>
<b>Date(s) of Experiment:</b>	4 <sup>th</sup> – 16 <sup>th</sup> December 2007

**Objective**

The granular films consisting of nanometer-sized magnetic metal particles embedded in an insulating matrix demonstrate interesting features in the spin transport phenomena and magnetoresistance [1]. At present we study the heterostructures GaAs/granular film SiO<sub>2</sub> containing x = 74 at.% of Co nanoparticles. These heterostructures show a positive injection magneto-resistance (IMR) to be equal to 5200 % in the in-plane-applied magnetic field of 2.3 T, and at the voltage 50 V, and at room temperature (Figure 1). For these structures electrons are injected from the granular film into GaAs substrate at positive voltages and the current density is high. When the applied voltage is negative, electrons drift from GaAs into the granular film and the current density is low. Such a transfer of spin-polarized electrons is intended for use in spintronic devices such as spin transistors, sensors and magnetic memory cells [2]. It is suggested that the magnetoresistance effect appears due to both the ferromagnetic layer in the granular film SiO<sub>2</sub> (Co) and the accumulation layer with polarized electrons formed in the semiconductor near the interface. Spins of Co nanoparticles in the ferromagnetic layer are polarized by the RKKY-like interaction through electrons of accumulation layer. According to our estimation the thickness h of the ferromagnetic layer in the granular film is 5–8 nm. The thickness d of the accumulation layer with polarized electrons is equal to 10–20 nm (synchrotron data) (Fig. 2).

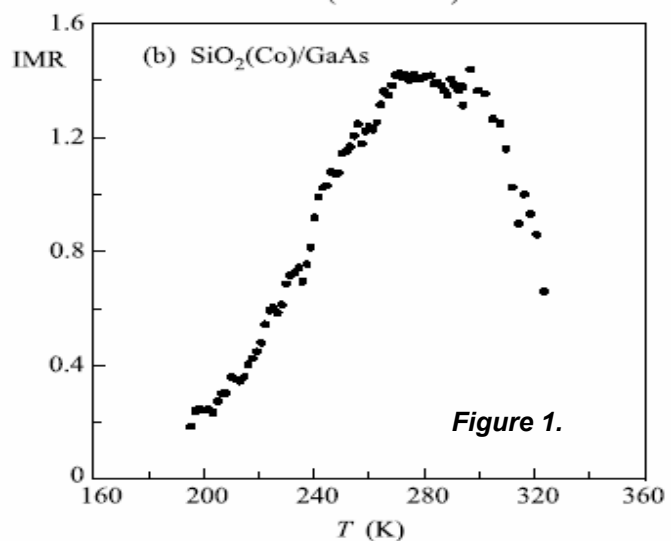
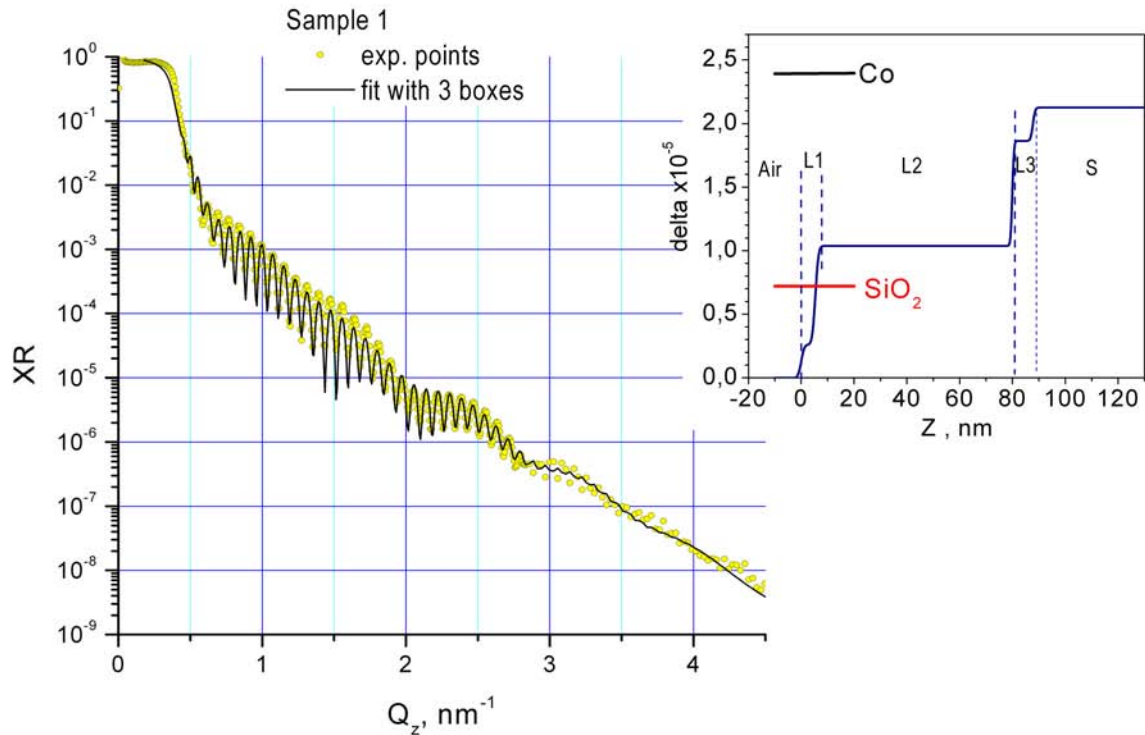


Figure 1.



**Figure 2:** Reflectivity profile of the synchrotron radiation from the heterostructure GaAs/granular film SiO<sub>2</sub> with Co nanoparticles and the three-layer model for description of the experimental data.

## Experiment

Composite heterostructure GaAs/granular film SiO<sub>2</sub> with Co nanoparticles was prepared by ion beam co-sputtering of composite quartz and cobalt targets. The average size of the ferromagnetic Co particles was determined from the small-angle X-ray scattering measurements: 3.5 nm. The thickness  $D$  of the granular film SiO<sub>2</sub> (Co) is equal to 40 nm and the thickness of the GaAs is 0.4 mm. The sample was covered by gold layers with a thickness 2.5 nm on the top and the bottom for measurement in the electric field.

The experiments were carried out at the NeRo reflectometer of FRG-1 research reactor in Geesthacht (Germany). A polarized beam of neutrons with an initial polarization of  $P_0 = 0.95$ , the neutron wavelength  $\lambda = 4.35 \text{ \AA}$  ( $\Delta\lambda/\lambda = 0.02$ ) was used. The scattered neutrons were detected by a position sensitive detector (PSD) with (256x256) pixels. The sample was set in a standard position to measure the reflectivity from the granular film of SiO<sub>2</sub> with Co on the GaAs substrate. The polarization followed the direction of the magnetic field (from 7 to 700 mT), which was applied perpendicularly to the incident beam and parallel to film surface. The reflected intensity was measured at the temperatures  $T = 150$ ,  $T = 300$  and  $T = 420$  K for two incident polarizations  $I^+(P_0)$  and  $I^-(P_0)$  along and opposite to the guiding magnetic field.

## Achievements and Main Results

Typical reflectivity profiles from the sample taken with the polarized neutrons at  $T = 150$  K are shown in Fig. 3 for the applied magnetic field  $H = 7$  and 700 mT. The data were taken in course of the remagnetization process i.e. after application of the opposite magnetic field of 900 mT. It is well seen that the granular film SiO<sub>2</sub> (Co) is magnetized for  $H=700$  mT what results in splitting of the profiles with polarization up (+) and polarization down (-). No splitting is observed for  $H=7$  mT i.e for the demagnetized film. Every experimental curve can be described with a model of two layers (L1 – gold and L2 – cobalt) and a substrate (sub – GaAs).

A strong deviation of the experimental data from the theoretical curves at low  $Q_z$  is connected with the small size of the sample with respect to the neutron beam. The results of the fit are following: the thickness of layer L1 is equal to 2.4 nm. The thickness of layer L2 is equal  $72 \pm 5$  nm, that is two times large than the thickness, which was calculated from ion beam co-sputtering method but it is in a good agreement with the synchrotron data (Fig. 2). The splitting of the reflectivity curve at  $H = 700$  mT occurs due to addition/subtraction of the magnetic scattering density  $N_m(L2)$  to/from the nuclear one  $N_n(L2)$ . The fit gives  $N_n(L2)$  value equal to  $2.56 \cdot 10^{-6} \text{ \AA}^{-2}$ , which matches together with expected value for the composite Co/SiO<sub>2</sub> in a ratio 0.75:0.25. The  $N_m(L2)$  value is equal to  $0.8 \cdot 10^{-6} \text{ \AA}^{-2}$  or magnetization  $M = 275 \text{ G} = 0.196 M_S$ . It is interesting to note that an additional magnetic contribution to the nuclear scattering density of the substrate is followed from the our fit. It is denoted as  $N_m(\text{sub})$  in Fig. 3. The appearance of this additional magnetization in the substrate near the interface can be related to the accumulation layer of polarized electrons observed in the synchrotron experiment ( Fig. 2).

**Figure 3:** The reflectivity profile of the polarized neutron beam from the heterostructure GaAs/granular film SiO<sub>2</sub> with Co nanoparticles at the magnetic field  $H = 7$  and  $700$  mT applied in the plane of the film. The inset shows a three-layer model for description of the experimental data.

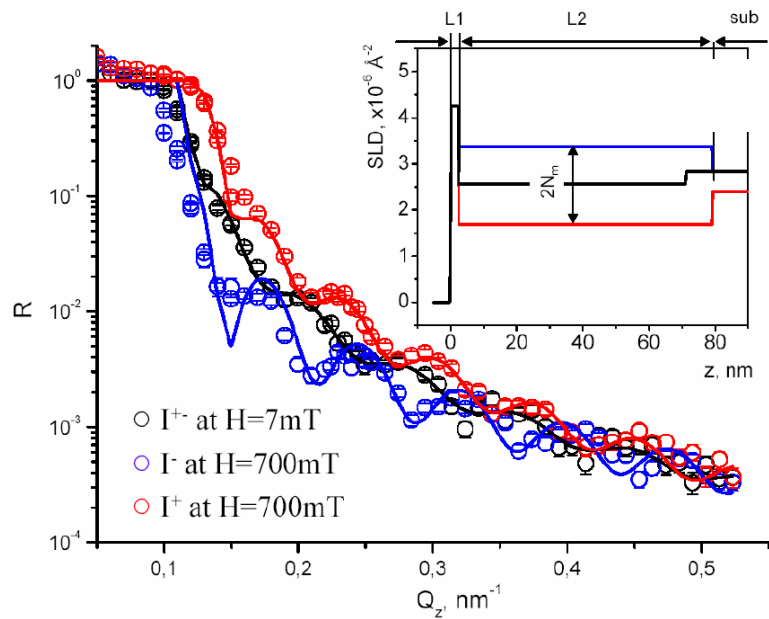
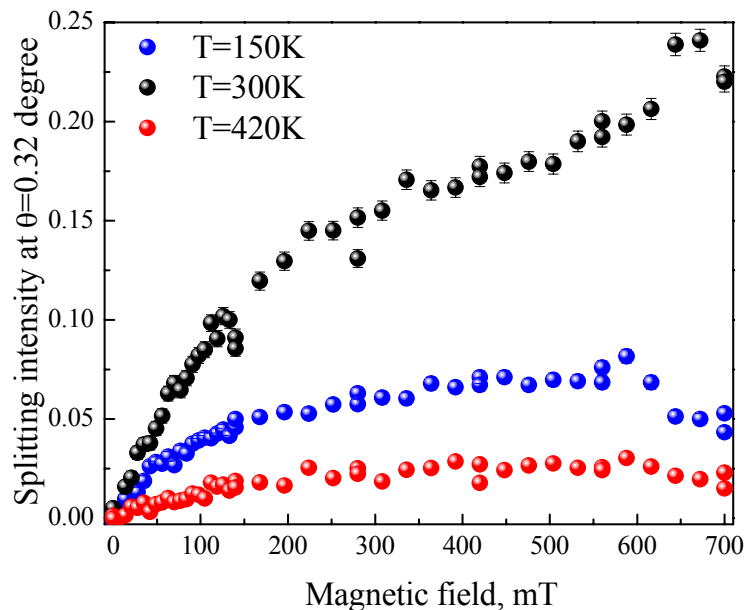


**Figure 4:** The magnetic field dependence of the difference between two intensities  $\Delta I = I^+(P_0) - I^-(P_0)$  taken at the angle  $2\theta = 0.32$  degree at three temperatures  $T = 150, 300$  and  $420$  K.




The difference (splitting) between two intensities with the incident polarization along  $I^+(P_0)$  and opposite  $I^-(-P_0)$  to the applied magnetic field was measured  $\Delta I = I^+(P_0) - I^-(-P_0)$  at the angle  $2\theta = 0.32$  degree as a function of the magnetic field at different temperatures of interest (Fig. 4). The temperature points  $T = 150$  K,  $300$  K and  $420$  K are positioned well below, exactly in the middle and well above the range, where the maximal IMR effect is observed (Fig. 1). The curves obtained characterize the magnetization of the magnetic layer of the sample. It is well seen that the saturation is reached at large fields for  $T = 150$  K and for  $T = 420$  K. On the contrary, the curve at  $T = 300$  K does not reach its saturation level up to  $H = 700$  mT. This can be connected to the different states of the magnetic layer at these three temperatures. The system at  $T = 150$  K is ferromagnetically ordered since the ferromagnetic Co particles are well correlated through the exchange. At  $T = 420$  K these particles are completely disconnected due to high temperature and the system become superparamagnetic. In the intermediated temperature at  $T = 300$  K there is a weak interconnection between the particles and the percolative scenario is realized.

Finally, we would like to thank our local contact Dr. Dieter Lott for his excellent support.

## References

- [1] K. Yakushiji, S. Mitani, K. Takanashi, J.-G. Ha, H. Fujimori, *J.Magn.Magn.Mater.* 212 (2000) 75
- [2] S. A. Wolf, D. D. Awschalom, R. A. Buhrman, J. M. Daughton, S. von Molnar, M. L. Roukes, A. Y. Chtchelkanova and D.M. Treger, *Science* 294 (2001) 1488

	<b>EXPERIMENTAL REPORT</b>	<b>GeNF NeRo</b>
<b>Neutron reflectivity studies of phospholipid layers on a thin titanium-alloy film on Si(100) substrate</b>		
<b>Proposer:</b> <b>Co-Proposer(s):</b>	<b>F. Feyerabend<sup>1</sup>, M. Störmer<sup>1</sup></b> <sup>1</sup> GKSS Research Centre Geesthacht, Germany	
<b>Experimental Team:</b> <b>User Group Leader:</b> <b>Instrument Responsible:</b>	<b>Dieter Lott<sup>1</sup></b> <b>Andreas Schreyer<sup>1</sup></b> <b>Dieter Lott<sup>1</sup></b>	
<b>Date(s) of Experiment:</b>	15 <sup>th</sup> – 22 <sup>nd</sup> August 2007	

## Objectives

Phospholipids (PL) are major constituents of cell membranes and play a crucial role in cellular processes such as signal transduction, calcification and apoptosis [1]. A potential application of phospholipids is their use as biomimetic implant coatings. Such coatings have been shown to improve cell differentiation [2]. In addition to the direct interactions between cells and coatings, another possible effect of the coatings is to modify the interactions of proteins with the implant surface. However, the characterization of such phospholipid layers is difficult because of the small dimensions: a phospholipid bilayer has a thickness about 4 nm in the dry state. Therefore, neutron reflectivity seems to be an appropriate measurement method.

## Experiment

Titanium alloy (Ti6Al7Nb) was deposited on the silicon substrates by sputter deposition with a layer thickness around 100 nm.

Phospholipid coating was done with the phospholipid 1-palmitoyl-2-oleoyl-sn-glycero-3-phospho-ethanolamine (POPE). POPE was solved in chloroform:methanol (80:20) and applied to the substrate. Afterwards the solvent was evaporated for 2 hours. The lipid layers were measured in this stage by unpolarized neutron reflectometry at NeRo.

Afterwards the samples were incubated in distilled water for 2 hours at 37° C under shaking conditions. After drying they were measured again

## Achievements and Main Results

Figure 1 shows the reflectivity curves taken at the different stages of the preparation of the sample. After applying the POPE solvent on the TiAlNb film, a strong peak appears at around  $Q_z = 0.113 \text{ \AA}^{-1}$  which is due to the repeat distance of the lipid chains with a value of about 5.6 nm. The strong intensity and small width of the peak indicates that the POPE film consist of many bilayers of lipids (multilayers) which even allows one to detect the second order at around  $0.225 \text{ \AA}^{-1}$ . After the incubation as described above the intensity of the first peaks reduces drastically while the second order could not be observed any more. By comparing the reflectivity curves for the initial pure TiAlNb film and the one after incubation one can clearly identify some broad additional intensity bump around the nominal  $Q_z$ -position of the multilayer peak of the lipid chains. This a clear indication that a small number of POPE layers is still present on the TiAlNb film after incubation. Further analysis of the neutron data to extract the exact number of remaining bilayers is on the way.


In the next steps, the the preparation technique will be optimized by further neutron reflectometry studies to examine the time dependence of the incubation process.

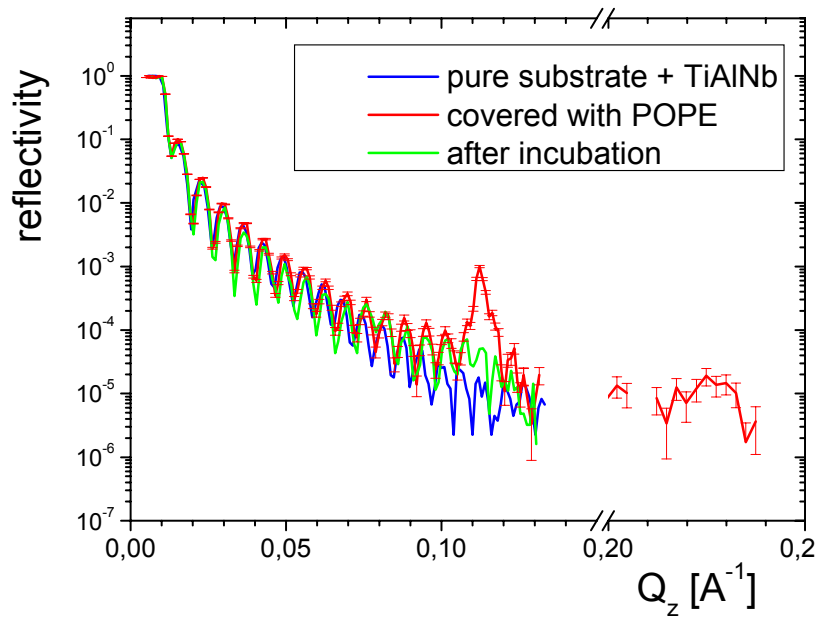


**Figure 1:**  
Unpolarized neutron reflectometry on the sample in different stages as indicated the legend.

## References

- [1] Bevers EM et al. Biol Chem 1998, 379, 973
- [2] Willumeit R et al. Eur Cell Mater 2007, 13, 11

	<b>EXPERIMENTAL REPORT</b>	<b>GeNF NeRo</b>
<b>Diffuse neutron scattering analysis on a nanostructured Ni dot array</b>		
<b>Proposer:</b> <b>Co-Proposer(s):</b>	<b>Wolfgang Kreuzpaintner<sup>1</sup>, Dieter Lott<sup>1</sup></b> <sup>1</sup> GKSS Research Centre	
<b>Experimental Team:</b> <b>User Group Leader:</b> <b>Instrument Responsible:</b>	<b>Wolfgang Kreuzpaintner<sup>1</sup>, Dieter Lott<sup>1</sup></b> <b>Andreas Schreyer<sup>1</sup></b> <b>Dieter Lott<sup>1</sup></b>	
<b>Date(s) of Experiment:</b>	24 <sup>th</sup> – 26 <sup>th</sup> August & 2 <sup>nd</sup> October 2007	

## Objectives

Preparation and characterization of laterally structured samples is of great importance for the understanding of inelastic neutron scattering of standing spinwaves in magnetic nanostructures.

Here we report on a diffuse neutron scattering investigation which – complementary to the results gained by x-ray methods – addresses the lateral structure of a laterally structured Ni sample as a preparatory experiment for magnetic and inelastic analysis.

## Experiment

For the experiment an 1" in diameter large and (by other methods) already pre-characterized thin polycrystalline, laterally structured Ni dot array sample was used. The total Ni structure has a thickness of approx. 12–13 nm and a lateral dot diameter of approx. 200 nm at a spacing of 730 nm arranged in a four fold symmetry. An SEM image is shown as an inset in figure 2.

Measurements were performed at room temperature for the as-prepared Ni sample without any applied external field at a neutron wavelength of 4.34 Å. The intensities were mapped by means of detector scans in up to  $2\theta = 11.78^\circ$  which corresponded to Q values of  $Q_z^{\max} = 0.10 \text{ \AA}^{-1}$  and  $Q_x = -3.7E-3 \text{ \AA}^{-1}$  to  $Q_x = +1.8E-3 \text{ \AA}^{-1}$ , respectively. In order to investigate the influence of the arrangement of the Ni dots in respect to the incident beam onto the diffusely scattered intensities, reciprocal space maps were taken for sample rotations with  $\Delta\phi = 3^\circ$  around the position at which the dot array is aligned with the incident beam .

## Achievements and Main Results

The collected data is presented in figure 1 for various rotation states. The corresponding reciprocal space maps calculated from the experimental results are shown in figure 2.

The vertical intensities on the right side of each raw data image correspond to the position of the primary beam. The diagonal intensity distribution give the specular reflectivity and the parabolic intensities are due to diffuse scattering on the lateral sample structure. The bisector of the specular beam and primary beam, an intensity minimum can be observed which is due to the sample horizon. Thus the signals on the right side of the bisector are intensities that penetrate through the sample below the sample plane after the scattering process.

By using neutrons one can probe regions of the reciprocal space that are not accessible by x-ray methods. The reciprocal space map collected by means of x-ray scattering is shown in figure 3 for reasons of comparison. Both methods give the same lateral structure spacing of



approximately 730 nm. The results gained from the neutron measurements are excellent and hence, for further sample analysis, polarized neutron scattering on NERO is proposed to probe also the diffuse magnetic properties of the laterally nanostructured sample.

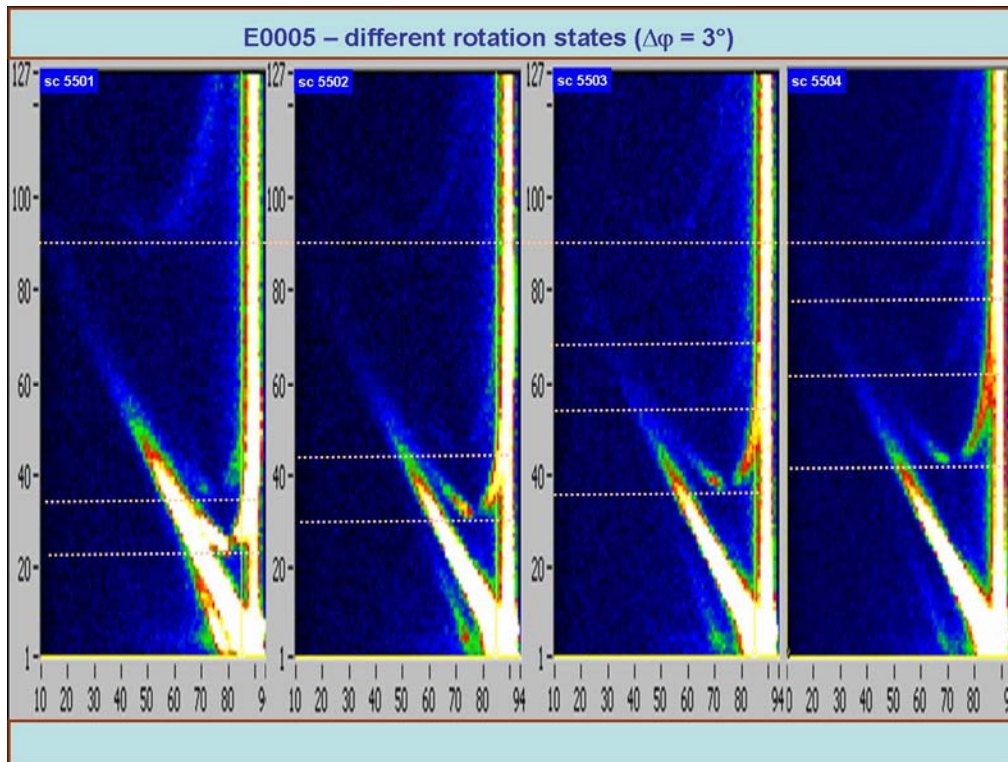


**Figure 1:** The collected raw data for various rotation states of the sample in  $\varphi$ . The horizontal channel numbers correspond to the various detector channels and the vertical channel numbers give the  $2\theta$  value. Shown are (from left to right) the rotation states of  $\varphi = -2^\circ$ ,  $\varphi = 1^\circ$ ,  $\varphi = 4^\circ$  and  $\varphi = 7^\circ$ .

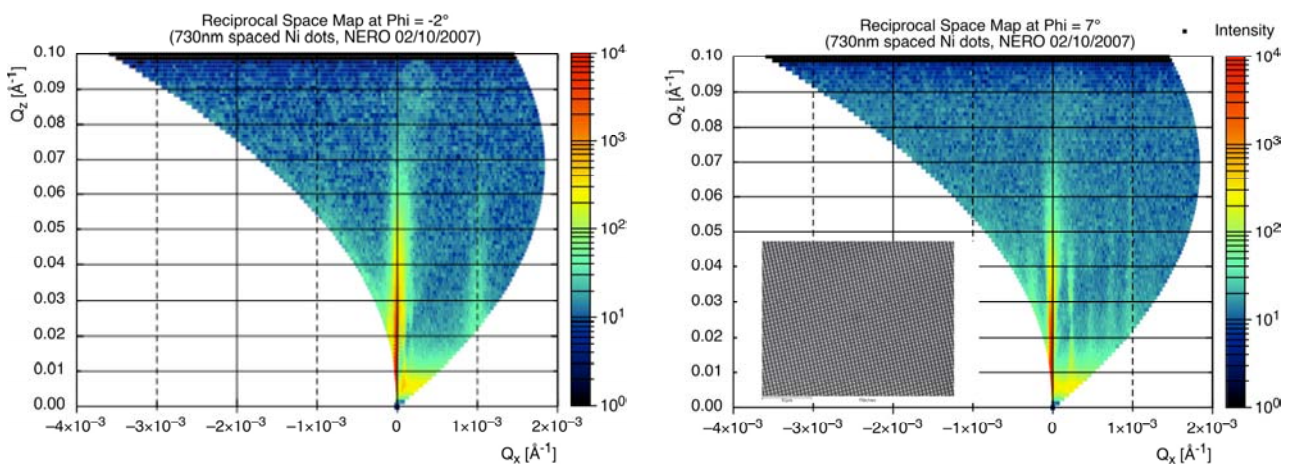


**Figure 2:** The reciprocal space maps for two of the rotation states of the sample in  $\varphi$ . The  $Q_x$  values is indirectly proportional to the laterally structure spacing. By increasing the rotation angle additional diagonal lattice components are observed, visible as additional intensities closer to the specular beam direction at  $Q_x = 0$ .



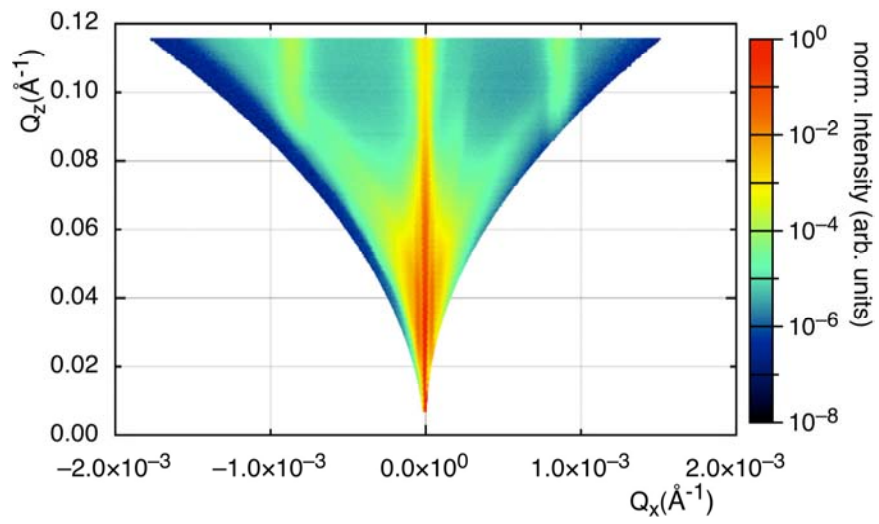


**Figure 3:** The reciprocal space map obtained by means of x-ray scattering. Intensities below the sample horizon cannot be probed due to absorption processes.



**Diffractometer for the analysis of residual stresses ARES-2**

**Short Instrument Description:**

Diffractometer for the analysis of residual stresses ('strain scanner') in specimens with technical sizes (up to approx. 200 kg) using thermal neutrons. Starting from the ground with a dance floor a completely new sample stage and detector mounting was installed in 2006, significantly improving the capability of handling large samples.

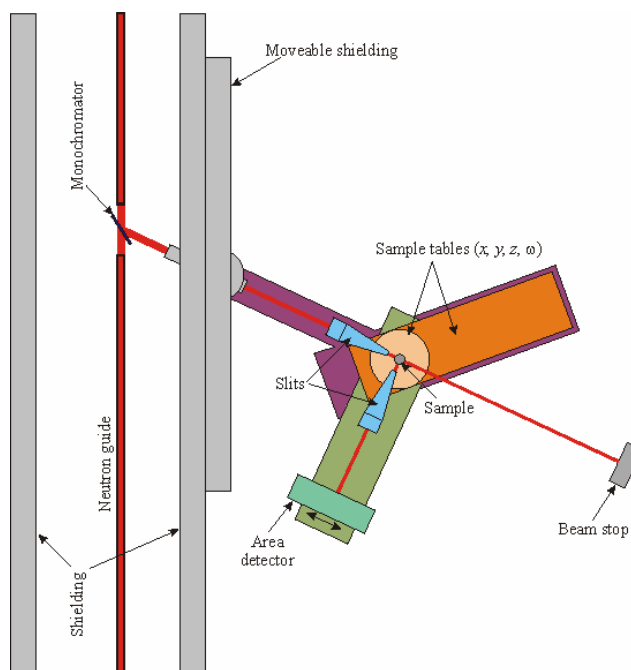
**Local Contact:**

**Dr. Peter Staron**

Phone/Fax : +49 (0)4152 87-1208 / +49 (0)4152 87-1356

E-mail: [peter.staron@gkss.de](mailto:peter.staron@gkss.de)


Schematic View of ARES-2:



**Instrument Details:**

Location at FRG-1:	beam line 7; thermal neutron guide (cross section $42 \times 90 \text{ mm}^2$ , supermirrors on top and bottom wall)
Monochromator:	elastically bent perfect Si monochromator, Si (311), double focussing
Take-off angle:	$57^\circ$ to $120^\circ$ , continuously selectable
Wavelength:	$\lambda = 0.16\text{--}0.23 \text{ nm}$ (with Si 311)
Flux at sample position:	$\Phi \approx 3 \cdot 10^5 \text{ cm}^{-2} \text{ s}^{-1}$
Sample movements:	x, y, z (range 400 mm), $\Omega$
Detector:	$^3\text{He}$ area detector (300 mm $\times$ 300 mm)
Sample environment:	Eulerian cradle (with x, y, z tables), load frame, furnace
Software:	PC programs for data reduction and analysis available



	<b>EXPERIMENTAL REPORT</b>	<b>GeNF ARES-2</b>
<b>Residual stresses in steel plates with a friction weld</b>		
<b>Proposer:</b>	<b>M. Piza</b> , PETROBRAS, Brasil	
<b>Co-Proposer(s):</b>	<b>P. Staron</b> , GKSS Research Centre Geesthacht, Germany	
<b>Experimental Team:</b>	<b>P. Staron</b>	
<b>User Group Leader:</b>	<b>P. Staron</b>	
<b>Instrument Responsible:</b>	<b>P. Staron</b>	
<b>Date(s) of Experiment:</b>	31 <sup>st</sup> October–29 <sup>th</sup> November.2007, 10 <sup>th</sup> –11 <sup>th</sup> December.2007	

## Objective

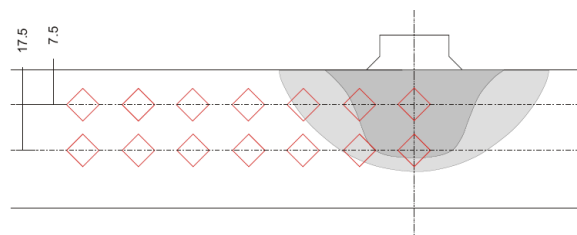
Efficient and reliable repair welding procedures are very important for some industrial equipment. Friction welding is a relatively new technique for repairing, and residual stresses generated by this technique can have a significant influence on the performance of repair welds. Therefore, residual stresses in eight 30 mm thick ferrite steel samples with friction point welds were determined to study the influence of welding parameters on the residual stress state. A friction point weld using a rotating rod had been applied in the centre of the plates, resembling a repair weld.

## Experiment

The investigated material is an unalloyed structural ferrite steel of grade S355 J2 G3 (old name: BS 4360 Gr 50D), corresponding to the German St 52-3 (DIN17100). The investigated samples had a size of 30 mm × 140 mm × 300 mm. The (211) reflection of the  $\alpha$  phase was measured at an angle of about 89° using a wavelength of 1.64 Å from a Si (311) monochromator. Since stress gradients are present in all three directions, a cubic gauge volume was used for scanning strains in radial, tangential, and axial directions. Because of the large sample thickness of 30 mm with a neutron path length in the material of 42 mm (and more in the weld region where a part of the rod used for welding was not removed), a large gauge volume with a nominal size of 5 mm × 5 mm × 5 mm was used. Preliminary measurements had shown that this spatial resolution is sufficient because the stress gradients around the weld cover a relatively large region [1]. The grain size of base material and weld was small enough to make sure that a large number of grains is included within the gauge volume. 14 points were measured in each sample along two 60 mm long lines in different depths, starting at the weld centre (Fig. 1).

**Figure 1:**

Sketch of the cross section of a 30 mm thick sample with point weld and heat affected zone. The positions and approximate size of the 14 measured volumes are indicated.



A small reference sample, in which macro-stresses can relax, was cut from one of the plates by electro discharge machining for the determination of the stress-free lattice parameter  $d_0$

and its variations in the weld. Significant variations of  $d_0$  from the base material into the weld are expected, depending on the exact chemical composition of the rod material.

### Achievements and Main Results


Significant differences in the radial and tangential strains are observed between two samples for which the data have partly been evaluated by now (Fig. 2). It was assumed for the evaluation that the stress in the through-thickness direction is zero for calculating  $d_0$ . The evaluation of the data of all eight samples will show in more detail how the stress state depends on the welding parameters. The results can help optimizing welding parameters with respect to welding induced residual stresses, as well as help evaluating finite element simulations of the welding process.

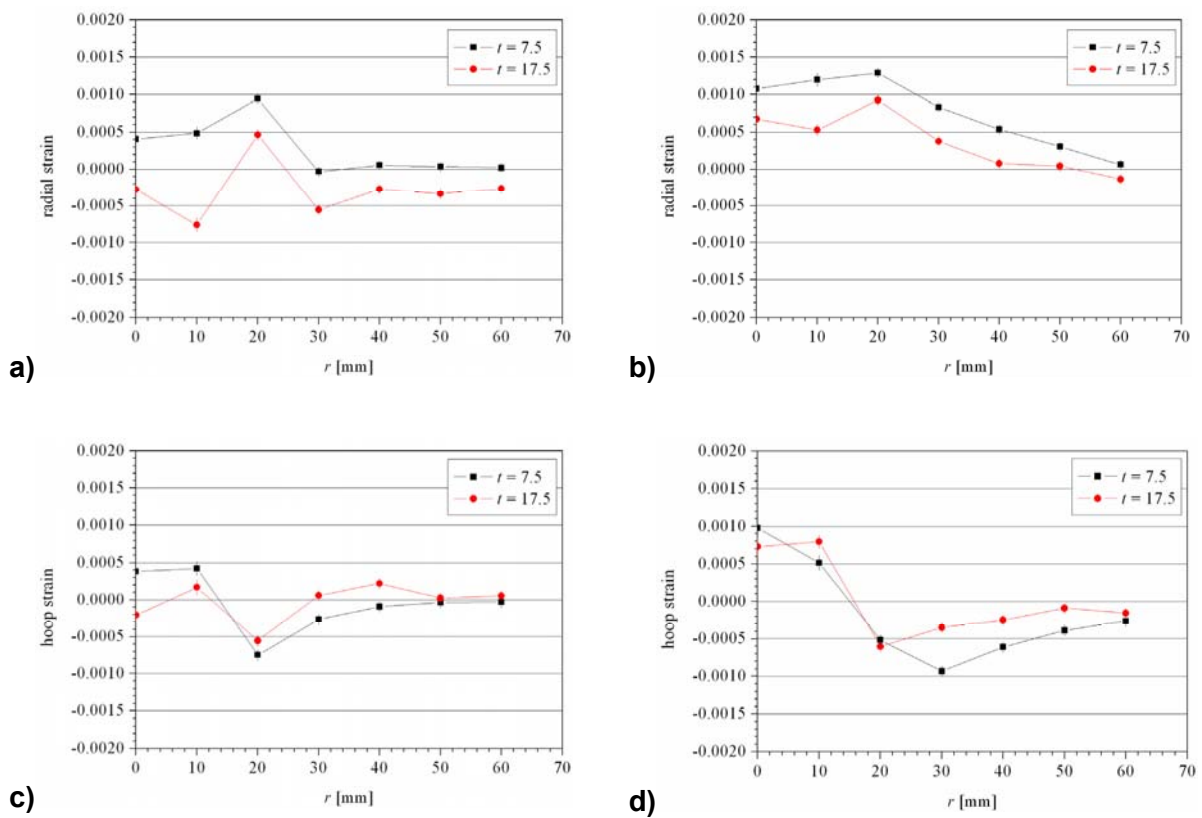


**Figure 2: Radial (a, b) and tangential (c, d) strains at two different depths  $t$  for two samples with different welding parameters.**

### Reference

[1] Piza M., Staron P., GeNF Experimental Report 2006, GKSS 2007/6, p. 165

	<b>EXPERIMENTAL REPORT</b>	<b>GeNF ARES-2</b>
<b>Residual stresses in a friction stir welded butt-joint of Al and steel</b>		
<b>Proposer:</b> <b>Co-Proposer(s):</b>	<b>J. Dos Santos<sup>1</sup></b> , <sup>1</sup> GKSS Research Centre Geesthacht, Germany <b>P. Staron<sup>1</sup></b>	
<b>Experimental Team:</b> <b>User Group Leader:</b> <b>Instrument Responsible:</b>	<b>P. Staron</b> <b>N. Huber<sup>1</sup></b> <b>P. Staron</b>	
<b>Date(s) of Experiment:</b>	17 <sup>th</sup> – 19 <sup>th</sup> December.2007	

## Objective

Dissimilar joints are important in many production processes, e.g. in the automobile industry. Aluminium alloys are used to save weight, while steel is used where higher strength is needed. However, producing reliable dissimilar joints can be challenging, depending on the details of the used material combination. Friction stir welding (FSW) is a solid-state joining technique that can overcome those problems that are related to melting of material. In this investigation, the residual stress distribution in a dissimilar Al-steel joint produced by FSW was determined.

## Experiment

A dissimilar joint of a ZStE260 microalloyed steel sheet and an Al sheet was produced in the GKSS FSW laboratory. The steel sheet had a thickness of 1.7 mm, the Al sheet of 1.5 mm. The final product had a size of approximately 300 mm × 315 mm. Internal strains were measured along a 180 mm long scan line in the middle of the sheet. Neutrons of 0.164 nm wavelength from an elastically bent perfect Silicon (311) monochromator were used. The (211) peak of the  $\alpha$  phase of the ferrite steel and the Al (311) peak was recorded with an area detector at an angle of about 89° and 84°. A matchstick-like gauge volume of nominal size 2×2×30 mm<sup>3</sup> was used for measurements of transverse ( $y$ ) and normal ( $z$ ) strains for improving the intensity. A cubic gauge volume of approximate size 2×2×2 mm<sup>3</sup> was used for measurements of longitudinal strains, because large stress gradients are expected in the transverse direction. In order to increase the number of diffracting grains for the small gauge volume, the gauge volume was shifted by 24 mm in longitudinal ( $x$ ) direction in eight steps during the measurement. Thus, approximately the same volume as in the two other directions is analysed. Since the nominal gauge volume is slightly larger than the sheet thicknesses, positioning was done carefully in order to minimize an influence of the sample position on the measured peak position.

## Achievements and Main Results

A plane stress state was assumed in the thin sheets for calculating  $d_0$ . There is an asymmetric strain pattern in the dissimilar weld with a much broader zone of tensile strain on the Al side of the weld and heat affected zone, and more compressive strain on the steel side farther away from the weld (Fig. 1). The zero position (weld line) in Figure 1 is given by the position of the tool pin. The distance between the points was 4 mm, dictated by the available beam time, which turned out to be too much. There is a very sharp rise of the longitudinal strain towards the weld on both sides of the weld.

Additional measurements are planned with higher spatial resolution in the weld zone. Moreover, the influence of variations of the welding parameters on the stress distribution can be studied.

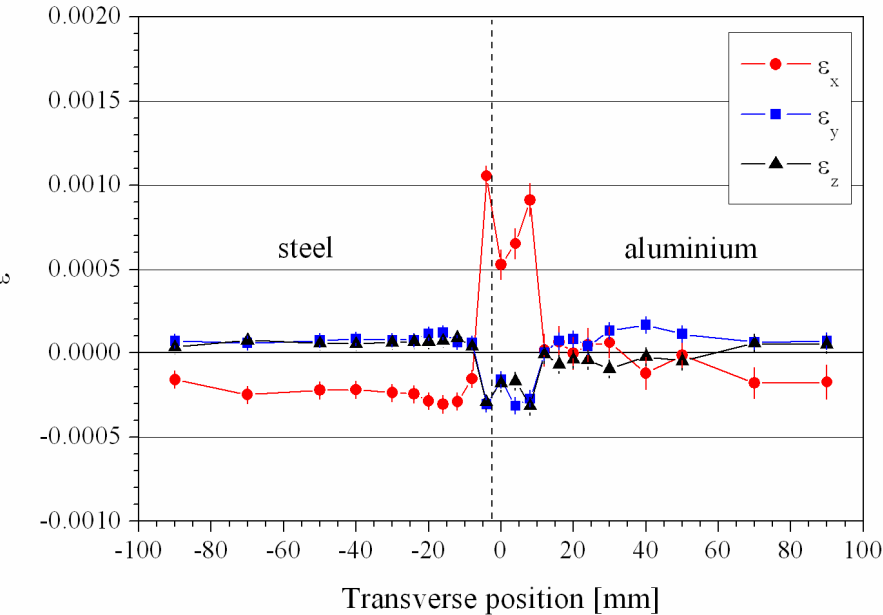


**Figure 1:** Longitudinal, transverse, and normal strains.



Residual stress in tool steel rods

**Proposer:** C. Redl, Böhler Edelstahl GmbH, Kapfenberg, Austria  
**Co-Proposer(s):** P. Staron, GKSS Research Centre Geesthacht, Germany

**Experimental Team:** P. Staron  
**User Group Leader:**  
**Instrument Responsible:** P. Staron

**Date(s) of Experiment:** 2<sup>nd</sup> – 16<sup>th</sup> May 2007

**Objective**

A feasibility study had shown that residual stress analysis is possible in specimens made of the tool steel 1.2343 (X38CrMoV5-1) produced by Böhler Edelstahl GmbH [1]. Thus, two additional specimens made of a slightly different material grade using different heat treatments were investigated. Rods with a length of 200 mm and a diameter of 20 mm were used for this study. One rod was gas quenched using nitrogen at 10 bar pressure, the other was additionally tempered.

**Experiment**

Scans were performed along a diameter in both samples using the (211) reflection of the  $\alpha$  phase. 2 mm wide slits with a height of 30 mm were used for measurements of radial and hoop strains. The slit in the incoming beam was set to 2 mm  $\times$  2 mm for measurements of axial strains. It was observed that the reflection from the hardened rod was symmetrically broadened to a width of 1.52° while the width of annealed iron was only 0.46° (Fig. 1). The peaks of the heat-treated rod are also broadened, but to a lesser width of 1.11°. It turned out that a correction of the peak position is required for the large peak widths, which comes from different absorption due to different path lengths within the gauge volume (Fig. 2). This correction was calculated numerically. Such a correction is not significant for peaks that are not broadened. The peak shift effect could probably be reduced by using a radial collimator.

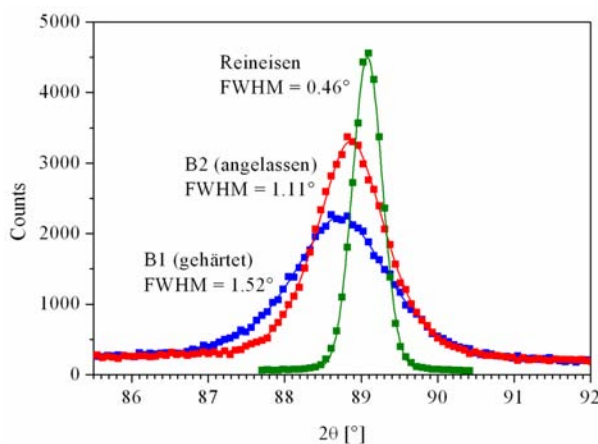


**Figure 1:** Exemplary peaks of hardened (B1) and heat-treated (B2) samples in comparison with annealed iron.

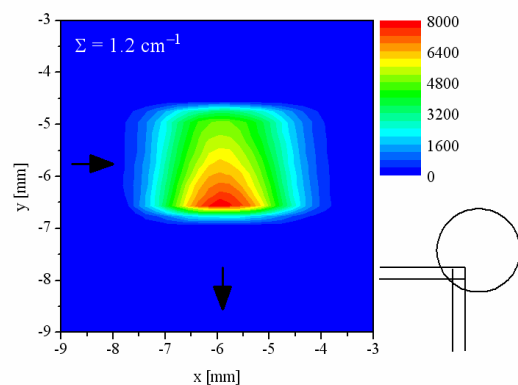


**Figure 2:** Distribution of intensity contribution within the gauge volume for steel at the location within the rod shown on the lower right side.

A possible origin of peak broadening could be the influence of micro segregation leading to fluctuations in the chemical composition on a microscopic scale. The presence of micro segregation is supported by the fact that an analysis of the peak width in terms of micro strains after Stokes and Wilson fails, because the peak width seems to be much too large to be explained by elastic strains only. In fact, micro segregation of Cr and Mo in this steel is well known.

### Achievements and Main Results


The strains determined in the hardened rod (Fig. 3) and in the tempered rod are close to zero. Expected differences in the residual stress state between the hardened and tempered material have not been observed. Already the hardened specimen seems to be free of macro stress. The development of residual stress depends on the size of the object and the rate of cooling from austenitization temperature. In the present case, the cooling rate seems to be too small to lead to the formation of significant residual stress in a rod with 20 mm diameter.

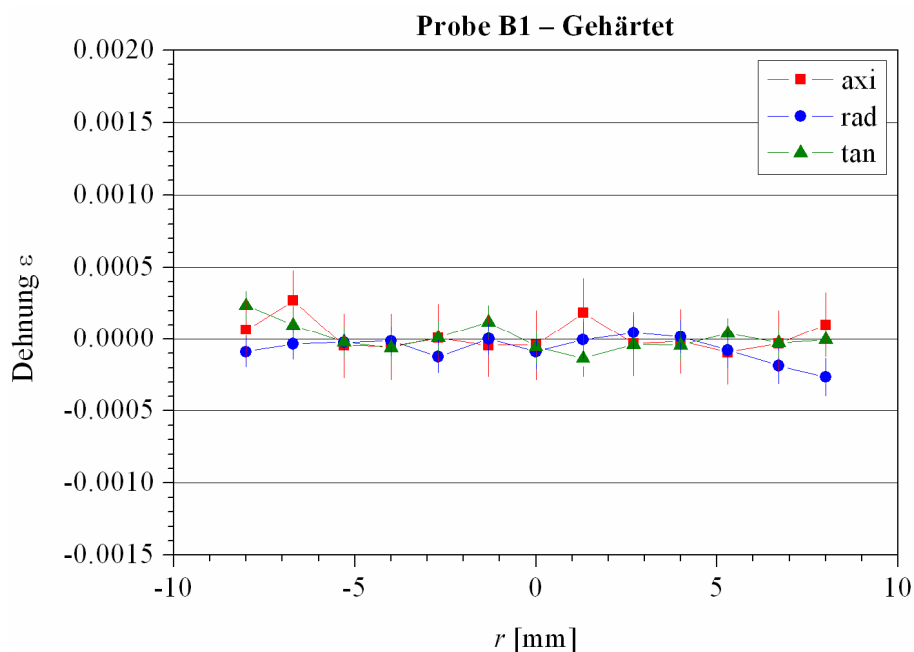


**Figure 3:** Axial, radial, and tangential strains for the hardened rod.

### Reference

[1] C. Redl, P. Staron, GeNF Experimental Report 2006, GKSS 2007/6, p. 161

	<b>EXPERIMENTAL REPORT</b>	<b>GeNF ARES-2</b>
<b>Residual stresses in a laser beam welded butt-joint of aluminium sheets</b>		
<b>Proposer:</b>	<b>W.V. Vaidya, M. Koçak<sup>1</sup></b> , <sup>1</sup> GKSS Research Centre Geesthacht, Germany	
<b>Co-Proposer(s):</b>	<b>P. Staron<sup>1</sup></b>	
<b>Experimental Team:</b>	<b>P. Staron</b>	
<b>User Group Leader:</b>	<b>N. Huber<sup>1</sup></b>	
<b>Instrument Responsible:</b>	<b>P. Staron</b>	
<b>Date(s) of Experiment:</b>	12 <sup>th</sup> – 16 <sup>th</sup> December.2007	

## Objective

Aluminium alloys are potential materials for lightweight structures in transportation industry. Laser beam welding (LBW) is, compared to the conventional fusion welding techniques, well suited for Al alloys because of the low localised heat input leading to low distortion [1]. In addition, high strength joints can be produced with high processing speeds. In an earlier investigation, the influence of different heat treatments on the residual stress distribution within and around the weld had been studied [2]. The weld in the T6 temper was investigated, however, the influence of a post-weld heat treatment again to T6 on the residual stress distribution remained open. This has been now supplemented in this investigation.

## Experiment

The investigated specimen was an aluminium sheet (AA6056) with a size of 500 mm × 500 mm and a thickness of 3.2 mm that has been joined using LBW. The sheet was in the T6 temper before welding. After welding, the sheet was given an additional T6 post-weld heat treatment. Internal strains were measured along a 140 mm long scan line in the middle of the sheet. Neutrons of 0.164 nm wavelength from an elastically bent perfect Silicon (311) monochromator were used. The Al (311) diffraction peak was recorded with an area detector at an angle of about 84°. A matchstick-like gauge volume of nominal size 2×2×30 mm<sup>3</sup> was used for measurements of transverse (*y*) and normal (*z*) strains for improving the intensity. A cubic gauge volume of approximate size 2×2×2 mm<sup>3</sup> was used for measurements of longitudinal strains, because large stress gradients are expected in the transverse direction. In order to increase the number of diffracting grains for the small gauge volume, the gauge volume was shifted by 24 mm in longitudinal (*x*) direction in eight steps during the measurement. Thus, approximately the same volume as in the two other directions is analysed. However, due to a technical problem up to now only one single step could be evaluated and, thus, the counting statistics as well as the grain statistics for the longitudinal direction is rather poor.

## Achievements and Main Results


A plane stress state was assumed in the thin sheet for calculating  $d_0$ . In general, a post-weld heat treatment is used not only for stress relief but also for recovery of strength in the weld. In the present case, the applied T6 post-weld heat treatment does not seem to be very effective in reducing residual stress, since a pronounced double tensile stress peak is still present in the weld region (Fig. 1). However, as shown in another investigation using small-angle neutron scattering, the T6 post-weld heat treatment is found to affect the distribution of strengthening precipitates in this sample [3].

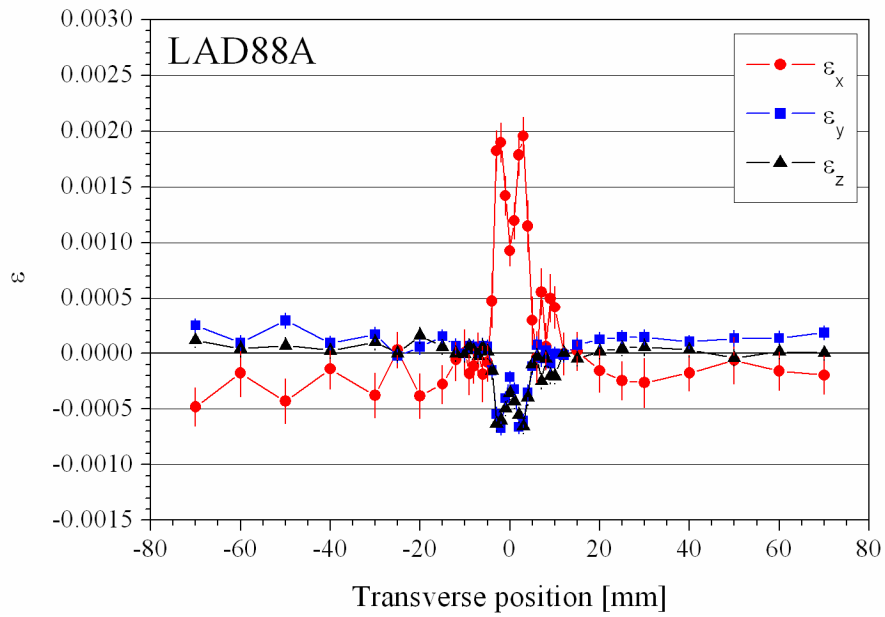


**Figure 1:** Longitudinal, transverse, and normal strains in the sample laser beam welded initially in the T6 temper and post weld heat-treated to T6 again.

### References

- [1] E. Schubert, M. Klassen, I. Zerner, C. Walz, G. Sepold, J. Mater. Processing Technol. 115 (2001) 2–8
- [2] W. V. Vaidya, M. Koçak, GeNF Experimental Report 2004, p. 147
- [3] P. Staron, W.V. Vaidya, GeNF Experimental Report 2007 (SANS-2 section of this document)

	<b>EXPERIMENTAL REPORT</b>	<b>GeNF ARES-2</b>
<b>Influence of the welding sequence on residual stresses in laser welded T-joints of an airframe aluminium alloy</b>		
<b>Proposer:</b>  <b>Co-Proposer(s):</b>	<b>Winulf Machold<sup>1</sup>, Funda Bayraktar<sup>1</sup>, Peter Staron<sup>1</sup>,</b> <sup>1</sup> GKSS Research Centre Geesthacht, Germany	
<b>Experimental Team:</b> <b>User Group Leader:</b> <b>Instrument Responsible:</b>	<b>Winulf Machold<sup>1</sup>, Funda Bayraktar<sup>1</sup></b> <b>Andreas Schreyer<sup>1</sup></b> <b>Peter Staron<sup>1</sup></b>	
<b>Date(s) of Experiment:</b>	10 <sup>th</sup> – 26 <sup>th</sup> .April.2007, 28 <sup>th</sup> June – 13 <sup>th</sup> July 2007, 27 <sup>th</sup> September – 04 <sup>th</sup> October.2007	

## Objective

Replacing rivets by laser beam welded (LBW) joints of aluminium alloys is a current topic in the aircraft industry [1, 2], which has been particularly realized for skin-stringer joints in the Airbus A380, A318 and A340. The major advantages of LBW joints are reduction of weight, fuel sparing, and a higher cargo load. Besides, the risk of corrosion damage is reduced, and faster manufacturing saves production costs [1, 2]. However, extension to T-joints of so-called clips to the skin is not yet achieved.

Due to the occurrence of cyclic loading during the flight of an airplane, the mechanical performance of welded aluminium joints depends on the distribution and the magnitude of residual stresses (RS). Especially, it is known that fatigue resistance and crack propagation behaviour is significantly improved by compressive residual stresses [3]. Start (run-in) and end (run-out) of the weld seam are most prone to crack initiation, and recent measurements have shown that longitudinal tensile stresses are lower at the run-in than at the run-out locations [4].

Therefore, in this study the effect of different welding sequences on the residual stress state was investigated [6]. While the usual welding sequence is from one clip end to the other, here it was additionally varied to welding from the clip ends to the middle (two run-ins at clip ends) and from the middle to the clip ends (two run-outs at clip ends). For this, a 2 mm thick clip was welded from one side to a 4.5 mm thick base plate using a 3.3 kW Nd:YAG laser source.

As LBW uses small focal points with high power density ( $\sim 10^6$  W/cm<sup>2</sup>), the welding speed becomes high, which implicates low heat input and, thus, low distortion. Consequently, LBW has proved to be very suitable for airframe components [2]. Nevertheless, LBW causes high cooling rates and high temperature gradients. Combined with the joint geometry and the material properties they define the shrinkage, which leads to residual stress. Neutron diffraction has been acknowledged very suitable for non-destructive RS evaluation, especially for the analysis of RS in bulk materials such as the aluminium plates in this study.

## Experiment

Current candidates for welded fuselage structures are high strength AlMgSiCu wrought alloys (6xxx series), such as AA 6013 and AA 6156 [1, 2]. The investigated samples consisted of a 4.5 mm thick AA 6156 T6 base plate and a 2 mm thick AA 6013 T6 clip. Additionally, half

of the base plates had 1.5 mm deep weight-reducing pockets (Fig. 1a). Since Mg and Cu improve the strength of the alloys and Si improves the weldability, an AA 4047 (12 % Si, eutectic AlSi) filler wire with a diameter of 1.2 mm was selected. A post-weld heat treatment was not applied.

During welding, the clip was fixed by a vacuum system and the plate was fixed by mechanical clamps. Such fixing minimizes thermal distortion and ensures a good precision of positioning. A 3.3 kW Nd:YAG laser was used, while the laser head was moved by an industry robot. The inert gas was helium, which affects the plasma flow out of the keyhole and consequently the formation of pores. The three different welding sequences are shown in Fig. 1b.

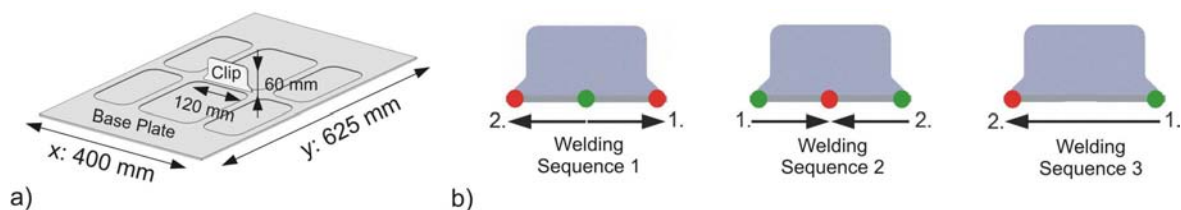


**Figure 1:** a) geometry of the samples with pockets, b) different welding sequences.

For the RS studies, a silicon crystal monochromator was used with a neutron wavelength of 1.64 Å. The shifts of the Bragg peaks were determined by an area detector with an angular resolution of 0.12° and with an active area of 300 mm × 300 mm. The lattice spacing given by the Miller indices  $hkl$  was calculated from the measured diffraction angles applying Bragg's equation. For peak fitting a pseudo-Voigt function was used. From this, the strain  $\varepsilon$  is obtained. In case of local plastic deformation as it occurs due to welding an appropriate reflection should be chosen to minimize the contribution of intergranular strains to the stress results. Thus, the Al(311) reflection was used. This reflection shows a good linearity of the strain-load behaviour, and the gauge volume is nearly cubic with  $2\theta = 84.38^\circ$ . The nominal size of the volume was defined by Cd slits to  $2 \times 2 \times 10 \text{ mm}^3$  for  $\varepsilon_x$  and  $\varepsilon_z$ . Because larger strain gradients are present in  $y$ -direction, for the strain  $\varepsilon_y$ , a gauge volume of  $2 \times 2 \times 2 \text{ mm}^3$  was used.

Due to the symmetry of a T-joint, the principle stress axes were assumed to coincide with the geometrical axes, so the generalized Hook's law for the diagonal components of the stress tensor was used. In case of Al the crystallographic anisotropy is small, so the macroscopic values  $E_{hkl} = 70 \text{ MPa}$  and  $\nu_{hkl} = 0.33$  were taken. Because of the heat treatment introduced by welding and the usage of base alloy deviant filler wire the chemical composition in the weld seam and in the heat affected zone (HAZ)  $d_0$  has to be considered as variable. Thus, a biaxial stress state with the condition  $\sigma_z = 0$  was assumed, which allows the determination of  $d_0$ . Due to the fact that the samples are thin sheets, this is a good assumption for the entire area except the very T-joint region. However, the changes of  $d_0$  in the weld and in the HAZ are expected to be small in case of the AA 61xx alloys. The strain was analysed along three scan lines perpendicular to the clip (middle and clip ends). Along each scan line, 19 data points were taken at the mid-thickness of the base sheet.

### Achievements and Main Results

As it can be seen in Figure 2, the largest distance of the data points to the clip surface was about 5 cm. Yet, these points are obviously not stress-free. Since the scan lines were in transverse direction, the tensile and compressive stresses in longitudinal direction should be in balance. Nevertheless, the entire stress dilatation of the whole sample has to be considered

as well as possible additions of small micro stresses. Taking this into account, the stress balance is well complied. In addition, there are tensile longitudinal stresses in the weld zone in all cases, which is typical for straight welding. The relatively high longitudinal stresses at the middle position show a lowering in the centre for some RS distributions (Fig. 2b and Fig.3b). This usually corresponds to a heat-affected weakening, which is typical for aluminium alloys. Also the maximum magnitudes of the measured stresses, which are due to the tensile yield strength, have characteristic values.

The comparison of the samples with pockets and without did not show significant differences. While the magnitudes of the stresses seem to be equal, the RS distributions show a slight broadening for the samples with pockets. However, a strong variation arises from the different welding sequences (Fig. 3). Generally, the maximum tensile stresses in the longitudinal direction vary strongly in a range of +50 MPa to +250 MPa. In transverse direction, the stresses are lower and partially compressive, while they also vary in a range of -100 MPa to +150 MPa. Independent from the weld sequence and the sample geometry, they are always compressive in the weld seam area of the run-in points. This applies especially to welding sequence 1, where the minimum transverse stress is -70 MPa or less. In contrast, the double run-out point of sequence 2 shows transverse tensile stresses with maxima of +150 MPa (Fig. 3).

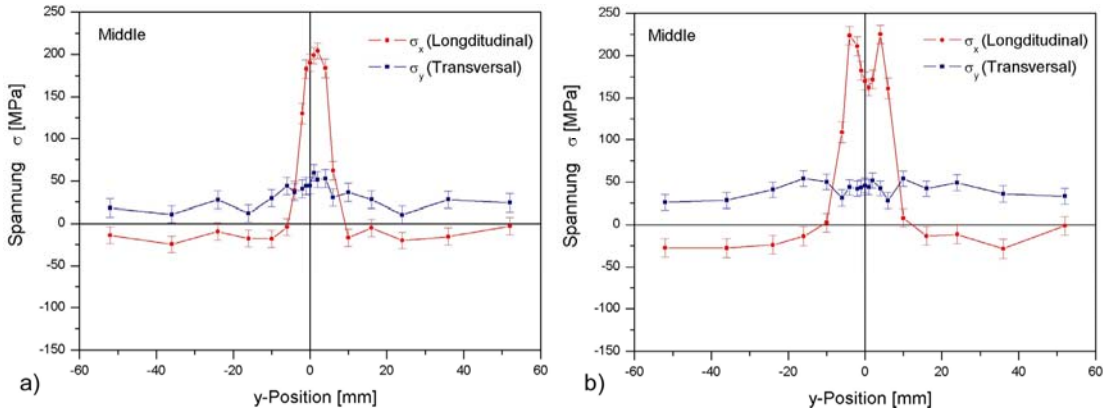


**Figure 2:** a) RS distributions for sample without pockets, welding sequence 3, b) RS distributions for sample with pockets, welding sequence 3.

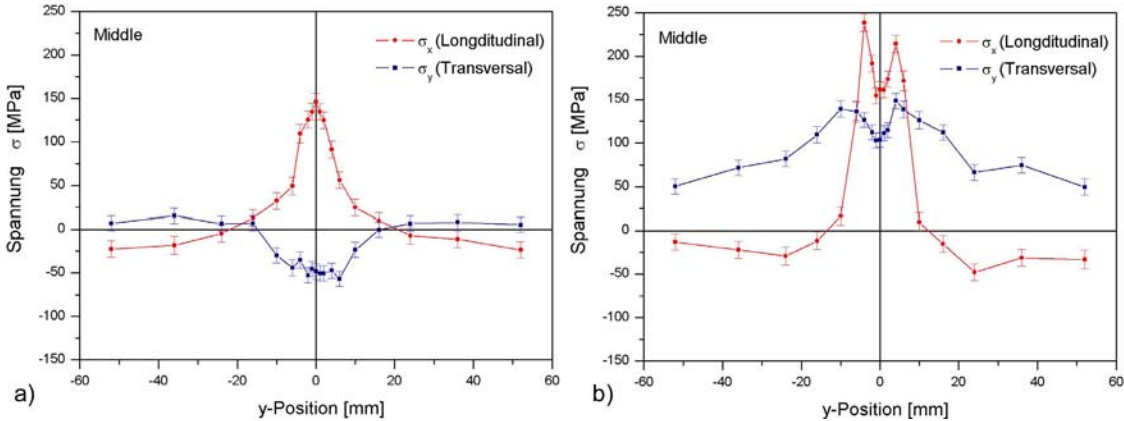


**Figure 3:** a) RS distributions in clip middle, welding sequence 1, b) RS distributions in clip middle, welding sequence 2.

With regard to the application in airframes, the measured RS should be considered in context of the fatigue behaviour. As a cyclic loading in transverse direction is influenced by transverse RS, for example welding sequence A should be clearly more resistant to an initiated crack in the middle of the clip than sequence B. This has already been acknowledged in fatigue tests [5].

## References

- [1] E. Schubert, M. Klassen, I. Zerner, C. Walz, G. Sepold: Light-weight Structures produced by Laser Beam Joining for Future Applications in Automotive and Aerospace Industry, *Journal of Materials Processing Technology*, 2001, Vol. 115, pp. 2–8
- [2] P. Leque, P. Lassince, T. Warner, G. M. Raynaud: Engineering for the Future: Weight Saving and Cost Reduction Initiatives, *Aircraft Engineering and Aerospace Technology*, 2001, Vol. 73, pp. 147–159
- [3] G. Glinka: Residual Stresses in Fatigue and Fracture: Theoretical and Experiments, *Advances in Surface Treatments*, 1987, Vol. 4, pp. 413–454
- [4] F.S. Bayraktar, P. Staron, M. Koçak, A. Schreyer: Residual Stress Analysis of Laser Welded Aluminium T-Joints, *Welding in the World*, 2007, Vol. 51, No 1-2, pp. 9–13
- [5] F.S. Bayraktar, M. Koçak, M. Horstmann, S. Riekehr: Fatigue Crack Behaviour of Laser Welded Skin-Clip Joints, *European Workshop on Short Distance Welding Concepts for Airframes*, 13–15 June 2007, GKSS Research Centre Geesthacht, Germany
- [6] W. Machold, P. Staron, F. Bayraktar, S. Riekehr, M. Koçak, A. Schreyer: Influence of the welding sequence on residual stresses in laser welded T-joint of an airframe aluminium alloy, *Proceedings of the MECA SENS conference and accepted for publishing in the Material Science Forum*, in press



Neutron texture diffractometer TEX-2

**Short Instrument Description**

The four circle neutron texture diffractometer is used to characterise textures in metallic, ceramic and geologic materials applying thermal, non-polarised neutrons.

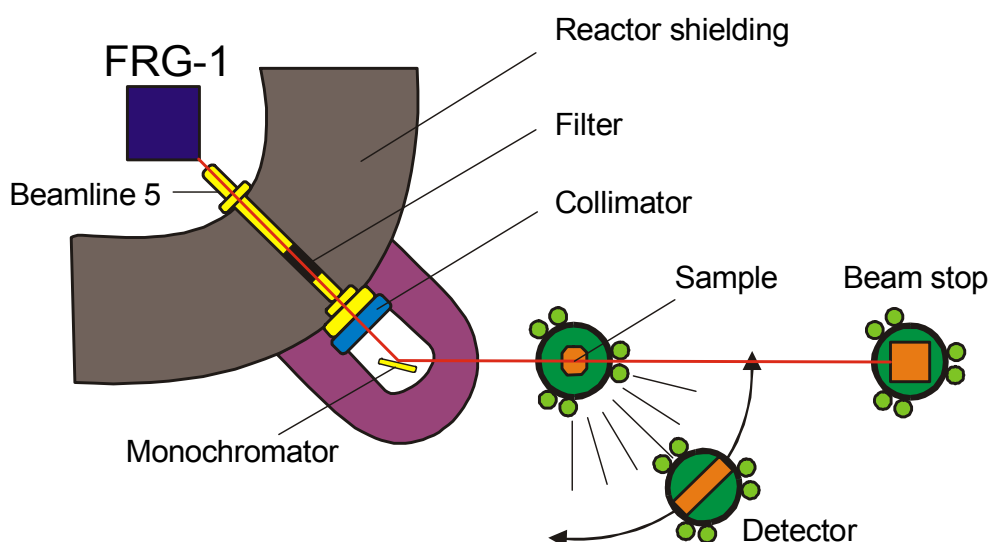
**Local Contact:**

**Prof. Dr. Heinz-Günter Brokmeier**

Phone/Fax: +49 (0)4152 87-1207 / +49 (0)4152 87-1338

e-mail: [brokmeier@gkss.de](mailto:brokmeier@gkss.de)

**Schematic View of TEX-2:**




**Instrument Details:**

Location at FRG-1:	beamline 5, thermal neutrons maximum beam cross section: 45 x 45 mm <sup>2</sup>
Primary collimation:	30', 42', 51'
Monochromator:	Cu (111), Cu (200), PG (002)
Take-off angle:	17.2°, 27.2°, 37.2°, 47.2°, 57.2°
Wavelength range:	$\lambda = 0.08\text{--}0.27$ nm (in steps)
Flux at sample position:	$\Phi = 0.3 - 2 \cdot 10^6$ cm <sup>-2</sup> s <sup>-1</sup>
Angular range	$\Phi$ : -360° to +360° X: -360° to +360° $\Omega$ : -46° to + 46° 2 $\Phi$ : -60° to +90°
Detector:	<sup>3</sup> He- single detector 2-D position – sensitive <sup>3</sup> He-detector 300 x 300 mm

**Instrument Details** (continued):

Sample geometries (standard):  (various):	cube 10 mm edge, sphere 15–20 mm $\varnothing$ cylinder 10–15 mm $\varnothing$ , 10–15 mm high e.g. wires, tubes, tensile samples
Distances: sample $^3\text{He}$ detector sample 2-D-detector	65–160 cm 60–120 cm
Sample environment:	– loading device: range of cycling load: tension up to 1.5 t, compression up to 2.0 t, – sophisticated set of sample holders

	<b>EXPERIMENTAL REPORT</b>	<b>GeNF TEX-2</b>
<b>Texture variation during heat treatment of extruded AZ31</b>		
<b>Proposer:</b>	<b>Sangbong Yi<sup>1</sup></b> , <sup>1</sup> Institut für Werkstoffkunde und Werkstofftechnik, TU Clausthal, Germany	
<b>Co-Proposers:</b>	<b>Heinz-Günter Brokmeier<sup>2</sup></b> <sup>2</sup> IWW-TEXMAT TU Clausthal, Geesthacht, Germany	
<b>Experimental Team:</b>	<b>H.-G. Brokmeier<sup>2</sup>, W. M. Gan<sup>2</sup>, Bernd Schwebke<sup>2</sup></b>	
<b>User Group Leader:</b>	<b>A. Schreyer<sup>3</sup></b> , <sup>3</sup> GKSS Research Centre Geesthacht, Germany	
<b>Instrument Responsible:</b>	<b>H.-G. Brokmeier<sup>2</sup></b>	
<b>Date(s) of Experiment:</b>	30 <sup>th</sup> March – 3 <sup>rd</sup> April 2007	

## Objective

The main objective of this study is to understand the recrystallization mechanism of magnesium alloy. Though there have been many researches on the dynamic recrystallization (DRX) of magnesium alloys, the studies on the static recrystallization (RX) are hardly to be found. This originates from the fact that the magnesium wrought alloys need to be deformed at high temperature such that the DRX occurs already during the deformation. Consequently, the classical RX, nucleation and the growth of nuclei, occur hardly in such DRXed status. Static recrystallization studies of other metals with hexagonal crystal structure, e.g. Ti, Zn, Zr, show that a certain orientation relationship between matrix and new grains, characterized by 30° rotation around the <00.1> axis, is associated with a high boundary mobility, while the nuclei are randomly oriented. Provided that this grain boundary characteristic is valid also for Mg alloys, however still unclear, some orientation changes following the above hypothesis should be observed also during grain growth. The main objective of the present study, as a preliminary experiment for understanding the recrystallization mechanism, is to investigate the orientation changes during heating of partially DRXed Mg alloy.

The typical texture component found in extruded AZ31 rods is strong <10.0> fiber texture component parallel to the extrusion direction. The present work reports the change of the <10.0> fiber texture component as a function of the annealing time at 400 °C.

## Experiment

The initial material is a round AZ31 rod, Mg - 3Al – 1Zn – 0.3 Mn in wt.-%, which was hydrostatically extruded at 350 °C with an extrusion ration of 14.4 : 1. The samples cut from the extruded rod were heat treated under ambient condition at 400 °C with different holding time, 3, 5, 10, 15, 30 min, and water quenched. The pole figure measurements were carried out at TEX-2 in GKSS research centre using neutron diffraction. The {10.0}, (00.2), {10.1}, {11.0} pole figures were used for calculating the ODF to a degree given by  $L_{max} = 22$ .

## Achievements and Main Results

The texture of the extruded rod is shown in Fig. 1 (a), in terms of the inverse pole figure at the extrusion direction (ED). As expected, the main texture component of the as-extruded sample is the <10.0> fibre parallel to the ED. The texture becomes weaker by the annealing. This weakening of the [10.0] fibre is clearly seen already after 3 min annealing at 400 °C. After 5 min of annealing new texture component appears, <11.0> parallel to the ED. The

intensity corresponding to this new component increases gradually with the annealing time. Furthermore, the  $\langle 11.0 \rangle$  fibre parallel to the ED becomes the main texture component from the annealing time of 15 min. Besides of understanding the kinetics of RX, this result can provide also the information for indicating the degree of the DRX during the extrusion, since the above listed textures (mixture of  $\langle 10.0 \rangle$  and  $\langle 11.0 \rangle$ ,  $\langle 10.0 \rangle$  or  $\langle 11.0 \rangle$  single fibre as main texture component) are found depending on the alloys and the working conditions.

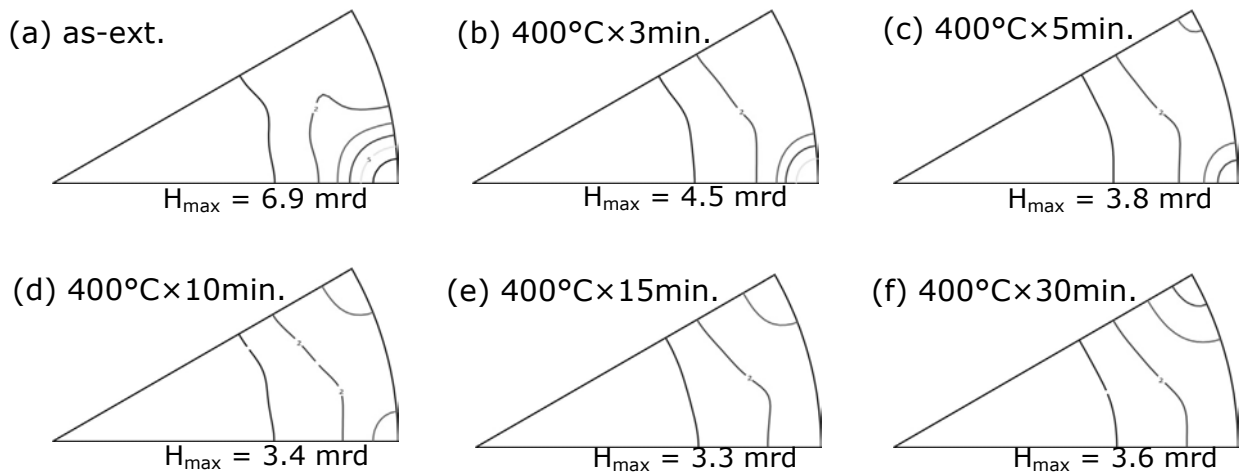



**Figure 1:** Inverse pole figures at ED of (a) the extruded rod and the heat treated samples at 400 °C with different annealing time; (b) 3min, (c) 5min, (d) 10 min, (e) 15 min and (f) 30 min. (level: 1, 2, 3, ... 6 mrd – multiple random).

Fig. 2 shows the variation of pole density as a function of the annealing time at 400 °C. The figure shows the exponential relation between the intensity change (decrease of  $\langle 10.0 \rangle$  pole and increase of  $\langle 11.0 \rangle$  pole parallel to the ED) and the holding time is found. The above mentioned grain boundary characteristics, i.e. high mobility of the boundaries having 30° rotation around the  $\langle 00.1 \rangle$  axis, explains very well the above results, since the  $\langle 10.0 \rangle$  and  $\langle 11.0 \rangle$  follow this orientation relationship. For understanding and confirming this relation between the texture developments and grain growth, further detailed studies are necessary, especially the microtexture and grain boundary characterisation. Further works will focus on the microstructure evolution after various heat treatments.

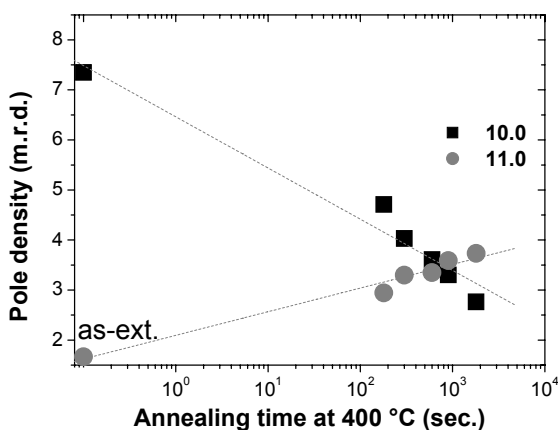


**Figure 2:** Variation of the  $\langle 10.0 \rangle$  and  $\langle 11.0 \rangle$  pole densities at the ED of the pole figure as a function of the annealing time at 400 °C.

	<b>EXPERIMENTAL REPORT</b>	<b>GeNF TEX-2</b>
<b>Texture measurements on ultrafine-grained aluminium produced by accumulative roll bonding</b>		
<b>Proposer:</b>	<b>Werner Skrotzki<sup>1</sup></b> <sup>1</sup> Institut für Strukturphysik, Abteilung Metallphysik, Technische Universität Dresden, 01062 Dresden, Germany	
<b>Co-Proposer:</b>	<b>Juliane Hüttenrauch<sup>1</sup></b>	
<b>Experimental Team:</b>	<b>W. M. Gan<sup>2</sup>, H.-G. Brokmeier<sup>2</sup>,</b> <sup>2</sup> IWW-TEXMAT TU Clausthal, Geesthacht, Germany	
<b>User Group Leader:</b>	<b>A. Schreyer<sup>3</sup>,</b> <sup>3</sup> GKSS Research Centre Geesthacht, Germany	
<b>Instrument Responsible:</b>	<b>H.-G. Brokmeier<sup>2</sup></b>	
<b>Date(s) of Experiment:</b>	23 <sup>rd</sup> – 28 <sup>th</sup> March 2007	

## Objectives

During recent years, bulk ultrafine-grained (UFG) materials, produced by severe plastic deformation (SPD) and with grain sizes in the range from 100 nm to less than 1  $\mu\text{m}$ , have received considerable scientific attention [e.g. 1]. Compared to their conventional grain-sized counterparts the UFG microstructure leads, beside many other enhanced properties in UFG-materials, to an extraordinary high strength and enhanced ductility [2]. While much is known about texture formation in SPD materials produced by equal channel angular pressing [e.g. 3], texture measurements on fcc metals subjected to accumulative roll bonding (ARB) are less frequent. ARB is a process where the rolled sheet is cut, polished, brushed, stacked and then roll-bonded (Fig. 1) [4, 5]. By repeating this procedure very high strains have been introduced successfully into different metals and alloys, and as a result, significant structural refinement has been achieved. Observations of the structural evolution during ARB have shown the formation of a lamellar structure at high strains, indicating a microstructural evolution similar to that which takes place during conventional rolling [6]. Similarly, texture formation should compare with that of rolling. However, because of repeated stacking of sheets containing a texture gradient characterized by plane strain deformation in the centre and a high portion of shear at the surface, marked differences are expected. Moreover, there are small zones heavily treated by brushing in order to accomplish good bonding.

In principal the ARB process may be easily integrated into existing industrial process chains. Thus, from the technological point of view, ARB is a highly promising process with a high light weight construction potential for the automobile and aircraft industry. Because of their significantly higher specific strength sheet like UFG workpieces should allow the production of lighter structural parts and, therefore, due to weight reduction contribute to save resources.

It is the aim of the present project to study in detail texture formation in aluminium as a function of ARB cycles.

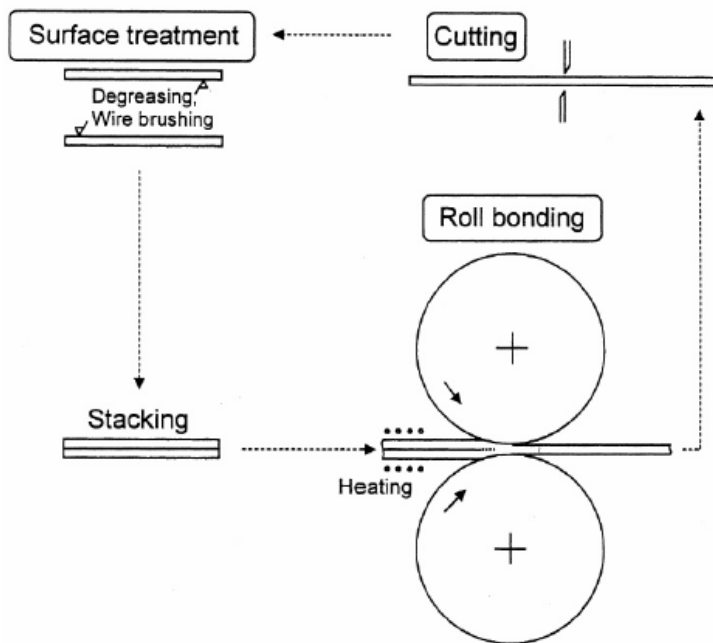


**Figure 1:**  
Principle of the accumulative roll-bonding process [4].

## Experiment

In this investigation sheets of aluminum of technical purity (AA 1050, 99.5 %) with an original thickness of 1 mm were used. After a recrystallization heat treatment at 520 °C for 1h the ARB-process was applied at room temperature to small strips of material, which had a width of 80–100 mm and a length of approximately 300 mm. The reduction of the thickness was set nominally to 50 % per rolling pass. After each pass (cycle) the surfaces were wire brushed, the sheet was folded at half of the length and the rolling process was repeated (Fig. 1). The number of cycles applied was eight leading to a sheet with 256 bonded layers.

Texture measurements were done by neutron diffraction on a stack of eight sheets with a size of 10 mm x 10 mm. Because of their high penetration depth neutrons allow bulk texture measurements. The orientation distribution function (ODF) was calculated from the measured pole figures (200, 220, 111) by using the harmonic method with a maximum series expansion coefficient of 22 [7].

## Achievements and Main Results

The starting texture (not measured so far) probably is a cube recrystallization texture.

During ARB the Copper component forms and strengthens up to the 6<sup>th</sup> cycle and slightly decreases afterwards. The Brass component is weak and has completely vanished after 8 cycles. Most interesting is the strong development of the rotated cube component, which exhibits the same behaviour as the copper component and is comparable in strength. This component is typical for simple shear which usually during rolling takes place in the surface layer of the sheets.

The textures shown are the bulk textures of the entire sheet thickness. Thus, with these textures it is possible to calculate the bulk properties of the ARB sheets. Calculations of the mechanical anisotropy of the sheets are in progress. To find out the spatial distribution of the different texture components as well as texture gradients within the layers of the ARB stack, electron back-scatter diffraction with high area resolution is planned.

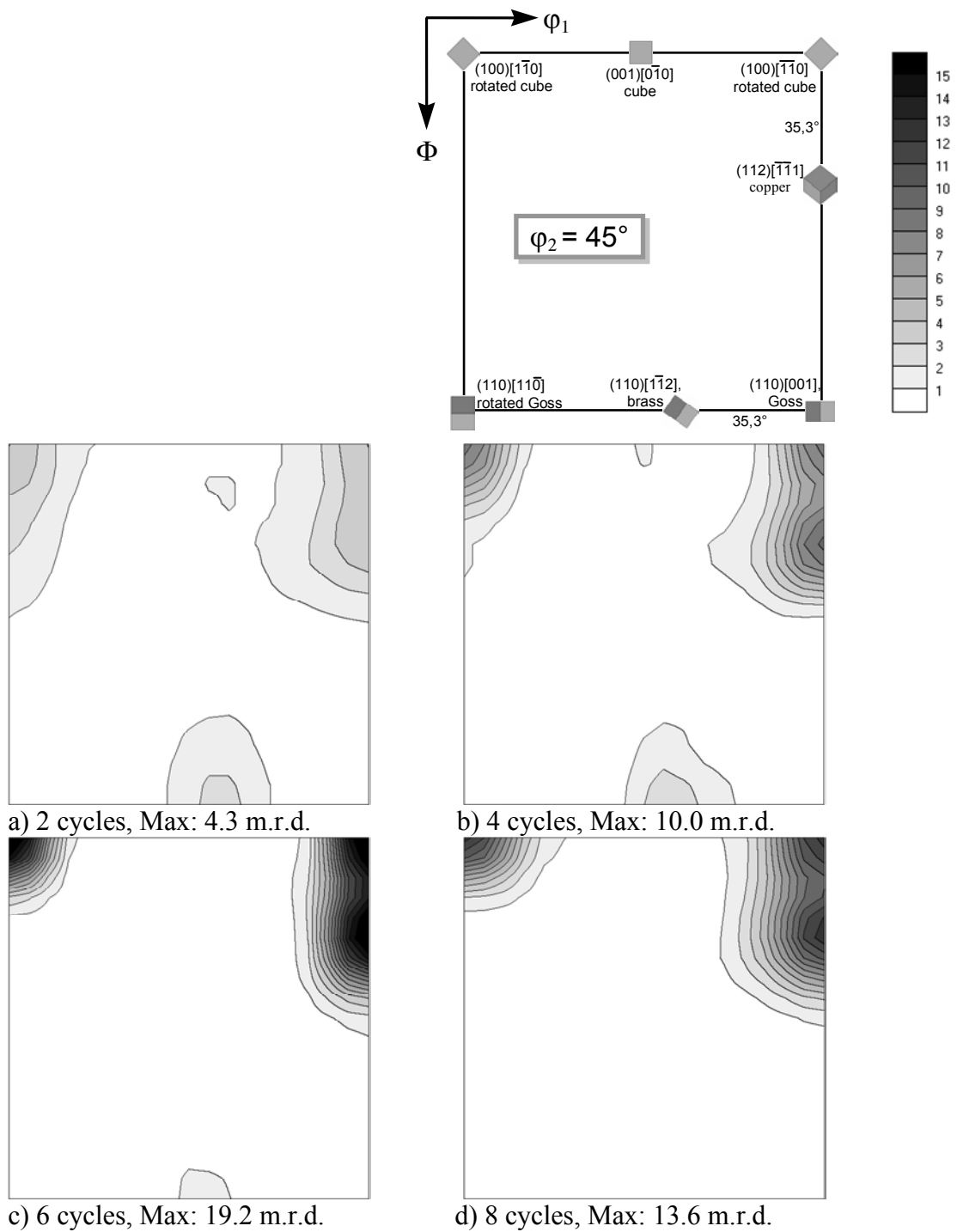
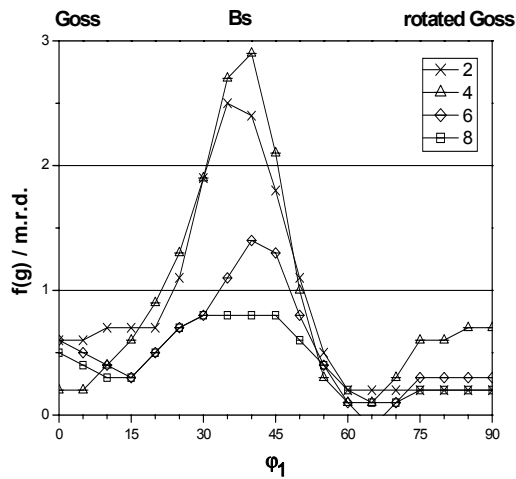
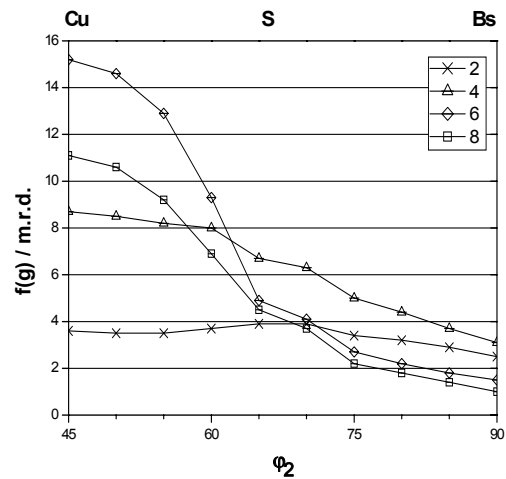


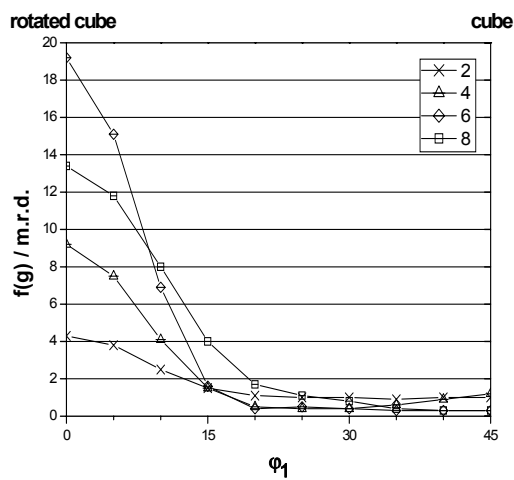
**Figure 2:** Texture of ARB AA1050 after (a) 2, (b) 4, (c) 6 and (d) 8 cycles displayed as ODF sections at  $\phi_2 = 45^\circ$ , intensities are given in multiples of a random distribution (m.r.d.). Keyfigure shows the position of the main texture components.



a)



b)



c)

**Figure 3:**  
Intensity along different fibres:  
(a)  $\alpha$ -fibre, (b)  $\beta$ -fibre and (c)  $\langle 100 \rangle$  ND-fibre.


## Acknowledgements

The ARB samples were kindly provided by Dipl.-Ing. I. Topic (Universität Erlangen).

## References

- [1] Valiev, R.Z., Estrin, Y., Horita, Z., Langdon, T.G., Zehetbauer, M., JOM 58 (2006) 33.
- [2] Höppel, H.W., May, J., Göken, M., Adv. Eng. Mat. 6 (2004) 219.
- [3] Tóth, L.S., Arruffat-Massion, R., Germain, L., Baik, S.C., Suwas, S., Acta Mater. 52 (2004) 1885.
- [4] Saito, Y., Utsunomiya, H., Tsuji, N., Sakai, T., Acta Mater. 47 (1999) 579.
- [5] Tsuji, N., Saito, Y., Utsunomiya, H., Tanigawa, S., Scripta Mater. 40 (1999) 795.
- [6] Huang, X., Tsuji, N., Hansen, N., Minamino, Y., Mater. Sci. Eng. A340 (2003) 265.
- [7] Dahms, M., Eschner, T., Quantitative Texturanalyse durch iterative Reihenzerlegung von Beugungs-Polfiguren (software manual) (1996).



	<b>EXPERIMENTAL REPORT</b>	<b>GeNF TEX-2</b>
<b>Texture investigation of magnesium alloys</b>		
<b>Proposer:</b>	<b>Tatiana Lychagina<sup>1</sup></b> , <sup>1</sup> Frank Lab of Neutron Physics, Joint Institute for Nuclear Research, Dubna, Russia	
<b>Co-Proposer(s):</b>	<b>Dmitry Nikolayev<sup>1</sup></b>	
<b>Experimental Team:</b>	<b>H.-G. Brokmeier<sup>2</sup>, W. M. Gan<sup>2</sup></b> <sup>2</sup> IWW-TEXMAT TU Clausthal, Geesthacht, Germany	
<b>User Group Leader:</b>	<b>A. Schreyer<sup>3</sup></b> , <sup>3</sup> GKSS Research Centre Geesthacht, Germany	
<b>Instrument Responsible:</b>	<b>H.-G. Brokmeier<sup>2</sup></b>	
<b>Date(s) of Experiment:</b>	6 <sup>th</sup> – 14 <sup>th</sup> September 2007	

## Objective

It is very important for industry to increase Mg alloy plasticity properties at room temperatures. The crystallographic texture affects the resulting plastic properties. The texture formation is defined by usage of different combination of thermomechanical treatments (different temperatures, different order of processing, etc.). The aim of proposed experiment is the investigation of the texture formation of Mg alloys (Mg-AZ31, Mg-AZ4.51). The motivation of usage of these alloys for our investigation is because they are most common, but still there are some open questions in their thermomechanical behaviour, their homogeneity and their anisotropic properties. The temperature and the degree of deformation could widely vary and this variations strongly influence resulting properties [1, 2]. The plastic properties of magnesium alloys are strongly depended on the crystallographic texture as demonstrated by Bohlen et al. [3] and Yi et al. [4]. That 's why it is very important to know orientation distribution for these materials. The alloys Mg-AZ4.51 and Mg-AZ31 were subjected to hot rolling at 420 °C, and warm rolling (start at 390 °C, finish at 200 °C). We had not investigated such combination of treatments (at first hot rolling, then warm rolling) for these alloys yet.

## Experimental

The texture of the samples was investigated by measuring the (002), (100), (101), (110) pole figures using the TEX-2 neutron diffractometer at the FRG-1 neutron source. It was measured four samples (two samples of the alloy Mg-AZ31 and two samples from alloy Mg-AZ4.51). All samples were prepared as the set of several sheets (width each of them is 1mm) to have a compact cube of about 2000 mm<sup>3</sup>. The preparation was very precisely so all sheet sections had identical sample orientation.

## Achievements and Main Results

It was measured four complete pole figures (PFs) for each sample (002), (100), (101), (110) (see Fig. 1). The all samples have rather strong texture (about 7 mrd in maximum on (002) for alloy Mg-AZ31 and 8.7/9.3 mrd on (002) for alloy Mg-AZ4.51). It could be concluded that the main texture character is axial.


On the basis of the measured pole figures it can be concluded that samples of the alloy Mg-AZ31 shows relatively homogenous texture. The another pair of samples (from alloy Mg-AZ4.51) has strong differences in the isolines shape for different samples, namely for the pole figure (101) maximum for one sample is symmetrical while for the other is not. Long axis of ellipsoidal isolines for minimum is oriented differently for the pole figures (100) and (110). Strong inhomogeneity motivates us for more thorough study of each piece that constituent a sample. The most suitable tool for that is the texture measurements by means of the hard X-rays.

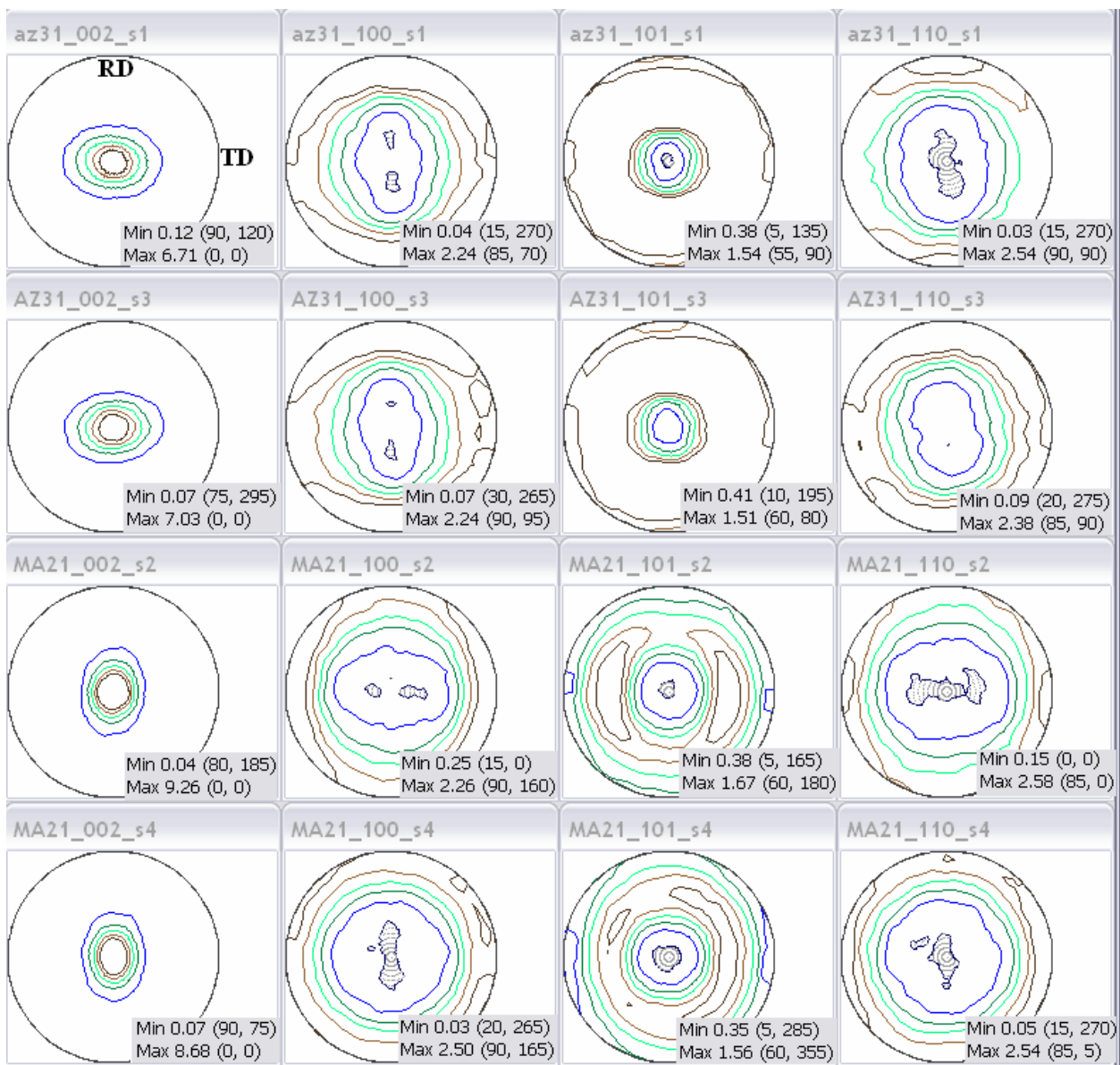


**Figure 1:** The experimental pole figures for two samples from alloy Mg-AZ31 (rows 1-2) and for two samples from alloy Mg-AZ4.51 (notation MA21) (rows 3-4). The position of sample coordinate system (rolling direction, transverse direction) is the same for all samples.

## References

- [1] Kochubey A.Ya., Serebryany V. N., Timofeev V. N. "TEM Investigation of Dislocations in Hot Deformed Mg-Al-Zn Alloy", Proc. FJH Symposium, School of Materials, University of Manchester, Manchester, 5th-7th Sept. 2006, Materials Sci. Forum Vol.550 (2007), pp. 259–264
- [2] Serebryany V. N., Kochubei A. Ya., Kurtasov S. F., Mel'nikov K.E. "Texture States of a Hot-Worked MA2-1 Magnesium Alloy", Russian Metallurgy (Metally), 2007, No 1, pp. 73–78
- [3] Bohlen J., Nürnberg M. R., Senn J. W., Letzig D., Agnew, S. "The texture and anisotropy of magnesium-zinc-rare earth alloy sheets, Acta Mat. Vol. 55 (2007), pp. 2101–2112
- [4] Yi S.-B., Davis C.H.J., Brokmeier H.-G., Bolmaro R. E., Kainer K. U., Homeyer J. "Deformation and Texture Evolution in AZ31 Magnesium Alloy during Uniaxial Loading, Acta Mat. Vol. 54 (2006), pp. 549–562
- [5] D. I. Nikolayev, T. A. Lychagina, A. V. Nikishin, V. V. Yudin, "Study of error distribution in measured pole figures", Solid State Phenomena Vol. 105, July 2005, Trans Tech Publications, pp. 77–82
- [6] D. I. Nikolayev, T. A. Lychagina, A. V. Nikishin, V. V. Yudin, "Investigation of measured pole figures errors", Materials Science Forum Vols. 495–497, Sep. 2005, Trans Tech Publications Proc. of ICOTOM 14, pp. 307–312

	<b>EXPERIMENTAL REPORT</b>	<b>GeNF TEX-2</b>
<b>Effect of texture on the damping behavior of the ECAPed AZ31 Mg alloy</b>		
<b>Proposer:</b>	<b>M.Y. Zheng<sup>1</sup>, K. Xiao<sup>1</sup>, K. Wu<sup>1</sup></b>	
<b>Co-Proposers:</b>	<sup>1</sup> School of Materials Science and Engineering, Harbin Institute of Technology, Harbin 150001, China <b>W. M. Gan<sup>1,2</sup>, H.-G. Brokmeier<sup>2</sup></b> <sup>2</sup> IWW-TEXMAT TU Clausthal, Geesthacht, Germany	
<b>Experimental Team:</b>	<b>W. M. Gan<sup>1,2</sup>, H.-G. Brokmeier<sup>2</sup></b>	
<b>User Group Leader:</b>	<b>A. Schreyer,</b> <sup>3</sup> GKSS Research Centre Geesthacht, Germany	
<b>Instrument Responsible:</b>	<b>H.-G. Brokmeier<sup>2</sup></b>	
<b>Date(s) of Experiment:</b>	4 <sup>th</sup> – 5 <sup>th</sup> April, 17 <sup>th</sup> – 18 <sup>th</sup> . August, 5 <sup>th</sup> – 12 <sup>th</sup> October 2007	

## Objective

Magnesium and its alloys are considered as high damping metals. In fact, damping capacity of Mg alloys depends on their chemical composition and microstructure, such as grain size and texture [1]. Therefore, it is necessary to investigate the damping capacity of Mg alloys having different composition and microstructure.

ECAP has been recognized as one of the most effective methods in producing bulk ultra-fine grained (UFG) materials with sub-microcrystalline structure for a wide range of materials, including magnesium alloys [2]. ECAP processed magnesium alloys, having different microstructure with conventional extruded or rolled magnesium alloy, exhibited high strength, high ductility as well as low temperature superplasticity due to the grain refinement and texture modification [3]. These novel microstructure obtained by ECAP may have a significant influence on the damping capacity of magnesium alloy. However, very few studies have been performed on the effect of ECAP on damping capacity of Mg alloys [4, 5]. In this research, the textures in as-extruded and EX+ECAPed AZ31 Mg alloys were measured, and the effect of texture on the damping capacity of the ECAPed magnesium alloy was analysed.

## Experiment

The material used in this investigation is commercial AZ31 magnesium alloy. The AZ31 ingot was hot extruded at 350 °C to give rectangular bars with 15 mm in thickness and 15 mm in width corresponding to a reduction ratio of 12:1. The extrusion rods were cut into 10×10×60 mm<sup>3</sup> rectangular billets for ECAP. The ECAP processing was conducted on the billets by the die with a channel angle of 90° using processing route B<sub>C</sub> and B<sub>A</sub>, respectively. The specimen was ECAP processed at 200 °C and 300 °C, respectively, up to 8 passes.

Texture measurements were carried out using neutron diffractometer TEX-2. Sample's coordination system is defined as shown in Fig.1. Four completed pole figures, i.e. (00.2), (10.0), (11.0), (10.1), were measured for the as-cast, as-extruded and EX+ECAPed AZ31 alloy.

## Achievements and Main Results

The pole figures of the as-extruded and as-ECAPed AZ31 alloy processed at 200 °C are shown in Figure 2. As shown in Figure 2 (a) and (b), the as-extruded AZ31 alloy exhibits an ED // <1010> fiber texture. ECAP can modify the texture in the magnesium alloy, and the textures formed in the ECAPed Mg alloy depend on the ECAP temperature, passes and route and subsequent treatment. As shown in Fig. 2 (c) and (d), after 6-pass ECAP at 200 °C, basal planes are inclined about 45° to the extrusion direction, and (1010) planes are parallel to the shear direction. After subsequent annealing, as shown in Fig. 2 (e) and (f), the texture keeps almost the similar except the higher intensity obtained in the as-annealed alloy.

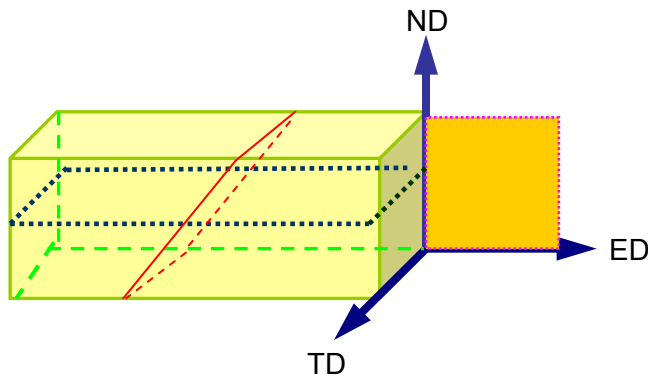


**Figure 1:**  
Definition of the coordination system for the texture measurement.

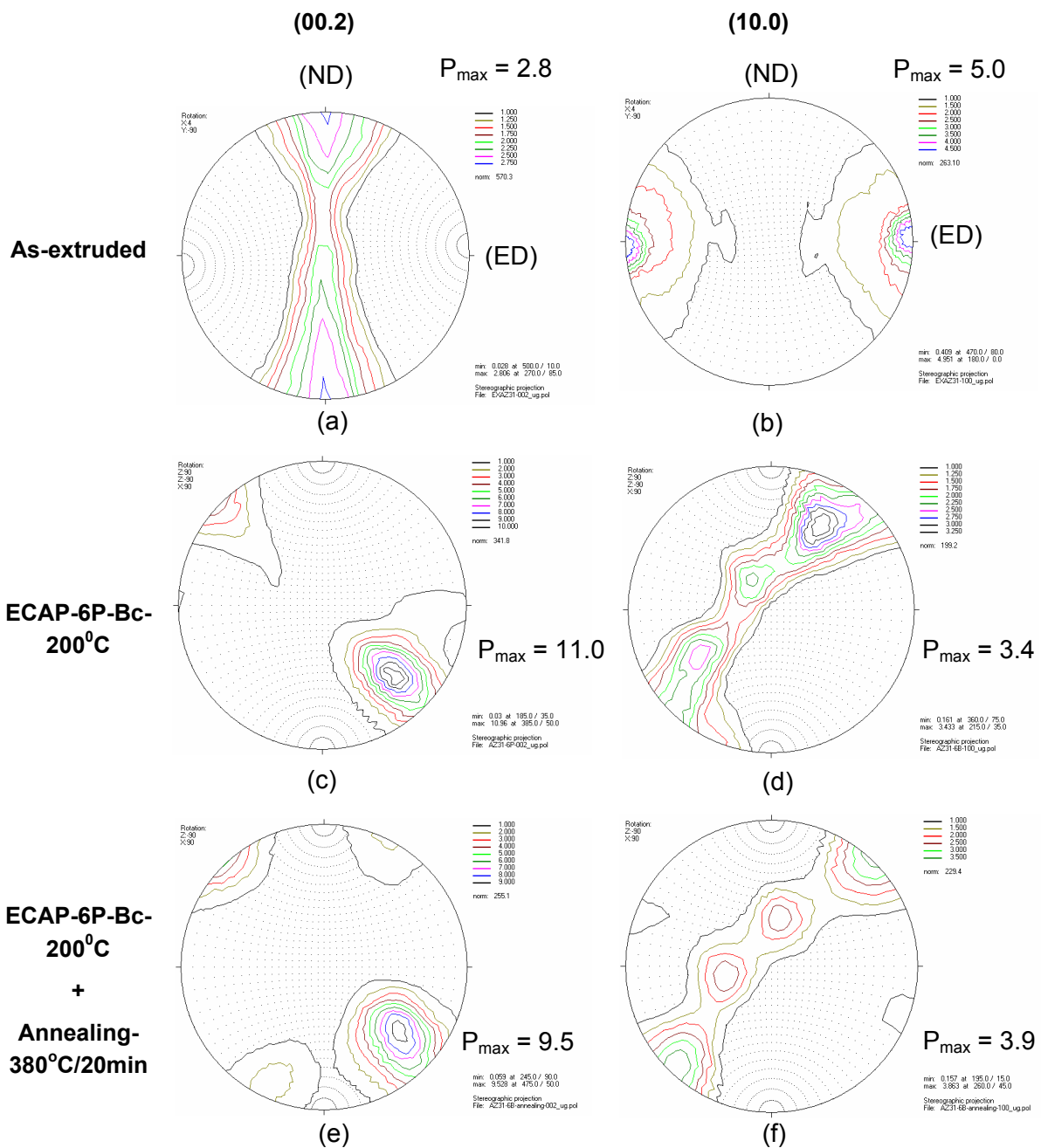


**Figure 2:** Pole figures of the AZ31 alloy: (a) and (b) as- extruded, (c) and (d) ECAPed at 200 °C for 6 passes using Bc route, (e) and (f) subsequently annealed at 380 °C for 20 min.

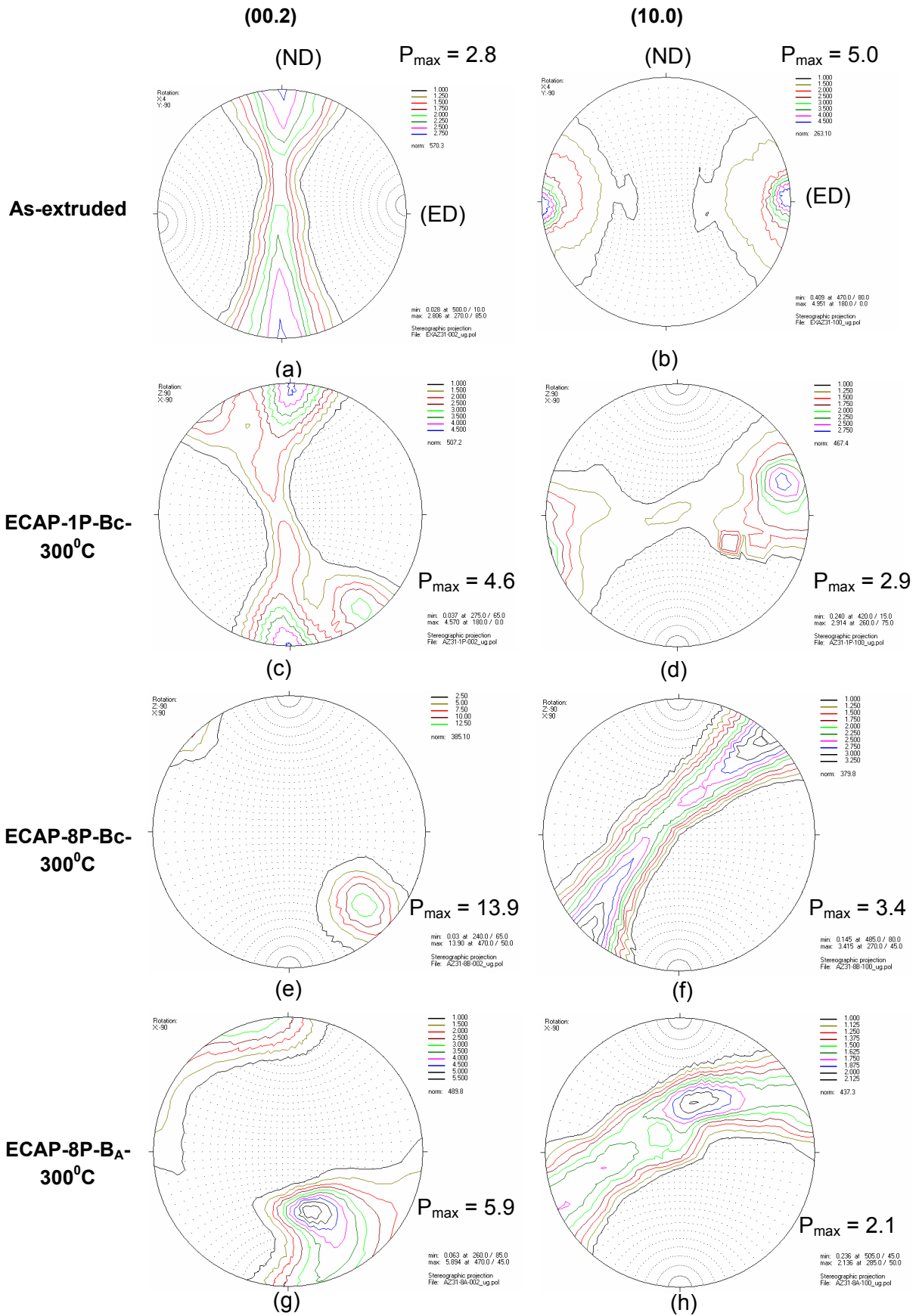



**Figure 3:** Pole figures of the AZ31 alloy. (a) and (b) as- extruded, (c) and (d) ECAPed at 300 °C for 1 pass using Bc route, (e) and (f) ECAPed at 300 °C for 8 passes using Bc route, (g) and (h) ECAPed at 300 °C for 8 passes using B<sub>A</sub> route.

## References

- [1] H. E. Friedrich, B. L. Mordike, *Magnesium Technology-Metallurgy, Design Data, Applications*. Springer-Verlag, Berlin, Heidelberg, 2006: 68–74
- [2] R. Z. Valiev, T.G. Langdon, *Progr. Mater. Sci.* 2006, 51: 881–981
- [3] M. Y. Zheng, S. W. Xu, X. G. Qiao, K. Wu, S. Kamado, Y. Kojima, H. G. Brokmeier. *Mater. Sci. Forum*, 2006, 503–504: 527–532
- [4] V. N. Chuvil'deev, T. G. Nieh, M.Y. Gryaznov, A. N. Sysoev, V. I. Kopylov. *Scr. Mater.*, 2004, 50: 861–865
- [5] M. Y. Zheng, X. S. Hu, S. W. Xu, X. G. Qiao, K. Wu, S. Kamado, Y. Kojima. *Mater. Sci. Forum*, 2007, 539–543: 1685–1690



	<b>EXPERIMENTAL REPORT</b>	<b>GeNF TEX-2</b>
<b>Texture measurements on ECAP deformed Al-Mg alloys</b>		
<b>Proposer:</b>	<b>Werner Skrotzki<sup>1</sup></b> Institut für Strukturphysik, Abteilung Metallphysik, Technische Universität Dresden, 01062 Dresden, Germany	
<b>Co-Proposer:</b>		
<b>Experimental Team:</b>	<b>W. M. Gan<sup>2</sup>, H.-G. Brokmeier<sup>2</sup>,</b> IWW-TEXMAT TU Clausthal, Geesthacht, Germany	
<b>User Group Leader:</b>	<b>A. Schreyer<sup>3</sup>,</b> <sup>3</sup> GKSS Research Centre Geesthacht, Germany	
<b>Instrument Responsible:</b>	<b>H.-G. Brokmeier<sup>2</sup></b>	
<b>Date(s) of Experiment:</b>	1 <sup>st</sup> – 4 <sup>th</sup> November 2007	

## Objectives

ECAP is at present one of the most promising techniques to produce bulk nanostructured or ultrafine-grained materials (UFG: grain size in the range of 100–1000nm) for structural applications. The process has received considerable attention in the last few years due to the advent of nano-technology, and it continues to receive attention of the scientific community due to its future industrial potential [1, 2]. In ECAP a billet is deformed in a narrow deformation zone at the plane of intersection of two die channels of equal area cross-section and the strain mode approximates closely to simple shear. As the overall billet geometry remains nearly constant during ECAP, multiple passes through the die are possible without any reduction in cross-sectional area. This allows materials to be deformed to very high plastic strains that cannot be readily obtained in more conventional processes, such as rolling. Large plastic deformation results in the development of texture, which will be demonstrated here for Al-Mg alloys. Special attention is focussed on the effect of Mg content. As has been determined by X-ray profile analysis, the highest Mg additions lead to a crystallite size and dislocation density of about 110 nm and  $5 \times 10^{14} \text{ m}^{-2}$ , respectively, yielding a Vickers hardness of 110 which is about a factor three higher than that of the coarse grained starting material [3].

## Experiment

The material used was produced by casting of 5N Al alloyed with different amounts of Mg (in wt.-%): 0.5, 1.0, 1.5, 2.0. To reduce small casting pores, the cast alloys were subjected to one ECAP pass and a subsequent recrystallization treatment at 673 K for 0.5 hours. For obtaining the UFG microstructure, eight ECAP passes using route B<sub>C</sub> (90° rotation between subsequent passes) were applied. The two channels of the ECAP die intersected rectangular with an outer curvature angle of 20°. Therefore, the equivalent strain imposed in each pass is about 1.05 [4]. The diameter and length of the cylindrical billets was 12 mm and 110 mm, respectively. Pressing was done with a velocity of 100 mm/min at room temperature using a lubricant containing ceramic particles.

Texture measurements were done by neutron diffraction on a rod section of 10 mm length taken from the middle part of the extruded billet. Because of their high penetration depth neutrons allow bulk texture measurements. The orientation distribution function (ODF) was calculated from the measured pole figures (111, 200, 220) by using LABOTEX software. Recalculated pole figures are projections in the ND-ED plane of the ECAP coordinate system.

## Achievements and Main Results

The shear process during ECAP produces a characteristic type of texture shown in Fig. 1. Due to the billet rotation of 90° between the passes the symmetry of the texture becomes

triclinic. Altogether, after eight ECAP passes using route B<sub>C</sub> the strength of texture is quite weak. However, there are some distinct changes of the intensity of certain ECAP texture components with increasing Mg content. A detailed analysis of the texture components with respect to intensity and deviation from ideal simple shear positions is in progress.

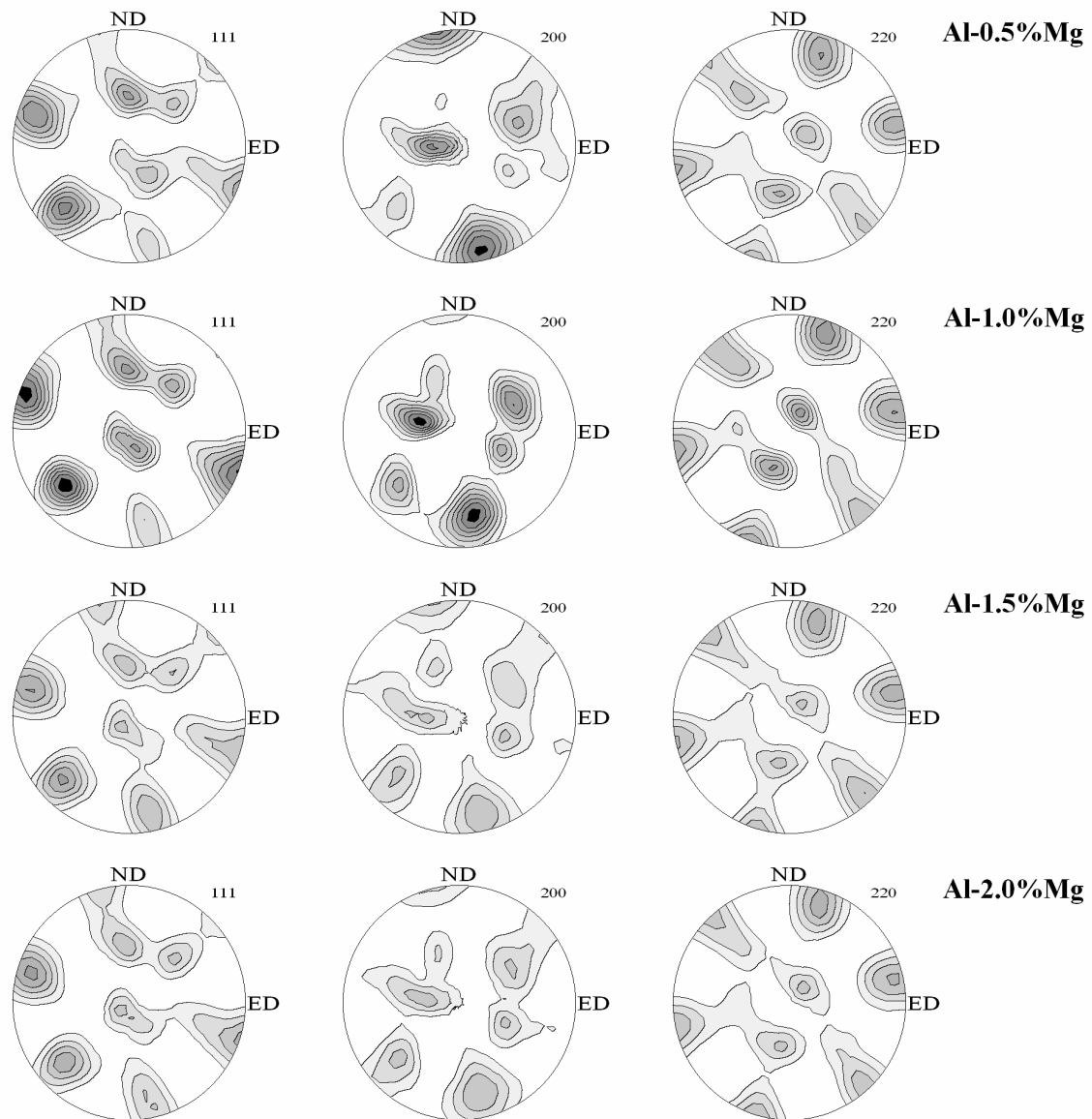


**Figure 1:** Recalculated (111), (200), (220) pole figures of Al alloyed with different amounts of Mg (in wt.-%): 0.5, 1.0, 1.5, 2.0 (intensity levels: 1.0, 1.3, 1.6, 1.9, 2.2, 2.5, 2.8 mrd, ND = normal direction, ED = extrusion direction).


### Acknowledgements

The ECAP samples were kindly provided by Dipl.-Ing. J. May, Universität Erlangen. Thanks are due to MSc R. Chulist for calculating the ODFs and T. Reiter for sample cutting.

### References

- [1] V. M. Segal, Mater. Sci. Eng. A 97 (1995), 157
- [2] R. Z. Valiev, Mater. Sci. Eng. A 234 (1997), 59
- [3] J. May, M. Dinkel, D. Amberger, H. W. Höppel, M. Göken, Metall. Mater. Trans. A 38 (2007), 1941
- [4] Y. Iwahashi, J. Wang, Z. Horita, M. Nemoto, T. G. Langdon, Scripta Mater. 35 (1996), 143



	<b>EXPERIMENTAL REPORT</b>	<b>GeNF TEX-2</b>
<b>Investigation on the texture gradient in the equal channel angular pressed (ECAP) pure Mg</b>		
<b>Proposer:</b>	<b>W. M. Gan<sup>1,2,3</sup>, M.Y. Zheng<sup>1</sup>, X. J. Wang<sup>1</sup>, H. Chang<sup>1</sup>, K. Wu<sup>1</sup></b> <sup>1</sup> Harbin Institute of Technology, Harbin, P. R. China	
<b>Co-Proposer(s):</b>	<b>H.-G. Brokmeier<sup>3</sup></b> <sup>3</sup> IWW-TEXMAT TU Clausthal, Geesthacht, Germany	
<b>Experimental Team:</b>	<b>W.M. Gan<sup>1,2,3</sup></b>	
<b>User Group Leader:</b>	<b>A. Schreyer<sup>2</sup>, <sup>2</sup>GKSS Research Centre Geesthacht, Germany</b>	
<b>Instrument Responsible:</b>	<b>H.-G. Brokmeier<sup>3</sup></b>	
<b>Date(s) of Experiment:</b>	13 <sup>th</sup> – 27 <sup>th</sup> October 2007	

## Objective

Equal channel angular pressing (ECAP) has been proved to be a promising severe plastic deformation technique which can effectively produce ultra-fined or nano-grained various bulk materials [1]. Microstructural homogeneity of the ECAPed materials is more important when considering the practical applications of this technique. Unique textures developed during ECAP have been increasingly investigated. Careful analysis of the texture makes it possible to estimate the mechanism responsible for the progress of plastic straining during ECAP. Due to the fact that some texture effects are still not understood, local texture measurements have been carried out firstly to see in-homogeneities during the ECAP process and secondly to find out way experimental and theoretical textures differ.

## Experiment

In order to get the local texture not only at the final ECAPed sample, the ECAP process was stopped after 50 % deformation. Thus the pure Mg sample consists of a first part from the ingoing channel, a second part directly from the 90° die angle area and a third part from the quadratic outgoing channel after shearing. The bulk texture over the whole sample cross section as well as a first part of local texture measurements were carried out by neutron diffraction with a Cu monochromator at TEX-2. Four pole figures (00.2), (10.0), (10.1) and (11.0) were measured.

## Achievements and Main Results

Figure 1 shows the (00.2) and (10.0) pole figures of the positions 0 to 7 which designate the corresponding regions in the ECAPed Mg sample as schematic shown in the top right. The initial as-extruded fiber texture was started to rotated from position 6 and a second shearing point occurred in (00.2) pole figure in position 0. At the deformation regions 1, 2, 3 and 4, there is an obvious change of the texture from position 1 to 4, 2 to 3, which indicates the shearing plane rotate from about 45° to 15°; one also can see that the local resolution is not sufficient to describe the texture gradient between these four positions. In position 5 we obtain the typical ECAPed texture as everyone reported, but not the same as the deformation region. Position 5 should include the texture information from positions 2 and 3, which can be further analyzed by hard x-ray. It is interesting to find that another weak shearing point occurred at position 7, which should be due to the friction effect of the channels.


Hence, local texture analysis on the half-ECAPed Mg can in detail illustrate the deformation history during ECAP processing, and the texture is still inhomogeneous after ECAP processing.

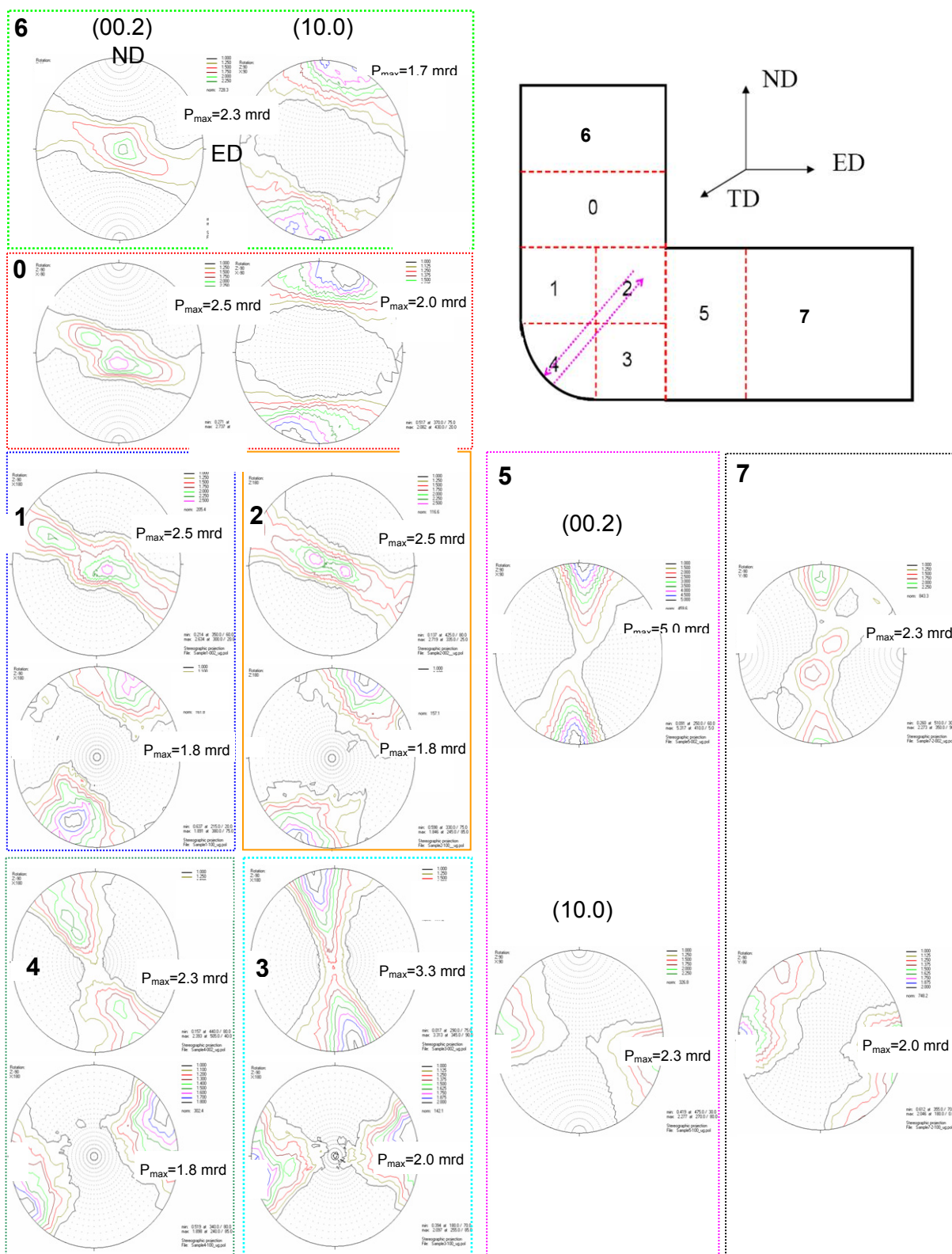


**Figure 1:** (00.2) and (0.0) pole figures of the different positions 0 to 7 in the ECAPed Mg corresponding to the top right schematic picture (Contour levels= 1.0, 1.25, 1.5, ... mrd (multiples of random diffraction)).

## Reference

- [1] Valiev R. Z.; Langdon T.G.; Principles of equal-channel angular pressing as a processing tool for grain refinement, Progress in Materials Science 51 (2006), 881–981

	<b>EXPERIMENTAL REPORT</b>	<b>GeNF TEX-2</b>
<b>Texture Development in AZ91 alloy and SiCp/AZ91 composites under extrusion processing</b>		
<b>Proposer:</b>  <b>Co-Proposer(s):</b>	<b>X. J. Wang<sup>1</sup>, W.M. Gan<sup>1,2, 3</sup>, M.Y. Zheng<sup>1</sup>, K. Wu<sup>1</sup>, H. Chang<sup>1</sup></b> <sup>1</sup> Harbin Institute of Technology, Harbin, P. R. China <b>H.-G. Brokmeier<sup>2, 3</sup></b> <sup>2</sup> GKSS Research Centre Geesthacht, Germany <sup>3</sup> IWW-TEXMAT TU Clausthal, Geesthacht, Germany	
<b>Experimental Team:</b> <b>User Group Leader:</b> <b>Instrument Responsible:</b>	<b>W. M. Gan<sup>1,2</sup>, H.-G. Brokmeier</b> <b>A. Schreyer<sup>2</sup></b> <b>H.-G. Brokmeier</b>	
<b>Date(s) of Experiment:</b>	1 <sup>st</sup> – 7 <sup>th</sup> May 2007	

## Objective

Particulate reinforced magnesium matrix composites (PRMgCs) have many advantages over monolithic Mg alloys, such as high specific strength and stiffness, high elastic modulus, increased creep and wear resistances [1, 2]. However, PRMgCs have low ductility due to the brittleness of the coarse second phases and their inhomogeneous distribution in matrix alloy. Microstructures must be optimized to develop high performance PRMgCs. Hot extrusion is a traditional processing which can effectively improve the mechanical properties of various materials. Current study was initiated to investigate the influences of SiC particulate on the development of texture under different extrusion conditions (temperature and ratio).

## Experiment

SiC-PRMgCs with different particle size and volume fraction have been fabricated by a high effective stir casting technique. The composites were extruded at different extrusion temperatures and ratios. Texture measurements were carried out by neutron diffraction with a Cu monochromator at TEX-2.

## Achievements and Main Results

The pole figures of composites extruded at different temperatures are shown in Figure 1. It is very difficult to measure the Mg (00.2) pole figure of extruded composites because of an overlap with a SiC diffraction peak. The orientation density of (10.0) pole figure is increased with extrusion temperature increasing. In Figure 2 one can also see a slight decrease of the orientation density of the (10.0) pole figure with increasing extrusion ratio which is due to the effect of SiC. But the (10.1) don't vary with extrusion ratio. The intensities of both (10.0) and (10.1) pole figures of 10 $\mu$ m10% composite are the highest among the composites with different particle sizes, as shown in Figure 3. But the orientation density of the (10.0) pole figure is decreasing and the orientation density of the (10.1) pole figure is increasing with increasing SiC volume fraction. Figure 5 indicates that texture intensity decreases with the increase of volume fraction of reinforced phase, which has been reported by many researches [2, 3]. In general, it has to be noticed that the texture sharpness of SiC-PRMgCs is much lower than for alloys due to the existence of SiC.

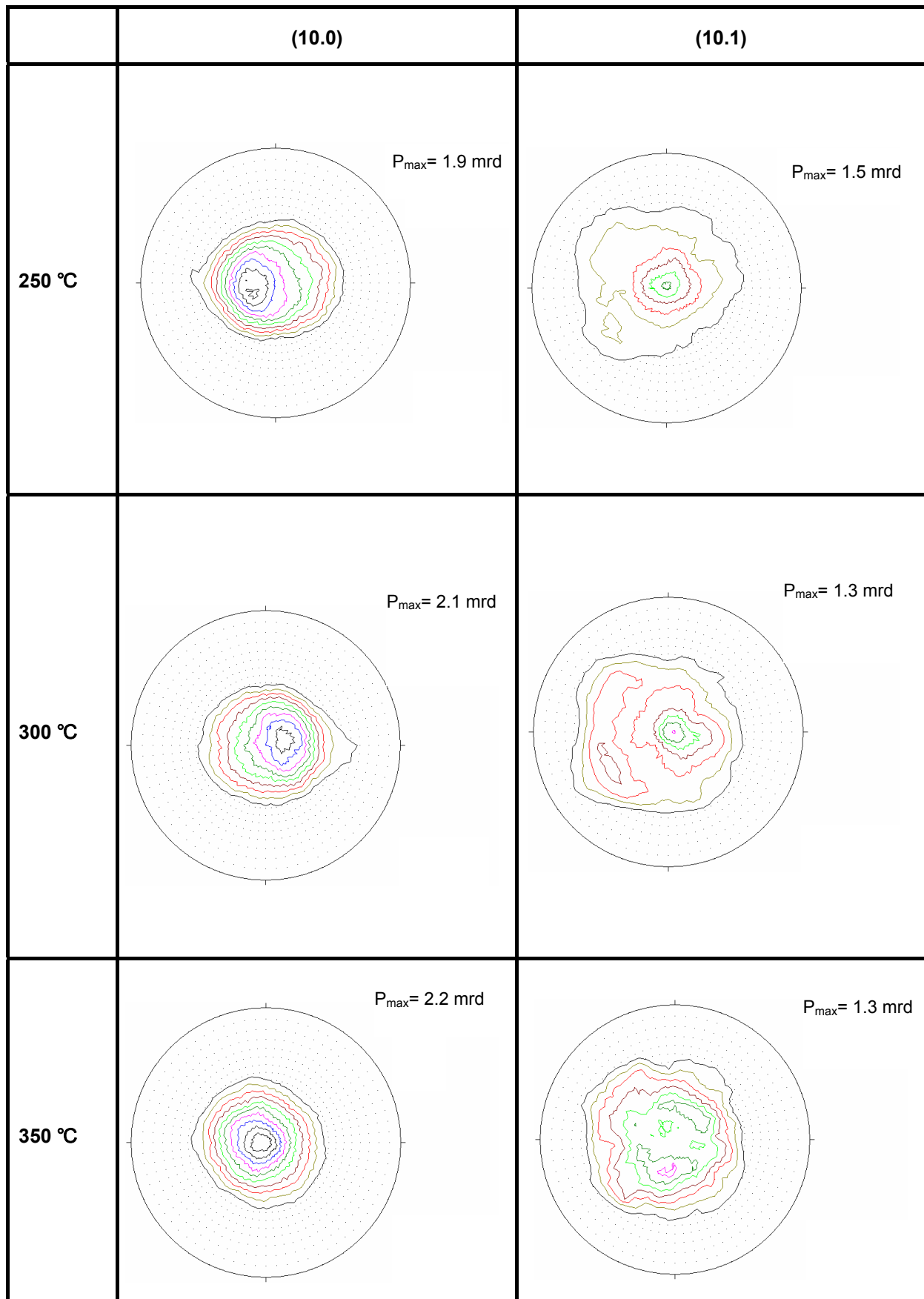


**Figure 1:** (10.0) and (10.1) pole figures of 10 $\mu$ m10% composites extruded at different temperatures (extrusion ratio of 12:1), (Contour levels= 1.0, 1.1, 1.2, 1.3 ..., mrd (multiples of random diffraction)).

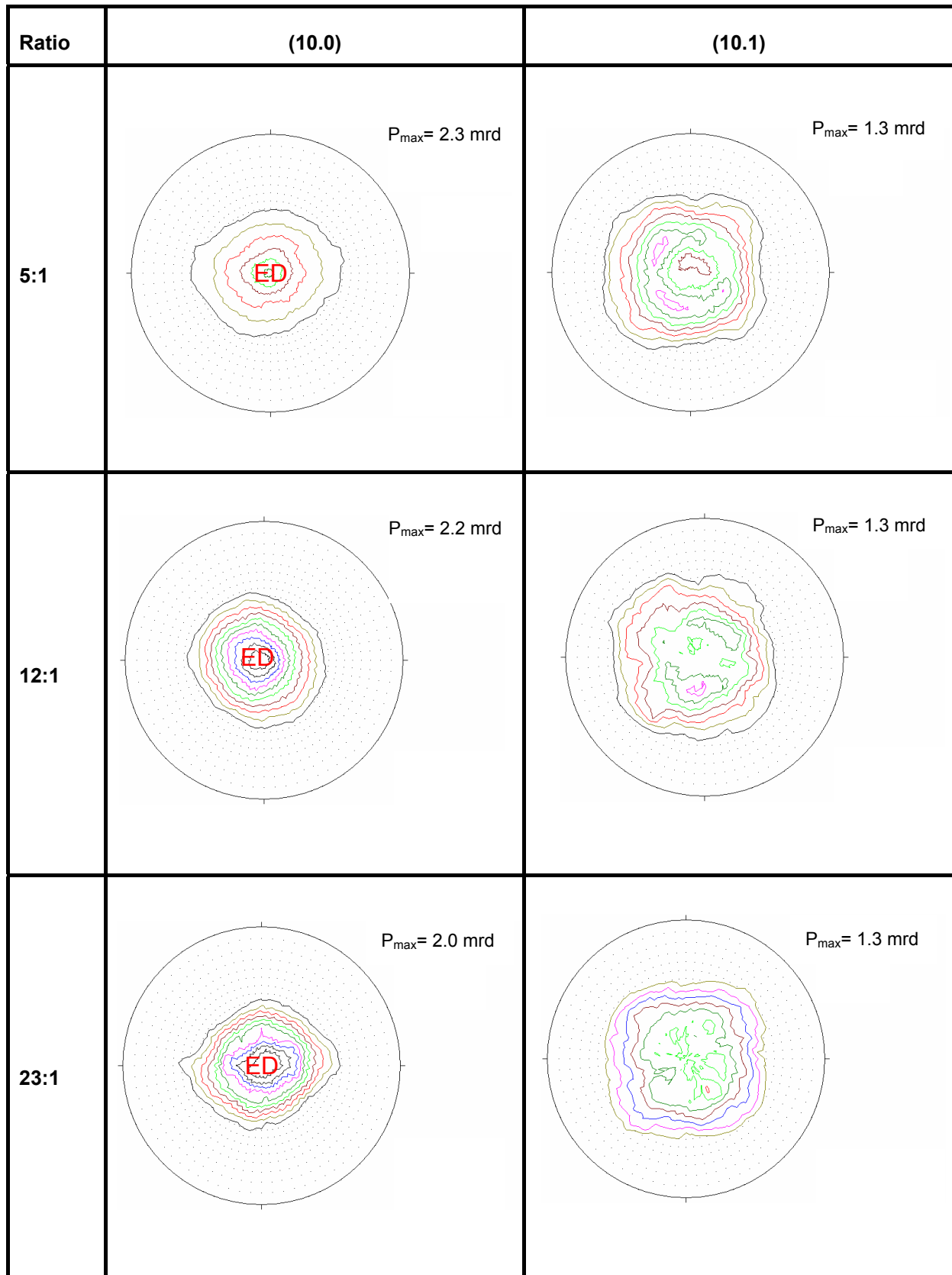


**Figure 2:** (10.0) and (10.1) pole figures of 10 $\mu$ m10% composites extruded at different ratios (extrusion temperature at 350 °C), (Contour levels = 1.0, 1.1, 1.2, 1.3 ...mrd).

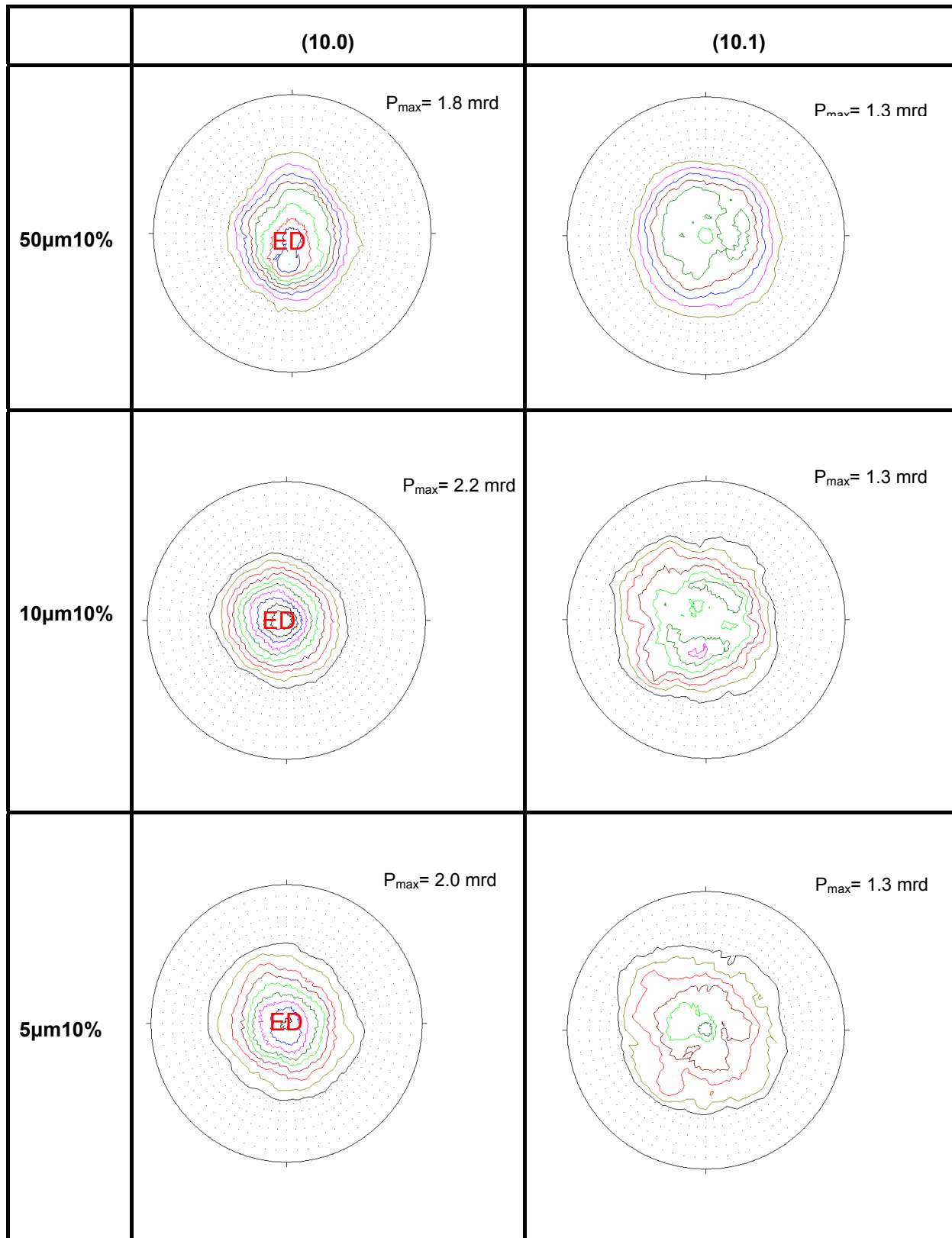


**Figure 3:** (10.0) and (10.1) pole figures of the as-extruded composites with different particle sizes (extrusion temperature at 350 °C and ratios of 12:1), (Contour levels = 1.0, 1.1, 1.2, 1.3 ... mrd).

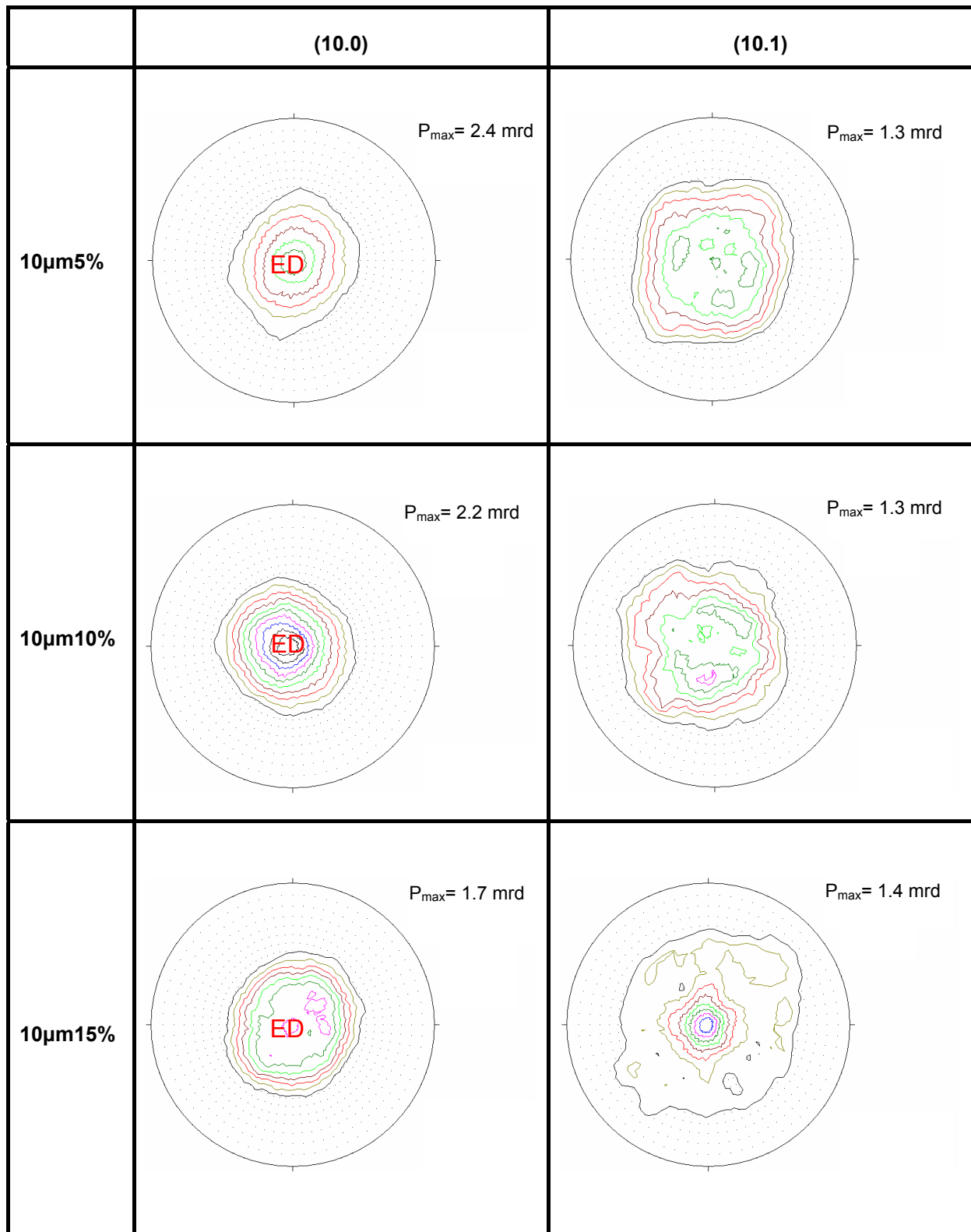



**Figure 4:** (10.0) and (10.1) pole figures of as-extruded composites with different volume fraction (extrusion temperature at 350 °C and ratios of 12:1), (Contour levels = 1.0, 1.1, 1.2, 1.3 ... mrd).

### References

- [1] K. F. Ho, M. Gupta, T. S. Srivatsan. Mater. Sci. & Eng. 2004, A369 (1-2): 302–308
- [2] S. Seshan, M. Jayamathy, S. V. Kailas, T. S. Srivatsan. Mater. Sci. & Eng. A. 2004, 363 (1-2): 345–351
- [3] H. Ferkel, B. L. Mordike. Mater. Sci. & Eng. A. 2001, 298 (1-2): 193–199





	<b>EXPERIMENTAL REPORT</b>	<b>GeNF TEX-2</b>
<b>Texture development of Mg AZ-80 and Mg-ZK60 extruded at different temperatures</b>		
<b>Proposer:</b>	<b>Muhammad Shahzad<sup>1</sup>, L. Wagner<sup>1</sup>, H.-G. Brokmeier<sup>1</sup></b> <sup>1</sup> Institute of Material Science and Engineering – TEXMAT – Clausthal University of Technology	
<b>Experimental Team:</b>	<b>W. M. Gan, B. Schwebke<sup>2</sup></b> <sup>2</sup> IWW-TEXMAT TU Clausthal, Geesthacht, Germany	
<b>User Group Leader:</b>	<b>A. Schreyer<sup>3</sup></b> , <sup>3</sup> GKSS Research Centre Geesthacht, Germany	
<b>Instrument Responsible:</b>	<b>H.-G. Brokmeier<sup>1</sup></b>	
<b>Date(s) of Experiment:</b>	25 <sup>th</sup> – 26 <sup>th</sup> April, 30 <sup>th</sup> April – 3 <sup>rd</sup> May 2007	

### Objective

It is known, that the crystallographic texture plays an important rule for the anisotropy of materials properties in Mg-alloys. Intense investigations were carried out worldwide to overcome this problem, because in practical application different behavior in case of a crush due to the strain direction is unwanted. Of basic interest is the investigation of Mg-alloys with optimized properties. Two important points are the grain size and the grain size distribution. Grain refinement can be done by severe plastic deformation (equal channel angular pressing or accumulative roll bonding) and by alloying elements to form precipitations. An earlier study performed to observe the effect of extrusion temperature on texture showed that ZK60 alloy results in stronger texture after extrusion than AZ80 alloy. Present study deals with the effect of extrusion ratio on texture evolution.

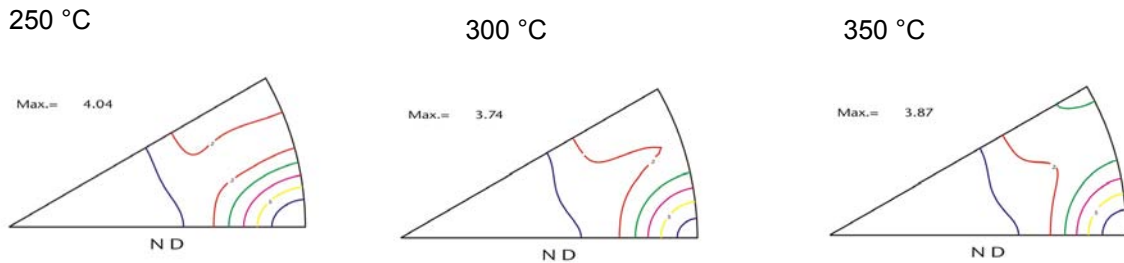
### Samples and Experiment

Ingot material with coarse AZ80 and ZK60 (~100 µm) was hot extruded by indirect extrusion. An extrusion ratio of 13 was realized in comparison to previously studied 46. To study the extrusion temperature on the final texture, the ingots were preheated at different temperatures, 250, 300 and 350 °C. Thereafter, neutron test samples were cut from each rod, so that cylindrical samples were obtained for a global texture measurement of the averaged crystallographic texture of each cylinder. The instrument TEX-2 at the FRG-1 was adjusted in a way, so that no overlapping reflections occur. The wavelength was 1.24 Å obtained by a graphite monochromator. According to a neutron flux of  $1 \times 10^6$  n/cm<sup>2</sup>sec, the total counting time for one sample was about 18h. For each sample four pole figures were measured, (10.0), (00.2), (10.1) and (11.0), to calculate the orientation distribution function (ODF). A windows PC based program of the iterative series expansion method was used for ODF-calucaltion.

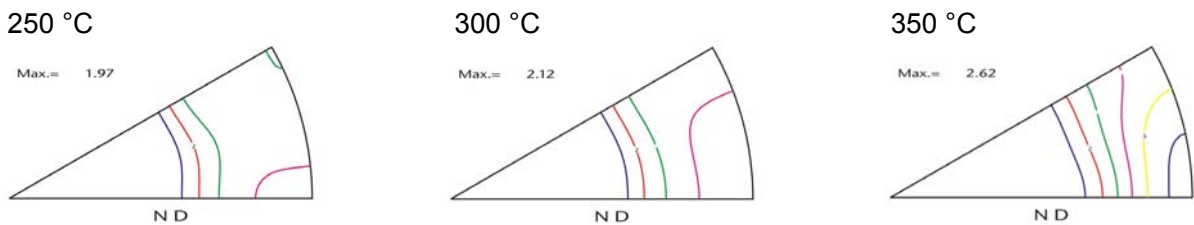
### Achievements and Main Results

Fig. 1 shows the inverse pole figures in the extrusion direction (ED) as a function of the extrusion temperature, ratio for both alloys. In all cases the main texture component is <10.0> fibre parallel to the extrusion direction, which is generally observed in extruded Mg. Independent on the extrusion conditions, AZ80 samples show always weaker texture than ZK60. Moreover, the strengthening of <11.0> parallel to the ED is clearly shown with increasing the extrusion temperature; this strengthening can also be expressed as spreading of the <10.0> component into <11.0> component. The appearance of <11.0> fibre after extrusion of Mg alloys indicates that the amount of the dynamic recrystallized grains increases with increase

of extrusion temperature. Further work underway to explain the difference of the texture, in quantitative as well as qualitative sense, between AZ80 and ZK60 samples, e.g. detailed investigations on the characteristics and vol. fraction of precipitates and the grain structure (vol. fraction of long extended grains and fine equiaxed-grains).



**Figure 1a:** Inverse pole diagram of AZ80 ER13 at 250 °C, 300 °C and 350 °C,




**Figure 1b:** Inverse pole diagram of AZ80 ER46 at 250 °C, 300 °C and 350 °C,

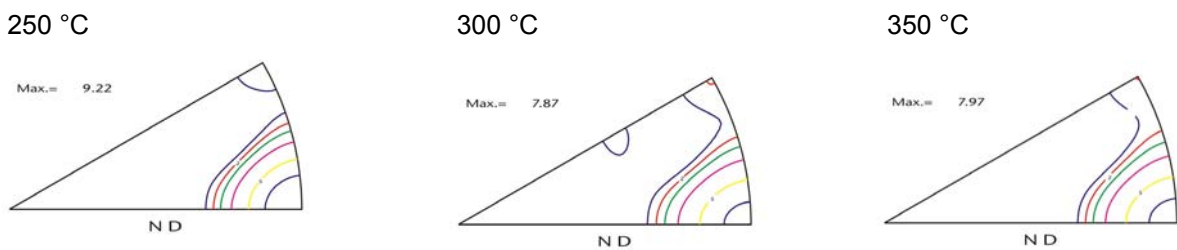


**Figure 1c:** Inverse pole diagram of ZK60 ER13 at 250 °C, 300 °C and 350 °C,

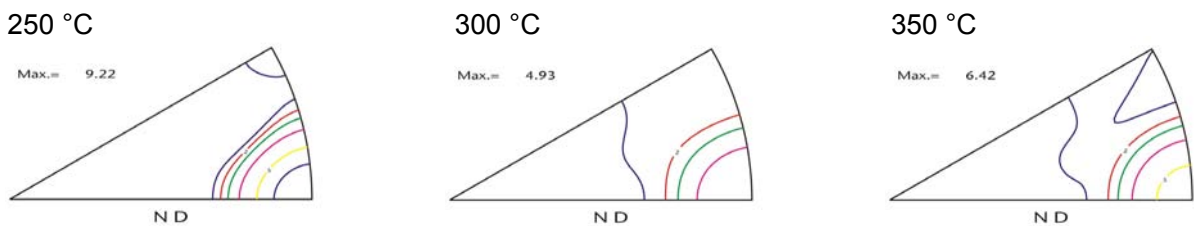


**Figure 1d:** Inverse pole diagram of ZK60 ER46 at 250 °C, 300 °C and 350 °C.

	<b>EXPERIMENTAL REPORT</b>	<b>GeNF TEX-2</b>
<b>Cast and rolling textures of NiMnGa alloys</b>		
<b>Proposer:</b>	<b>Werner Skrotzki<sup>1</sup></b> <sup>1</sup> Institut für Strukturphysik, Abteilung Metallphysik, Technische Universität Dresden, 01062 Dresden, Germany	
<b>Co-Proposer:</b>	<b>Robert Chulist<sup>1</sup></b>	
<b>Experimental Team:</b>	<b>Heinz-Günter Brokmeier<sup>2</sup></b> <sup>2</sup> Institut für Werkstoffkunde und Werkstofftechnik, TU Clausthal	
<b>User Group Leader:</b>	<b>H.-G. Brokmeier</b>	
<b>Date(s) of Experiment:</b>	16 <sup>th</sup> – 19 <sup>th</sup> July, 19 <sup>th</sup> – 23 <sup>rd</sup> August 2007	

## Objectives

NiMnGa alloys close to the stoichiometric composition Ni<sub>2</sub>MnGa belong to the quite new family of ferromagnetic shape memory alloys. These alloys are characterized by magnetically induced reorientation (MIR) resulting from the motion of twin boundaries under the influence of a magnetic field [1, 2]. Plastic deformation of NiMnGa single crystals by twin boundary motion leads to a maximum magnetic field induced strain (MFIS) of about 10 %. To our knowledge, until now MFIS has not been reported for NiMnGa polycrystals. However, since for broad technical applications growth of single crystals is quite time consuming and cost intensive it is necessary to investigate polycrystalline samples on their suitability for MFIS. To approach MFIS of single crystals the crystallographic texture of polycrystalline samples is of particular concern. Thus, the present work focuses on texture analyses of NiMnGa polycrystals fabricated with two different techniques: directional solidification and plastic deformation by hot rolling. To examine the texture of coarse grained NiMnGa alloys in a statistically relevant way diffraction of neutrons has been applied. The texture results are discussed with respect to the material, processing and phase transformations.

During cooling from high temperatures NiMnGa alloys experience different phase transitions, from B2 (cubic) via L2<sub>1</sub> (cubic, austenite) to martensitic structures (7M modulated, orthorhombic, space group Fmmm; 5M modulated and non-modulated, both tetragonal, space group I4mmm) [3–5]. The martensitic crystal structures in NiMnGa are strongly composition dependent [6–8]. In the hot rolled alloy investigated here 7M and NM martensitic structures have been observed simultaneously. In general, the phase transformations from austenite to martensite are characterized by specific orientation relationships with some variants being preferred.

## Experiment

The two polycrystalline samples studied were fabricated by directional solidification (Ni<sub>48</sub>Mn<sub>30</sub>Ga<sub>22</sub>) and hot rolling (Ni<sub>50</sub>Mn<sub>30</sub>Ga<sub>20</sub>). The martensitic transition for Ni<sub>48</sub>Mn<sub>30</sub>Ga<sub>22</sub> takes place at a temperature of -5–5 °C, that means at room temperature the alloy is in the austenitic state, and for Ni<sub>50</sub>Mn<sub>30</sub>Ga<sub>20</sub> at 90–100 °C. Directional solidification was carried out under Ar atmosphere. A prealloy was prepared by induction melting of pure elements (Ni 99.98, Mn 99.8, Ga 99.999) [9]. The casting process was performed in an Indrudet S investment casting machine followed by furnace-cooling to room temperature. The cast sample

had a diameter and length of 10 mm and 50 mm, respectively. Coarse columnar grain growth was achieved by using a hot mould with a cooled copper plate at the bottom. The mould was heated in a separate furnace to a temperature close to melting. The cylindrical sample cut from the cast ingot above about 1 cm from the bottom had a diameter and height of 8 mm and 15 mm, respectively. The second sample was plastically deformed by hot rolling. The ingot (7.9 x 11.9 x 44 mm<sup>3</sup>) canned in steel, was rolled at a temperature of 1000 °C up to 50 % reduction and then air-cooled to room temperature.

The texture of the two samples was measured by neutron diffraction at GKSS Research Centre Geesthacht, Germany. Due to the high penetration depth of neutrons, texture measurements with this radiation in transmission allows for collecting orientation data from a large sample volume, i.e. with a good grain statistics. Due to the fact that the rolled sample consists of more than one phase, some diffraction peaks from different phases may overlap. Therefore, the orientation distribution functions (ODF) were only calculated with the measured pole figures belonging to non-overlapping peaks. With the ODF all pole figures desired can be recalculated. Processing of the texture data was done with the Labotex software.

### Achievements and Main Results

The directionally solidified sample is characterized by long columnar grains with a width of about 0.5 mm. The austenitic phase has a strong  $\langle 100 \rangle$  fibre texture around the growth direction (GD) (Fig. 1).

The microstructure of the hot rolled alloy is recrystallized with an equiaxed grain size of about 400  $\mu\text{m}$ . Neutron diffraction shows that the polycrystal investigated simultaneously contains two martensitic structures, 7M and NM. The texture of both phases investigated by neutron diffraction is a weak  $\{111\}\langle 112 \rangle$  rolling texture (Figs. 2, 3). It has been formed during hot rolling in the B2 phase field.

The  $\langle 100 \rangle$  fibre texture existing in the directionally solidified NiMnGa alloy is typical for cast cubic crystals with the  $\langle 100 \rangle$  fibre axis aligned along the temperature gradient determining GD [10].

The texture of the hot rolled alloy most probably has been produced by dynamic recrystallization in the B2 field. It is a typical recrystallization texture of body-centred cubic metals [11]. No obvious variant selection took place during phase transformation from the cubic L2<sub>1</sub> phase to the martensitic phases.

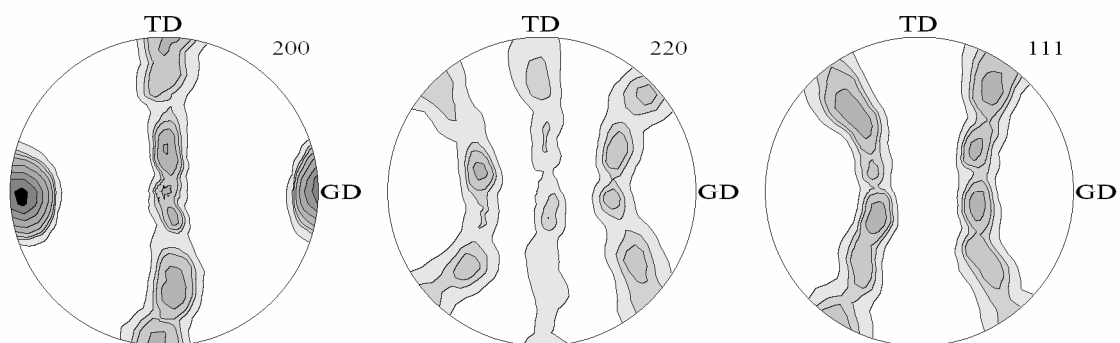


**Figure 1:**  $\{200\}$ ,  $\{220\}$ ,  $\{111\}$  pole figures of the austenitic phase in the directionally solidified sample (intensities: 1.0, 2.0, 2.5, 3.3, 4.9, 7.3, 9.6, 12.0 mrd, GD = growth direction, TD = transverse direction).

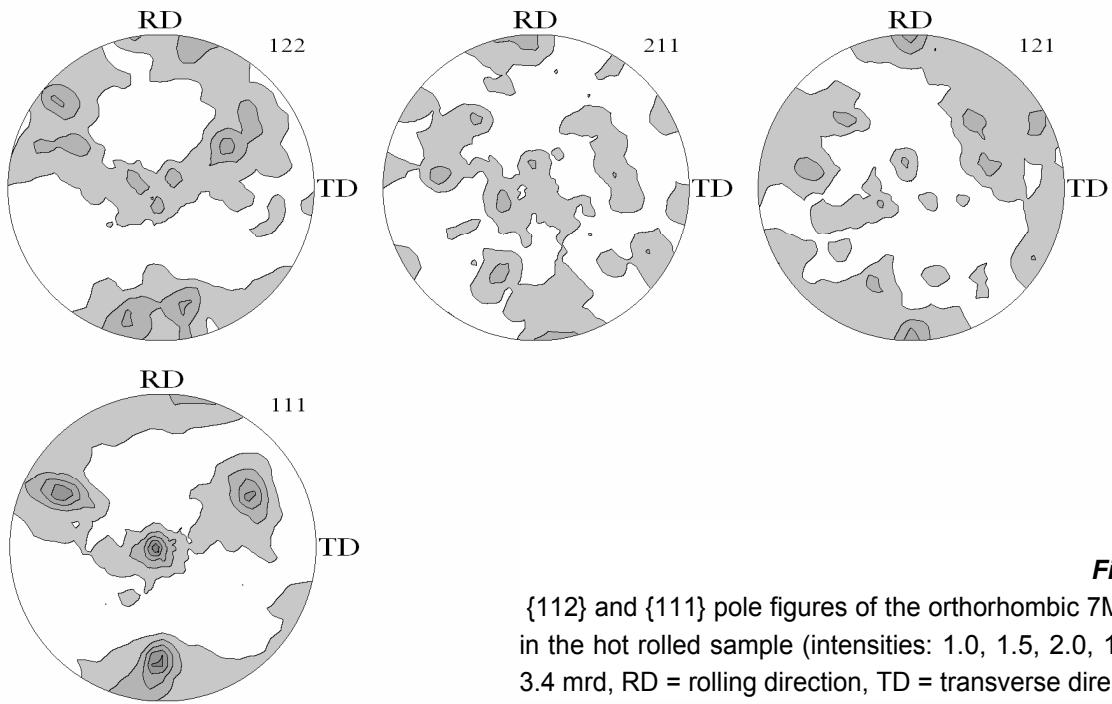


**Figure 2:**  $\{112\}$  and  $\{111\}$  pole figures of the orthorhombic 7M phase in the hot rolled sample (intensities: 1.0, 1.5, 2.0, 1.5, 3.0, 3.4 mrd, RD = rolling direction, TD = transverse direction).

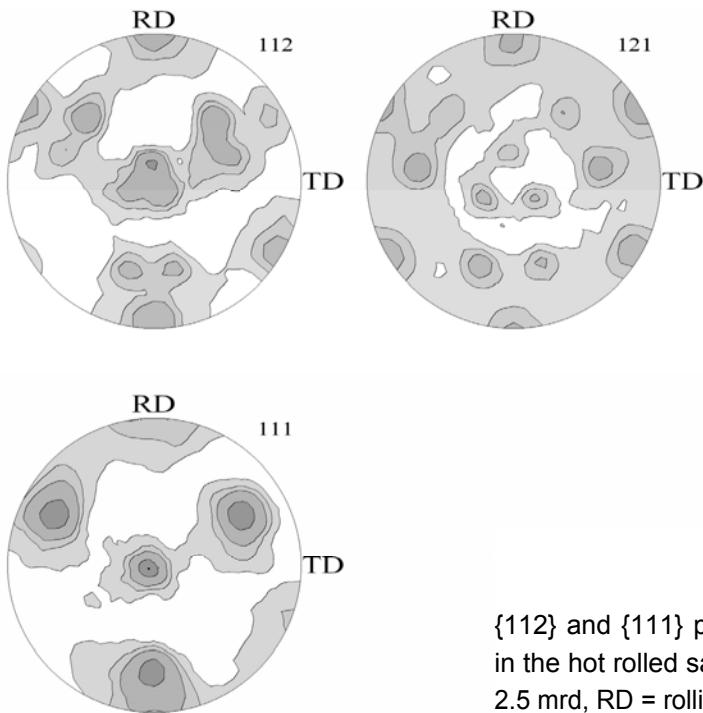



**Figure 3:**  $\{112\}$  and  $\{111\}$  pole figures of the tetragonal NM phase in the hot rolled sample (intensities: 1.0, 1.3, 1.6, 1.9, 2.2, 2.5 mrd, RD = rolling direction, TD = transverse direction).

### Acknowledgements

The work has been carried out within the priority program SPP 1239 “Magnetic shape Memory: Change of microstructure and shape of solid materials by external magnetic fields” of the German Research Society (DFG) under contract Sk 21/22-1. Thanks are due to H.-T. Reiter for sample cutting.

## References

- [1] Müllner, P., Chernenko, V. A., Wollgarten, M., Kosterz, G., Appl. Phys. Lett. 92 (2002) 6708
- [2] Müllner, P., Chernenko, V. A., Kosterz, G., J. Magn. Magn. Mater. 267 (2003) 325
- [3] Chernenko, V. A., Scripta Mater. 40 (1999) 523
- [4] Ullakko, K., Huang, J. K., Kantner, C., Kokorin, V. V., O'Handley, R.C., Appl. Phys. Lett. 69 (1996) 523
- [5] Martynov, V. V., J. de Physique IV 5 (1995) 5
- [6] Pons, J., Chernenko, V. A., Santamarta, R, Cesari, E., Acta Mater. 48 (2000) 3027.
- [7] Chernenko, V. A., Pons, J., Segui, C., Cesari, E., Acta Mater. 50 (2002) 53
- [8] Wedel, B., Suzuki, M., Murakami, Y., Wedel, C., Suzuki, T., Shinto, D., Itagaki, K., J. Alloys Comp. 290 (1999) 137
- [9] Pötschke, M., Gaitzsch, U., Roth, S., Rellinghaus, B., Schultz, L., J. Magn. Magn. Mater. 316 (2007) 383
- [10] Wassermann, G., Grewen, J., Texturen metallischer Werkstoffe, Springer, Berlin (1962)
- [11] Raabe, D., Lücke, K., Mater. Sci. Eng. 157-162 (1994) 597

	<b>EXPERIMENTAL REPORT</b>	<b>GeNF TEX-2</b>
<b>Texture Characterization of Pb and Pb-62%Sn alloys deformed by ECAE</b>		
<b>Proposer:</b>	<b>R. E. Bolmaro</b> , Instituto de Física Rosario – Materials Science Laboratory. CONICET-UNR. Rosario. Argentina	
<b>Co-Proposer(s):</b>	<b>V. L. Sordi, M. Ferrante</b> , Departamento de Engenharia de Materiais – Universidade Federal de São Carlos. Brazil	
<b>Experimental Team:</b>	<b>H.-G. Brokmeier, W. M. Gan, Bernd Schwebke</b> IWW-TEXMAT TU Clausthal, Geesthacht, Germany	
<b>User Group Leader:</b>	<b>A. Schreyer</b> , GKSS Research Centre Geesthacht, Germany	
<b>Instrument Responsible:</b>	<b>H.-G. Brokmeier</b>	
<b>Date(s) of Experiment:</b>	10 <sup>th</sup> – 15 <sup>th</sup> April, 19 <sup>th</sup> May – 24 <sup>th</sup> June, 29 <sup>th</sup> June – 2 <sup>nd</sup> July, 2007	

## Objective

ECAE has been one of the most prolific techniques in the study of severe deformations of metallic alloys. Severe deformation on low melting temperature alloys has been scarcely studied due to the high dynamic recrystallization effects they usually present. In the current presentation we show ECAE deformation experiments performed in a 120° tool at room temperature in pure Pb and near eutectic composition Pb-62%Sn alloy. The samples were passed 5 times in a route A. Metallographic observation after each pass showed a completely recrystallized structure. Due to the high absorption presented by Pb for X-rays the textures were measured by neutron diffraction. Because of their high penetration and superior statistical capabilities the textures showed well defined patterns even in the cases when the strengths were rather weak.

## Experiment

The texture of the pure Pb-samples was investigated by measuring three reflections (111), (200), (220). Due to the overlapping between cubic Pb and tetragonal Sn, the number of measurable reflections is restricted. In the case of Pb-Sn composites Pb (200) and Pb (220) are of good quality as well as Sn (220), Sn (211) and Sn (301). This choice of reflections takes a little longer counting time as expected. According to the high penetration power obtained at the neutron diffractometer TEX-2 the quantitative texture result is an average over the whole ECAP-cross section.

## Achievements and Main Results

Textures are shown in Fig. 1 as (200) pole figures for as cast and 1 to 5 passes for pure Pb and Pb-62%Sn samples. Both starting textures are Cube oriented probably due to the solidification process. The Cube texture for the single phase as cast sample is quite strong and might be influencing the development on the first pass. For the pure Pb samples the rotation of the Cube texture with respect to the sample axes is kept constant and equal to ~ 26.56°, all along the different deformation passes. There are no major changes on the texture patterns despite some small strength variations.

On the textures belonging to the Pb-rich phase, of the Pb-62%Sn sample, the Cube component is still noticeable with lower sharpness. The different components are more unstable and seem to evolve oscillating with no clear tendency. The rotation angle between the weak Cube texture and the sample axes is in between 18° and 20°. The high proportion of the Sn-rich second phase plays a major role in the stabilization of the orientation of the Cube texture

of Pb-rich phase at a lower angle of rotation. Also the relatively high content of Sn (close to 29 at. %) may change the SFE and texture. Sn-rich phase textures are shown in Fig. 2 where the regular twisted pattern can be seen.

Part of the current results has been sent to the 15<sup>th</sup> International Conference on Textures of Materials (ICOTOM 15<sup>th</sup> – June 1<sup>st</sup> – 5<sup>th</sup>, 2008) [4].

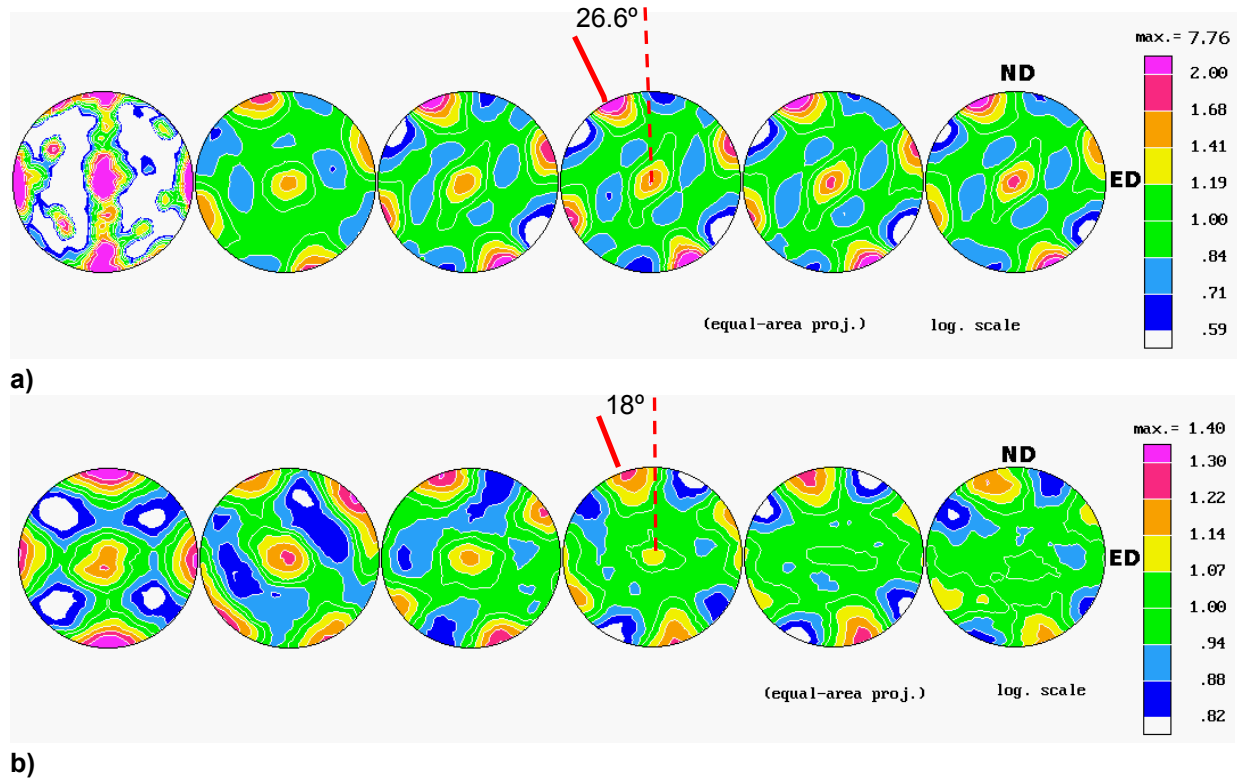


**Figure 1:** (200) pole figures of Pb and Pb rich phase in as cast samples and after 1 through 5 passes. a) Pure Pb samples. b) Pb-62%Sn samples.

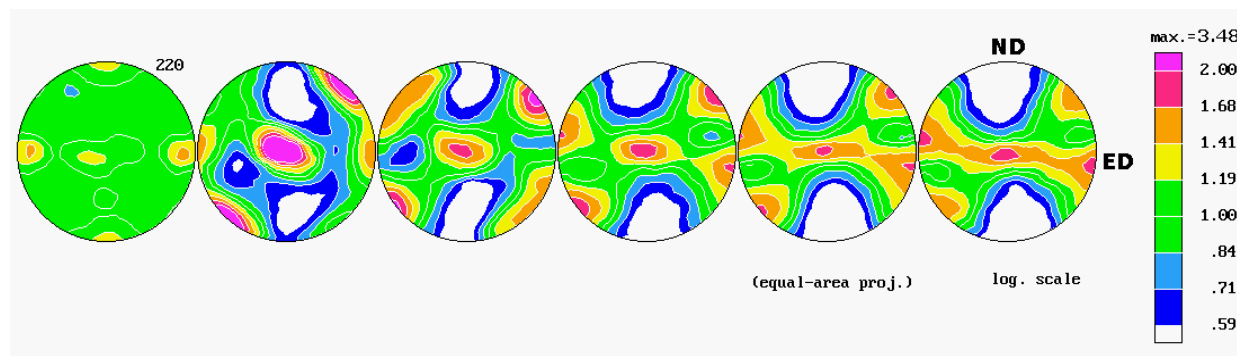



**Figure 2:** (220) pole figures of Sn rich phase in as cast samples and after 1 through 5 passes.

## References

- [1] H.-G. Brokmeier, W. Böcker and H. J. Bunge. "Neutron Diffraction Texture Analysis in Extruded Al-Pb Composites". *Text. and Microstructures*, 8-9, 429–441 (1988).
- [2] H.-G. Brokmeier. "Experimental textures of Al-Pb, Al-Cu and Fe-Cu metal-metal Composites". *Mat. Sci. Eng A175*, 131–139 (1994).
- [3] H.-G. Brokmeier, K. Helming and T. Eschner. "Pb Texture of Pb-Al Composites Determined by the Iterative Series Expansion Method and the Component Method". *Mat. Sci. Forum.* 157-162, 633–638 (1994).
- [4] R. E. Bolmaro, V. L. Sordi, M. Ferrante, WeiMin Gan, H.-G. Brokmeier. "Cube Texture Due to Dynamic Recrystallization in Pb and Pb-62%Sn Alloys Under Equal Channel Angular Extrusion Processing". 15<sup>th</sup> ICOTOM. June 1<sup>st</sup> – 5<sup>th</sup>, Pittsburgh. USA.



	<b>EXPERIMENTAL REPORT</b>	<b>GeNF TEX-2</b>
<b>NiTi – Shape Memory Alloy Texture</b>		
<b>Proposer:</b>	<b>Wolfgang W. Schmahl, Casjen Merkel, Andreas Götz</b> Dpt.für Geo- und Umweltwissenschaften, Sektion Kristallographie, Ludwig-Maximilians Universität München	
<b>Experimental Team:</b>	<b>H.-G. Brokmeier ,W. M. Gan, Bernd Schwebke</b> IWW-TEXMAT TU Clausthal, Geesthacht, Germany	
<b>User Group Leader:</b>	<b>A. Schreyer</b> GKSS Research Centre Geesthacht, Germany	
<b>Instrument Responsible:</b>	<b>H.-G. Brokmeier</b>	
<b>Date(s) of Experiment:</b>	10 <sup>th</sup> – 15 <sup>th</sup> July 2007, 25 <sup>th</sup> – 30 <sup>th</sup> September 2007	

## Objective

The shape memory effect is the ability of a material to recover its pristine shape upon heating. The effect is based on deformation by ferroelastic switching of the twin domain structure of the monoclinic phase under stress. The newly formed twin structure is then (meta-) stable even when the stress is released and heating results in a phase transformation to the cubic B2 phase, which transforms back on cooling to the original structure and shape in a stress-free environment. NiTi-SMA's provide a tunable martensitic transition temperature which varies strongly with Ni-content and makes this material especially relevant for widespread medical and engineering applications such as mobile phone antennas, durable frames, arterial implants, micro actuator valves, pipe fittings, and orthodontic wires. However, the application of stress onto a shape memory alloy produces a pronounced crystallographic texture in these materials, and any pre-existing texture due to materials processing greatly affects the recoverable strain in engineering applications. Complete bulk neutron diffraction texture measurements on the mechanism of ferroelastic twin reorientation have been performed to support recently performed *in situ* measurements (at the FRM II) on a monoclinic-martensitic engineering SMA (Ni<sub>50.14</sub>Ti<sub>49.86</sub>). In this measurements the tensile axis is perpendicular to the diffraction plane limiting the information on materials texture within the obtained data. Therefore the complete texture has been measured before (0.0 % strain) and after a recoverable tensile deformation of up to 4.5 % strain.

## Experiment

The measurements have been performed at TEX-2 on one sample (Ni<sub>50.14</sub>Ti<sub>49.86</sub>) at the gauge area (deformed texture from the previous *in situ* experiment at FRM II) and at the fixing point (undeformed texture), which yields both textures at once (in 5 h) and requires no additional sample environment. The used Cell parameters for the monoclinic NiTi are: a = 2.900, b = 4.615, c = 4.124  $\alpha = \beta = 90.00$ ,  $\gamma = 97.130$ .

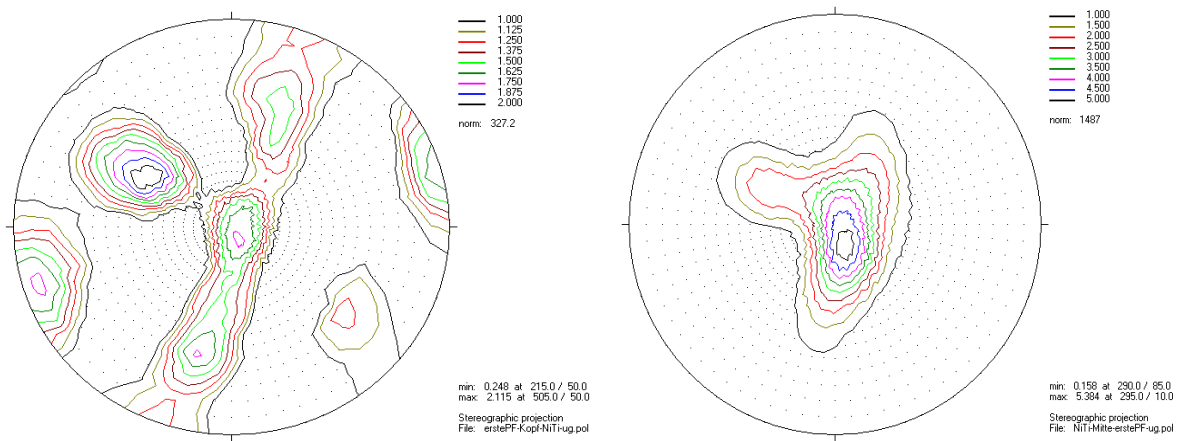



**Figure 1:** (l) Pole figure (No. 1) of  $\text{Ni}_{50.14}\text{Ti}_{49.86}$  SMA before the tensile experiment, i.e. in the fixing point (undeformed texture). The material is strongly pretextured due to extrusion moulding. (r) Pole figure (No. 1) of the measured texture within the gauge length (deformed texture). The (010) pole clearly accumulates at the center of the pole figure.

### Achievements and Main Results

The measurement validated the texture evolution as a function of strain as estimated from the spherical harmonic refinement of the measurement at FRM II (cf. figure 2). The (010) pole corresponds to the long axis of the transformation strain ellipsoid. The original material is already pretextured by mechanical processing. The application of stress orients the domains in a way to align martensite (010) with the load axis. Thus we show with these experiments, that the formerly believed “elastic part” of the stress/strain hysteresis curve is associated with domain alignment, which is due to domain wall movements similar to ferromagnetic hysteresis.

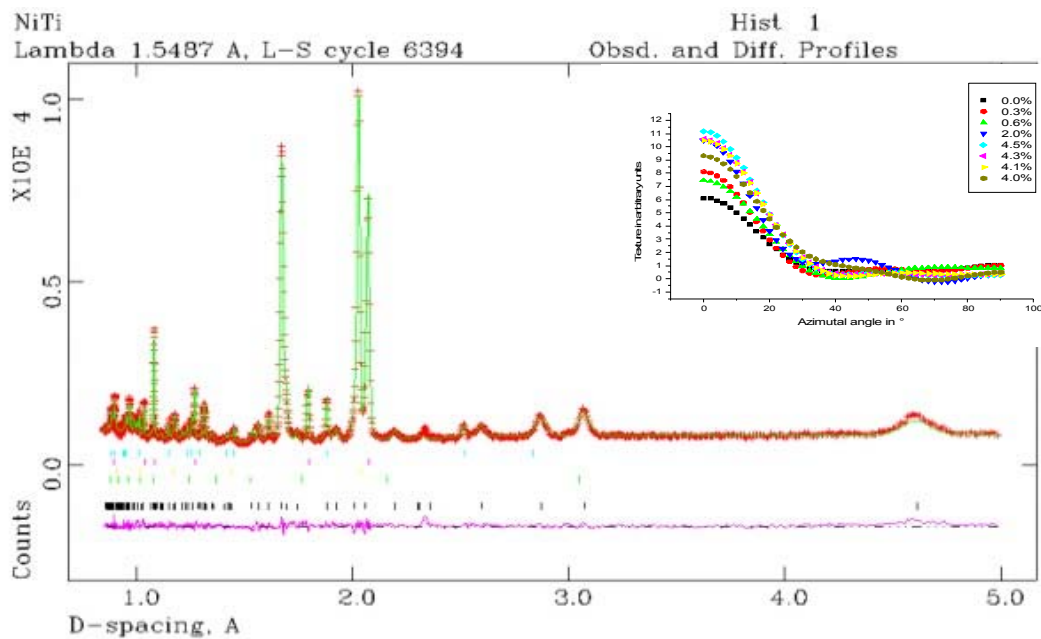


**Figure 2:** Diffraction pattern of type M NiTi at 4.5 % strain (SPODI, FRM II). Inner figure: Development of texture as a function of strain displayed by the pole density of the (010) pole as obtained from Rietveld refinement using a spherical harmonics description of the orientation density function (ODF). The azimuthal angle is defined as the angle between the pole and the load axis.

	<b>EXPERIMENTAL REPORT</b>	<b>GeNF TEX-2</b>
<b>Texture of hematite ore deformed to high strains in torsion</b>		
<b>Proposer:</b>	<b>H. Siemes</b> Institut für Mineralogie und Lagerstättenlehre, RWTH-Aachen	
<b>Experimental Team:</b>	<b>H.-G. Brokmeier, W. M. Gan, Bernd Schwebke</b> IWW-TEXMAT TU Clausthal, Geesthacht, Germany	
<b>User Group Leader:</b>	<b>A. Schreyer</b> , GKSS Research Centre Geesthacht, Germany	
<b>Instrument Responsible:</b>	<b>H.-G. Brokmeier</b>	
<b>Date(s) of Experiment:</b>	24 <sup>th</sup> August – 5 <sup>th</sup> September 2007, 14 <sup>th</sup> – 20 <sup>th</sup> September 2007	

## Objective

The microstructure and crystallographic preferred orientation (texture) of banded iron ores from the Iron Quadrangle in Minas Gerais, Brazil and from other localities was the objective of numerous publications, e.g. Quade et al. 2000, Rosiere et al. 2001, Bascou et al. 2002. Compression experiments revealed first insights in the development of preferred orientation (Siemes et al. 2003). In order to simulate the origin of hematite textures torsion experiments were performed on hematite ore from the Sishen Mine, South Africa, comprising a modal composition of 99.5 % hematite with varying fine grain sizes and a very weak texture. The specimens (10 mm length, 15 mm diameter) were deformed by means of a HTP-torsion apparatus (Paterson & Olgaard, 2000) at the GFZ, Potsdam.

## Experiment

Preferred orientation was measured by means of neutron diffraction (Brokmeier et al. 1998, Jansen et al. 2000) on small prismatic samples of 2.5 x 2.5 x 10 mm<sup>3</sup> close to the periphery of the deformed specimens, the volume of strongest shear strain. Preliminary results as the experimental textures depending on temperature, shear strain, and shear strain-rate are presented at conferences (Siemes et al. 2006a,b) and in the experimental report for the year 2006.

## Achievements and Main Results

Experimental textures depending on the microstructure of the starting material was the subject of research of the last year. Figure 1 shows the microstructure of three blocks with different grain sizes. Block05 reveals a rather homogeneous grain distribution with a mean of <5µm. Block08 is composed of layers with coarse grains of 9.8 µm and fine grains similar to the grain size of block05. Block12 is coarse grained with a mean of 17.2 µm. The experiments on three specimens are presented here as an instructive example. After deformation under approximately the same conditions the microstructure of all three specimens consists of recrystallized grains with mean diameters around 10 µm (Fig. 2 to 4). With increasing grain diameter of the starting material the maximum density of the 0003-reflection decreases from 11.9 m.r.d. to 3.4 m.r.d. and accordingly the texture index J decreases from 3.53 to 1.52. On the other hand the parameters for the assumed dislocation glide mode increase with increasing starting grain size, the stress exponent from n=2.0 to n=2.8 and the activation energy from Q=189 kJmol<sup>-1</sup> to Q=234 kJmol<sup>-1</sup>.

Undeformed Sishen ore

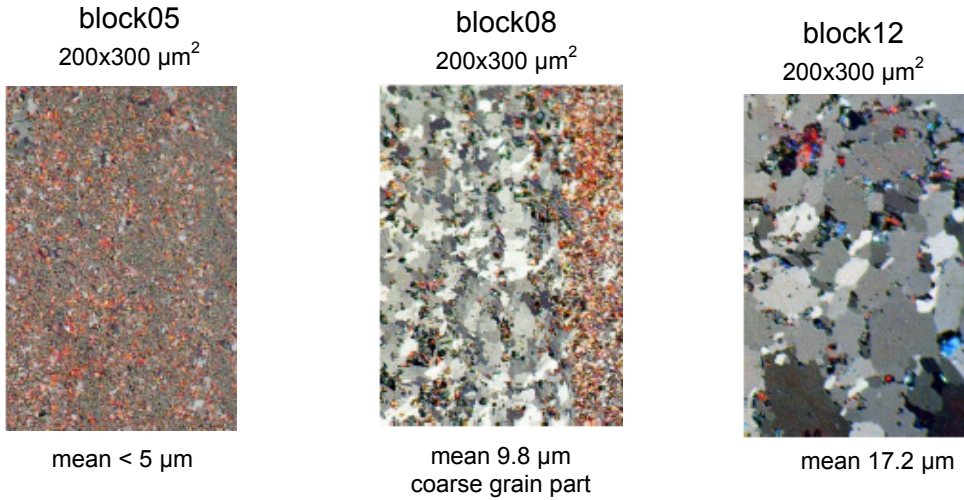


Figure 1.

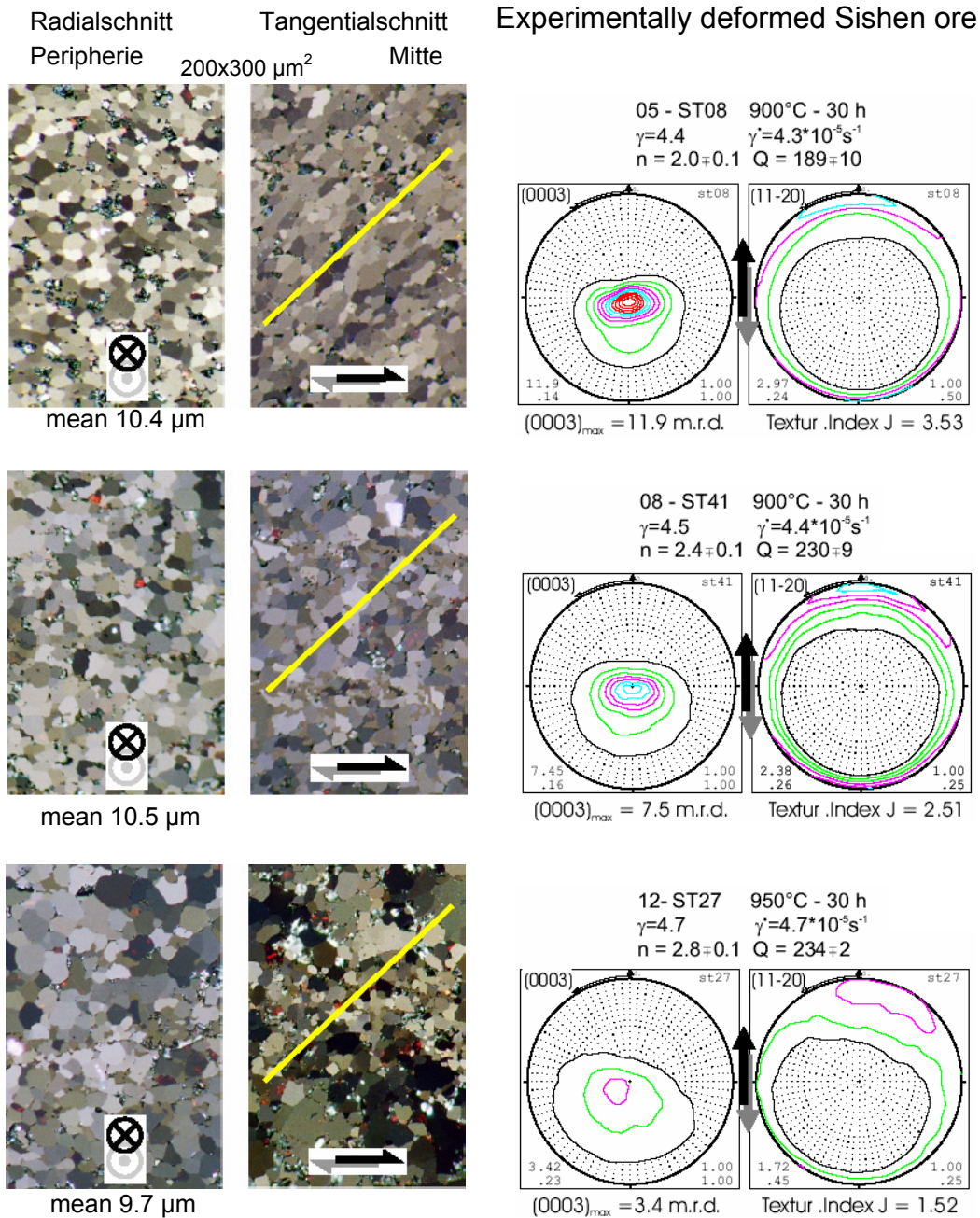


Figure 2.

Figure 3.

Figure 4.

## Conclusions

Shear deformation of hematite results in a recrystallized polygonal microstructure with a typical preferred orientation which strongly resemble naturally deformed iron ores. The behavior of the dislocation glide mode parameters depending on the grain size of the Sishen ore is still subject of our research.

## Acknowledgements


The authors are grateful to the DFG for financial support and the staffs of the involved institutions for their technical support. The management of Kumba Resources is thanked for supplying suitable hematite ore from the Sishen Mine, South Africa for our experiments.

## References

- Bascou, J., Raposo, M. I. B., Vauchez, A., Egydio-Silva, M., 2002. Titanohematite lattice-preferred orientation and magnetic anisotropy in high-temperature mylonites. *Earth and Planetary Science Letters* 198, 77–92
- Brokmeier, H.-G., Zink, U., Schnieber, R., Witassek, B. (1998) TEX-2, texture analysis at GKSS Research Center (instrumentation and application). In: Schwarzer, R. (Ed.). *Texture and Anisotropy of Polycrystals*. Materials Science Forum 273–275, 277–282
- Jansen, E., Schäfer, W., Kirfel, A. (2000) The Jülich neutron diffractometer and data processing in rock texture processing. *Journal of Structural Geology* 22, 1559–1564
- Paterson, M.S., Olgaard, D.L. (2000) Rock deformation tests to large shear strains in torsion. *Journal of Structural Geology* 22, 1341–1358
- Quade, H., Rosière, C.A., Siemes, H., Brokmeier, H.-G., 2000. Fabrics and textures of Precambrian iron ores from Brazilian deposits. *Zeitschrift für angewandte Geologie, Sonderheft* 1, 155–162
- Rosière, C.A., Siemes, H., Quade, H., Brokmeier, H.-G., Jansen, E.M. (2001) Microstructures, textures and deformation mechanisms in hematite. *J. of Structural Geology* 23, 1429–1440
- Siemes, H., Klingenberg, B., Rybacki, E., Naumann, M., Schäfer, W., Jansen, E., Rosière, C.A. (2003) Texture, microstructure, and strength of hematite ores experimentally deformed in the temperature range 600° to 1100°C and at strain rates between  $10^{-4}$  and  $10^{-6}$  s<sup>-1</sup>. *Journal of Structural Geology* 25, 1371–1391
- Siemes, H., Klingenberg, B., Rybacki, E., Naumann, M., Walter, J. M., Jansen, E., Kunze, K. (2006a). Textures of naturally and experimentally deformed hematite ores. *Workshop Neutrons for Geoscience*, 14. July 2006, Garching
- (2006b) Mikrostruktur und Textur bei Scherverformungsversuchungen an Hämatiterzen. In: Schreyer, A., Willumeit, R., Röhlberger, R., Incochia-Hermes, L., Griewatsch, K., Hrsg., *Programm und Abstracts, Deutsche Tagung für Forschung mit Synchrotronstrahlung, Neutronen und Ionenstrahlen an Großgeräten 2006*, Hamburg 4.–6. Oktober, D-P399





	<b>EXPERIMENTAL REPORT</b>	<b>GeNF TEX-2</b>
<b>Texture Characterization of a poly-structured rock from Sierras de Córdoba (Argentina)</b>		
<b>Proposer:</b>  <b>Co-Proposer(s):</b>	<b>R. E. Bolmaro</b> , Instituto de Física Rosario – Materials Science Laboratory. CONICET-UNR. Rosario, Argentina  <b>R. D. Martino</b> , CONICET y Cátedra de Geología Tectónica. F.C.E.F. y N. Universidad Nacional de Córdoba. Av. Velez Sarsfield 299. 5000-Córdoba, Argentina	
<b>Experimental Team:</b>  <b>User Group Leader:</b> <b>Instrument Responsible:</b>	<b>W. M. Gan, B. Schwebke, H.-G. Brokmeier</b> Institut für Werkstoffkunde und Werkstofftechnik, TU Clausthal, Germany <b>A. Schreyer</b> , GKSS Research Centre Geesthacht, Germany <b>H.-G. Brokmeier</b>	
<b>Date(s) of Experiment:</b>	18 <sup>th</sup> – 19 <sup>th</sup> April, 15 <sup>th</sup> – 28 <sup>th</sup> June, 3. July 2007	

### Objective

The study of the cinematic behaviour of the central sierras in Córdoba, Argentina, requires the characterization of the thermo-mechanic geological processes that have imprinted many of the chemical, microstructural and geometrical features visible nowadays. One very promising rock vein is called the La Yeya region. The rock is a very complex metamorphic rock including fine albite and quartz. Quartz might be the main phase for acquiring fine information about the deformation process. Meanwhile the albite could be used later to confirm the deformation path and for the understanding of the micromechanical processes themselves and their influences on the final microstructure.

### Experiment

Because of the strong overlap between the peaks of both phases only a few pole figures could be retrieved. Fig. 1 shows a neutron diffraction pattern with the identification of the main peaks.

### Achievements and Main Results

Fig. 2 shows the pole figures characterizing the main available orientations for Quartz. Fig. 3 shows the only clean, no overlapped, pole figure available for albite. Textures are very weak but well defined. The results are still on the process of analysis and correlation with geologic regional data.

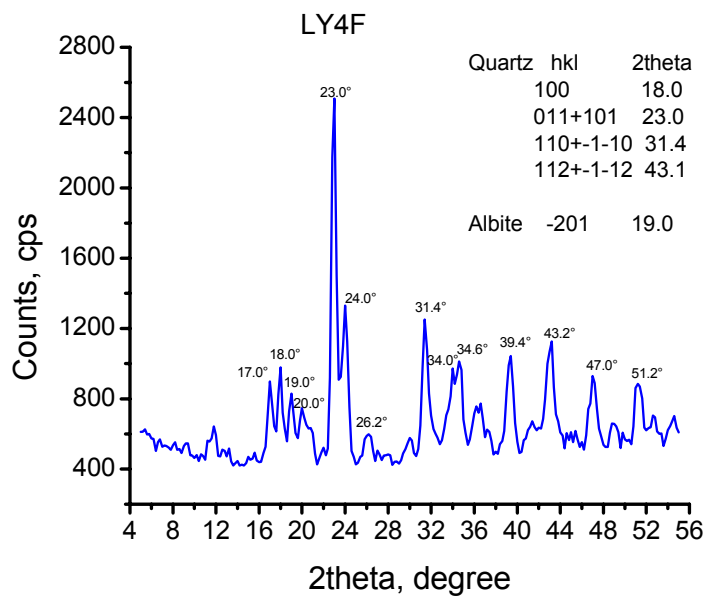


**Figure 1:**  
Neutron diffraction pattern  
for composite sample.

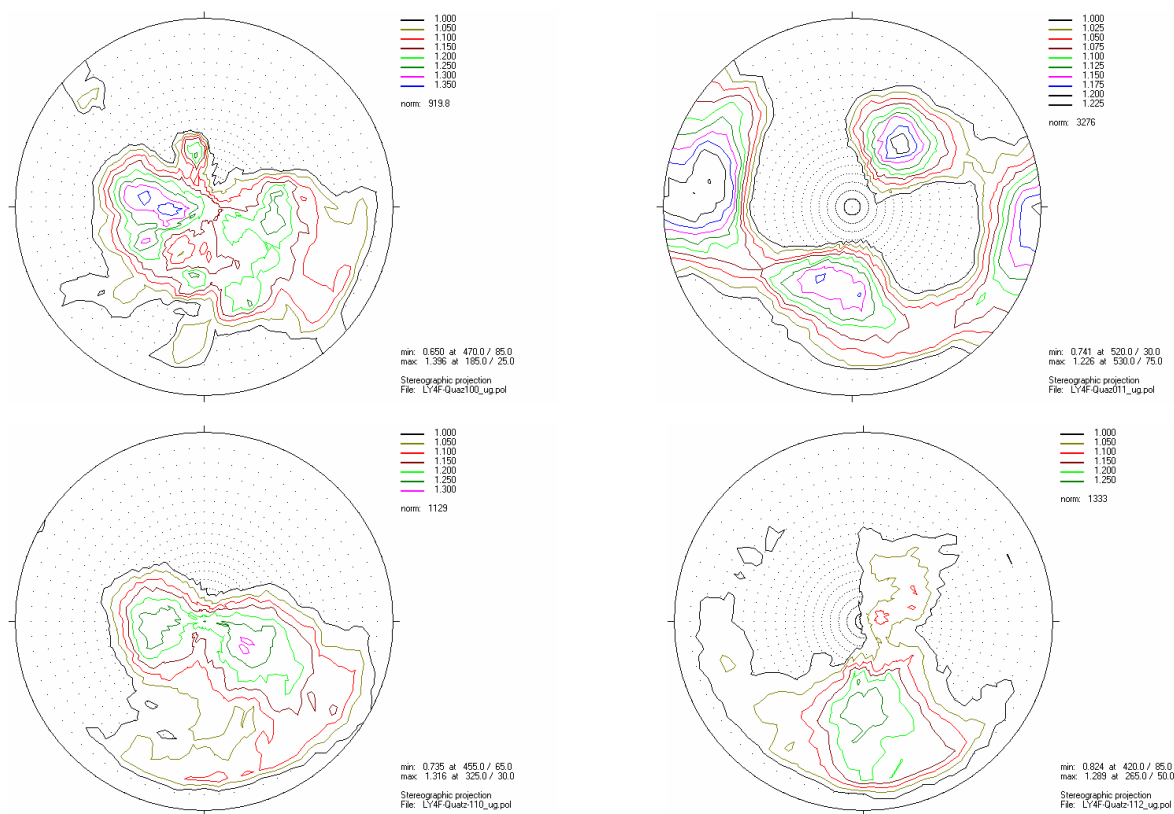



**Figure 2:** (100), (011), (110) and (112) pole figures for quartz phase.

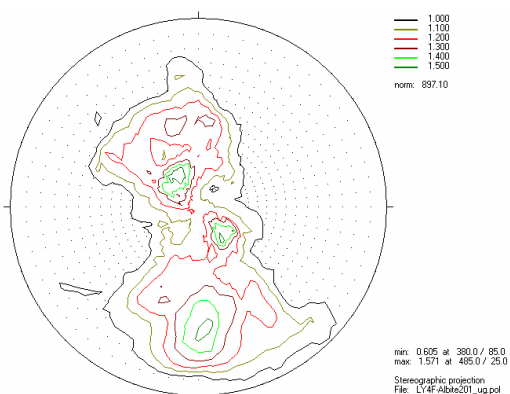


**Figure 3:**  
(-201) pole figures for Albite phase.



	<b>EXPERIMENTAL REPORT</b>	<b>GeNF TEX-2</b>
<b>Texture Characterization of FeMn Shape Memory Alloys</b>		
<b>Proposer:</b>	<b>R. E. Bolmaro</b> , Instituto de Física Rosario – Materials Science Laboratory. CONICET-UNR. Rosario. Argentina	
<b>Co-Proposer(s):</b>	<b>A. V Druker</b> , Facultad de Ciencias Exactas, Ingeniería y Agrimensura – Universidad Nacional de Rosario. Argentina	
<b>Experimental Team:</b>	<b>H.-G. Brokmeier, W. M. Gan</b> Institut für Werkstoffkunde und Werkstofftechnik, TU Clausthal, Germany	
<b>User Group Leader:</b>	<b>A. Schreyer</b> , GKSS Research Centre Geesthacht, Germany	
<b>Instrument Responsible:</b>	<b>H.-G. Brokmeier</b>	
<b>Date(s) of Experiment:</b>	20 <sup>th</sup> – 24 <sup>th</sup> April, 27 <sup>th</sup> – 29 <sup>th</sup> April, 4 <sup>th</sup> – 8 <sup>th</sup> May 2007	

## Objective

FeMn Shape Memory Alloys (SMA) are promising materials for technological applications for tube sealing and joints. Due to its characteristic anisotropy it is known that textures should play a role on the recovery properties. The current experiments are devoted to study texture development due to different rolling thermo-mechanical processes applied to FeMn SMA. Rolling is usually idealized as a plane strain deformation process. However, friction with rolling tools and geometric compatibility render heterogeneous deformation fields. Textures are usually heterogeneous through the thickness of the rolled sheets. Because of the high absorption presented by Fe for Cu X ray radiation the usual X ray diffraction tools can be used to characterize local through thickness textures. On the contrary, obtaining average textures is not feasible and a high penetration technique, as neutron diffraction, is needed. We will use those capabilities on the current experiments.

## Experiment

Overlapping among the HCP and FCC phases precludes measurement of all necessary pole figures to calculate ODFs. However, enough poles were available to judge main texture characteristics for both phases.

The processing of both samples (G3 and G4) are similar: a) Raw material rolled at 1000 °C. The X-ray diffraction pattern showed  $\gamma$  phase (FCC) and a small amount of  $\epsilon$  (HCP) martensite formed on cooling. Peaks  $\{111\}_{fcc}$  and  $\{0002\}_{hcp}$  are overlapped when both phases coexist. b) 35 % reduction in rolling at 600 °C. c) 67 % reduction in rolling at 1000 °C d) 20 % reduction in rolling at 650 °C. e) 15 minutes annealing at 600 °C. f) Tensile strain of just 3 % is applied, which induce an incomplete martensitic transformation.

The only difference between G3 and G4 is that G4 was subject to an extra 40% reduction at 600 °C immediately after step d). Pole figures taken by X ray diffraction showed a weak texture in both phases. That makes the samples the perfect candidates to be measured by neutron diffraction.

## Achievements and Main Results

Experimental textures were processed by popLA software and the results are shown as recalculated pole figures which were pretty much in coincidence with the experimental ones. Textures are shown in Fig. 1a) and b) for FCC phase as (100) pole figures for both samples (G3 and G4). The textures are very weak and the rolling direction is only noticeable by the

orientation of the (100) directions on the rolling (left of the figure) direction. The influence of the extra 40 % reduction on sample G4 is evident through the texture. Fig 2 a) and b) show pole figures for the HCP phases of both samples.

Parts of the current results have been sent to the 15<sup>th</sup> International Conference on Textures of Materials (ICOTOM 15<sup>th</sup>, June 1<sup>st</sup> – 5<sup>th</sup> 2008) [2].

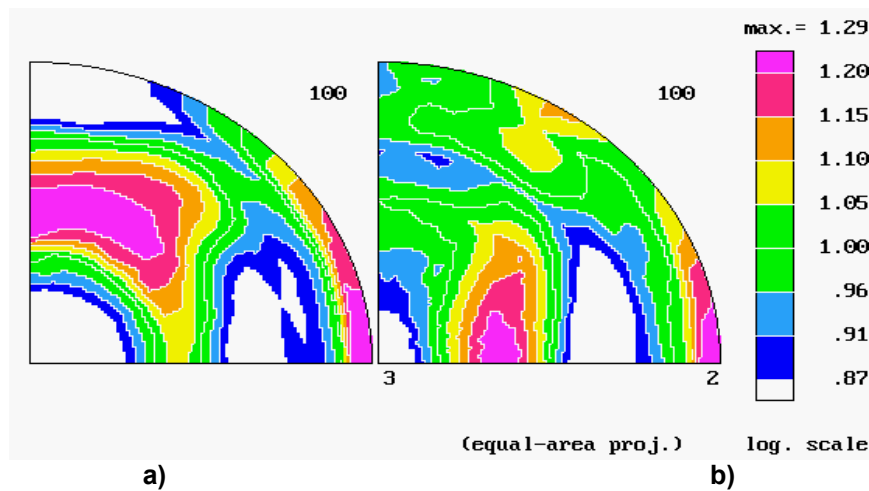


**Figure 1:** (100) pole figures for FCC phases a) sample G3 b) sample G4.

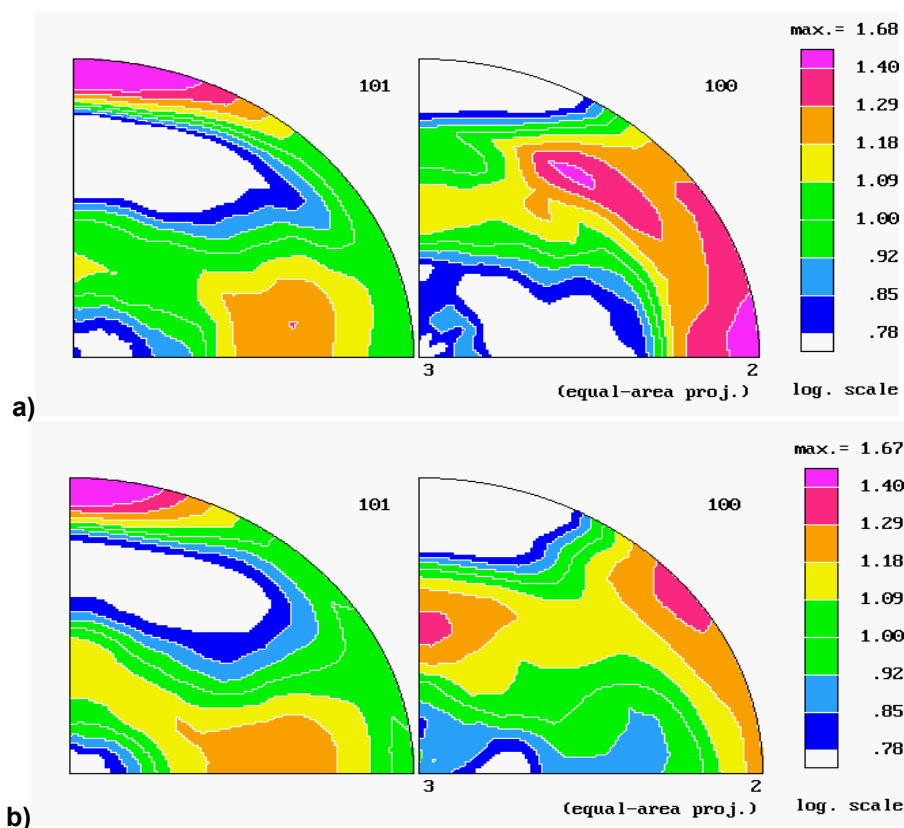


**Figure 2:** Pole figures for the HCP phases of both samples: a) sample G3V, and b) sample G4.

## References

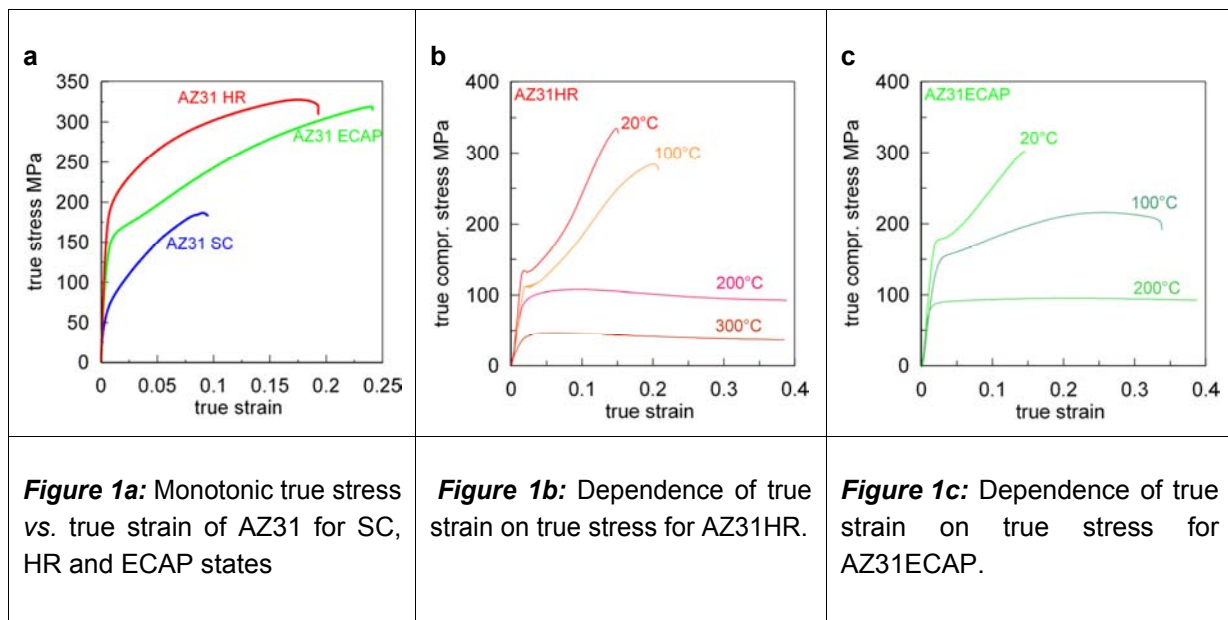
- [1] A. Druker, C. Sobrero, H.-G. Brokmeier, J. Malarría, R. Bolmaro. "Texture Evolution During Thermomechanical Treatments in Fe–Mn–Si Shape Memory Alloys". Mat. Sci. and Eng. A. on line June 2006
- [2] C. Sobrero, A. V. Druker, J. Malarría, U. Garbe, H.-G. Brokmeier, A. Roatta and R. E. Bolmaro. "Texture heterogeneities on rolled Fe-Mn-Si SMA and its influence on shape memory effects". 15<sup>th</sup> ICOTOM, June 1<sup>st</sup>-5<sup>th</sup>. Pittsburgh. USA

**Texture of Mg-AZ31 after squeeze casting (SC), hot rolling (HR) and equal channel angular pressing (ECAP)**

<b>Proposer:</b>	<b>Zuzana Zuberova, H.-G. Brokmeier</b> Institute of Material Science and Engineering – TEXMAT – Clausthal University of Technology
<b>Experimental Team:</b>	<b>W. M. Gan, B. Schwebke</b> IWW-TEXMAT TU Clausthal, Geesthacht, Germany
<b>User Group Leader:</b>	<b>A. Schreyer</b> , GKSS Research Centre Geesthacht, Germany
<b>Instrument Responsible:</b>	<b>H.-G. Brokmeier</b>
<b>Date(s) of Experiment:</b>	06 <sup>th</sup> – 09 <sup>th</sup> July 2007, 28 <sup>th</sup> – 30 <sup>th</sup> October 2007

**Objective**

Mechanical properties of Mg alloys strongly depend on chemical composition of materials, production technique and consequently on the crystallographic texture and microstructure. The aim of proposed experiment was to use the crystallographic texture for a better understanding of the materials properties as tensile strength, yield strength, ductility, creep resistance, thermal stability and fatigue of ECAPed, hot rolled and squeeze cast Mg-AZ31. In figures 1a, b and c two examples of the process dependent properties are shown. For example the yield strength varies between 86.2 MPa (SC), 163.7 MPa (ECAP) and 213.8 MPa (HR).



**Experiment**

The global texture determination was performed at the TEX-2 four-circle diffractometer using a neutron diffraction system. The neutron wave length was 1.332 Å. Four complete Mg pole figures were measured using samples of about 1 cm<sup>3</sup> in volume.

## Achievements and Main Results

*Squeeze cast* material shows nearly random distribution with a maximum pole figure intensity of 1.1 m.r.d. (multiple random distribution), which is close to ideal random texture intensity defined as 1.0 m.r.d. Fig. 2 shows a random texture of AZ31SC in the case of (10.0) pole figure.

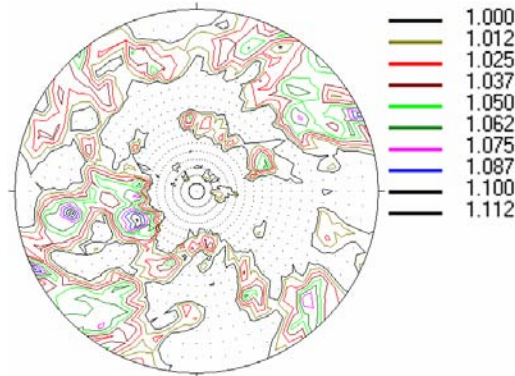
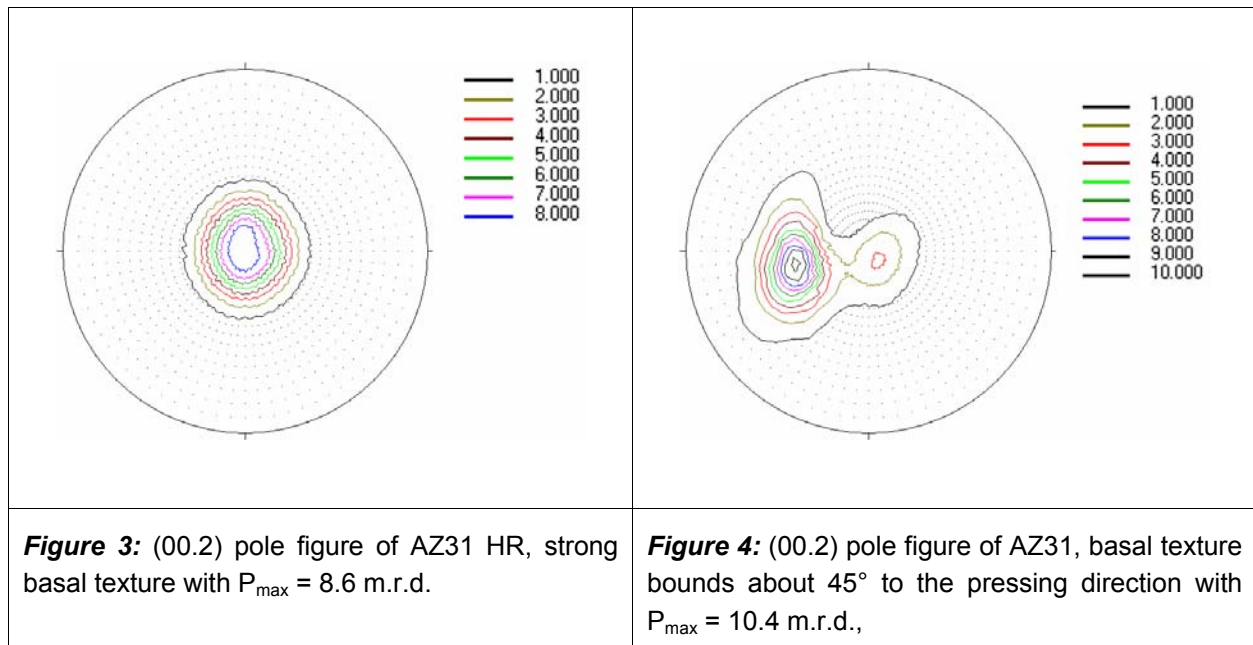


**Figure 2:** (10.0) pole figure of AZ31 SC, maximum pole figure intensity  $P_{\max} = 1.1$  m.r.d. indicates a nearly random texture.

In the case of *hot rolled* material the typical basal type texture is obtained with a strong fiber axis of  $P_{\max} = 8.6$  m.r.d, see figure 3. Due to the shear deformation during ECAP processing the basal planes tend to orient parallel to the shear plane. This can be seen by the texture of the ECAP-sample in figure 4. The basal pole is rotated about  $45^\circ$  compared to the plane strain deformation of hot rolling. Moreover, it can be seen that the texture sharpness increases to  $P_{\max} = 10.4$  mrd in the ECAP sample.



The difference in the crystallographic texture is responsible for the variation in tensile and compressive behaviour as shown in figure 1. A detailed relationship between crystallographic texture and anisotropic properties is given by Sangbong Yi (PhD-Thesis Clausthal University of Technology 2005).

**Polarised diffractometer POLDI**

**Short Instrument Description:**

With the polarised diffractometer 3-D depolarisation analysis is used to investigate magnetic properties and correlations in magnetic materials. With minor modifications a time of flight option in non-polarised mode is additionally available for the purpose of dosimeter calibration.

**Local Contact:**

**Jochen Fenske**

Phone/Fax : +49 (0)4152 87-1224 / +49 (0)4152 87-1338

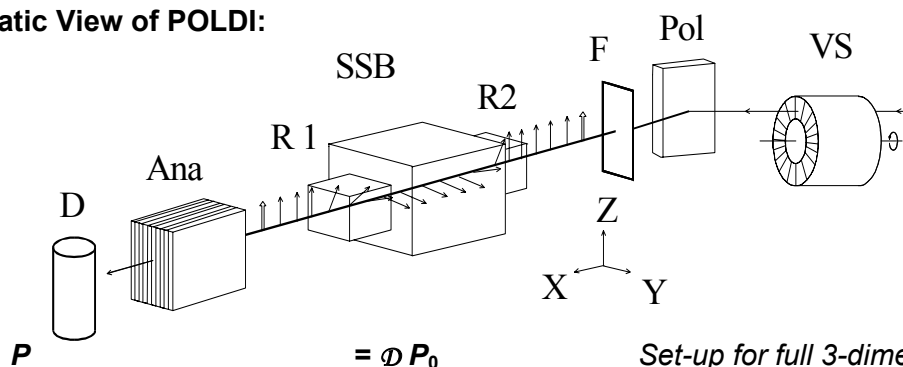
e-mail: [jochen.fenske@gkss.de](mailto:jochen.fenske@gkss.de)

**Dr. Dieter Lott**

Phone/Fax : +49 (0)4152 87-1372 / +49 (0)4152 87-1338

e-mail: [dieter.lott@gkss.de](mailto:dieter.lott@gkss.de)

**Schematic View of POLDI:**



**Instrument Details:**

Location at FRG-1:	beamline 7, thermal neutrons cross section 10 x 4 cm <sup>2</sup> ,
Polariser / monochromator (Pol)	Cu <sub>2</sub> MnA (111), PG(002), Si (311) doubly focussing; helical slot selector (VS)
Take-off-angle:	10° < 2 Θ <sub>M</sub> < 65°
Wavelength:	λ = 0.1 to 0.36 nm, 2 <sup>nd</sup> order suppression by velocity selector (VS)
Flux at sample position:	Φ <sub>max</sub> = 0.8 · 10 <sup>5</sup> cm <sup>-2</sup> s <sup>-1</sup> (polarised)
Analyser (Ana):	Co/Ti-supermirror
Overall polarisation:	0.94
3D depolarisation analysis in transmitted beam:	accuracy < 1 % for any component of D
Sample environment fitting in the magnetically shielded sample box (SSB) for 3D depolarisation analysis:	– refrigerator T > 12 K, – DC magnetic field < 160 A/cm – pulsed field < 8.0 kA/cm
Detector (D):	<sup>3</sup> He-counter
Instrument control/data acquisition:	remote internet PC control IEEE bus, serial bus and special interfaces



**Investigation of temperature behaviour of the magnetic phase transition in Fe<sub>50</sub>Pt<sub>50-x</sub>Rh<sub>x</sub> thin films**

<b>Principal Proposer:</b>	<b>P. Mani<sup>1</sup>, D. Lott<sup>2</sup>, J.Fenske<sup>2</sup></b> <sup>1</sup> MINT Center, University of Alabama, Tuscaloosa, Al, USA <sup>2</sup> GKSS Research Centre Geesthacht, Inst. of Material Science, Germany
<b>Co-Proposer(s):</b>	
<b>Experimental Team:</b>	
<b>User Group Leader:</b>	<b>J. Fenske<sup>2</sup></b>
<b>Instrument Responsible:</b>	
<b>Date(s) of Experiment:</b>	2007

### Objective

In the last years, perpendicular recording has been in the focus of scientific and technological interest in the search for materials to overcome the limitations in storage density of conventional magnetic recording media. Promising media such as FePt, have a high perpendicular anisotropy providing good thermal stability. However, the high anisotropy leads also to high coercivity fields and therefore to high write fields. In order to lower the high coercivity soft magnetic underlayer are needed. A possible candidate for such an underlayer is the L1<sub>0</sub> structured Fe<sub>50</sub>Pt<sub>50-x</sub>Rh<sub>x</sub> film. The bulk system shows an antiferromagnetic (AF) phase at low temperature and ferromagnetic (FM) phase at high temperature [1]. In the low temperature state the AF phase stabilizes the magnetization state of the recording media and at high temperature state the FM phase leads to a strong reduction of the write field [2].

In an earlier report we showed the behaviour of the half order peaks (00½) and (½00) of a 200 nm Fe<sub>50</sub>Pt<sub>40</sub>Rh<sub>10</sub> film in a temperature range between 12 K and 325 K [3]. In this report we focus on the (002), (200), (001) and (100) reflections in a temperature range up to 450 K. Also the data of a second 200nm film with a 17.5 % Rh concentration is reported.

### Experiment

With the neutron diffractometer POLDI temperature dependent measurements were performed in a temperature range between 12 K and 450 K on the Fe<sub>50</sub>Pt<sub>40</sub>Rh<sub>10</sub> film and between 12 K and 325 K on the Fe<sub>50</sub>Pt<sub>32.5</sub>Rh<sub>17.5</sub> film. Additional measurements for the Fe<sub>50</sub>Pt<sub>40</sub>Rh<sub>10</sub> film were performed on the three axis spectrometer IN12 at ILL.

### Achievements and Main Results

#### Fe<sub>50</sub>Pt<sub>40</sub>Rh<sub>10</sub>

The neutron diffraction measurements show clearly six peaks, three in-plane and three out-of-plane. From structure factor calculations for the L1<sub>0</sub> configuration we could determine their nature. The (00½), (½00) and (100) reflections a pure antiferromagnetic peaks, while the (002), (200) and (001) peaks are nuclear Bragg peaks with a possible ferromagnetic contribution.



As discussed in an earlier experimental report [3] the peak intensity of both antiferromagnetic half order peaks decreases with increasing temperature. By fitting the data using the power law,  $I(T) = (I_0[1 - T/T_c]^\beta)^2$  we get a transition temperature of about 331 K and 284 K respectively. At the same time the peak intensity of the (100) reflection increases with temperature, up to 300 K. Above 300 K the intensity decreases with increasing temperature.

The integrated intensities of the (002), (200) and (001) reflections are nearly constant about the entire temperature range. The constant intensity together with the structure factor calculations indicate that these peaks are pure nuclear Bragg-peaks with no FM contribution.

The decrease of the intensity of the half order peaks with the increase of the (100) peak suggests a reorientation of the magnetic moments. This reorientation is accompanied by a transition from a dominantly AF out-of-plane order to an AF in-plane order. Above 450 K an AF-PM phase transition takes place.

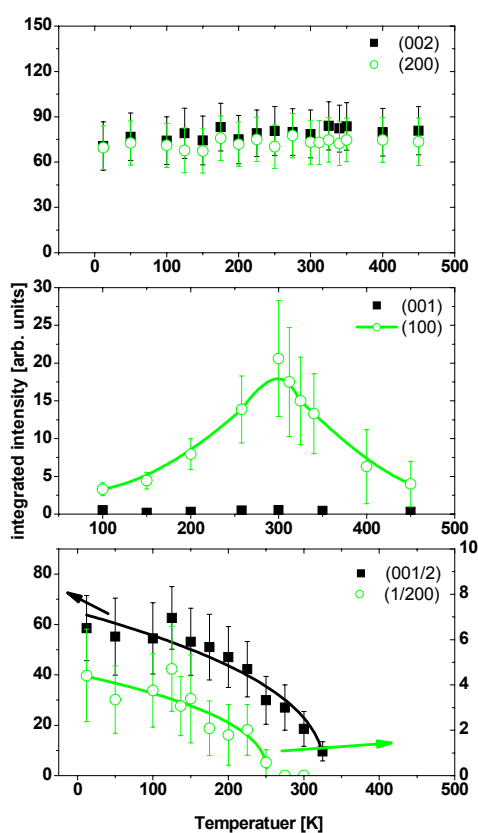


**Figure 1:**

Temperature dependence of the integrated neutron diffraction intensity of three in-plane (200), (100), ( $\frac{1}{2}00$ ) (open circles) and three out-of-plane (002), (001), ( $00\frac{1}{2}$ ) reflections (solid squares) of the  $\text{Fe}_{50}\text{Pt}_{40}\text{Rh}_{10}$  film. The line of the (100) peak is a guide to the eye. While the lines for the ( $00\frac{1}{2}$ ) (solid line) and ( $\frac{1}{2}00$ ) (dashed line) peaks are fits to the power law. Further details are in the text.

### **$\text{Fe}_{50}\text{Pt}_{32.5}\text{Rh}_{17.5}$**

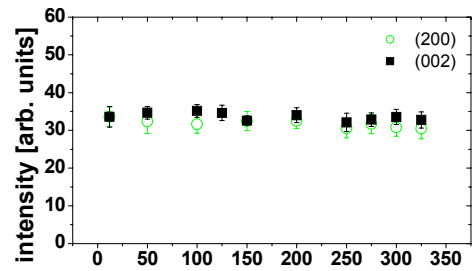
For the  $\text{Fe}_{50}\text{Pt}_{40}\text{Rh}_{10}$  film we could find only four peaks, two out-of-plane and two in-plane. As discussed before the (002) and (200) peaks are nuclear Bragg-peaks with a possible FM contribution and the ( $00\frac{1}{2}$ ) and ( $\frac{1}{2}00$ ) reflections are pure antiferromagnetic peaks. The (001) and (100) peak could not be observed.

The half order peaks show the same temperature behaviour as for the  $\text{Fe}_{50}\text{Pt}_{40}\text{Rh}_{10}$  film, i.e. a decrease of its intensity with increasing temperature. However, the transition temperature for both peaks is with 356K, 26K higher than for the  $\text{Fe}_{50}\text{Pt}_{40}\text{Rh}_{10}$  film. The (002) and (200) reflections behave very similar to the second order reflections for the  $x=10$  film, but show a slight tendency of a decreasing peak intensity with increasing temperature. This indicates the presence of a small FM contribution.

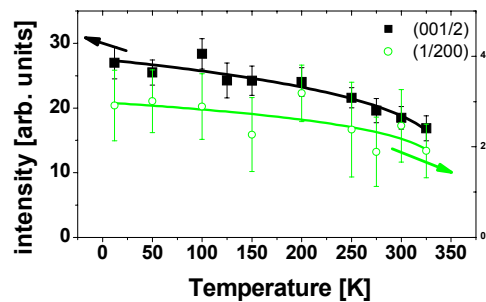


### Figure 2:

Temperature dependence of the integrated neutron diffraction intensity of two in-plane (200), ( $\frac{1}{2}00$ ) (open circles) and two out-of-plane (002), ( $00\frac{1}{2}$ ) reflections (solid squares) of the  $\text{Fe}_{50}\text{Pt}_{32.5}\text{Rh}_{17.5}$  film. The lines for the ( $00\frac{1}{2}$ ) (solid line) and ( $\frac{1}{2}00$ ) (dashed line) peaks are fits to the power law. Further details are in the text.



**No (001) peak  
No (100) peak**



The magnetic structure of both films could be solved by neutron diffraction measurements. The data reveal an AF-PM phase transition for the  $\text{Fe}_{50}\text{Pt}_{40}\text{Rh}_{10}$  and the  $\text{Fe}_{50}\text{Pt}_{32.5}\text{Rh}_{17.5}$  film above 450 K and 357 K, respectively. The former one shows an additional transition from AF out-of-plane to AF in-plane order at 300 K. A coexistence of an AF/FM phase for the  $\text{Fe}_{50}\text{Pt}_{32.5}\text{Rh}_{17.5}$  film at low temperature could not be excluded and has to be verified in future neutron diffraction experiment with and without polarization analysis.

Following these measurements, a detailed study of the (002) and (200) peak is planned to examine the possibility of a FM contribution to the nuclear Bragg peaks. Additionally, measurements of  $\text{Fe}_{50}\text{Pt}_{50-x}\text{Rh}_x$  films of the same thickness but with different Rh concentration will be performed to examine the temperature behaviour of the samples in the dependence of the composition.

### References

- [1] Takizawa, K.; Ono, T.; Miyajima, H.; Journal of Magnetism and Magnetic Materials 226 (2001), 572
- [2] Thiele, J.-U.; Maat, S.; Fullerton, E.E.; Applied Physic Letters 82 (2003), 2859
- [3] Mani, P.; GeNF – Experimental Report 2006 (2007), GKSS 2007/6, 215



Geesthacht neutron radiography and tomography facility GENRA-3

**Short Instrument Description**

The Geesthacht neutron radiography and tomography facility serves as an instrument for non-destructive testing and damage analysis of materials and technical structures by static and dynamic imaging. The ability of light elements, e.g. hydrogen or boron, to absorb neutrons allows unique analysis possibilities.

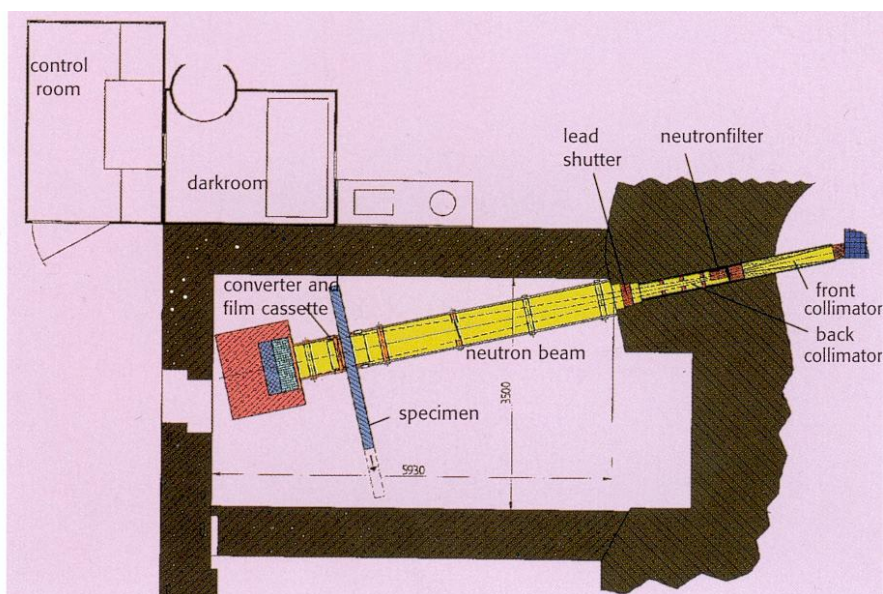
**Local Contact:**

**Dr. P. Klaus Pranzas**

Phone/Fax : +49 (0)4152 87-1326 / +49 (0)4152 87- 41326

e-mail: [pranzas@gkss.de](mailto:pranzas@gkss.de)

**Schematic View of GENRA-3:**



**Instrument Details:**

Location at FRG-1:	beamline 13, thermal neutrons
Collimation ratio:	100 to 300
Flux at sample position:	$\Phi_{\text{therm}} = 1.4 \cdot 10^6 \text{ cm}^{-2} \text{ s}^{-1}$ $\Phi_{\text{epi}} = 8 \cdot 10^3 \text{ cm}^{-2} \text{ s}^{-1}$ with 4 cm Bi-filter at position: 2 m from beam exit available filters: 9 cm Bi-filter combined with 10 cm Be 0.2 cm Cd
max. size of specimen:	100 x 200 cm <sup>2</sup>
Image:	15 x 15 cm <sup>2</sup> to 45 x 45 cm <sup>2</sup>
Detecting: direct imaging	Gadolinium foil: max 14 x 17 inch Gd-scintillation screen connected to an image intensifier video camera
indirect imaging	transfer material: Indium, Dysprosium
Sample handling	Remote control of specimen, e.g. for scan purposes



**Neutron Radiography Characterization of the  
Hydrogen Distribution in RT Hydride Tanks**

<b>Proposer:</b>	<b>P. Klaus Pranzas<sup>1</sup>, <sup>1</sup>GKSS Research Centre Geesthacht, Germany</b>
<b>Co-Proposer(s):</b>	<b>Oliver Metz<sup>1</sup>, Martin Dornheim<sup>1</sup></b>
<b>Experimental Team:</b>	<b>Oliver Metz<sup>1</sup>, Heinz-Werner Schmitz<sup>1</sup></b>
<b>Group leaders:</b>	<b>Rüdiger Bormann<sup>1</sup>, Andreas Schreyer<sup>1</sup></b>
<b>Instrument Responsible:</b>	<b>Heinz-Werner Schmitz<sup>1</sup>, P. Klaus Pranzas<sup>1</sup></b>
<b>Date(s) of Experiment:</b>	September 2007

### Objective

Room temperature metal hydrides are used for the reversible storage of hydrogen at ambient conditions. The commercially available material "C5" contains e.g. Mn (51.31 %), Ti (27.13 %), V (13.95 %), Fe (2.98 %), Zr (2.97 %) and Al (0.27 %). The available hydrogen storage capacity is approximately 1.6 wt.-%. As a first step to an *in situ* study, a tank with the room temperature hydride powder "C5" was filled with different amounts of hydrogen and measured with neutron radiography. The aim of this study is the *in situ* characterisation of the hydrogen absorption and desorption in commercially available room temperature hydrides in order to visualise the hydrogenation and powder compaction of the material inside the tank. The results of these investigations are necessary for the optimisation of tank design and construction of metal hydride hydrogen storage tanks.

### Experiment

The stainless steel tank (304L AISI) with a free volume of 285 cm<sup>3</sup> was filled with approximately 500 g metal hydride powder "C5". Hydrogen pressures up to 30 bars were used corresponding to a maximum amount of hydrogen of about 90 litres.

The neutron radiography experiments were performed in the irradiation chamber of GENRA-3 at distance P = 4 m in the hutch, resulting in a distance to the source of about 6 m. The neutron beam parameters are:

P [m]	4
Size [cm <sup>2</sup> ]	45x45
Flux [n cm <sup>-2</sup> s <sup>-1</sup> ]	3.5·10 <sup>5</sup>
L/D	300
Exposure time [min]	60

The direct gadolinium method was used to record the radiography images. The gadolinium converter was placed behind the film (back screen) because of the high absorption of Gd. During neutron capture Gd emits 70 keV of conversion electrons to the film.

## Achievements and Main Results

The resulting neutron radiography images are shown in figure 1.

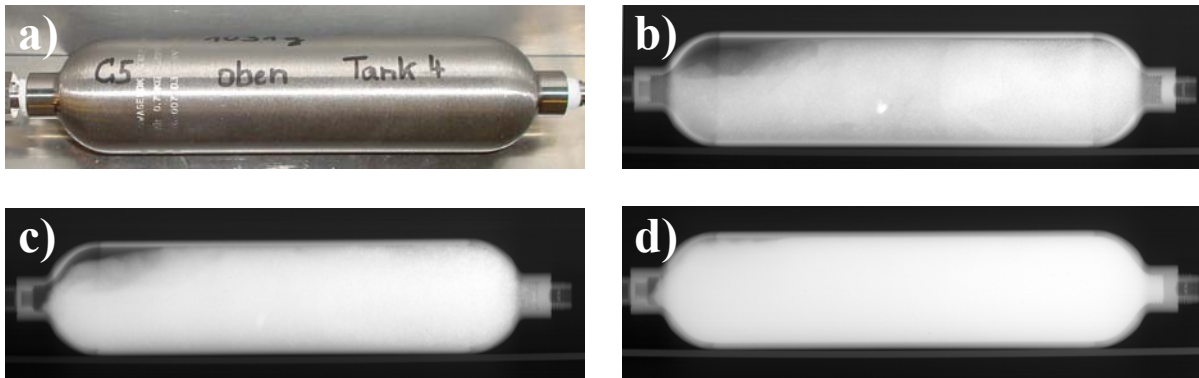


**Figure 1:** a) Photo of a hydrogen tank filled with the room temperature metal hydride “C5”, b)–d) Neutron radiography images of this tank filled with different amounts of hydrogen: b) empty, c) 9 litres H<sub>2</sub>, d) 90 litres H<sub>2</sub>.

In the empty state (Fig. 1b) the tank is not completely filled (up to 80 %) with the room temperature metal hydride. The neutron absorption is already quite high due to the high neutron absorption cross sections of the elements Mn, Ti and V which are the main components in the metal hydride. With increasing hydrogen content (Fig. 1c + d) higher neutron absorption is visible due to the hydrogen (brighter white colour of the tank content). During the absorption process the hydrogen distribution is homogeneous over the whole tank. The swelling of the metal hydride material due to the hydrogen absorption is also verified in these images.

This is the first step to an *in situ* characterisation with neutron radiography and tomography of the hydrogen absorption and desorption in metal hydride tanks using different metal hydrides and tank geometries.

**Note:**

The following research projects have been supported by the European Commission under the 6th Framework Programme through the Key Action: Strengthening the European Research Area, Research Infrastructures. Contract n°: RII3-CT-2003-505925':

*M. Almgren, M.-J. Stébé*

Contrast variation SANS studies of micelles in mixed perfluorinated and normal non-ionic surfactants

*M. Almgren*

Contrast variation SANS studies of micelles in mixed perfluorinated and hydrogenated surfactants

*L. Vekas, D. Bica, M.V. Avdeev*

SANS analysis of ferrofluids produced by laser pyrolysis

*M. Balasoiu, M.L. Craus, A.M. Moisin, V.Tripadus*

Effect of Ce and Gd doping on the microstructure properties of PT ceramics investigated by SANS

*S. Filippov, P. Štěpánek*

Conformation of hydrophilic polymers hydrophobically modified by sterically-hindered phenols

*J. Preu, T. Gutberlet, T. Heimburg*

Interaction of Angiotension II with lipid membranes

*M. Knaapila, A. Monkman*

A SANS study of polyfluorene phase behaviour in solution

*J. Preu, T. Gutberlet, T. Heimburg*

Network formation in lipid membranes

*A. Michels, R. Birringer, P. K. Pranzas*

Magnetic microstructure of nanocrystalline gadolinium

*E. Eidenberger, P. Staron*

SANS experiments with unpolarized neutrons to study precipitation of intermetallic phase in a Fe-Co-Mo alloy

*E. Eidenberger, S. Mayer, P. Staron*

SANS experiments with unpolarized neutrons to study precipitations in hot-work tool steels

*A. Michels, M. Elmas, F. Döbrich, J. Kohlbrecher, R. Birringer*

Dipole-Field-Induced Spin Disorder In Nanoporous Inert-Gas Condensed Materials

*S. King, H. Jarvie*

Fractal Structure of Natural Aquatic Nanocolloids

The support by the European Commission is gratefully appreciated by the authors and proposers.





## **Appendix I**

**Reports of experiments carried out  
at the instruments REFSANS and SRESS-SPEC  
at the GKSS outstation at the Forschungsneutronenquelle  
Heinz Maier-Leibnitz (FRM II) in Garching  
in support of internal and external users.**

**These reports have been taken from  
FRM II Annual Report 2007.**

(Reprinted by courtesy of  
Forschungsneutronenquelle Heinz Maier-Leibnitz (FRM II), Garching)



## 2.6 Integration of a new sample goniometer and a further double disc chopper (SC-2) in the ToF-Neutron Reflectometer REFSANS

R. Kampmann<sup>1</sup>, M. Haese-Seiller<sup>1</sup>, J.-F. Moulin<sup>1</sup>, V. Kudryashov<sup>2</sup>, B. Nickel<sup>4</sup>, E. Sackmann<sup>3</sup>, A. Schreyer<sup>1</sup>

<sup>1</sup>GKSS Forschungszentrum, Institut für Werkstofforschung, D-21502 Geesthacht, Germany

<sup>2</sup>Petersburg Nuclear Physics Institute, Gatchina, 188350, Russian Federation

<sup>3</sup>Technische Universität München, Physik Department, E22, D-85747 Garching, Germany

<sup>4</sup>Ludwig-Maximilians-Universität, Geschwister-Scholl-Platz 1, D-80539 München, Germany

### New sample goniometer at REFSANS

REFSANS has been designed as a novel ToF neutron reflectometer [1, 2] for comprehensive analyses of surfaces and interfaces. A new sample goniometer could be purchased in 2007 to enable samples inside of large and heavy (up to 200 kg) environments to be analysed at REFSANS. The goniometer comprises x-, y- and z-translation tables, one rotation table and two cradles (Fig. 2.21). The distance from the symmetry centre of the cradles to their upper surface amounts to 300 mm.

### Slave-Chopper-2

SC-2 was installed in the beam guide chamber of REFSANS in January 2007. The SC-2 discs-5 and -6 have one large window ( $W_{5,0}$  and  $W_{6,0}$ ) with an

opening of  $120^\circ$  and 5 small windows with openings of only  $1^\circ$  ( $W_{5,1} \dots W_{5,5}$ : Fig. 2.22a; disc-5) and  $3^\circ$ ,  $1^\circ$ ,  $2^\circ$ ,  $1^\circ$  and  $5^\circ$  ( $W_{6,1} \dots W_{6,5}$ : Fig. 2.22b; disc-6). The angular separation between the closing sides of the small windows of both discs is  $10^\circ$  whereas the gap between the first small and the  $120^\circ$  window amounts to  $20^\circ$ . The linear table is installed in REFSANS vertically and the beam passes SC-2 to the right of the axis if viewed in beam direction. This corresponds to a beam position above the axis in Fig. 2.22a and 2.22b.

SC-2 can be used in different operation modes by adequate setting of the phases of disc-5 and disc-6. For reflectometry and GISANS measurements the phases may be set such that SC-2 opens only one window with an angular width between  $0^\circ$  and  $120^\circ$  in order to define the wavelength range to be used for an experiment. In the calibration mode usually up to 11 small windows with widths between  $1^\circ$  and  $5^\circ$  are adjusted such that only neutrons of various wavelengths  $\lambda_i$  can pass through SC-2. In the inelastic mode only one or a few small windows are opened for inelastic measurements. Furthermore, for reflectivity measurements with a very broad wavelength range SC-2 will not be rotated and

the beam penetrates its windows. These different operation modes lead to the unconventional design of discs-5 and -6.

### High precision neutron reflectometry at REFSANS

High resolution reflectometry needs precise measurements of both the incidence angle and the wavelength. The incidence angle can accurately be measured at REFSANS by means of the high spatial resolution of the 2D-detector (FWHM  $\approx 2$  mm in vertical direction [3]) and the long distance of up to  $\approx 12$  m which can be set between the sample and the detector.

The installation of SC-2 allows of performing accurate  $\lambda$ -calibrations. Those measurements are performed by setting discs-5 and -6 of SC-2 such that only intensity peaks are transmitted. An example of a primary beam and calibration measurement as performed in the frame of measurements for proposal 1542 is shown in Fig. 2.23: The continuous spectrum in Fig. 2.23a represents the primary beam measurement with non rotating discs-5 and -6 and a sample detector distance of 6697 mm (REFSANS-parameter table=6m). At short flight times ( $t <$



Figure 2.21: Sample goniometer of REFSANS with a sample aligned in the beam.

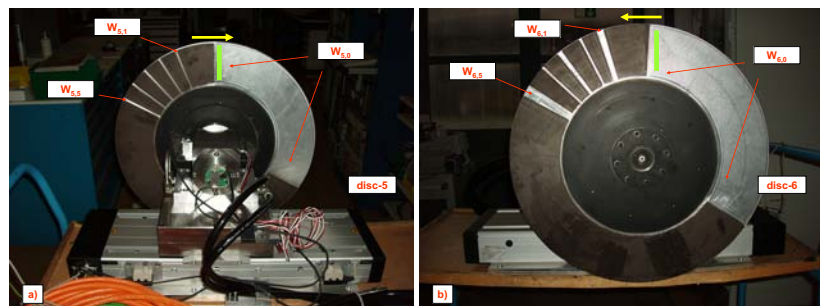


Figure 2.22: Views of SC-2 with rotation drive and linear table in beam direction (Fig. 2.22a) and against it (Fig. 2.22b). The yellow arrows indicate the rotation direction, the green bar indicates the beam area.

35 ms) the spectrum reflects the cold spectrum of neutron guide NG-2b. After  $\approx 35$  ms the transmission of the chopper decreases more and more and vanishes at  $\approx 70$  ms. This results from the window setting of the Master-Chopper (MC) and Slave-Chopper-1 (SC-1) for this measurement.

After the primary beam measurement SC-2 was started and the phases of disks 5 and -6 were set such that the small window peaks formed by disk-6 were observed with flight times  $t_{6,i} < 30$  ms and those from disk-5 at  $t_{5,i} > 40$  ms. A further calibration peak ( $t_{5,6} \approx 37$  ms) is formed by the large windows of disc 5 and -6. Afterwards the calibration peaks were measured at further distances between the sample and the detector corresponding to differences in flight length of  $\pm 5$  m (Fig. 2.23b). The time differences of the peak positions

are used to determine the velocity and thus the wavelength of the neutrons. It is pointed out that these measurements can be performed in short measuring time, they lead to a very precise lambda-calibration for a set of very different wavelengths.

Such calibration measurements by use of SC-2 significantly improved the reconstruction of reflectivity curves because the flight time at REFSANS depends not only on the wavelength but also on the openings of the windows of the MC and SC-1 ( $\gamma_{MC}$  and  $\gamma_{SC-1}$ ) and further on the phase shift between the closing of MC and the opening of SC-1 ( $\delta_{MC,SC-1}$ ). This results from the fact that  $\gamma_{MC}$ ,  $\gamma_{SC-1}$  and  $\delta_{MC,SC-1}$  define both the position and the starting time of the neutron packages in dependence of the wavelength. After putting SC-2 into operation these parameters are de-

termined from lambda-calibrations by fitting the observed peak arrival times to the chopper settings.

The neutron reflectivity of a film from an implant coating with cell membrane mimics exemplifies the performance of REFSANS for high precision reflectometry (proposal 1542). Firstly, the reflectivity from a metallic Ti-alloy (Ti-6Al-4V; 100nm) sputtered onto a Si wafer was measured at REFSANS. Measurements were performed at different incidence angles as indicated in Fig. 2.24. Afterwards the metallic film was coated with POPE (Palmitoyl-Oleoyl Phosphatidyl-Ethanolamine). Significant changes of the reflectivity curve were observed after ageing of the POPE and adhesion of proteins (fetal bovine serum, containing 3–4.5 g Protein / dl; see Fig. 2.24).

## Use of REFSANS in 2007

REFSANS could not be used for user proposals to the expected extend. This was due to technical reasons resulting from faulty soft- and hardware systems controlling the neutron optics and the choppers. A strong reduction in staff members from April to November 2007 made running of REFSANS further difficult. Nevertheless, REFSANS has been improved technically and measurements in the frame of exciting internal and external proposals could successively be performed.

## Acknowledgements

The great contribution of the technical department of GKSS to constructing and manufacturing of REFSANS components is gratefully acknowledged. The development of REFSANS has been supported by the German Federal Ministry of Education, Research and Technology (BMBF) under contracts 03-KA5FRM-1 and 03-KAE8X-3.

## References

- [1] Kampmann, R., Haese-Seiller, M., Marmotti, M., Burmester, J., Deriglazov, V., Syromiatnikov, V., Okorokov, A., Frisius, E., Tristl, M., Sackmann, E. *Applied Physics A*, 74,

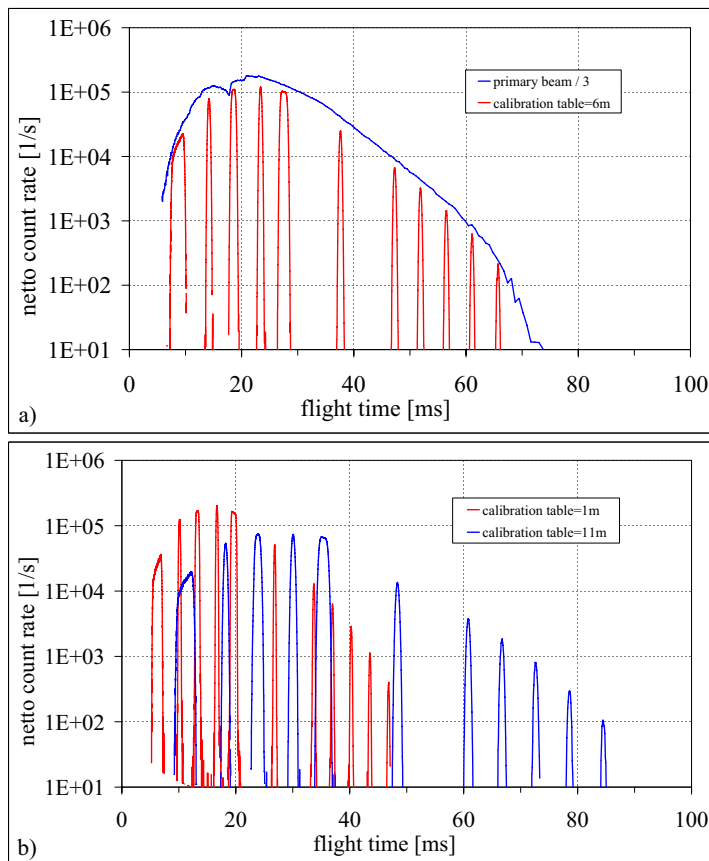


Figure 2.23: Primary beam measurement and  $\lambda$ -calibration at REFSANS. Measurement of the primary beam was performed with non rotating SC-2 at table = 6m corresponding to a sample detector distance of 6697 mm (Fig. 2.23a). The  $\lambda$ -calibration was performed by running SC-2 in calibration mode and setting the detector to table = 1m, 6m and 11m 2.23a and Fig. 2.23b.

(2002), 249–251.

- [2] Kampmann, R., Haese-Seiller, M., Kudryashov, V., Deriglazov, V., Trisl, M., Daniel, C., Toperverg, B., Schreyer, A., Sackmann, E. *Physica B*, 350, (2004), e763–e766.
- [3] Kampmann, R., Marmotti, M., Haese-Seiller, M., Kudryashov, V. *Nuclear Instruments and Methods A*, 529, (2004), 342–347.

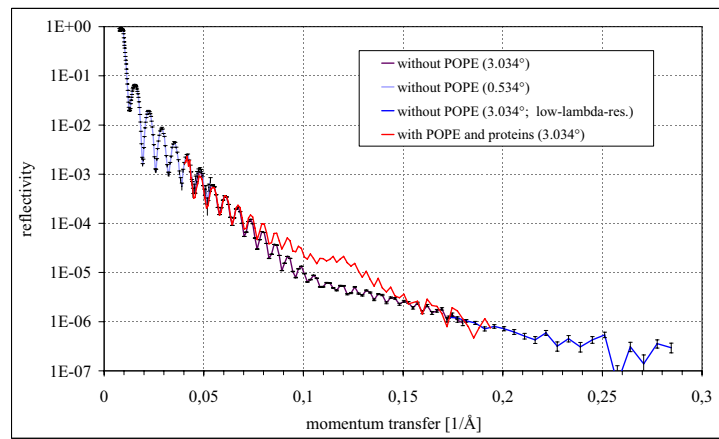


Figure 2.24: Implant coating with cell membrane mimics: Reflectivity curves without POPE phospholipid (see text) and with POPE and proteins are shown (proposal 1542: F. Feyerabend et al.).



## Interaction of Glucagon-like Peptide-1 with DOPC bilayer

Pauline Vandoolaeghe, Fredrik Tiberg, Tommy Nylander (Lund U.)

Kirstin Seidel, Bert Nickel (LMU)

Glucagon-like peptide-1 (GLP-1) (cf figure 1) is derived from the transcription product of the [proglucagon](#) gene. The major source of GLP-1 in the body is the [intestinal L cell](#) that secretes GLP-1 as a [gut hormone](#). GLP-1 possesses several physiological properties that make it a subject of intensive investigation as a potential treatment of diabetes.<sup>1,2</sup> Indeed, GLP-1 contributes to the normalization of elevated glucose levels through regulation of insulin and glucagon secretion, gastric emptying, satiety and body weight.

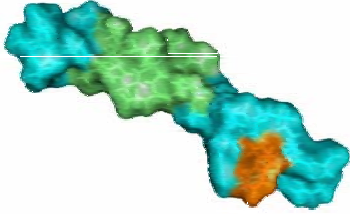


Figure 1: Image of Glucagon-like peptide 1 created with PyMOL.<sup>3</sup>

To investigate the potential of GLP-1 as treatment of diabetes, it is interesting to study its interaction with membranes. Biological studies have been performed on the action of this peptide in the body, but to our knowledge, no physicochemical studies have been done on model systems. Such studies are important for fundamental understanding of the interaction and action of the peptide on the membrane. The experiment involves biophysical and surface chemical studies of the interactions of GLP-1 with model systems. Ellipsometry has been used and allows us to study the adsorption of the peptide on model systems consisting of lipid bilayers supported on surfaces (see figure 2).

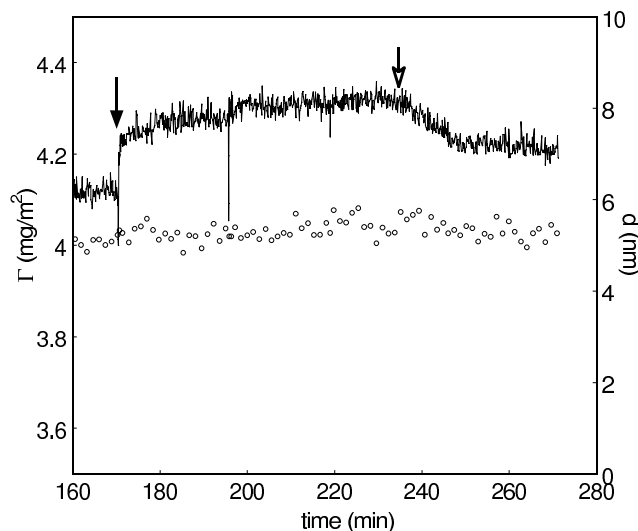


Figure 2: Adsorbed amount (line) and thickness (open symbols) as measured by ellipsometry after addition of 80  $\mu$ g/mL of GLP-1 on a DOPC bilayer (formation of the bilayer not shown here). The filled arrows correspond to additions and the open arrows correspond to rinsing.

Neutron reflectivity experiments were performed to gain insight on the detail of structural modifications occurring as the GLP-1 is interacting with the bilayers, using phospholipids with perdeuterated acyl chains.

Neutron reflectivity measurements were carried out on REFSANS reflectometer at FRMII, Garching, Germany. The instrument was used in the conventional reflection geometry. The chopper device was set to get a fixed wavelength resolution, which was not changed during the experiment to avoid problems with the energy selection. The distance between the slit and the sample was measured by

means of a ruler. The alignment of the sample was made in this way: a rough alignment of the  $0^\circ$  angle was made by using a water level. A height scan was then performed at low incident angle. A finer alignment of the incident angle was done by measuring at different angles and calculating the offset of the angle values. In the same way, measurements were performed at different detector distances to determine the offset of this parameter.

Measurements were performed at  $0.8^\circ$  with detector distance of 11 m and at  $3.2^\circ$  with detector distance of 6 m. These settings allow us to measure up to a momentum transfer of  $0.15 \text{ \AA}^{-1}$ .

The supported d-DOPC bilayer was formed on a silica surface by adsorption/deposition from an aqueous solution where the phospholipid is solubilised with a sugar surfactant, n-dodecyl- $\beta$ -D-maltopyranoside (DDM), at a ratio of 1:6.<sup>4</sup>

Adsorption of GLP-1 on this bilayer (figure 3) showed a change in the properties of the bilayer. We studied the effect of rinsing on the system, and we obtained a reflectivity curve which is in between the curves corresponding to the DOPC bilayer before and after the GLP-1 adsorption, which is indicative of some GLP-1 molecules being removed from the layer while some molecules stayed adsorbed inside or on top of the bilayer.

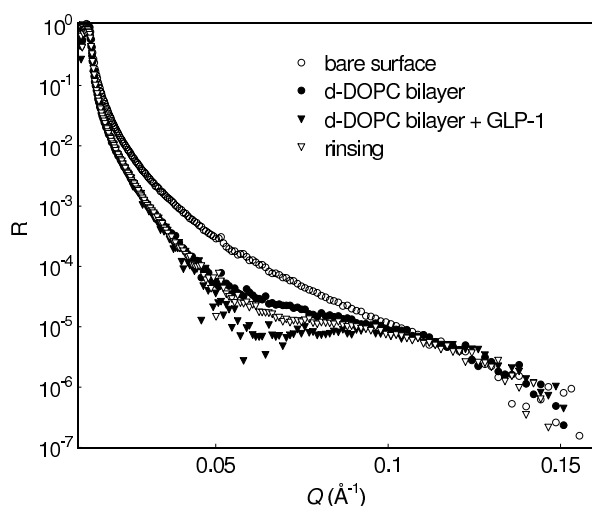


Figure 3: Reflectivity curves of the adsorption of  $80 \mu\text{g/mL}$  GLP-1 on d-DOPC bilayer in an acetate buffer  $10 \text{ mM}$  at  $\text{pH } 4.5$  in  $\text{D}_2\text{O}$ . Note that there is a shift in  $Q$  values as apparent from the low critical edge. This shift will be calculated after analysis of some test measurements performed after the experiment.

These neutron reflectivity measurements have been successful. The preliminary data have now to be corrected for an apparent shift in  $Q$  values and data analysis needs to be done to determine whether the peptide inserts in the bilayer or adsorbs on top. Analysis will also allow calculating the amount of peptide going in the layer after addition, as well as the amount remaining on the layer after rinsing, and enable detailed comparison with ellipsometry data obtained.

1. Toft-Nielsen, M. B.; Madsbad, S.; Holst, J. J., Determinants of the effectiveness of glucagon-like peptide-1 in type 2 diabetes. *Journal of Clinical Endocrinology and Metabolism* 2001, 86, (8), 3853-3860.
2. Meier, J. J.; Weyhe, D.; Michaely, M.; Senkal, M.; Zumtobel, V.; Nauck, M. A.; Hoist, J. J.; Schmidt, W. E.; Gallwitz, B., Intravenous glucagon-like peptide 1 normalizes blood glucose after major surgery in patients with type 2 diabetes. *Critical Care Medicine* 2004, 32, (3), 848-851.
3. [http://www.bioquest.org/bedrock/problem\\_spaces/trpcage/molecules.php](http://www.bioquest.org/bedrock/problem_spaces/trpcage/molecules.php)
4. Tiberg, F.; Harwigsson, I.; Malmsten, M., Formation of model lipid bilayers at the silica-water interface by co-adsorption with non-ionic dodecyl maltoside surfactant. *European Biophysics Journal with Biophysics Letters* 2000, 29, (3), 196-203.



Action of lipase on solid-supported layers formed from the adsorption of cubic liquid crystalline nanoparticles on hydrophilic surfaces  
Pauline Vandoolaeghe, Tommy Nylander (Lund U.)

Kirstin Seidel, Bert Nickel (LMU)

Lipases (triacylglycerol hydrolases) are important enzymes, which catalyze the formation or hydrolysis of lipids and are used industrially as detergent enzymes, in paper and food technology, in the preparation of fats, and as biocatalysts for the organic synthesis [1]. Lipases play also an important physiological role in the fat digestion [2]. It is therefore of importance to understand, predict and control reactions catalyzed by lipases. The natural substrates for lipases, acyl glycerols, do not form bilayers, but rather form non-lamellar structures with inverse curvature. Glycerol monooleate (GMO), which is hydrolysed to oleic acid and glycerol in the presence of lipases, forms a cubic liquid crystalline phase in the excess of water [3]. This phase can be dispersed into various types of discrete colloidal nanoparticles with the particle size in the range of 50 – 500 nm [3,4]. Key properties such as particle size, nanostructure, morphology and stability of these liquid crystalline nanoparticles (LCNP) can be easily tuned and controlled predictably and reproducibly by mixing with other lipid components and by varying the preparation technique [5].

Cubic liquid crystalline nanoparticles with an internal reverse bicontinuous cubic structure (Cubosome<sup>®</sup>) is one good candidate to be used as carriers for dietary, cosmetic, nutritional, diagnostic and pharmaceutical agents, as they offer the possibility to incorporate large amounts of both hydrophilic and hydrophobic molecules thanks to their “channel structure”. Almost no information on the surface interactions of non-lamellar liquid crystalline particles is available. Such studies are important for fundamental understanding of the barriers and uptake mechanisms of encapsulated active components, fusiogenic properties of the delivery system, and for colloidal stability, e.g. on storage.

The experiment involved biophysical and surface chemical studies of the adsorption of self-assembled lipid structures with surfaces, as well as the action of lipase on the layer formed.

Ellipsometry has been used extensively in our work and this allows us to study the adsorption of the nanoparticles on hydrophilic surfaces [6] and TLL action (see figure 1).

Neutron reflectivity experiments were performed to gain insight on the detail of structural modifications occurring as the nanoparticles are interacting with the surfaces and are hydrolyzed by the lipase.

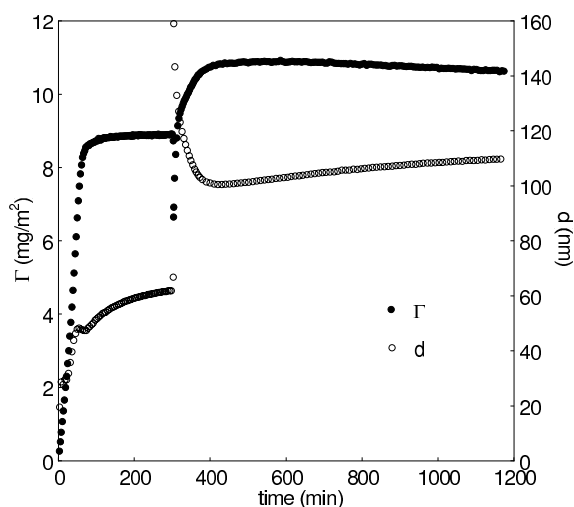


Figure 1: Adsorbed amount (filled symbols) and thickness (open symbols) by ellipsometry after injection of 0.05 mg/mL GMO-based CPNPs in presence of NaCl 0.1 M at pH 4.5.

Neutron reflectivity measurements were carried out on REFSANS reflectometer at FRMII, Garching, Germany in October 2007. The instrument was used in the conventional reflection geometry. The chopper device was set to get fixed a wavelength resolution  $\Delta\lambda/\lambda$ . The distance between the slit and the sample was measured by means of a ruler. The alignment of the sample was made in this way: a rough alignment of the  $0^\circ$  angle was made by using a water level. A height scan was then performed at low incident angle. A finer alignment of the incident angle was done by measuring at different angles and calculating the offset of the angle values. In the same way, measurements were performed at different detector distances to determine the offset of this parameter.

Measurements were performed at  $0.8^\circ$  with detector distance of 11 m and at  $3.2^\circ$  with detector distance of 6 m. These settings allow us to measure up to a momentum transfer of  $0.15 \text{ \AA}^{-1}$ .

Adsorption on hydrophilic surfaces was studied for Glycerol Monooleate (GMO) based-cubic phase nanoparticles (CPNPs) in presence of electrolytes, NaCl 0.1 M and CaCl<sub>2</sub> 0.017M at pH 4.25. The lipase used was from the fungi *Thermomyces lanuginose* (TLL).

The reflectivity curve obtained in D<sub>2</sub>O is given in figure 2. We observed a peak appearing at high  $q$  ( $\sim 0.11 \text{ \AA}^{-1}$ ), indicative of the formation of a multilayer at the interface. This is indicative of either the particles keeping their structure upon adsorption on the surface, or the particles dissociating at the interface and growing in an organized manner at the surface. Note that these data are preliminary and there is a shift in  $Q$  values, which still has to be determined.

When injecting a high concentration of the lipase TLL, the reflectivity curve obtained is similar to the one of the bare surface, which indicates that the organized structure is destroyed and the layer is completely removed from the surface.

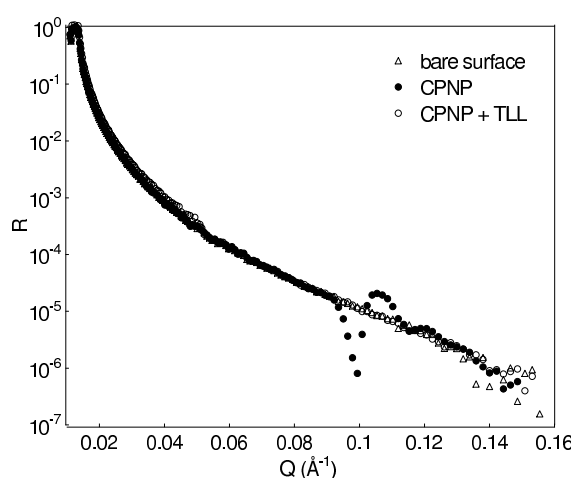


Figure 2: Reflectivity curves for the bare surface (open triangles), after adsorption of GMO-based CPNP 5 wt% (filled circles) and after hydrolysis by TLL (open circles) on silica surfaces at pH 4.25, in presence of NaCl 0.1M and CaCl<sub>2</sub> 0.017M in D<sub>2</sub>O.

Neutron reflectivity measurements allow us to have more information about the structure formed on the silica surfaces when the nanoparticles adsorb and the layer formed could be used to investigate the action of a lipase on this immobilized structure. We should now investigate the action of lipase at smaller concentrations, to be able to observe the intermediate states formed upon hydrolysis.

- [1] Svendsen, A. *Biochim. Biophys. Acta.* 2000, 1543, 223-238.
- [2] Patton, J. S., Carrey, M. C. *Science* 1979, 204, 145-148.
- [3] Larsson, K. *J. Phys. Chem.* 1989, 93, 7304-7314.
- [4] Gustafsson, J.; Ljusberg-Wahren, H.; Almgren, M.; Larsson, K. *Langmuir* 1997, 13, 6964-6971.
- [5] Barauskas, J.; Johnsson, M.; Joabsson, F.; Tiberg, F. *Langmuir* 2005, 21, 2569-2577.
- [6] Vandoolaeghe, P.; Tiberg, F.; Nylander, T. *Langmuir* 2006, 22, 9169-9174.

# Annexin binding to phospholipid membranes

K. Seidel, P. Vandoolaeghe, B. Nickel

Ludwig-Maximilians-Universität, Departement für Physik, Lehrstuhl Rädler, Geschwister-Scholl Platz 1, 80539 München

We study the interaction of proteins with phospholipid membranes. A suitable and well-established model system for surface sensitive studies are substrate supported membranes [1]. The protein that was investigated in this study, Annexin II, is a peripheral membrane protein that binds to negatively charged lipids in a calcium dependent manner [2]. There are two possible conformations the protein may bind to a lipid membrane that differ in the height of the protein layer (figure 1). The primary goal of this work was to reveal the actual conformation.

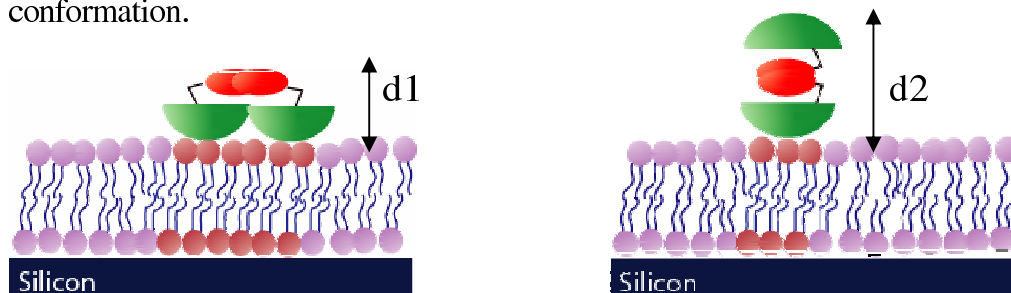


Figure 1: Phospholipid membrane with bound Annexin II. Shown are the two possible conformations that differ in height of Annexin II.

Reflectivity measurements were conducted at REFSANS. We used a microfluidic chamber that allows for the control of the quality of the membrane by fluorescence microscopy and neutron measurements at the same sample. Our substrates consist of  $100 \times 50 \times 10 \text{ mm}^3$  silicon block with oxide layers of 1000nm, to minimize quenching of fluorescence dyes during fluorescence microscopy.

The first measurement was the bare substrate in D<sub>2</sub>O mounted on the fluidic cell. 3 angles were measured: 0.5, 2 and 3 degrees. The distances of the detector were 5m for 0.5 and 2 degrees and 11m for 3 degrees. The instrument was used in time of flight mode at three different chopper settings that set wavelength distribution and resolution. The slit opening before the sample was 0.8, 3.4 and 5mm respectively.

After this measurement the chamber was filled with 100nm vesicles of a 3:1 1-Palmitoyl-2-Oleoyl-*sn*-Glycero-3-Phosphocholine (POPC): 1-Palmitoyl-2-Oleoyl-*sn*-Glycero-3-[Phospho-L-Serine] (Sodium Salt) (POPS) where the POPS is negatively charged. As fluorescent probe 0.5 mol% of Texas Red DHPE lipid was added to this mixture.

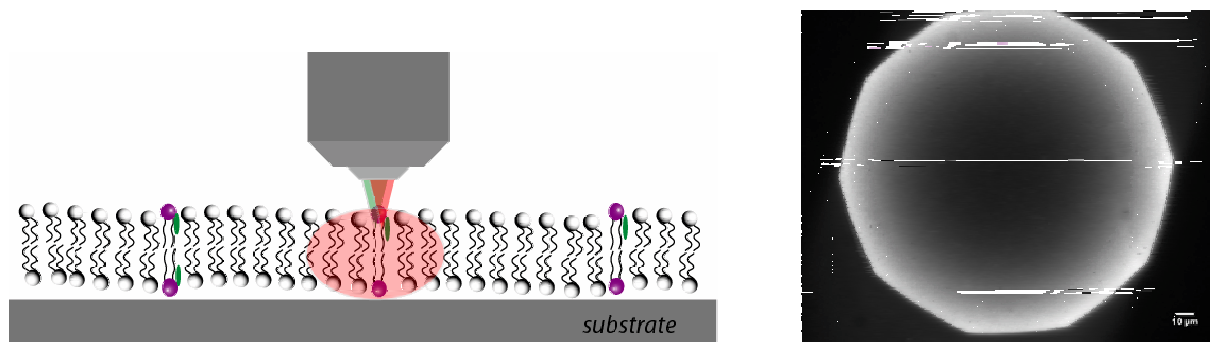


Figure 2: Fluorescence microscopy picture of a 3:1 POPC:POPS membrane after vesicle spreading with osmotic pressure. The picture was taken after 50min of continuous bleaching. The white rim indicates a high mobility of the membrane lipids and thus an intact membrane.

To gain fluid bilayers of such a mixture on silicon, vesicle spreading with osmotic pressure was used. Figure 2 shows the microscope image of such a membrane after 50min of continuous bleaching. The clearly visible white rim indicates an intact and fluid membrane [3]. After the control by fluorescence microscopy the sample was returned to the sample stage of REFSANS and measured 0.8 and 3 degrees. The slit opening was 0.6 and 3mm. The detector sample distances were 5 and 11m. Different chopper settings were used for each angle.

Afterwards measurements of the protein layer bound to the membrane were taken at 0.8, 3 and 4.5 degrees incident angle, using detector distances of 5m, 11m and 2m. The slit opening before the sample was 0.6mm, 3mm and 4mm. Different chopper settings for each incident angle to optimize flux were used.

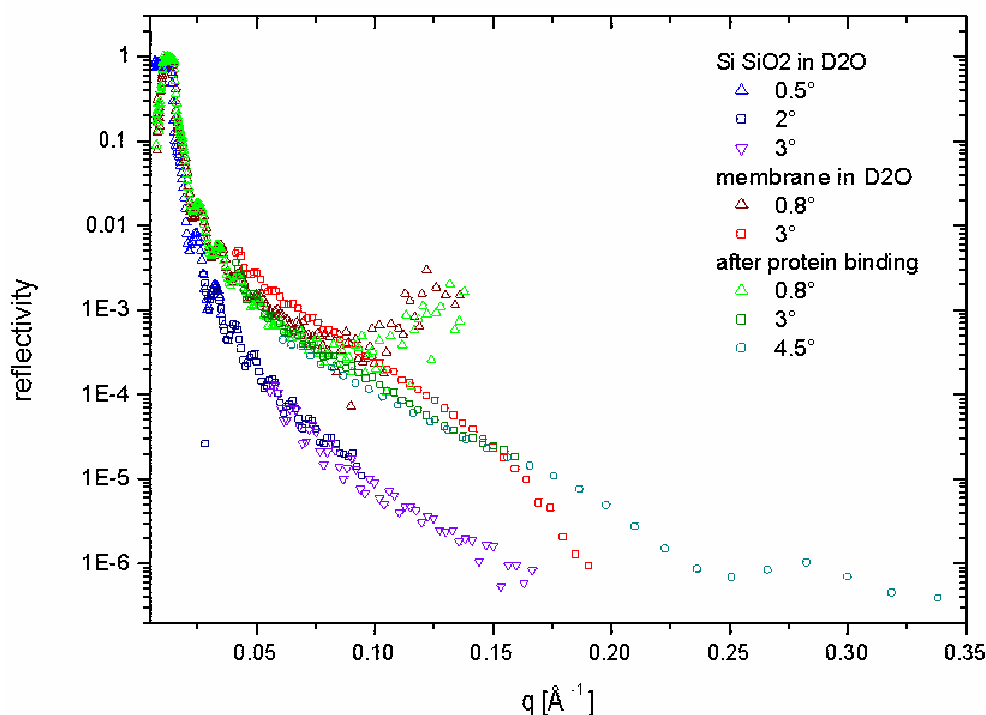


Figure 3: Summary of reflectivity data of the siliconblock with oxide layer in D2O (blue and purple data points), after vesicle spreading (red data points) and binding of the protein (green data points)

Figure 3 summarizes the experimental data. Intensities have been normalized to the incident beam intensity. The  $q$  values were calculated from the time of flight, the distance sample detector and the incident angle of each measurement. As can be clearly seen the data measured at different angles do not overlap properly. Furthermore the total reflection edge does not fit to the expected value.

The main conclusion from this experiment is to use, at this point, only one chopper detector setting for all incident angles to overcome problems in the data analysis. This has been done in the following experiment (see report P. P. Vandoolaeghe ). The Annexin experiment has to be repeated in February 08.

## References

- [1] M. Hochrein, C. Reich, B. Krause, J. Rädler and B. Nickel, Langmuir 22, 538, (2006)
- [2] M. Menke, M. Ross, V. Gerke, and C. Steinem, Chem. Bio. Chem 5, 1003, (2004)
- [3] M. R. Horton, C. Reich, A.P. Gast, J. Rädler, B. Nickel, Langmuir 23, 6263, (2007)

## Improved order in thick tri-block copolymer films by different annealing strategies, No. 1337

### Experimental team:

**E. Metwalli**<sup>1</sup>, **P. Müller-Buschbaum**<sup>1</sup>

<sup>1</sup>TU München, Physik-Department LS E13, James-Franck-Str. 1, D-85748 Garching, Germany

Instrument: REFSANS, 11-26-2007 to 11-29-2007

Local contact: J.-F. Moulin, R. Kampmann

The plan for this experiment at REFSANS was to investigate alternative routes towards a tri-block copolymer film structure with increased order. The examined model system consisted of the A-B-A type tri-block copolymer poly-paramethylstyrene-b-poly-styrene-b-poly-paramethylstyrene with a fully deuterated central polystyrene block, denoted P(pMS-b-Sd8-b-pMS), and both components being nearly symmetrical in the number of monomer units. The selected molecular weight was  $M_w = 280\,000$  g/mol (narrow molecular weight distribution  $M_w/M_n = 1.1$ ). Due to the high molecular weight, the strong segregation regime was addressed. Films were prepared by spin-coating on pre-cleaned silicon substrates. In previous experiments at the D22 instrument at ILL Grenoble a powder-like disordered lamellar morphology had been observed [1]. The samples consisted of thick films on Si substrates which were annealed in a toluene vapour atmosphere. Obviously, in these films interfacial interactions with the atmosphere and the substrate did not allow for the formation of a regular lamellar structure. However, applications based on tri-block copolymer films acting as templates require a good alignment of the lamellae with respect to the interfaces.

Following the proposal we prepared P(pMS-b-Sd8-b-pMS) films which differed in the post production treatment. In addition to these samples we made a reference sample, which was prepared identically to the samples which had been investigated at the D22. To test the performance of the REFSANS instrument we started with this sample. The idea was, on the one hand, to get well controlled starting conditions for the experimental settings of the REFSANS instrument and on the other hand, to have a direct comparison with the D22 performance.

Unfortunately, the start was delayed by the dismounting of the previous experiment at REFSANS and moreover, it turned out that the instrument had serious problems with motor movements. To solve the technical problems we lost mainly the first day.

After performing the measurement of the reference sample, two additional difficulties occurred, namely severe problems with the beam profile and the intensity. The beam profile was not acceptable due to the absence of one well-defined peak in the incidence neutron beam. Instead of one Voigt-type peak a double peak was present. The problem with the beam profile was fixed by changing the neutron beam part in front of the sample (removal of 2 neutron guides) and thereby increasing the resolution. The biggest problem, however, was the dramatic low neutron flux. In 24 hours counting time, we missed a serious factor compared to the ILL experiment. Problems with non-reproducible slit movements prevented us from getting back to the former REFSANS performance. The time loss due to all these problems was so dramatic that none of the actually planned experiments could be performed. It was not even possible to obtain a measurement with a statistics comparable to earlier D22 experiments.

So basically technical problems prevented the intended experiments and we ask for another complete REFSANS beamtime to repeat the plan under better REFSANS conditions.

[1] Müller-Buschbaum, P.; Bauer, E.; Maurer, E.; Cubitt, R. *Langmuir* **2006**, *22*, 9295.



## Buried layers in thin, lamellar diblock copolymer films

### Experimental team:

Z. Di<sup>1</sup>, C.M. Papadakis<sup>1</sup>

R. Kampmann<sup>2</sup>, M. Haese-Seiller<sup>2</sup>

<sup>1</sup>Physikdepartment E13, Technische Universität München

<sup>2</sup>GKSS, Geesthacht

REFSANS, December 2007

Local contact: R. Kampmann, M. Haese-Seiller

Diblock copolymers form spontaneously oriented structures in thin film geometry, which may be useful for a number of applications, such as the creation of nanoporous films. The aim of our investigation was to gain detailed information on the lamellar structure in thin diblock copolymer films. In supported films of a poly(*d*-styrene)-*b*-butadiene (*d*PS-PB) diblock copolymer (molar mass 150 kg/mol), we have detected using grazing-incidence small-angle neutron scattering (GISANS) that the lamellae are perpendicular to the substrate [1], in agreement with our results on non-deuterated PS-PB [2]. However, one may anticipate a thin overlayer of PB because of its lower surface tension than *d*PS or a buried layer of *d*PS or PB near the substrate surface (Fig. 1). The existence of such layers is important for the accurate calculation of the free energy of the films, which allows the prediction of their orientation [3]. Since the neutron contrast between *d*PS and PB is significantly higher than the X-ray contrast between PS and PB, we carried out neutron reflectometry (NR) in order to detect possible buried layers or overlayers. A buried layer of PB leads to modulations of the Kiessig fringes (Fig. 1) having a period of  $\Delta q_z = 2\pi/D_{\text{buried}}$ . Such a layer is expected to have a thickness of approximately a quarter of the lamellar thickness, i.e. the thickness of one PB block.

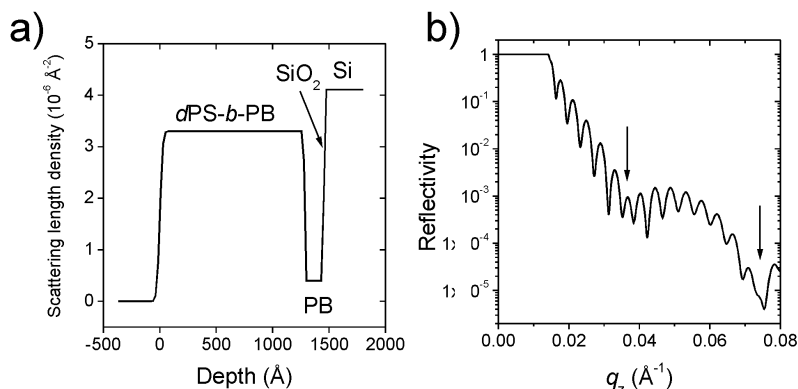


Fig. 1: Scattering length density profile of a thin film consisting of perpendicular lamellae and a thin buried PB layer (a). The corresponding NR curve (b) shows modulations of the Kiessig fringes, their minima are marked by arrows.

Two films from *d*PS-PB (molar mass 150 kg/mol) were prepared by spin-coating from toluene solution onto Si wafers with a native oxide layer. Concentrations of 20 and 30 mg/ml were used, resulting in film thicknesses of 1300 Å and 5000 Å, respectively, as determined using ellipsometry. The sample sizes were 3 × 8 cm<sup>2</sup>. Care was taken to produce films with a homogeneous thickness over the entire area. The lamellar thickness is 920 Å. The sample-to-detector distance was 10 m. NR experiments were carried out at the ToF-reflectometer REFSANS. Incident angles  $\alpha_i = 0.40^\circ$ ,  $1.00^\circ$  and  $1.50^\circ$  were used. The measuring times per angle amounted to more than 8 h per angle. A preliminary conversion of the 2D images to NR curves was carried out by the REFSANS team.

The NR curve from the thin film shows that the expected critical angle of total external reflection of the polymer was well recovered. The dynamic range amounts to nearly 6 decades (Fig. 2a). The curve shows well-resolved Kiessig fringes which indeed reveals the expected modulation (arrow in Fig. 2a). The minimum is at the position expected for a thin PB layer (Fig. 1b). However, the curves measured at different incident angles do not overlap but are shifted along  $q_z$ . Especially the curve

## Buried layers in thin, lamellar diblock copolymer films

measured at  $0.4^\circ$  deviates from the one at  $1.0^\circ$ . This is also reflected in the plot of the positions of the minima (Fig. 2b). Not only are the curves shifted, but they are also distorted. Film thicknesses between 1330 and 1950 Å are obtained.

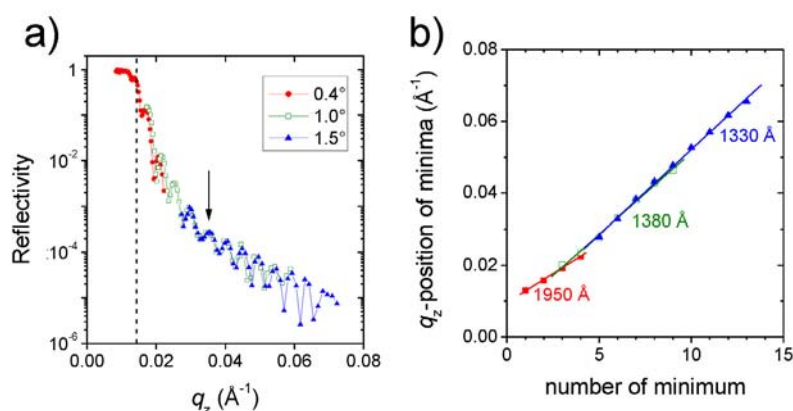


Fig. 2: (a) NR curve of the thin film (1300 Å) measured using the incident angles given. The dashed line denotes the critical  $q_z$ -value of the polymer film. The arrow marks the minimum of the modulation. (b) Positions of the minima of the Kiessig fringes in (a). The film thicknesses calculated from the slope of the fitted lines are given. Same symbols as in (a).

The thick film has a film thickness of 5000 Å. Optimizing the resolution, Kiessig fringes could indeed be resolved (Fig. 3a). However, they are weak, and no modulation was present. This is probably due to the high thickness of the film which approaches the bulk limit. The decay does not fit to the expected critical angle of the polymer. Again, there is a severe mismatch of the  $q_z$ -values calculated for each angle (Fig. 3b): The slopes differ by 12%, and the minima are significantly shifted. The curve measured at  $0.4^\circ$  seems to be shifted/distorted.

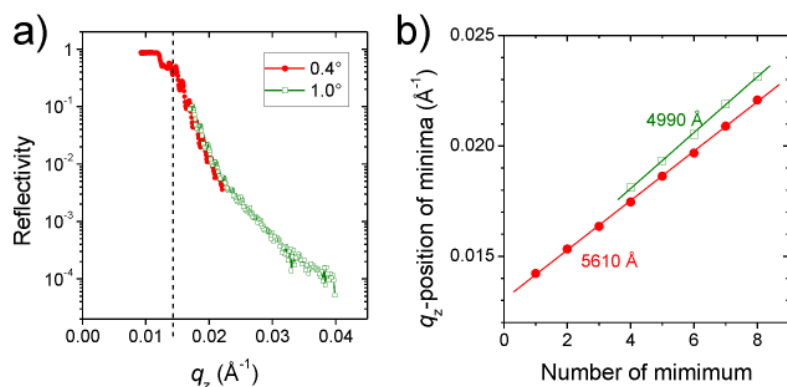


Fig. 3: (a) NR curve of the thick film (5000 Å) measured using the incident angles given. The dashed line denotes the critical  $q_z$ -value of the polymer film. (b) Positions of the minima of the Kiessig fringes in (a). Same symbols as in (a).

In order to get better knowledge on the absolute value of  $q_z$  and to characterize the NR around the critical angle, the NR curve of a blank Si wafer was measured as well. However, more than three months after the experiment, the data have not been provided by the REFSANS team yet, in spite of a large effort from our side. Neither have correct  $q_z$ -values been provided.

We conclude that the experiment was very successful. However, the measuring times (in total several days per sample!) appear unusually long. Moreover, since a part of the data has not been made available to us and no help has been provided by the REFSANS team for correcting the wrong  $q_z$ -scales, we cannot analyse the data further or even publish them.

1. Z. Di, C.M. Papadakis, R.Kampmann, M. Haese-Seiller, V. Kudryashov, Exp. Report 399, FRM II, 2008.
2. D.-M. Smilgies, P. Busch, C.M. Papadakis, D. Posselt, *Synchr. Rad. News* **15**, no. 5, p. 35 (2002). P. Busch, D.Posselt, D.-M. Smilgies, D. Posselt, B. Rheinländer, F. Kremer, C.M. Papadakis, *Macromolecules* **36**, 8717 (2003). C.M. Papadakis, P. Busch, D. Posselt, D.-M. Smilgies, *Adv. Solid State Phys.* **44**, 327 (2004). P. Busch, D. Posselt, M.Rauscher, D.-M. Smilgies, C.M. Papadakis, *Macromolecules* **40**, 630 (2007). C.M. Papadakis, Z. Di, C. Darko, D. Posselt, D.-M. Smilgies, M.A. Singh, in: *Lecture Notes in Physics: Applications of Synchrotron Light to Non-Crystalline Diffraction in Materials and Life Sciences*, in print.
3. I.I. Potemkin, *Macromolecules* **37**, 3505 (2004). I.I. Potemkin, P. Busch, D.-M. Smilgies, D. Posselt, C.M. Papadakis, *Macromol. Rapid. Commun.* **28**, 579 (2007).



# Lipidschichten auf Titan, Proposal No. 1542

## Experimental team:

Frank Feyerabend<sup>1</sup>, Michael Störmer<sup>1</sup>, Dieter Lott<sup>1</sup>, Vasyl Haramus<sup>1</sup>, Regine Willumeit<sup>1</sup>, Martin Haese-Seiler<sup>1</sup>, Reinhard Kampmann<sup>1</sup>

<sup>1</sup>GKSS Forschungszentrum Geesthacht

Instrument: REFSANS, 13.09. – 07.10. 2007

Local contact: Reinhard Kampmann, Martin Haese-Seiler

## Objectives

Phospholipids (PL) are major constituents of cell membranes and play a crucial role in cellular processes such as signal transduction, calcification and apoptosis [1]. A potential application of phospholipids is their use as biomimetic implant coatings. Such coatings have been shown to improve cell differentiation [2]. In addition to the direct interactions between cells and coatings, another possible effect of the coatings is to modify the interactions of proteins with the implant surface. All lipids coatings are so far not covalently linked to the surface because the preparation is based on the self assembly of multilamellar lipid layers by evaporation of a solvent. Only from the cellular reaction we can judge that a lipid film must be present even after exposure to water or growth medium. However the independent prove and characterization of such an existing lipid bi – or multi layer is of utmost importance for further studies of cellular interaction. We therefore assume that neutron reflectivity seems to be an appropriate measurement method and that REFSANS shows high enough intensity and the wide q-range necessary to evaluate layer thicknesses from several 100 nm down to the scale of a single lipid bilayer in the range of about 4 nm in dry state.

## Experimental

Titanium alloy (Ti6Al7Nb) was deposited on the silicon substrates by sputter deposition with a layer thickness around 100 nm.

Phospholipid coating was done with the phospholipid 1-palmitoyl-2-oleoyl-sn-glycero-3-phospho-ethanolamine (POPE). POPE was solved in chloroform:methanol (80:20) and applied to the substrate. Afterwards the solvent was evaporated for 2 hours. The lipid layers were measured in this stage by neutron reflectometry at REFSANS.

Afterwards the samples were incubated in distilled water for 2 hours at room temperature. After drying they were measured again. A schematic drawing of the supposed layer composition is given in Figure 1.



Figure 1: Supposed layer composition after the different treatments.

## Results and Discussion

Figure 2 shows the reflectivity curves taken at the different stages of the preparation of the sample. After applying the POPE solvent on the TiAlNb film, a strong peak appears between a momentum transfer of 0.1 and 0.12 1/Å which is due to the repeat distance of the lipid chains. The strong intensity and small width of the peak indicates that the POPE film consist of many bilayers of lipids

## Lipidschichten auf Titan, Proposal No. 1542

(multilayers) which even allows one to detect the second order at around 0.22 1/Å. After the incubation as described above the intensity of the first peaks reduces drastically while the second order could not be observed any more. By comparing the reflectivity curves for the initial pure TiAlNb film and the one after incubation one can clearly identify some broad additional intensity. This a clear indication that a small number of POPE layers is still present on the TiAlNb film after incubation.

In the next steps, the the preparation technique will be optimized by further neutron reflectivity studies to examine the time dependence of the incubation process. Moreover, the adhesion of proteins should be measured.

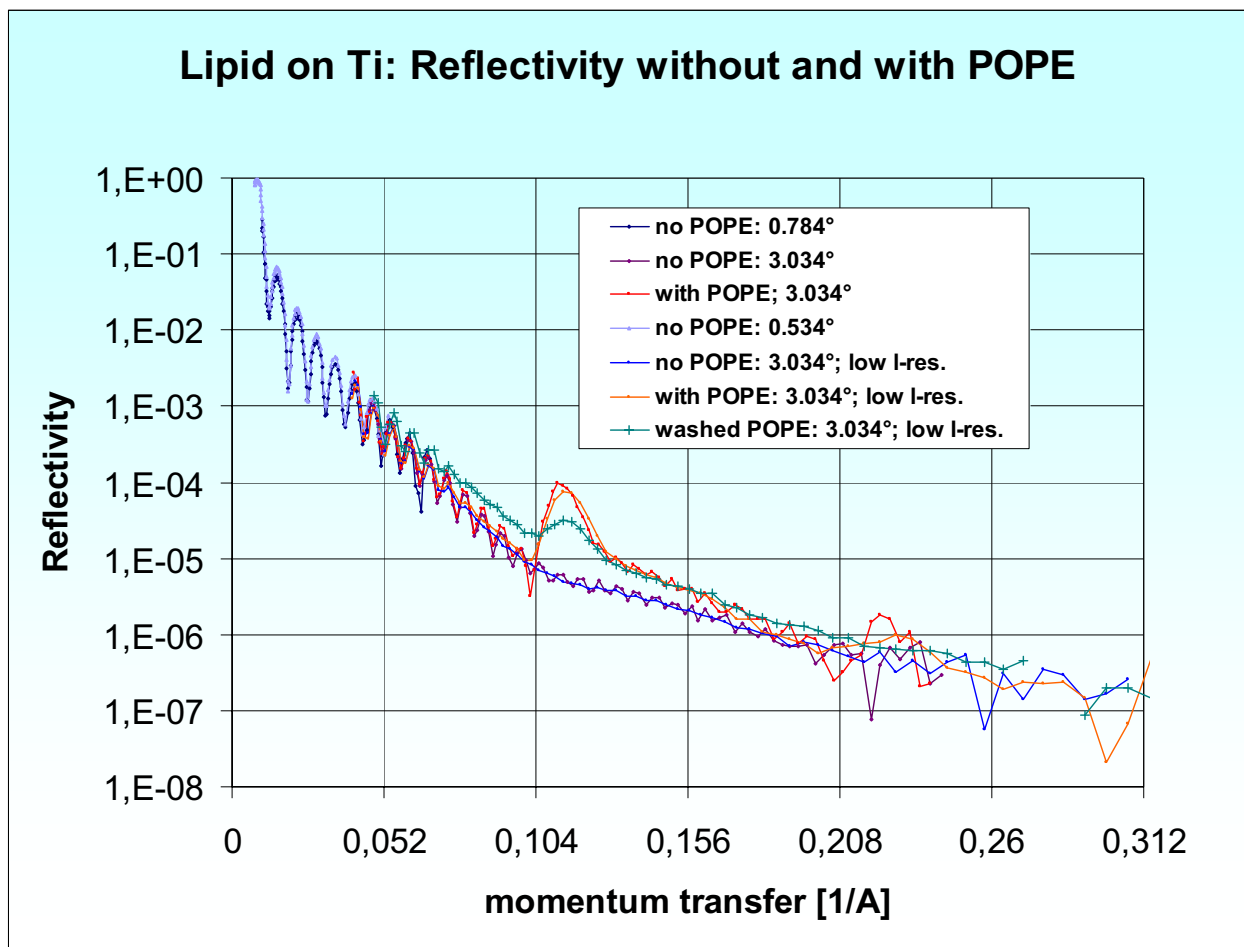


Figure 2: Reflectivity at different resolutions on the sample in different stages as indicated in the legend.

### Literature

- [1] Bevers EM et al. *Biol Chem* **1998**, 379, 973.
- [2] Willumeit R et al. *Eur Cell Mater* **2007**, 13, 11.

## <GISANS on REFSANS>, <1707>

### Experimental team:

W. Kreuzpaintner<sup>1</sup>, Jean-Francois Moulin<sup>1</sup>

<sup>1</sup> GKSS Forschungszentrum GmbH, Max-Planck-Straße 1  
21502 Geesthacht

Instrument: **REFSANS, December 21-24 2007**

Local contact: **Jean-Francois Moulin, Martin Haese-Seiller, Reinhard Kampmann**

### Introduction

Grating incidence small angle neutron scattering allows to address wide ranges of the reciprocal space which by other scattering geometries is not accessible. REFSANS is ideal for small angle neutron scattering and with its TOF option allows to apply the entire available neutron wavelength spectrum for the experiment and also allows the analysis of wavelength spectra for inelastic scattering which are intended for the future.

We here briefly report on Grating incidence small-angle neutron scattering investigation which - complementarily to the results gained by x-ray methods - addresses the lateral structure of the prepared laterally structured Ni sample as preinvestigative experiment for inelastic measurements under grazing incidence geometry.

### Experimental

For the experiment a 1" in diameter large and (by other methods) well pre-characterized thin polycrystalline laterally structured Ni sample with a total Ni structure thickness of approx. 13 nm and a lateral dot diameter of 200 nm at a spacing of 700 nm arranged in a square symmetry was used. An SEM image is shown in figure 1 and its diffusely scattered intensities as function of the sample rotation is shown in figure 2.

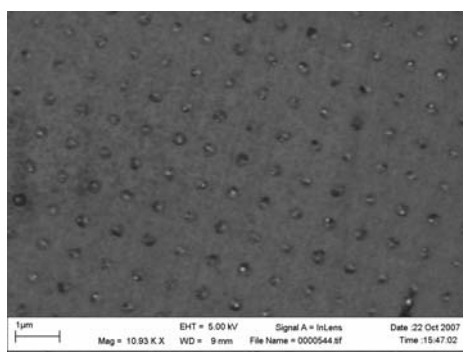


Figure 1: SEM image of the investigated Ni dot array sample on Si showing its lateral structure.

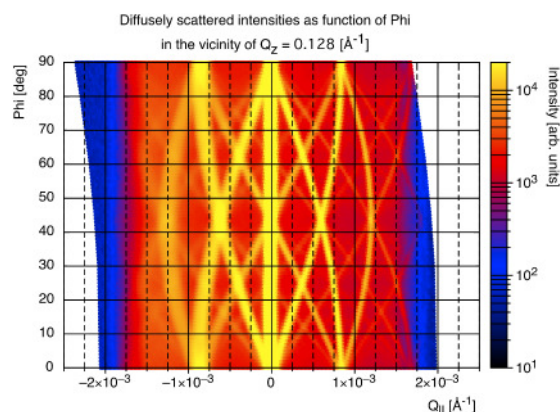


Figure 2: Diffusely scattered X-ray intensities as a function of the sample rotation obtained by rocking scans.

Measurements were performed at room temperature without any applied external field utilizing the full neutron spectrum available at REFSANS.

The incidence angle was  $0.348^\circ$  and the detector sample to detector distance was chosen such that the detector was in the focal point of the neutron beam and was measured to 9.35 m. Apart from quickly recording primary beam spectra and the position of the totally reflected neutron beam, two measurements were performed: one with the sample aligned such that the axis of the lateral structure on the sample surface was aligned parallel to plane defined by the primary and the

## <GISANS on REFSANS>, <1707>

specular beam direction and one such that the lateral structure was rotated approximately  $-4^\circ$  counterclockwise to this direction.

During the experiment REFSANS performed superbly and no problems with the machine were encountered.

### *Results and discussion*

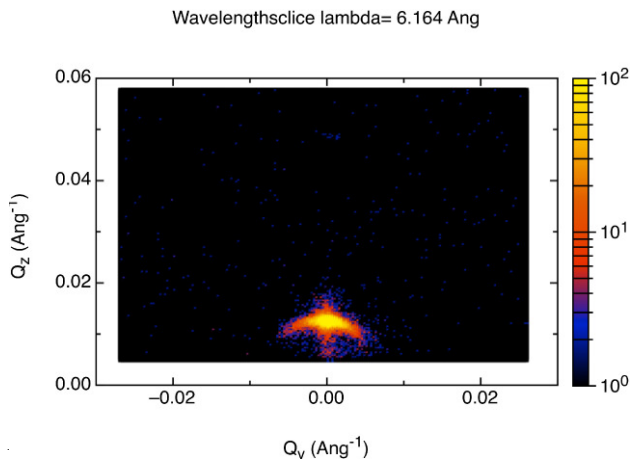


*Figure 3: GISANS as measured with the beam direction parallel to one axis of the Ni dot array.*

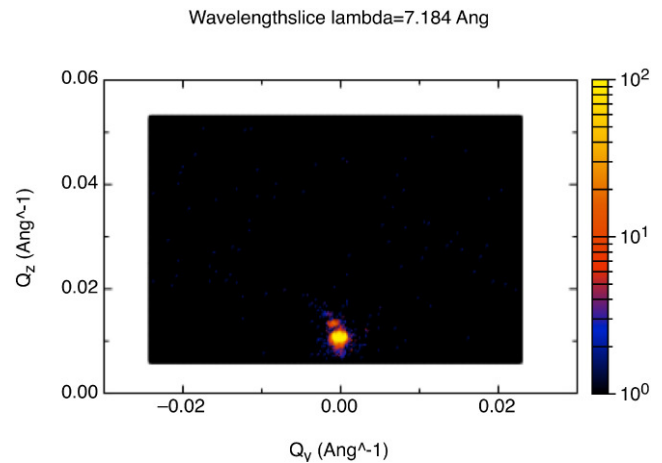


*Figure 4: GISANS as measured with the rotated sample.*

Figure 3 and figure 4 show the reciprocal space maps of the GISANS measurements at wavelength slices of 6.164 Angstrom and 7.184 Angstrom respectively as obtained from the DART and NESTOR evaluation software package available at REFSANS. The difference in the scattered intensities is only due to the rotation of the sample around its out of plane axis as the data was already converted into Q values and hence is wavelength independent. The next step in the evaluation of the data will be to integrate the intensities in the reciprocal space over the entire wavelength spectrum instead of only using a single wavelength slice.

As data analysis is in its early stages, we currently cannot make a detailed interpretation of the obtained data. However, if comparing first REFSANS results with the results gained by x-ray measurements on the same sample approximately the same order of magnitude in the structure size, with a slight discrepancy is obtained whose origin must still be investigated and could be a mistake in our data analysis.

# Texture evolution in tungsten wire, proposal no. 664

## Experimental Team:

**J. Ocenasek<sup>1</sup>, C. Krempaszky<sup>1,2</sup>, U. Garbe<sup>3</sup>, J. Repper<sup>1</sup>, E. Werner<sup>2</sup>**

<sup>1</sup>) Christian-Doppler Laboratorium für Werkstoffmechanik von Hochleistungslegierungen

<sup>2</sup>) Lehrstuhl für Werkstoffkunde und Werkstoffmechanik, TU München, Boltzmannstraße 15, D-85748 Garching, Germany

<sup>3</sup>) FRM-II, TU München, Lichtenbergstr. 1, D-85747 Garching, Germany

Instrument: Stress-Spec

Period: 29<sup>th</sup> January 2007 – 4<sup>th</sup> February 2007 (7 days)

Local contact: Michael Hofmann

## Introduction

Tungsten wire used in lightening industry is produced from sintered tungsten rods which are rolled, swaged and hammered prior to the multi-pass drawing process. During this severe deformation process (mostly during first drawing steps) longitudinal intergranular cracks sometimes occur, which are known as splits and are considerably undesirable. This problem has not been yet fully understood, but it is apparent that not only the residual stresses of first order, but also the stress localization at grain boundaries and second order residual stresses are of importance. Therefore the optimization of drawing process parameters requires the knowledge of micro-structural material behaviour at the intergranular level. During the production process, tungsten is repetitively highly deformed affecting significantly the development of microstructure and texture. Originally equiaxed grains get highly elongated in the longitudinal section. Furthermore, the BCC tungsten grains rotate leading to a pronounced (110) fibre texture.

High-quality texture measurements of different wire diameters are necessary to identify the microstructure of tungsten wires during wire processing and are essential for calibrating numerical models used for the texture prediction.

Tungsten wires of three different diameters (1.0mm, 2.5mm and 3.5mm) were chosen for the texture measurements. Two additional samples (C and E) were prepared by removing the wire surface in acid in order to measure only the inner volume of the wire which is not affected by the friction with drawing die, see Table 1.

**Table 1 – Notation of the samples**

Sample	Wire diameter	Diameter reduction
A	3.5 mm	no reduction
B	2.5 mm	no reduction
C	2.5 mm	to 1.1mm
D	1.0 mm	no reduction
E	1.0 mm	to 0.3mm

The measurements of three crystallographic planes (110), (200) and (211) were attempted.

## Measuring details

The neutron beam was monochromatized with the Pyrolitic Graphite (002) monochromator which provided a wavelength of 2,41Å. To achieve a bigger angle scale on one measuring position a PSD detector in a distance of 79cm to the sample position was used.

### Discussion on results

Drawn tungsten wires of smaller diameter exhibit more pronounced (110) texture, the measurement of the (110) reflection was successful even on single wires with the diameter of 0.3mm. As an alternative to sample containing a single wire a pack of 24 wires was measured to achieve better statistic. Texture measurements on the finer samples with the diameter of 0.3mm in other crystallographic directions than (110) exhibited poor quality. As an example the (110) fibre texture is shown in Fig 1.

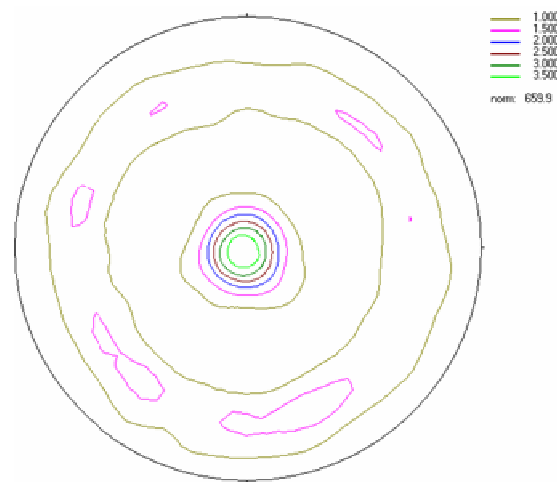


Fig 1 The (110) pole figure of the sample B; equal area mapping; the centre of the pole figure corresponds to the wire axis

# Texture Proposal for Mg samples. Analysis of the effect of Sn and strain rate in the texture for HPDC alloys, Proposal no 767

Gurutze Arruebarrena<sup>1</sup>, Iñaki Hurtado<sup>1</sup>, Menachem Bamberger<sup>2</sup>, Uwe Wasmuth<sup>3</sup>, Ulf Garbe<sup>4</sup>

<sup>1</sup> *University of Mondragon, Mondragon, Spain*

<sup>2</sup> *Technion – Israel Institute of Technology, Haifa, Israel*

<sup>3</sup> *Institute of Metal Forming and Casting (UTG), TU München, Germany*

<sup>4</sup> *Research Reactor Munich (FRM II), TU München, Germany*

Instrument: Stress-Spec, 02.07.2007-05.07.2007

Local contact: Michael Hofmann

The present report makes reference to the results obtained during the second part of the scheduled experiments time (02.07.2007-05.07.2007) and bring together with the results obtained in the first part, with the aim of writing the full report.

The aim of the proposal is to analyse the influence of texture in the mechanical behaviour of two High-Pressure Die-Cast Mg alloys. The alloy AM50 and an alloy based on the AM50 but modified with Sn (denoted as 60226), were tested at different strain rates. It is observed that the 60226 alloy presents higher mechanical properties, but when raising the strain rate, the elongation is reduced. The texture measurements at fracture were analysed in the first part of the experiments, and the second part wished to understand the texture development during deformation of the alloy AM50 at low strain rate. The results obtained in the first part of the experiments did not show any differences in texture between AM50A and 60226 alloys. For a better understanding of the texture development in a tensile test, the evolution of texture with elongation should be analysed. In-situ tensile testing is not still possible in the Stress-Spec. In order to obtain samples with different deformation levels, tensile tests were stopped when certain % of elongation was reached. It was only possible to stop the testing with low strain rates, and because of the similar behaviour in texture of both alloys, a single alloy was selected for this investigation. The bigger use in the industry of the commercial AM50A alloy was the reason why this alloy was selected for further study instead of the newly developed 60226 alloy. There are still few investigations concerning the texture evolution of the commercial AM50A alloy.

The initial deformation section of the tensile samples is 6 mm in diameter. Figure 1 shows the tensile engineering curve of the AM50A alloy, where the development of texture during testing was analysed at different deformation levels. Tensile testing was stopped at 4 different strain levels (1%, 5%, 10% and 15%), and the deformations of 20% and 26% were obtained at fracture of two different samples. The dimensions of the samples were defined by ASTM-E8M standard for HPDC samples and an extensometer with a gauge length of 50 mm was used. The most deformed part of the tested samples, about one centimetre in length including the fracture zone when samples reached fracture, was used for the texture measurements in the Stress-Spec instrument. Non-tested samples were also investigated to have a reference of their initial state. Two diffraction angle ranges,  $2\theta$ , were chosen for the texture measurements. The first one includes the diffraction peaks  $(10\bar{1}0)$ ,  $(0002)$  and  $(10\bar{1}1)$ . The second range includes the peaks  $(11\bar{2}0)$  and  $(10\bar{1}3)$ .

Figure 2 shows the  $(10\bar{1}0)$  pole figures obtained in the AM50A samples at different strain levels. The evolution of the texture in a tensile test can be observed in this figure. The as-cast sample prior to testing is a non-textured sample, presenting a near random distribution of grains (mrd max. 1,1) what could be expected from the solidification conditions. A texture generates in the tensile testing, getting more intensity in the 0 0 degrees in the  $(10\bar{1}0)$  pole figures. Nevertheless, a change in the main orientation is observed in the 26% elongated sample.

Texture Proposal for Mg samples. Analysis of the effect of Sn and strain rate in the texture for HPDC alloys, Proposal no 767

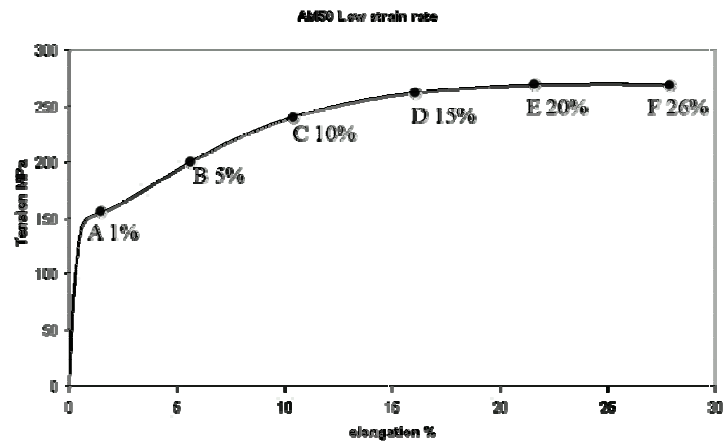


Figure 1 – Engineering tensile curve of the alloy AM50A, showing the points of deformation where texture was measured

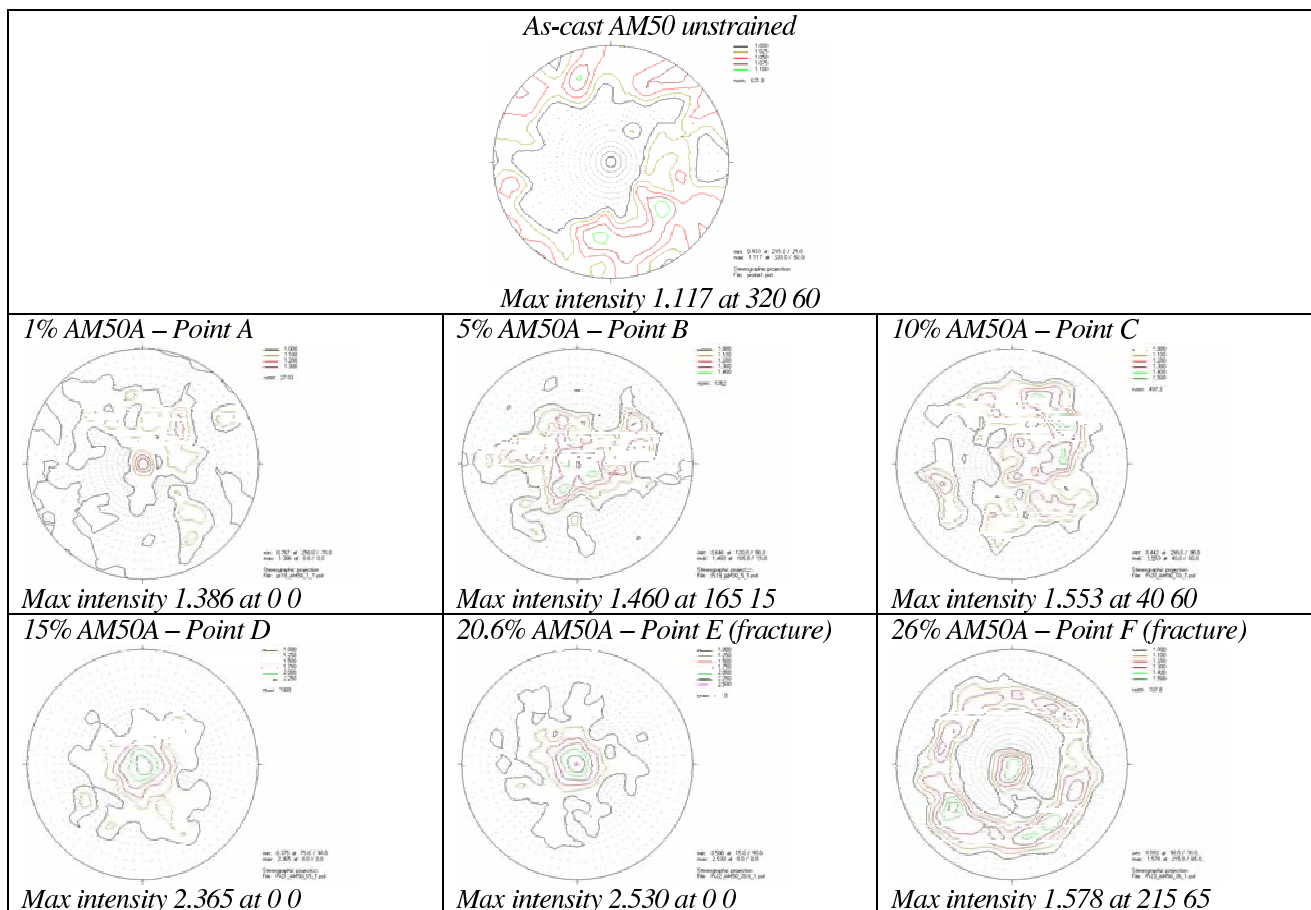


Figure 2. Pole figures for the diffraction peak  $(10\bar{1}0)$ .

The sample references correspond to the deformation conditions described in Table I

An article is expected to be published with the results obtained in the Stress-Spec, where microstructures of the samples will also be discussed and compared to the texture development. Further experiments may be required to verify a second preferred orientation on the  $(11\bar{2}0)$  plane.



# Texture evolution of AZ31B Mg alloy sheet samples deformed at high speed and medium temperatures, 917

## Experimental team:

Ibai Ulacia<sup>1</sup>, Iñaki Hurtado<sup>1</sup>, Gurutze Arruebarrena<sup>1</sup>, Michael Worswick<sup>2</sup>, Ulf Garbe<sup>3</sup>

1 University of Mondragon, Mondragon, Spain

2 University of Waterloo, Waterloo, Canada

3 GKSS Outstation FRM II, Germany

Instrument: Stress-Spec, 25.09.2007-28.09.2007 & 15.10.2007-16.10.2007

Local contact: Michael Hofmann

The present report makes reference to the results obtained during the proposal with ID: 917. The aim of the proposal was to analyse the influence of texture in the mechanical behaviour of a wrought magnesium alloy AZ31B of 1 mm thickness that was previously tested at different strain rates and temperatures. It is observed from the tensile tests that increasing the strain rate, both, the flow stress and the elongation increase. Besides, the temperature increase produces a decrease of the flow stress for the whole strain rate tested. However at quasi-static strain rates a softening behaviour is observed that it is not so evidence at high strain rates.

With the purpose of determining the reason of the different behaviour at different strain rates samples from the fracture zone of tensile tested specimens were studied in the Stress-Spec instrument. In table I the analysed specimens are shown. Two diffraction angle ranges,  $2\theta$ , were chosen for the texture measurements. The first one, from 31 to 43 degrees, includes the diffraction peaks  $(10\bar{1}0)$ ,  $(0002)$  and  $(10\bar{1}1)$ . The second range includes the peaks  $(11\bar{2}0)$  and  $(10\bar{1}3)$ .

Table I – Tensile test samples of AZ31B sheet

Reference	Tensile test condition – Direction	Sample dim. (mm <sup>3</sup> )	YS (MPa)	E %
AZ31B-0	As received (Not tested)	12.5x~5x1		
QS21RD	0.001s <sup>-1</sup> & 21°C – Rolling Direction	12.5x~5x1	145	22
QS21TD	0.001s <sup>-1</sup> & 21°C – Transversal Direction	12.5x~5x1	170	19
QS250TD	0.001s <sup>-1</sup> & 250°C – Transversal Direction	6x~5x1	65	53
HSR21TD	1000s <sup>-1</sup> & 21°C – Transversal Direction	1.75x~5x1	280	25.5
HSR250TD	1000s <sup>-1</sup> & 250°C – Transversal Direction	1.75x~5x1	225	20

When comparing the texture state of the different samples, all the general tendencies shown for each peak are comparable. As an example of the results, figure 1 shows the evolution of the peak  $(10\bar{1}0)$ .

It is also remarkable that the measuring time is quite high for the small samples used in the high strain rate testing (approximately 36h.) while it is considerably smaller for the biggest dimension samples.

## Texture evolution of AZ31B Mg alloy sheet samples deformed at high speed and medium temperatures, 917

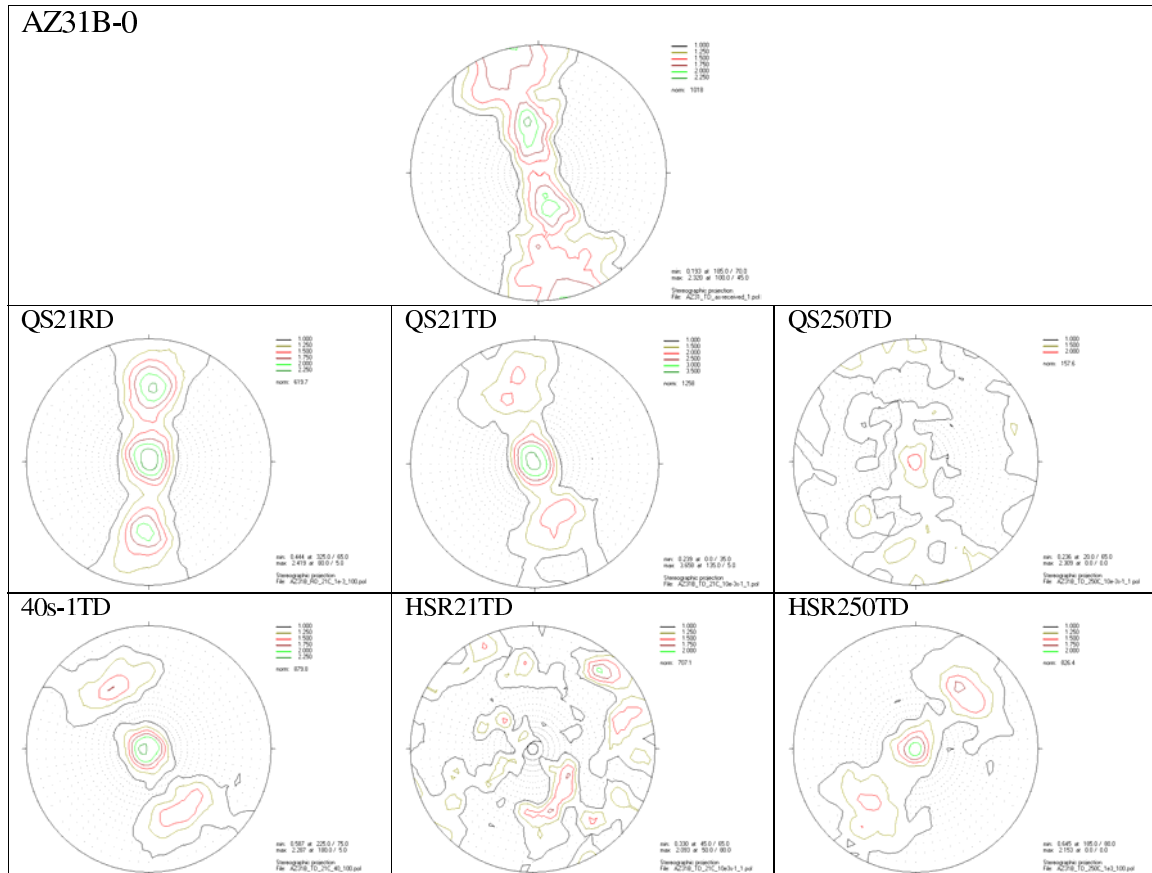


Figure 1. Pole figures for the diffraction peak  $(10\bar{1}0)$ .  
The sample references correspond to the deformation conditions described in Table I

From the figures, the first conclusion that can be observed is that the initial material has a clear texture (mrd max. 2.25), common in wrought materials after rolling process. However the commercial material acquired for this study was totally annealed (O condition) and this initial texture was not expected. This initial texture when deformed at low and intermediate strain rates is increased when testing at room temperature (mrd max. 3.5). On the other hand, when the strain rate is higher ( $1000s^{-1}$ ) and also at room temperature, it can be seen that there is not a preferential direction (random), thus there is not texture. At elevated temperatures, it can be observed that the texture decreases for the quasi-static strain rates due to the new grains that are formed as a consequence of the dynamic recrystallization that undergoes. Furthermore at high strain rates it is observed that the preferential direction is kept, although the intensity is a bit lower. It can be seen that for the samples with an increase in elongation the texture was decreased (QS250TD and HSR21TD).

These results help to properly know the initial material that is being studied. It can be outlined that the studied magnesium alloy experiences extremely different microstructural behaviour depending on the strain rate range. Although some points were clarified, the whole study is not completed yet and others aspects will be studied in the next period of measurements at the Stress-Spec. It would also be interesting to test samples deformed at high strain rate at different deformation values before breaking (i.e. 5%, 10%, 15% deformation). These new results would help to understand how the texture evolves from the initial state to the final one, giving a hint on the deformation behaviour of the material.

## **Appendix II**

**Reports of experiments carried out  
at the GKSS outstation at DESY in Hamburg  
in support of internal and external users.**

**These reports have been taken from  
HASYLAB Annual Report 2007.**

(Reprinted by courtesy of DESY, Hamburg)



# New developments at the Engineering Materials Science Beamline HARWI II

*T. Lippmann, L. Lottermoser, F. Beckmann, R. V. Martins, T. Dose, R. Kirchhof and A. Schreyer*

*GKSS Forschungszentrum Geesthacht, Max-Planck-Str. 1, 21502 Geesthacht, Germany*

2007 was the first year of full user-mode at the engineering materials science beamline Harwi II. In addition to the scheduled experiment time for users and for in-house research, a fraction of the beamtime was dedicated for testing and commissioning of new equipment as introduced below. Last year, the first test experiments using the double-crystal Laue-type high-energy monochromator had shown that the beam stability of the monochromatic beam was not sufficient. A drift of the reflection positions was observed during a complete DORIS run, which was ascribed to heat load of the square-centimetre-sized beam on the first crystal. Thus, a simple water-cooled crystal-cooler was installed (Fig. 1), which can be equipped with up to 3 crystals. Further stability tests this year have now shown that the reflection positions do not change more than a few  $10^{-4}$  degree over weeks, which is sufficient for most of the experiments.

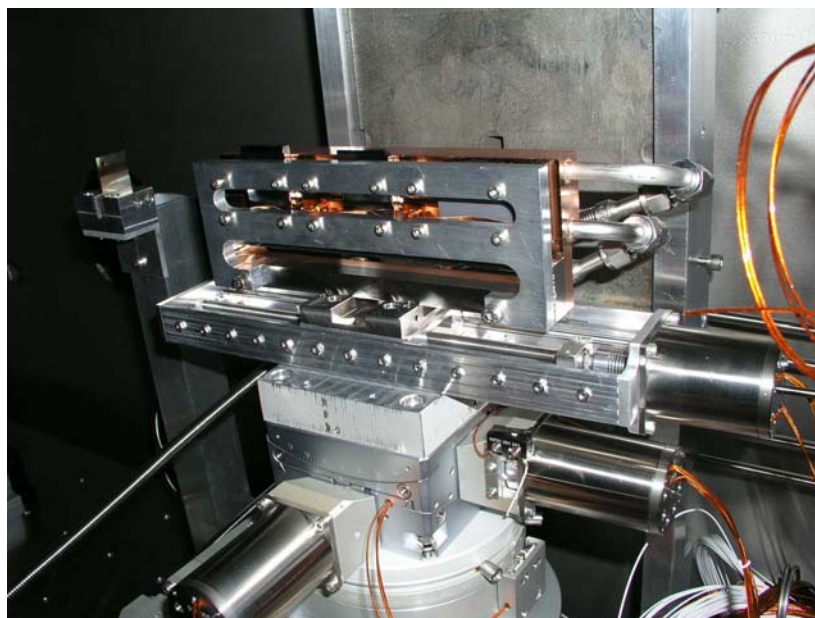


Figure 1: Snapshot of the high-energy monochromator's first tower. The crystal changer is equipped with three crystals: Si 111 (left), Si 111 annealed (middle) and SiGe 111 (right). Polished faces of the crystals are pressed on the polished backside of the copper cooler, which has several holes to let the beam through.

A further improvement of the monochromator was the outfitting with Silicon-Germanium (SiGe) gradient crystals. The gradient crystals have been manufactured by the Institut für Kristallzüchtung (IKZ), Berlin, and the first pair of SiGe 111 has recently been installed and tested. At our standard energy of 100 keV the intensity gain is approximately a factor of 20 compared to the annealed Si 111 crystal pair (compare Fig. 1 in [1]), i.e. a flux of  $5 \times 10^{11}$  photons/sec/mm<sup>2</sup> in the beam centre can now be achieved. Details concerning the use of these gradient crystals as monochromators can be found in [2].

In order to allow a supervision of the operation of the monochromators, e.g. during the alignment, video cameras are looking through the inspection windows and an LED illumination equipment has been installed in the tank. It can be operated and dimmed from outside of the hutch via remote control in order to allow optimal illumination conditions.

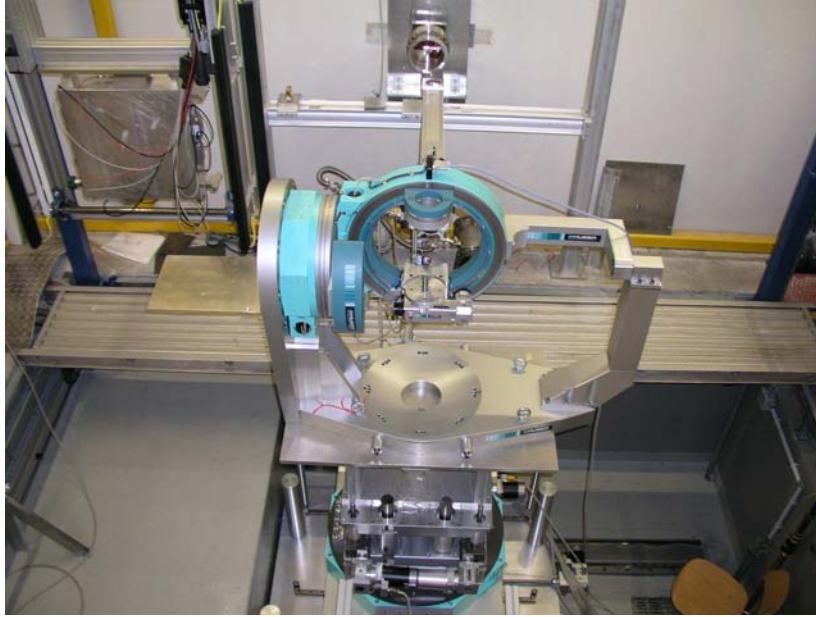


Figure 2: A view from above into the diffractometer pit. The sample tower of the materials science diffractometer was equipped with the Eulerian cradle in vertical scattering geometry.

At the beginning of this year the sample tower of the materials science diffractometer has been delivered and installed. The tower consists of a permanently installed and a variable part, and it is mounted on rails located at the bottom of the diffractometer pit, so that the whole tower can be moved in and out of the beam without deinstallation of any equipment. The 'permanent' part consists of an xyz–alignment table ( $x, y: \pm 200$  mm,  $z: \pm 250$  mm), where  $y$  is parallel to the beam and  $z$  is the height. On top of the table a tilt segment ( $\pm 5^\circ$ ) and a Huber 480 circle are mounted. Some technical details are shown in Tab. 1.

Table 1: Technical parameters of the sample tower of the materials science diffractometer.  
'Permanent' part of sample tower:

$z_1$	translation (height)	$\pm 250$ mm
$x_1$	translation ( $\perp$ beam)	$\pm 200$ mm
$y_1$	translation ( $\parallel$ beam)	$\pm 200$ mm
$\alpha_i$	tilt	$\pm 5^\circ$
$\omega$	circle	$\pm 180^\circ$
Maximum upload of 'permanent' part		600 kg

'Variable' part of sample tower:

$\chi$	tilt	$\pm 7^\circ$
$\phi$	tilt	$\pm 7^\circ$
$z_2$	translation (height)	$\pm 100$ mm
$x_2$	translation ( $\perp$ beam)	$\pm 500$ mm
$y_2$	translation ( $\parallel$ beam)	$\pm 500$ mm
Maximum upload of 'variable' part		100 kg

The 'variable' part can either be a double–tilt segment combined with a further xyz–combination, a Eulerian cradle (Fig. 2) mounted in a frame for either horizontal or vertical scattering geometry, or

large sample environments, e.g. a stress rig (Fig. 3, [1]), ovens, cryostats, magnets, etc. Completion of the diffractometer (detector tower) and of the cover of the pit are foreseen in the near future.



Figure 3: Sample tower of the materials science diffractometer equipped with the stress rig.

Since a growing number of experiments is dedicated to in-situ studies (e.g. in-situ welding, see below), a new, fast area detector (Mar555) was bought, installed and tested (Fig. 4). Technical parameters are shown in Tab. 2. First test experiments have been performed at 100 keV, e.g. [3, 4]. Fig. 4 shows the detector mounted on carrier 1 of the detector portal. Meanwhile, it is mounted on carrier 2 and the Mar345 image plate scanner is mounted on carrier 1, so that users can easily change between them. The handshake between the detector and the diffractometer is currently performed via TTL signals and VME I/O registers.

Table 2: Some technical parameters of the Mar555 detector.

Active area	430 mm × 350 mm
Pixel size	140 μm × 140 μm
Dynamic range	16 bit (18 with expansion)
Operated at	25° C
Read-out time	typically 920 msec
Weight (Harwi detector)	35 kg

Fig. 5 shows a friction stir welding test machine, which was operated at the Harwi II beamline in the first half of 2007. Friction stir welding is a method, which has been extensively investigated at the GKSS research centre during the last years. During the process, a fast rotating pin is pressed on and moved along the seam, thus heating and conclusively joining the components. In-situ





Figure 4: The Mar555 detector mounted on carrier 1 of the detector portal.

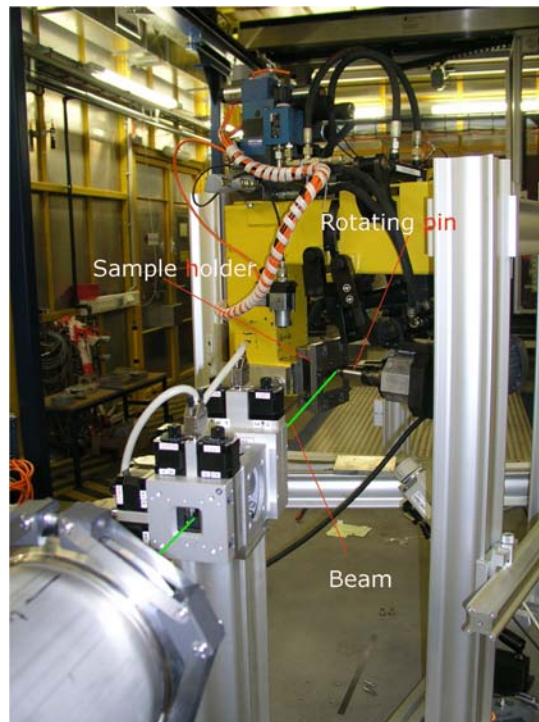


Figure 5: The friction stir welding test machine mounted on top of the 'user table'.

investigations will allow to study the stress and temperature dynamics as a function of parameters such as tool type, speed and material. In particular, the material investigation in the plastic regime is of interest for the optimization.

The test machine was a 'conventional' apparatus, which was already available in the Materials Science Institute at GKSS, and for our tests it was simply mounted within a special frame located on the 'user table' in the experimental hutch. Meanwhile, a special in-situ welding machine (FlexiStir) has been constructed (Fig. 6), and the first experiments are scheduled for December 2007.

Since each of the different experiments in the experimental hutch in principal needs to control





Figure 6: The in-situ friction stir welding apparatus FlexiStir.

the components in the optics hutch, the latter are controlled via a separate computer running the Hasylab control software Spectra Online. The connection is established by using ethernet and the socket based network device concept of the software. As an example, the diffractometer computer, which is also running Spectra Online, can address the monochromator, the counters, the shutter etc. as remote devices.

A new data acquisition software for the DENEX wire detector was developed by GKSS and has been installed on a Windows system. Communication between the detector software and the LINUX-based diffractometer control has also been realized via a socket communication port. If the image plate scanner is used, both control computers use ssh to copy command files to the MAR scanner.

## References

- [1] T. Lippmann, F. Beckmann, R.V. Martins, L. Lottermoser, T. Dose, A. Schreyer, HASY-LAB Annual Report 2006.
- [2] S. Keitel, PhD thesis, DESY-Thesis-1999-026, ISSN 1435-8085.
- [3] G. Zickler et al., this Annual Report.
- [4] T. Lippmann, this Annual Report.



# First Feasibility Study for High-Energy *in-situ* SAXS Investigation of a Friction Stir Welding Process at HARWI II

R.V. Martins<sup>1</sup>, S. Sheikhi, T. Fischer, C. Weis Olea, L.A. Bergmann, T. Lippmann, P. Staron, J. dos Santos, and A. Schreyer

GKSS-Research Centre Geesthacht GmbH, Max-Planck-Str. 1, 21502 Geesthacht, Germany

<sup>1</sup>now: JRC, Institute for Energy, Westerduinweg 3, 1755 LE Petten, The Netherlands

Metallurgical reactions such as precipitation forming, recrystallisation, and phase transformations during thermo-mechanical processing are principally responsible for the microstructure and mechanical properties of metallic engineering materials. For many decades these reactions have been studied in detail to optimise thermo-mechanical process parameters. During welding processes such as Friction Stir Welding (FSW) the localised heat input and deformation process leads to non-equilibrium microstructures in the join region. This alters the properties of the base material in the join region and can compromise the integrity of the metallic joint.

A Virtual Institute IPSUS, lead by GKSS, has been set up in 2007. The main strategic research topic of this Virtual Institute is the understanding of non-equilibrium metallurgical phenomena (i.e. precipitation, recrystallisation and phase transformation under high heating and high cooling rates) in metallic joints on lightweight materials, using *in-situ* synchrotron-based diffraction techniques. In the framework of this project this first feasibility test was carried out with a small *in-situ* FSW device. A first *ex-situ* SAXS experiment with high-energy X-rays at HARWI II had been successfully carried out beforehand [1]. At the time of the present experiment a dedicated *in-situ* FSW device was in the design phase at GKSS and is, by now, operational [2].

The aims of the experiment with the small *in-situ* FSW device were twofold. The first aim was to gather experience for future *in-situ* experiments of that kind and to optimise the experimental parameters. The second aim was to produce input for the design optimisation of the dedicated *in-situ* FSW device while still in the design phase. Figure 1 shows a picture of the experimental setup with the small *in-situ* FSW device.



Figure 1: View of the experimental setup with *in-situ* FSW device for high-energy SAXS studies at HARWI II.

The photon energy chosen was 72 keV, in order to be above the edge energy of Tungsten, the material of the beamstop, on one hand, and to have, on the other hand, a high photon transmission for the aluminum sample. The beamsize was confined by a first slit pair about 5 m before the sample to a size of  $1 \times 0.2 \text{ mm}^2$  (H x V). A second slit pair, 850 mm before the sample, was used for the cleaning up of the beam. The beamstop itself was, as in the first SAXS test at HARWI II [1], a simple block, matted on one side and moved from the bottom into the beam, hereby blocking also the lower half of the diffraction signal. It was placed 1 m behind the sample. The detector, a MAR345 online image plate scanner, was positioned at a distance of 6680 mm behind the sample. The beam incident angle with respect to the 4 mm thick Al sheets to be welded was  $20^\circ$ , leading to an illuminated gauge volume length of about 15 mm in the horizontal plane. In the present test the FSW process was slowed down in the way that the rotating tool advanced with a speed of 0.45 mm/s. That allowed an exposure time of 40 s during which the tool passed completely along the illuminated volume. These welding conditions are not close to real FSW conditions but they were judged to be sufficient for the aims of this experiment.

Figure 2 shows the results from one of the welded sheets. The gauge volume was at a distance of 2 mm below the tool shoulder in the heat affected zone of the weld. The material investigated was Al alloy AA6056-T6 which shows in its initial state (dotted line) the presence of precipitates which enhance the mechanical strength of this alloy. During the welding process it can be seen that these precipitates dissolve almost completely due to the heat input (solid line).

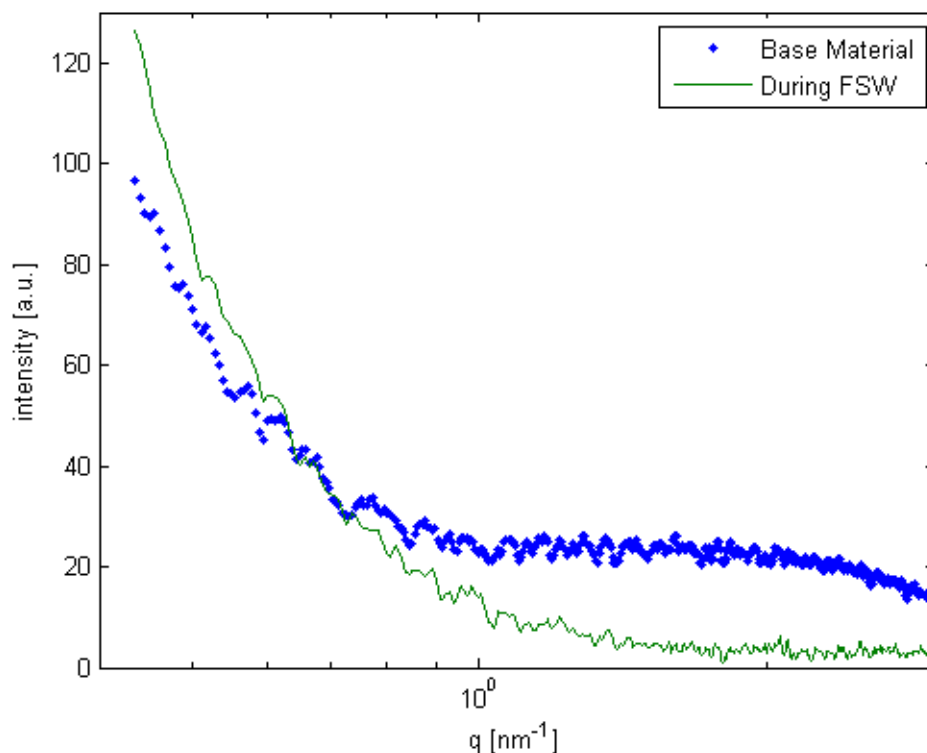


Figure 2: Results from the first *in-situ* SAXS studies of a FSW process.

## References

- [1] P. Staron et al., this annual report
- [2] T. Lippmann et al., this annual report

# The DITO-Experiment at the HARWI II Beamline

B. Hasse<sup>1</sup>, H. Rahn<sup>2</sup>, S. Odenbach<sup>2</sup>, F. Beckmann<sup>3</sup>, W. Reimers<sup>1</sup>

<sup>1</sup>TU Berlin, Institute for Materials Science and Technology, Sekr. BH18, Ernst-Reuter-Platz 1, D-10587 Berlin

<sup>2</sup>TU Dresden, Institute of Fluid Mechanics, Chair of Magnetofluidynamics, George-Bähr-Str.3, 01069 Dresden

<sup>3</sup>GKSS-Forschungszentrum Geesthacht, Max-Planck-Strasse 1, 21502 Geesthacht

The investigation of structural and mechanical properties within the bulk of engineering components and materials with high spatial resolution is of great interest. Among others, crack propagation or strain stress fields are leading to a better understanding of fatigue behaviour and corrosion. Useful methods for such characterisations are diffractometry and tomography. For these purpose a new experiment for position sensitive diffractometry [1] and tomography called DITO was built and commissioned this year at the HARWI II beamline [2]. With the available high photon energies up to 150 keV it is possible to investigate the bulk of metallic samples of a few millimetres thickness with both methods. The diffractometry detector allows the investigation of the phase composition as well as phase sensitive determination of residual stresses with a spatial resolution below 10  $\mu\text{m}$  while the tomography detector can either measure in high resolution mode with a spatial resolution of 2  $\mu\text{m}$  or in high speed mode recording a whole tomogram within 60 seconds. The high speed tomography can be used to investigate dynamical processes in that time regime while the high resolution setup is useful for structural investigations of various objects.

The general setup of the diffractometry instrument has been described in [3]. The experiment is typically operating in the energy range of 20 to 100 keV with beam dimensions of 40 x 3  $\text{mm}^2$  allowing the investigation of metallic samples with several millimetres in diameter. The whole setup is shown in figure 1. It consists of the diffractometry detector, the tomography detector and a sample stage with x-y-z-table and  $\phi$ -circle.

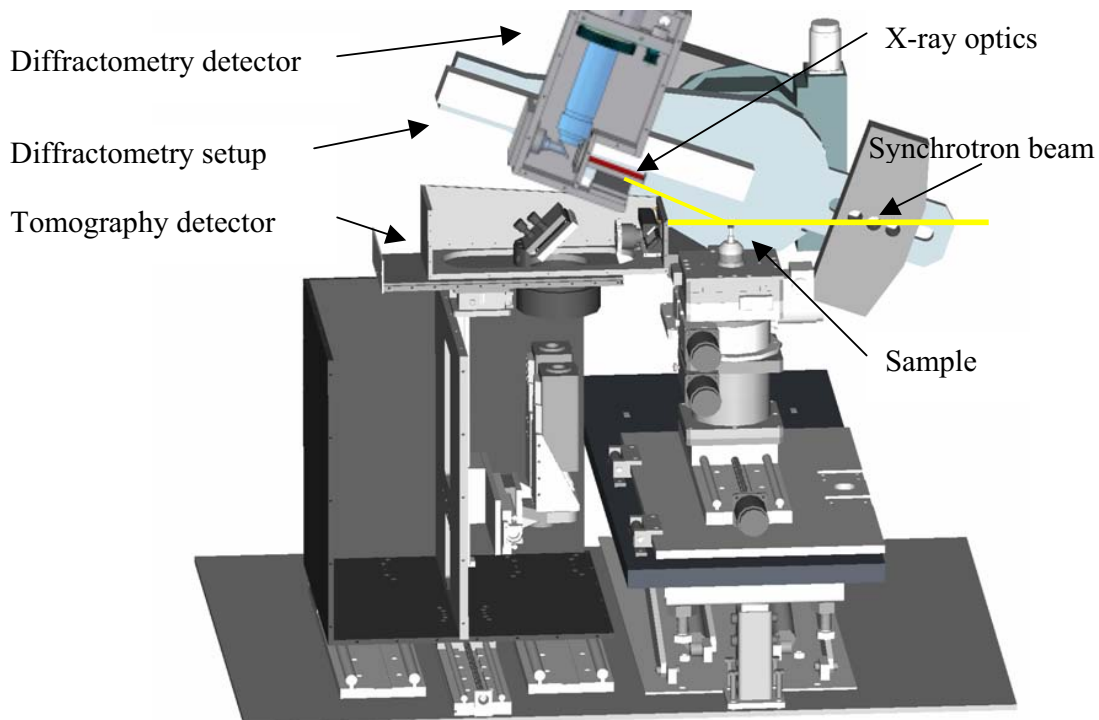


Figure 1: Setup of the DITO-experiment. Close up sketches of the detectors are given in figures 2 and 3.

For the diffractometry detector the development of a new X-ray optic was necessary to prevent cross firing of the diffracted radiation. For this purpose different capillary structures are used [4]. A structure of borosilicate glass is used in the energy range from 20 to 45 keV. This structure has an outer diameter of 8 mm and capillaries with diameters of 5  $\mu\text{m}$ . For higher energies a structure with capillaries of borosilicate glass in a matrix of lead glass with capillary diameters of 10  $\mu\text{m}$  and an outer diameter of 3 mm is available. Due to the high lead content cross firing of radiation is suppressed even at energies of 80 keV. Both structures are 100 mm long allowing the investigation of Bragg spots at low  $2\theta$  angles recording intensity from the primary beam with the detector. The use of such structures for collimating X-rays and the investigation of the bulk structure of specimen was shown by Wroblewski and Bjeoumikhov [5].

In the housing of the tomography detector two CCD-Cameras are installed. One CCD allows high resolution measurements with a spatial resolution down to 2  $\mu\text{m}$ , while the second one is a high speed camera for fast scans with 14.7 frames per second. With this setup it is possible to record a whole tomogram in a few seconds and therefore to investigate dynamic processes in that timescale. In both detectors the X radiation is converted to visible light with  $\text{CdWO}_4$  luminescence crystals. The visible light is projected with mirrors and focused with lenses on the CCD cameras. The detector parameters are given in table 1, the design of the detectors is shown in figures 2 and 3.

Table 1: Parameters of the detectors.

	Diffractometry detector	Tomography detector	
		High resolution	High speed
Number of pixels	1024 x 1024	4008 x 2672	2048 x 2048
Pixelsize	24 $\mu\text{m}$ x 24 $\mu\text{m}$	9.1 $\mu\text{m}$ x 9.1 $\mu\text{m}$	7.37 $\mu\text{m}$ x 7.37 $\mu\text{m}$
Dynamic range	12 bit or 16 bit	14 bit	14 bit
Speed	5 frames per second (12 bit) or 1 fps (16 bit)	5 fps	14.7 fps
Magnification	4fold (fix)	0.98 – 5.62	0.97 – 6.87
Spatial resolution	6 $\mu\text{m}$	2 $\mu\text{m}$	40 $\mu\text{m}$

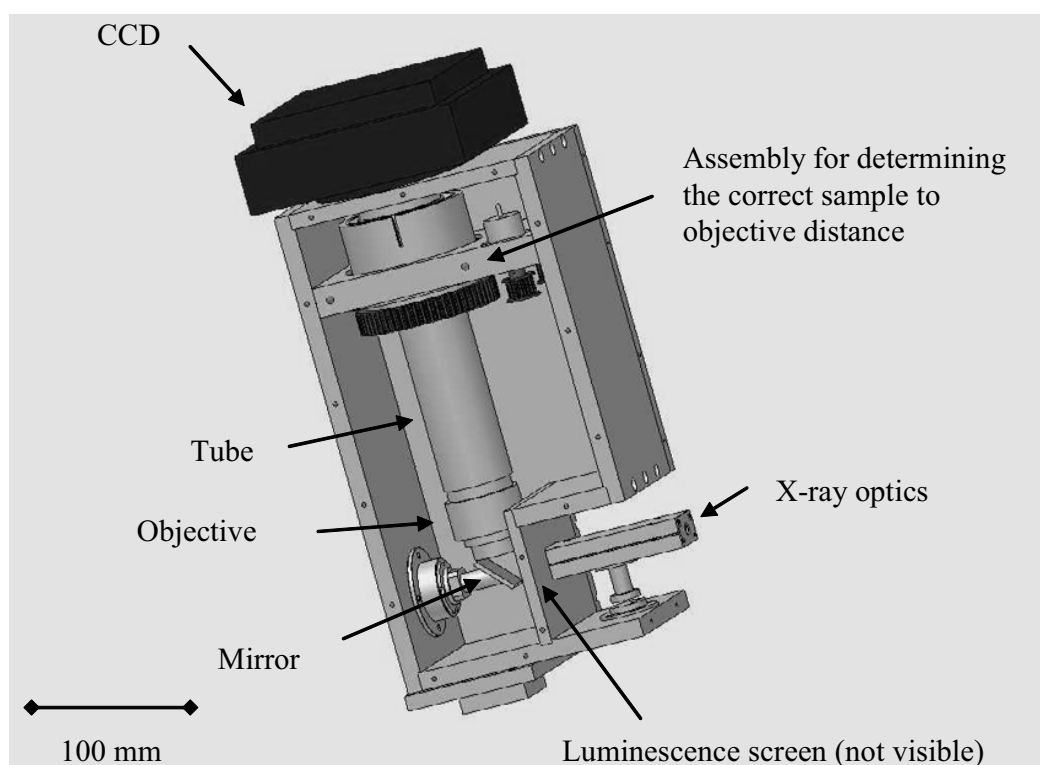


Figure 2: Design of the diffractometry detector.



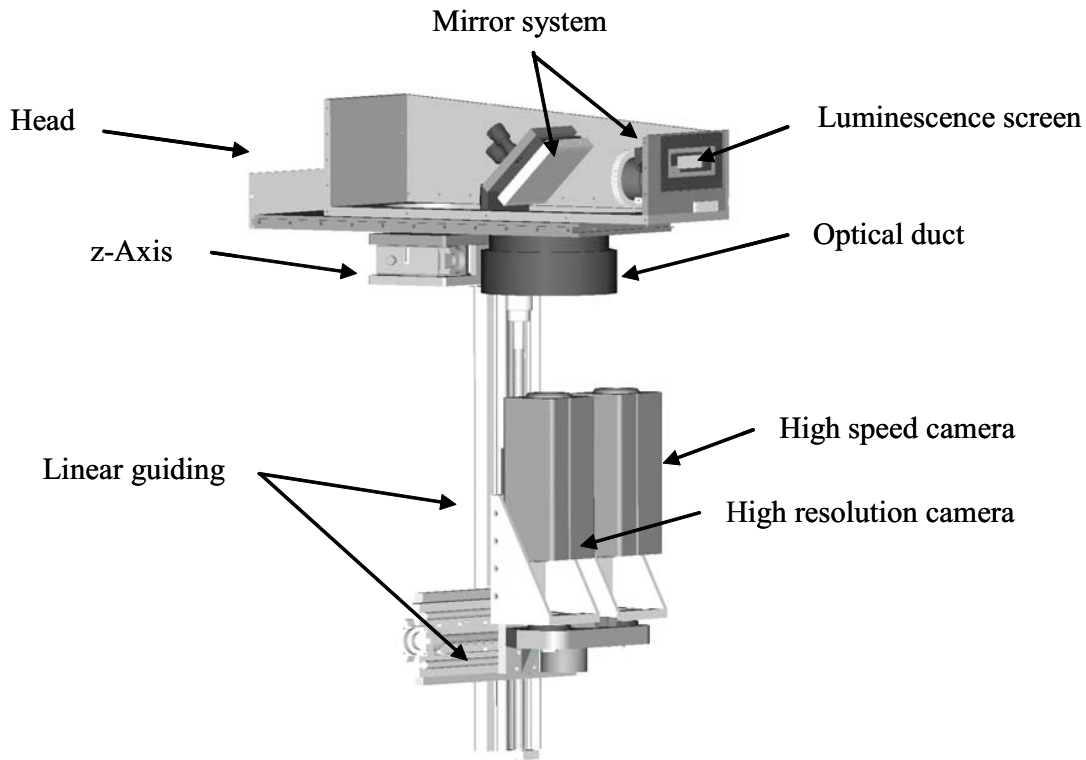


Figure 3: Design of the tomography detector. The special feature of this tomography set up is that the detector consists of two different cameras, which are used alternatively. With one camera tomograms with high resolution are achievable, while the other allows ultra-fast scanning.

The setup was assembled in January 2007. Since then many measurements were performed. With the tomography setup different samples have been measured, first results from a study about a new cancer treatment with ferrofluids, a suspension of nanoparticles in a carrier liquid, are submitted for publication [6]. The research helped to understand the treatment process. The diffractometry detector was mainly used to characterize the new developed X-ray optics. The structures were aligned in a way that the primary beam propagates parallel to the capillary axes. The beam was scanned while the capillary structure moved horizontally or vertically through the beam. The results for the structure made of borosilicate glass are shown in figure 4. The internal structure of the array is clearly visible in figures 4a and b. Single capillaries are grouped together to sub arrays, which are further elongated. With these capillary bundles the complete array is formed. The figures 4c and d are showing the intensities of the whole images as function of the scan angle. Differences in the width of the resulting peaks have their origin in the different divergence of the monochromatic beam.

The functionality of the detector was tested using a sample of aluminium and aluminium oxide. The result of a detector scan is shown in figure 5. The visible Bragg-spots have a size of 60 to 120  $\mu\text{m}$ . In these measurements no substructure of the capillary array is visible because the intensity of the diffracted beam is approximately two orders of magnitude lower than the intensity of the direct beam shown in figure 4.

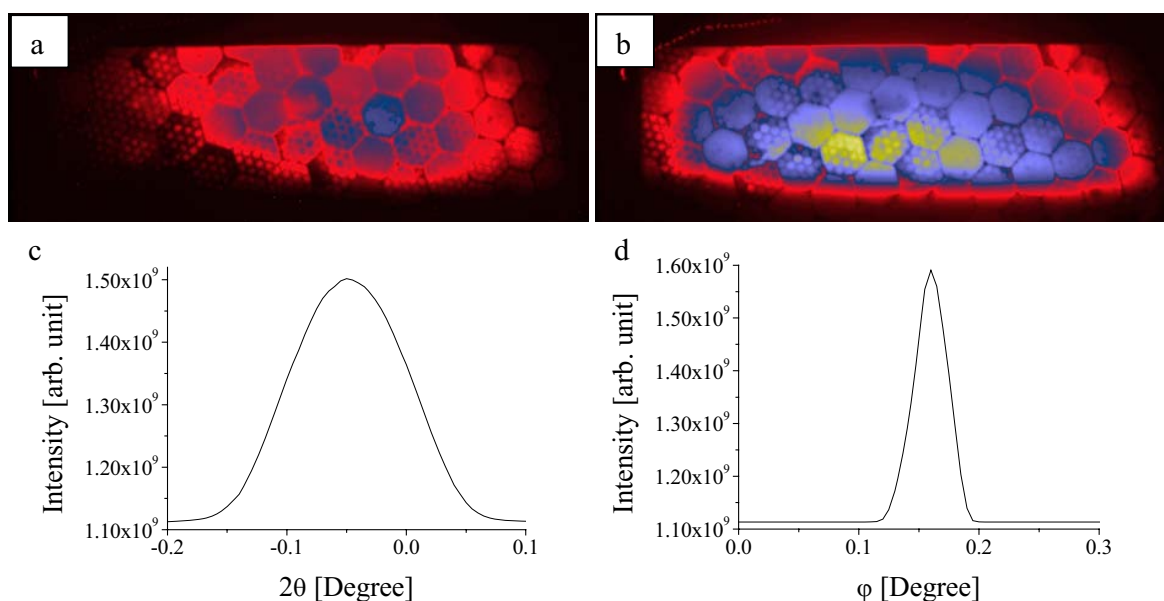


Figure 4: Characterisation of the capillary structure made of borosilicate glass at a photon energy of 20 keV. Figures a) and b) are showing the primary beam, a) in the rising edge, b) in the peak maximum. The single capillaries of the structure are clearly visible. In figures c) and d) the total intensities of the images are given as function of the angle in vertical and horizontal direction respectively. The different width of the peaks occurs due to different divergence of the monochromatic beam.

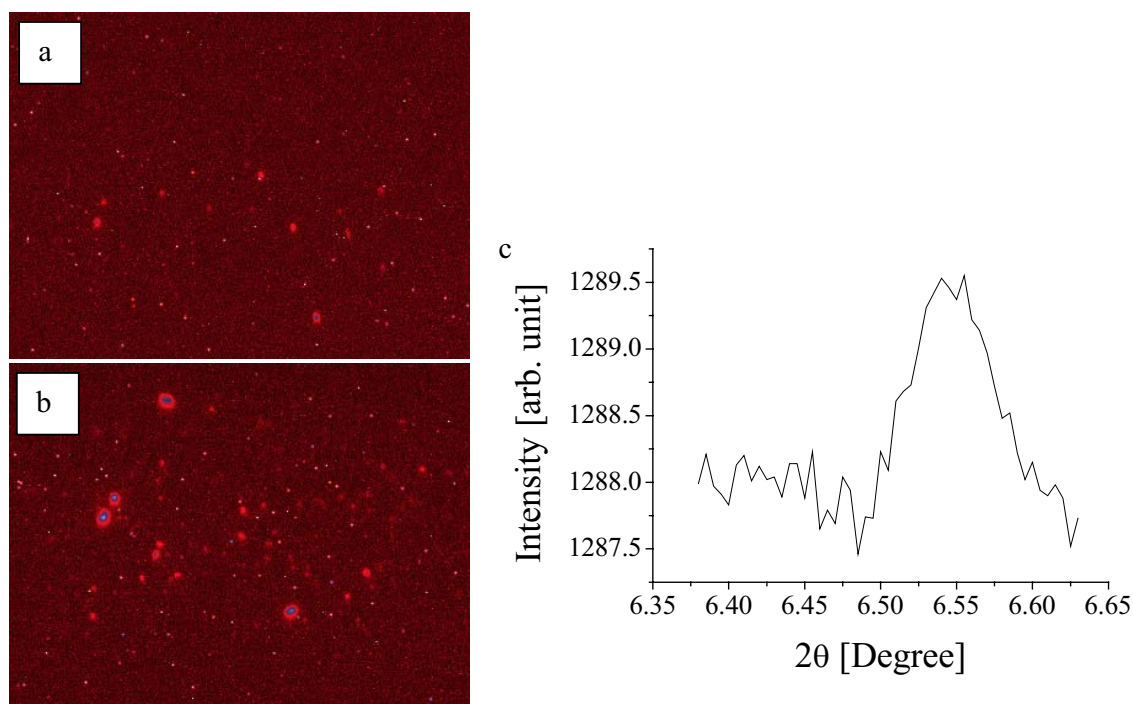


Figure 5: Bragg-spots of aluminium oxide (a) and aluminium (b) together with the overall intensities of the images as function of the  $2\theta$  angle (c) measured at a photon energy of 45 keV. The image size of Figures a) and b) is  $2.4 \times 1.8 \text{ mm}^2$ . Here spatially resolved data are shown. The visible spots have their origin in different sample positions. The images are enhanced for display, therefore the scaling of the intensity is different. The reflex of the aluminium oxide is not visible in Figure c) because the intensities of the Bragg spots are too weak compared to the noise in the images. The noise has its origin in high energetic X-ray photons and cosmic particles hitting either the luminescence screen or the CCD.



The authors wish to thank all colleagues and technical staff from the HASYLAB, the GKSS and the technical universities in Berlin and Dresden who helped during the construction, fabrication, instalment, and commissioning of the experiment.

Financial support by the BMBF (05 KS4KT2/0) and the DFG (OD18/9 within SPP1104) is gratefully acknowledged.

## References

- [1] T. Wroblewski, S. Geier, R. Hessmer, M. Schreck, and B. Rauschenbach: *Rev. Sci. Instrum.* Vol. 66 (1995), p. 3560
- [2] F. Beckmann, T. Donath, J. Fischer, T. Dose, T. Lippmann, L. Lottermoser, R.V. Martins, and A. Schreyer: *Proc. SPIE* 6318 (2006), p. 631810-1
- [3] B. Hasse, M. Kocak, and W. Reimers, *Mater. Sci. Forum* 524-525, 279 (2006)
- [4] Available at the company IfG in Berlin Adlershof (Germany), <http://www.ifg-adlershof.de/>
- [5] T. Wroblewski and A. Bjeoumikhov: *Nucl. Instrum. Meth. Phys. Res. A*, Vol. 538 (2005), p. 771
- [6] H. Rahn, I. Gomez-Morilla, R. Jurgons, Ch. Alexiou and S. Odenbach, submitted to *J. Phys.: Condens. Matter*



## Design of the Imaging Beamline at PETRA III

*A. Haibel, F. Beckmann, T. Dose, S. Utcke, J. Herzen, H.-U. Ruhnu, R. Kiehn, and A. Schreyer*

*GKSS-Research Centre Geesthacht GmbH, Max-Planck-Str. 1, 21502 Geesthacht, Germany*

Since Mai 2007 the GKSS Research Centre Geesthacht is responsible for construction, operation and funding of the Imaging Beamline IBL at PETRA III. The beamline is structured into an optics hutch and two experimental stations for different tomographic setups.

To generate the monochromatic X-ray beam two types of monochromators will be installed in the optics hutch. A silicon single crystal monochromator, designed by DESY will be used for tomographic methods, which need a very high monochromatization (e.g. vector tomography, absorption edge tomography, diffraction tomography). For applications, which need particularly high flux (e.g. for fast in situ experiments) a double multilayer monochromator will be designed. The energy range for both types of monochromators will be tunable between 5 and 50 keV.

For micro tomography a hutch in large distance from the source (80-88 m) is planned.

Due to the divergence of the low- $\beta$  X-ray beam the field of view at this distance is large enough to investigate samples of some millimetres diameter in (sub)-micrometer resolution. Here, fields of application encompass questions from materials science (e.g. imaging and quantitative analysis of pores, cracks, precipitations, phase transitions) as well as problems in the area of biology or medicine (e.g. structures of bones, tissues, teeth, plants, insects). To achieve spatial resolutions near the physical limit, high precision air bearing stages will be used for the sample rotation as well as for the camera movement. In addition a special sample positioning system was designed, which is integrated into the aperture of the rotation stage to guarantee extremely low tilt errors of the samples and wired via sliding contacts which allows a continuous rotation. Further a motorized microscope optics made of X-ray resistant glasses will be implemented. Due to an automatic sample changer and respective software the measurements will be automated to a large extent.

The possibility to focus the X-ray beam into the nanometer range will be used for nano tomographic imaging. Therefore, a second hutch for nano tomography is planned at a distance of 62-71 m from the source. On the one hand a combination of hard X-ray microscopy with tomography will be realized by means of compound parabolic refractive lenses. Here, the large distance of about 18 m between both hutches will be used for magnifying the X-ray images. The samples will be positioned in the nano tomography hutch and the images will be detected in 18 m distance of the micro tomography hutch. Due to the parabolic shape of the lenses undistorted radiographic images and thus precise tomographic images are expected. On the other hand by using crossed cylindrical nano focus lenses, Fresnel lenses or Kirkpatrick-Baez Multilayer mirrors cone beam geometry for magnifying imaging will be realized. In both cases a spatial resolution below 100 nm will be expected for micrometer sized samples.

In close cooperation with other beamline scientists and future users the general design of the beamline was presented and discussed in a first workshop, which took place on September 14, 2007.

After completion of the imaging beamline and the high-energy materials science beamline at PETRA III four complementary tomography stations will be managed by the GKSS at DESY. The HARWI setup for high-energy tomography (16-150 keV) and the BW2 setup for tomography at lower energies (6-24 keV), both at DORIS III, are characterized by a large field of view and an excellent absorption contrast. The tomography facilities at PETRA III (imaging beamline, energy range 5-50 keV and HEMS beamline, energy range 30-150 keV) distinguish themselves with high flux at small fields of view and high coherence, i.e. they fulfil excellently the qualifications for phase contrast or holo tomography, for nano tomography and for high speed or in situ tomography.

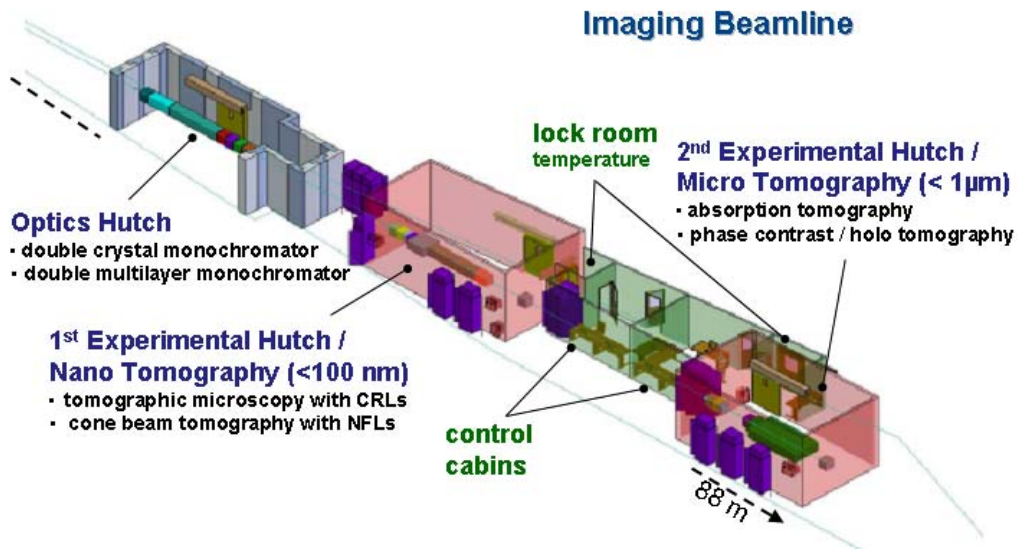


Figure 1: Schematic view of the imaging beamline IBL.

# Status and Design of the HEMS Beamline at PETRA III

N. Schell, R.V. Martins, A. Haibel, F. Beckmann, H.-U. Ruhnu, R. Kiehn, and A. Schreyer

GKSS-Research Centre Geesthacht GmbH, Max-Planck-Str. 1, 21502 Geesthacht, Germany

The future High Energy Materials Science Beamline HEMS at PETRA III [1] will have a main energy of 120 keV, fully tunable in the range of 50 to 300 keV, and will be optimized for sub-micrometer focusing with Compound Refractive Lenses (CRLs) and Kirkpatrick-Baez (KB) Multilayer mirrors. Design, construction, operation and main funding are the responsibilities of the Research Center Geesthacht, GKSS. Approximately 70 % of the beamtime will be dedicated to Materials Research, the rest reserved for "general physics" experiments supported by DESY.

*Fundamental research* will encompass metallurgy, physics, chemistry and biology. For first experiments in investigating grain-grain-interactions a dedicated 3D-microstructure-mapper has been designed. *Applied research* for manufacturing process optimization will benefit from the high flux in combination with ultra-fast detector systems allowing complex and highly dynamic *in-situ* studies of micro-structural transformations. The beamline infrastructure will allow easy accommodation of large user provided equipment. Experiments targeting the *industrial user community* will be based on well established techniques with standardised evaluation, allowing "full service" measurements. Environments for strain mapping on large structural components up to 1 t will be provided as well as automated investigations of large numbers of samples, e.g. for tomography and texture determination.

The current design for the beamline (P07 in sector 5 of the future experimental hall) consists of a nearly five meter in-vacuum undulator source (U19-5) optimized for high energies, a general optics hutch, an in-house test facility and three independent experimental hutches working alternately, plus additional set-up and storage space for long-term experiments, compare Fig. 1. HEMS should be operational in late spring 2009 as one of the first beamlines running at PETRA III.

The current design of HEMS has been introduced to the user community at the conference MECA SENS IV [2] as well as in the 2<sup>nd</sup> GKSS / DESY Workshop: High Energy Materials Science at PETRA III, held at DESY on November 2, 2007. Major experiments are clearly defined and the essential instruments designed and partly purchased, e.g. an improved HUBER surface diffractometer with premonochromator for the investigation of liquids as designed by H. Reichert [3], or a customized 1 t hexapod from Physik Instrumente Karlsruhe [4].

## References

- [1] [http://petra3.desy.de/beamlines/work\\_packages/e1036/e1557/index\\_eng.html](http://petra3.desy.de/beamlines/work_packages/e1036/e1557/index_eng.html)
- [2] N. Schell, R.V. Martins, F. Beckmann, H.-U. Ruhnu, R. Kiehn, A. Schreyer, *accepted* for publication in Materials Science Forum (Conference proceedings of the 4<sup>th</sup> Conference on Stress Evaluation, MECA SENS IV, in Vienna, Austria, 24-26 September, 2007)
- [3] H. Reichert, V. Honkimäki, A. Snigirev, S. Engemann, H. Dosch, Physica B 336, 46 (2003)
- [4] [Information on http://www.physikinstrumente.com/](http://www.physikinstrumente.com/)

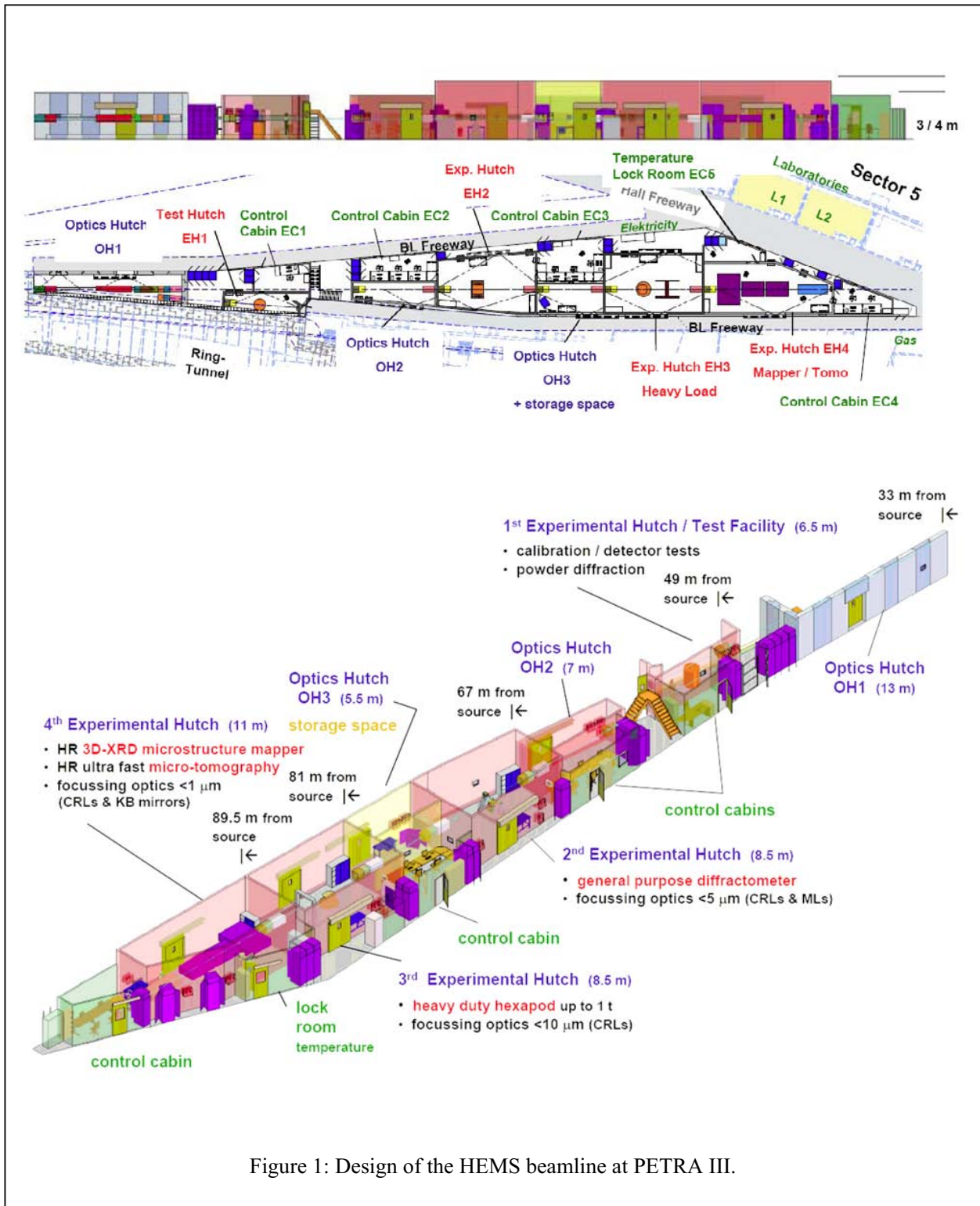


Figure 1: Design of the HEMS beamline at PETRA III.

# 2<sup>nd</sup> GKSS / DESY Workshop High Energy Materials Science at PETRA III

*N. Schell*

*GKSS-Research Centre Geesthacht GmbH, Max-Planck-Str. 1, 21502 Geesthacht, Germany*

On November 2, 2007, the second GKSS / DESY Workshop: “High Energy Materials Science at PETRA III” took place on the DESY site. The agenda is shown in the attached program. The status and design of the HEMS Beamline [1] together with detailed specifications of its major experimental components (improved surface diffractometer [2], 3D-XDS mapper, customized 1t hexapod for heavy-duty sample/environment handling [3],  $\mu$ -tomography set-up) were introduced to the future user community of the HEMS Beamline.

The design and construction of various pieces of equipment was motivated by clearly defined in-house research requirements of the main funding organisation GKSS and its cooperation partners at universities, other research facilities or industry, as well as possible future upgrades in extrapolation of current HASYLAB experiments.

Another major aim of the HEMS staff was the fine-tuning of the best possible optics to realize the envisioned experiments. Therefore, emphasis was put on the optics experience gained at other 3<sup>rd</sup> generation synchrotron radiation sources, i.e. listening to experts from the ESRF and APS.

The 30 registered participants as well as many spontaneous drop-ins enjoyed lively and highly focused discussions on the HEMS case. General agreement was reached on the recommendation to optimise the optics for the unique high-energy characteristics of HEMS, to guarantee highest stability of the beam and to realize a flexible bending option in Rowland circle geometry with a double-Laue horizontal fixed-exit monochromator.

## References

- [1] [http://petra3.desy.de/beamlines/work\\_packages/e1036/e1557/index\\_eng.html](http://petra3.desy.de/beamlines/work_packages/e1036/e1557/index_eng.html)
- [2] H. Reichert, V. Honkimäki, A. Snigirev, S. Engemann, H. Dosch, *Physica B* **336**, 46 (2003)
- [3] Information at <http://www.physikinstrumente.com/>

# 2<sup>nd</sup> GKSS / DESY Workshop

## High Energy Materials Science at PETRA III

Friday 2 November 2007

DESY, Notkestr. 85, 22607 Hamburg, building 25f, room 456

### 1<sup>st</sup> Part: Presentation of the GKSS High Energy Materials Science beamline (HEMS)

Time	Title	Presenter
09:00-09:15	<i>Welcome</i>	A. Schreyer (GKSS), E. Weckert (DESY)
09:15-10:10	<i>Status and design of HEMS</i>	N. Schell (GKSS)
10:10-10:30	<i>Stress and strain mapping</i>	R. Martins (EC JRC Petten)
10:30-11:00	<i>Tomography at PETRA III</i>	A. Haibel (GKSS) / F. Beckmann (GKSS)

Coffee break: 11:00 – 11:30

### 2<sup>nd</sup> Part: Trends and upgrades for high energy synchrotron radiation beamlines

Time	Title	Presenter
11:30-12:00	<i>High energy optics</i>	J. Patommel (TU Dresden)
12:00-12:30	<i>Focussing experience at ESRF</i>	V. Honkimäki (ESRF)
12:30-13:00	<i>Focussing experience at APS</i>	S. Shastri (APS)

Lunch break: 13:00 – 14:00

### 3<sup>rd</sup> Part: Possible experiments

Time	Title	Presenter
14:00-14:30	<i>Surface and interface studies</i>	H. Reichert (MPI)
14:30-14:50	<i>High energy diffraction at BW5</i>	M. v. Zimmermann (HASYLAB)
14:50-15:10	<i>Tomography combined with diffraction</i>	A. Pyzalla (MPI)
15:10-15:30	<i>Pump and probe experiments</i>	J. Pelka (IFPAN)

Coffee break: 15:30 – 16:00

Time	Title	Presenter
16:00-16:20	<i>Applications of analytical synchrotron radiation techniques in friction-based joining methods</i>	S. Amancio (GKSS)
16:20-16:40	<i>Complementarity to neutrons</i>	P. Staron (GKSS)
16:40-17:00	<i>Residual stress analysis of single grains at HEMS</i>	W. Reimers (TU-Berlin)

### 4<sup>th</sup> Part: Round table discussion



# Autumn School on Application of Neutrons and Synchrotron Radiation in Engineering Materials Science

*T. Wroblewski*

The Virtual Institute 'Photon and Neutron Research on Advanced Materials' [1] was established as a collaboration of the three Helmholtz research centers DESY, GKSS, and HMI and the universities TU Berlin, TU Clausthal, TU Dresden and TU Wien (meanwhile replaced by the MPI Düsseldorf).

The Large Scale Facilities of the Helmholtz Society with photon and neutron sources offer unique possibilities by complementary use of these probes for structural analyses of advanced engineering materials. By using photons delivered by a synchrotron radiation source and by using neutrons, information about materials microstructures can be obtained non-destructively in the near-surface region as well as in the bulk of samples and components. Compared to conventional laboratory X-rays the spatial resolution achievable using synchrotron radiation can be improved by up to several orders of magnitude.

Diffraction methods reveal information about crystalline phase volume fractions, texture and residual stresses, while tomography provides complementary 3-dimensional images of the material's microstructure. Both diffraction and tomography have increasing impact in the fields of design of tailored materials, their processing and lifetime assessment.

The integration of complex experimental techniques and specialized engineering material knowledge requires coordinated R&D actions such as this Virtual Institute to provide system solutions for ever increasing demands in the field of high-performance engineering materials and systems. The combination of different expertise and the demonstration of successful examples are also important for problem and innovation oriented co-operations with industry either bilateral or e.g. in BMBF - and EU-projects by the participation of the partners of this Virtual Institute. In this context, a joint presentation of the Virtual Institute PNAM was planned via seminars, workshops and internet.

One step towards this aim was the establishment of a biannual autumn school on the 'Application of Neutrons and Synchrotron Radiation in Engineering Materials Science' which took first place 2005 in Ammersbek near Hamburg. The second school in this series took place at the same location from September 17 to 21, 2007. The covered topics reached from the properties of neutrons and of synchrotron radiation to those of materials like residual stress texture and how these are influenced due to different treatments.

During the second day, different imaging and scattering techniques were presented, and the application to various problems in engineering materials science was demonstrated.

While speakers related to the virtual institute gave lectures on the first two days, the third day was used for a look beyond the fence with talks from industry and other neutron and synchrotron radiation sources.



Figure 1: Participants and Lecturers of the autumn school in front of the Haus am Schüberg

The last two days were dedicated to visits to DESY and GKSS. The 50 participants were divided into two equally sized groups of which one first visited DESY and then GKSS, and the other the opposite way round. Unfortunately, practical training was only possible at GKSS due to a service week at DESY, which on the other hand enabled the visit of otherwise not accessible installations like the tunnel of the DORIS storage ring.

A book covering the topics of the first school in 2005 will be published soon by Wiley.

## References

- [1] <http://www.tu-berlin.de/~pnam>

# Analysis of volume strain in notched tensile specimens by SR-based microtomography

H.-A. Crostack, J. Nellesen<sup>1</sup>, G. Fischer<sup>1</sup>, F. Beckmann<sup>2</sup> and J. Herzen<sup>2</sup>

Lehrstuhl für Qualitätswesen, Fakultät Maschinenbau, TU Dortmund, 44221 Dortmund, Germany

<sup>1</sup>RIF e.V., Joseph-von-Fraunhofer-Str. 20, 44227 Dortmund, Germany

<sup>2</sup>GKSS Research Center, Max-Planck-Str. 1, 21502 Geesthacht, Germany

The localisation of strain in metallic materials is of great practical interest, since this process plays an important role for the locus and the type of the successive failure of a component. Moreover, the behaviour during machining is influenced by this process. In addition, strain localisation can lead to undesired roughness of the surface of a part and diminished fracture strain. In order to affect this strain localisation in the framework of material optimisation knowledge about the effects of alloy composition, precipitation state, microstructure and loading conditions (strain rate, temperature, multiaxiality, ...) is needed. In case of reinforcement of a metallic material by dispersion of brittle particles the impact of volume (fraction), shape, orientation and arrangement of the particles on the localisation has to be considered accessorially. In the case of composites the different mechanical behaviour of the phases and the actual condition of the phase interfaces have to be taken into account.

For the analysis of this phenomenon a holistic, three-dimensional approach is chosen using experimentally obtained 3D-images of the microstructure in different load or deformation stages. 3D-images of microstructure are acquired by X-ray tomographic microscopy (XTM). On the basis of these images models are generated which are used in FE-simulations of the material behaviour. From the comparison between the experimentally observed and the simulated behaviour and parameter studies understanding of the localisation process can be deduced. A detailed description of this approach can be found in [1].

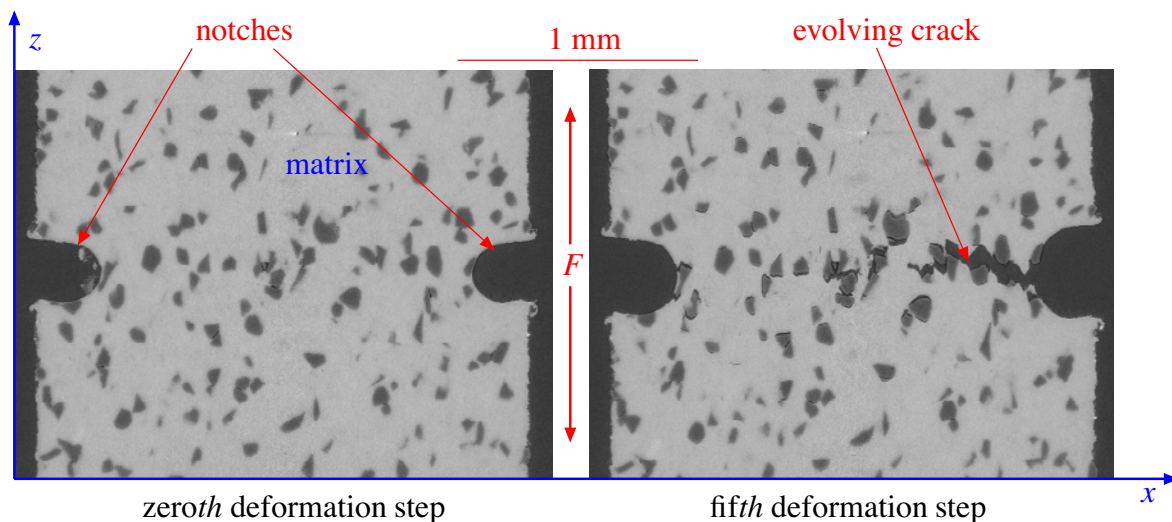


Figure 1: 2D-images of microstructure from the bulk of a notched tensile specimen consisting of the Al/B<sub>4</sub>C-composite in different stages of deformation representing nearly the same microstructural region; no deformation (left); advanced deformation and damage initiation (right)

In the scope of the experiments the particle-reinforced metal matrix composite Al/B<sub>4</sub>C was investigated which was manufactured by plasma spark sintering. The composite mainly consists of high-purity (99.99% Al) aluminium which shows a ductile behaviour. In this matrix brittle B<sub>4</sub>C-particles are dispersed whose mean particle diameter amounts to 44.5  $\mu\text{m}$  (corresponding to the

commercial grade: FEPA no. 240) with a volume fraction of 5% (= 4.68 % mass fraction). Due to the remarkable concentration of boron this composite is qualified as a neutron absorber. Since no brittle interphases precipitate at the interface between the Al-matrix and the  $B_4C$ -particles this material is also of interest beyond nuclear power technology [2].

Experiments were carried out at beamline BW2. Monochromatic photons of  $E = 22$  keV were selected by a double-crystal monochromator in Bragg-reflection arrangement. After each deformation step the gauge length (cross-sectional area  $A = 2$  mm<sup>2</sup>) of the tiny dog-bone shaped specimen was imaged by XTM in the unloaded state.

From the right 2D-image ( $xz$ -slice) in fig. 1 extracted from the 3D-tomogram it is obvious that a crack propagates through the specimen which originates from the right notch. During the visual inspection of the vicinal  $xz$ -layers it turns out that the crack might be caused by an agglomeration of particles in the neighbourhood of the right notch. Although the left notch is a little bit deeper the crack originates from the base of the right notch. Accordingly, the colour-coded 3D distribution of equivalent strain  $\varepsilon_{equ}$  (cf. fig. 2) shows elevated strain values in the neighbourhood of the right notch already in the third stage of deformation.

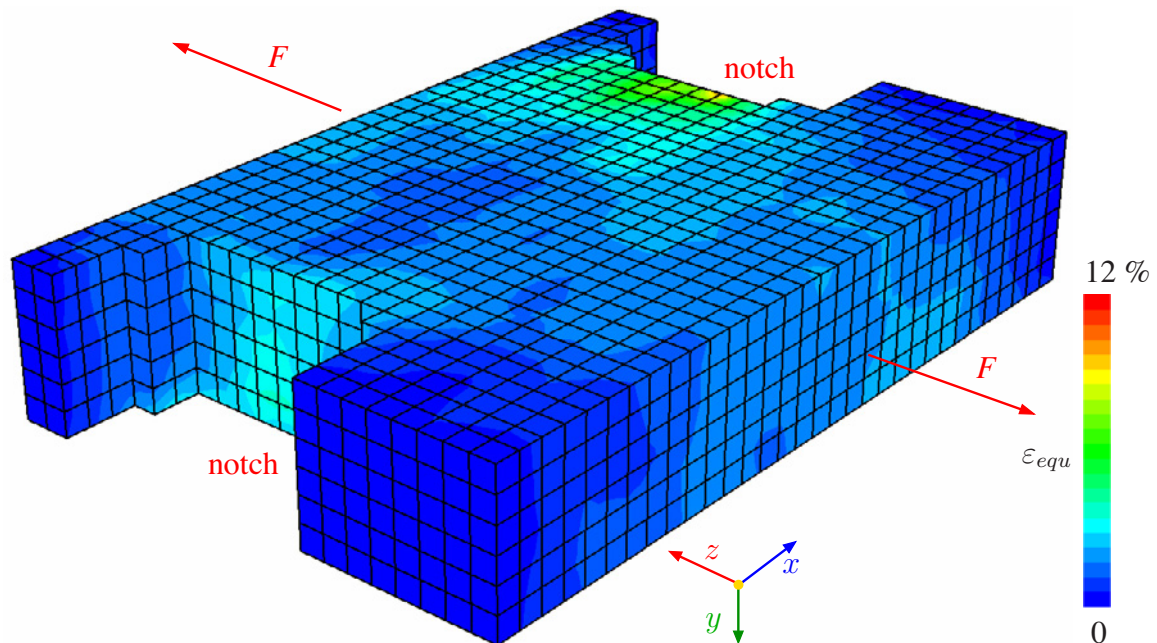


Figure 2: Colour-coded 3D-distribution of equivalent strain  $\varepsilon_{equ}$  in the gauge length of the notched tensile specimen at the third deformation step; elevated strain can be found in the vicinity of the notch bases, especially in the region of the right notch where a crack is initiated

## References

- [1] H.-A. Crostack, J. Nellesen, G. Fischer, S. Schmauder, U. Weber, F. Beckmann, Proc. SPIE 6318, 63181A-1-12 (2006).
- [2] M. Kouzeli, C.S. Marchi, A. Mortensen, Mater. Sci. Eng. A 337, 264 (2002).



# Application of $\mu$ -CT for structure analysis of porous media

A. Waske<sup>1</sup>, S. Odenbach<sup>1</sup>, M. Pulkin<sup>2</sup>, F. Beckmann<sup>3</sup>

<sup>1</sup>TU Dresden, Professur für Magnetofluidodynamik, 01062 Dresden, Germany

<sup>2</sup>Universität Bremen, Inst. Keramische Werkstoffe und Bauteile, 28359 Bremen, Germany

<sup>3</sup>GKSS, Max-Planck-Str.1, 21502 Geesthacht, Germany

This project is part of the DFG graduate research training school “PoreNet”, which focuses on fundamental research on non-metallic porous media. An important aspect for the characterisation of such media is the non-destructive analysis of their structure, e.g. porosity and pore size distribution. In this project,  $\mu$ -CT analysis is employed in combination with other experimental techniques covered by the research training school, like Hg-intrusion or particle laser induced fluorescence (LIF), to explore structure issues. One particular focus lies on structure parameters that are strongly linked to an (industrial) use of the porous media – like surface area, connectivity, and homogeneity.

As one example for employing a porous ceramic for a technical application, we present studies of a freeze gelation ceramic [1] which can be used for very different purposes, for instance acoustic damping in gas turbines or the inclusion of living cells in bio-compatible scaffolds. The ceramic is produced by freezing the slurry together with a foaming agent and subsequently removing excess water. Since the freezing starts from one defined sample side, one objective of the tomography studies is to evaluate pore parameters as a function of the distance from the starting front of the freezing. For the freeze gelation ceramic shown in figure 1, two tomograms have been taken at different heights above the freezing front, which have been analysed regarding their pore size distribution. The image processing techniques involved have been employed earlier in our group to study porous metallic foams [2]. Additionally, the connectivity of the pores and the homogeneity of the sample are important characteristics to study in future, since the freeze gelation ceramic is intended to be used as an acoustic absorber.

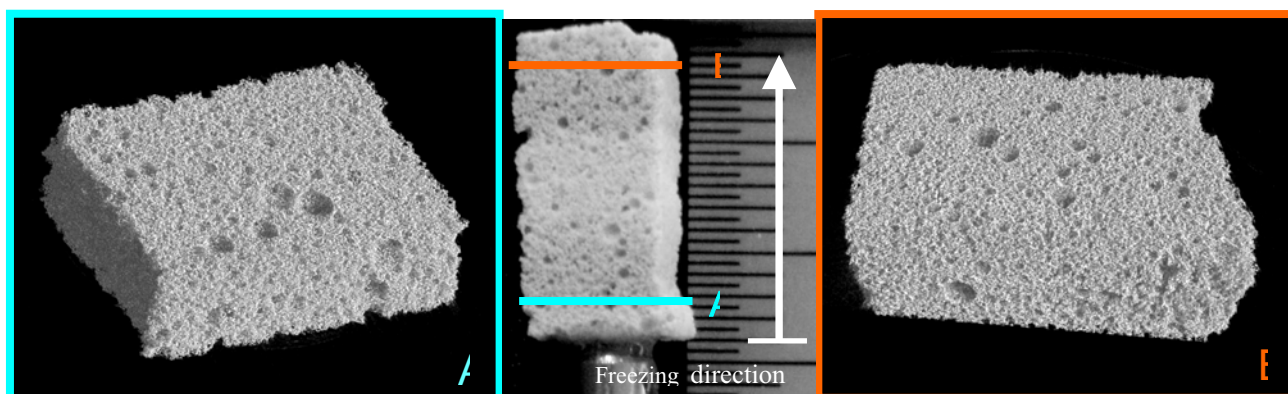


**Fig. 1:** Freeze gelation ceramic with direction of freezing front indicated (middle). Two tomograms have been taken close to (A, left) and further away from the freezing front (B, right).

The pore size distribution is based on a granulometry algorithm, which is applied to the binarised image. In this case, the binarisation has been done by fitting the bimodal histogram

with two Gauss curves. The intersection point of the curves has been set as threshold. The results are shown in figure 2: the pore size distribution extracted from the tomographic data clearly follows a logarithmic normal distribution. The mean diameters of the pores for cut A and B are  $d = 67,2$  microns and  $d = 89,7$  microns, respectively, which implies that the mean pore diameter increases as the distance from the freezing front gets larger. This is might most likely be due to the fact that at cut B the foaming agent has had more time to act on the slurry before it froze, hence creating larger pores. The results from the mercury intrusion experiment – a method averaging over the whole sample- reveal slightly smaller pore diameters, reflecting that only the pores cross sections which can be penetrated by the mercury will be measured.

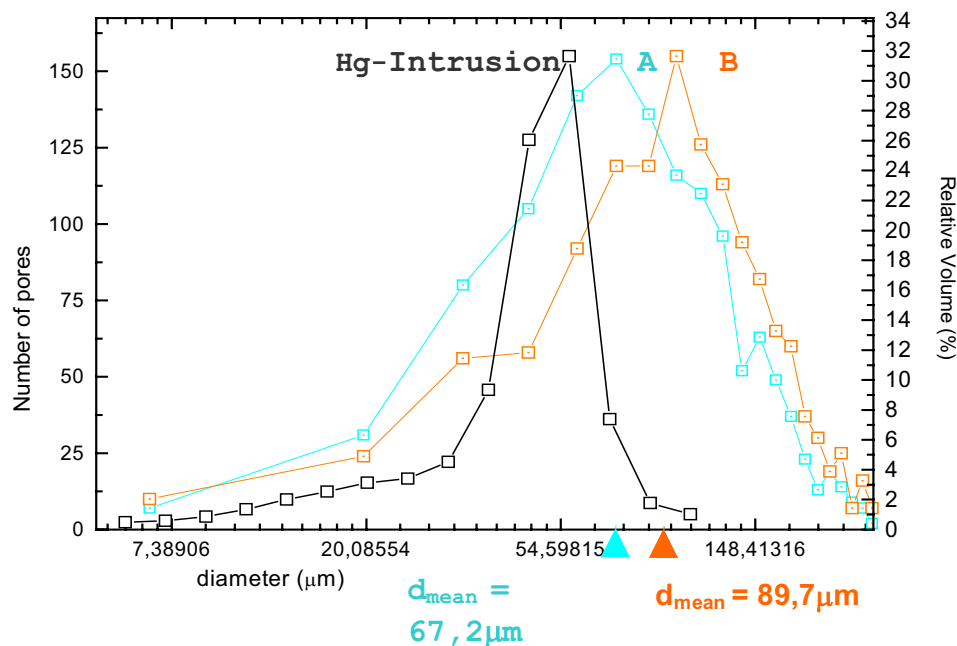


**Fig. 2:** Pore size analysis of freeze gelation ceramic (cyan and orange curve) compared to experimental data from mercury intrusion (black).

We thank J. Herzen and B. Hasse for support during beam times.

## References

- [1] U. Soltmann, H. Bottcher, D. Koch, G. Grathwohl (2003) Freeze gelation: a new option for the production of biological ceramic, *Materials Letters*, 2005. 57: p. 2861-2865.
- [2] O. Brunke, S. Odenbach, F. Beckmann (2004) Quantitative methods for the analysis of synchrotron- $\mu$ CT datasets of metallic foams, *EPJ of Applied Physics*, 2005. 29: p. 73-81.

# ASAXS of Light Metal Hydride Composites

U. Bösenberg<sup>1</sup>, K. P. Pranzas<sup>1</sup>, C. Nwakwu<sup>1</sup>, J. M. Bellosta von Colbe<sup>1</sup>, G. Goerigk<sup>2</sup>, U. Vainio<sup>3</sup>,  
M. Dornheim<sup>1</sup>, R. Bormann<sup>1</sup>, A. Schreyer<sup>1</sup>

<sup>1</sup>Institute of Materials Research, GKSS Research Centre Geesthacht, Max-Planck Str. 1, 21502 Geesthacht, Germany

<sup>2</sup>Institute of Solid State Physics, Research Centre Jülich, 52425 Jülich, Germany

<sup>3</sup>HASYLAB at DESY, Notkestraße 85, D-22603 Hamburg, Germany

Light weight metal hydrides are favoured materials for hydrogen storage in mobile application. Due to the high requirements on the materials concerning storage capacity, reaction thermodynamics and kinetics novel functional materials need to be developed. One promising new class of materials are the *Reactive Hydride Composites* (RHC) [1,2]. These systems show reduced total reaction enthalpies at high storage capacities. The system of e.g.  $2\text{LiH} + \text{MgB}_2 + 4\text{H}_2 \leftrightarrow 2\text{LiBH}_4 + \text{MgH}_2$  has a theoretical storage capacity of 11.4 wt% hydrogen and an equilibrium pressure of 1bar  $\text{H}_2$  at 170°C. During the endothermic desorption reaction the exothermic formation of  $\text{MgB}_2$  proceeds and is thereby lowering the total reaction enthalpy. The system shows very sluggish kinetics and can therefore only be operated at temperatures above the thermodynamic equilibrium. With cycling and suitable additives the kinetics is significantly improved by an order of magnitude [3]. However, the catalytically active species and the mechanism for the enhanced sorption reactions are not yet identified. In order to approach this questions and based on previous experience with  $\text{MgH}_2$  [4], anomalous small angle X-ray scattering (ASAXS) was performed at beamline B1 (formerly JUSIFA) at Hasylab, DESY, Hamburg. Prior to the small angle scattering investigations, absorption curves were measured revealing changes in the chemical state of the initial additive during preparation and cycling. Already after milling, a shift towards a lower valence-state takes place. Upon cycling this effect becomes apparently stronger, however, the state of metallic Vanadium was not reached. From these absorption measurements three energies with a variation in  $f'$  by a factor of two were determined.

ASAXS measurements were performed near to the K-absorption edge of Vanadium at 5247, 5467 and 5475 eV (Vanadium-K: 5465 eV). Two sample-to-detector distances, 935 and 3635mm, were used to cover a 'q' range ( $q = 4 \cdot \pi \cdot \sin \theta / \lambda$ ) from 0.003 to 0.4  $\text{\AA}^{-1}$ . The samples with thickness of 20-150 $\mu\text{m}$  were prepared between two layers of Kapton tape. SAXS curves were corrected for detector sensitivity, empty beam, dark current and transmission. The macroscopic differential scattering cross section  $d\Sigma/d\Omega$  was obtained by calibration with a reference glassy carbon sample.

The energy dependence of the small angle X-ray scattering near the K-absorption edge of Vanadium is used to access directly the resonant scattering contribution of the Vanadium based additives. The form factor is derived by the methods described in [5]. In Figure 1 the obtained scattering curves are shown for composite material of  $2\text{LiH} + \text{MgB}_2 + 0.1 \text{VCl}_3$  in the milled, absorbed and desorbed state. The fits obtained using a correlation lengths model are shown as solid lines.

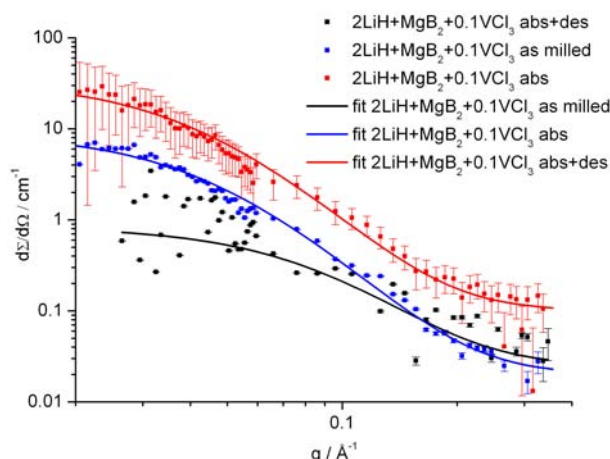


Figure 1: Separated scattering curves of  $2\text{LiH} + \text{MgB}_2 + 0.1 \text{VCl}_3$  composites

Typical correlation lengths of 10-25 Å are estimated for the V-based additive phase using the model described in [6]. With cycling, a tendency to larger values was found. The scattering decay of about  $q^{-2.5}$  indicates a weakly segregated network of V-based particles in the grain boundaries.

Recently, further ASAXS experiments of this RHC system with Zr-based additives were performed, measuring near to the K-absorption edge of Zirconium (Zirconium-K: 17998 eV). As a first result the difference scattering curve between the scattering curves measured at the calibrated energies of 18006 eV and at 17200 eV is shown in figure 2 for the samples based on  $2\text{LiH}+\text{MgB}_2+0.1\text{ZrCl}_4$  compounds.

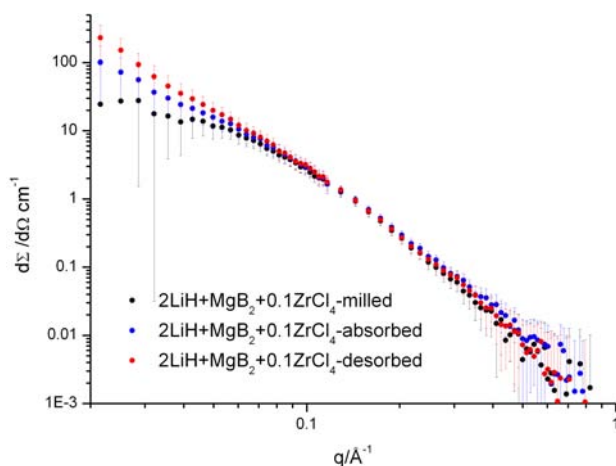


Figure 2: Difference scattering curves of  $2\text{LiH}+\text{MgB}_2+0.1\text{ZrCl}_4$  composites in different cycling stages

These curves represent the scattering of the Zr-based structures in the nanocrystalline metal hydrides. Indicated by higher intensities at small  $q$ -values a shift towards larger correlation lengths can be identified with the cycling of the material, indicating coarsening of Zr-based particles. Further evaluation and analysis concerning the size of the Zirconium based compounds and its changes upon cycling as well as a comparison to the V-based additives is currently performed and will be published soon.

## References

- [1] G. Barkhordarian, T. Klassen, M. Dornheim, R. Bormann, J. Alloys Compd. 440 1-2, L18-L21 (2007)
- [2] J. Vajo, S.L. Skeith, F. Mertens, J. Phys Chem B Lett. 109, 3719, (2005)
- [3] U. Bösenberg, S. Doppiu, L. Mosegaard, G. Barkhordarian, N. Eigen, A. Borgschulte, T. R. Jensen, Y. Cerenius, O. Gutfleisch, T. Klassen, M. Dornheim, R. Bormann, Acta Mater. 55, 3951-3958 (2007)
- [4] P.K. Pranzas, M. Dornheim, U. Boesenberg, J.R. Ares Fernandez, G. Goerigk, S.V. Roth, R. Gehrke, A. Schreyer, J. Appl. Cryst. 40, S 383 - S 387 (2007)
- [5] G. Goerigk, R. Schweins, K. Huber, M. Ballauff, Europhys. Lett. 66(3), 331-337 (2004)
- [6] G. Goerigk and D.L. Williamson, J. of Non.Cryst. Solids 281, 181-188 (2001)



# Cast textures of NiMnGa alloys

R. Chulist<sup>1</sup>, M. Pötschke<sup>2</sup>, U. Garbe<sup>3</sup>, C.-G. Oertel<sup>1</sup>, W. Skrotzki<sup>1</sup> and T. Lippmann<sup>3</sup>

<sup>1</sup> *Institut für Strukturphysik, Technische Universität Dresden, D-01062 Dresden, Germany*

<sup>2</sup> *Institut für Metallische Werkstoffe, Leibniz-Institut für Festkörper- und Werkstoffforschung, D-01069 Dresden, Germany*

<sup>3</sup> *Institut für Werkstoffforschung, GKSS Forschungszentrum, D-21502 Geesthacht, Germany*

NiMnGa alloys close to the stoichiometric composition Ni<sub>2</sub>MnGa belong to the quite new family of ferromagnetic shape memory alloys. These alloys are characterized by magnetically induced reorientation (MIR) resulting from the motion of twin boundaries under the influence of a magnetic field [1,2]. Plastic deformation of NiMnGa single crystals by twin boundary motion leads to a maximum magnetic field induced strain (MFIS) of about 10%. To our knowledge, until now MFIS has not been reported for NiMnGa polycrystals. However, since for broad technical applications growth of single crystals is quite time consuming and cost intensive it is necessary to investigate polycrystalline samples on their suitability for MFIS. To approach MFIS of single crystals the crystallographic texture of polycrystalline samples is of particular concern. Thus, the present work focuses on texture analyses of NiMnGa polycrystals fabricated with directional solidification. To examine the texture of coarse grained NiMnGa alloys in a statistically relevant way diffraction of synchrotron radiation has been applied. The texture results are discussed with respect to the material, processing, phase transformations and MFIS.

The polycrystalline sample (Ni<sub>50</sub>Mn<sub>29</sub>Ga<sub>21</sub>) studied was fabricated by directional solidification. The martensitic transition for Ni<sub>50</sub>Mn<sub>29</sub>Ga<sub>21</sub> takes place at a temperature of 55°C. Directional solidification was carried out under Ar atmosphere. A prealloy was prepared by induction melting of pure elements (Ni 99.98, Mn 99.8, Ga 99.999) [9]. The casting process was performed in an Indrudet S investment casting machine followed by furnace-cooling to room temperature. The cast sample had a diameter and length of 10 mm and 50 mm, respectively. Coarse columnar grain growth was achieved by using a hot mould with a cooled copper plate at the bottom. The mould was heated in a separate furnace to a temperature close to melting. The cylindrical sample cut from the cast ingot above about 1 cm from the bottom had a diameter and height of 8 mm and 15 mm, respectively.

The texture was measured by diffraction of high-energy synchrotron radiation (100 keV) using the GKSS materials science beamline HARWI-II at DESY in Hamburg, Germany. Due to the high penetration depth of high-energy X-rays, texture measurements in transmission allow for collecting orientation data from a large sample volume, i.e. with a good grain statistics. Due to the fact that the sample consists of more than one phase, some diffraction peaks from different phases may overlap. Therefore, the orientation distribution functions (ODF) were only calculated with the measured pole figures belonging to non-overlapping peaks. With the ODF all pole figures desired can be recalculated. Processing of the texture data was done with the Labotex software.

The directionally solidified sample is characterized by long columnar grains with a width of about 0.5 mm. During cooling from the melt it experiences several phase transformations: B2 → L<sub>21</sub> → martensite. Three modulated and non-modulated martensitic structures may exist (one orthorhombic (7M) and two tetragonal (5M and NM)) [3-5]. The martensitic crystal structures in NiMnGa are strongly composition dependent [6-8]. X-ray diffraction shows that the polycrystal investigated simultaneously contains two martensitic structures, 7M and NM. Both phases have a strong <100> fibre texture around the growth direction (GD) (Figs. 1, 2). In the orthorhombic 7M and tetragonal NM case, six and three martensitic variants, respectively, may exist. The numbers are reduced to three and two in the case of <100> fibre textures. During formation of the martensitic phases a variant selection took place favouring one of the <100> directions parallel to GD (Figs. 1, 2). Using the Labotex software the volume fractions (full width at half maximum of 20°) of the different variants are for the 7M structure: 40% [001], 33% [010], 17% [100]. In the case of the NM structure it is: 40% [001] and 55% <100>, rest phase.

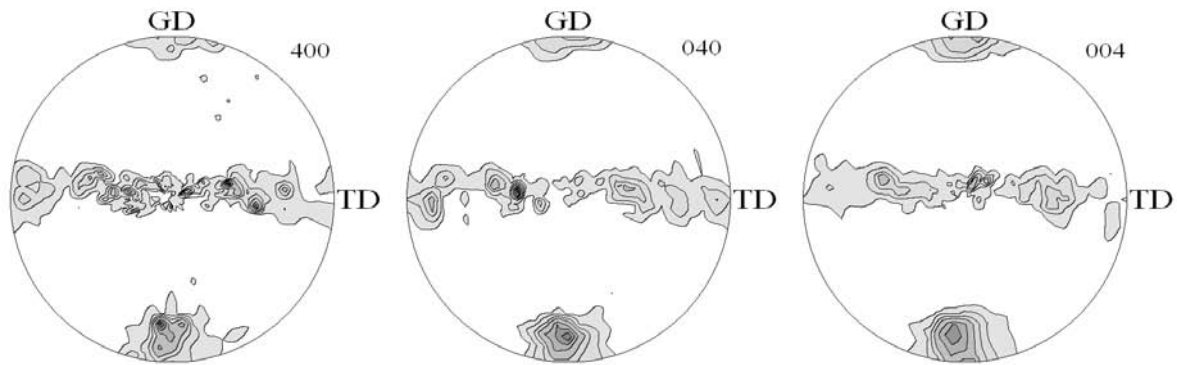


Fig. 1:  $\{400\}$  pole figures of the orthorhombic 7M phase in the directionally solidified sample measured with synchrotron radiation (intensities: 1.0, 4.0, 8.0, 12.0, 16.0, 20.0, 24.0, 28.0 mrd, GD = growth direction, TD = transverse direction).

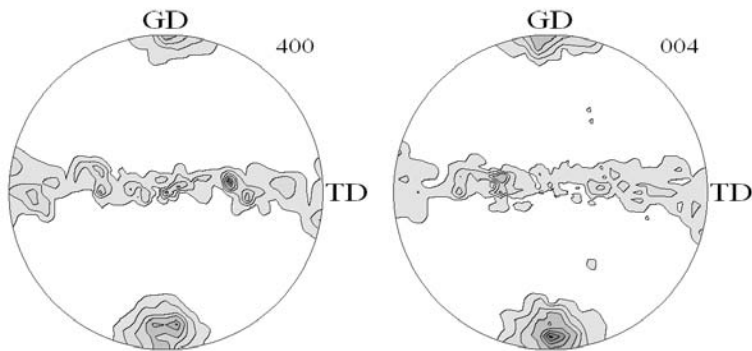


Fig. 2:  $\{400\}$  pole figures of the tetragonal NM phase in the directionally solidified sample measured with synchrotron radiation (intensities: 1.0, 4.0, 8.0, 12.0, 16.0, 20.0, 24.0, 28.0 mrd, GD = growth direction, TD = transverse direction).

The  $\langle 100 \rangle$  fibre texture existing in the directionally solidified NiMnGa alloy is typical for cast cubic crystals with the fibre axis aligned along the temperature gradient determining GD [10]. The variant selection during the martensitic phase transformation is such that mainly the shortest lattice parameter is parallel to GD, which for 7M is  $c$  and for NM is  $a$ . Before discussing the reason of this kind of variant selection, further investigations are necessary to check if this finding is of statistical relevance. Moreover, it is of particular interest to find out if the material can be trained to increase the intensity of the main variant.

## References

- [1] P. Müllner, V.A. Chernenko, M. Wollgarten and G. Kostorz, *Appl. Phys. Lett.* 92, 6708 (2002)
- [2] P. Müllner, V.A. Chernenko and G. Kostorz, *J. Magn. Magn. Mater.* 267, 325 (2003)
- [3] V.A. Chernenko, *Scripta Mater.* 40, 523 (1999)
- [4] K. Ullakko, J.K. Huang, C. Kantner, V.V. Kokorin and R.C. O'Handley, *Appl. Phys. Lett.* 69, 523 (1996)
- [5] V.V. Martynov, *J. de Physique IV* 5, 5 (1995)
- [6] J. Pons, V.A. Chernenko, R. Santamarta and E. Cesari, *Acta Mater.* 48, 3027 (2000)
- [7] V.A. Chernenko, J. Pons, C. Segui and E. Cesari, *Acta Mater.* 50, 53 (2002)
- [8] B. Wedel, M. Suzuki, Y. Murakami, C. Wedel, T. Suzuki, D. Shinto and K. Itagaki, *J. Alloys Comp.* 290, 137 (1999)
- [9] M. Pötschke, U. Gaitzsch, S. Roth, B. Rellinghaus and L. Schultz, *J. Magn. Magn. Mater.* 316, 383 (2007)
- [10] G. Wassermann and J. Grewen, *Texturen metallischer Werkstoffe*, Springer, Berlin (1962)

# Characterization of Ti6Al4V/Al7020-T6 friction welds using SR $\mu$ CT

J. Herzen<sup>1</sup>, F. Beckmann<sup>1</sup>, T. Donath<sup>1</sup>, V. Ventzke<sup>1</sup>, K.-H. Bohm<sup>1</sup>, P. Merhof<sup>1</sup>, M. Watzlaw<sup>2</sup>, M. Kocak<sup>1</sup>, and A. Schreyer<sup>1</sup>

<sup>1</sup>Institute of Materials Research, GKSS Research Centre, Max-Planck-Str. 1, 21502 Geesthacht, Germany

<sup>2</sup>GEA Tuchenhagen, Flow Components, Berliner Straße 25, 21514 Büchen, Germany

Friction welding is an advanced joining technique used for dissimilar materials like Al-based alloys and high-strength metals like Ti-based alloys. Because of the difference in melting points of these materials, the use of conventional fusion welding processes are not very suitable. Friction welding combines high-speed and a melt-free welding of the components and is used in aerospace field or nuclear industry. The joining mechanism is supposed to be based on cohesion and adhesion between the materials Ti6Al4V and Al7020-T6.

A study of crack initiation in Ti6Al4V/Al7020-T6 friction welded joints was performed using synchrotron-radiation-based micro-computed tomography (SR $\mu$ CT) at the beamline BW2 at HASYLAB [1]. The joints were analysed before and after a strength load to study the crack initiation. The results presented below show a friction welded joint that was cut cylindrically with a diameter of 3.5 mm from the weld and analysed by SR $\mu$ CT using a photon energy of 24 keV and a pixel size of 2.3  $\mu$ m. A measured spatial resolution of 4.72  $\mu$ m was achieved. Crack volume and position were determined using 3D-image-processing techniques.

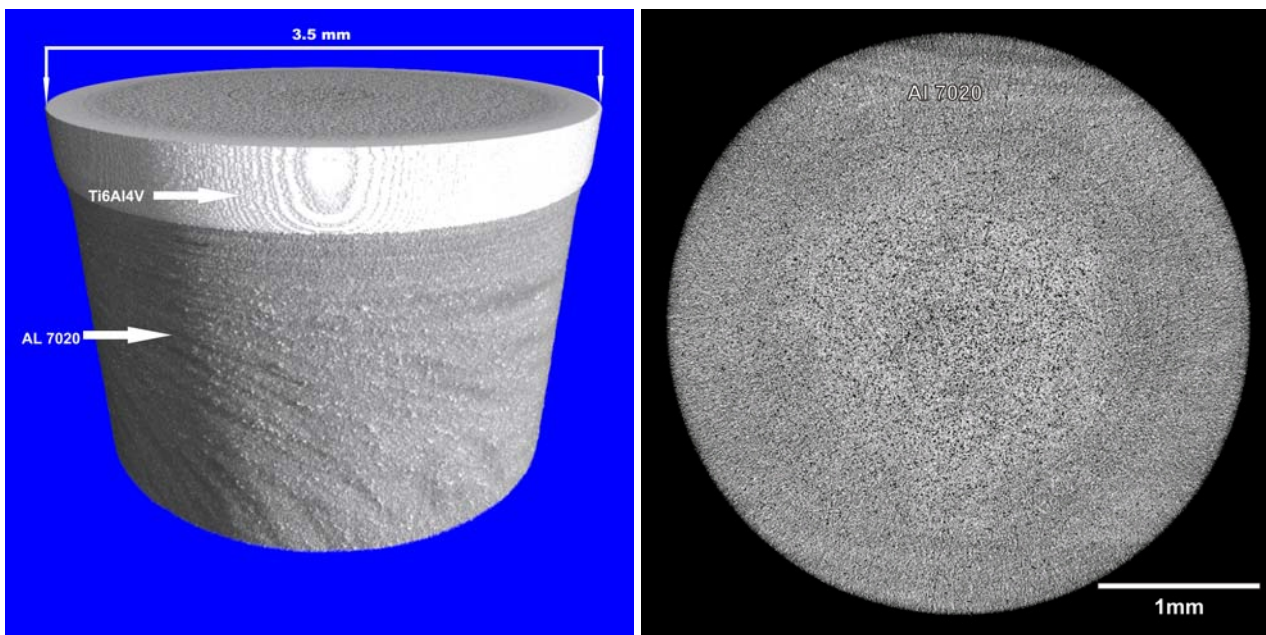


Figure 1: 3D view (on the left) and a slice from the tomogram (on the right: a slice from the region of Al 7020-T6) of a Ti6Al4V/Al7020-T6 friction welded joint without strength load. There are no cracks before strength loading, only some inhomogeneities inside the Al7020-T6 caused by the joining process.

Figure 1 shows a 3D view and a tomogram of a friction welded joint before loading. The Ti6Al4V was too highly absorbing at the energy of 24 keV, thus there is no information about the direct joining layer. Within the Al7020-T6 there is a non-homogeneous structure given by precipitation and dispersoids commonly appearing in Al alloys. The same joint after a strength load is presented in figure 2. Cracks can now be seen, but only in the region of the weaker aluminium Al7020-T6 and they are located on the surface of the joint outside of the interface between Al7020-T6 and Ti6Al4V. An SR $\mu$ CT measurement at the beamline HARWI II using a photon energy of 70 keV, that penetrates also the Ti6Al4V, confirms the results, that no cracks were initiated within the

titanium Ti6Al4V. In figure 3 the largest cracks within the loaded joint are labelled and their depth  $d$  from the surface and their distance  $a$  from the joining layer are listed in the table 1.

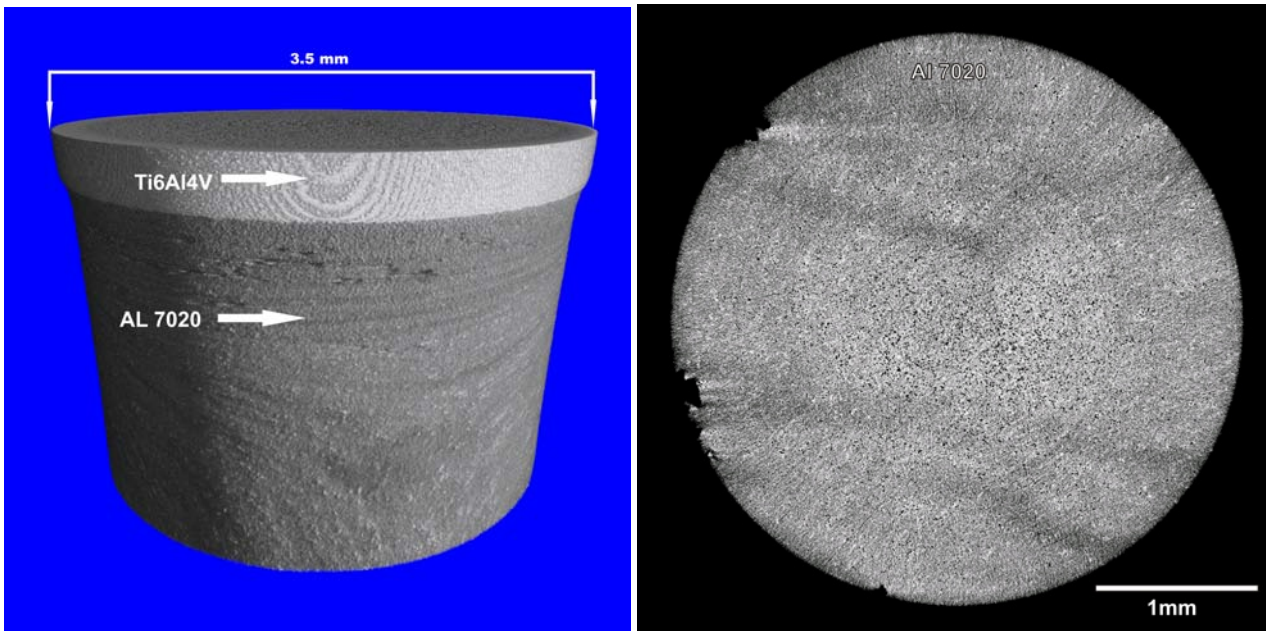


Figure 2: 3D view (on the left) and a slice from the tomogram (on the right: a slice from the region of Al 7020-T6) of a Ti6Al4V/Al7020-T6 friction welded joint after a strength load for crack initiation. In the region of the weaker material Al 7020-T6 cracks were initiated, which are located only on the surface of the sample (see right figure: black areas at the edges) and in a certain distance from the joining layer.

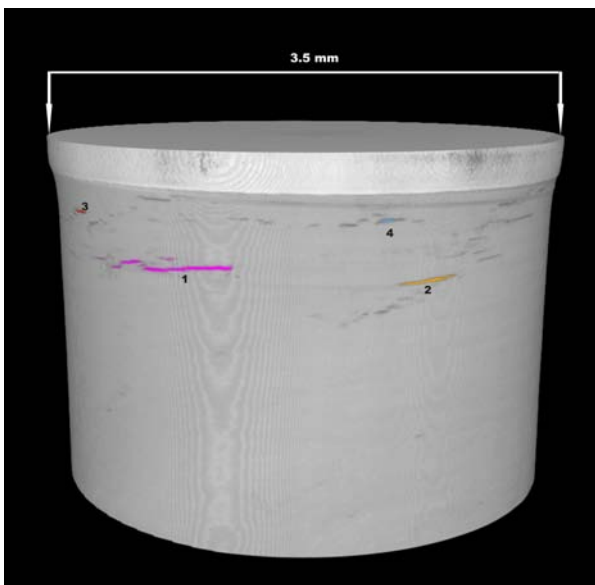


Figure 3: Volume rendering of a Ti6Al4V/Al7020-T6 friction welded joint after a strength load for crack initiation with labelling of the four largest cracks. For label parameters see table 1.

Crack label	Depth $d$ ( $\mu\text{m}$ )	Distance from joining layer $a$ ( $\mu\text{m}$ )	Colour
1	21.5	213.9	purple
2	30.1	257.1	yellow
3	31.9	94.8	red
4	21.8	70.9	blue

Table 1: List of parameters for the crack labels of a Ti6Al4V/Al7020-T6 friction welded joint after a strength load. The four largest cracks are labelled in figure 3.

The SR $\mu$ CT study shows non-destructively that all the initiated cracks are located within the weaker material Al 7020-T6. No cracks are found inside the joining layer. Hence, the joint will break outside the joining layer in the region of Al 7020-T6 first.

## References

- [1] F. Beckmann et al. (2006) SPIE Proceedings 631810-11.

# Charge density analysis of spinels with the use of the high-energy synchrotron radiation

*J. Warczewski<sup>1</sup>, T. Śliwińska<sup>1</sup>, G. Urban<sup>1</sup>, J. Fijak<sup>1</sup>, T. Lippmann<sup>2</sup>*

*<sup>1</sup>University of Silesia, Institute of Physics, Department of Physics of Crystals,  
Uniwersytecka 4, 40-007 Katowice, Poland*

*<sup>2</sup>GKSS Research Center, Max-Planck-Str. 1, D-21502 Geesthacht*

The charge density investigations play an important role in order to determine crystalline and electronic structures of many compounds. There are many publications concerning the magnetic crystals (spinel), especially with respect of their potential for industrial applications. For example the electronic companies, such as IBM, undertake major research efforts in order to understand in more detail such effects as e.g. magnetoresistance.

Spinel compounds with the general formula  $ACr_2X_4$  (where  $A = Cd, Zn, Hg, Ga, Cu$ ;  $X = S, Se, O$ ) have been analysed during the last decades due to their interesting electric, thermal and magnetic properties [1 – 5]. The spinels are perfect materials for many current technological applications such as magnetic sensors used as the read-write heads in the computer hard discs or as the temperature sensors. The advantages of applying synchrotron radiation are especially pronounced when the heavier atoms are present in the compounds under study (for example  $Cd, In, Hg, Ga$ ). The use of the synchrotron allows us to measure very small crystal samples at short wavelength, and thereby drastically decreases the sources of uncertainty such as the absorption of the X-ray beam in the crystal [6].

The measurements reported here will allow us to apply the Hirshfeld method with the goal to create maps of the electron density, even in the case of investigating such heavy elements as  $In$  and  $Ga$ , which are present in many spinels. The application of the Hirshfeld method for the precise refinement of the deformation functions of the electron density of the heavy elements is not really feasible using the conventional X-ray sources. Probably, this is the reason for the fact that very accurate maps of the electron density in the magnetic spinel crystals are not available so far. The Hirshfeld approach presents a research method for the understanding the structure in more detail as well as the influence of the electronic effects and, therefore, it is of great value for physics.

The experiment was performed on the materials science diffractometer at the GKSS materials science beamline HARWI-II at DESY, Hamburg, Germany. The following samples of single crystals have been investigated:  $CdXGa_1-XCr_2Se_4$ ,  $CdXIn_1-XCr_2Se_4$ . We used the high-energy synchrotron radiation approximately 100 keV in order to reduce both absorption and extinction [7]. We also used the MAR345 image plate camera for the quick data collection of our samples.

In this report we would like to focus on the data concerning  $CdXIn_1-XCr_2Se_4$ . This spinel has the cubic structure (space group  $Fd-3m$ ,  $a = 10.755 \text{ \AA}$ ). We performed the data collection for this crystal at room temperature and collected 180 frames with a  $\Delta\omega$  of  $1^\circ$  and additionally 90 frames with a  $\Delta\omega$  of  $2^\circ$  using a 6 mm Fe absorber in the beam in order to account for the strong reflections. The data images for  $CdXIn_1-XCr_2Se_4$  from the MAR345 were processed with XDS program package [8]. The initial structure refinements with SHELXL is in progress [9] as well as the conventional refinement with the assumption of spherical atomic scattering factors and the deformation refinement in which the experimental electron distribution will be fitted to the multipole deformation functions.

## References

- [1] J. Warczewski, J. Krok-Kowalski, P. Gusin, T. Sliwinska, G. Urban, L.I. Karoleva, A. Pacyna, E. Malicka, T. Mydlarz, S. Matyjasik, *J. Alloys and Comp*, in press
- [2] J. Krok-Kowalski, J. Warczewski, L. I. Koroleva, K. Krajewski, P. Gusin, H. Duda, P. Zajdel, A. Pacyna, T. Mydlarz, S. Matyjasik, R. V. Demin, *J. Alloys and Comp*, 377 (1-2) (2004) 53
- [3] D. R. Parker, M. A. Green, S. T. Bramwell, A. S. Wills, J. S. Gardner, D. A. Neumann, *J. Am. Chem.Soc.* 126 (2004) 2710
- [4] T. Groń, H. Duda, J. Warczewski, *J. Phys.* 49 (1988) 869
- [5] J. Warczewski, J. Krok-Kowalski, P. Gusin, H. Duda, J. Fijak, K. Kozerska, K. Nikiforov, A. Pacyna, *J. of Non-Linear Optics, Quantum Optics*, 30 (3-4) (2003) 301
- [6] P. Coppens, B. Iversen, F. K. Larsen, *Coordination Chemistry Reviews* 249 (2005) 179
- [7] T. Lippmann, J.R. Schneider, *J. Appl. Cryst.* 33 (2000), 156 – 167.
- [8] W. Kabsch, *J. Appl. Cryst.* 26 (1993) 795-800
- [9] G. M. Sheldrick, SHELXL-97 – A program for crystal structure refinement



# Deformation Analysis of Multi-Anvil High-Pressure Assemblies by Synchrotron based X-Ray Attenuation Contrast Tomography

*H.J. Mueller, F. Beckmann<sup>1</sup>, C. Lathe, A. Haibel<sup>1</sup>, M. Wehber, and J. Herzen<sup>1</sup>*

*GFZ Potsdam in der Helmholtz-Gemeinschaft, Dept. 5, Telegraphenberg, Potsdam, D-14473, Germany*

*<sup>1</sup>GKSS-Research Centre, Max-Planck-Straße 1, Geesthacht, D-21502, Germany*

Contrary to diamond anvil cells multi-anvil devices are characterized by its much bigger (several orders of magnitude) specimen volume and much smaller temperature gradient along the sample. The compression is really 3-dimensional. 6 (single-stage multi-anvil, e.g. MAX80) or even 8 anvils (double-stage multi-anvil, e.g. MAX200x) move toward the sample center simultaneously. The sealing process is the result of a complicate interaction of elastic and plastic deformation limited by internal friction. Consequently even minor dimensional changes and material replacements can modify the whole deformation and pressure generation behavior dramatically. Basing on theory and experimental experience the optimization is finally performed by trial and error, i.e. a new design element is tracked as long as the result can be improved. The problem is the interpretation of the experimental results in terms of design elements, i.e. answering the question in detail why the last design version improved or degraded the result at a time. It is very unpromising to disassemble a strongly deformed high pressure set-up, especially if it is embrittled by thermal treatment. Thus X-ray attenuation contrast tomography is an extraordinary and indispensable tool for the post-experiment clarification of deformation facts.

The experiment was performed at the high-energy materials science beamline HARWI-II using a photon energy of 65 keV. The resulting tomogram is calculated from 720 projections equally stepped between 0 and  $\pi$  sample rotation. The field of view of the X-ray detector was set to 14.9 x 4.6 mm<sup>2</sup> with a pixel size of 9.69  $\mu$ m showing a measured spatial resolution of about 19  $\mu$ m. The total reconstructed volume consists of 1535 x 1535 x 471 voxel representing 14.9 x 14.9 x 4.6 mm<sup>3</sup>. For visualization we use the software VGStudio MAX 1.2 of Volume Graphics GmbH Heidelberg, Germany.

Figure 1 shows the 3-dimensional view of a 6/4 assembly after a long-run high-pressure, high-temperature experiment at MAX80. The outer aliform parts are the gaskets sealing the set-up formed from the boron epoxy cube in the gap between the anvils. After all this experiment was disrupted by a blow-out, i.e. viscous parts, e.g. the graphite heater and the sodium chloride pressure standard dislocate from the center to the outer parts of the assembly and broke a gasket away resulting in a sudden decompression of the set-up accompanied by anvil rupture. Even though the assembly is widely destructed figures 1b and 1c clearly show the reason why. The copper rings of the power supply line are undersized. During gasket creation they were extruded. The graphite heater had followed this weak spot resulting in the blowout. The solution is reinforcing of the metal rings and reducing the diameter of the inner parts in proportion to the total cube size. This can easily be done using 3-dimensional CAD-software. Synchrotron based X-ray attenuation contrast tomography significantly accelerates and quantifies these optimization processes.

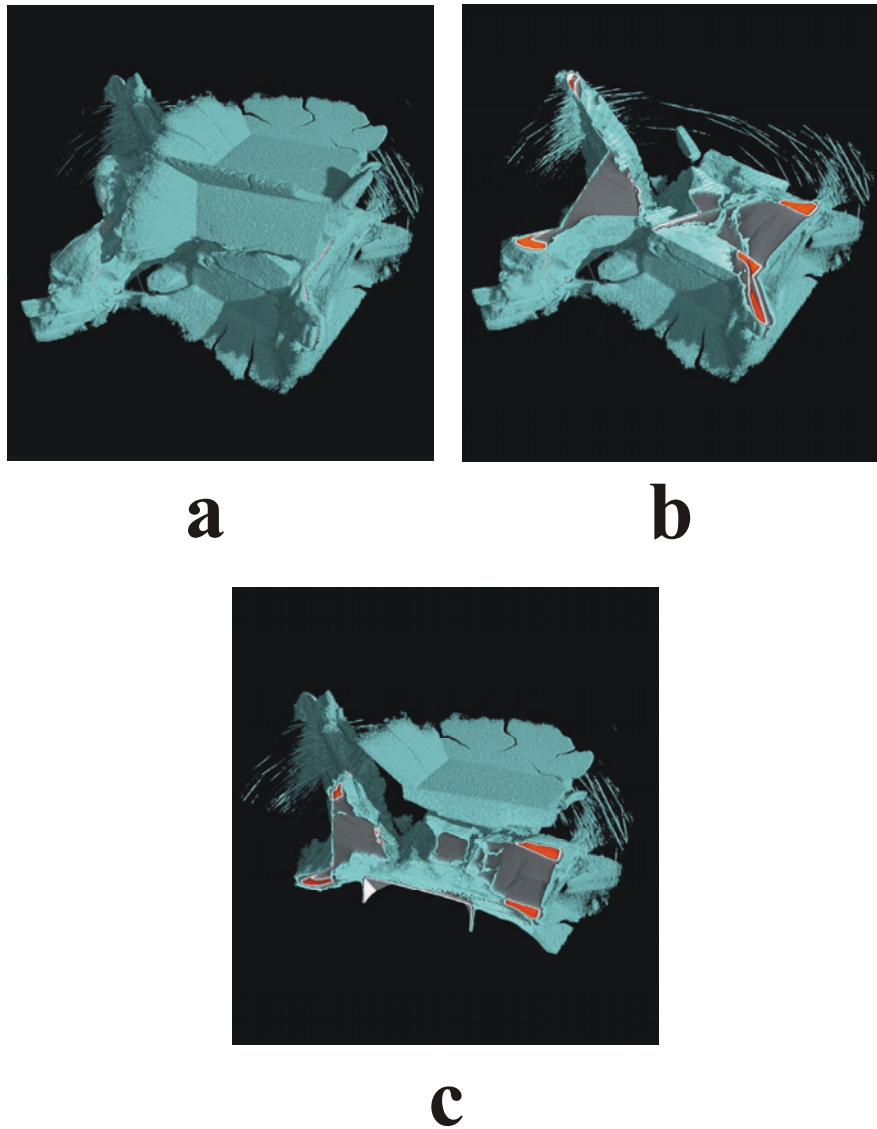


Figure 1: Synchrotron based X-ray attenuation contrast tomography of a multi-anvil set-up. The experiment was performed at beamline HARWI-II using a photon energy of 65 keV. The total reconstructed volume is  $14.9 \times 14.9 \times 4.6 \text{ mm}^3$ :  
a) total view, b, c) cross section.

## References

- [1] T. Donath, F. Beckmann, and A. Schreyer, *J. Opt. Soc. Am. A.*, 23 (5), 1048-1056 (2006)
- [2] F. Beckmann, T. Donath, J. Fischer, T. Dose, T. Lippmann, L. Lottermoser, R.V. Martins, and A. Schreyer, *Proc. SPIE Vol. 6318* (2006)
- [3] H.J. Mueller, F.R. Schilling, C. Lathe, J. Lauterjung, *High Pressure Research* 26, Vol. (4), pp. 529-537, 2006.



# Determination of residual stress depth fields in welded joints after different mechanical surface treatments

*Th. Nitschke-Pagel, I. Weich<sup>1</sup>, R. Martins<sup>2</sup>, T. Fischer<sup>3</sup>*

*Institut of Joining and Welding, Technical University of Braunschweig, Langer Kamp 8, 38106 Braunschweig, Germany*

*<sup>1</sup>Institut for Rehabilitation of Buildings and Structures, Technical University of Braunschweig, Pockelsstr. 3, 38106 Braunschweig, Germany*

*<sup>2</sup>JRC, Institute for Energy, Westerduinweg 3, 1755 LE Petten, The Netherlands*

*<sup>3</sup>GKSS Research Centre, Institute of Materials Research, Max-Planck-Str. 1, 21502 Geesthacht - Germany*

The current study has been conducted in the range of a BMBF project “REFRESH-Lebensdauererlängerung bestehender und neuer geschweißter Stahlkonstruktionen“. The objective of this project is to investigate methods to increase the fatigue strength and fatigue life of existing and new welded structures. The beneficial effects of mechanical post weld treatment methods, their quality control and possible design concepts are analysed [1].

Shot peening and different peening methods (Ultrasonic Impact Treatment, UIT and High Frequency Impact Treatment, HiFIT) provide a way of increasing the fatigue strength of welded structures. These methods introduce compressive residual stresses in the surface layers in combination with cold hardening. The depth of the penetration of the compressive residual stresses is quite different. After shot peening the maximum compressive residual stresses usually can be found in depth of 0.1...0.2 mm, whereas new high frequency peening methods shall produce a depth of more than 1 mm.

In order to optimize the peening parameters and to come up with a local fatigue life assessment approach a detailed knowledge about the residual stress distribution at the surface and the distribution under the surface is necessary. It is not confirmed, whether a maximization of the penetration depth of the compressive residual stresses leads to higher benefit with regard to the fatigue strength of welded joints or the maximization of near surface compressive residual stresses. Therefore, residual stresses and especially the stress gradient in the influenced layers are of greatest importance regarding the influence of the residual stresses on the fatigue strength.

The surface residual stresses have been measured by X-ray diffraction (XRD), residual stresses in the bulk by neutron diffraction (ND) [2]. The gap between the surface and the bulk region can only be closed with help of electrochemical removal of surface layers or by applying the hole drilling method. Both procedures destroy the sample and are limited in their accuracy: the surface removal causes changes of the original residual stress field and the hole drilling results are limited by plastification processes. Therefore, synchrotron radiation has been used in order to analyse the residual stresses in the treated area.

For the experiment 8 mm thick slices out of MAG-welded steel grade S355J2 and S690QL were cut out and shot peened or alternatively treated with HiFIT or UIT. Synchrotron diffraction measurements have been performed in transmission at the beamline HARWI II of the GKSS with a monochromatic beam with a wavelength of 0,154Å (120keV). The strains were evaluated using the {211}-reflex of the ferrite. In order to exclude influences of vertical misalignments of the specimen the surface was coated with copper powder, so that the {200}-reflex of the strainfree copper could be used as a reference. Strain measurements have been conducted in an area of +/- 2mm from the weld toe up to a depth of 2 or 6 mm. The beam size has been defined as 0.5 mm x 0.5 mm for the UIT and HiFIT treated specimens and as 0.25 for the shot-peened ones. The residual stresses were calculated assuming plane residual stresses and linear elastic material behaviour.

The residual stress obtained for the UIT- and HiFIT-treated specimens out of steel grade S355J2 are plotted in figure 1. Compressive residual stresses which can be correlated with the treatment process are found up to a depth of 1.2...1.4 mm, the transition to the equilibrium tensile stresses in the adjacent depth zone between 1.2 and 1.8 mm. The greatest amount of the compressive residual

stresses is between -200 and -300 MPa. In the deeper zone tensile residual stresses occur. The maximum of the residual stresses in the HiFIT-treated zone appears at a depth of 0.8 mm slightly eccentric. These results correspond very well to measurements carried out with the hole drilling method on peened specimens of the basic material. The eccentricity can be explained by the different material conditions in the welded zone and the base material and must be also correlated to geometrical effects of the weld toe. The results for the HiFIT and UIT treated S690QL show similar results. Up to a depth of 1.5mm compressive residual stresses occur. It is obvious that the influence of the treatment is only given in the treated area.

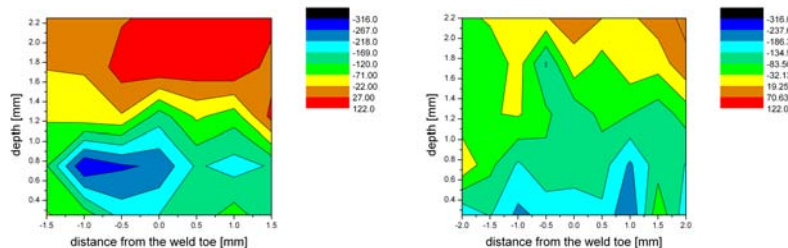


Figure 1: Transverse residual stresses [MPa] in the HiFIT- (left) and UIT-treated (right) zone.

Shot peening of the S355J2 causes compressive residual stresses up to a depth of 0.2 mm (figure 2). Regarding the S690QL compressive residual stresses of -200MPa have been measured up to a depth of 1.2 mm (figure 2). However, the residual stress depth distributions due to shot peening could not be sufficiently investigated with experimental setup used in the described experiments. The corresponding results obtained with help of XRD-measurements will be presented later.

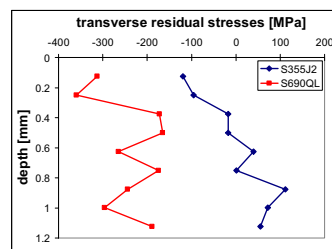


Figure 2: Transverse residual stresses [MPa] after shot peening

In summary, the results prove that the penetration depth of the beneficial compressive residual stresses caused by the peening methods is around 1 to 1.5 mm with a maximum underneath the surface at approximately 0.5 mm. At a depth of 2 mm tensile stresses occur. Therefore, the penetration is higher as induced by shot peening. However, experimental results about the fatigue behaviour reveal, that the higher penetration depth not necessarily leads to an improved fatigue behaviour. Nevertheless, the results of residual stress measurements after application of different measurement techniques match very well if the boundary conditions of the different techniques are taken into account carefully.

*We thank the GKSS and HASYLAB for providing beamtime for this project and the Bundesministerium für Bildung und Forschung for the financial support.*

## References

- [1] Weich, I.; Ummenhofer, T.; Nitschke-Pagel, Th.; Dilger, K., High Frequency Peening Methods – Fatigue Improvement and Design Concepts, Proc. of the IIW International Conference Welding and Materials, Kozuh., Z., Bauer, B. (Hrsg.), 2007, Croatian Welding Society, pp 141 – 150
- [2] Th. Nitschke-Pagel, K. Dilger, I. Weich, T. Ummenhofer, Residual stresses and near surface material condition of welded high strength steels after high frequency mechanical post-weld treatments, IIW Document XIII-2153-07 (2007)

# Influence of the characteristic microstructural length in MMCs on the tomographic analysis of volume strain

H.-A. Crostack, J. Nellesen<sup>1</sup>, G. Fischer<sup>1</sup>, F. Beckmann<sup>2</sup> and J. Herzen<sup>2</sup>

Lehrstuhl für Qualitätswesen, Fakultät Maschinenbau, TU Dortmund, 44221 Dortmund, Germany

<sup>1</sup>RIF e.V., Joseph-von-Fraunhofer-Str. 20, 44227 Dortmund, Germany

<sup>2</sup>GKSS Research Center, Max-Planck-Str. 1, 21502 Geesthacht, Germany

Localisation of volume strain in tensile specimens can be analysed by X-ray tomographic microscopy. The basic prerequisite for this tomographic approach is that microstructure shows some contrast in the tomograms. In particle-reinforced metal matrix composites (MMC<sub>p</sub>) this requirement is often met due to differences in the linear attenuation coefficient between the phases. These differences lead to grey level gradients in the tomograms which are exploited. Thus, the dispersed brittle particles act as marker for strain.

For strain analysis done by the authors pairs of computer tomograms of the less deformed (reference) and the more deformed microstructure are iteratively matched in that manner described below [1]:

Regularly distributed cuboid regions are defined in the reference tomogram on a rectangular grid. They represent the local microstructure in the less deformed state. For each cuboid region a corresponding (more or less same but deformed microstructural) hexahedral region in the tomogram of the more deformed specimen is iteratively searched. During this iteration procedure an affine and a radiometric transform are optimised with the least squares method. From the affine transform the deformation gradient  $\mathfrak{F}$  and subsequently the Laplacian strain tensor are computed. The size of the cuboids has to be adapted to the characteristic microstructural length which is given by the mean distance between the particles in case of MMC<sub>p</sub>.

In the scope of the studies particle reinforced reinforced metal matrix composites have been investigated which are used for cutting segments of rotating tools for stone machining. Two different commercial available segments consisting of a cobalt matrix with dispersed diamonds and WC-particles have been studied. Experiments were performed at beamline HARWI-II with monochromatic photons (energy  $E = 82$  keV and  $E = 100$  keV, respectively).

At a glance, the differences in microstructure can be spotted in fig. 1. In the two-dimensional tomogram region on the left only two large diamonds are visible. The diameter of the diamonds averages about  $300 \mu\text{m}$ . The composite on the right contains quite a lot diamonds (dark) with a mean diameter of approximately  $90 \mu\text{m}$ .

The studies aim at sampling strain with the highest possible spatial resolution, i.e. minimum cuboid dimensions. Since the strain analysis algorithm makes use of markers the lower limit of the cuboid dimensions corresponds to the mean distance between the dispersed particles. For both composites the mean distance between the WC-particles (bright, diameter  $\approx$  few microns) is smaller than the one between the diamonds (cf. fig. 1).

In the first case (left column) the cuboid dimension is  $42^3$  voxels and the spacing between the cuboid centers is 8 voxels. The voxel edge length amounts to roughly  $10 \mu\text{m}$ . For the second composite (right column) the cuboid is also formed like a cube but the edge length is only 32 voxels and the spacing is 12 voxels. The effective voxel edge length amounts to  $3.3 \mu\text{m}$ . The size of the images in the left column is  $121 * 241$  voxels whereas the width and height of pictures in the right column amounts to 585 and 511 voxels, respectively.

The comparison of the colour-coded smoothed maps of equivalent strain  $\varepsilon_{equ}$  which are overlaid over the images of microstructure reveal that regions of elevated strain can be found mostly in the neighbourhood of the diamonds. Due to the relative large dimensions of the cuboids high strain values can also be seen inside the diamonds in some places, which is not expected in view of the brittleness of diamond. In future work the cuboid dimensions will further be reduced for the second composite (right column in fig. 1) in order to avoid this effect.

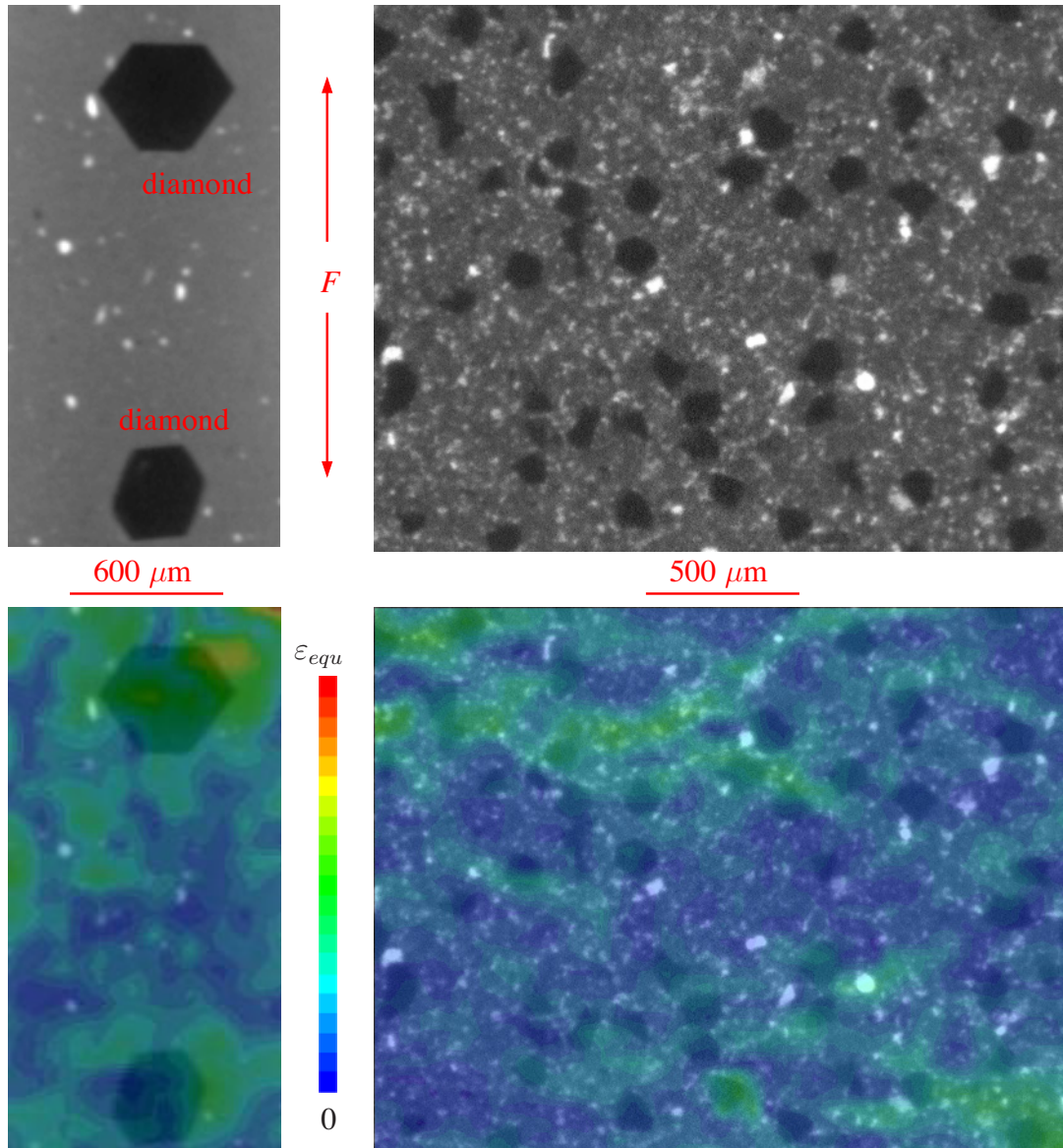


Figure 1: Comparison of microstructure of different particle-reinforced metal matrix composites and colour-coded overlaid distribution of equivalent strain  $\varepsilon_{equ}$ , composite with  $300 \mu\text{m}$  (left column) and  $\approx 90 \mu\text{m}$  diamonds (right column)

This work is financially supported by the German Research Foundation (DFG) in the scope of the research project CR4/111-1 which is gratefully acknowledged.

## References

- [1] H.-A. Crostack, J. Nellesen, G. Fischer, S. Schmauder, U. Weber, F. Beckmann, Proc. SPIE 6318, 63181A-1-12 (2006).



# ***In-situ* High-Temperature SAXS Studies of the Precipitation Kinetics in a Fe-Co-Mo Alloy**

G.A. Zickler<sup>1,2</sup>, E. Eidenberger<sup>2</sup>, E. Stergar<sup>2</sup>, H. Leitner<sup>1,2</sup>, H. Clemens<sup>2</sup>, T. Lippmann<sup>3</sup>, P. Staron<sup>4</sup>,  
T. Fischer<sup>3</sup>, A. Schreyer<sup>4</sup> and R. Nowak<sup>5</sup>

<sup>1</sup>Christian Doppler Laboratory for Early Stages of Precipitation, University of Leoben, Franz-Josef-Str. 18,  
A-8700 Leoben, Austria

<sup>2</sup>Dept. Physical Metallurgy and Materials Testing, University of Leoben, Franz-Josef-Str. 18, A-8700 Leoben, Austria

<sup>3</sup>GKSS at DESY, Notkestr. 85, D-22607 Hamburg, Germany

<sup>4</sup>GKSS Research Centre Geesthacht, Max-Planck-Str. 1, D-21502 Geesthacht, Germany

<sup>5</sup>HASYLAB/DESY, Notkestr. 85, D-22607 Hamburg, Germany

The increasing demand for better economy, higher operating efficiency, and the related reduction of emissions have prompted intensive research on advanced high-performance structural materials. Modern steels belong to this group of high-performance materials, which display excellent wear resistance, high strength, and high resistance against microstructural changes under operating conditions. The development of new advanced materials requires comprehensive understanding of the occurring solid-state phase transformations, precipitation reactions, and their effects on the mechanical properties [1].

The investigated material is based on a ternary Fe-Co-Mo alloy with the nominal chemical composition: Fe base, 25 at% Co, 15 at% Mo, and Ni, Cr, V, W, Cu, Si, C as micro alloying additions. Previous transmission electron microscopy, atom probe tomography, and small-angle neutron scattering experiments displayed that the alloy shows precipitation reactions of the nanometre-sized intermetallic  $\mu$  phase ((Fe,Co)<sub>7</sub>Mo<sub>6</sub>). The  $\mu$  phase is precipitated during heat treatments of the alloy and causes the extraordinary mechanical properties. The scattering contrast (electron density contrast) between the  $\mu$  phase and the matrix was calculated to be  $(\Delta\eta)^2 = 1.8 \times 10^{19} \text{ cm}^{-4}$ , which is sufficient to study the precipitation kinetics by small-angle X-ray scattering (SAXS).



Figure 1: High-temperature scattering furnace [2] for *in-situ* SAXS studies of the precipitation kinetics at the high-energy materials science beamline HARWI-II (W2).

SAXS experiments using high-energy synchrotron radiation in combination with an *in-situ* high-temperature furnace are powerful tools for studying phase transformations and precipitation reactions in bulk samples (diameter: 5.0 mm). SAXS experiments were performed for the first time at the GKSS high-energy materials science beamline HARWI-II (W2) at HASYLAB/DESY. Figure 1 shows the high-temperature furnace [2] and the setup at the beamline. For the *in-situ* high-temperature experiment, a nominal photon energy of 100 keV and a sample-to-detector distance of 9.8 m were chosen. The specimens were solution treated at 1180°C for 5 min before the experiment and isothermally aged at various temperatures between 425 and 525°C (heating rate: 100 °C min<sup>-1</sup>) in the evacuated *in-situ* scattering furnace. SAXS patterns were taken continuously during the *in-situ* heat treatment. An image plate detector (mar345, Marresearch) and a novel direct conversion selenium detector (mar555, Marresearch) were used, respectively, to detect the scattered photons. The SAXS patterns covered a range of scattering vector of 0.1 nm<sup>-1</sup> <  $q$  < 5.0 nm<sup>-1</sup>, where the length of the scattering vector is given by  $|\mathbf{q}| = q = (4\pi / \lambda) \sin \theta$ , with  $2\theta$  being the scattering angle and  $\lambda$  the wavelength. The scattering patterns were corrected for background scattering, electronic noise, transmission, and polarisation by using the data reduction program FIT2D. All specimens showed isotropic scattering patterns, which were azimuthally averaged for equal radial distances from the central beam (Figure 2). The SAXS curves show a characteristic maximum, which shifts at 500°C from 0.9 nm<sup>-1</sup> at the early stages of precipitation to 0.4 nm<sup>-1</sup> in the observed time range.

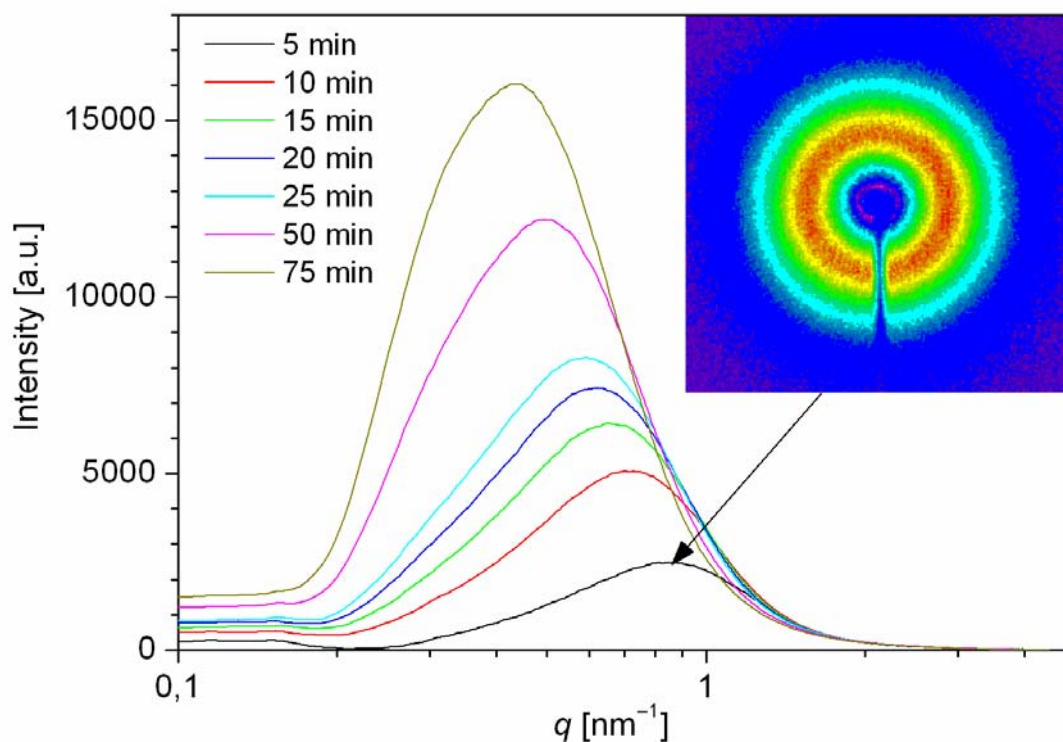


Figure 2: A typical series of azimuthally averaged SAXS patterns of the Fe-Co-Mo alloy heat-treated at 500°C for various ageing times. The insert shows a two-dimensional intensity distribution (detector image).

The SAXS signal will be evaluated by modelling of the scattering curve, using particle form factor, size distribution of the precipitates, and structure factor due to dense packing of the precipitates. This approach should provide information about size, shape, and volume fraction of the intermetallic  $\mu$  phase. Detailed evaluation of the data, including model fitting of the SAXS curves is currently in progress.

## References

- [1] Y. Geller, Tool Steels (translated from Russian by V. V. Afanasyev) Mir Publishers, Moscow (1978)
- [2] M. von Zimmermann and R. Nowak, HASYLAB Annual Report (2004)

# Investigation of the creep cavity evolution in steel by synchrotron micro-tomography

C. Barbatti<sup>1</sup>, A. Isaac<sup>1</sup>, F. Sket<sup>1</sup>, K. Dzieciol<sup>1</sup>, F. Beckmann<sup>2</sup>, J. Herzen<sup>2</sup>,  
A. Borbély<sup>1</sup>, A. Pyszalla<sup>1</sup>

<sup>1</sup>Max-Planck-Institute for Iron Research GmbH, Max-Planck-Strasse 1, 40237 Düsseldorf, Germany

<sup>2</sup>GKSS–Research Centre, Institute for Materials Science, Max-Planck-Strasse 1, 21502 Geesthacht, Germany

The efficiency of electricity-generating plants and gas turbines depends strongly on their components' sustainability of loading at high temperatures. The service lifetime of these components in most cases is controlled by creep-induced cavity growth. In order to quantify the remnant lifetime of creep loaded components models have been proposed, which are based on parameters characterizing microstructure damage [1]. Microscopic methods have been used to determine, for example, the fraction of grain boundaries damaged by cavities, however these procedures to determine creep damage only rely on information obtained from two-dimensional images. Since microscopy necessitates cutting the sample, only a snap-shot of the damage evolution was available. Synchrotron tomography provides data of damage in the bulk, which often significantly differs from damage at the surface [2], and it reveals the chronology of damage events in case of in-situ tests.

Using a combination of fast tomography [3] and diffraction with white high-energy synchrotron radiation [4] we could recently determine the creep pore evolution and texture formation during creep of a brass alloy [5]. More recently [6], in-situ investigations of the evolution of creep cavity size, shape, and spatial orientation in a brass alloy (Cu-40Zn-2Pb) using synchrotron X-ray tomography enabled a quantitative description of the time dependence of cavity morphology and size distributions. Besides, the results of the experiments allowed following the coalescence of cavities giving rise to pores with complex shapes.

The aim of this work is to obtain a detailed quantification of the creep pore evolution in standard Cr-Mo steels, which are the standard materials e.g. in power plant components subjected to creep. This includes a quantitative determination of the distributions of the morphology, orientation and size of the cavities.

Specimens of standard steel grade 1.4112 (0.85-0.95%C, 1.0%Si, 1.0%Mn, 0.04%P, 0.015%S, 17-19%Cr, 0.9-1.3%Mo, 0.01-0.12%V) with a diameter of 1mm and an active length of 2mm were produced. The creep tests were carried out using a miniature creep device developed earlier for in-situ experiments, which is suited for the loads necessary to obtain significant creep pore growth during measurement times of a few hours. The synchrotron X-ray tomography experiments were performed at the experimental station W2 (HARWI II) using monochromatic beam at 55keV during two measurement sessions. Information on the number and volume fractions of cavities was extracted from the tomograms using a numerical code written in interactive data language (IDL) developed in-house.

The creep curve obtained during the complete creep test for steel 1.4112 under tensile load of 422 MPa at 740°C is shown in **Fig.1**. Samples were obtained by interrupting the test at several different times. **Fig.2** provides a macroscopic isometric view of 3D reconstructions of the sectioned volumes revealing creep damage evolution in the sample with cavities highlighted in blue. The tensile load axis coincides with the vertical axis in this figure. The macroscopic view indicates an increase in the number of creep cavities with time. The inhomogeneity of the distribution of the cavities along the longitudinal section of the sample is also visible, there are

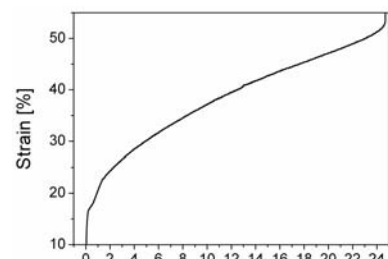


**Fig.1:** Creep curve for steel 1.4112 subjected to 422 MPa at 740 °C.

substantially more creep cavities at the top of the sample compared to the bottom. This is due to a temperature gradient of approximately 46°C along the sample.

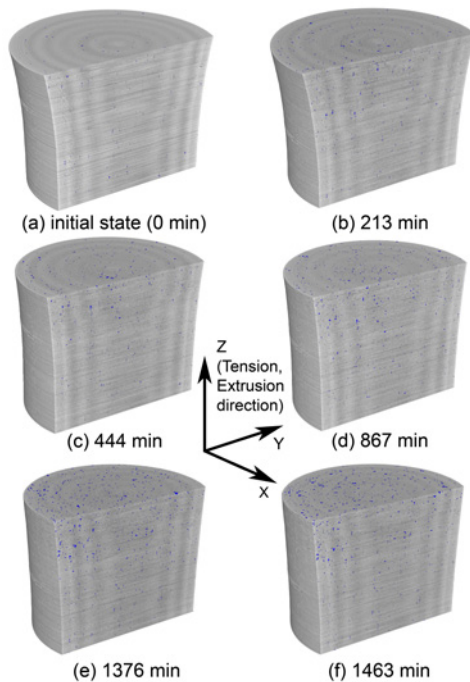


**Fig.2:** Tomography revealing the cavities in the initial condition and at different times during the creep test. The diameter of the samples is 1 mm

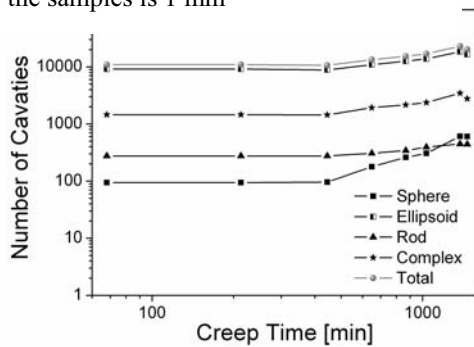


**Fig.3:** The evolution of the number of cavities (given for the different shapes and in total) as a function of creep time.

**Fig.3** shows the evolution of the number of cavities corresponding to different shapes. These results show that both in the initial state and throughout the creep test ellipsoids are the most numerous and govern the creep behavior for this material. Only a comparatively low number of cavities are rod and sphere shaped, approximately one order of magnitude less than the complex shaped cavities. Up to 400 minutes into the creep test the number of cavities does not increase considerably. After 400 min the increase in the number of cavities becomes visible with the highest rate in the sphere shaped cavities.

The results for the total cavity volume show a similar behavior, with the number of ellipsoid cavities dominating the creep behavior. As for the average cavity volume (**Fig.4**), the results indicate a slight increase in the average cavity size for all the different shapes. The predominance of ellipsoid-shaped cavities suggests that creep in Cr-Mo steel follows a diffusion-controlled mechanism. The relatively large reconstructed volume (several mm<sup>3</sup>) ensures that the quantified cavity distributions are representative.

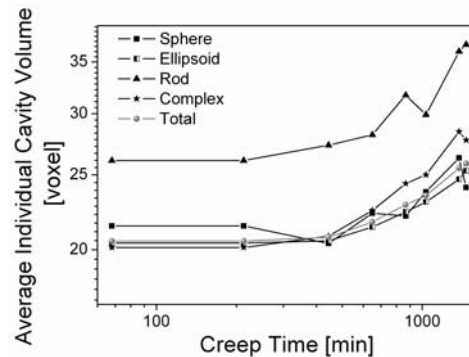


**Fig.4:** The evolution of the average individual cavity volume (given for the different shapes and in total) as a function of creep time.

## References

- [1] H. Riedel, Fracture at High Temperatures (Springer-Verlag, Berlin, 1987).
- [2] J. -Y. Buffière, E. Maire, P. Cloetens, G. Lormand, R. Fougères, Acta Mat. 47, 1613 (1999).
- [3] M. Di Michiel et al., Rev. Sci. Inst. 76 (2005).
- [4] W. Reimers, A. Pyzalla, M. Broda, G. Brusch, D. Dantz, K.-D. Liss, T. Schmackers, T. Tschentscher, J. Mat. Sci. Letters 19 (1999) 581 – 583.
- [5] A. Pyzalla, B. Camin, T. Buslaps, M. Di Michiel, H. Kaminski, A. Kottar, A. Pernack, W. Reimers, Science 308 (2005) 92-95.
- [6] A. Isaac, F. Sket, W. Reimers, B. Camin, G. Sauthoff, A. Pyzalla, Mater. Sci. Eng. A (2007), doi:10.1016/j.msea.2007.05.108.



# Local phase analysis in the welded seam of a FW Al7020/Ti6Al4V sample

H.-G. Brokmeier<sup>1,2</sup>, S. Lenser<sup>1,2</sup>, V. Ventzke<sup>2</sup>, A. Rotkirch<sup>3</sup>, T. Wroblewski<sup>3</sup>

<sup>1</sup>Institut für Werkstoffkunde und -technik, TU-Clausthal, Agricolarstr. 6, D-38678 Clausthal-Zellerfeld, Germany

<sup>2</sup>GKSS-Forschungszentrum, Max-Planck-Str., D-21502 Geesthacht, Germany

<sup>3</sup>HASYLAB at DESY, Notkestr. 85, D-22603 Hamburg, Germany

Welding techniques to join different types of materials such as Al with Ti, Mg with Al or Al with steel are of great importance for advanced products to optimize materials properties, the total weight at a reasonable prize. As part of the PNAM activities (PNAM – Photon and Neutron Research on Advanced Materials) laser beam welding, friction welding and friction stir welding have been tested. From the view of crystal physics the joining at the atomic level is one of the basic questions. In the present investigation the friction welding of Al7020 with Ti6Al4V was studied to determine possible intermetallic components in the welded zone. It has to be noticed that friction welding is technique where one part was fixed in the joining device while the other part was rotated very fast and finally compressed for some seconds to the first part. The operation temperature is much lower than the melting temperatures, so that a solid state process takes place. The three different joining techniques mentioned above have very different welded seams and heat affected zones. Friction welding has a very narrow welded seam, which means a high local resolution is necessary to examine the formation of new phases. Thus, an experiment at G3 with a high resolution using a polycapillary in front of a 2D detector was used. The investigation was carried out with 7 keV, so that a sample plate with part I (Al7020) and with part II (Ti6Al4V) was prepared. A  $2\theta$  area between  $40^\circ$  and  $44^\circ$  was chosen, which allows a good separation between  $\alpha$ -Ti the main part of Ti6Al4V and  $\alpha_2$ -Ti<sub>3</sub>Al. Because of the small effect we expect, the spectra along y were added together. The following figures show the schematic sketch of the welded sample (Fig.1) and intensity distribution over the welded seam (Fig.2).

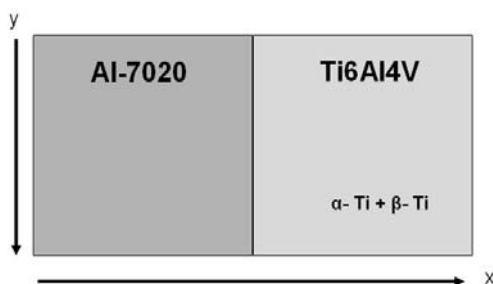


Fig. 1: Sketch of the FW-sample (Al7020/Ti6Al4V)

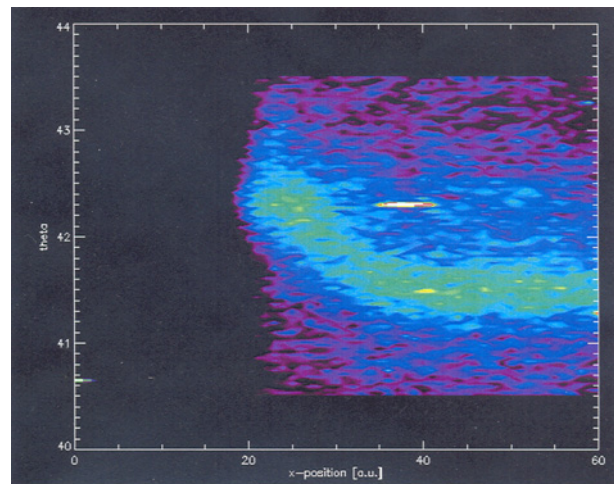


Fig. 2: Intensity distribution over the welded seam for  $2\theta$   $40^\circ$  to  $2\theta$   $44^\circ$  to

The white spot belongs to an electronical signal of the detector electronics, which do not belong to the sample. The blue colour belongs to the Ti-part of the sample plate. Due to the special scattering properties of Ti, the welded seam can be detected very precisely at the

beginning of the black zone. A curling of only 5 pixels (65 $\mu$ m) is the local expansion of the welded seam. In order to describe the results one can see in figure 2 a theoretical calculation of some possible crystallographic phases were carried (cubic Al, hexagonal  $\alpha$ -Ti, cubic  $\beta$ -Ti, hexagonal  $\alpha_2$ -Ti<sub>3</sub>Al, tetragonal  $\gamma$ -TiAl).

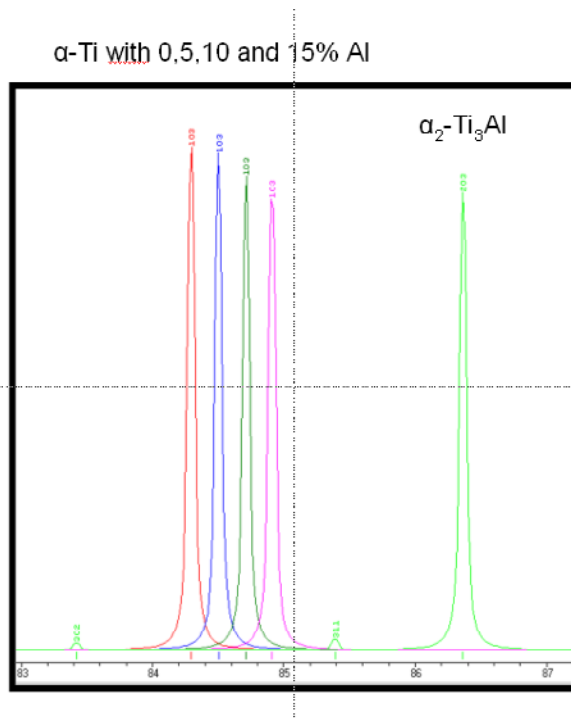


Figure 3: Theoretical powder pattern for some phases in the system Ti-Al

Figure 3 shows a set of the (10.3) reflection of hexagonal  $\alpha$ -Ti for different Al contents. Due to the Al content the lattice constants of the Ti(Al) mixed crystal can vary from  $a=2.953 - 2.923\text{ \AA}$  and  $c=4.686-4.466\text{ \AA}$ . According to the expected processing temperatures an Al – content of about 6-7% can be solved in the Ti lattice. The reflection at about  $86.2^\circ 2\theta$  belongs to the intermetallic  $\alpha_2$ -Ti<sub>3</sub>Al.  $\alpha_2$ -Ti<sub>3</sub>Al has also a hexagonal crystal structure as a  $\alpha$ -Ti but with an ordering of Al. The weak intensity band between  $\alpha$ -Ti and  $\alpha_2$ -Ti<sub>3</sub>Al is part of the transition zone between both phases of about 10 pixels (130 $\mu$ m). It has to be noticed that  $\alpha_2$ -Ti<sub>3</sub>Al is a stable crystallographic phase not only on the exact stoichiometry, so that the Al-content can vary and a shift of the  $\alpha_2$ -Ti<sub>3</sub>Al is possible.

### Discussion:

Looking on the Ti-Al phase diagram, one recognizes a solubility of 15% Al in Ti, which results in a peak shift to higher Bragg's angles. The friction welding process leads to a diffusion of Al atoms into the hexagonal  $\alpha$ -Ti crystal lattice. These first Al atoms can be solved in the hexagonal  $\alpha$ -Ti crystal lattice without any ordering. With increasing Al-content a peak shift is observed as known for mixed crystals. A further increase of the Al-content in the Ti-lattice results in an ordering of the Al atoms at discrete lattice positions which belong to a new crystallographic structure, the intermetallic  $\alpha_2$ -Ti<sub>3</sub>Al with a stoichiometric ratio of 3:1.

This experiment is a first indication of the crystal physics effect of the joining process between Al7020 and Ti6Al4V by diffusion of Al into the hexagonal  $\alpha$ -Ti crystal. A very small bonding layer of intermetallic  $\alpha_2$ -Ti<sub>3</sub>Al and another bonding layer with a continuous increase of the Al-content in the  $\alpha$ -Ti crystal are observed. More experiments are necessary to concentrate on possible other intermetallic phases particular between the small band of  $\alpha_2$ -Ti<sub>3</sub>Al and Al. Previous investigations on massive Al-Ti composites have shown that  $\gamma$ -TiAl and Al<sub>3</sub>Ti are possible candidates to fill this gap.

# Microtomography Study of Crack Propagation within Laser Welded Al-Alloy T-Joints

*J. Herzen, F. Beckmann, T. Donath, F. S. Bayraktar, S. Riekehr, M. Kocak, and A. Schreyer*

*Institute of Materials Research, GKSS Research Centre, Max-Planck-Str. 1, 21502 Geesthacht*

The use of advanced joining techniques like laser welding or friction stir welding in aircraft production could reduce the weight of aircrafts and, hence, their fuel consumption significantly. Currently only few parts of the aircrafts are welded. A better understanding of crack propagation and crack-pore interaction within the welds would help to establish these techniques for the fabrication of welded parts of the aircrafts.

A study of crack propagation in laser welded aluminium alloy T-joints was performed using synchrotron-radiation-based micro-computed tomography (SR $\mu$ CT) at the beamline HARWI II at HASYLAB [1]. Different aluminium alloys, which are known for their high or low pore level after welding, were used. A crack was initiated into the weld and the T-joints were analysed before and after cyclic loading to study the crack propagation. The results presented below show a test measurement of a laser welded aluminium T-joint of AA6013 T6 and AA2139 T3. The weld was cut cylindrically with a diameter of 6 mm from the T-joint and analysed by SR $\mu$ CT using a photon energy of 40 keV. A spatial resolution of 10.45  $\mu$ m was achieved.

Figure 1 shows the laser welded aluminium alloy T-joint, that was used for the test measurement. The cylindrical weld was cut from the region marked below. The tomogram is shown in figure 2. It is almost free of artefacts and allows to visualize different sort of pores within the weld. All different materials used in the T-joint can be clearly separated, as well as the weld itself due to the high density resolution.

The SR $\mu$ CT at HARWI II due to its superior density resolution allows to visualize non-destructively the distribution of pores and to separate all materials within the laser welded T-joints. The SR $\mu$ CT enables to study the crack propagation in interaction with pores inside the welds free of any artefacts.

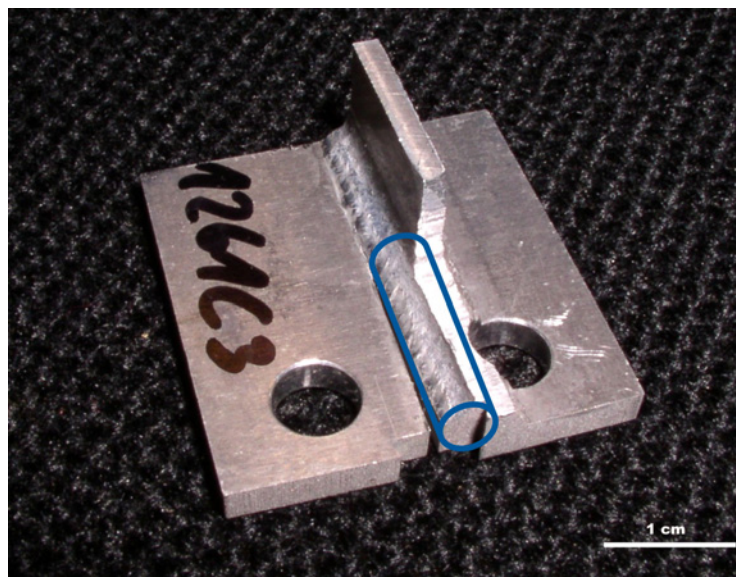


Figure 1: A laser welded aluminium alloy T-joint for the microtomography study. The skin consists of AA2139 T3 and the clip of AA6013 T6.

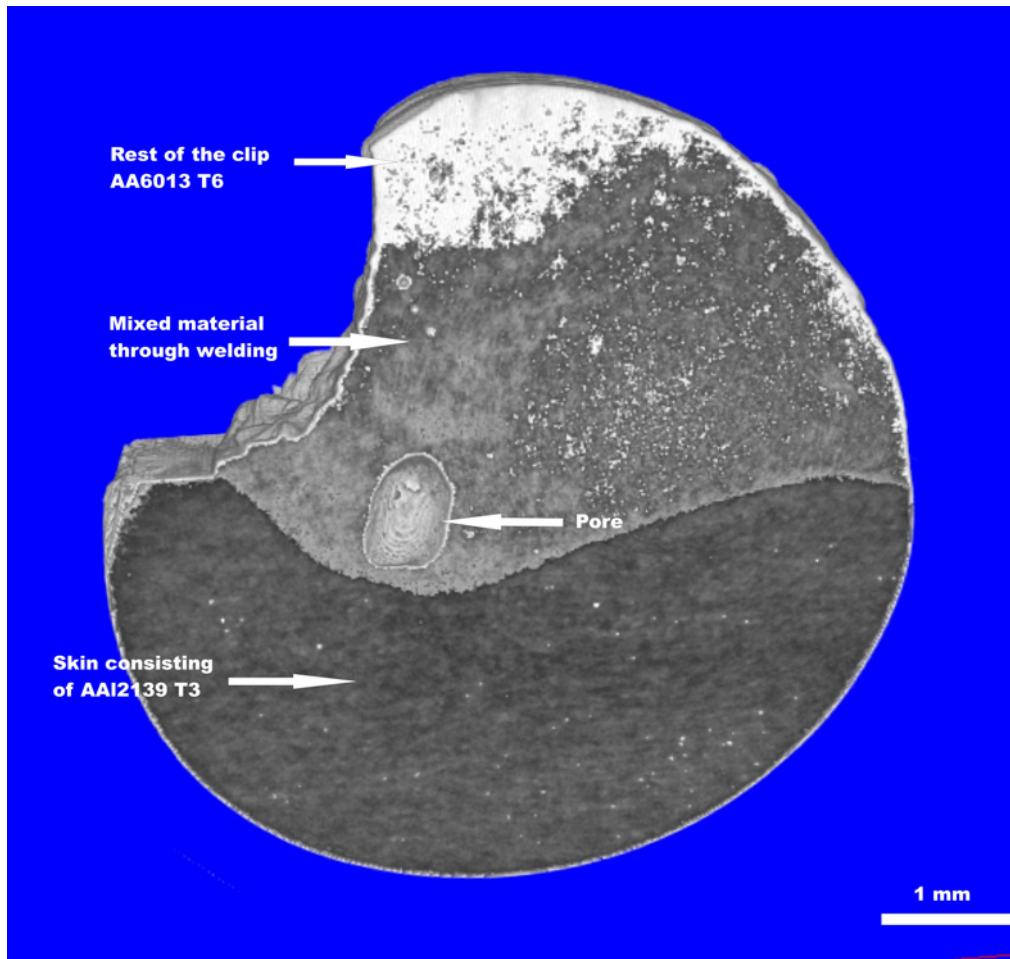


Figure 2: Virtual cut from a 3D view of a laser weld (tomogram measured using an energy of 40 keV at the beamline HARWI II at HASYLAB, DESY). The sample was cut cylindrically from a welded T-joint before the measurement. Not only the process pores are visible, but also the different materials can be clearly separated from the grey values of the tomogram.

## References

- [1] F. Beckmann et al. (2006) SPIE Proceedings 631810-11.
- [2] V. Ventzke et al. (2007) Proceedings of the European Workshop on „Development of Short Distance Welding Concepts for Airframes (WEL-AIR)“, GKSS Research Center, Geesthacht, Germany

# **$\mu$ CT analysis performed with DiTo: Identification of sources for malfunctions in sensors**

*H. Rahn<sup>1</sup>, I. Gomez-Morilla<sup>1</sup>, R. Baumann<sup>2</sup>, S. Fasoulas<sup>2</sup>, J. Herzen<sup>3</sup>, F. Beckmann<sup>3</sup>  
and S. Odenbach<sup>1</sup>*

<sup>1</sup>TU Dresden, Professur für Magnetofluidodynamik, 01062 Dresden, Germany

<sup>2</sup>TU Dresden, Professur für Raumfahrtssysteme/-Nutzung, 01062 Dresden, Germany

<sup>3</sup>GKSS, Max-Planck-Str.1, 21502 Geesthacht, Germany

Cutting-edge miniaturised gas sensor systems are being designed and manufactured at the Institute for Aerospace Engineering of TU Dresden in the frame of a ESA funded research project. These systems enable the simultaneous in-situ measurement of O<sub>2</sub> and CO<sub>2</sub> as well as volume/mass flow rates for human respiratory investigations [1].

The sensors are produced by screen printing techniques, consist of up to 20 layers of different materials and layouts, and are based on ion conducting ceramic materials, e.g. yttria-doped zirconia. In these ceramics ion conductivity is increased significantly above 400 °C. Therefore an electrical resistor is included in one of the layers to heat up the element and maintain stable operating conditions.

A major aim of this study is the serial production of these products. For this, the miniaturisation and the reproducibility (both structurally and operational) are two important aspects to be investigated. Thanks to their layout, the structural analysis can be performed non-destructively by micro-computed tomography. In addition, by analysing the structure of both functioning and malfunctioning sensors and comparing them, it is possible to relate the performance (or lack of it) with the structure, and connect the findings to improve the reproducibility of the production.

A series of measurements has been performed with DiTo [2] in order to identify any structural differences between working and faulty sensors, and relate these to the malfunctionality that the faulty sensors present. All tomographic examinations within this series have been performed with a photon energy of 60 keV and an optical magnification of 2.6, leading to a spatial resolution of 6  $\mu$ m. The sensors are 3 mm wide and 20 mm long, so they can not be analysed entirely in one scan. The images have therefore been acquired in horizontal slices of 1.2 mm in height and stacked together to form the whole 3D image without losing of information. The region of interest is about 5 mm long, so the rendered images are composed of 5 stacked slices.

An example of this comparison analysis is presented below. Figures 1a and 1b show optical photographs of two different CO<sub>2</sub> sensors. The first one works, while the second one failed during the testing phase due to over-heating. It can be easily seen that the top ceramic layer is damaged in the second one. That could be a reason for the malfunctionality, but there may be structural changes in other layers that can not be seen with pure optical methods. For this reason, tomography analysis was performed with DiTo.



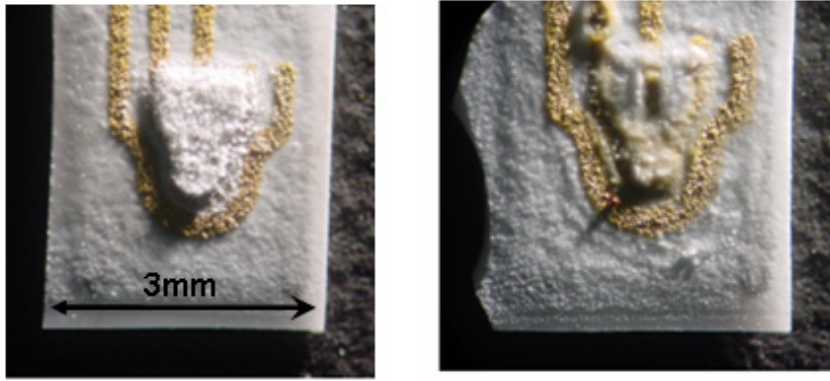


**Fig. 1: Optical photograph of (a) working sensor and (b) malfunctioning sensor.**

Figures 2a and 2b show cross sections of rendered images of the reconstructed tomography data sets collected from the sensors shown in Fig 1a and 1b. The histograms from both images have been treated equally, and both images can be compared directly. There are three major differences. In the faulty sensor there is a lack of a coating layer, which is present in the working sensor (represented in light green in the image). This is attributed to evaporation due to the over-heating. In addition, the electrode structure appears changed in density. This can not be identified in the optical image. Finally there is damage in the faulty sensor's electrode.

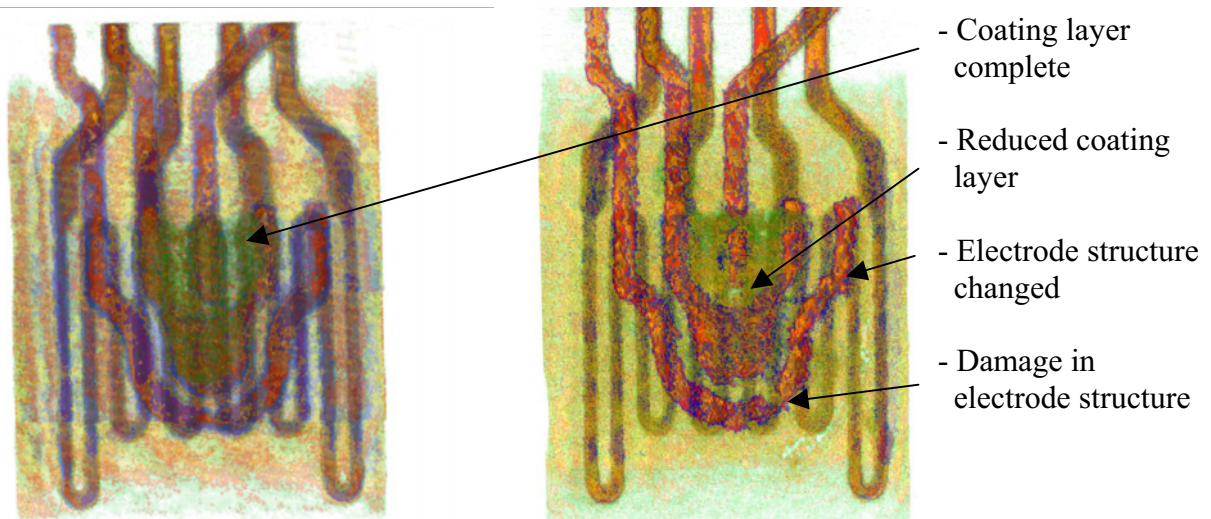


**Fig. 2: Tomography rendered images (a) a working sensor and (b) malfunctioning sensor.**

More comparisons have been performed, and structural changes have been identified and related to different malfunctions in faulty sensors. These findings have contributed to the re-design of the production process.

1. S.Fasoulas, R. Baumann, Gläser, C. Gritzner, F. Hammer, J. Heisig, R. Kahle, T. Kirschke, T. Schmiel, M. Völkel, Report No. ILR-RSN P 06-07, 2006.
2. B. Hasse, H. Rahn, S. Odenbach, F. Beckmann, W. Reimers, *The DITO-Experiment at the HARWI II Beamline*. HASYLAB Annual Report 2007, 2007.

# Porosity Evaluation in NiTi Intermetallics for Advanced Biomedical Components

A. Pozdnyakova<sup>1</sup>, A. Giuliani<sup>1</sup>, F. Beckmann<sup>2</sup>, J. Herzer<sup>2</sup> and M. G. Ortore<sup>1</sup>

<sup>1</sup>Università Politecnica delle Marche, Dipartimento di Scienze Applicate ai Sistemi Complessi, Via Brecce Bianche, 60131 Ancona, Italy

<sup>2</sup>GKSS-Research Centre, 21502 Geesthacht, Germany

Microstructural features of Nickel-Titanium (NiTi) samples produced by two different low cost and advanced techniques were investigated by means of X-Ray micro-computed tomography ( $\mu$ -CT) at the high-energy materials science beamline HARWI-II at the DORIS III storage ring. We investigated two sets of NiTi specimens:

1. NiTi sintered by Metal Injection Molding (MIM) with an heating rate of 10 K/min to 1270°C in argon atmosphere, before and after different Impulse Electric Current Treatment (IECT).
2. NiTi produced from superelastic powder by Mechanical Alloying & Hot Pressing (MA&HP), in particular one part of samples was produced from powder after milling.

The experimental equipment was set in order to obtain spatial resolution of 9  $\mu\text{m}$ . The sample-manipulator provides a high precision rotation (each step is 0.250°), translation and reposition of the sample. Data were processed by using the program VGStudio<sup>®</sup>MAX<sup>°</sup>1.2.1 using pixel linear dimension equal to 9.23  $\mu\text{m}$ . According to the above mentioned parameters, the three-dimensional reconstructions of investigated samples and quantitative evaluation of pores were obtained for each type of samples. In order to gain a good statistical quality of data analysis, the whole sample volume was investigated, and obtained results were normalized on individual volume Vs to perform a valuable comparison between different samples.

For the first set of samples we chose photon energy equal to 60 keV. We obtained three-dimensional reconstructions of all the investigated samples and pore size distribution, as reported in Fig.1. The more efficient IECT treatment was found to be at intermediate current values. In this case, IECT treatment had no noticeable effect on the sample porosity in the range  $>10^4 \mu\text{m}^3$ . On the other side, the carrying out of IECT reduces the pore volume in the range of volumes  $<10^4 \mu\text{m}^3$ . It follows that the treatment can possibly induce the coalescence phenomenon in already porous samples [1].

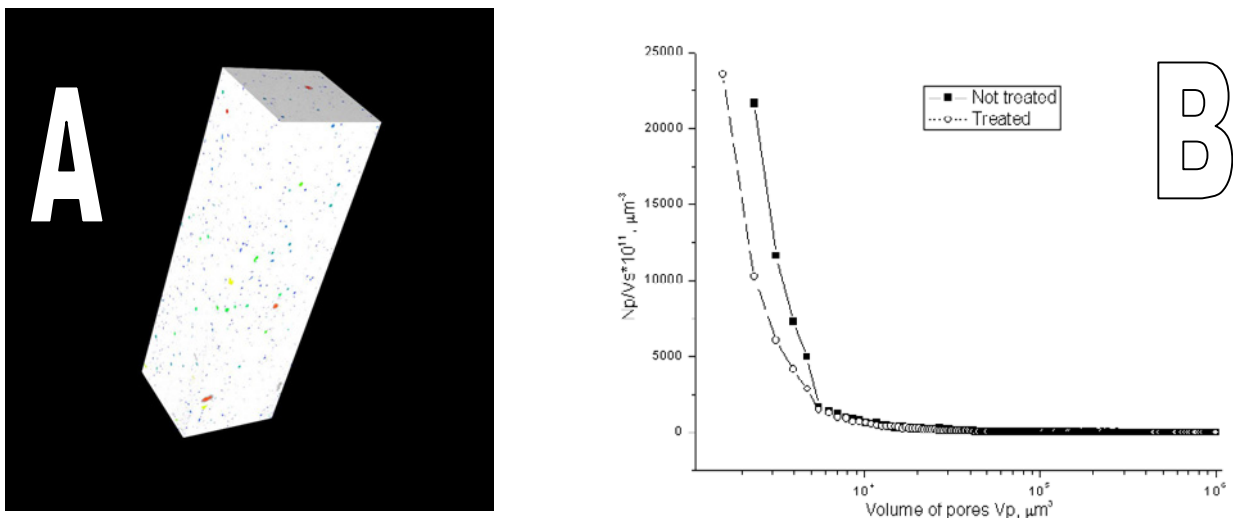


Fig. 1. A. Three-dimensional reconstruction of the not treated investigated sample. B. Comparison between pores distribution in NiTi samples before and after IECT treatment.

For the second set of samples, photon energy of 70 keV was used. Results obtained after the data analysis of these samples are presented in the Fig. 2. Since we performed an average on different parts of the samples, in the milled sample we determined noticeable error bars, indicating a not homogeneous porosity in the specimens. However, we can observe a bigger number of pores for milled samples. Further it also was stated that milled samples contain a bigger number of pores in the range up to  $5 \times 10^3 \mu\text{m}^3$ .

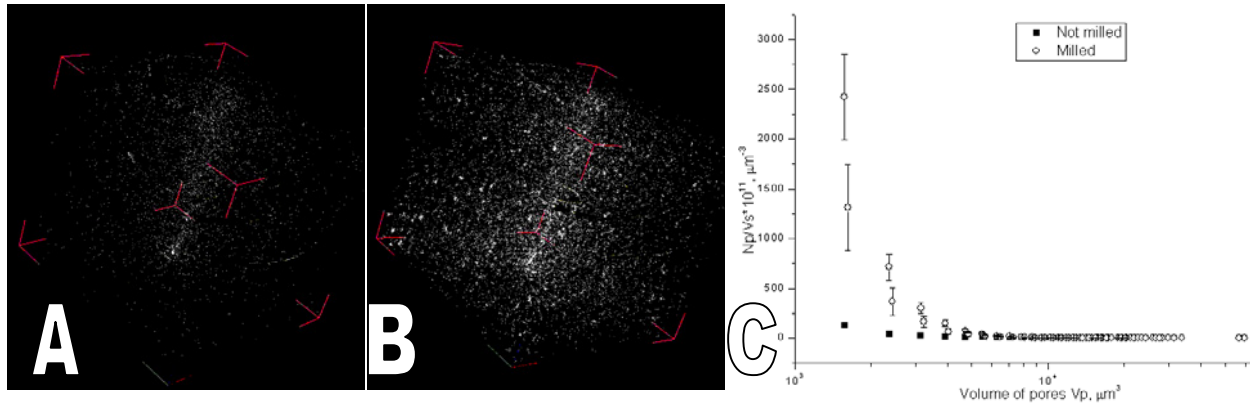


Figure 2: A.B. Three-dimensional reconstruction of pores: sample produced from superelastic powder (A) and the other from this powder after ball milling (B). C. Comparison in pores volume distribution.

We remark that different porosity of the NiTi alloys corresponds to different bone ingrowth, in particular increasing porosity can improve bone growth. Consequently NiTi elastic modulus can decrease to values comparable to bone ones.

In conclusion, our results point out that both types of samples present good potential in biomedical application field [2]. In fact, according to different treatments it was possible to modify NiTi alloys porosities, which can be associated to different possible biomedical applications.

## References

- [1] J. M. Sánchez, A. Ordóñez, R. González, International Journal of Refractory Metals & Hard Materials 23, 193–198 (2005)
- [2] D.C. Lagoudas, E.L. Vandygriff, Journal of Intelligent Material Systems and Structures 13, 837 - 850 (2002)



# Process $\mu$ -CT for observation of transport phenomena in porous media - a first test

A. Waske<sup>1</sup>, S. Odenbach<sup>1</sup>, F. Beckmann<sup>2</sup>

<sup>1</sup>TU Dresden, Professur für Magnetofluidodynamik, 01062 Dresden, Germany

<sup>2</sup>GKSS, Max-Planck-Str.1, 21502 Geesthacht, Germany

Porous ceramics exhibit a large range of specific properties that make them interesting for industrial and highly demanding applications, like their extremely large specific surface ( $> 500 \text{ m}^2/\text{g}$ ) and their ability to withstand mechanical stress and thermal shock. For applications where liquid or gas flow through the porous medium is involved, like in filtration or chemical reactor devices, open-cell structures are used. Understanding the 3D behaviour of processes in such porous media have recently become the focus of extensive research [1],[2].

This project is supported by the DFG graduate research training school “PoreNet”, which is dedicated to fundamental research on non-metallic porous media. We will employ process  $\mu$ -CT – i.e. tomographic analysis with extremely reduced scan times [1] – to explore liquid and multiphase flow in porous ceramics. As a first test of the process  $\mu$ -CT facility used, a sequence of tomograms of a (static) ceramic sample has been acquired. The scan times, i.e. the overall time to take one tomogram, range from  $t = 424 \text{ s}$  to  $t = 5 \text{ s}$ . For referencing, the sample has additionally been analysed with a “normal”  $\mu$ -CT scan (Fig.1), which, for comparison, took approximately 90 min.

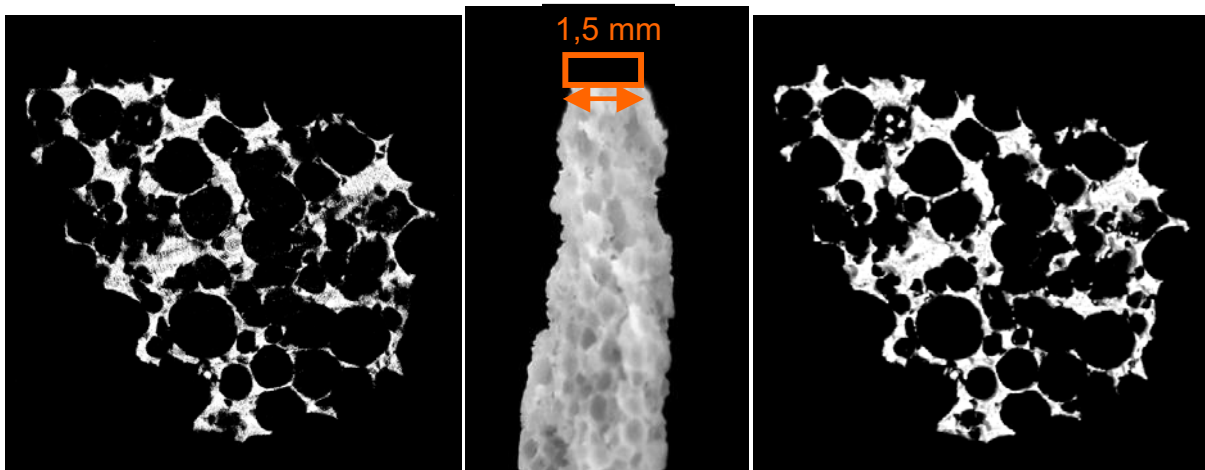


**Fig. 1:** Thermal insulation ceramic used as a test sample for ultra fast tomography (middle) with analysed region indicated. *Right:* XY-slice using “normal” tomography ( $t_{\text{scan}} \sim 90 \text{ min}$ ). *Left:* Same slice taken with ultra fast tomography ( $t_{\text{scan}} \sim 5 \text{ s}$ ) showing remarkable similarity.

The tomograms reconstructed up to now show remarkable similarity despite their large scan time difference. The image analysis planned will on one hand focus on how image quality depends on the decreasing scan time. On the other hand, we will evaluate how rotational axis movement during the

exposure affects image quality, since the sample is not stopped for exposure but keeps revolving during one scan. We expect to find decreasing image quality further away from the centre of rotation.

The data analysis of this test experiment will enable us to customize planned process  $\mu$ -CT filtration experiments by finding the most suitable scan setting, resolution and sample structure.

We thank J. Herzen and B. Hasse for support during the beam times.

## References

- [1] M. Dierick, J. Vlassenbroeck et al., High-speed neutron tomography of dynamic processes, *Nuclear Instruments and Methods in Physics Research A* 542, 296–301 (2005)
- [2] F.A.H. Al-Abduwani, R. Farajzadeh et al., Filtration of micron-sized particles in granular media revealed by x-ray computed tomography, *Review of scientific instruments* 76, 103704 (2005)
- [3] A. Pyzalla et al., Simultaneous Tomography and Diffraction Analysis of Creep Damage, *Science* 308, 92-94 (2005)

# Residual Stress Investigation at HARWI II of Dissimilar Overlap Friction Stir Welds Made from Aluminum and Steel

R.V. Martins<sup>1</sup>, S. Sheikhi, J. dos Santos, and A. Schreyer

GKSS-Research Centre Geesthacht GmbH, Max-Planck-Str. 1, 21502 Geesthacht, Germany

<sup>1</sup>now: JRC, Institute for Energy, Westerduinweg 3, 1755 LE Petten, The Netherlands

The joining of dissimilar materials is of great interest for the weight and cost reduction in the production of components, e.g., for cars and aeroplanes. Material of higher strength can be joined to the base structure where the demands in terms of strength and resistance are higher than for the rest of the component. In the present experiment a total of four different overlap Friction Stir Welds (FSW) made from dual-phase steel alloy DP600 and Al alloy AA5754-H22 were investigated. DP600 has a great forming and hardening potential and is mainly used in car industry, e.g., to produce high strength parts of car seats or vehicle wheels. AA5754 is also dominantly used in car manufacturing, e.g., for inner body panels. The specimens investigated vary in their welding parameters. The aim of this experiment was to investigate the influence of the welding parameter variations on the residual stress state of the welded panels.

Figure 1 shows a sketch of the experimental setup in transmission geometry at the HARWI II beamline [1]. The monochromatic beam had an energy of 100 keV and was confined by slits to  $2 \times 0.2 \text{ mm}^2$  (HxV), the smaller size being in the direction of the expected steep stress gradient. The  $\text{Al}\{311\}$  and  $\text{Fe}\{211\}$  reflections were used to measure the lattice spacing variations in both materials. Simulations showed that the overlap of the  $\text{Fe}\{211\}$  and  $\text{Al}\{222\}$  peak introduces an acceptable error between 0.5 and  $3 \times 10^{-4}$  for the  $\text{Fe}\{211\}$  peak position determination. Especially in the weld zone, due to expected weak influence of the texture, this error is almost negligible. In addition, copper powder was directly attached to the specimen and measured simultaneously to account for changes of the sample-to-detector distance, which, otherwise, would lead to erroneous results.

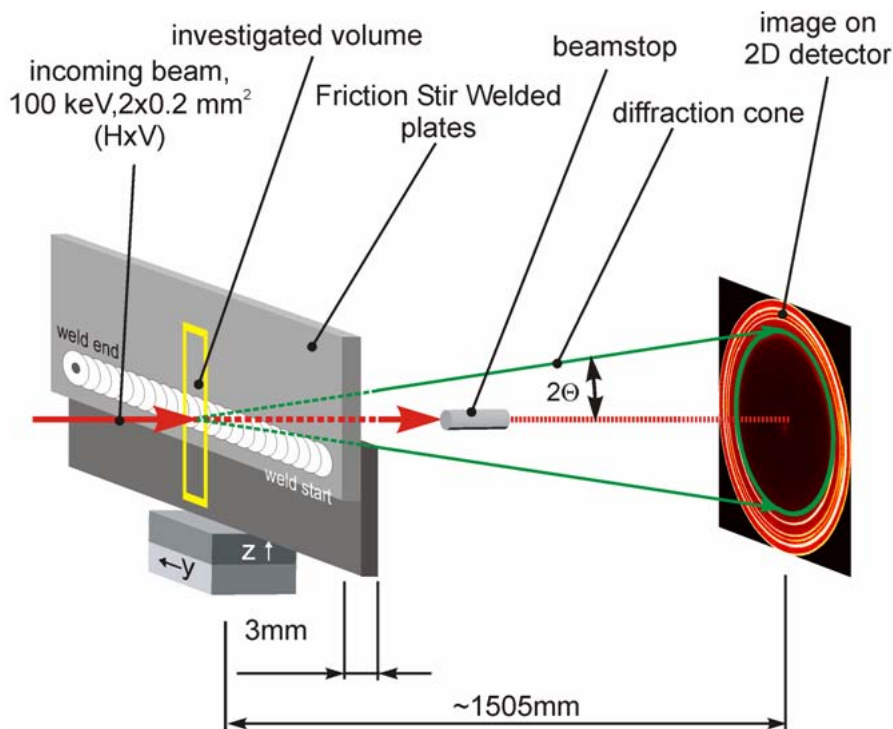


Figure 1: Schematic of the experimental setup for residual strain measurements in overlap FSW specimens at HARWI II.

The strong low order reflections from steel and aluminum, less appropriate for macroscopic strain measurements, were masked with a lead plate on the detector to avoid saturation of the image plate (MAR345). The exposure time was 60 s per image.

Figure 2 illustrates a subset of the results obtained. It shows the residual stress distribution for the longitudinal stress component (parallel to weld line) in the steel part of Al/St FSWs welded with different parameters. The weld line is at 0 mm and the overlap region of the aluminum and steel sheet extends from -20 to +20 mm. The results for the steel show that in both cases (sample A and D) the residual stress observed is very close to the yield strength, indicated by the thick solid line. In the case of aluminum the maximum observed residual stress was around 70% of its yield strength.

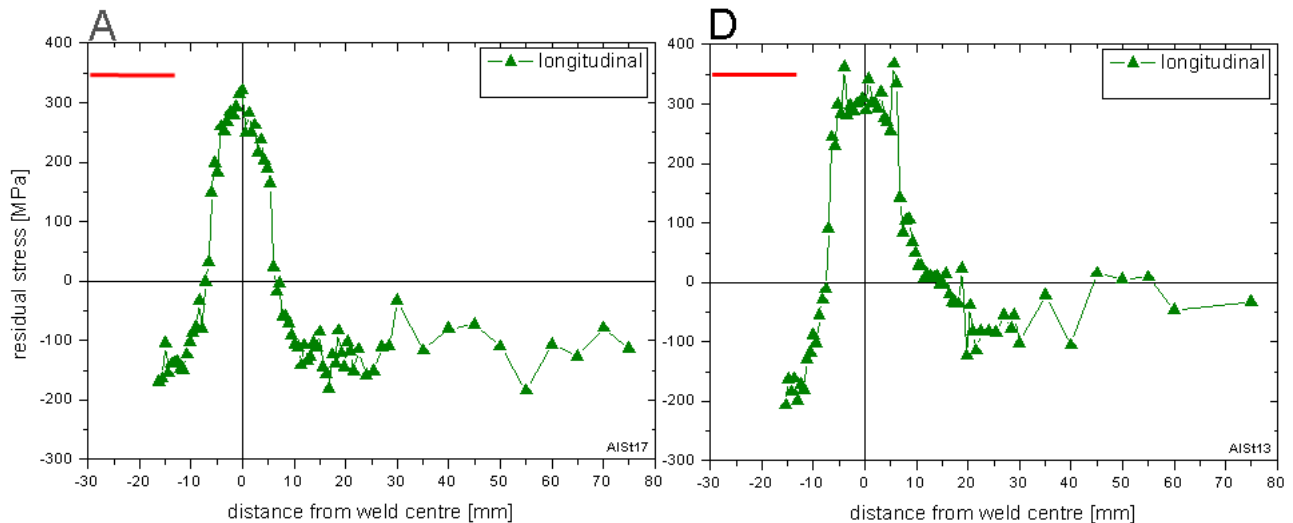


Figure 2: Residual stress in longitudinal direction measured in steel plate of Al/St overlap FSWs. Sample D (right) was welded with 10% lower tool rotation and 25% lower tool advancing speed than sample A (left).

The results indicate that high welding and tool rotation speeds result in steeper stress gradients in steel (cf. Figure 2, sample A) and almost symmetric stress profiles in both materials, aluminum and steel. Low welding and tool rotation speeds result in broader stress profiles in steel (cf. Figure 2, sample D) and an asymmetry of the profiles in both materials.

Additional investigations will be carried out on these samples and will focus on the tensile strength and the microstructure in the weld region.

## References

- [1] T. Lippmann et al., this annual report

# Residual stress mapping in laser welded T-joints of an airframe aluminium alloy

W. Machold, R.V. Martins<sup>1</sup>, P. Staron, A. Schreyer

GKSS Research Centre, Max-Planck-Strasse 1, 21502 Geesthacht, GERMANY

<sup>1</sup>now: JRC, Institute for Energy, Westerduinweg 3, 1755 LE Petten, THE NETHERLANDS

The development of new materials and new joining techniques is an important task in the aircraft industry. Compared with conventional manufacturing, not only costs can be reduced by using faster processes, but also mechanical properties such as corrosion susceptibility can be improved; above all, weight can be reduced. Weight reduction again comes along with fuel sparing, less CO<sub>2</sub> emission and a higher cargo load. A possibility to achieve such advantages is replacing rivets in the fuselage by laser beam welding (LBW) using high strength wrought Al alloys (e.g. 6xxx series) [1, 2]. By now, this has already been realized for skin-stringer joints in some parts of the Airbus A380, A318 and A340. However, extension to T-joints of so-called clips to the skin is not yet achieved.

For the current study, samples consisting of a 4.5 mm thick AA 6156 T6 base plate and a 2 mm thick AA 6013 T6 clip were produced to resemble welded clip-skin joints. As it is established in the aircraft industry, the base plates had 1.5 mm deep weight-reducing pockets (Fig. 1a). The total length of the weld was 120 mm and it was welded from one side using a 3.3 kW Nd:YAG laser source with 12% Si-containing filler wire. No post-weld heat treatment was applied.

High-energy synchrotron radiation can easily penetrate thin aluminium sheets and is well known to be suitable for investigations of residual stresses (RS), which affect the fatigue resistance and crack propagation of welded joints due to cyclic loading [3]. With the high intensity of a synchrotron source it is possible to generate 2-dimensional stress maps with good spatial resolution. Typically, start (run-in) and end (run-out) of the weld seam are most prone to crack initiation. Since previous measurements have shown significant differences between the RS distributions of run-in and run-out locations [4], two different welding sequences were developed. While the usual welding is from one clip end to the other, in this study it was varied to welding from the middle to the clip ends in the first case and from the clip ends to the middle in the second case (Fig. 1b). Different stress gradients along the weld as well as perpendicular to the weld were expected for the different welding sequences; therefore, two-dimensional stress maps are required for an analysis of the optimum welding sequence.

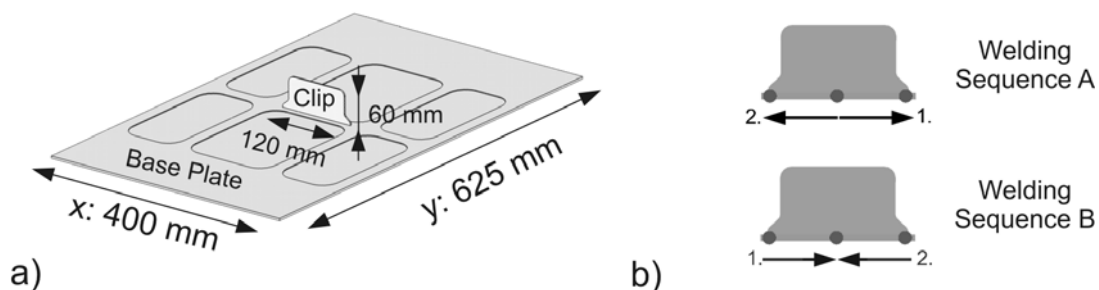


Figure 1: a) Geometry of the samples; b) Different welding sequences.

The strain measurements were carried out in transmission at the beamline HAWRI II at a photon energy of 115 keV and a beam size of 1×1 mm<sup>2</sup>. Therefore, the base plate of the samples was oriented perpendicular to the beam. At a distance of 1.9 m from the sample a MAR345 image-plate detector with a diameter of 345 mm was placed, so the Al(111), Al(200), Al(220), and the Al(311) peak could be observed. To determine the exact distance between sample and detector, a copper powder was attached to the surface of the samples. A macro stress free lattice parameter was obtained in an outer corner of the samples. Since the crystallographic anisotropy is small in case of Al, the macroscopic values for Young's modulus and Poisson ratio  $E = 70$  MPa and  $\nu = 0.33$  were

used. Assuming a biaxial stress state with principle stress axes according to the sample geometry, two-dimensional stress maps were calculated. Each map covers an area of  $180 \times 60 \text{ mm}^2$  symmetric to the clip and consists of  $31 \times 16 = 496$  points.

The stress maps show that a significant difference arises from the different welding sequences (Fig. 2). This is in good agreement with neutron stress measurements of the same samples, where only line scan measurements could be realized. The stresses vary in a range of  $-150 \text{ MPa}$  to  $+250 \text{ MPa}$ . This is the value limited by the tensile yield strength, which was also tested. However, in the maps a patch-like variation of the stress values can be observed. This effect is caused by a non-ideal ratio of the gauge volume to the grain size of the material. With regard to the application in airframes, the measured RS should be considered in the context of fatigue behaviour. As a cyclic loading in transverse direction is influenced by transverse RS, for example welding sequence A should be more resistant to crack initiation and lead to a reduced crack propagation speed in the middle of the clip than sequence B. This has already been acknowledged in fatigue tests.

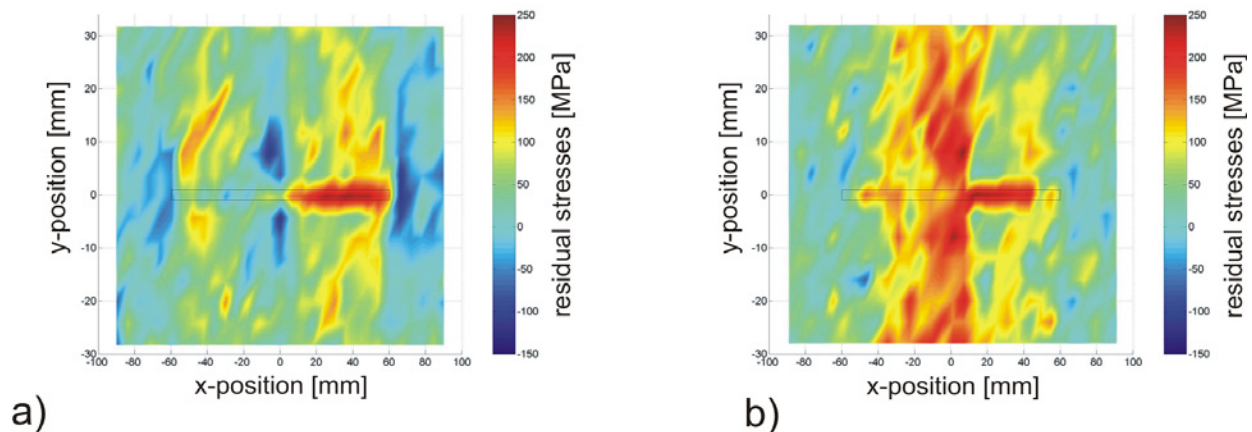


Figure 2: a) Residual stresses in transverse direction for welding sequence A; b) Residual stresses in transverse direction for welding sequence B.

## References

- [1] E. Schubert, M. Klassen, I. Zerner, C. Walz, G. Sepold: Light-weight Structures produced by Laser Beam Joining for Future Applications in Automotive and Aerospace Industry, *Journal of Materials Processing Technology*, 2001, Vol. 115, pp. 2-8
- [2] P. Leque, P. Lassince, T. Warner, G. M. Raynaud: Engineering for the Future: Weight Saving and Cost Reduction Initiatives, *Aircraft Engineering and Aerospace Technology*, 2001, Vol. 73, pp. 147-159
- [3] J. D. Almer, J. B. Cohen and B. Moran: The Effects of Residual Macro stresses and Micro stresses on Fatigue Crack Initiation, *Materials Science and Engineering A*, 05.2000, Vol. 284, Issues 1-2, pp. 268-279
- [4] F.S. Bayraktar, P. Staron, M. Koçak, A. Schreyer: Residual Stress Analysis of Laser Welded Aluminium T-Joints, *Welding in the World*, 2007, Vol. 51, No 1-2, pp. 9-13

# Residual stress measurement of laser beam welded butt joints at the materials science beamline HARWI II

T. Fischer , R.V. Martins<sup>1</sup>, A. Schreyer

GKSS Research Centre, Max-Planck-Strasse 1, 21502 Geesthacht, GERMANY

<sup>1</sup>now: JRC, Institute for Energy, Westerduinweg 3, 1755 LE Petten, The Netherlands

In civil aircraft production advanced welding techniques, like laser beam welding (LBW) and friction stir welding (FSW) are used to reduce weight and production costs. The way towards a rivet-free aircraft is supported by LBW and the development of new weldable, high-strength aluminium alloys. In this study residual stresses in laser beam welded butt joints of aerospace grade aluminium alloy AA6056-T6 were characterized using high energy synchrotron radiation. Because of its improved corrosion resistance and good weldability alloy AA6056-T6 (AlMgSi) will substitute standard AA2024 alloy (AlCu) for the manufacturing of forthcoming aircraft fuselage skins.

The samples were CO<sub>2</sub> laser beam welded butt joints of sheets made from Al-alloy AA6056 in T6 condition. The thickness of the samples was 3.2 mm and 6 mm. Metallographic investigations show the usual large pancake shaped grains with diameters up to 300  $\mu\text{m}$  and a thickness of 60  $\mu\text{m}$  in the parent material. In the weld seam exists a dendritic grain structure. The weld seam was 2.5 mm large. This large grain size makes the measurements with high spatial resolution more difficult due to the poor grain statistics. The strain scanning was performed at the high energy synchrotron beamline HARWI II of the GKSS research centre at HASYLAB. The diffraction experiments were carried out in transmission geometry, using photons with an energy of 80 keV. A Cu powder reference sample was directly attached to the investigated area for the determination of the Al<sub>311</sub> peak shifts. The beam size on the specimen was 6 x 0.2 mm<sup>2</sup>, the large dimension of the beam was parallel to the weld line. A large sample-detector-distance of about 8600 mm ensures a high angular resolution for the peak position determination. The distance between the measuring points was 0.2 mm in the welding area and up to 2 mm in the base material. This yielded a very detailed profile of the residual stress for the longitudinal as well as the transversal component. For the measurement of

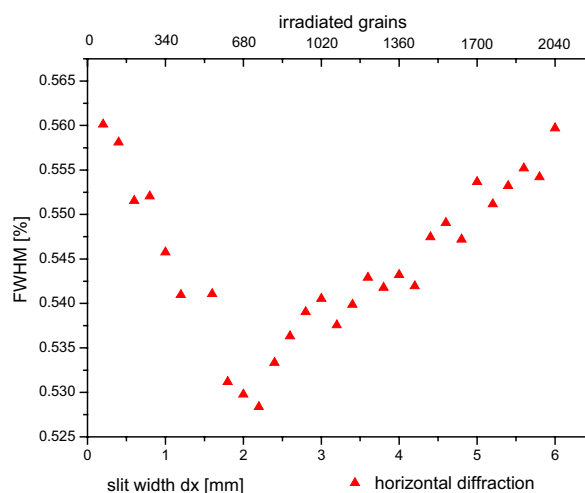


Fig.1 : Variation of the Full Width at Half Maximum of Al-Peaks due to beam divergence resp. coarse grain effects

the unstrained lattice parameter, a 3 mm wide bar was cut out of the weld seam. The influences of the gauge volume size and grain statistics on the strain measurements were systematically



investigated. The results (fig. 1) show that, with the given beam parameters, the optimum gauge volume size for the peak position determination is a beam width of 2 mm. A small gauge volume leads to a low number of irradiated grains and poor statistics. With a wide beam size the diffraction peaks are blurred due to the divergence of the beam.

The residual stress profiles of the 3,2 mm thick sheets are shown in fig. 2. They were corrected for  $d_0$  variations. The results show high tensile stresses of 210 MPa parallel to the weld at  $\pm 2.6$  mm from the weld centre, i.e. in the heat affected zone (HAZ). In the weld centre the stresses are below

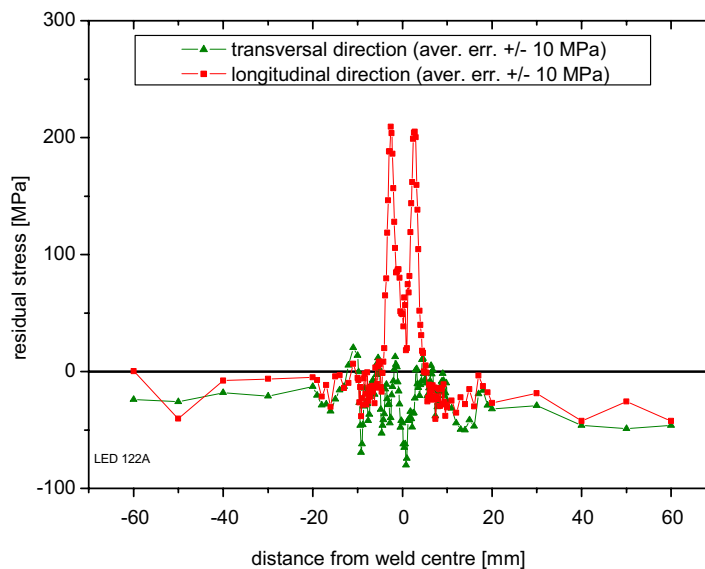


Fig. 2: Residual stress profile of the LBW butt joint for transversal and longitudinal direction

100 MPa. A dip at  $\pm 10$  mm from the centre with longitudinal stresses down to -40 MPa is observed. The comparison with the neutron data [2] shows, that the use of high energetic synchrotron radiation is expedient. Due to high spatial resolution, these small-scale effects could be observed. The longitudinal forces are balanced by compressive stresses in the far field, which are not symmetric to the weld line. The transverse stress component exhibits mostly stresses between +20 and -70 MPa with strong oscillations in the weld region and the HAZ. Due to the beam geometry and divergence, the measurement of this component was much more sensitive to coarse grain effects than the longitudinal one.

## References

- [1] P. Leque, P. Lassince, T. Warner, G. M. Raynaud, "Engineering for the Future: Weight Saving and Cost Reduction Initiatives"  
Aircraft Eng. and Aerospace Tech., 2001, Vol. 73 , pp. 147-159
- [2] P. Staron, W.V. Vaidya, M. Kocak, J. Homeyer, J. Hackius, "Residual stress in laser beam welded butt joint of airframe alloy AA6056"  
Mat. Sci. Forum Vol. 524-525 (2006) pp.413 - 418



# Residual stresses in individual crystallites

M. Moscicki<sup>1</sup>, A. Borbély<sup>1</sup>, H. Pinto<sup>1</sup>, A.R. Pyszalla<sup>1</sup>,  
R.V. Martins<sup>2</sup>, T. Fischer<sup>2</sup>, T. Lippmann<sup>2</sup>, C. Paulmann<sup>3</sup>

<sup>1</sup>Max-Planck-Institut für Eisenforschung GmbH, Max-Planck-Strasse 1, 40237 Düsseldorf, Germany

<sup>2</sup>Institute for Materials Research, Dept. WFN (Neutron-/Synchrotron Scattering), GKSS-Research Center, D-21502 Geesthacht, Germany

<sup>3</sup>Mineralogisch-Petrographisches Institut, Universität Hamburg, D - 20146 Hamburg, Germany

The deformation behavior of polycrystals and its modeling are matter of great technological interest, since structural components are mostly made of polycrystalline materials. So far, several models have been proposed to describe the plastic deformation behavior of polycrystals, however, all them rely on assumptions and simplifications regarding the grain-to-grain interactions. In the last decade the significance of these grain-to-grain interactions during static or dynamic loading is particularly increasing due to the frequent use of miniaturized components.

The aim of the project is the description of deformation behavior of individual crystallites in a model polycrystalline material containing a few grains. Two different experiments (ex-situ and in-situ) were carried out on wires of 200 $\mu\text{m}$  and 300 $\mu\text{m}$  in diameter (steel grade numbers 1.4310 (X10CrNi18-8) and 1.4841 (X15CrNiSi25-20)). Both steels had an austenitic microstructure with a grain size of about 100 $\mu\text{m}$ , which was achieved by an adequate heat treatment. Of particular interest was to study the influence of crystallographic orientation of component grains on the stress state and reorientation during plastic straining.

In order to automatize a procedure for stress analysis simultaneously in several individual grains with highest achievable spatial resolution, diffraction experiments using monochromatic synchrotron radiation at HASYLAB have been carried out. The experimental stations Harwi-II and F1 were used, the first equipped with a MAR345 image-plate detector with a pixel size of 150  $\mu\text{m}$ , and the latter equipped with a MarCCD-camera with a pixel size of 79 $\mu\text{m}$ .

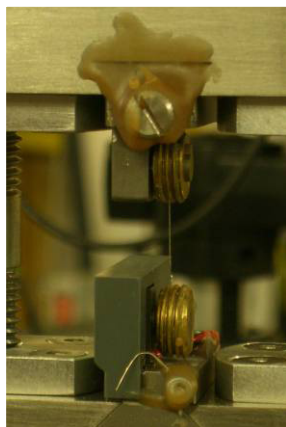


Fig.1. Wire mounted in a miniaturized tensile test device for 'in-situ' experiments

At Harwi-II two radiation energies were used (60 or 120 keV) and sample-to-detector distances were set in the range from 1100 to 1800 mm. At F1 the radiation energy was 31 keV and the sample-to-detector distances were varied between 140 and 300mm. The beam size was about 1000x500 $\mu\text{m}^2$  (Harwi-II) or 500x200 $\mu\text{m}^2$  (F1), which assured the illumination of the sample over its whole diameter.

For the 'in-situ' experiment the sample was mounted on a small-tensile machine (Fig.1), which was placed on x-y stage allowing a good alignment in the diffractometer. The stage (with the test machine) was rotated about an axis ( $\omega$ ) perpendicular to the x-y plane in steps of  $\Delta\omega$ . The grains fulfilling the Bragg condition during the rotation step gave rise to diffracted beams, which were collected by the detector aligned perpendicular to the direct incoming beam. To obtain the most information from the illuminated grains the sample was rotated in an interval of 360°. During each exposure, the sample was oscillated by  $\pm\Delta\omega/2$ . After each 360° cycle the strain on the wire was increased achieving strains as large as 36%.

For the automatic data evaluation a MATLAB code is being developed in order to index the spots recorded. The software (Fig.2) is based on image analysis and finds reflections meeting certain criteria, e.g. threshold intensity values, FWHM of reflection and  $2\theta$  position, and sorts them into groups (individual crystallites). The assignment is made on crystallographic criteria only [1,2], i.e. the angles between reflections from the same grain match some well known theoretical angles corresponding to the crystal-structure in case.

The developed algorithm works as follows. On each image the beam centre is determined and the 2D-diffraction pattern is transformed from the Cartesian into the polar coordinate system. In order to find the  $2\theta$  positions of each  $\{hkl\}$  family a 360° integration over the  $\chi$ -angle is carried out and the average  $2\theta$  positions around, which the automatic reflection search will work are

marked. In order to define the directions of the scattering vectors the automatic procedure searches across the mosaic spread of each single reflection spot obtained for the maximum intensity

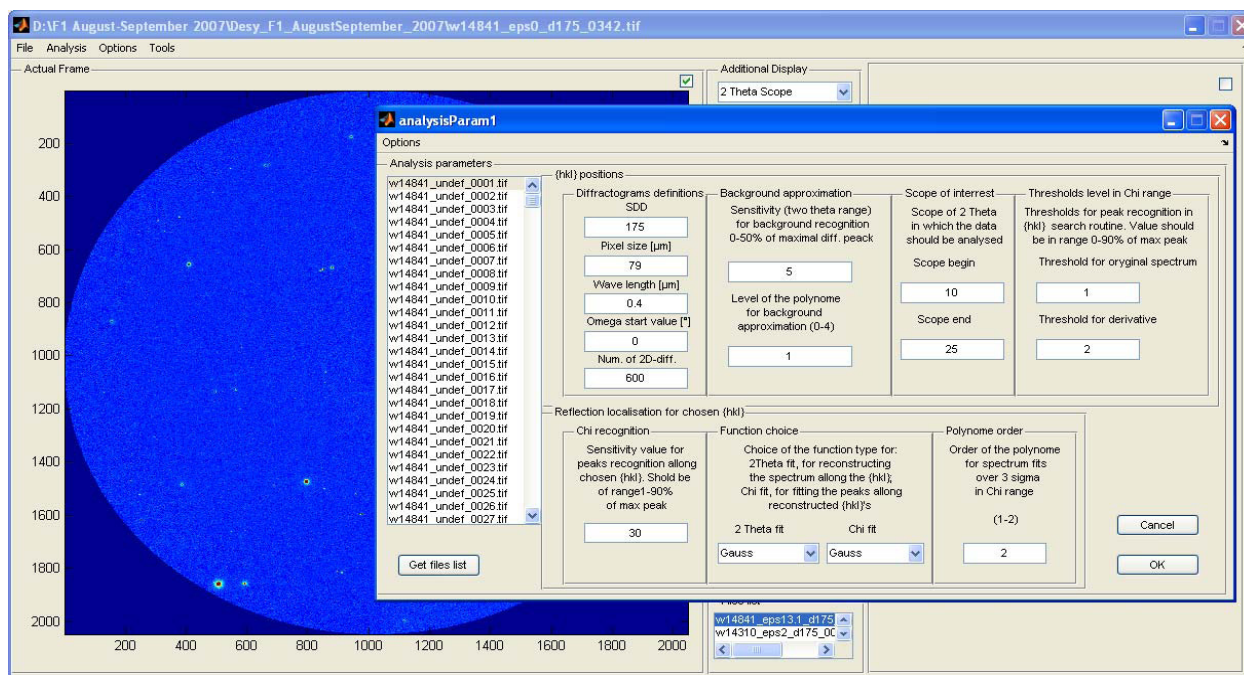


Fig.2. The interface of the software for diffraction patterns analysis

positions ( $\chi_{\max}$ ,  $\omega_{\max}$ ). Nonlinear least square routines are applied to fit the  $\chi$ ,  $\omega$  and  $2\theta$ -positions, with Gaussian and Pseudo-Voigt functions, respectively. The indexing software was tested on model simulations, which allowed the estimation of the error incorporated in the calculation of grain position and orientation unavoidable in the experiment.

The result of the last stage is a list of grains in the illuminated area. Each grain holds an assigned list of reflections sorted in  $hkl$  orders. The present algorithm decreased considerably the analysis time, which for indexing 128 grains took less than 5 min on usual PC. Based on the new simulation tool factors giving impact on the precision of the analysis can be further investigated. Beside grain orientations the software is capable to calculate the position of the grains in the sample. Calculation of the grain position is done independent from grain orientation and it was shown that has accuracy better than 1 pixel. This is of course still large with regard of the sample diameter. The accuracy of the Euler angles describing the grain orientation is of the order of the  $\Delta\omega$  step used during the simulation (measurement).

The evaluation of strain/stress tensors of individual grains, however, still requires further software development by incorporating the  $2\theta$  shifts of the reflections from the value corresponding to unstrained crystal. Such calibration spectra from a powder sample of the same materials as well as from  $\text{CeO}_2$  powder used for calibration of the sample-detector distance were also measured.

## References

- [1] H.F. Poulsen et al., J.Appl. Cryst (2001), 34, 751-756
- [2] E.M. Lauridsen et al., J.Appl. Cryst (2001), 34, 744-750
- [3] A.P.Hammersley et al., High Pressure Research (1996), 14, 235-248

# Texture and physical Properties of Dual-Phase steels

H. Klein, A. Wetzel, <sup>1</sup>M. Masimov and <sup>2</sup>T. Lippmann

GZG, Dept. of Crystallography, Univ. of Göttingen, Goldschmidtstr.1, 37077 Göttingen, Germany

<sup>1</sup>Salzgitter Mannesmann Forschung, Eisenhüttenstr.99, 38239 Salzgitter, Germany

<sup>2</sup>GKSS Research Center, Max-Planck-Str.1, 21502 Geesthacht, Germany

Dual-phase steels very sensitively change their texture and with it their anisotropic properties after heat treatment. A cold rolled dual-phase steel was annealed at 780°C and 900°C and quenched under different conditions. From the different samples textures were measured using high-energy synchrotron radiation and conventional X-rays in order to compare the differences between these methods on the basis of the calculation of anisotropic properties [4].

Texture measurement with high-energy-synchrotron radiation was carried out at the GKSS materials science beam-line HARWI II at DESY, Hamburg, Germany. A beam-energy of ~100keV was chosen and a beam cross section of 1mm x 1mm. The diffracted intensity was recorded by a mar345 area detector. The synchrotron texture measurements were carried in the conventional step scan mode in a range of the orientation angle  $\omega$ :  $-80^\circ \leq \omega \leq +80^\circ$  in steps of  $\Delta\omega=1^\circ$ , the recording-time was 2sec per 2-dimensional image [1].  $\text{Co}_{K\alpha}$  radiation was used for the texture measurements using conventional X-rays. With a Seifert PTS goniometer incomplete pole figures were measured in the ranges:  $0^\circ \leq \alpha \leq 70^\circ$  with  $\Delta\alpha=5^\circ$  and  $0^\circ \leq \beta \leq 360^\circ$  in steps  $\Delta\beta=3.6^\circ$ . Three pole figures of the bcc phase were measured: (110), (200) and (211). To get a comparable information to the synchrotron method a special sample preparation was used: the sandwich technique. This technique allows the measurement of the global texture because it uses a texture measurement of the transverse plane of a sample[2]. From the data of the diffraction experiments the orientation distribution function was calculated in order to compare the different measurement methods and different treatments. The orientation distribution function was calculated on the basis of the harmonic method after Bunge[3]. Fig.1 shows three Orientation distributions in  $\varphi_2=45^\circ$ -sections of the dual-phase steel in different stages. The textures in Fig.1 are calculated from conventional X-ray measurements. In fig.1a the typical cold rolled texture of bcc iron is to be seen. After annealing at 780°C and fast quenched to room temperature the texture become weaker (fig.1b), it is very weak after heating up to 900°C and a slow cooling down. Fig.2 shows the texture of the same samples, but measured using high-energy synchrotron radiation. The level lines in fig. 1 and fig. 2 are comparable. One can observe, that the textures become weaker, because with hard X-rays the real global texture is measured, in contrast to the conventional X-ray measurements.

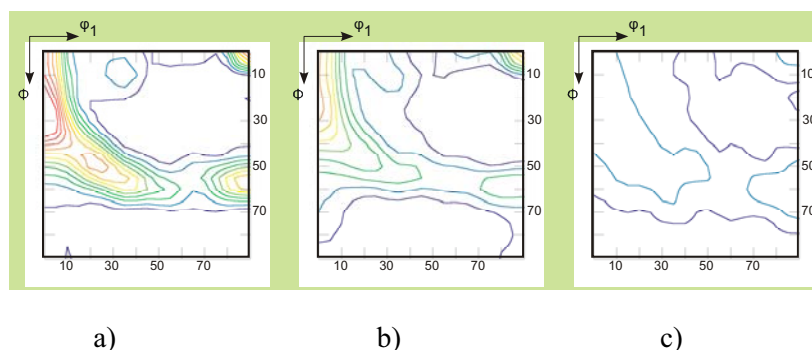


Fig.1: Orientation Distribution Function in  $\varphi_2=45^\circ$ -sections of a dual-phase steel: a) cold rolled, b) annealed at 780°C and fast quenched, c) annealed at 900°C and slowly cooled down. Measured with conventional X-rays.

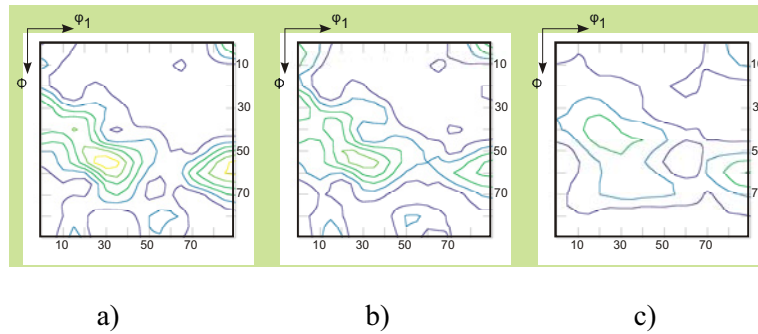


Fig.2: Orientation Distribution Function in  $\phi_2=45^\circ$  sections of a dual-phase steel: a) cold rolled, b) annealed at  $780^\circ\text{C}$  and fast quenched, c) annealed at  $900^\circ\text{C}$  and slowly cooled down. Measured with high-energy synchrotron radiation.

From Orientation Distribution Functions the anisotropic Young's modulus was calculated. Fig.3 shows the Young's modulus as a function of the angle from rolling to transverse direction for different annealing and cooling strategies. Calculations of anisotropic properties on the basis of texture measurements using high-energy synchrotron radiation are very close to calculations on the basis of global texture measurements with conventional X-rays. Because of the high penetration depth of the synchrotron radiation a larger diffracted volume can be measured. This leads to a better information about the global texture and thus about the anisotropic properties.

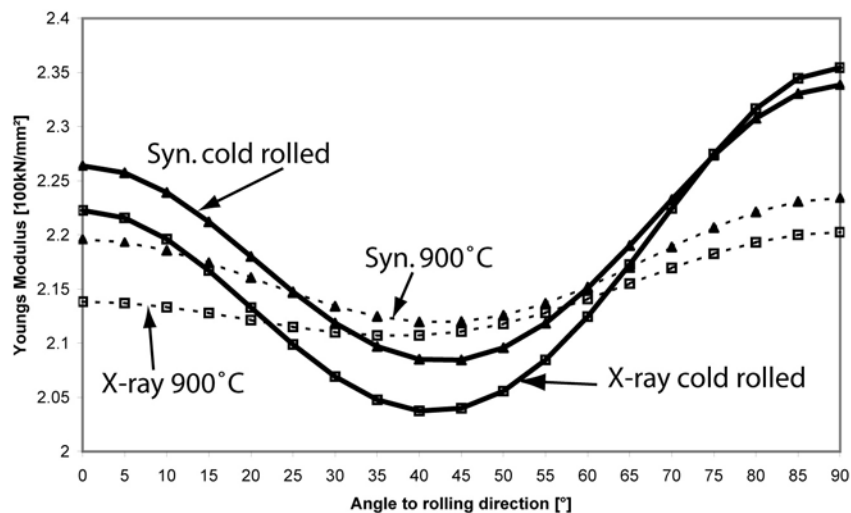


Fig.3: Anisotropic Young's modulus of a dual-phase steel treated under different conditions –cold rolled and annealed at  $900^\circ\text{C}$  and slowly cooled- and different measurement methods of textures: High-energy synchrotron radiation and conventional X-rays.

## References

- [1] H.J. Bunge, H.Klein, L. Wcislak, U. Garbe, W. Weiß and J.R. Schneider, Textures and Microstructures, 35, 253 (2003).
- [2] H. Klein, C. Heubeck and H.J. Bunge, Mat. Sci. Forum, 157-162, 1423 (1994)
- [3] H. J. Bunge, Texture Analysis in Material Science, 2th ed., Cuvillier Verlag Göttingen (1993)
- [4] A. Wetzel, Diploma thesis, Göttingen (2007)

# Texture gradient in dissimilar laser welded Al-alloys (AA5083-H111 with AA6013-T6)

S. Lenser<sup>1,2</sup>, T. Lippmann<sup>2</sup> and H.-G. Brokmeier<sup>1,2</sup>

<sup>1</sup>Institute for Materials Research (TEXMAT), Clausthal University of Technology, Agricolastr. 6, 38678 Clausthal-Zellerfeld, Germany

<sup>2</sup>GKSS-Research Center, Max-Planck-Str., D-21502 Geesthacht, Germany

With the availability of high-energy lasers the laser beam welding could be implemented in the joining of Al alloys. This method permits high welding speeds under obtainment of very narrow seams. Two different types of rolled Al-sheets (AA5083-H111 and AA6013-T6) were used as examination object. A more fine-grained AA5083H-111 was joined together with a more coarse-grained AA6013-T6 by means of a robot. The process was made by an Nd:YAG-Laser. The welding process was performed with different speeds of the robot between 1.8 m/min and 2.6 m/min. The presented results are focused on 1.8 m/min laser beam welding.

Texture measurements were performed at the GKSS Materials Science high-energy beamline HARWI II at the GKSS outstation at Desy, Hamburg using a 2-dimensional image plate detector (MAR345). The selected wavelength was set to 0,123 Å. The sheets were prepared as a sample of 60 mm x 3 mm. In order to enhance the grain statistics each picture has been recored during a sample rotaion of 5 degrees. Local texture measurements were carried out on 5 different positions. Of special interest of this investigation is the modification of the crystallographic texture in the head affected zone (HAZ) compared to the texture of the base materials. The measured data were used to calculate the orientation distribution function (ODF) by using the iterative series expansion method.

Figure 1 shows the microstructure (base materials, head affected zone and welding seam) with the rolling direction of the sheets and four measured positions of the welded sheets.

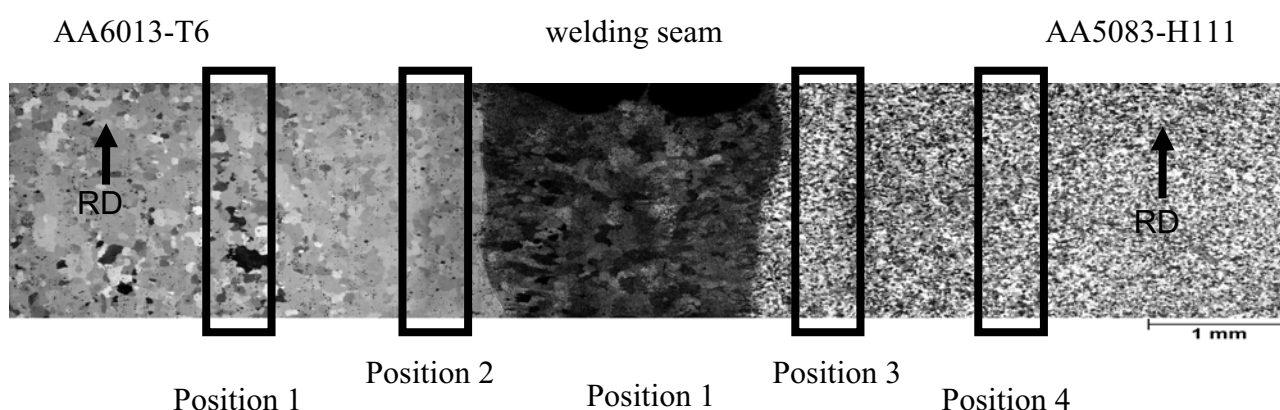


Figure 1: Microstructure of laser beam welded dissimilar Al-alloys with four measured positions.

Position 1 and 4 shows the crystallographic texture of the base alloys. Therefore in this area no influence of the welding process is observed in comparison to position 2 and 3.



Figure 2 presents four measured (111) pole figures. The welding seam is located perpendicular to the plane of projection. The orientation of the weld goes from the north towards south in the pole figures.

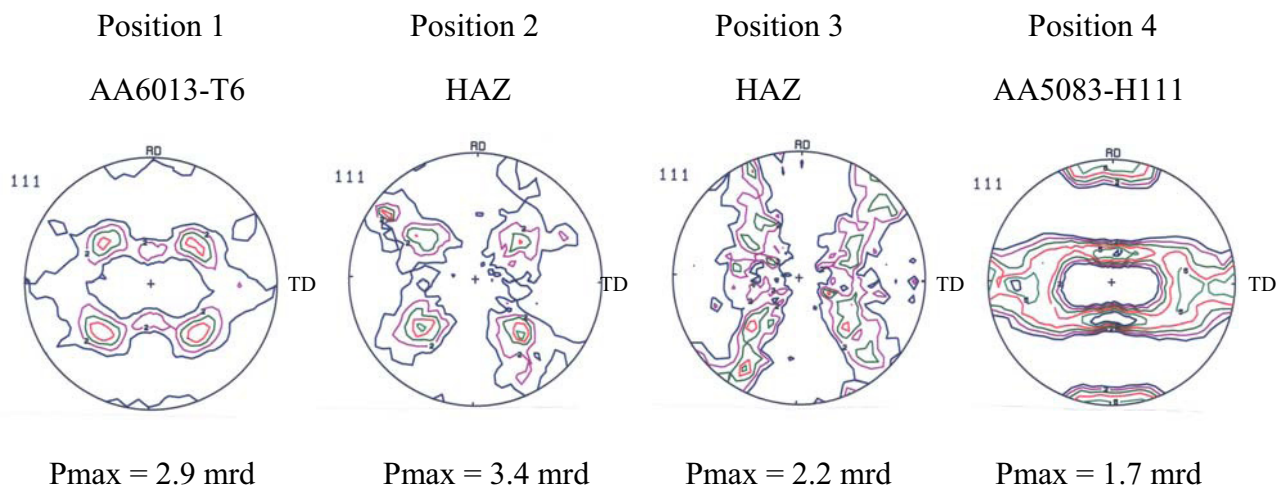


Figure 2: Measured (111) pole figures

The initial state of the crystallographic texture is presented of position 1 (AA6013-T6) and position 4 (AA5083-H111) in figure 1. A5083-H111 has a relatively weak texture with the brass component  $\{110\}\langle 112 \rangle$  and the Cu component  $\{112\}\langle 111 \rangle$  as majority. A much softer cube component  $\{001\}\langle 100 \rangle$  is also available. The texture of AA6013-T6 is little sharper than the AA5083-H111 texture. Strong cube  $\{001\}\langle 100 \rangle$  and Goss  $\{110\}\langle 001 \rangle$  components indicate the recrystallisation of this material. Smaller BS and G/B components complete the crystallographic texture of AA6013-T6 [1]. The texture of the HAZ is different. The HAZ between AA6013-T6 and the weld (figure 2, position 2) shows a strong cube component  $\{001\}\langle 100 \rangle$ . As minority component one obtained the Goss  $\{110\}\langle 001 \rangle$  component and a weak S component  $\{124\}\langle 634 \rangle$ . The HAZ between AA5083-H111 and the weld (figure 2, position 3) shows a  $\langle 001 \rangle$  fiber texture.

This results are compatible to the microstruktur (light microscopy). The influence of the welding process is shown in different grain sizes and grain orientations in compartion of base materials and HAZ.

## References

- [1] H.-G. Brokmeier, S. Lenser, R. Schwarzer, V. Ventzke, S. Riekehr, M. Kocak, J. Homeyer, Materials Science Forum Vols. 539-543, 3894 (2007)

# Texture gradient in the ECAPed pure Mg

W.M. Gan<sup>1, 2, 3</sup>, H.-G. Brokmeier<sup>1, 2</sup>, B.Schwebke<sup>1, 2</sup>, H. Chang<sup>3</sup>, M.Y. Zheng<sup>3</sup>, K. Wu<sup>3</sup>

<sup>1</sup>GKSS-Forschungszentrum, Max-Planck strasse 1, D21502 Geesthacht, Germany.

<sup>2</sup>Institute for Materials Science and Engineering, TU-Clausthal, D38678 Clausthal, Germany.

<sup>3</sup>School of Materials Science and Engineering, Harbin Institute of Technology, 150001 Harbin, P. R. China.

Equal channel angular pressing (ECAP) has been proved to be a promising severe plastic deformation technique which can effectively produce ultra-fined or nano-grained various bulk materials [1]. Microstructural homogeneity of the ECAPed materials is more attractive when considering the practical applications of this technique. Unique textures developed during ECAP have been increasingly investigated. A study of the nature of the evolution of the predominant crystallographic orientation is of primary importance in ECAP processing, and careful analysis of the texture makes it possible to estimate the mechanism responsible for the progress of plastic straining during ECAP. Due to the fact that some texture effects are still non-understood local texture measurements have been carried out firstly to see inhomogeneities during the ECAP process and secondly to find out way experimental and theoretical textures differ.

In order to get the local texture not only at the final ECAPed sample the ECAP process was stopped after 50% deformation. Thus the pure Mg sample consists of a first part from the ingoing channel, a second part directly from the 90° die angle area and a third part from the quadratic outgoing channel after shearing. The bulk texture over the whole sample cross section as well as a first part of local texture measurements were carried out by neutron diffraction with a Cu monochromator at TEX-2, GKSS. Fig. 1 shows the (00.2) and (10.0) pole figures of the positions 1, 2, 3 and 4. In position 1 and 2 the crystallographic texture is close to the initial texture of the sample before ECAP. Moreover, it can be found that there is an apparent change of the crystallographic texture at the deformation regions particular from 2 to 3, from 3 to 4 and from 1 to 4. One also can see that the local resolution is not sufficient to describe the texture gradient between these four positions. Neutron texture analysis is restricted by the sample volumes. Therefore hard x-rays at HARWI-II-W2 were used to increase the local resolution. The texture evolution in the deformation regions 1, 2, 3, 4 (see figure 1) was measured from bottom to top at each step of 1 mm. That means 5 measurements for each position (position 1a, 1b, 1c, 1d, 1e). In Fig. 2 an image plate picture of pure Mg powder taken with the MAR555 and its sum pattern integrated over the Debye-Scherrer cone is shown. Texture measurements were done with the MAR345 detector and the MAR555 detector, on one hand get fast measurements using the new MAR555 and second to compare data quality between the two detectors. The data evaluation of the measurements from November 2007 is in work. The texture measurements were carried out in steps of 5° in  $\omega$  rotation from -90° to 90° for complete pole figure without any sample symmetry. Integral intensities will be calculated to obtain a set of five pole figures (10.0), (00.2), (10.1), (10.2) and (11.0). It has to be pointed out that one texture measurement able for a quantitative texture analysis using complete pole figures needs only 10 min by the MAR555 detector. Primary results of the top and bottom parts at the positions 1a and 1e, 2a and 2e, 3a and 3e as well as 4a and 4e are shown in Fig. 3. It can be found that the (00.2) reflection can qualitatively describe the texture evolution. For all combinations one can see very clearly, that the intensity distributions around the Debye-Scherrer cones vary, which indicates the crystallographic texture. Moreover, one can recognize that these intensity variations along the Debye-Scherrer cones differ from top to bottom for any position. That means we expect a strong texture gradient after quantitative texture evolution.

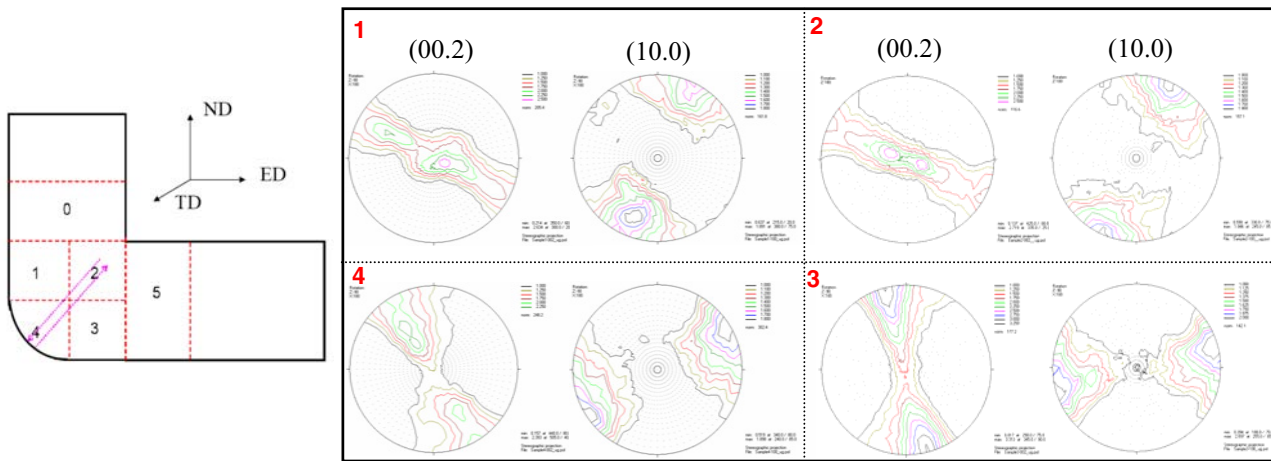


Fig. 1 (00.2) and (10.0) pole figures at different positions (schematic shown in left) in the deformation region of the ECAPed pure Mg by neutron diffraction at TEX-2.

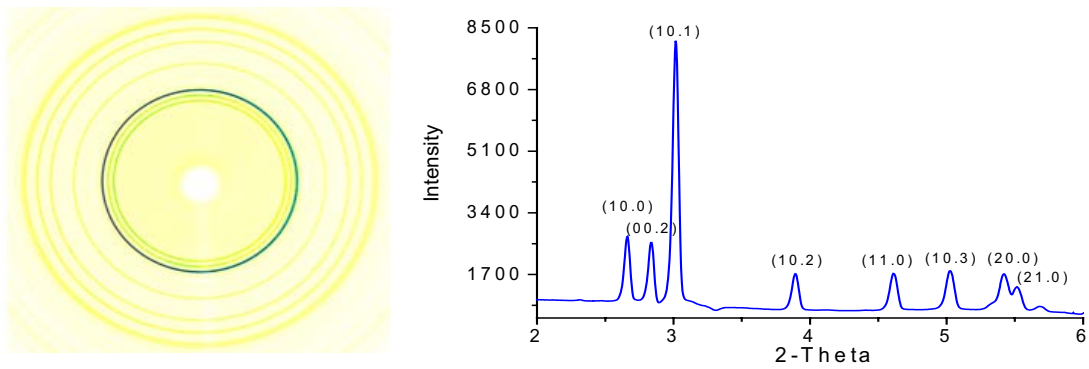


Fig. 2 Image plate picture (MAR555) of an Mg powder (left) and its sum diffraction pattern (right).

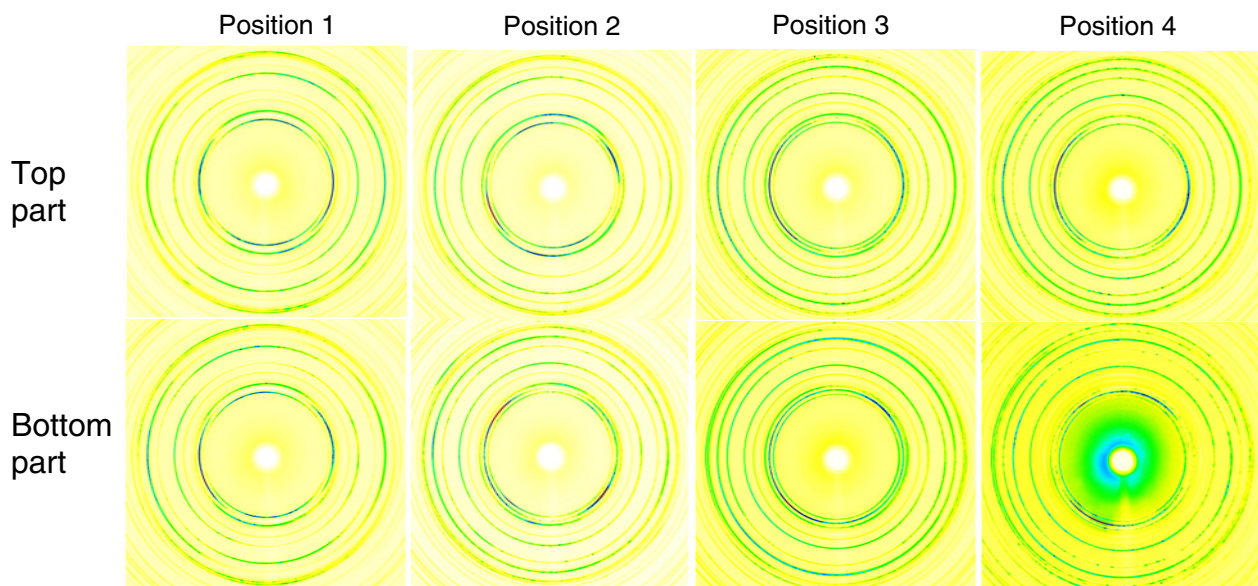


Fig. 3 MAR555 area detector pictures for top and bottom parts in the positions 1, 2, 3 and 4.

## References

- [1] R.Z. Valiev, T.G. Langdon, Prog. in Mater. Sci 51, 931 (2006)



# Texture inhomogeneity in titanium deformed by ECAP

W. Skrotzki<sup>1</sup>, B. Klöden<sup>1,2</sup>, A. Lankau<sup>1</sup>, R. Chulist<sup>1</sup>, V. Kopylov<sup>3</sup>, H.-G. Brokmeier<sup>4</sup>

<sup>1</sup> Institut für Strukturphysik, Technische Universität Dresden, D-01062 Dresden, Germany

<sup>2</sup> Fraunhofer-Institut für Fertigungstechnik und Angewandte Materialforschung, Winterbergstr. 28, D-01277 Dresden, Germany

<sup>3</sup> Physico-Technical Institute, National Academy of Sciences, Minsk, Belarus

<sup>4</sup> GKSS Forschungszentrum, Max-Planckstr., D-21494 Geesthacht, Germany

Equal channel angular pressing (ECAP) is one of the most promising methods of severe plastic deformation (SPD) leading to bulk ultrafine to nanocrystalline materials. Compared to the conventional coarse-grained counterparts such materials possess a much higher strength simultaneously keeping sufficient ductility [1]. During SPD the materials develop a pronounced texture, which in ECAP due to predominantly simple shear in the intersection plane of the two channels is a shear texture. This texture may produce a strong anisotropy of certain properties, like mechanical and magnetic properties. Moreover, it has been shown that in ECAP processed materials there exists a texture gradient with respect to intensity and deviation from the ideal texture components from top to bottom of the billets [2, 3]. It is the aim of the present paper to study in detail the texture inhomogeneity of ECAP processed pure titanium. In contrast to Ti alloys, strong and ductile pure Ti because of its excellent biocompatibility and corrosion resistance is of particular interest for biomedical and orthopaedic applications such as implants and miniaturized medical instruments.

A billet (14 x 14 x 120 mm<sup>3</sup>) cut from a hot-rolled plate of commercially pure titanium (VT1-00, supplied by Verkhnyaya Salda Metallurgical Production Association, Russia, impurities in wt. %: Fe < 0.2, Si < 0.08, C < 0.05, O < 0.1, N < 0.04, H < 0.008) was deformed by ECAP using four passes of route B<sub>C</sub>, i.e. after each pass the billet was rotated first 90° clockwise about the transverse direction (TD) in order to insert the billet front first into the channel (along the normal direction (ND)) and then 90° clockwise about the rotated extrusion direction (ED) axis. The intersection angle of the square channels was 90° without rounding of the corners. ECAP was performed isothermally at 380°C ( $T/T_m = 0.34$ ,  $T_m$  melting temperature) using a pressing speed of 0.4 mms<sup>-1</sup>. In order to approach the simple shear condition along the intersection plane as good as possible the contact friction was minimized by lubrication with a mixture of flaked graphite, MoS<sub>2</sub> and engine oil. Additionally, a back-pressure of 240 MPa (0.2 of forward pressure) was applied [4]. The accumulated shear strain is about 8.

The microstructure was investigated in scanning electron microscopes (SEM, Zeiss DSM 962 and LEO 1530) with orientation imaging microscopy (OIM) based on electron backscatter diffraction (EBSD) using HKL software.

Global texture measurements of the starting and ECAP processed material were done by neutron diffraction [5]. The pole figures measured are (10-10), (10-11), (11-20) and (0002). To examine the homogeneity of ECAP deformation, the local texture was analyzed by high-energy synchrotron radiation (100 keV) using beam line BW5 at DESY-HASYLAB in Hamburg, Germany. The sample for texture measurements with synchrotron radiation was a pin of (2 × 2 × 14) mm<sup>3</sup> taken from the centre as well as 3 mm from each side wall of the billet with the long sample axis directed from the top to the bottom. The texture was measured at 7 positions along this direction with an aperture of (2 × 0.5) mm<sup>2</sup> in volumes of about 2 mm<sup>3</sup>. Details about synchrotron texture measurements as well as texture representation are given in [2, 6]. The pole figures constructed from the Debye-Scherrer rings are the same as for neutron diffraction. These pole figures have been taken to calculate the orientation distribution function (ODF) using the program LABOTEX. The intensity and Euler angles of the main texture component have been determined from the ODF sections at  $\varphi_2 = 25^\circ$  or  $\varphi_2 = 30^\circ$ . The sample and crystal coordinate systems used (ED, TD, ND and 1, 2, 3, respectively) to describe the textures are given in [2].

The starting rolled material is partially recrystallized with a grain size smaller than about 100 μm. The initial texture is (0001)<10-10> with a ±40° rotation about the rolling direction. This texture is

generally observed for hot-rolled Ti [7]. After 4 passes of ECAP route B<sub>C</sub> the material has a grain size smaller than 1 μm. The largest grains which could be measured by EBSD probably are dynamically recrystallized. The global texture may be characterized by a predominant elliptical component located around  $\varphi_1 = 225^\circ$ ,  $\phi = 45^\circ$  and  $\varphi_2 = 30^\circ$  with  $\Delta\varphi_1 = 20^\circ$ ,  $\Delta\phi = 40^\circ$  and  $\Delta\varphi_2 = 20^\circ$ . Its volume fraction is about 20%. The texture sample symmetry is triclinic. Local texture measurements by synchrotron radiation reveal that within the cross-section of the billet there is a texture gradient with respect to intensity and orientation of the main component. On the left and right side of the billet the intensity slightly decreases from the top to the bottom except in the lower 20% where it increases again. The texture gradient with respect to  $\varphi_1$  and  $\phi$  is about  $-1^\circ/\text{mm}$  and  $1^\circ/\text{mm}$ , respectively. A local variation of  $\varphi_2$  is within  $5^\circ$ . The intensity also decreases from the left to the right side. The angular spread from the left to the right side at a given position is smallest in  $\varphi_1$  when it is largest in  $\phi$  and vice versa. The texture type observed compares quite well with that measured by Yu et al. [8] after the same ECAP process. The texture inhomogeneity of a Ti sample billet processed 8 passes ECAP route B<sub>C</sub> through a round die has been investigated by Bonarski and Alexandrov [9]. They observed a decrease of the maximum ODF intensity from the centre to the edge of the billet. However, a direct comparison of the texture type is not possible.

The texture of route A ECAP processed face-centred cubic metals is quite inhomogeneous from the top to the bottom of the billet [2, 3]. With increasing number of passes it becomes more homogeneous. The non-uniform texture in ECAP processed Ti is in line with these observations. However, in route B<sub>C</sub> ECAP processed Ti a texture gradient also exists from the left to the right side of the billet. The texture heterogeneity may be explained by Tóth's flow line model [10] yielding an increasing flow line coefficient from the top to the bottom of the billet and here, due to a  $90^\circ$  rotation about ED, also from the left to the right side.

The texture observed compares well with the stable orientations found in simulations on simple shear deformation of hexagonal metals [11, 12]. In the present case a P fibre texture is observed with a strong elliptical component at  $\varphi_1 = 225^\circ$ ,  $\phi = 45^\circ$  and  $\varphi_2 = 30^\circ$ . The P fibre is due to prismatic and pyramidal slip [11], indicating that these slip modes predominate the texture development in Ti. Surprisingly, there exists some similarity of the main texture component found with that observed in magnesium deformed in the same way, although this material primarily deforms on the basal system. However, in contrast, in magnesium the component has a pronounced spherical shape and is more rotated towards the shear plane normal. An explanation of this behaviour may be given by the texture simulations planned.

## References

- [1] R.Z. Valiev and T.G. Langdon, *Prog. Mater. Sci.* 51, 881 (2006)
- [2] W. Skrotzki, N. Scheerbaum, C.-G. Oertel, R. Arruffat-Massion, S. Suwas and L.S. Tóth, *Acta Mater.* 55, 2013 (2007)
- [3] W. Skrotzki, N. Scheerbaum, C.-G. Oertel, H.-G. Brokmeier, S. Suwas and L.S. Tóth, *Acta Mater.* 55, 2211 (2006)
- [4] V.I. Kopylov, In: *Investigations and Applications of Severe Plastic Deformation*, T.C. Lowe and R.Z. Valiev (eds.), Kluwer Academic Publishers, Netherlands, 23 (2000)
- [5] H.-G. Brokmeier, *Habilitation thesis*, TU Clausthal (1995)
- [6] W. Skrotzki, B. Klöden, R. Tamm, C.-G. Oertel, U. Garbe and E. Rybacki, *Textures Microstruct.* 35, 163 (2003)
- [7] A.K. Singh and R.A. Schwarzer, *Z. Metallkd.* 91, 702 (2000)
- [8] S.H. Yu, D.H. Shin and S.K. Hwang, In: *Ultrafine Grained Materials III*, Y.T. Zhu, T.G. Langdon, R.Z. Valiev, S.L. Semiatin, D.H. Shin and T.C. Lowe (eds.), TMS (The Minerals, Metals & Materials Society), 227 (2004)
- [9] J. Bonarski and I.A. Alexandrov, In: *Nanomaterials by Severe Plastic Deformation*, M.J. Zehetbauer and R.Z. Valiev (eds.) Wiley-VCH Verlag GmbH & Co. KGaA, Weinheim, 309 (2004)
- [10] L. Tóth, *Adv. Eng. Mat.* 5, 308 (2003)
- [11] B. Beausir, L.S. Tóth and K.W. Neale, *Acta Mater.* 55, 2695 (2007)
- [12] B. Beausir, S. Suwas, L.S. Tóth, K.W. Neale and J.-J. Fundenberger, *Acta Mater.* (2007), in press

# Charge density studies of various sulfides.

T. Lippmann

GKSS Forschungszentrum Geesthacht, Max-Planck-Str. 1, 21502 Geesthacht, Germany

Charge density studies have been performed on various sulfides, i.e. pyrite ( $\text{FeS}_2$ ), chalcopyrite ( $\text{CuFeS}_2$ ), pyrargyrite ( $\text{Ag}_3\text{SbS}_3$ ), proustite ( $\text{Ag}_3\text{AsS}_3$ ) and sphalerite ( $\alpha\text{-ZnS}$ ). As has been pointed out by Gibbs *et al.* [1], 'sulfides comprise an important class of minerals that exhibit a range of M-S, M-M and S-S bonded interactions and structure types [2] in concert with a host of important electronic, magnetic and catalytic properties. If we are to understand and exploit their manifold uses, an understanding of the connection between the bonded interactions and the properties of the electron density distribution at the atomic level is required.' This statement is underlined by the growing importance of sulfides as advanced engineering materials, e.g. in solar cell industries.

The investigated structures have been selected for several reasons: Pyrite and sphalerite have well-known and well-investigated structures and the results of these experiments can easily be compared to literature data. Thus, the experiments serve as a quality benchmark test. Moreover, pyrite has also been investigated at beamline BW5 recently [3]. Chalcopyrite is characterized by two different transition metals, i.e. differences in the chemical bonding should be found. Pyrargyrite and proustite are iso-structural, i.e. only differ by one atom and it is interesting to investigate, if this difference can be properly worked out using the data. In addition, appropriate crystals of all mentioned structures were available.

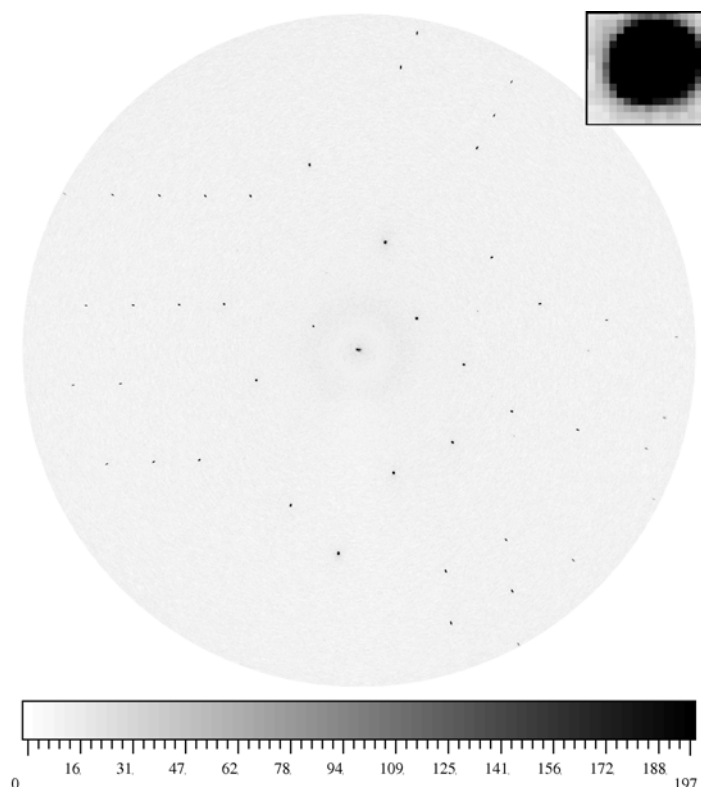


Figure 1: Mar345 raw data (sphalerite measurement). The inset shows a magnification of one of the low-order reflections.

Data have been recorded on the materials science diffractometer at the GKSS materials science beamline HARWI-II at DESY, Hamburg, using 100 keV radiation and a Mar345 image plate detector.  $\Delta\omega$  of  $1^\circ$  (sphalerite:  $2^\circ$ ) and various illumination times between 15 and 90 seconds have been used, depending on the size of the crystals.

A special feature has to be mentioned for the sphalerite data collection. The crystal has been remeasured using the new Mar555 detector (direct conversion selenium detector). This detector is characterized by its short read-out time (less than one second per image, i.e. less than half an hour for the complete data collection) and by its negligible point-spread function (comp. insets of Figs. 1 and 2). Data reduction using XDS [4] and Automar [5] are currently under progress.

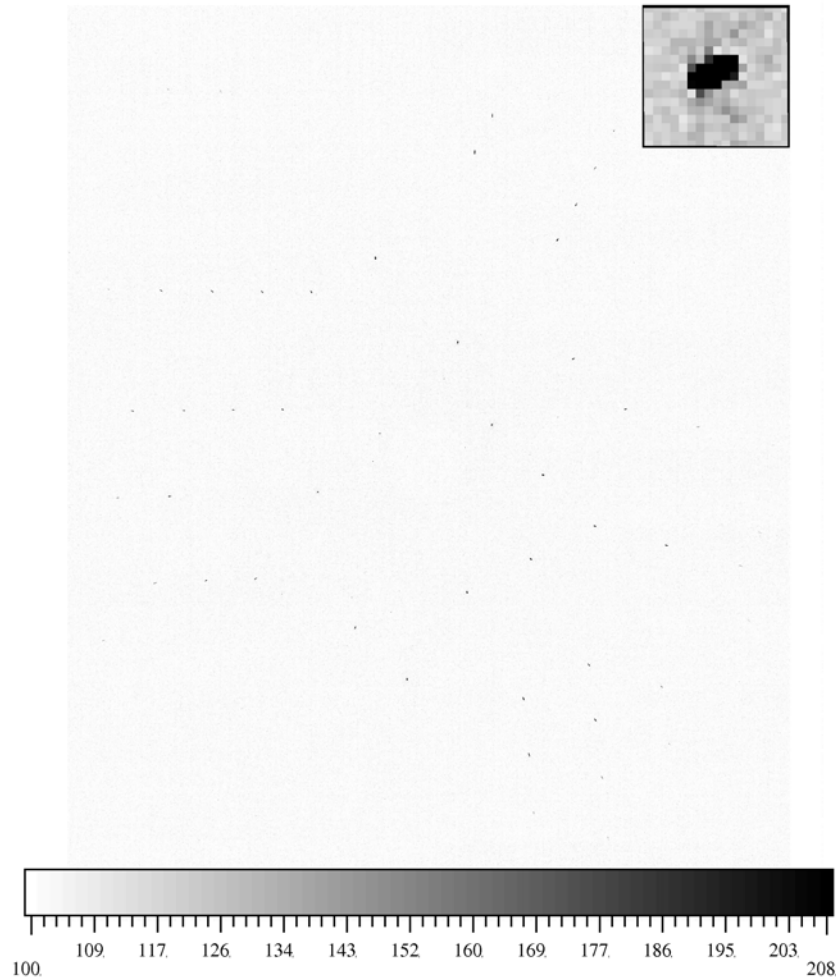


Figure 2: Mar555 raw data. The inset shows the same reflection as in Fig. 1. Energy and sample-detector distance have been kept constant.

## References

- [1] J. Gibbs et al., *Z. Kristallogr.* (2008), in press.
- [2] E. Makovicky, *Rev. Mineral. Geochem.* 61 (2006), 7 – 125.
- [3] T. Lippmann, *Hasylab Annual Report 2006*.
- [4] W. Kabsch, *J. Appl. Cryst.* 26 (1993), 795 – 800.
- [5] K. Bartels and C. Klein, *Automar users guide*, 2003.

# Solution Structure from Small to Wide Angle X-ray Scattering of Surface Functionalized Polyethylene Imine

B. Angelov<sup>1</sup>, U. Vainio<sup>2</sup>, N. Pasquier<sup>3</sup>, T. Li<sup>1,4</sup>, R. Gehrke<sup>2</sup> and R. Willumeit<sup>1</sup>

<sup>1</sup>*Institute of Materials Research, GKSS Forschungszentrum, Max-Planck-Str. 1, 21502 Geesthacht, Germany*

<sup>2</sup>*HASYLAB c/o DESY, Notkestr. 85, 22603 Hamburg, Germany*

<sup>3</sup>*DWI an der RWTH Aachen e.V. und ITMC, RWTH Aachen, Pauwelsstr. 8, 52056 Aachen, Germany*

<sup>4</sup>*Department of Biomedical Engineering, Zhejiang University, Zheda Str.38, 310027 Hangzhou, China*

In this report, we present SAXS results for the solution structure of a partially branched polyethylene imine (PEI) that has covalently anchored functional groups. Branched PEI with primary, secondary and tertiary amine groups in a ratio 31:39:30 (a commercially available derivative) was functionalized with cationic and hydrophobic groups (ref. 1). The hydrophobic/hydrophilic balance of the modified PEI was controlled via the conditions of the chemical synthesis [1].

The investigated model polymers have application in delivery of DNA and other negatively charged drug molecules into the cell. Intensive investigations were carried out to establish their interactions with cells and model lipid membranes. Surface modification allows for a better tuning of the interactions of such polymers with cell membranes.

Our experiments were performed at beamline B1 of the DORIS III storage ring at the synchrotron radiation facility HASYLAB/DESY in Hamburg, Germany. The beam size was 1.0 mm × 1.0 mm on the sample. The measurements were carried out at a fixed energy of 15998 eV, corresponding to a wavelength  $\lambda = 0.77 \text{ \AA}$ . The scattered intensity was recorded with a two-dimensional (2D) gas detector, which area was divided in 256 × 256 pixels. The 2D SAXS data were circularly integrated, normalized, background subtracted, and calibrated by silver behenate standard.

The X-ray scattering pattern of 2 mg/ml functionalized PEI (synthesis described in ref.1) in aqueous solution was measured at room temperature (Fig.1). The small angle scattering curve (Fig. 1a) shows the presence of small peaks near  $q = 0.13 \text{ \AA}^{-1}$  and  $0.23 \text{ \AA}^{-1}$ . From the data regularization procedure, by means of GNOM software [3], the pair distance distribution function  $p(r)$  was obtained (Fig. 1b). A local maximum of  $p(r)$  is presented near 6 Å.

The subsequent three-dimensional reconstruction of PEI solution structure was done using DAMMIN software [4]. The required template for the fitting of the regularized curve was prepared from random sequential aggregation (RSA) of uniform spheres. Such a template has been already employed successfully in protein surface modelling [5]. Our studies reveal that the RSA template better accounts for the inherent disorder of PEI than a periodic lattice. PEI is a cationic polymer composed of one type repetitive units at variance to proteins, which are heteropolymers. This is an advantage for the reconstruction of PEI structure, which has not been reconstructed so far. In the literature, there are some data from transmission electron microscopy at low resolution, where details below 20 nm are unresolved. The reconstructed PEI, presented on Fig.1c, exhibits branches. Their maximum diameter was determined to be 110 Å. The overall structure is modelled using 153 single spheres of 8 Å diameters. Since the branched PEI does not have a unique structure in solution, the presented model should be considered as an “equivalent” structure that exactly reproduces the measured scattering curve.

The obtained results will be compared with light scattering and small angle neutron scattering experiments in a future work. The structural studies will be extended to different stereo-chemical modifications of PEI.

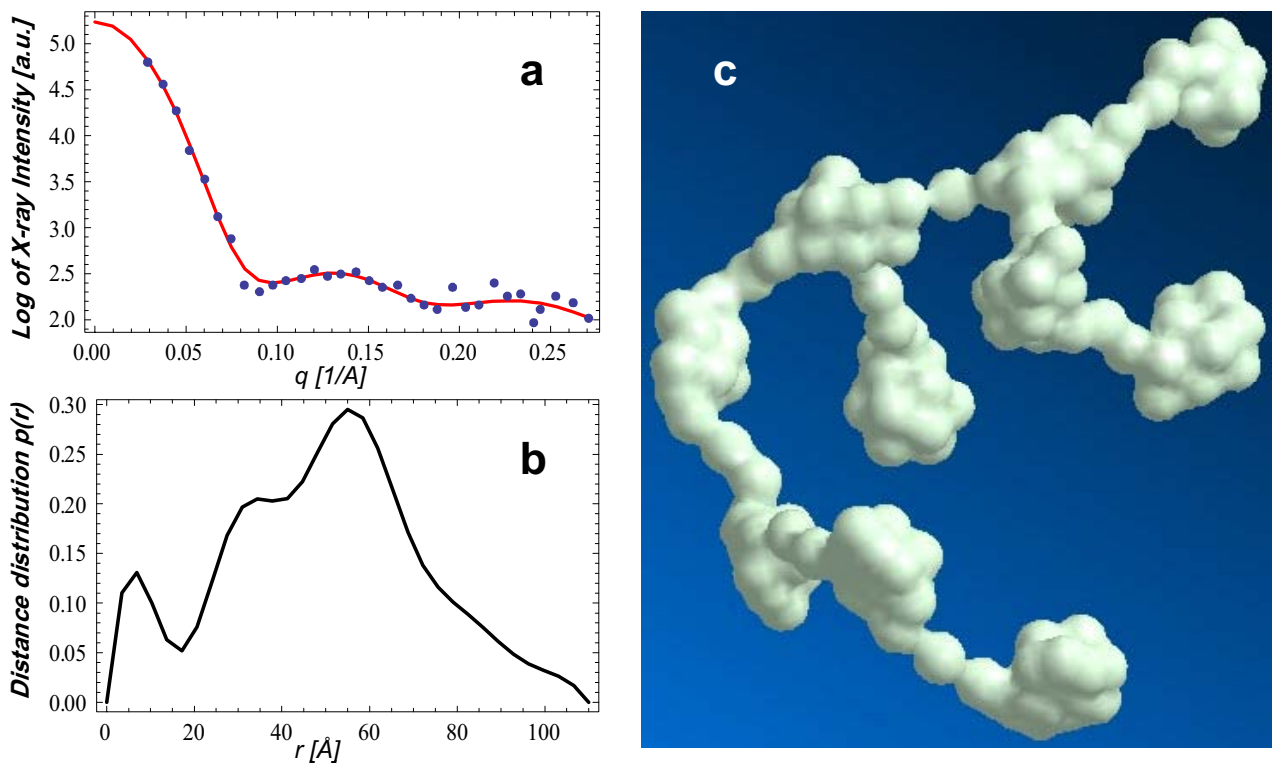


Figure 1: Example of measured X-ray scattering intensity of surface functionalized polyethylene imine (a), the corresponding  $p(r)$  distance distribution function (b), and a reconstruction of the polymer structure (c).

## Acknowledgement

The research of B.A. on PEI structure is funded by BMBF (BMBF-Projekt „Strukturbildende Copolymere zur Primären und Sekundären Ausrüstung von Oberflächen mit funktionalen und schaltbaren Eigenschaften“, 03X0019). T.L. acknowledges IAESTE grant.

## References

- [1] Pasquier, N.; Keul, H.; Heine, E.; Moeller, M.: *Biomacromolecules*, **8**, 2874, (2007)
- [2] Svergun, D. I.: *J. Appl. Crystallography*, **25**, 495, (1992)
- [3] Svergun, D. I.: *Biophysical Journal*, **76**, 2879, (1999)
- [4] Angelov, B.; Sadoc, J. F.; Jullien, R.; Soyer, A.; Mornon, J. P.; Chomilier, J.: *Proteins-Structure, Function and Genetics*, **49**, 446, (2002)

# The interaction of membrane-active molecules with model membranes

*S. Linser, A. Rzeszutek, B. Angelov, S.S. Funari<sup>1</sup> and R. Willumeit*

*GKSS Research Center, Max - Planck - Str. 1, 21502 Geesthacht, Germany*

*<sup>1</sup> HASYLAB, Notkestrasse 85, 22603 Hamburg, Germany*

The search for alternatives for conventional antibiotics due to the uprise of resistances of pathogenic bacteria is not new, but still of prior interest. Beside antibacterial peptides that belong to the innate immune system of almost all species, also synthetic molecules that mimic the properties of these peptides have become promising candidates as alternatives. Our intend is to investigate the mechanism of action of antibacterial peptides and antibacterial polymers.

In our previous Hasylab reports we found that the antibacterial peptides NKCS and derivatives thereof shifted the inverse hexagonal phase transition temperatures of POPE, DOPE-trans and DiPOPE model membranes to higher values [1 and references therein]. In this report we investigated the influence of 8 new peptide derivatives of NKCS and functionalized polyethylene imine (PEI) [2] polymers on phospholipid model membranes. Furthermore, a first attempt was made to measure the influence of salt on the scattering of the negatively charged lipid POPG.

The SAXS measurements of vesicles were prepared in 10 mM sodium phosphate buffer (NaP) pH 7 for DOPE-trans and DiPOPE and 10 mM NaP plus 1 M sodium chloride (NaCl) buffer for POPG with a final lipid concentration of 25 mg/ml. Temperature dependent SAXS measurements were performed at the Soft Condensed Matter Beamline A2.

The results we found are in a good agreement with our previous experiments. All tested peptides shifted the inverse hexagonal phase transition temperature in a concentration dependent manner to higher values. The only exception was a randomly scrambled peptide sequence that corresponds to the less active second half of the peptide NKCS, which showed no effect on the phase transitions. Like it was found before for NKCS, the effect on DiPOPE was more pronounced than for DOPE-trans, which indicates an importance of the acyl chain length of the lipids.

The polymer PEI showed strong interaction with model membranes and even destructive properties at higher concentrations.

The addition of salt to the buffer used for POPG liposomes preparation resulted in a completely different scattering pattern of POPG (figure 1). When POPG was measured in 10 mM sodium phosphate buffer there is no signal visible, what can be due to the low concentration of the lipid and/or a precipitation of the sample. Usually the scattering of the unilamellar POPG vesicles exhibit no sharp peaks but a broad signal. After addition of 1 M sodium chloride to the buffer, the prepared POPG vesicles showed two sharp peaks at 30°C (figure 1), which were visible during the whole temperature scan from 30 to 60°C. This finding has to be repeated during our next experiments and also the interaction of our cationic peptides with the negatively charged POPG membranes will be investigated.

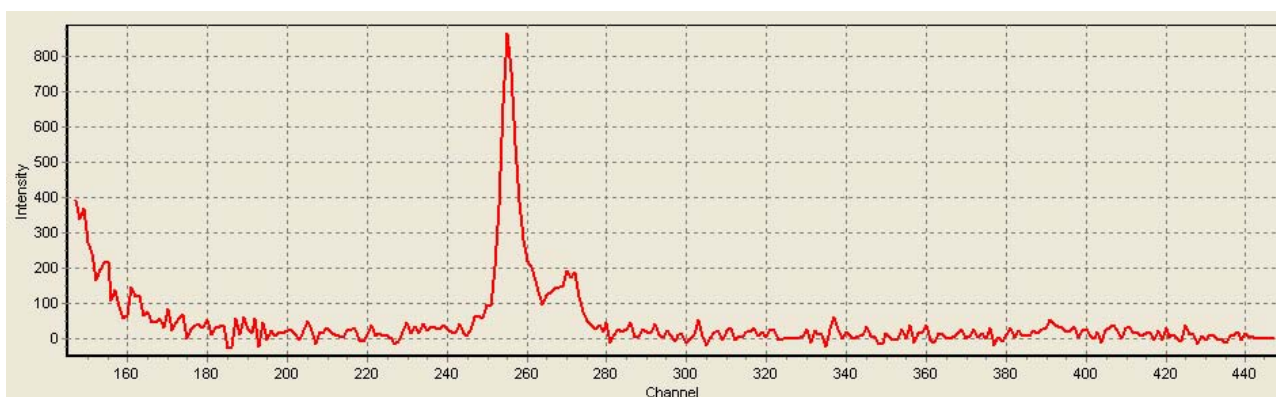


Figure 1: Diffraction pattern of POPG in 10mM NaP+1M NaCl Buffer at 30°C.

**Abbreviations used:** DOPE-trans: 1,2-dielaidoyl-sn-glycero-3-phosphatidylethanolamine; DiPOPE: 1,2-dipalmitoleoyl-sn-glycero-3-phosphatidylethanolamine; POPG: 1-palmitoyl-2-oleoyl-sn-glycero-3-[Phospho-rac-(1-glycerol)]

### Acknowledgements

We would like to thank Jessica Rutz and Tao Li for experimental help during the synchrotron measurements.

### References

- [1] S. Linser, S.S. Funari and R. Willumeit, *Hasylab Annual Report* (2006)
- [2] Pasquier, N.; Keul, H.; Heine, E.; Moeller, M.: *Biomacromolecules*, 8, 2874, (2007).



# Bone-Cartilage-Interface of the Vertebral Endplate

Susanne Drews, Magdalena Müller-Gerbl, Felix Beckmann<sup>1</sup>, Julia Herzen<sup>1</sup>, Oliver Brunke<sup>2</sup>,  
Thomas Hemberger<sup>2</sup> and Bert Müller<sup>3</sup>

*Institute of Anatomy, University of Basel, Pestalozzistr. 20, 4056 Basel, Switzerland*

<sup>1</sup>*GKSS-Research Centre, Max-Planck-Strasse 1, 21502 Geesthacht, Germany*

<sup>2</sup>*phoenixlx-ray Systems+Services GmbH, Niels-Bohr-Strasse 7, 31515 Wunstorf, Germany*

<sup>3</sup>*Biomaterials Science Center, University of Basel, 4031 Basel, Switzerland*

Bone-cartilage-interface is the venue of many degenerative and inflammatory diseases such as osteoarthritis or rheumatoid arthritis. Of special interest, here, is the morphology of the calcified cartilage [1]. For its visualization, one uses histological sectioning combined with optical microscopy or magnetic resonance tomography (MRI). Both methods allow simultaneously visualizing bony and cartilaginous tissue with different spatial resolution and contrast. Histology laterally provides sub-micrometer resolution, but the resolution in the third direction is worse and the data acquisition becomes time-consuming. MRI is best suited for soft tissue contrast, but only yields limited contrast for calcified bone. Even more important, the spatial resolution does not reach the cellular level required for the detailed analysis of the tissue's morphology.

Micro computed tomography ( $\mu$ CT) is well established to quantitatively characterize bone with true micrometer resolution in the three orthogonal directions, non-destructively, so that histology could be performed subsequently. The surrounding soft tissue components, however, are often hardly visible or even invisible. Better density resolution or contrast can be reached applying synchrotron radiation, which is so intense that a monochromator can be inserted and, thus, the beam hardening is drastically reduced. The present study is the comparison of sophisticated conventional  $\mu$ CT with synchrotron radiation-based  $\mu$ CT (SR $\mu$ CT) characterizing the morphology of a part of the human spine.

The specimen selected consisted of the two vertebral bodies, the inter-vertebral disc and the anterior and posterior longitudinal ligament. From the visual inspection, it showed no sign of illness or degeneration. Both conventional  $\mu$ CT and SR $\mu$ CT in absorption contrast mode are employed to three-dimensionally visualize the transitional zone between vertebral body and inter-vertebral disc of the lumbar motion segment.

The  $\mu$ CT measurements were done with a nanotom<sup>®</sup>-CT system (phoenixlx-ray, Wunstorf, Germany) equipped with a 180 kV high-power nanofocus<sup>®</sup> tube with Mo-Target, a 5 mega-pixels high-contrast flat panel detector (Si-photodiode array) with the pixel size of 50  $\mu$ m. The  $\mu$ CT-parameters were 80 kV and 180  $\mu$ A (14.4 W) and the 3  $\mu$ m focus spot size. The data acquisition was done with 1,200 projections by 360° rotation. The voxel size corresponded to 10.0  $\mu$ m. The total duration for acquisition and reconstruction processes was about 80 min.

The SR $\mu$ CT measurements were carried out with the absorption contrast set-up at the beamline W 2, operated by the GKSS Research Centre, using the photon energy of 28 keV. The spatial resolution determined by the modulation transfer function at a metallic edge corresponded to 13.9  $\mu$ m at a pixel size of 6.8  $\mu$ m. The projections were recorded with an asymmetric rotation axis and 360° rotation to increase the spatial resolution almost by a factor of two with respect to the conventional 180° rotation. For reconstruction by means of the filtered back projection in each case two out of the 1441 projections were combined. To obtain the 3D dataset of the region of interest, 4 tomograms shifted by 2.3 mm were combined.

Figure 1 shows axial slices of the PMMA-embedded sample virtually cut through the bone cartilage interface. The image on the top was obtained from the conventional  $\mu$ CT. The image on the bottom shows a corresponding slice obtained from SR $\mu$ CT. Although the sample showed macroscopically no signs of degenerative processes, in both pictures the interfaces appear irregular. One finds hyper-mineralized regions at the bone cartilage interface.

One of the main challenges in the  $\mu$ CT is the differentiation or segmentation cartilage from the embedding material, because the absorption is almost identical. This interface can hardly be seen in the slices represented in Figure 1 for both techniques. It is, however, impossible to distinguish

between the hyaline cartilage layer at the endplate and the remaining inter-vertebral disc, which mainly consists of fibro-cartilage. Comparing SR $\mu$ CT with the conventional  $\mu$ CT, one recognizes some differences related to the number and extension of different artefacts. Conventional  $\mu$ CT provides in some regions low-noise data, but near the bone the star-like artefacts are so prominent that the segmentation of the low-contrast features becomes impossible.

In summary, both conventional and SR $\mu$ CT offers the visualization of cartilage near the bony tissue. By increasing the time for the measurement, the signal-to-noise ratio becomes better and better but the prominent artefacts in conventional  $\mu$ CT as the result of inhomogeneous distribution of stronger absorbing bony tissue prevent the segmentation of the cartilage. For SR $\mu$ CT the segmentation seems to be possible but requires long periods of the expensive beamtime.

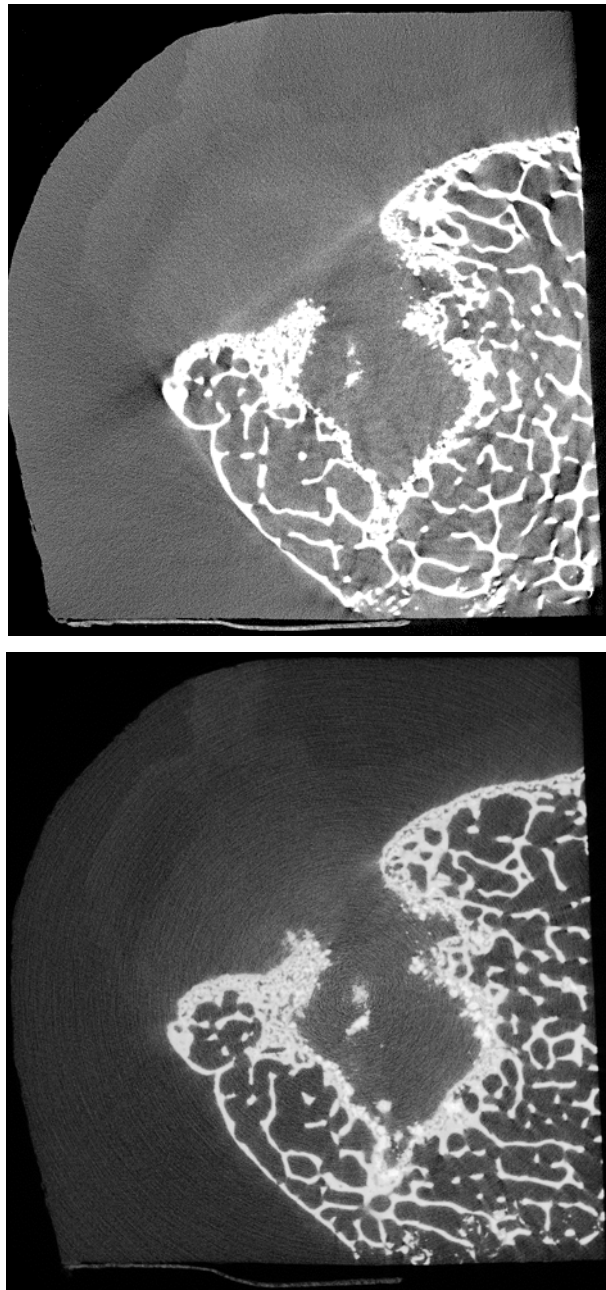


Figure 1: The axial slices through the spine segment are scaled that one can recognize the differences between cartilage and bare PMMA embedding. The image on the top is acquired with conventional  $\mu$ CT, whereas the slice on the bottom is obtained with SR $\mu$ CT.

## References

- [1] D.B. Burr, *Osteoarthr. Cartil.* 12, 20 (2004)

# Brain Vessel Staining for the Visualization with Micro Computed Tomography

*Marco Dominietto, Felix Beckmann<sup>1</sup>, Julia Herzen<sup>1</sup>, and Bert Müller<sup>2</sup>*

*Institute for Biomedical Engineering, ETH Zürich, Wolfgang Pauli-Str. 10, 8093 Zurich, Switzerland*

*<sup>1</sup>GKSS-Research Centre, Max-Planck-Strasse 1, 21502 Geesthacht, Germany*

*<sup>2</sup>Biomaterials Science Center, University of Basel, c/o University Hospital, 4031 Basel, Switzerland*

The visualization of the 3D vessel network is crucial for studying the physiological processes related to angiogenesis and vascular disease. High-resolution tomography can serve to uncover the smallest capillaries, which have the diameter of about 5  $\mu\text{m}$  [1]. The aim of this work is to set-up a protocol to stain the vessels of cancerous tissue in mouse models down to the capillary level. The data obtained will be used for comparisons with simulations of angiogenesis [2].

A female nude mice (Balb/c), weight 24.5 g, was used for this experiment performed in strict adherence to the Swiss law for animal protection. The contrast agent was a suspension of barium sulfate made of 15 g barium in 200 ml physiological solution. The suspension was filtered (pore size 40  $\mu\text{m}$ , BD Falcon, USA) to obtain particles with dimensions comparable to the diameters of micro-vessels. Before injection, the suspension was made homogeneous using the ultrasonic bath Sonorex Digital 10P, Bandelin at the temperature of 37 °C for a period of 10 min. The mouse was anesthetized by an intra-peritoneal injection of 350  $\mu\text{m}$  Ketamine/Xylazine. Subsequently, the animal was perfused with 10 ml phosphate-buffered saline and 10 ml barium sulfate suspension via the left ventricle of the heart applying the peristaltic pump (Watson Marlow 101 U/R) as similarly described in [3]. The brain was isolated, fixed in 4% para-formaldehyde and transferred into Eppendorf containers for the imaging using synchrotron radiation-based micro computed tomography (SR $\mu$ CT).

The SR $\mu$ CT-measurement of the barium sulfate-stained brain was carried out at the beamline BW 2 using the photon energy of 19 keV. The pixel length was set to 3.9  $\mu\text{m}$ . The spatial resolution determined by means of the modulated transfer function of a highly absorbing metal edge corresponded to 7.2  $\mu\text{m}$ . The rotation center of the Eppendorf container was asymmetrically placed to the detection unit that the projections at each rotation angle  $\alpha$  can be combined with the one at  $\alpha + 180^\circ$ . 1801 projections between 0° and 360° were recorded to reconstruct the brain vessel network by means of the standard filtered back-projection algorithm.

The vascular network is clearly visible in the projections recorded (see Figure 1, top). Therefore, local tomography could be applied easily, in order to increase the spatial resolution avoiding recording the surrounding container and liquid free of tissue. The distribution of the barium sulfate, however, is inhomogeneous as observable in the projection and better transparent in the reconstructed and visualized 3D data (Figure 1).

In summary, although the injection of the barium sulfate in the left ventricle leads to better perfusion results than the intra venous injection in the tail, the size distribution of the barium sulfate is of crucial importance and has to be tailored. This is because the entire contrast agent goes directly into the arterial blood without passing through the lungs that makes a sort of physiological filter for the larger particles. We do expect the resolution of the network of capillaries using barium sulfate only with grain sizes of up to 5  $\mu\text{m}$ . Based on the expected results, one can treat the tomographic data to compare them with the simulations of tumor growth. This comparison will allow validating the simulations and, thus, contributing to the tumor treatment for the benefit of patients.

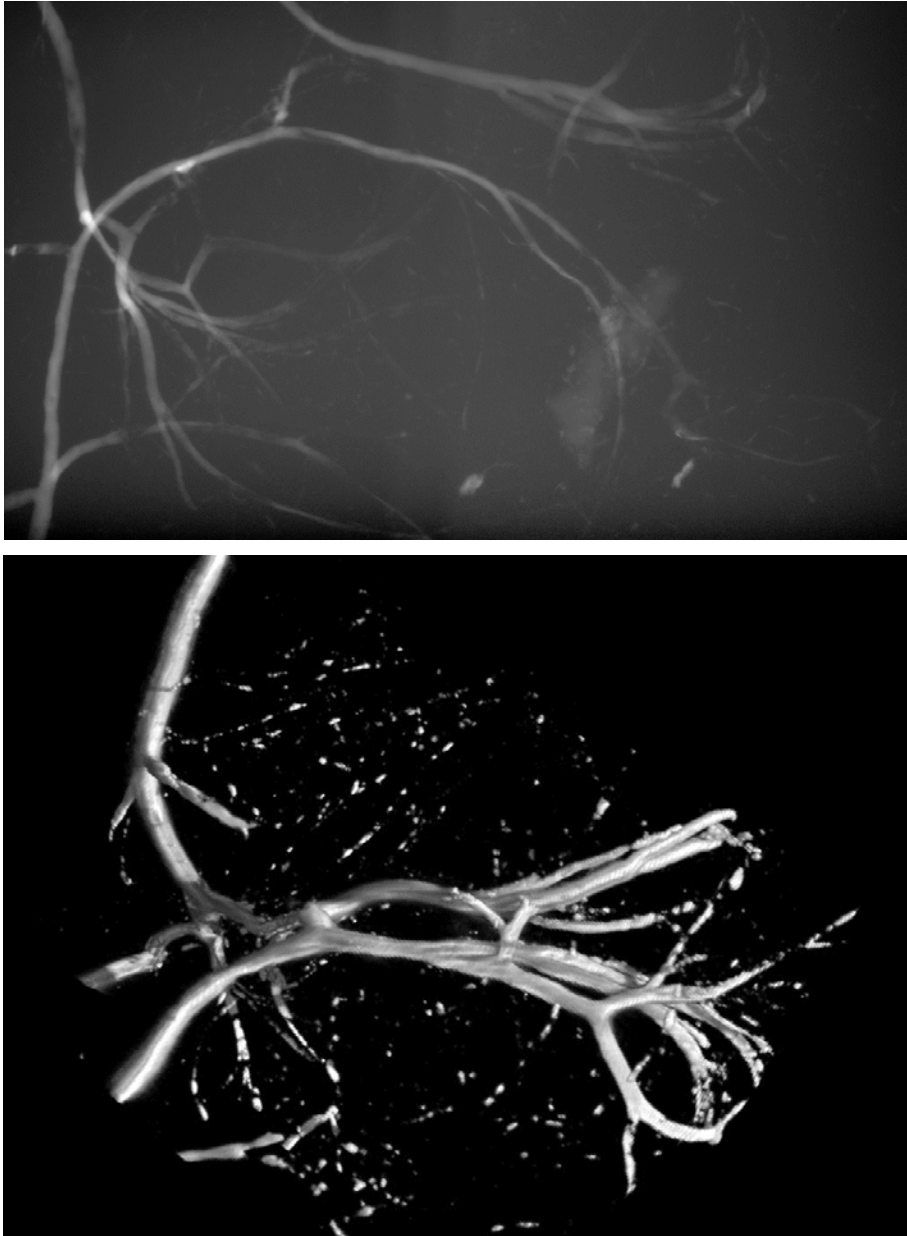


Figure 1: Projection and 3D image generated by VGStudio Max 1.2 (Volume Graphics, Heidelberg, Germany) of the vascular network of mouse brain stained with barium sulfate.

## References

- [1] B. Müller et al., Nucl. Instrum. Meth. B 246, 254 (2006)
- [2] B.A. Lloyd et al., LNCS 4792, 874 (2007)
- [3] K. Myojin et al., Am. J. Neuroradiol. 28, 953 (2007)

# Chemical and morphological characterisation of insect brains

M. Kühbacher, B. Grünewald<sup>1</sup>, G. Falkenberg<sup>2</sup>, E. Welte<sup>2</sup>,  
J. Herzen<sup>3</sup>, F. Beckmann<sup>3</sup> and A. Kyriakopoulos

Department of Molecular Trace Element Research in the Life Science, Hahn-Meitner-Institut, Glienicker Str. 100,  
14109 Berlin, Germany

<sup>1</sup>Institut für Neurobiologie, Freie Universität Berlin, 14195 Berlin, Germany

<sup>2</sup>Hamburger Synchrotronstrahlungslabor HASYLAB at Deutsches Elektronen-Synchrotron DESY, Notkestr. 85,  
22603 Hamburg, Germany

<sup>3</sup>GKSS-Research Center Geesthacht, Institute for Materials Research, Max-Planck-Strasse 1,  
21502 Geesthacht, Germany

Different synchrotron radiation based methods were used to investigate insect brains with a specific focus on chemical imaging. In previous studies, we found a specific distribution of trace metals in the central nervous system (CNS) of rodents [1]. Metals and metalloids are involved in the production of free radicals, the causing factor for oxidative stress. However, metals and metalloids are also necessary components of specific antioxidant enzymes [2]. The identification of metalloproteins and the determination of their cellular and subcellular distribution will provide valuable hints with regard to the functions and the biological role of the metals and metalloids in question. In brain tissues, knowledge about the spatial distribution of certain metals, as iron, copper, zinc and manganese, may help to explain age-related changes in the central nervous system (CNS). A wide variety of neuropathological manifestations including elevations in protein oxidation, protein aggregation, and cytotoxicity may be the result of age-related alterations in the metal-homeostasis.

In order to analyze the elemental distribution in three dimensions tomographic as well as confocal methods can be applied. In figure 1 the reconstructed image of microtomographic data from a honeybee comb hiding a larva is shown. The data were obtained by absorption contrast at the BW2 beamline. The measurements were performed with photon energies of 8 and 9 keV. The chosen animal models honeybee and fruit fly allow measurements without sectioning the brain tissue as well as *in vivo* measurements.

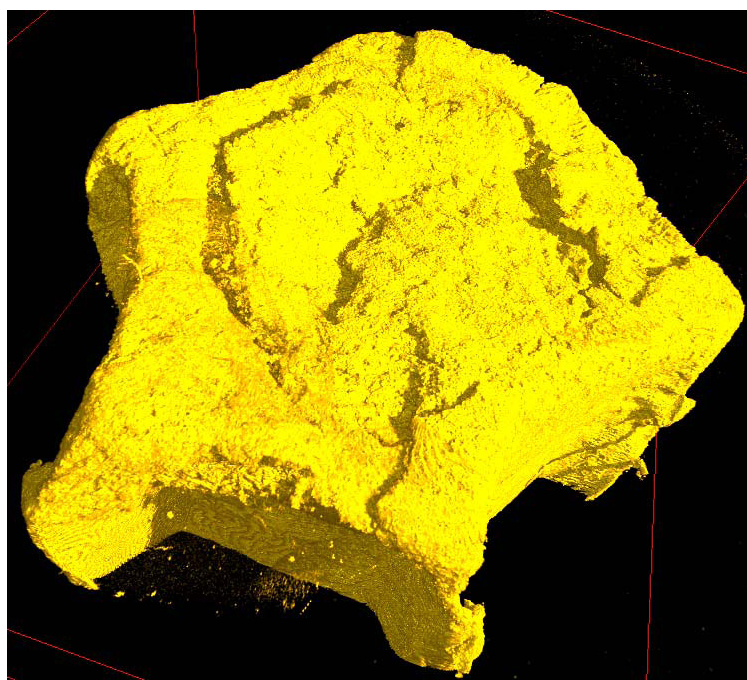


Figure 1: Honeybee comb (with living larva inside) investigated with microtomography.

Synchrotron radiation based microtomography allows us to visualize the internal microscopic structure of small brains like insect brains. While classical tomography provides a spatial resolution in the millimeter range, microtomography is expanding the spatial resolution down to the micrometer range.

Beside other tomographic techniques based on absorption, phase-contrast, or X-ray scattering, X-ray fluorescence computed tomography achieves multi-element capability by recording characteristic X-ray emission. For the investigation of the elemental distribution in two dimensions the micro-synchrotron radiation X-ray fluorescence procedure ( $\mu$ -SRXRF) at beamline L was used by scanning with a focused beam of synchrotron radiation. In addition, XANES, performed at beamline A1, was used for the characterisation of the metals iron, copper and zinc in the insect brains.

## References

- [1] M. Kühbacher, G. Weseloh, A. Thomzig, H. Bertelsmann, G. Falkenberg, M. Radtke, H. Riesemeier, A. Kyriakopoulos, M. Beekes, D. Behne, *Analysis and localization of metal- and metalloid containing proteins by synchrotron radiation x-ray fluorescence spectrometry*. X-Ray Spectrometry 34, 2: 112-117 (2005)
- [2] NE. Savaskan, AU. Bräuer, M. Kühbacher, A. Kyriakopoulos, O. Ninnemann, D. Behne, R. Nitsch, *Selenium deficiency increases susceptibility to glutamate-induced excitotoxicity*. FASEB J 17(1): 112-114 (2003)
- [3] R. Menzel, M. Giurfa, *Cognitive architecture of a mini-brain: the honeybee*. Trends in Cognitive Sciences 5, 2: 62-71 (2001)
- [4] B. Grünewald, *Morphology of feedback neurons in the mushroom body of the honeybee, Apis mellifera*. J. Comp. Neurol. 404: 114-126 (1999)
- [5] R. Brandt, T. Rohlfing, J. Rybak, S. Krofczik, A. Maye, M. Westerhoff, H.C. Hege, and R. Menzel, *Three-Dimensional Average-Shape Atlas of the Honeybee Brain and Its Applications*. The Journal of Comparative Neurology 492: 1-19 (2005)

# Improving the knowledge of integration of medical devices in bone; a comparison of 3D SR $\mu$ CT data to histomorphometrical data obtained on cut and ground sections

C.B. Johansson<sup>1</sup>, J. Lindblad<sup>1</sup>, H. Sarve<sup>2</sup>, R. Bernhardt<sup>3</sup>, F. Beckmann<sup>4</sup>, J. Herzen<sup>4</sup>  
G. Borgefors<sup>2</sup>, D. Scharnweber<sup>3</sup>

<sup>1</sup>Department of Clinical Medicine, Örebro University, SE-701 82 Örebro, Sweden.

<sup>2</sup>Centre for Image Analysis, Swedish University of Agricultural Sciences, SE-751 05 Uppsala, Sweden.

<sup>3</sup>Max-Bergmann-Center of Biomaterials, Institute of Materials Science, Dresden University of Technology, D-01062 Dresden, Germany.

<sup>4</sup>Institute for Materials Research, GKSS Research Centre Geesthacht, D-21502 Geesthacht, Germany.

## Introduction

The aim of our research is to find, and apply techniques that will help us to understand the mechanisms of integration of biomaterials in bone tissue. We will combine traditional 2D histomorphometrical data (bone to implant contact and bone area around the implants) with the acquired 3D SR $\mu$ CT data. Bone area measurements obtained on the 2D sections versus bone volumes obtained on the 3D reconstructed volumes are of immediate interest. We foresee that combining information obtained with a number of different techniques will help us to gain further understanding of the integration of biomaterials.

## Materials and Methods

Bone blocks with screw shaped implants (diam. 2.2 mm and 3.2 mm long) of commercially pure titanium were retrieved from rat bone after 4 weeks of follow up (samples from spongy type bone; implants were inserted in the femur chondyle region). The animals had been *in vivo* labeled with 3 different fluorescent dyes (clinical antibiotic).

Laboratory processing resulted in embedment of all samples in resin. The samples had an outer diameter of 10 mm and a length of 13 mm.

All samples were imaged with the SR $\mu$ CT device of the GKSS at beamline W2 using a photon energy of 50 keV. To achieve maximal contrast and to reduce the amount of noise in the images, blocks of  $2 \times 2$  pixels of the detector were binned together. To maintain the best possible resolution, the tomographic scans were acquired with the axis of rotation placed near the border of the detector, and with 1440 equally stepped radiograms obtained between  $0^\circ$  and  $360^\circ$ . Before reconstruction combination of the projection of  $0^\circ - 180^\circ$  and  $180^\circ - 360^\circ$  were built. A filtered back projection algorithm was used to obtain the three-dimensional data of X-ray attenuation for the samples. The field of view of the X-ray detector was set to 6.76 mm  $\times$  4.51 mm (width  $\times$  height) with a pixel size of 4.40  $\mu$ m showing a measured spatial resolution of about 11  $\mu$ m. A slice through a reconstructed data volume can be seen in Figure 1 (middle).

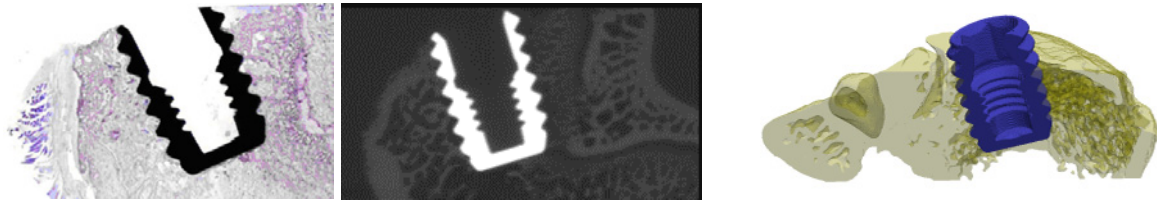


**Figure 1:** SR $\mu$ CT image of commercially pure titanium implant inserted in rat-tibia bone for 4 weeks. **Left:** Histologically stained undecalcified cut and ground section (10  $\mu$ m) of the corresponding sample with implant inserted in rat spongy type bone. **Middle:** Slice through the reconstructed data. **Right:** 3D rendering of a preliminary segmentation of the data into implant (blue) and surrounding bone material (yellow).

### Processing

Fifteen  $\mu$ m thin undecalcified cut and ground sections, demonstrating adequate fluorescent labeled bone tissue, have been extracted from the imaged implants, resulting in histological “routine sections”, see Figure 1 (left). Relevant histomorphometrical data is extracted from these sections using computer aided image analysis in either a semi-automatic or a fully automatic manner [1]. The location of the histological sections will be found in the SR $\mu$ CT volumes using image registration, and the measurements of bone area outside the implants will be compared to

- a) bone area measurements from simulated sections of the SR $\mu$ CT data at the same location
- b) bone volume measurements from the whole SR $\mu$ CT volume.

The availability of registered 2D histological data provides a good reference for the method enabling comparative analysis, while the 3D measurements will show the strengths of the new image modality. Methods for the 2D-3D registration have been developed and are currently going through evaluation and fine tuning. Image segmentation of the SR $\mu$ CT is underway. A preliminary result of segmentation of the data into two classes, implant and bone is visualized in Figure 1 (right). A challenge is to see if it is possible to separate new bone growth from older bone, in the SR $\mu$ CT data.

### Acknowledgements

This project was partly supported by the IA-SFS project RII3-CT-2004-506008 of the Framework Program 6.

### References

- [1] H. Sarve, J. Lindblad, C. B. Johansson, G. Borgefors, V. F. Stenport. *Quantification of Bone Remodeling in the Proximity of Implants*, Proceedings of the 12th International Conference on Computer Analysis of Images and Patterns (CAIP), LNCS-4673, pp. 253-260



# Micro computed tomographic analysis of a tumour tissue with DiTo

H. Rahn<sup>1</sup>, J. Gomez-Morilla<sup>1</sup>, R. Jurgons<sup>2</sup>, Ch. Alexiou<sup>2</sup>, J. Herzen<sup>3</sup>, F. Beckmann<sup>3</sup>  
and S. Odenbach<sup>1</sup>

<sup>1</sup>Chair of Magnetofluidynamics, Technische Universitaet Dresden, Dresden 01062, Germany

<sup>2</sup>Department of Otorhinolaryngology, Head and Neck Surgery, University of Erlangen-Nürnberg, Erlangen, Germany

<sup>3</sup>GKSS, Max-Planck-Str.1, 21502 Geesthacht, Germany

Within the frame of the research project SPP1104 funded by DFG, two different cancer treatment methods have been investigated. Both methods, Magnetic Drug Targeting (MDT) and Hyperthermia (HT), coincide in the use of ferrofluids (magnetic nanoparticles in an appropriate carrier liquid), but they differ in their approach. They both make use of the strong influence of magnetic fields on nanoparticles, with the aim of treating the cancer locally while reducing, or even eliminating, the side effects that usually occur during conventional cancer treatments.

In the case of MDT, starch coated nanoparticles are used as drug carriers. The chemotherapeutic agent mitoxantrone is bounded chemically to the nanoparticles and injected into the artery which supplies the tumour. By applying a strong magnetic field gradient, the nanoparticles can be directed through the vessels and delivered into the desired area: the tumour tissue. Therefore drugs can be accumulated where they are needed and not spread in the patient's body. For this research project tumours have been grown in rabbits and treated with MDT. After the treatment, the tumour tissue has been resected from the animals, fixated in formalin and embedded in paraffin, ready for the analysis.

To achieve a successful cancer therapy, a calculated dose of drugs should end up within the tumour tissue. To analyse the distribution of drugs connected with nanoparticles, several techniques have been applied. The most straightforward method is the analysis by electron or optical microscopy of histological cuts [1-6]. This technique provides useful information but only in 2 dimensions, furthermore the sample is destroyed.

To receive 3-d information about the distribution of the particles within the tumour tissue, we are carrying out micro-computed tomography analysis ( $\mu$ CT) [7].

The tomographic examination of the tumour sample has been performed in 2 different CT laboratories, a conventional X-ray cone beam  $\mu$ CT laboratory and DiTo, a new  $\mu$ CT apparatus based on synchrotron radiation at DESY/HASYLAB, which has been installed and commissioned during the last year. With the conventional  $\mu$ CT set-up at TU Dresden a spatial resolution of 40  $\mu$ m can be achieved and we can observe that the nanoparticles are accumulated within the tumour tissue as desired. Figure 1 shows nanoparticles accumulated in 2 isolated areas within a particular tumour sample[8].

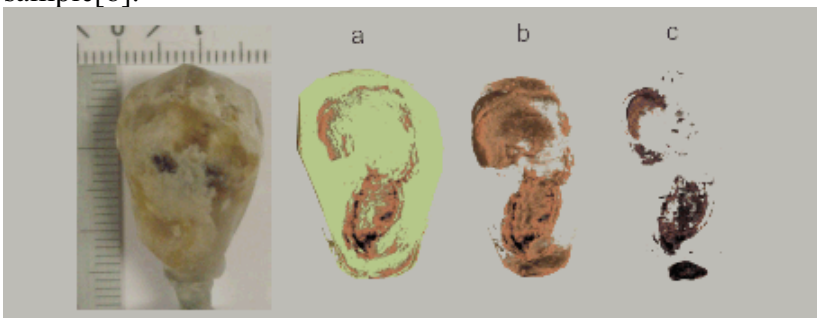


Fig.: 1 Tumour sample, photography of the tumour; computed representation of frontal slice of a) the tumour sample embedded in paraffin; b) tumour tissue with nanoparticles; c) the area with highest density: nanoparticles contained within the tissue.

The same sample has been analysed with DiTo, where a principle spatial resolution of 1.3  $\mu$ m can be achieved.

Figure 2 shows a tomogram slice of this sample taken with DiTo. The scan has been performed at the photon energy of 20 KeV, with an optical magnification of 1.8 (restricted by the dimensions of the sample) and a spatial resolution of 10 $\mu$ m. With the high resolution, structures within the areas where particles have been detected with the cone beam laboratory set up can be differentiated. One

sees clearly one of the larger vessels (dark blue and red labelled zones) inside the tumour filled with magnetic nanoparticles and a region around the vessels where particles have been transferred into the tissue. Moreover the green region at the upper left edge of the tomographic cross section indicates particles, which have been enriched in the tissue due to the magnetic forces exerted by a magnet located in the respective area. This information is of great importance for the further development of this innovative cancer treatment method [8].

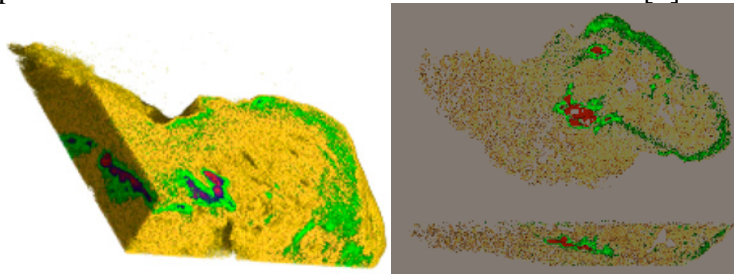


Fig.: 2 Tumour sample analysed by DiTo at Hasylab in DESY/Hamburg

Acknowledgements: This project is funded by DFG with OD18/9 within SPP1104

## References

- [1] C. Seliger et al., *In vitro investigation of the behaviour of magnetic particles by a circulating artery model*. Journal of Magnetism and Magnetic Materials, 2007. 311(1): p. 358-362
- [2] I. Hilger et al., *Developments for the minimally invasive treatment of tumours by targeted magnetic heating*. Journal of Physics: Condensed Matter, 2006. 18(38): p. S2951-S2958
- [3] C. Alexiou et al., *Targeting cancer cells: magnetic nanoparticles as drug carriers*. European Biophysics Journal, 2006
- [4] C. Alexiou et al., *Magnetic drug targeting - Biodistribution of the magnetic carrier and the chemotherapeutic agent mitoxantrone after locoregional cancer treatment*. Journal of Drug Targeting. 11(3): p. 139-149
- [5] C. Alexiou et al., *Locoregional Cancer Treatment with Magnetic Drug Targeting*. Cancer research, 2000. 60(23): p. 6641 - 6648
- [6] C. Alexiou et al., *Magnetic mitoxantrone nanoparticle detection by histology, X-ray and MRI after magnetic tumor targeting*. Journal of Magnetism and Magnetic Materials, 2001. 225(1-2): p. 187-193
- [7] O. Brunke et al., *Determination of the magnetic particle distribution in tumour tissue by means of x-ray tomography*. Journal of Physics: Condensed Matter, 2006. 18(38): p. S2903-S2917.
- [8] H. Rahn, I. Gomez-Morilla, R. Jurgons, Ch. Alexiou, S. Odenbach, *Micro computed tomography analysis of ferrofluids used for cancer treatment*. submitted to Journal of Physics: Condensed Matter, 2007

# Micro-CT studies of normal and pathological cranial sutures – a new insight

*Tobias Schmidt<sup>1</sup>, Julia Herzen<sup>2</sup>, Felix Beckmann<sup>2</sup>, Jan Regelsberger<sup>3</sup>*

<sup>1</sup> *Doctoral candidate at Department of Neurological Surgery, University of Hamburg, c/o University Hospital Hamburg-Eppendorf, 20246 Hamburg, Germany*

<sup>2</sup>*GKSS-Research Center, Max-Planck-Straße 1, 21502 Geesthacht, Germany*

<sup>3</sup>*Department of Neurological Surgery, University Hospital Hamburg-Eppendorf, 20246 Hamburg, Germany*

**Introduction:** Our present understanding of cranial suture biology is based on morphological studies, mainly recruited from rats and birds. Normal and pathological growth patterns in humans have been derived from these observations containing not proved assumptions. More detailed morphological analyzes of human sutures are still missing.

**Methods:** Histological investigations and microtomographic scans were performed to analyze five normal sutures at different time stages of the fusion process and five pathological synostotic sutures of different sites. Contrary to the customary micro-CT technique a unique synchrotron radiation source with a monochromator could have been used generating an exceptional high image resolution with 3D-reconstructions of the affected bones.

**Results:** Joint like bony edges of the normal sutures are seen in the first month of life interlocking with increasing age. At the age of 12 month bony thickness and suture width do not allow a further movement of the adjacent bony plates. Marked thickening of the diploe with ridging of the bone was only found in sagittal synostosis but not in coronal and lamdoid suture synostosis. On micro-CT all synostotic sutures turned out to show only partial fusions and moreover the ultrastructural features of the non-fused sections showed no differences compared to the normal sutures.

The specimens were imaged by microtomography in absorption mode utilizing synchrotron radiation at beamline BW2 at Hamburger Synchrotronstrahlungslabor HASYLAB at Deutsche Elektronen Synchrotron DESY (Hamburg, Germany) using 16 keV photon energy. The measured spatial resolution corresponded to 7.3 micrometers.

**Discussion:** Against previous assumptions partial fusions in suture synostosis may be the rule and seems to express a dynamic fusion procedure completing over time. Microtomographic analyzes of the non-fused sections in synostosis were unsuspecting compared to normal sutures. Therefore an early surgical correction in the very first months of life may be advisable to achieve a complete normalization of the abnormal head shape with a minimal effort and less invasiveness.

**Conclusion:** Microtomographic investigations of normal and pathological sutures were helpful to increase our knowledge of cranial suture pathology. Further electronmicroscopic and histochemical studies are now on their way to examine if very early and simple craniotomies could be as effective as the present complex reshaping procedures in suture synostosis.

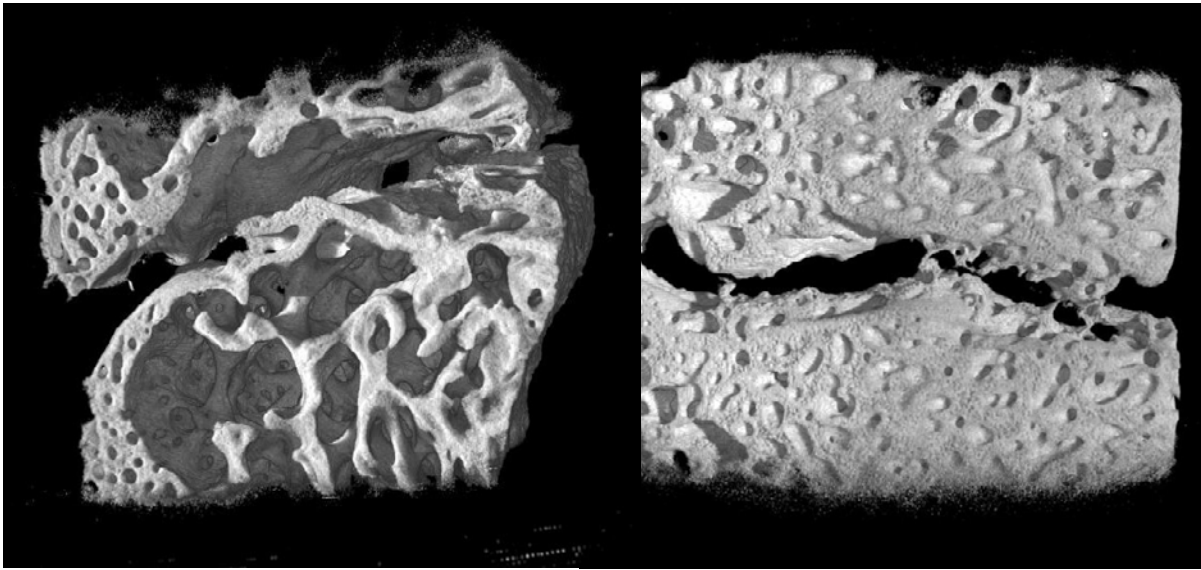


Figure 1 and 2: 3D reconstructed synchrotron-radiation based micro-computed tomography of a cranosynostotic sagittal suture in fusion process. The field of view of the CCD-detector was 7.5 mm x 5.2 mm.

## References

- [1] Anderson PJ, Netherway DJ, David DJ, Self P. Scanning electron microscope and micro-CT evaluation of cranial sutures in health and disease. *J Craniofac Surg.* 2006 Sep;17(5):909-19.
- [2] Ozaki, Wayne M.D., D.D.S.; Buchman, Steven R. M.D.; Muraszko, Karin M. M.D.; Coleman, Daniel Ph.D. Investigation of the Influences of Biomechanical Force on the Ultrastructure of Human Sagittal Craniosynostosis. *Plastic & Reconstructive Surgery.* 102(5):1385-1394, October 1998.

# Morphogenesis during asexual bud formation and growth in the poriferan *Tethya wilhelma*

J.U. Hammel<sup>1</sup>, J. Herzen<sup>2</sup>, F. Beckmann<sup>2</sup> and M. Nickel<sup>1</sup>

<sup>1</sup>Institut für Spezielle Zoologie und Evolutionsbiologie mit Phyletischem Museum, Friedrich-Schiller-Universität Jena, Ebertstr. 1, D-07743 Jena, Germany

<sup>2</sup>GKSS Forschungszentrum, Max-Planck-Str. 1, 21502 Geesthacht, Germany.

## Background

Sponges (Porifera) are sessile, filter feeding animals. They inhabit mainly the sea, but also a smaller number of fresh water species are known. Sponges are a comparatively old phylum in the context of evolution of multicellular animals. They are the oldest and most basal recent multicellular animals. Some sponges show distinct motions, which definitely seem to be coordinated. This is in contrast to the knowledge that these animals lack real muscle tissue and raises the question: How are contractions and coordination processes in sponges mediated? Sponges already evolved biochemical modules serving as building blocks for complex mechanical effector systems and integration systems. For this reason sponges are suitable model organisms to study the evolution of contraction systems leading to the development of muscles.

The highly contractile and locomotory poriferan *Tethya wilhelma* [1] is our model to investigate early evolved metazoan contractile tissues and coordination mechanisms [2]. Under laboratory conditions, the main reproduction mode of this sponge is asexual. Buds form at the tip of filaments protruding from the globular body of the mother sponge. The structural basis of the filaments is a dynamic composite of silica scleres and collagen, representing extensions of the radial skeleton bundles in this species [3]. During bud formation, a high number of cells, representing

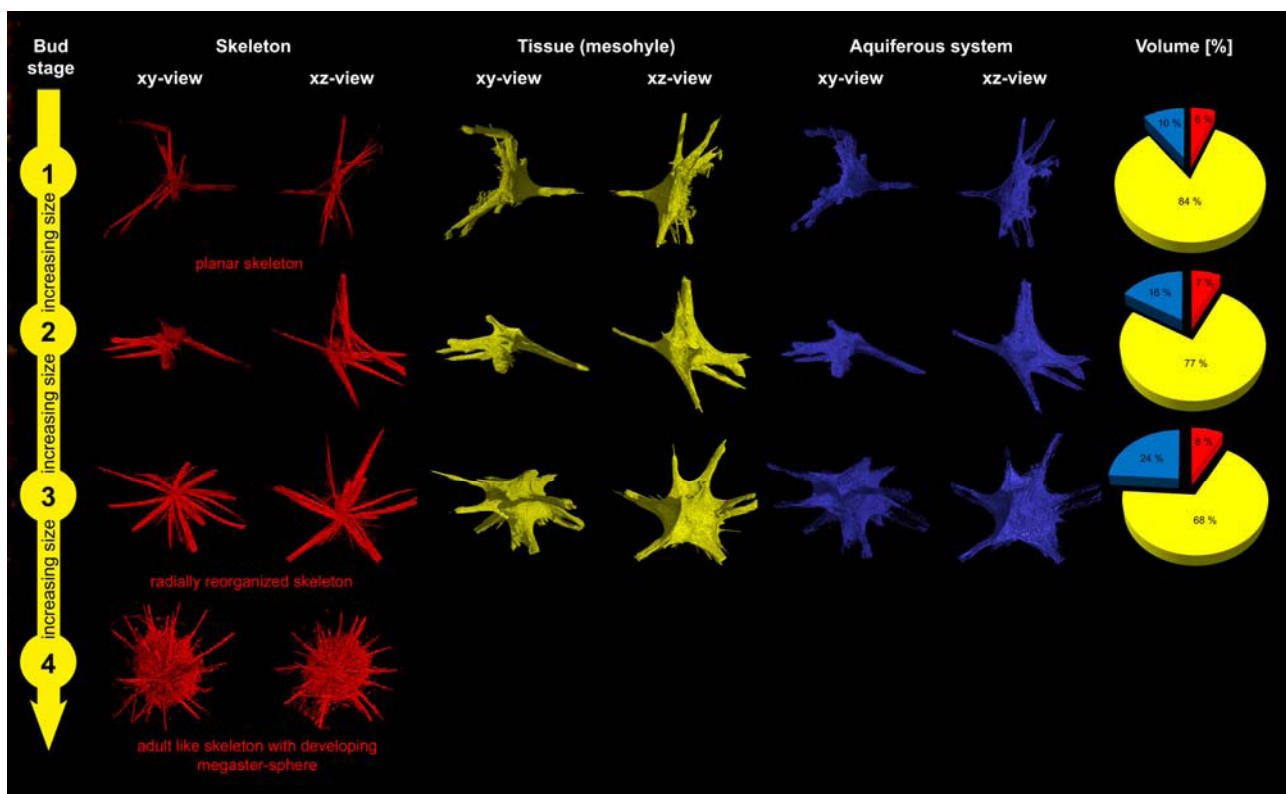


Figure 1. Segmented renderings of different stages of *T. wilhelma* bud development based on SR $\mu$ CT data from OsO<sub>4</sub>-fixed and dried specimens. Increasing bud size is correlated with further developed bud stages. Skeleton (red), sponge tissue (yellow) and aquiferous system (blue). Increasing bud size corresponds with



later bud stages. Proportions (%) of skeleton, sponge tissue and aquiferous system on slices of 2.99  $\mu\text{m}$  are given in the corresponding colours.

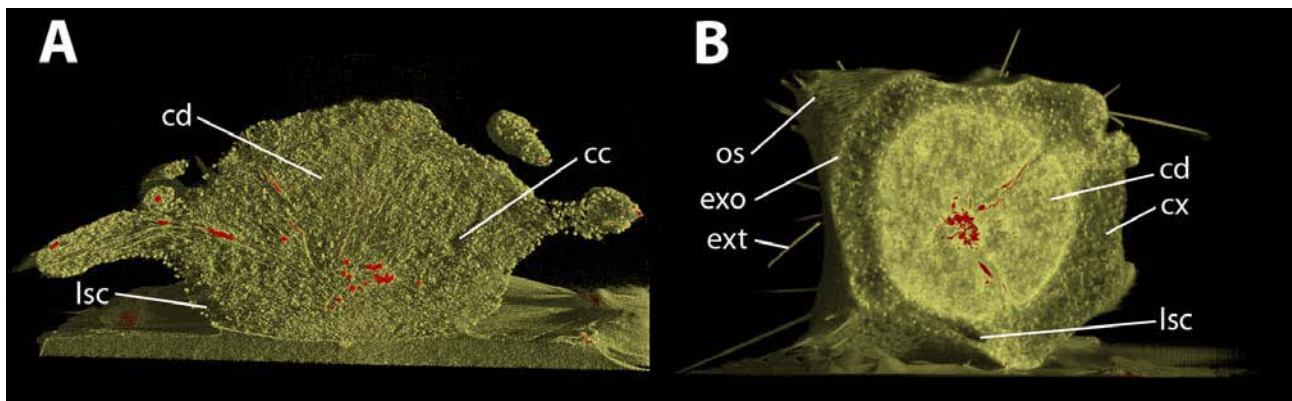


Figure 2. Rendering of SR $\mu$ CT data from OsO<sub>4</sub>-fixed and dried *T. wilhelma* buds, (A) early bud stage, (B) late bud stage, already detached from the mother sponge: sponge tissue (yellow), skeleton (red), choanoderm (cd), cortex (cx), current canal (cc), exopinacoderm (exo), body extension (ext), lacunar system cavity (lsc), ostia (os).

various cell types, migrate from the mother sponge along the filaments into the tips. All major spicule types of the siliceous skeleton are transferred into the bud, too and are arranged into the typical pattern of three skeletal superstructures of the adult sponge [3, 4] during growth of the bud. The analysis of the onset of contractile behaviour and response during bud development in correlation to the morphogenesis of the functional sponge body structures will help to understand the contractile effector systems. For this reason, we applied buds of different size and developmental stages to synchrotron radiation based microtomography studies to obtain detailed data on the organisation of skeleton elements, tissue differentiation and development of the aquiferous system.

### Methodology

Buds of *T. wilhelma* were collected from adult specimens kept in a tropical aquarium in our lab and subsequently frozen in liquid nitrogen. The buds were fixed via freeze-substitution in Methanol containing 1% OSO<sub>4</sub>, 2.5% Glutaraldehyde and 2.5 % H<sub>2</sub>O [4]. Samples were finally critical point dried. SR $\mu$ CT scans were performed at Hasylab Beamline BW2 at 11keV and 14.5 keV, yielding final resolutions of between 2.84  $\mu\text{m}$  and 3.01  $\mu\text{m}$  respectively.

### Preliminary results and outlook

With increasing bud size, the juvenile sponges change their habit from a more planar organisation to the globular shape of the adult organism, and the skeleton develops its typical megasclere bundles and megastar sphere (Fig.1). In addition, the aquiferous system starts to develop discrete channels and together with the differentiation of the tissue into cortex and choanoderm. The lacunar system can be observed at this point, too (Fig.1, Fig.2). Our results clearly shows that the juvenile sponges already display an almost adult like body organization [4] when they detach from the mother sponge.

The data sets obtained by SR $\mu$ CT at Hasylab Beamline BW2 allow for qualitative as well as quantitative 3D analysis of morphology during bud formation. in order to correlate them with preceded SR $\mu$ CT studies of adult sponges [3, 4]. The formation of defined body structures and skeletal superstructures will help to understand morphogenesis. In addition, this morphological knowledge will allow for pioneering new methodologies of genetic manipulation in sponges.

### References

- [1] M. Sarà, A. Sarà, M. Nickel, F. Brümmer, Stuttgarter Beiträge zur Naturkunde Serie A. 631: 1-15 (2001).
- [2] M. Nickel, Journal of Experimental Biology 209: 2839-2846 (2006).
- [3] M. Nickel, E. Bullinger & F. Beckmann, Zoomorphology 125: 225-239 (2006).
- [4] M. Nickel, T. Donath, M. Schweikert & F. Beckmann, Zoomorphology 125, 209-225 (2006).

# Morphological evaluation of a rat joint – epiphyseal cartilage and joint cartilage

R. Zehbe<sup>1</sup>, A. Halbe<sup>2</sup>, C. Brochhausen<sup>3</sup>, F. Beckmann<sup>2</sup>, J. Herzer<sup>2</sup>, U. Gross<sup>4</sup>, C.J. Kirkpatrick<sup>3</sup> and H. Schubert<sup>1</sup>

<sup>1</sup> TU Berlin, Institute of Materials Science and –technologies, Englische Str. 20, 10587 Berlin, Germany

<sup>2</sup> GKSS Research Center Geesthacht, Max-Planck-Str.1, 21502 Geesthacht, Germany

<sup>3</sup> Johannes Gutenberg University, REPAIRlab, Institute of Pathology –Langenbeckstr. 1, 55101 Mainz, Germany

<sup>4</sup> Charité University Medicine Berlin, Biomaterials Research, Assmanshauser Str.4-6, 14197 Berlin, Germany

The scientific investigation of the human body with respect to pathological anatomy probably dates back to Giovanni Battista Morgagni’s work from 1761, on “De sedibus et causis morborum per anatomem indagatis”. Nearly one century (1859) later, Virchow developed the concept of correlating tissue structure with its function in his work on “cellular pathology” [1]. Since this time, histology has become the principal and probably most fundamental characterization methodology in pathology-related science. Histological methodology requires tissue fixation, dehydration, paraffin embedding and finally sectioning into micrometer sized (4-5  $\mu\text{m}$ ) thin slices for light microscopical analysis. Light optical limitations, like refraction, are the principal limiting factors for sophisticated analysis of the three-dimensional tissue structure.

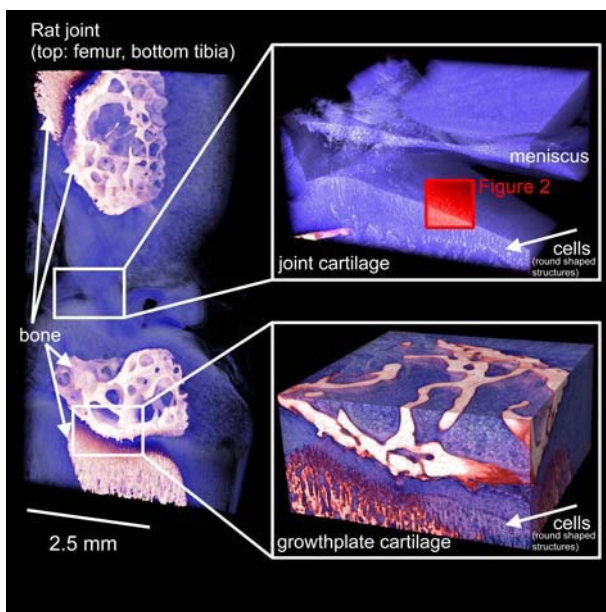


**Figure 1:** Three-dimensional representation of a joint (Sprague Dawley rat), showing joint- and epiphyseal cartilage

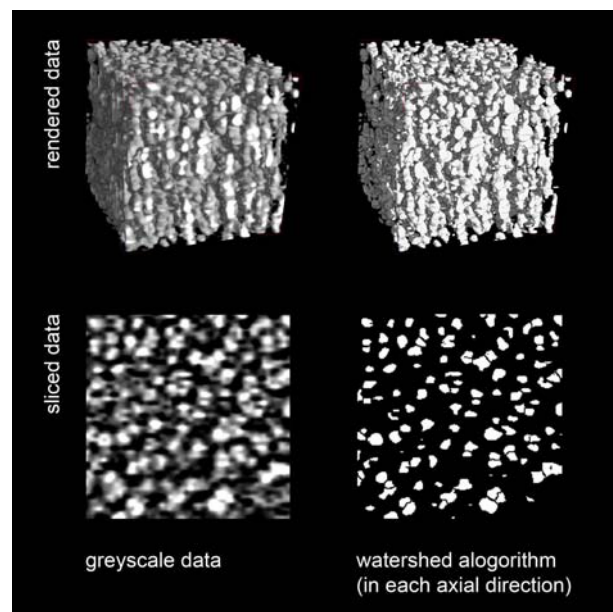


**Figure 2:** Cubic volume of joint cartilage showing the highly oriented cell distribution within the tissue

In X-ray-based analytical techniques, for example in micro computed tomography, the refractive limitations of matter, as found in native tissue, are less evident. Furthermore, due to the small wavelength of X-rays, tissue matter is nearly transparent for this radiation.

In 1989, Feldkamp et al. [2] pioneered computed tomography, investigating the three-dimensional structure of bone. Major progress in experimental setups became possible due to advancements in computer technology and in X-ray beam quality. Synchrotron beamlines as a source for X-rays with exceptional properties (e.g. high brilliance, high energy, monochromaticity and beam parallelism) opened up the possibility to investigate even soft tissues such as cartilage. Currently, both experimental constellations and subsequent computing capabilities achieve a quality and a spatial

resolution, which permit imaging of single cells in native tissues [3]. Therefore, this method is applicable to a quantitative analysis of the spatial distribution of cells inside a given tissue volume.

For a better differentiation between certain tissue components, especially cells versus extracellular matrix, a common approach is to label these components with metals [4, 5]. However, homogeneous metal labelling in large samples may be problematic due to diffusion limitations of the metal stain. Thus, the outer regions are highly contrasted, whereas the inner regions are lesser contrasted. Furthermore, metal labelling may introduce artefacts as a result of the great difference in absorption contrast of stained and unstained structures. Here, we demonstrate that metal labelling might not be necessary to analyze the spatial distribution of cells in native tissue.

A knee joint of a 4-week-old Sprague Dawley rat was characterized using the GKSS synchrotron micro computed tomography setup at the HASYLab beamline BW2. The joint originated from a previous histological study [6] showing both the articular cartilage region with the menisci as well as the region of the epiphyseal growth plate, with the adjacent tibia (bottom) and femur (top). The rat joint (Figure 1) was analyzed by absorption tomography at approximately 10 keV with an effective voxel size of 3.97  $\mu\text{m}$  using a  $\text{CdWO}_4$  scintillator. Due to the limited field of view in height, the SR- $\mu\text{CT}$  data was stitched from four subsequent tomographic measurements and was afterwards merged into a single data set. The data showed no major artefacts (e.g. ring artefacts).

Concerning cellular details, cells are detectable in both epiphyseal and articular cartilage (indicated by arrows in the expanded images of Figure 1). Exemplarily, a cubic volume from the joint cartilage part has been separated, saved as multi-image TIF-stack and then binarized using ImageJ (<http://rsb.info.nih.gov/ij/>). Finally, using ImageJ, we used the watershed algorithm on the entire TIF-stack in each axial direction to separate cell structures (Figure 2). The ImageJ 3D-object-counter plugin was used to analyze the volume of each object in the TIF-stack (Figure 3). The total volume fraction of cells was 12.75% with an average cell volume of 923  $\mu\text{m}^3$ . The resulting calculated cell density was  $1.38 \cdot 10^5$  cells/ $\text{mm}^3$ . This value is in line with data in the literature, assuming the cell densities between  $3.00 \cdot 10^4$  cells/ $\text{mm}^3$  and  $1.10 \cdot 10^5$  cells/ $\text{mm}^3$  measured by confocal microscopy [7].

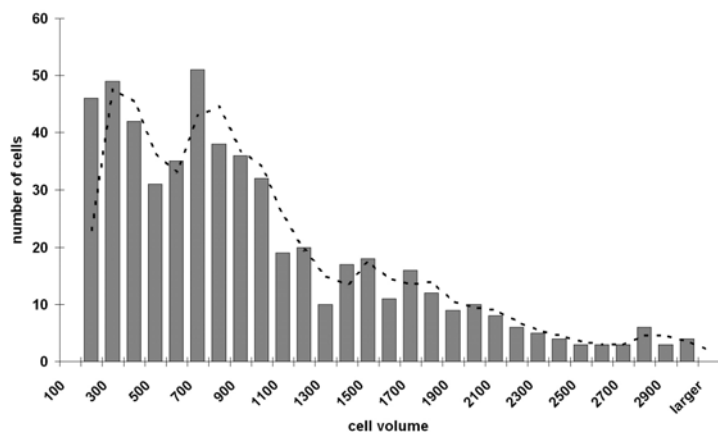


Figure 3: Histogram of cell volume in binarized Stack

## References

- [1] R. Virchow, Die Cellularpathologie in ihrer Begründung auf physiologische und pathologische Gewebelehre, Verlag von August Hirschwald, Berlin (1859)
- [2] L.A. Feldkamp, S.A. Goldstein, A.M. Parfitt, G. Jasion, M. Kleerekope, J Bone Min Res 4, 3-11 (1989)
- [3] R. Zehbe, C. Brochhausen, A. Haibel, S. Halstenberg, U. Gross, C.J. Kirkpatrick, H. Schubert, Tissue Engineering Research, Novapublishers 2008
- [4] R. Zehbe, A. Haibel, C. Brochhausen, U. Gross, C.J. Kirkpatrick, H. Schubert, Int J Mat Res 98, 562-568 (2007)
- [5] B. Müller, M. Riedel, P.J. Thurner, Microsc. Microanal. 12, 97-105 (2006)
- [6] C. Brochhausen, R. Zehbe, U. Gross, H. Schubert, C.J. Kirkpatrick, J Appl Biomat Biomech 5, 70-81 (2007)
- [7] M. Wong, P. Wuethrich, P. Egli, J Orthop Res 14(3) 424-432 (1996)



# Morphology of Osteoblast-Derived Histoids

*B. Saldamli<sup>1,2</sup>, J. Herzen<sup>3</sup>, F. Beckmann<sup>3</sup>, J. Tübel<sup>4</sup>, R. Burgkart<sup>4</sup>, H.-F. Zeilhofer<sup>2</sup> and B. Müller<sup>5</sup>*

<sup>1</sup>*Oral, Cranio-Maxillofacial and Facial Plastic Surgery, J.W. Goethe University, 60590 Frankfurt am Main, Germany*

<sup>2</sup>*Hightech-Research Center, University Hospital Basel, 4031 Basel, Switzerland*

<sup>3</sup>*GKSS-Research Centre, Max-Planck-Strasse 1, 21502 Geesthacht, Germany*

<sup>4</sup>*Department of Orthopedic Surgery, Klinikum rechts der Isar, TU Munich, 81675 Munich, Germany,*

<sup>5</sup>*Biomaterials Science Center, University of Basel, c/o University Hospital, 4031 Basel, Switzerland*

Cell cultures are established in vitro models for studying tissue related processes. For many decades cells have been cultivated just in monolayers on dishes. The importance of the third dimension for cell biology has been recently better understood. Human tissues are usually organized in three-dimensional (3D) space. The growing knowledge has attracted further attention to the 3D culturing of cells. The characterization of 3D cultures is often based on methods adapted from the ones established for monolayer cultures. These methods, however, encounter certain restrictions, especially when the 3D spatial organization has to be evaluated. Histological sectioning allows studying this aspect. Unfortunately, the extracted information is restricted to the rather arbitrarily selected slices. In addition, because of the destructive nature of this method, further studies on the samples are often impossible. Micro computed tomography using synchrotron radiation (SR $\mu$ CT) provides almost isotropic spatial resolution down to about 1  $\mu$ m, which corresponds to the sub-cellular level. Some pioneer studies have already successfully applied SR $\mu$ CT for the visualization and even quantification of biological meso- and microstructures [1, 2]. The aim of the present study was to explore the power of SR $\mu$ CT for the non-destructive characterization of scaffold-free 3D cell cultures termed histoids.

Primary human osteoblasts, isolated from femur neck spongy bone were expanded as 2D culture in non-mineralizing osteogenic medium. A thick cellular membrane with abundant matrix that lost partially surface contact formed. This was intentionally released and randomly folded. The histoid grew in non-mineralizing osteogenic medium during 80 weeks and reached a size of approximately 1 cm in diameter. Prior to characterization, the histoid was fixed in formalin, post-fixed with osmium tetroxide and embedded in paraffin.

SR $\mu$ CT in the absorption contrast mode at the beamline BW 2, HASYLAB at DESY, Hamburg, Germany, served for the visualization the internal microscopic structure of the histoid using a photon energy of 24 keV. To investigate the entire sample five tomographical scans were performed and registered after reconstruction. The reconstructed 3D volume consists of 1535 x 1535 x 2037 voxels, representing the volume of 8.2 x 8.2 x 10.9 mm<sup>3</sup>. The measured spatial resolution, determined by the modulated transfer function [3] corresponds to about 9.1  $\mu$ m at a voxel length of 5.3  $\mu$ m. Figure 1 shows three 2D slices through the reconstructed volume perpendicular to each other together with a 3D representation on smaller scale.

The SR $\mu$ CT yields details about the 3D spatial organization of the histoids. Information about the composition of the extra-cellular matrix, the cell morphology and the type as well as the cellular processes such as viability, proliferation and death, however, have still to be provided by histological methods. The SR $\mu$ CT is a non-destructive approach for the identification and selection of areas of interest in 3D space prior to histological sectioning. Our study of the millimeter-sized, scaffold-free histoids demonstrates that the micro-architecture and the features on the cellular level can be made visible and quantified in 3D space with high precision.

The project was partially funded by the Bayerische Forschungsstiftung and HASYLAB at DESY, Hamburg, Germany.

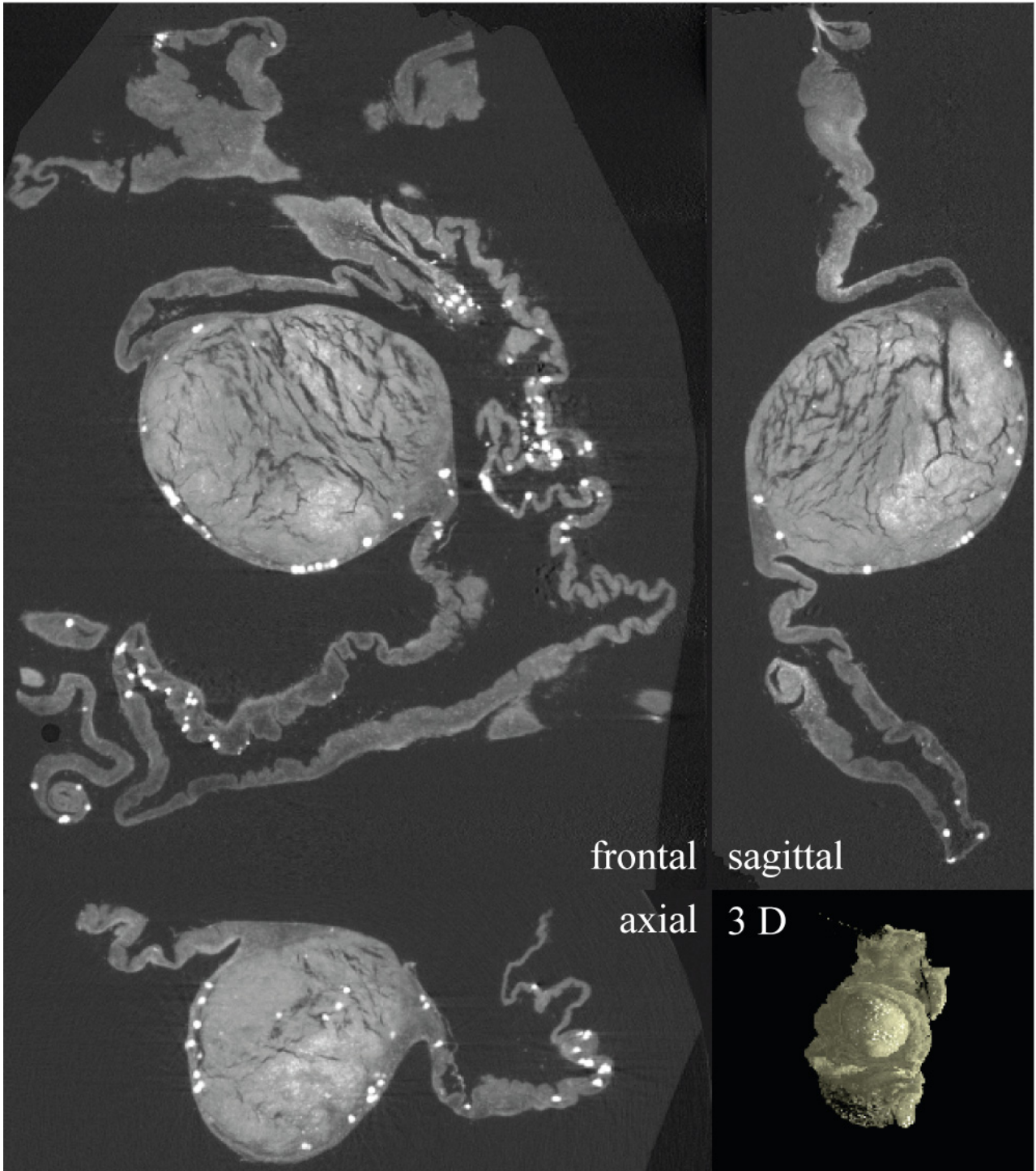


Figure 1: Frontal, sagittal, and axial SR $\mu$ CT-slices of the scaffold-free histoid. The 3D image, on the smaller scale, should give the reader an impression on the morphology of the histoid.

## References

- [1] B. Müller, P. Thurner and M. Riedel, *Microsc. Microanal.* 12, 97 (2006)
- [2] M. Dalstra, P.M. Cattaneo and F. Beckmann, *Orthod. Craniofacial Res.* 9, 199 (2006)
- [3] B. Müller et al., *Proc. SPIE* 4503, 178 (2001)

# Renal calculi microtomography

G.Taton, E. Rokita, A.Wrobel<sup>1</sup>, F. Beckmann<sup>2</sup>, P. Thor<sup>3</sup>, M.Worek<sup>4</sup>

Jagiellonian University Medical School, Department of Biophysics, Lazarza 16a, 30531 Cracow, Poland

<sup>1</sup>Jagiellonian University, Institute of Physics, Reymonta 4, 30059 Cracow, Poland

<sup>2</sup>GKSS-Research Center, Max-Planck-Straße 1, 21502 Geesthacht, Germany

<sup>3</sup>Jagiellonian University Medical School, Chair of Pathophysiology, Czysta 18, 31121 Cracow, Poland

<sup>4</sup>St. Lukas Hospital, Department of Urology, Lwowska 171a, 33100 Tarnów, Poland

The aim of the study was the investigation of renal calculi structure with the use of microtomography utilizing synchrotron radiation. Two problems are considered: (1) if the renal calculi developed in the first and second stage of nephrolithiasis episodes have similar microstructure and (2) what is the structure of stones which elemental composition is different from the average renal calculi population.

The renal calculi developed in the first and second nephrolithiasis episodes were collected from three patients in a standard medical procedure applied in nephrolithiasis (6 samples). A piece of the stones with dimensions suitable for the microtomographic measurements were prepared and measured.

Additionally the samples of renal stones with unusual elemental composition were chosen and prepared for measurements. The elemental composition was previously investigated by IR spectroscopy. The cases characterised by unusual concentrations of Mg, Ca and S were taken into consideration (5 samples). In this part of the study the structure as well as the density distributions will be studied so the density standard was also investigated. The standard was prepared as the pastille-sandwich made from 5 layers of substances observed in typical renal stones (uric acid, hydroxyapatite, struvite, cysteine and calcium oxalate).

Finally 12 samples were investigated (11 renal stone pieces and density standard). The beamline BW2 equipped with microtomographic scanning system was utilized. The energy of 21 keV was applied. Achieved image resolution was about 7.6  $\mu\text{m}$ . The 3D images of investigated samples were reconstructed. Achieved voxel size in reconstructed images is about 4  $\mu\text{m}$ . Samples of reconstructed images are presented in fig. 1 and fig. 2.

The quantitative analysis of collected data is in progress and its results will be reported in the future.

## Acknowledgement

*Work supported by the European Community - Research Infrastructure Action under the FP6 "Structuring the European Research Area" Programme through the Integrated Infrastructure Initiative "Integrating Activity on Synchrotron and Free Electron Laser Science" Contract RII3-CT-2004-506008 (IA-SFS).*

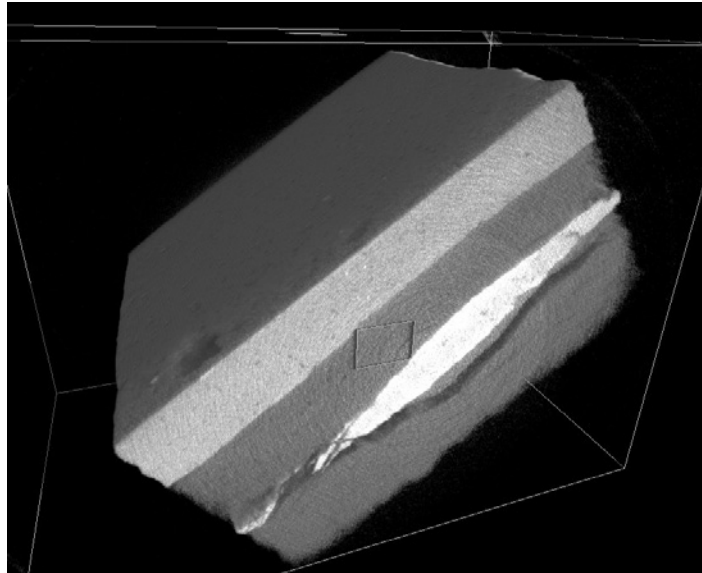


Figure 1: The reconstructed 3D image of investigated density standard. The structure of sandwich layers is well visible.

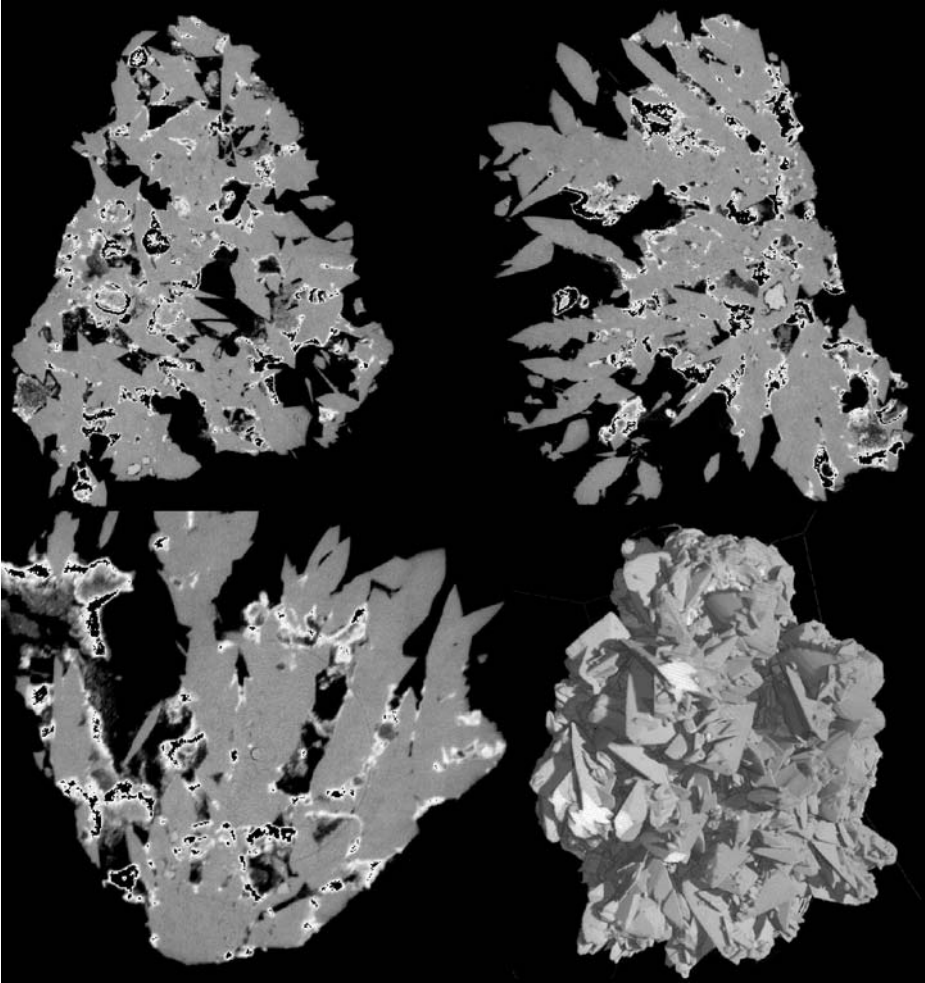


Figure 2: The reconstructed 3D image of a renal calculi sample and its cross sections in orthogonal directions.

# SR $\mu$ CT analysis of bone regeneration based on bio-mimetically coated scaffolds in critical size defects of the sheep tibia

R. Bernhardt, C. Rentsch<sup>1</sup>, B. Rentsch<sup>2</sup>, A. Breier<sup>3</sup>, A. Biewener<sup>1</sup>, F. Beckmann<sup>4</sup>, J. Herzen<sup>4</sup>  
D. Scharnweber, H. Zwipp<sup>1</sup>

Max Bergmann Center for Biomaterials Dresden, Technische Universität Dresden, Germany

<sup>1</sup>Department of Trauma and Reconstructive Surgery, University Hospital „Carl Gustav Carus“, Dresden, Germany

<sup>2</sup>Catgut GmbH, Markneukirchen, Germany

<sup>3</sup>Leibniz Institute of Polymer Research, Dresden, Germany

<sup>4</sup>Institute for Materials Research, GKSS Research Centre Geesthacht, Germany.

## Introduction

Posttraumatic or tumour related large defects in long bones are still a challenge to reconstructive surgery. The innovative idea of our project is to construct a Polycaprolactone-co-Lactide (PCL) cell scaffold, which has the shape of a spongy 3-dimensional disc. The scaffold should provide a temporary matrix for cell migration, proliferation and differentiation as well as interconnecting pores for vascularisation in critical size defects. An ideal filling of long bone defects of nearly any size will be provided by piling up scaffolds, which should be degraded over time and totally remodelled with new bone. To analyze the osteogenic and vascularisation potential we have coated the scaffolds with collagen type I (coll I) and chondroitin sulfate (CS), seeded ovine mesenchymal stem cell (oMSC) and investigated the formation of bone inside the scaffolds in a sheep model, which is close to human conditions in anatomy and weight bearing conditions.

To describe the formation of new bone with a high spatial resolution the synchrotron microcomputer tomography (SR $\mu$ CT) is a useful technique. Our aim is to detect and quantify mineral zones inside the explanted scaffold samples and correlate this information with the healing time, properties of the scaffold material and with histological findings.

## Material and Methods

Embroidered scaffolds of PCL were coated with coll I + CS, oMSC were seeded, and the so prepared constructs were implanted in a critical size defect in sheep tibia for 12 weeks. The bone defect was prepared by cutting out a 3 cm bone fragment and fixed to the tibia by medullar nailing (Fig. 1 A). X-ray controls were performed postoperative (Fig. 1 B) and at 8 and 12 weeks after surgery. For the SR $\mu$ CT-investigations and histological analysis segments of about 5 cm length, including the defect zone and stationary tibia bone, were prepared. With the GKSS SR $\mu$ CT-device

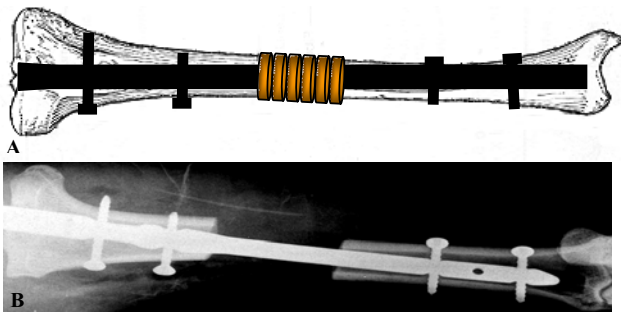


Figure 1: Scaffold implantation in critical size defect in sheep tibia. A: piled up scaffolds for defect filling in long bones, stabilized with a medullar nail (schematic image). B: postoperative x-ray of the defect zone in sheep tibia

at HASYLAB beamline BW2 a single tibia segment with a diameter of about 4 cm was investigated. The photon energy was set to 60 keV. With an optical magnification of 0.878 an image resolution of 27  $\mu$ m was reached. At least 5 positions along the defect zone were investigated using two 360° scans for each position.



## Results

Two of ten operated sheep showed a stable bone bridged defect. Three animals demonstrated a distinct formation of new bone, three confirmed a slight structure of new bone, and two sheep could not be evaluated because of osteosynthetic failure. Figure 2 shows the conventional CT data and histological staining of an explant from a sheep treated with coll I + CS scaffold implants. The visualisation from the SR $\mu$ CT investigation, shown in Figure 3, reveals tissue with different mineralisation degrees around and inside the scaffold.

Figure 2: First results of explanted sheep tibiae with implanted coll I + CS scaffolds A: 3D reconstruction of a clinical tomographic analysis of explanted sheep tibia, new bone is bridging the defect. B: van Goldner staining of defect zone green – bone matrix, red bone marrow (1.6 x magnification).

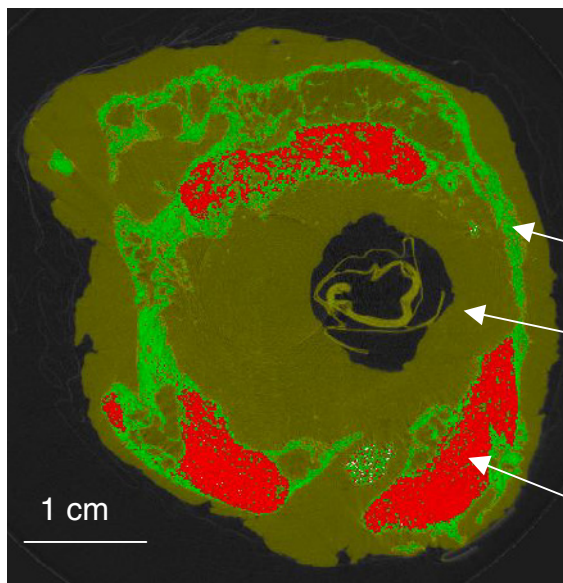
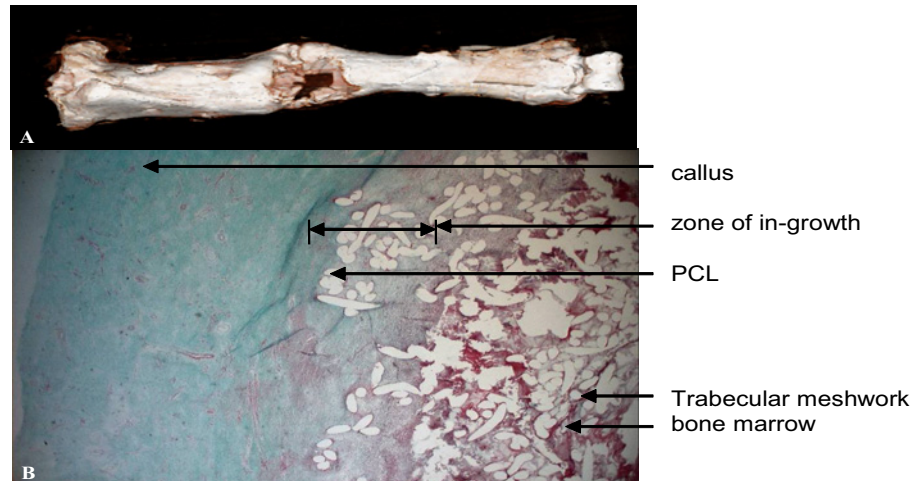


Figure 3: Reconstruction of absorption data for mineralised tissue from SR $\mu$ CT-measurements at GKKS beamline W2 using a photon energy of 60 keV.

- Bone structure with lower mineralisation degree
- soft tissue/scaffold
- Bone structure with higher mineralisation degree

## Conclusion:

The combination of conventional CT, SR $\mu$ CT, and histology allows the detailed analysis of tissue response to scaffolds in tissue engineering applications. The bio-mimetically coated scaffold qualifies as excellent bone tissue engineering implants, because (i) no repelling reaction to the material could be observed, (ii) no signs of necrosis were detected over the whole implant volume, (iii) substantial vascularisation was observed as a prerequisite for native bone regeneration, and (iv) significant bone regeneration occurred over large areas of the defect zone. With the SR $\mu$ CT-measurement, the formation of bony tissue could be visualised inside the scaffold. In addition the SR $\mu$ CT data have the advantage of a quantitative as well as a spatial analysis of bone formation in relation to the experimental conditions. However, the size of the sample was not optimal for SR $\mu$ CT-measurements. A separation of the tibia in two or four parts along the z-axis prior to the measurements will be considered for future experiments. This will also improve the overall resolution of the SR $\mu$ CT-information. The experiments are still in progress. The goal of our scaffold concept is to reach clinical application.

# SR $\mu$ CT-based study of external and internal structures of adults and larvae of Endopterygota (Hexapoda)

Frank Friedrich<sup>1</sup>, Hans W. Pohl<sup>1</sup>, Frank Hünefeld<sup>1</sup>, Felix Beckmann<sup>2</sup>,  
Julia Herzen<sup>2</sup> and Rolf G. Beutel

<sup>1</sup>Institut für Spezielle Zoologie und Evolutionsbiologie, FSU Jena, 07743 Jena, Germany

<sup>2</sup>GKSS-Research Centre, Max-Planck-Str. 1, 21502 Geesthacht, Germany

## Background

The investigations at DESY were carried out in the framework of an extensive phylogenetic project (DFG: BE 1789/4-1) aiming at the clarification of the relationships within the most species rich group of organisms, the holometabolous insects or Endopterygota (ca. 800.000 spp.) [1]. More than 30 ingroup taxa representing all conventional endopterygote orders and four outgroup taxa will be included in the phylogenetic analyses. With a combination of different traditional (dissection, histology) and modern techniques (SEM, CLSM,  $\mu$ CT), an extensive and well documented morphological data set will be compiled and finally combined with molecular data. Following a total evidence approach the phylogeny of Endopterygota will be reconstructed with cladistic software programmes and evolutionary scenarios will be developed on the basis of the results.

## Material and specimen preparation

Adults of Neuroptera (2 genera), Megaloptera, Hymenoptera, Trichoptera, Lepidoptera, Mecoptera, Siphonaptera, and Diptera were examined, and the larval head of *Nevrorthus* (Neuroptera). All specimens were either fixed in ethanol (70%, 100%) or FAE (Formaldehyde-ethanol-acetic acid) and critical point dried. Adults were cut into two halves at the anterior abdominal segments. Protruding structures such as wings antennae and legs were cut off near their base in order to minimise the field of view for a maximal scan resolution. The specimens were mounted on cylindrical metal carriers with superglue.

## Results

The synchrotron radiation based micro computed tomography (SR $\mu$ CT) applied to adult and immature specimens yielded results of superior quality, allowing a highly efficient computer based three dimensional reconstruction of external and internal features (Figs 1, 2). The maximum resolution obtained was 4.4 $\mu$ m. In contrast to experiments carried out at other institutions (e.g., Center for Synchrotron Radiation Research and Instrumentation [CSRRI], Illinois Institute of Technology) [2] it is possible to use a stable SR-beam at low photon energy (8 KeV) at the beamline BW2, which allows to discern different tissue types such as cuticle, musculature and elements of the nervous system very easily by its specific density. The distinctly different greyscales allow not only an efficient reconstruction of separate internal body parts (e.g. nervous system), but are essential for the morphological interpretation of complex structures.

## Outlook

SR $\mu$ CT is likely a key innovation in insect morphology and has the potential to trigger a major renaissance in this discipline. Most systematists agree that most reliable results are obtained with a combination of molecular data and an extensive and well documented set of morphological characters. The use of SR $\mu$ CT will contribute to a major progress in insect phylogeny in the near future.

## Acknowledgements

We gratefully acknowledge the opportunity to use the DESY facilities and the support of the Endopterygota project by the DFG (BE 1789/4-1).

## References

- [1] Beutel, R. G., and H. Pohl, H. Systematic Entomology, 31, 202-219, (2006)
- [2] Beutel, R. G., S.-Q. Ge, and T. Hörschemeyer, T. Cladistics, (online early)

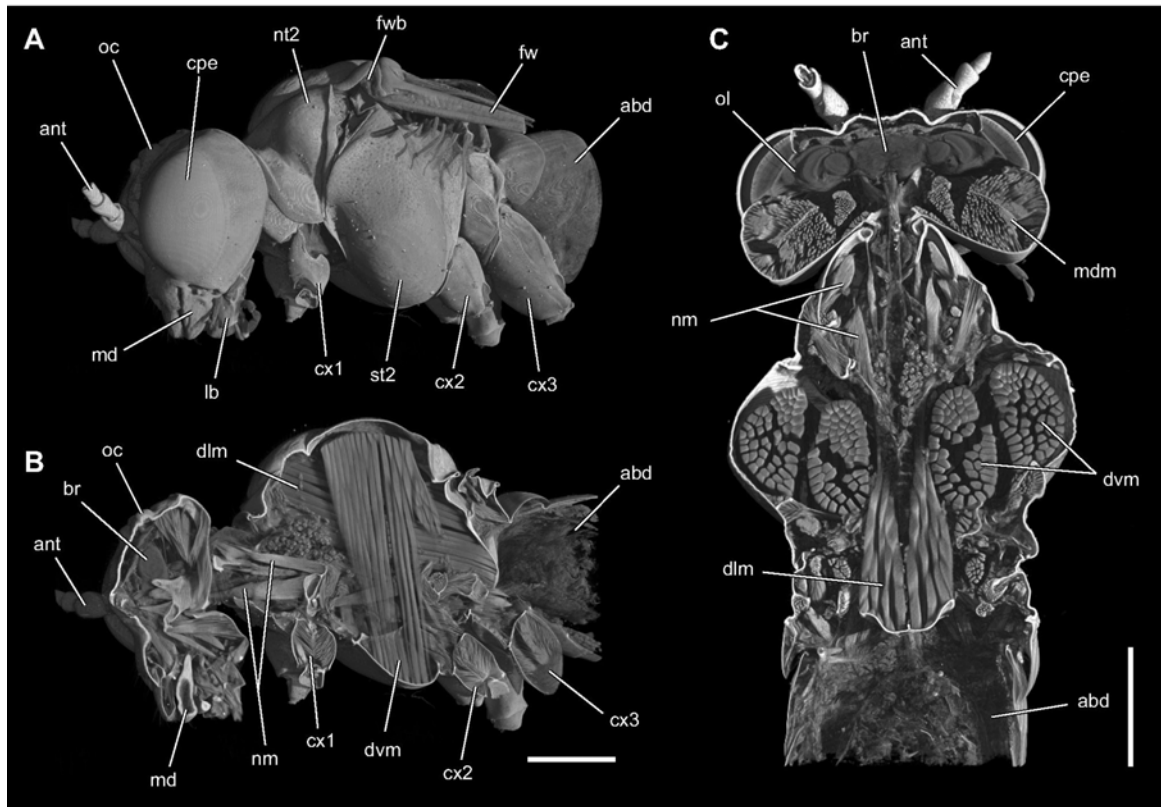


Figure 1: External and internal anatomy of the head and thorax of the sawfly *Tenthredo vespa*. Reconstruction based on SR $\mu$ CT data (2x binned) using myVGI. **A.** Lateral view. **B.** Sagittal section. **C.** Horizontal section. abd – abdomen, ant – antenna, br – brain, cpe – compound eye, cx1/2/3 – pro-/meso-/metacoxae, dvm/dlm – dorso-ventral and dorsal longitudinal parts of indirect flight muscles, fw – fore wing, fwb – fore wing base, lb – labium, md – mandible, mdm – mandibular muscle, nm – neck muscles, nt2 – mesonotum, ol – optical lobes of the brain, oc – ocellus, st2 – mesosternum. Scale bar: 1mm.

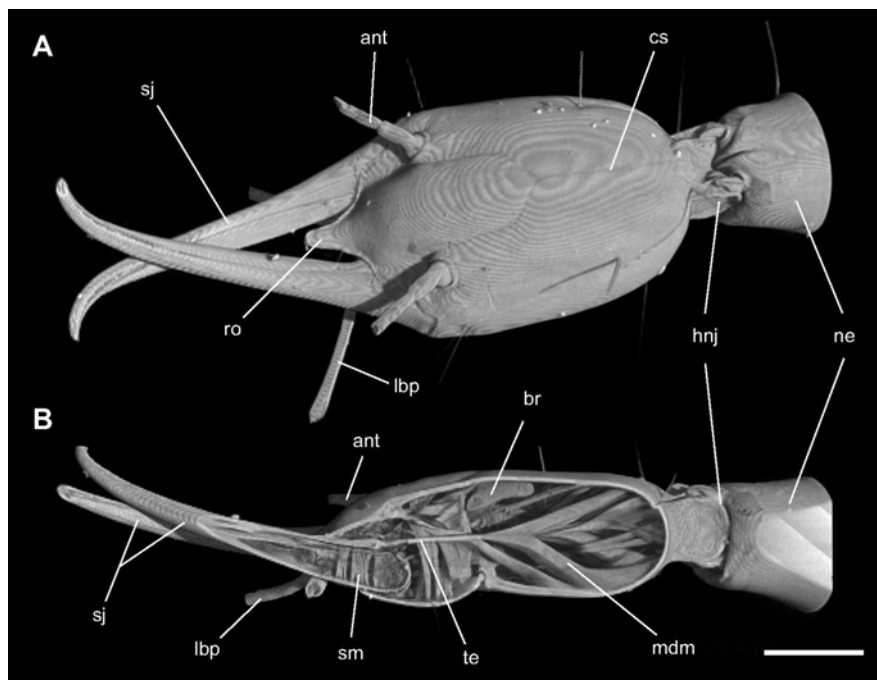


Figure 2: Head of the minute aquatic larva of *Nevrorthus* (Neuroptera). Reconstruction based on SR $\mu$ CT data (2x binned) using myVGI. **A.** Dorsolateral view. **B.** Sagittal section. ant – antenna, br – brain, cs – coronal suture, hnj – head-neck joint, lbp – labial palp, mdm – mandibular muscle, ne – neck, ro – rostrum, sj – sucking jaw, sm – sucking muscles, te – tendon. Scale bar: 500 $\mu$ m.



# Structural Investigations of Artificial Bone

M. Strobl<sup>1</sup>, C. Ritzoulis<sup>2</sup>, G. Choinka<sup>1</sup>, C. Tsiptsias<sup>3</sup>, V. Vasilakos<sup>3</sup>, C. Panayiotou<sup>3</sup>, F. Beckmann<sup>4</sup>,  
J. Herzen<sup>4</sup> and T. Donath<sup>4</sup>

<sup>1</sup>Hahn-Meitner Institute, Glienickerstrasse 100, D14109 Berlin, Germany

<sup>2</sup>ATEI of Thessaloniki, PO Box 141, 57400 Thessaloniki, Greece

<sup>3</sup>Aristotle University of Thessaloniki, University Campus, Greece

<sup>4</sup>Institute for Materials Research, GKSS-Research Center, 21502 Geesthacht, Germany

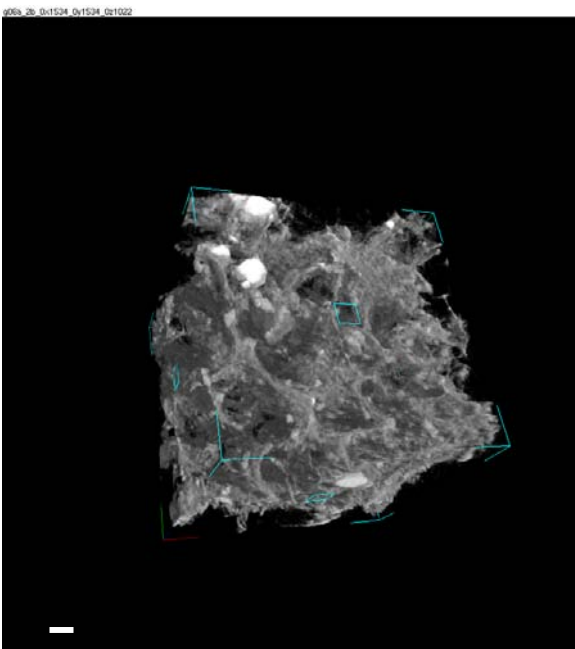
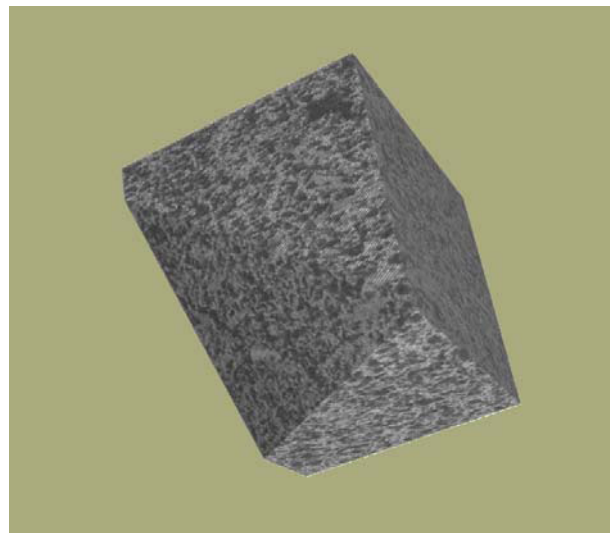
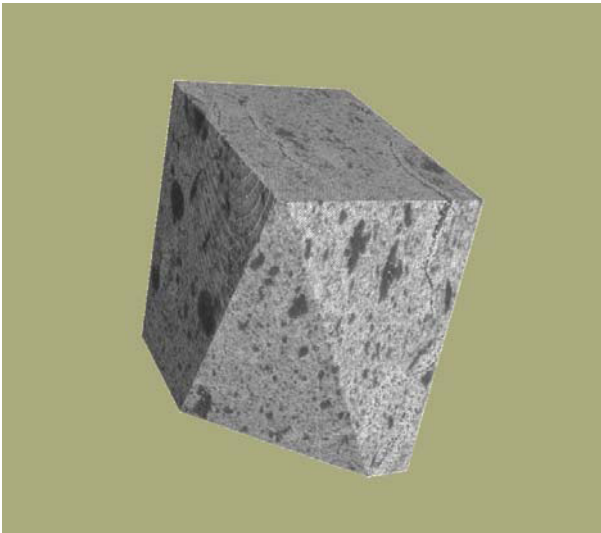
Artificial bone made of calcium-rich milk protein sodium caseinate and bone-compatible mineral hydroxyapatite, designed for utilization as artificial bone substitute, has been subjected to imaging/tomography at beamline BW2. The samples have been prepared by means of a micro-templating process [1].

The samples studied contain either only one population of pores (one below 10 microns or one at some tens of microns) (“monomodals”), or both populations (“bimodals”), the latter being a necessary pre-requirement for the application of such materials as bone substitutes. Previous experiments held using the double crystal diffractometer V12a at HMI / BENSC provided a useful insight in terms of data on the bone porosity in the 0.1–10  $\mu\text{m}$  region [2]. The experiments of the present session focus on the characterization mainly of the larger pores, and the tomographic examination/rendering of the entire structure in the micron scale.

A first analysis of the tomographic data provided three-dimensional information on our visually opaque samples, which is not feasible with other methods, such as SEM or confocal microscopy. The results verify the co-existence of two distinct pore populations, one in the order of <10 microns, one in the order of some tens of microns. Valuable information has been obtained concerning the pore volume fraction and size distribution. Correlation of this information with the process conditions for each sample can aid the amelioration/optimization of the materials manufacture and their final properties.

An additional point of interest has been the verification of the interconnectivity of the pores, manifested as a bicontinuous solid – gaseous network. This interconnectivity between the tens-of-microns-sized pores is essential, as to allow the bone-reinforcing cells to move through the structure.

As the interpretation/quantification of the data continues, the proposers believe that this project has been successful in its aims, providing valuable information on the structure and composition of this new and potentially useful biomedical application. A submission for publication of the above results is currently underway.



Figures: Top: Two representative samples with different pore size distributions. Bottom: left: Tomographic rendering for a bi-continuous network of artificial bone + bimodal pores; right, typical pore size distribution for a sample with a bimodal size distribution. The bar stands for approximately 40 microns.

## References

- [1] C. Ritzoulis, N. Scoutaris, K. Papademetriou, S. Kokkou S., S. Stavroulias S. and C. Panayiotou  
J. Biomed. Mat. Res. A 71, 675 (2004)
- [2] M. Strobl, W. Treimer, C. Ritzoulis, A. G. Wagh, S. Abbas, I. Mankeb J. Appl. Cryst. 40, s1-3 (2007)

## Acknowledgement

The authors would like to acknowledge the valuable assistance and support received from the GKSS group.

# Synchrotron based high resolution X-ray computed microtomography of freeze dried amphibians

*T. Kleinteich and A. Haas*

*Biozentrum Grindel und Zoologisches Museum Universität Hamburg, Martin-Luther-King-Platz 3,  
20146 Hamburg, Germany*

Evolutionary research in biology relies on the comparison of different individuals of different species in order to explore the history of today's biodiversity. The applications of synchrotron based high resolution X-ray computed microtomography ( $\mu$ CT) in the comparative field of evolutionary biology are virtually infinite (for examples see [1]). In this study, we use  $\mu$ CT imaging to investigate the evolution of a particular group of amphibians; caecilians.

Caecilians (scientific name: Gymnophiona) are limbless, fossorial amphibians. The Gymnophiona comprise 171 species that are restricted to the tropics [2]. Caecilians show a variety of feeding modes during development (suction feeding, biting, rasping; [3], [4]). This project focuses on the anatomical and functional demands of different feeding modes on caecilian skulls and head muscles. It was necessary to have  $\mu$ CT datasets of different developmental stages and to collect  $\mu$ CT data from different species for comparison.

$\mu$ CT data of adult caecilians (4 individuals; 4 species) was collected within 72 h at beamline W2; developmental stages (6 specimens; 3 species) have been  $\mu$ CT scanned at beamline BW2 in a 48 h shift. The specimens had been decapitated and their heads were freeze dried prior to the  $\mu$ CT imaging procedure. Because the lengths of the samples exceeded the area that could be penetrated by the X-ray beam at once, several scans were performed for different regions of the specimens; the separate datasets were combined afterwards.

The resulting datasets show high detail in hard and soft tissues. The resolution of the  $\mu$ CT data (voxel-sizes) ranges from 2  $\mu$ m to 9  $\mu$ m, depending on the size of the sample. Single muscle fibers, nerves, and connective tissues can be identified in the datasets. The richness in detail of our datasets is significantly higher, especially within soft tissues, than in any previously published vertebrate  $\mu$ CT scan (e.g. [5] and references therein).

The  $\mu$ CT data was used for the comparison of caecilian anatomy in different species and developmental stages (Fig. 1A, B). The jaw closing musculature shows notable differences in the topographic relationships to other muscles and to the squamosal bone. The musculature that acts on the hyobranchium (i.e. gills and gill arches) in aquatic caecilians is well developed and covers the ventral and lateral side of the caudal head region; in caecilians that capture their prey by biting or that receive their nutrition by rasping, the hyobranchial musculature comprises less muscles and covers only the ventral side of the animal. A muscular tongue is absent in aquatic developmental stages but present in all other investigated specimens.

Physical models of the skulls of 3 specimens have been created using a rapid prototyper with the  $\mu$ CT datasets as input data (Fig. 1C; cooperation with Dr. Adam Summers, UC Irvine). The models are up scaled in size and can easily be manipulated by hand. Interacting with the physical models gives new insights into the functional anatomy of caecilian heads. It is possible to interactively explore the degrees of freedom for movements of different bones in caecilian skulls.

The high detail within soft tissues, especially musculature, of the  $\mu$ CT data made it possible to automatically measure the angles of muscle fibres in caecilians. The muscle fibre angles can be used in a lever arm model to estimate bite forces in the caecilian jaw closing mechanism.

Results that were based on the  $\mu$ CT datasets have been presented in a talk at the International Conference on Vertebrate Morphology (ICVM) in Paris [6] and in a seminar talk at the Museum of Vertebrate Morphology at UC Berkeley (MVZ).

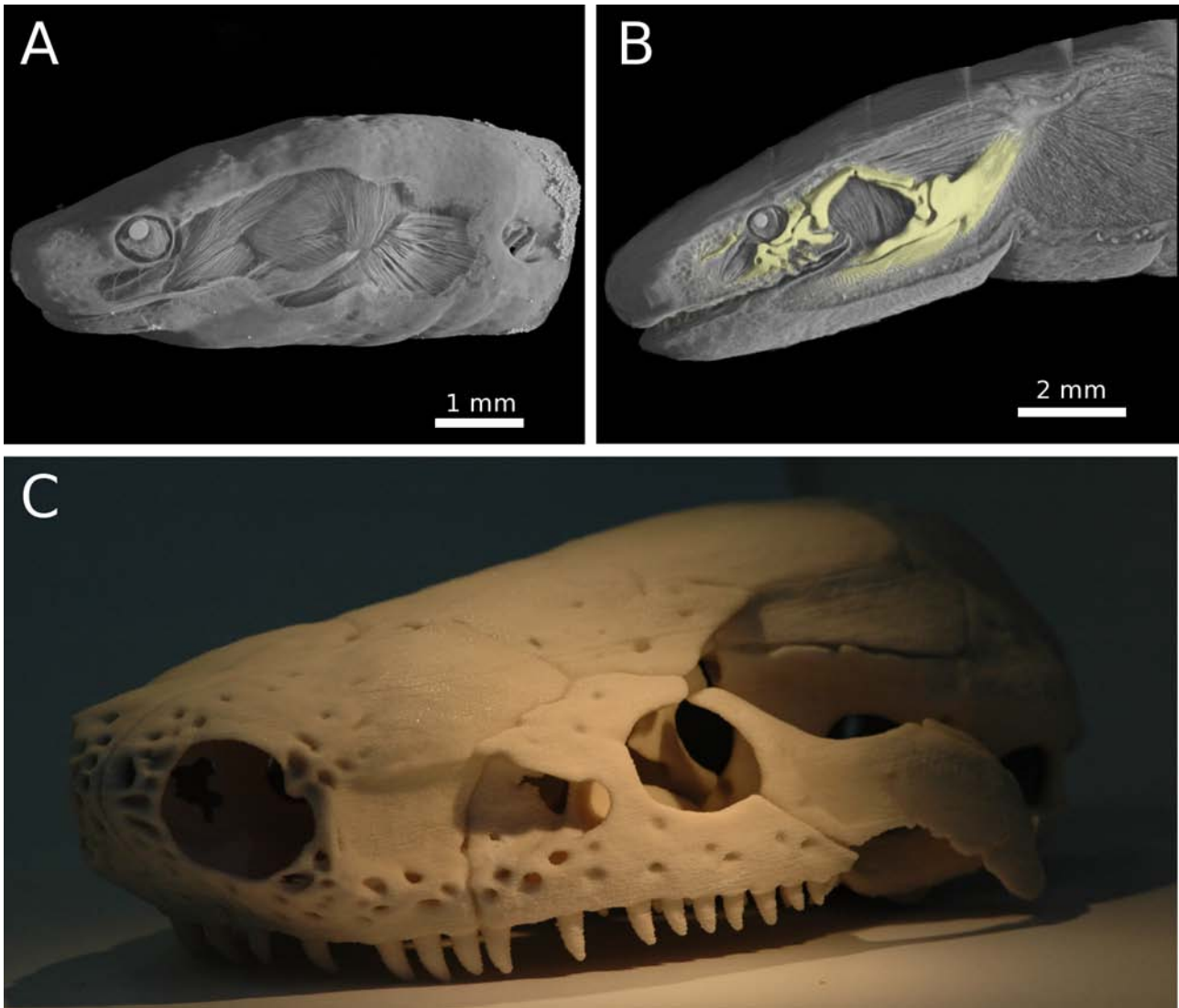


Figure 1:  $\mu$ CT data in the study of caecilian evolution. A: Lateral view of a larval specimen of *Ichthyophis kohtaoensis* (specimen ZMH A08978; GKSS-ID: zim10); skin partially removed. B: Lateral view of an adult specimen of *I. kohtaoensis* (ZMH A08981; zim03); different planes of section for soft tissues and cranial bones. There are notable differences in the orientation and the presence of muscles between larva and adult within the same species. C: Physical model of an adult *Typhlonectes natans* (ZMH A08984; zim02) generated by rapid prototyping. The model is up scaled in size and can easily be manipulated by hand.

## References

- [1] O. Betz, U. Wegst, D. Weide, et al., *J. Microsc.* 227, 51–71 (2007)
- [2] D.R. Frost, *Amphibian Species of the World: an online reference*. Version 5.1 (2007)
- [3] S.M. Deban, J.C. O'Reilly, K.C. Nishikawa, *Am. Zool.* 41, 1280–1298 (2001)
- [4] A. Kupfer, H. Müller, M.M. Antoniazzi, et al., *Nature* 440, 926–929 (2006)
- [5] Digital Morphology Group, University of Texas, <http://www.digimorph.org> (2007)
- [6] T. Kleinteich, *J. Morphol.* 268, 1093 (2007)

# Vessel Tree Visualization with Synchrotron Radiation-based Micro Computed Tomography

Marco Dominietto, Sebastian Friess<sup>1</sup>, Silke Grabherr<sup>2</sup>, Julia Herzen<sup>3</sup>, Felix Beckmann<sup>3</sup>, and Bert Müller<sup>4</sup>

*Institute for Biomedical Engineering, ETH Zürich, Wolfgang Pauli-Str. 10, 8093 Zurich, Switzerland*

*<sup>1</sup>Gloor Instruments AG, Brauereistrasse 10, 8610 Uster, Switzerland*

*<sup>2</sup>Institut de Médecine Légale, Centre Hospitalier Universitaire Vaudois, Rue du Bugnon 21, 1005 Lausanne, Switzerland*

*<sup>3</sup>GKSS-Research Centre, Max-Planck-Strasse 1, 21502 Geesthacht, Germany*

*<sup>4</sup>Biomaterials Science Center, University of Basel, c/o University Hospital, 4031 Basel, Switzerland*

The 3D visualization of vascular networks applying contrast agents and taking advantage of micro computed tomography is of prime importance in angiographic studies, especially for assessing phenotypes of genetically modified mice or for examining tumor tissues. In the present study we compare the established barium sulfate stain [1] with a very recently developed iodine-based, oily contrast agent termed Angiofil® [2]. Using the liquid Angiofil® one avoids the sedimentation often observed in suspensions with the dense and heavy salts [1], which is reflected in the images by non-connected vessels. The possibility to tailor the viscosity of the Angiofil® changing the ratio with its solvent should lead to the selective, caliber depending demonstration of the vessels. The oily contrast agent is expected to remain in the vessels without penetrating through the walls. Angiofil® is also an alternative to casting using for example polyurethane-based systems [3]. Note that casting is a time-consuming procedure, which often fails to maintain the entire vascular network including capillaries.

Two female nude mice (Balb/c), weight 24 to 26 g, were used in strict adherence to the Swiss law for animal protection. The animals administrated with a mask face were anesthetized using isoflurane (3%). The contrast media were injected into the tail vein of the mouse. The first contrast agent was a suspension made of 15 g barium sulfate and 200 ml physiological solution. The suspension was filtered (BD Falcon, USA, pore size 40  $\mu\text{m}$ ,) in order to inject a volume of 500  $\mu\text{l}$  only containing particles with dimensions comparable to the diameters of micro-vessels. Just before the injection the suspension was mixed at the temperature of 37 °C for a period of 10 min (Sonorex Digital 10P, Bandelin). The second contrast agent was the solution of 20  $\mu\text{l}$  Angiofil® and 60  $\mu\text{l}$  solvent.

Using the barium sulfate suspension, the mouse survived and, thus, it was sacrificed after about 5 min. Because of the solvent used for the Angiofil® staining, the mouse died after about 2 min. Subsequent to the procedures, several organs, namely brain, lungs, heart, liver, spleen, and kidneys were isolated to study the metabolism of the two contrast agents. For the  $\mu\text{CT}$  experiments the tissues were fixed in 4% para-formaldehyde and transferred into Eppendorf containers for the  $\mu\text{CT}$  measurements.

For each tissue sample one projection was acquired to check the presence of the contrast agent in the vessels. We found that only the lungs were well filtrated with the contrast agents. In the case of barium sulfate this is explained by the size of the salt particles, which corresponds to values between 1 and 40  $\mu\text{m}$  and is, therefore, often larger than the arterial capillaries. Consequently, the lung may act as ‘physiological filter’ for particles larger than 5  $\mu\text{m}$ . In the case of Angiofil® big emboli into the heart chambers were detected, which probably caused the death of the mice and prevented significant flow via the arteries to the other organs.

The synchrotron radiation-based micro computed tomography (SR $\mu\text{CT}$ ) measurement of the barium sulfate stained lung was carried out at the beamline W 2, operated by the GKSS-Research Center, using the photon energy of 38 keV. This value is just above the K-edge of barium. Therefore, we

have found lower absorption values for the photon energy of 32 keV, indicating rather high amounts of barium are present in the mouse lung. The pixel length corresponded to  $6.8 \mu\text{m}$ . The spatial resolution of  $13.7 \mu\text{m}$  was determined by means of the modulated transfer function. The 3D dataset of the lung (see Figure 1) was obtained combining 5 tomograms at different heights each by means of the standard filtered back-projection reconstruction algorithm out of 720 projections. The SR $\mu$ CT of the Angiofil®-stained lung was performed at the beamline BW 2 using again 721 projections, the photon energy of 17 keV and the pixel size of  $7.0 \mu\text{m}$ .

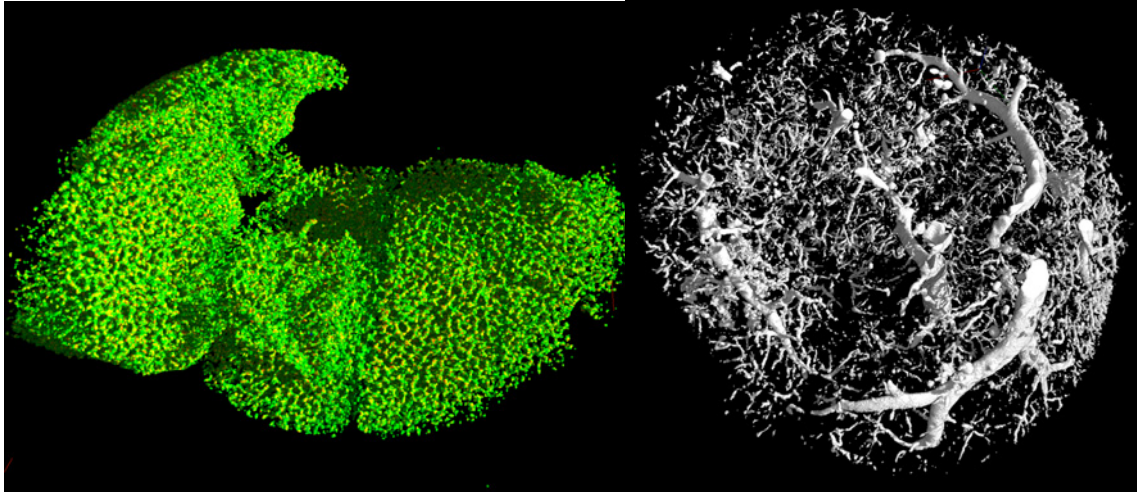


Figure 1: SR $\mu$ CT-based 3D visualization of mouse lungs perfused with barium sulfate micro-particles (left) and Angiofil® (right). The images are generated by means of the software VGStudio Max 1.2 (Volume Graphics, Heidelberg, Germany).

## References

- [1] B. Müller et al., Nucl. Instr. Meth. B 246, 254 (2006)
- [2] S. Grabherr et al., Microsc. Res. Techn. submitted (2007)
- [3] T. Krucker et al., Microsc. Res. Techn. 69, 138 (2006)

# Visualizing the Root-PDL-Bone Interface – The Key to Understanding Alveolar Bone Remodelling

*M. Dalstra, P.M. Cattaneo, J. Herzen<sup>1</sup> and F. Beckmann<sup>1</sup>*

*Dept. of Orthodontics, University of Aarhus, Vennelyst Boulevard 9, 8000 Aarhus C, Denmark*

*<sup>1</sup>GKSS Research Center Geesthacht, Max-Planck-Str. 1, 21502 Geesthacht, Germany*

The root-PDL-bone (RPB) interface is important for a correct understanding of the load transfer of masticatory forces and orthodontic loads from the teeth via the periodontal ligament and the alveolar bone to the rest of the jaw. For the approximation of the magnitude of the contact stresses between root and bone for a given load applied to a tooth normally a smooth ellipsoidal RPB surface is assumed, but how valid is this assumption really? It is the aim of this study to assess the three-dimensional structure of the RPB interface in human material using high-resolution micro-tomography.

The experiments which could be performed in 2007 are part of a larger project to study the 3D structure of alveolar bone in human jaw segments [1,2,3]. For the experiments a human mandibular jaw segment, obtained at autopsy from a 22 year old male donor was available. The segment contained two premolars and two molars and it was embedded in a block of methylmetacrylate ( $\varnothing$  28 mm, height 30 mm) for conservation purposes. The block was first scanned as a whole using the microtomography device of GKSS at beamline W2 with a photon energy of 64 keV. Normally, tomographical scans are performed with this device by acquiring 720 X-ray attenuation projections equally stepped between 0 and  $\pi$ . However, as the width of the sample was larger than the field of view of the detector, a special scanning technique had to be used. The detector was set to a field of view of 14.7 mm x 9.8 mm (width x height), pixel size 9.6  $\mu$ m, and a measured spatial resolution of 31.4  $\mu$ m. The rotation axis was set near the border of the detector and the scan was performed obtaining radiograms between 0 and  $2\pi$ . Before reconstruction the projections of  $0 \dots \pi$  and  $\pi \dots 2\pi$  were combined to build one tomographical scan from  $0 \dots \pi$  for the entire scanned height. This procedure had to be repeated at 7 slightly overlapping heights to cover the full length of the sample. Finally, a back-filtered projection algorithm was used to obtain the 3D data of the X-ray attenuation for the entire sample. After this scanning session, the block containing the sample was trimmed to allow easy access to the first molar. This tooth and its surrounding bone were then removed with a 10mm hollow core drill. From the resulting cylindrical sample 6 smaller samples of the RPB complex (2 from the mesial surface, 2 from the distal surface and 2 from the interradiolar area) were drilled out in the buccolingual direction with a 1.5mm hollow core drill. These samples were subsequently scanned at beamline BW2 with a photon energy of 19 keV. The detector was set to a field of view of 2.24 mm x 1.49 mm (width x height), pixel size 1.5  $\mu$ m, and a measured spatial resolution of 4.1  $\mu$ m. Also here, scanning had to be repeated at 6 or 7 slightly overlapping heights to cover the full lengths of the samples and a back-filtered projection algorithm was used to obtain the 3D data of the X-ray attenuation for the entire sample.

Using synchrotron radiation as an X-ray source has the advantage that the gray values of the scans are a direct reflection of the densities of the scanned tissues. Therefore not only could a clear distinction between enamel, bone, dentine and cementum be made, but also between areas within bone with different degrees of mineralization. The scans of the entire segment showed alveolar bone with a thin lamina dura, often not thicker than the PDL, supported by an intricate trabecular network (Figure 1). Although featuring many openings between the PDL and the bone marrow on the other side to allow blood vessels to transverse, the lamina dura seems smooth at this resolution. First at high resolution, however, it becomes evident that in fact it is not, but is irregular with bony spiculae and pitted surfaces (Figure 2). Microfractures (most likely due to the drilling process) also become visible at this magnification and seem to occur at sharp corners of the bony surface and then follow osteonal boundaries. This leads to the conclusion that the magnitude of the stresses in the bone can be much higher than would be expected from a smooth continuous alveolus and this might explain why tooth movement can be achieved with even low orthodontic forces.



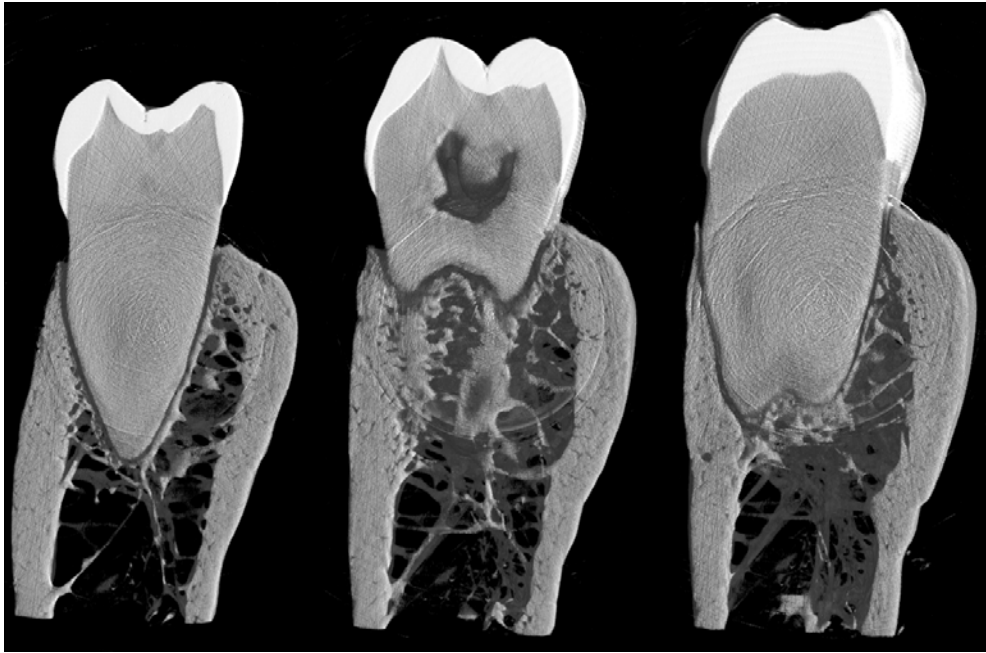


Figure 1: Cross-sections through the distal root (left), the interradicular area and the mesial root (right) of the first molar. Note the thin lamina dura of the alveolus surrounding the roots.

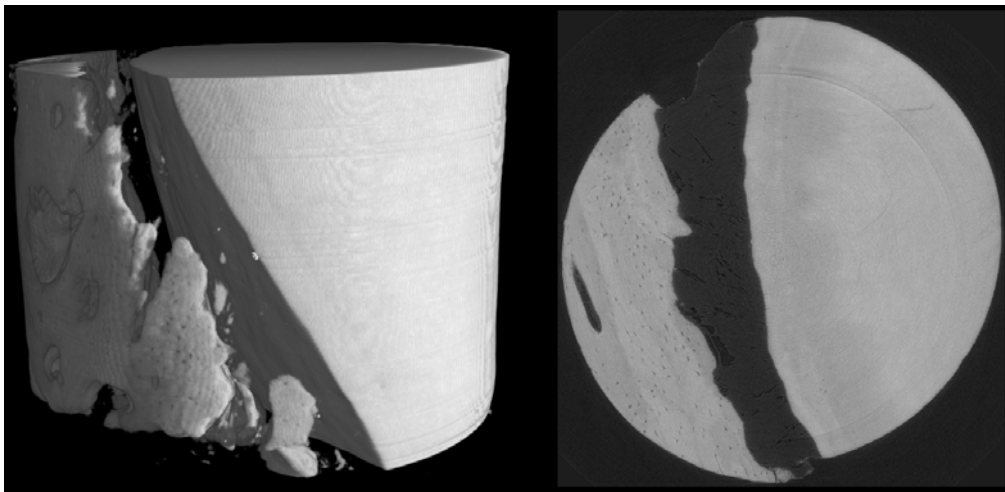


Figure 2: 3-D reconstruction of part of one of the smaller samples (left). Note the gap of the PDL running diagonally with the bone on the left side. On the right, a single slice from the 3D dataset is shown. Note the rough surface of the alveolar bone.

**Acknowledgments:** This work has been financially supported by the European Commission (IHP-contract I-20060192 EC), The Danish Research Council for Natural Sciences (DANSYNC program) and the Aarhus University Research Fund (E-2004-SUN-1-120).

## References

- [1] M. Dalstra, P.M. Cattaneo, F. Beckmann, M.T. Sakima, C. Lemor, M.G. Laursen, and B. Melsen, *Developments in X-Ray Tomography V*, 631804-1 (2006)
- [2] M. Dalstra, P.M. Cattaneo, and F. Beckmann, *Orthod. Craniofac. Res.* 9, 199 (2006)
- [3] M. Dalstra, P.M. Cattaneo, T. Donath, J. Herzen, and F. Beckmann, *HASYLAB Ann. Rep.*, 1305 (2006)



# Non-destructive Phase Analysis of Historical Objects of Art

H. Klein, C.E. Tommaseo, L. Raue<sup>1</sup>, M. Brandt<sup>2</sup> and T. Lippmann<sup>3</sup>

GZG, Dept. of Crystallography, Univ. of Göttingen, Goldschmidtstr.1, 37077 Göttingen, Germany

<sup>1</sup>Dept. Microstructure Physics & Metal Forming, Max Planck Institute for Iron Research GmbH, Max-Planck-Str.1, 40237 Düsseldorf, Germany

<sup>2</sup>Dom-Museum Hildesheim, Am Domhof 4, 31134 Hildesheim, Germany

<sup>3</sup>GKSS Research Center, Max-Planck-Str.1, 21502 Geesthacht, Germany

Often it is difficult to determine the date and place of origin of a historical object. Then it is helpful to know the materials composition, this can be a fingerprint in order to find an answer of the questions. Beyond it texture and microstructure investigations can help to deduce the production processes of the historical objects[1,2].

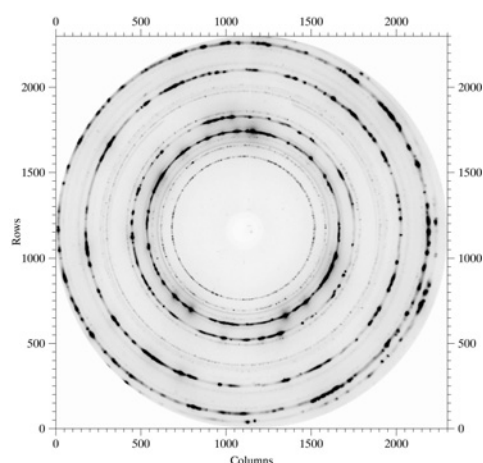
In the most cases such objects of art do not allow destructive analyses. X-ray experiments can perform non-destructive examinations of the phase composition of the materials. Quantitative phase analysis (Rietveld-method) allows to determine the base material and its impurities. But conventional X-ray analysis is – in this case – not the right tool. High-energy synchrotron radiation allows high penetration depth and an excellent angular resolution [1]. The experiments were performed end of November 2007 at the GKSS materials science beamline HARWI II at DESY, Hamburg, Germany. The beam energy was about 100keV and a mar345 detector was used to record the diffraction images.

Different objects of art (12<sup>th</sup> and 13<sup>th</sup> century) cast in bronze – using lost-wax bronze foundry - from the Dom-Museum of the cathedral of Hildesheim (Germany) were examined. Because of the short time the images were not analysed using the Rietveld-method, this will be done in the following weeks. Here, some examples of the examined objects and their related diffraction images are shown.

Figure 1a shows a crucifix which was fire gilded. The diffraction image shows beside the strong copper-alloy reflexions some characteristic lines of the contamination (Au, Pb, etc.) (fig. 1b). In figure 2a a lion candle holder cast in bronze is to be seen. In the diffraction image also large grains can be seen (fig. 2b). A large object of art is the knob of the baptistery of the cathedral of Hildesheim (12<sup>th</sup> century) (fig.3a). It is a good sample for the use of high-energy synchrotron radiation because of its size (approx. 40cm and 15 kg) and its high wall thickness. In the 2d-diffraction image (fig. 3b) we see large grains of the copper-alloy and reflections of the contaminations.



a)

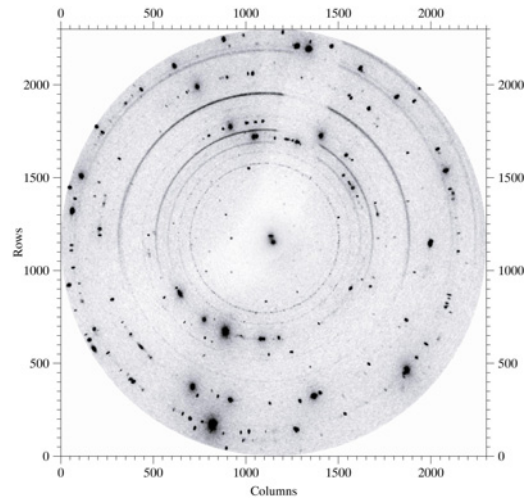


b)

Figure 1: Bronze crucifix and related diffraction image



a)

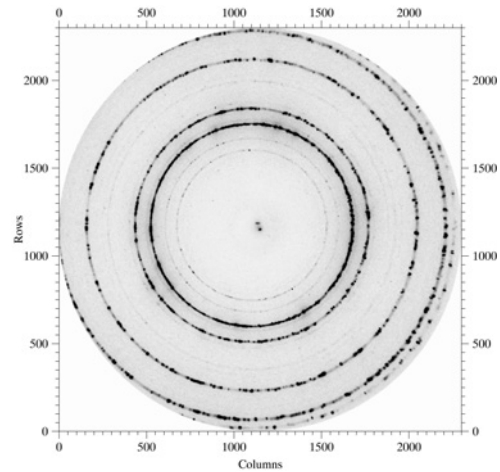


b)

Figure 2: Lion candle holder cast in bronze and the diffraction image



a)



b)

Figure 3: Cast bronze knob of the baptistry of the cathedral of Hildesheim

In order to examine historical objects of art the high-energy synchrotron radiation is an ideal tool to determine quantitatively the composition of phases and of the microstructure. Using more sophisticated methods – texture and grain size and grain shape measurements – one can follow the production process.

## References

- [1] H.J. Bunge, L. Wcislak, H. Klein, U. Garbe and J.R. Schneider, *Advanced Engin. Mater.*, 4, 300 (2002).
- [2] H.J. Bunge, H.Klein, L. Wcislak, U. Garbe, W. Weiß and J.R. Schneider, *Textures and Microstructures*, 35, 253 (2003).

# Synchrotron radiation micro computer tomography (SR $\mu$ CT) as high resolution technique to study skeletal deformations in medaka (*Oryzias latipes*)

Frank Neues,<sup>a</sup> Roland Goerlich,<sup>b</sup> Jörg Renn,<sup>c</sup> Felix Beckmann,<sup>d</sup> Matthias Eppe<sup>a</sup>

<sup>a</sup> Inorganic Chemistry, University of Duisburg-Essen, Universitaetsstrasse 5-7, 45117 Essen, Germany Fax: +49 201 183-2621; Tel: +49 201 183-2402; E-mail: matthias.eppe@uni-duisburg-essen.de

<sup>b</sup> Department of Molecular Biotechnology, RWTH University Aachen, Worringerweg 1, 52074 Aachen, Germany

<sup>c</sup> Department of Biological Sciences, National University of Singapore, 14 Science Drive 4, Singapore 117543, Singapore

<sup>d</sup> GKSS Research Center Geesthacht, Institute for Materials Research, c/o GKSS at DESY, Notkestrasse 85, 22607 Hamburg, Germany

Synchrotron radiation micro computer tomography (SR $\mu$ CT) offers the possibility to investigate biomineralized structures in high detail. Two animals of adult medaka fish (*Oryzias latipes*) were analyzed by SR $\mu$ CT: The wild-type animal was developed normally whereas the second animal showed an idiopathic deformation of the cranial and axial skeleton. These deformations could be followed in the macro- and on the microscale (i.e. on the level of the individual ribs and fin bones). Our study clearly demonstrates that SR $\mu$ CT is an excellent technique to study alterations in the skeletal structure of adult medaka in detail.

We used adult wild-type medaka of the Carbio (Carolina Biological Supplies) strain, obtained originally from the laboratory of Manfred Scharl (University of Wuerzburg, Germany) and kept as closed colony lines at the RWTH Aachen since several generations. Less than 1 % of the offspring shows non-lethal skeletal deformations. Possible explanations for these deformations are idiopathic mutations of hitherto unknown genetic background. However, we cannot exclude non-genetic factors as cause. For the present study, we used such an adult medaka and designate it as fish having idiopathic deformations. The animals were anesthetized and subsequently killed by CO<sub>2</sub> gas.

The sample (one whole fish each) was dehydrated in a graded ethanol row. The sample was subsequently placed for 30 min at 4 °C in solutions of 30 %, 50 %, 74 %, 90 %, 95 %, and 100 % (twice) aqueous ethanol. For embedding, the epoxide precursor was prepared by mixing 24 g Agar 100 epoxy resin (equivalent to Epon 12), 22 g DDSA (hardener), 6 g MNA (hardener) and 1.5 g BDMA (accelerator). This mixture was stored at -20 °C. The fish was subsequently placed into graded solutions of the epoxide precursor in ethanol (v/v): 60 min (4 °C) in 50 % (twice), 60 min (4 °C) in 80 %, 6 h (4 °C) in 80 %, 6 h (25 °C) in 100 %, and 2 d (60 °C) in 100 % for polymerization.

SR $\mu$ CT was carried out at beamline BW2 at HASYLAB/DESY (Hamburg, Germany). The synchrotron radiation was monochromatized to 19 keV. Projection images were recorded in steps of 0.25° from 0° to 180° of 13 or 10 (wild type or deformed animal, respectively) height segments, giving 13 or 10 discrete segments of the intact sample which were then electronically reassembled. The detector was a KX2 instrument (Apogee Instruments; 14-bit digitalization at 1.25 MHz, 1536·1024 pixel; each 9·9  $\mu\text{m}^2$ ). For normalization of the recorded data, flat field images of the beam were recorded every eight projections. Reconstruction was performed using a filtered backprojection algorithm. 3D renderings were created with the program VG Studio MAX 1.2. The voxel edge length after reconstruction was 6.55  $\mu\text{m}$ .

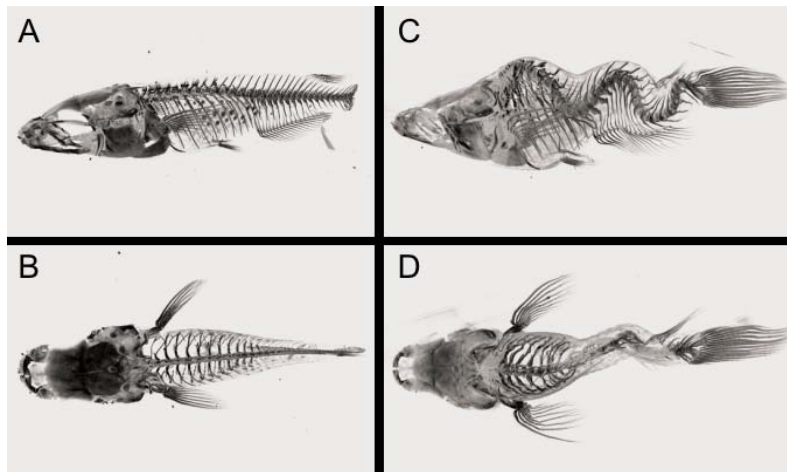


**Figure 1:** Representations of wild-type healthy (A, B) and deformed fish (C, D) in lateral (A, C) and dorsal view (B, D).

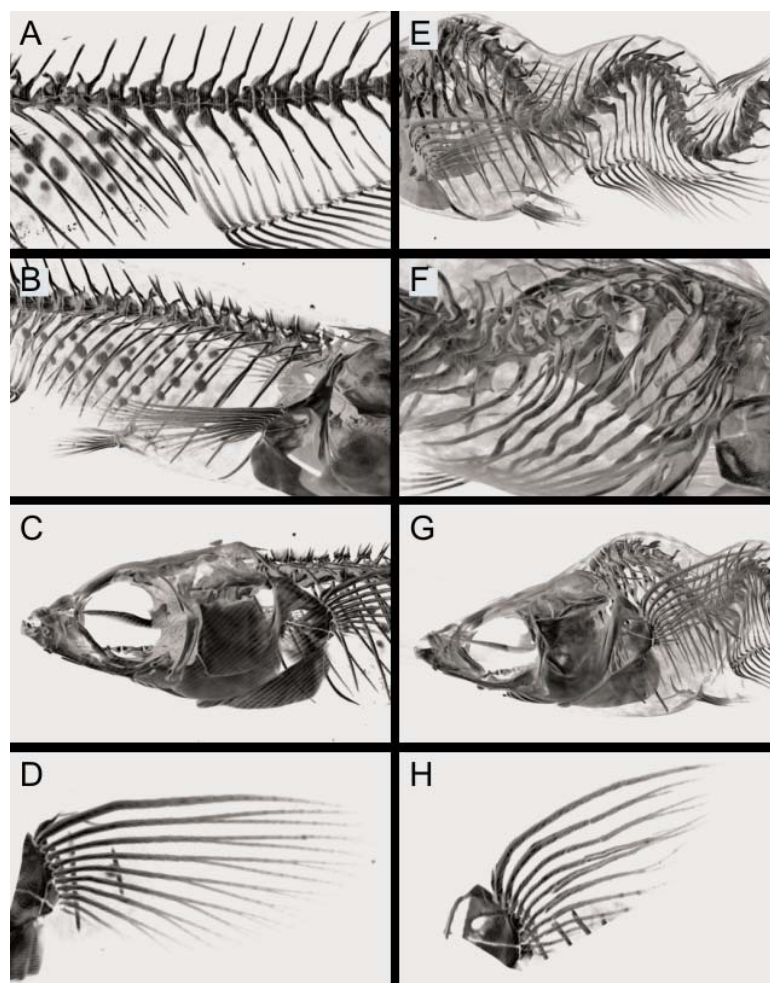


**Figure 2:** Magnified views of wild-type (A, B, C, D) and deformed (E, F, G, H) medaka (head pointing to the left, except for B and F). Shown are the vertebral column (A, D), the rib cage (B, E) and the pectoral fin (C, F).

## References

- [1] F. Neues, R. Goerlich, J. Renn, F. Beckmann, M. Epple, "Skeletal deformations in medaka (*Oryzias latipes*) visualized by synchrotron radiation micro-computer tomography (SR $\mu$ CT)", *Journal of Structural Biology* 160 (2007) 236-240.

# Self-Association of Maltoside and Melibioside Glycolipids

P. Garidel<sup>a</sup>, J. Howe<sup>b</sup>, G. Milkereit<sup>c</sup>, M. Rössle<sup>d</sup>, S. Linse<sup>e</sup>, S. Gerber<sup>e</sup>, R. Willumeit<sup>e</sup>, T. Gutschmann<sup>b</sup>,  
V. Vilf<sup>e</sup> and K. Brandenburg<sup>b,\*</sup>

<sup>a</sup>Martin-Luther-Universität Halle-Wittenberg, Institut für Physikalische Chemie, Mühlpforte 1, 06108 Halle/Saale

<sup>b</sup>Forschungszentrum Borstel, Leibniz-Zentrum für Medizin und Biowissenschaften, Parkallee 10, 23845 Borstel

<sup>c</sup>GKSS Forschungszentrum, Max-Planck-Straße, 21502 Geesthacht

<sup>d</sup>European Molecular Biology Laboratory, EMBL c/o DESY, Notkestr. 85, 22603 Hamburg

<sup>e</sup>Universität Hamburg, Institut für Organische Chemie, Martin-Luther-King-Platz 6, 20146 Hamburg

In the recent years, glycolipids with short-sugar chains have attracted much attention due to an astonishing number of biological functions of short-sugar-headgroup lipids [1]. Furthermore, glycolipids as amphiphilic molecules form thermotropic liquid crystalline phases in their pure state upon heating as well as lyotropic liquid crystalline phases in the presence of solvent (e.g. water). The driving force for this formation of different mesophases is an intermolecular “microphase” separation, which in the case of amphiphilic molecules leads to self-association according to the hydrophobic effect and the formation of an aggregate structure with separated regions for the hydrophobic and hydrophilic moieties, enabling the maintenance of van der Waals interactions in the hydrophobic region. This paper summarises the biophysical properties of two glyco glycerol lipids bearing maltose (wedge-shaped) and melibiose (tilted) disaccharide carbohydrate headgroups and an 1,3-dimyristyl-glycerol backbone (Figure 1). The biophysical properties are investigated and discussed in terms of their chemical structures. The thermotropic properties of these compounds and the aggregate structures in water were investigated by means of Fourier-transform infrared spectroscopy (FTIR), differential scanning calorimetry (DSC), film-balance measurements and small-angle X-ray scattering (SAXS) (see [2]).

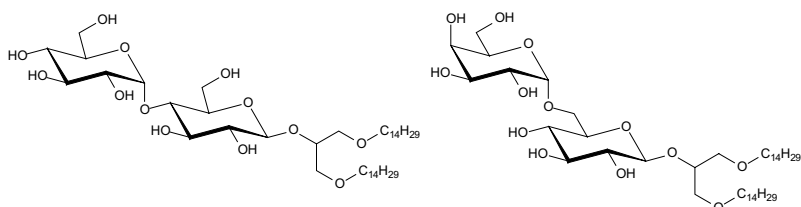


Figure 1. Chemical structures of the investigated glycolipids (**Left**) 1,3-Di-*O*-tetradecyl-2-*O*-[4'-*O*- $\alpha$ -D-glucopyranosyl]- $\beta$ -D-glucopyranosyl]-sn-glycerol (DMMA), (**Right**) 1,3-Di-*O*-tetradecyl-2-*O*-[6'-*O*- $\alpha$ -D-galactopyranosyl]- $\beta$ -D-glucopyranosyl]-sn-glycerol (DMME).

The lipids were synthesised and purified as described previously [2]. X-ray diffraction measurements were performed at the European Molecular Biology Laboratory (EMBL) outstation at the Hamburg synchrotron radiation facility HASYLAB using the SAXS camera X33. Differential scanning calorimetry (DSC) measurements were performed with VP-DSC and MC-2 calorimeter (MicroCal, Inc., Northampton, MA, USA) at a heating and cooling rate of 1 °C·min<sup>-1</sup>. The infrared spectroscopy measurements were performed on an IFS-55 spectrometer (Bruker, Karlsruhe, Germany) in transmission mode. Film balance measurements were performed on a film balance equipped with a Wilhelmy plate (Riegler-Kirstein, Mainz, Germany) with the help of a dipper device.

The gel to liquid crystalline phase transition temperature  $T_c$  (investigated by DSC and FTIR) of DMMA depended on the storage and hydration conditions (Figure 2, left), a precooled sample having a  $T_c$  around 45 °C, and a freshly prepared sample around 33 °C. In contrast, the phase transition temperature for the gel to liquid crystalline phase of DMME was always found at 25 °C (data not shown). This is confirmed by the infrared spectroscopic data. The compounds displayed thermotropic multilamellar phases (Figure 2, middle, right). In the gel phase, DMMA formed also a crystalline phase of orthorhombic symmetry, and DMME an interdigitated phase. Surface pressure isotherms of the lipids on water and buffer showed that DMMA covers only a small surface area (30 Å<sup>2</sup>) whereas DMME requires 50 Å<sup>2</sup> of space on the surface. Films of DMMA can be compressed up to a maximum compressibility  $\Pi_{max}$  of 54 mN·m<sup>-1</sup> whereas the tilted DMME forms less stable films with  $\Pi_{max}$  of 34 mN·m<sup>-1</sup>. These different structural characteristics reflect the different conformations of the disaccharide head groups. The presence of the  $\alpha 1 \rightarrow 4$  linked maltose head group in (DMMA) and an  $\alpha 1 \rightarrow 6$  linked melibiose head group in DMME induces geometrical structures ranging from a slightly wedge-shaped towards a more tilted structure, and as a consequence of Israelachvili's packing model, to the formation of different phases. In addition, the structural constraints of DMME allow the formation of a phase with interdigitated hydrocarbon chains (for more details see [2]).

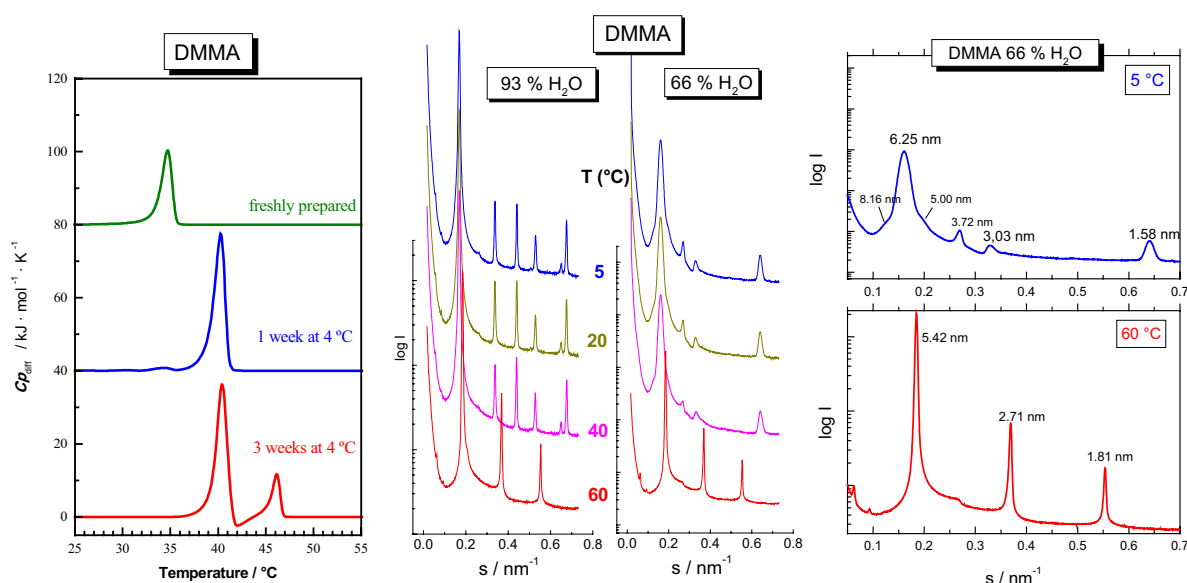


Figure 2. **(Left)** DSC first heating scans of DMMA after different storage times at 4 °C. The excess specific heat  $C_{p,diff}$  of the calorimetric sample cell as compared to the reference cell is plotted versus temperature.

Small-angle X-ray diffraction patterns of DMMA **(Middle)** at 93 % and 66 % water content in dependence on temperature. **(Right)** at 66 % water content and 5 (top) and 60 °C (bottom) (adapted from [2]).

## References

- [1] W. Curatolo, Biochim. Biophys. Acta 906, 137-160 (1987)
- [2] P. Garidel et al. Chem. Phys. Lipids, in press, doi:10.1016/j.chemphyslip.2007.09.004 (2007)